The Local Scouring Phenomenon at Bridge Abutments Terminating in the Floodplain Zone

Salah Kouchakzadeh

A Dissertation
Submitted to School of Graduate Studies
under the supervision of
Dr. R. D. Townsend

in partial fulfilment of the requirements
for the degree of
Doctor of Philosophy in Civil Engineering

Department of Civil Engineering
Faculty of Engineering
University of Ottawa
Ottawa, Canada K1N 6N5
December 1996

The Doctor of philosophy in Civil Engineering is a joint program between
Carleton University and the University of Ottawa, which is administered
by the Ottawa-Carleton Institute for Civil Engineering

National Library
of Canada

Acquisitions and
Bibliographic Services Branch

395 Wellington Street
Ottawa, Ontario
K1A 0N4

Bibliothèque nationale
du Canada

Direction des acquisitions et
des services bibliographiques

395, rue Wellington
Ottawa (Ontario)
K1A 0N4

Your file Votre référence

Our file Notre référence

ISBN 0-612-19978-9

ABSTRACT

This study examines the local scouring phenomenon associated with bridge abutments exposed to combined main-channel (MC) and floodplain (FP) flows. The principal goal of the study was to develop and validate, based on a comprehensive physical-model testing programme that considered different abutment shapes, an improved relationship for predicting maximum scour depth.

A relationship was established among sediment size, flow depth and longitudinal channel slope for initiating the *threshold* condition of bed material movement. This relationship facilitated the selection of sediment size and channel bed slope for the various experiments, which were performed in a compound channel under *interacting* (combined MC and FP flows) and *non-interacting* (isolated FP flow) conditions. *Clear-water* approach-flow conditions were utilized throughout the testing programme. A flow visualization technique was employed to study the various patterns of the combining flows in the MC/FP junction regions. It determined both the flow deflection angle and the extent of the influence zone (a portion of the channel width beyond the abutment) whose discharge, Q_w, contributes to the scour development.

Maximum scour depths produced under *interacting* conditions were observed to be 15% to 30% greater than those observed for *non-interacting* conditions. This important observation clearly demonstrated the need to properly account for *compound-channel* effects in the simulation exercise.

The scour prediction relationship presented herein is based on a dimensional analysis of the relevant parameters and incorporates the data obtained from the laboratory studies performed in a compound channel using *vertical-wall*, *wing-wall*, *semi-circular*, and *spill-through* abutment shapes. The model indicates a very good agreement between predicted and observed maximum scour depths for bridge abutments terminating in the FP zone.

In the name of God

ACKNOWLEDGEMENTS

The author wishes to express his sincere appreciation to his supervisor, Dr. R.D. Townsend, for his guidance, advice, and encouragements during the course of this research.

The scholarship provided by the Ministry of Culture and Higher Education of the I.R. of Iran is gratefully acknowledged.

Particular thanks are due to my brother, Mozaffar, for all his support especially for developing the data acquisition system. The test section for this research program was prepared at the workshop of the Civil Engineering Department. I am grateful to the workshop staff, Mr. C. Lavigne and Mr. B. Cotter, who were responsible for the preparation of the test section.

I would like to express my special thanks to my wife, Nahleh, and children, Amir, Mahmoud, and Yasir for their patience and continuous support throughout this work.

TABLE OF CONTENTS

CHAPTER ONE

CHAPTER TWO

CHAPTER THREE

CHAPTER FOUR

CHAPTER FIVE

CHAPTER SIX

CHAPTER SEVEN

LIST OF SYMBOLS

a = constant coefficient
A = numerical constant
A = the channel cross-sectional area
A$''$ = sediment coefficient
A$'$ = sediment coefficient
A_a = flow area of an approach cross-section which is obstructed by a roadway embankment.
b = pier diameter
b = constant coefficient
B = channel width
B = numerical constant
c = cohesiveness
C = constant coefficient
C_D = drag coefficient
C_L = lift coefficient
D = particle diameter
$\overline{D}$ = the average diameter of grains
D_{50} = median grain diameter
D_s= effective grain size or roughness element
D_v = vortex diameter
F_* = dimensionless shear stress
F_a = Froude number in the floodplain upstream of the end of the abutment
F_n = force acting normal to the bed slope
F_t = force acting parallel to the slope
g = acceleration due to gravity
H = total flow depth in the main channel
K = numerical constants
$K_{\alpha L}$ = a coefficient accounts for the effects of the flow angle of attack on the local scour depth at rectangular bridge piers

k_1, k_2, k_3 = particle shape factors
K_D = sediment size factor
K_G = approach channel geometry factor
K_I = flow intensity factor
K_L = abutment length factor
K_θ = abutment alignment factor
K_s = abutment shape factor
K_σ = sediment gradation factor
K_y = flow depth factor
l = Prandtl's mixing length
L = abutment length
L' = projected length of abutment normal to the flow
L^* = width of the flood channel
L_e = equivalent length of the abutment
M = discharge contraction ratio
n = Manning roughness coefficient of the main channel
n_a = Manning roughness coefficients of the floodplain
N = numerical constant
P = wetted perimeter
Q = total approach discharge
Q_a = flow intercepted by the abutment and diverted towards the main channel
Q_o = that portion of the flow in the approach section with a width equal to the opening width
$(Q_s)_I$ = rate of sediment going into the scour hole
$(Q_s)_o$ = rate of sediment going out of the scour hole
Q_w = discharge moving in a specific width of the channel, w, in a streamwise direction
r = numerical constant
R = hydraulic radius
R_{*e} = sediment Reynolds number
t = time
t_e = required period to reach the equilibrium scour depth
u_* = shear velocity
u_{*c} = critical shear velocity

u_b = flow velocity at the bottom of the channel
u_{bc} = critical flow velocity at the bottom of the channel
U_a = depth averaged flow velocity at the abutment end
U_o = approach mean velocity of the undisturbed flow
V = volume of scour hole
w = effective width
W = submerged particle weight
y_a = flow depth in the floodplain
y_o = approach uniform flow depth
y_s = scour depth at time t
y_{se} = equilibrium scour depth
y_w = average depth of flow in the width w
α_o = opening ratio
α = flow angle of attack for rectangular bridge piers
β = flow deflection angle
θ = angle of the abutment alignment ($\theta < 90°$ if it points downstream)
κ = Von Karman's universal constant
ρ = density of water
ρ_s = density of bed material
$\sigma_g = \sqrt{D_{84}/D_{16}}$ = geometric standard deviation of the bed material
τ_o = bed shear stress
τ_c = critical shear stress
τ' = intensity of shear at boundary associated with sediment particle
ν = kinematic viscosity of the fluid
ψ = particle shape factor
φ = angle of repose of bed material
ω = particle fall velocity

LIST OF ABBREVIATIONS

A/D = analogue to digital conversion
AI = analogue indicator
Al = abutment alignment factor
DI = differential input mode
FP = floodplain
FS = factor of safety
G = cross-sectional geometry and flow distribution factor
GID = ground isolating device
I/O = input output transfer
LMT = lateral momentum transfer
MC = main channel
PCVC = precision current to voltage current
PDI = pseudo-differential input mode
SC = semi-circular
SE = single-ended input mode
Sh = abutment shape factor
ST = spill-through
VW = vertical-wall
WW = wing-wall

LIST OF FIGURES

Figure page

Figure page

Figure page

Figure page

Figure page

Figure page

Plate **page**

LIST OF PLATES

LIST OF TABLES

CHAPTER ONE

INTRODUCTION

1.1- STATEMENT OF PROBLEM

The massive piers and short spans of old arch bridges resulted in extreme contractions of the flow section and, consequently, severe scour of the channel bed. However, improved construction methods and materials, and advanced techniques of analysis and design helped engineers construct bridges having relatively small piers and long spans. Yet, the list of the failed bridges due to excessive scour around piers and abutments continues to lengthen.

Since the early times of bridge construction, scour of the streambed remains the major cause of bridge failure (Laursen and Toch, 1956). After an extensive study of the potential for bridge failures, the state of New York classified *hydraulic* (scour, ice, debris) as the first mode of the most significant failure modes for bridges within the state (Shirole and Holt, 1991). The data of New York State's bridge failures database are summarized in Table 1.1. The Table shows bridge failures according to the failure modes recorded in the U.S. and in the state of New York since 1950 and indicates that about 60 % of the bridge failures were attributed to scour and other related hydraulic conditions.

In an extensive study of bridge failure in the United States, Brice and Blodgett (1978) reported that damage to bridges and highways from major regional floods in 1964 and 1972 amounted to about $100,000,000 per event. Of the 108 major bridge failures recorded in New Zealand during the period 1960-1984, 29 were attributed to abutment scour (Melville, 1992). Kandasamy and Melville (1989) found that six of 10 bridge failures that occurred in New Zealand during Cyclone Bola were related to abutment or approach scour. A survey of roading expenditure in New Zealand as the result of damage due to scour showed that about 50% of total expenditure was for bridges, and of this abutments and approaches comprised more than 70% (Melville, 1992).

Table 1.1- Summary of the bridge failure survey in the U.S. (Shirole and Holt, 1991)

Failure modes	Number of failures due to failure mode	
	U.S. bridge failures	New York bridge failures
Hydraulics	494	43
Collision	108	16
Overloads	84	21
Nature	24	3
Miscellaneous	39	9
Fire	24	1
Deterioration	36	15
Earthquake	14	0
Total identified failures (since 1950)	823	108

Scouring of the bridge foundations is the most common cause of flood damage to bridges. During the Spring floods of 1987, 17 bridges in New York and New England were damaged or destroyed by scour. In 1985, 73 bridges were destroyed by floods in Pennsylvania, Virginia, and West Virginia. A 1973 national study for the FHWA (Federal Highway Administration) of 383 bridge failures caused by catastrophic floods showed that 25% involved pier damage and 72% involved abutment damage. A second more extensive study done in 1978 indicated local scour at bridge piers to be a problem about equal to abutment scour problems (Richardson et al., 1991a).

During the last five decades, researchers have proposed more than 35 formulae for local scour prediction at bridge piers. Comparison between field data and the results of prediction equations have been the subject of study of many researchers in order to select an appropriate equation for a specific site. However, only a few equations have been proposed to predict local scour near bridge abutments (Copp et al., 1988). Scouring at abutments bear similarity to scouring around spur-dikes and most of the recent information about abutments comes from studies that have been performed at the University of Auckland (Breusers and Raudkivi, 1991). However, the way the experiments were conducted does not represent many of the conditions typically encountered in the field.

Most equations for predicting local scour at abutments are based on laboratory data compiled using abutments projecting into a stream having uniform flow velocity distribution and flow depth upstream of the abutment. In other words, the *laboratory* situation simulates abutments sitting in the main channel (MC) of watercourse rather than in the floodplain (FP). In the *field* situation, however, due to vegetative cover and the elevated terrain, lower flow velocities and shallower flow depths exist in the FP where bridge abutments are usually located. Because of the methods by which laboratory-scale experiments were conducted, the traditional abutment scour equations only predict the maximum scour that could occur. Therefore, using present abutment scour equations, a designer usually obtains excessively conservative estimates of maximum scour depth even for situations that might have little or no scour depths (Richardson and Richardson, 1993b).

The usual configurations for bridge abutments include: wing-wall (WW), vertical-wall (VW), spill-through (ST), and semi-circular (SC) abutments. Figures 1.1 to 1.4 show different views of these abutment shapes. Bridge abutments might terminate in the FP or can encroach on the MC of a watercourse. Also, they can be set perpendicular to or at an angle to the flow. Scour at abutments can be either *live-bed* or *clear-water* scour. Finally, there can be varying amounts of *overbank* flows that are intercepted by the approaches to the bridge and returned to the stream at the abutment. All of these factors affect the magnitude of scour depth at bridge abutments (Richardson et al., 1991b).

Table 1.2- Summary of abutment scour cases (Richardson et al., 1991b)

Case	Abutment location	Overbank flow	$(L/y_o)^*$	Bedload	Abutment type
1	project into channel	No	<25	Live bed clear water	VW or ST
2	project into channel	Yes	<25	Live bed clear water	VW or ST
3	set back from MC	Yes	<25	Clear water	VW or ST
4	relief bridge on FP	Yes	<25	Clear water	VW or ST
5	at edge of MC	Yes	<25	Live bed	VW or ST
6	not designated	Yes	>25	Not designated	ST
7	skewed to stream	—	—	—	—

* The ratio of abutment length to flow depth

Scour at abutments can be divided into seven cases which are given in Table 1.2 and illustrated in Figure 1.5. Laursen (1980) has developed equations for these cases. However, as yet none of his equations has been verified in the field. Many abutment scour prediction equations, among them Laursen's (1962a, 1980), Liu et al.'s (1961), Froehlich's (1989), and Melville's (1992), are presented in chapter two.

Present scour equations estimate excessive abutment scour when they are applied to field situations. This is because these equations were based on *physical model* studies that did not correctly represent field conditions. Most existing laboratory data were obtained by installing a defined-length abutment in a shallow-flow flume having a rectangular cross section and a flat sand bed. The uniformities of both the flow depth and the lateral velocity distribution across the laboratory flume are the main characteristics of the *approach flows* of these studies (Figure 1.6).

On a real FP, because of the variations in roughness, the velocity profile is not uniformly distributed (Figure 1.7). In the field case the returning flow produces less turbulence and vortices at the end of the abutment because the overbank flow may return to the MC in a less-concentrated manner upstream of the abutment. Temporary storage in the overbank attenuates the passing flood hydrograph as it moves through a bridge crossing reach. This also tends to reduce the magnitude of returning overbank flow and, subsequently, the severity of abutment scour. The overbank-flow portion, which is redirected to the MC, cannot be directly related to the abutment length, *L*, that projects into the flow. These characteristics of actual floods have not been properly represented by laboratory models.

So far, the following conditions have generally prevailed in laboratory studies of abutment scour:

- the abutment length, *L*, determines the magnitude of the overbank flow that is forced back into the channel at the abutment;
- there is an essentially uniform velocity distribution across the fume; and

- flumes of constant cross-sectional area and shape (rectangular) are used.

A careful inspection of the conditions under which past laboratory studies were conducted points to the significant differences between those laboratory-scale scour studies and actual field conditions. Hence, traditional predictive abutment scour equations are flawed because they are based exclusively on the available laboratory studies. In the field, because little relation exists between the abutment length and overbank flows, applying traditional scour prediction equations generally results in gross over-estimation of abutment scour (Richardson and Richardson, 1993a). Therefore, for field situations, flawed equations will be obtained if the abutment length is used in the formulation. The discharge ratio Q_w/Q_a, however, is a significant variable to determine scour depth because when two flows at different velocities (angle and magnitude) intersect, turbulence, shear, and vortices are generated which scour the bed. Q_a is the returning overbank flow in the vicinity of the abutment end and Q_w is the discharge moving in a specific width of the flume, w, in a streamwise direction through the bridge opening adjacent to the bridge.

1.2- SCOPE OF RESEARCH

One of the most urgent needs for predicting abutment scour depth is to properly simulate field conditions in the laboratory studies. Abutment scour depends on the interaction of the flow obstructed by the abutment and the flow in the channel adjacent to the abutment. In order to develop a reliable abutment scour prediction equation, variables which directly contribute to local scour must be incorporated. It is suggested that the flow ratio Q_w/Q_a, be incorporated in the abutment scour equation. Also, the Froude number should be incorporated in the abutment scour formulation because it describes the main flow characteristics relating to the process.

This study experimentally investigates the local scouring process at the ends of bridge abutments terminating in the FP of a compound channel having a trapezoidal MC. Unlike all previous physical modelling studies on this topic, this study was performed in a compound-shaped laboratory channel in order to investigate the impact on local scouring of the important *main channel/floodplain* (MC/FP) interaction process (as recommended in Richardson and Richardson, 1993a). The main objective of the study was to develop an improved relationship for predicting maximum local scour depth at bridge abutments based on a more realistic simulation of conditions normally encountered in the field.

1.3- OUTLINE OF THESIS

Chapter two of the thesis deal with contributions and advancements relating to the field of local scour at bridge sites. In cases where information on bridge abutment scour were missing, special attention was paid to aspects of bridge pier scour that bear similarity to that of bridge abutments. The mechanics of local scour at bridge piers and abutments and the influence of factors governing local scour are covered. Abutment scour depth prediction formulae are also included. Since the present study deals with certain aspects of compound channel flows, relevant materials regarding the flow interaction phenomena (between the MC and the FP zones) are reviewed in the last section of chapter two.

The theoretical basis describing the threshold condition of particle movement is covered in the first section of chapter three. The second section reviews the universal velocity distribution law and describes the method by which the equivalent sand roughness can be evaluated. The third section of chapter three deals with the dimensional analysis related to the scour phenomena considered in the study.

Chapter four describes the experimental apparatus used and the data acquisition system specifically designed for this study. The original compound flume and the modified test section required for this study, the pump, flow and scour depth measurement devices, and velocity measurement devices are described in the first part of this chapter. The second part deals with the procedures followed to design and test a data acquisition system for velocity measurements.

Experimental set-up and other conditions govern the selection of experimental parameters, such as: longitudinal channel bed slope, discharge range, required flow depth in the FP, and model bridge abutment length. Governing conditions were thoroughly investigated by a series of preliminary tests so as to select the most appropriate channel-bed material and other important parameters for the main tests. The results of these preliminary tests led to the selection of proper bed material size, channel longitudinal slopes, required FP flow depths, model bridge abutment lengths, and the discharge range to generate the required near-normal flow depth. In addition to the results of the preliminary tests, the methods by which the governing condition were investigated are presented in chapter five.

Chapter six deals with the analysis of the data. In the first section of this chapter the flow data are analysed to determine the shear velocity distribution in the FP for interacting and non-interacting flow conditions. The flow deflection angle and the effective width that contribute in the discharge ratio were examined; the discharge ratio for the interacting flow conditions were then determined. The analysis of the scour data is presented in the second section of chapter six. The variations in scour depth with influencing parameters are examined and the relationships between relative scour depth and discharge ratio are presented. In this section the scour data are also compared with the results of previous scour prediction formulae. The third section deals with the scour data for non-interacting flow conditions; the scour depth for interacting and non-interacting flow conditions are compared in this section. The proposed scour prediction model for abutments located and terminating in the FP is presented in the last section of chapter six. The summary and conclusions are given in chapter seven.

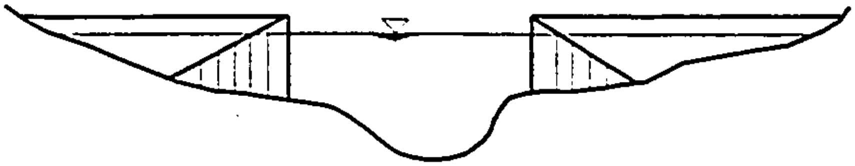

Elevation

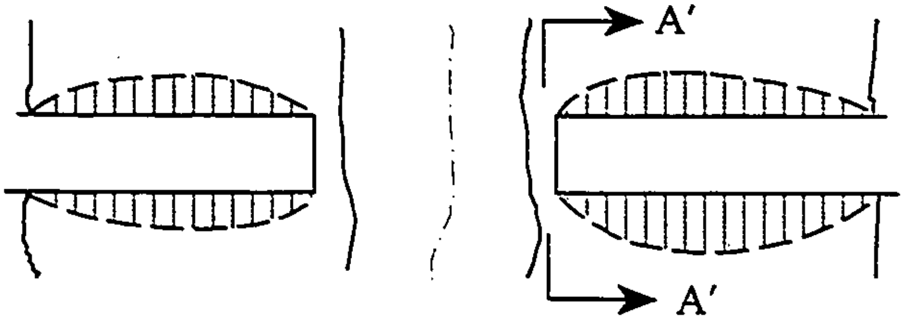

Plan

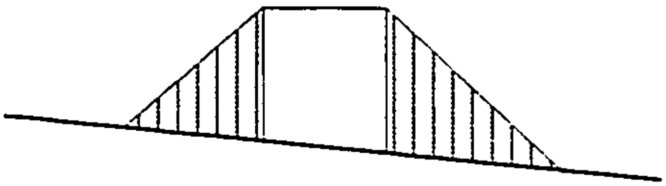

Section A-A′

Figure 1.1- Wing-wall abutment

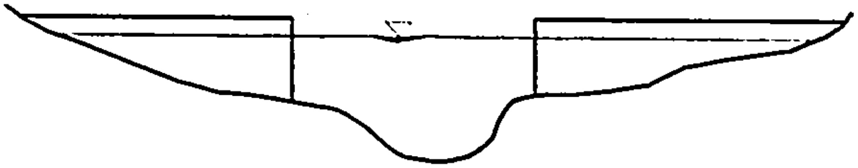

Elevation

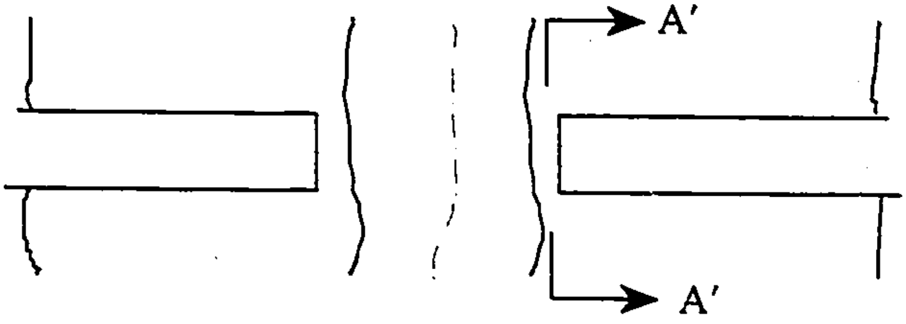

Plan

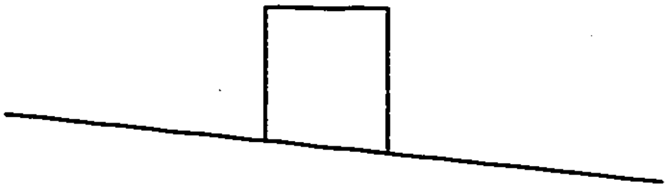

Section A-A′

Figure 1.2- Vertical-wall abutment

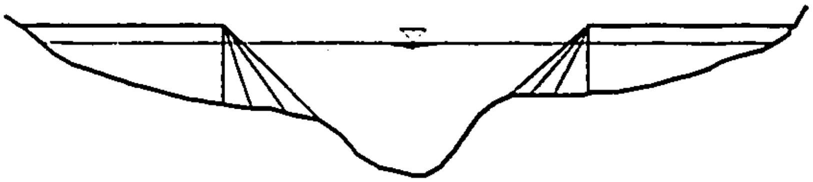

Elevation

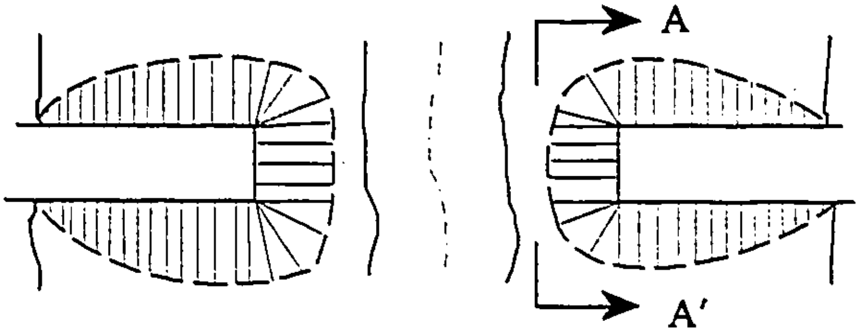

Plan

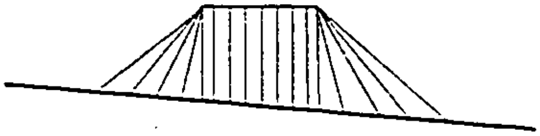

Section A-A'

Figure 1.3- Spill-through abutment

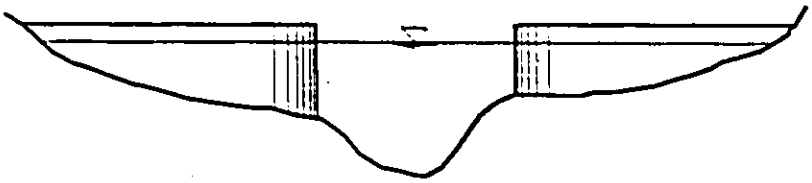

Elevation

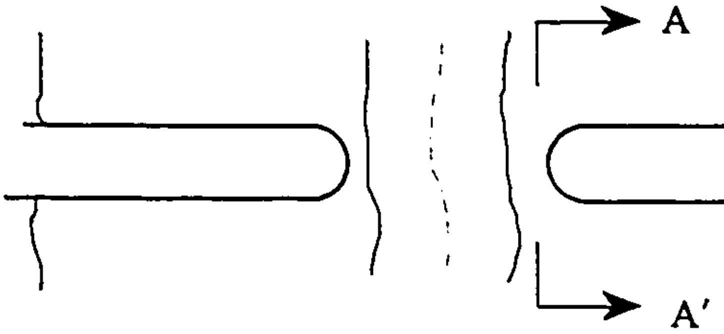

Plan

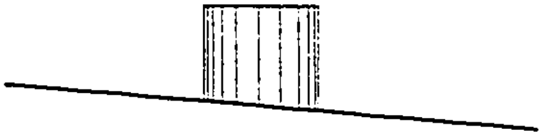

Section A-A'

Figure 1.4- Semi-circular abutment

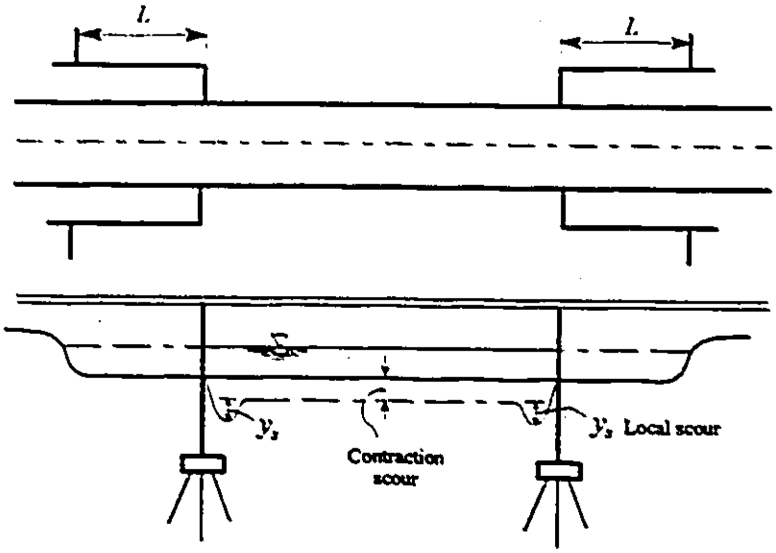

Case 1: Abutments project into channel, no overbank flow

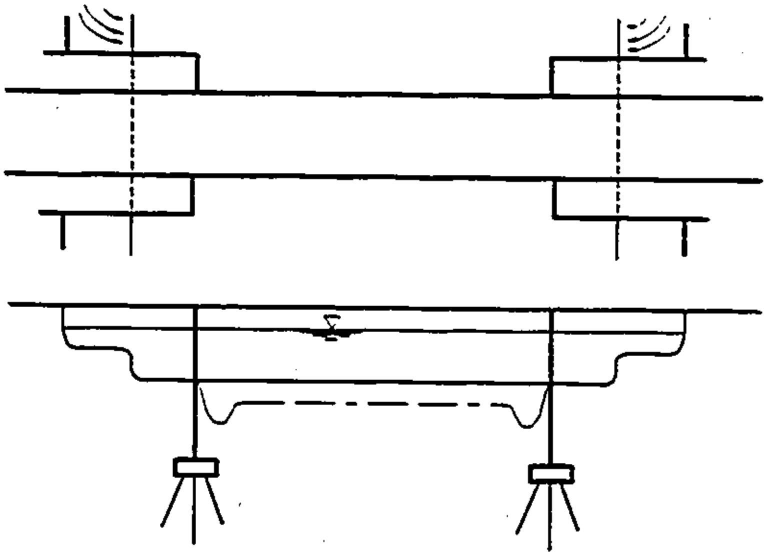

Case 2: Abutments project into channel, overbank flow

Figure 1.5- Abutment cases

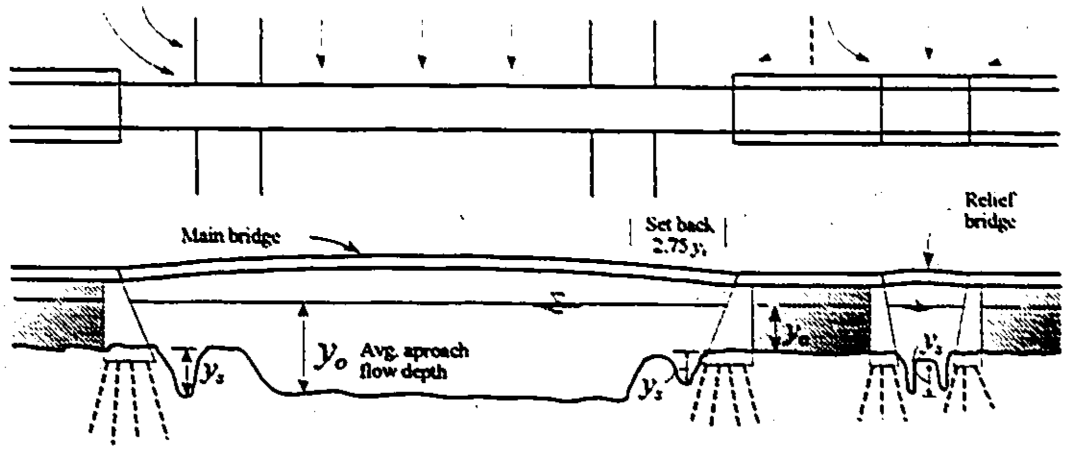

Case 3: Abutments setback from the channel more than 2.75 y_s
Case 4: Relief bridge

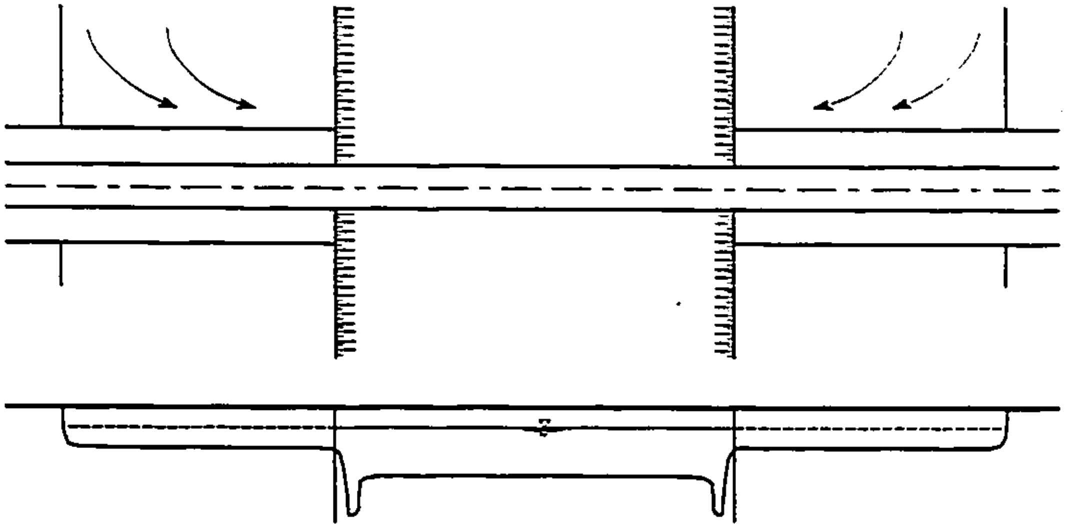

Case 5: Abutments set at edge of channel, overbank flow

Figure 1.5- Abutment cases (Cont'd)

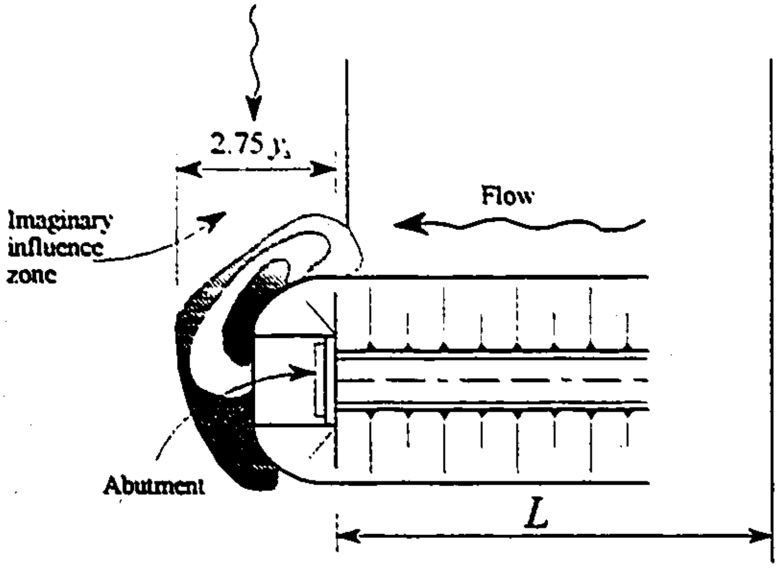

Case 6: Ratio of $Ly_o > 25$

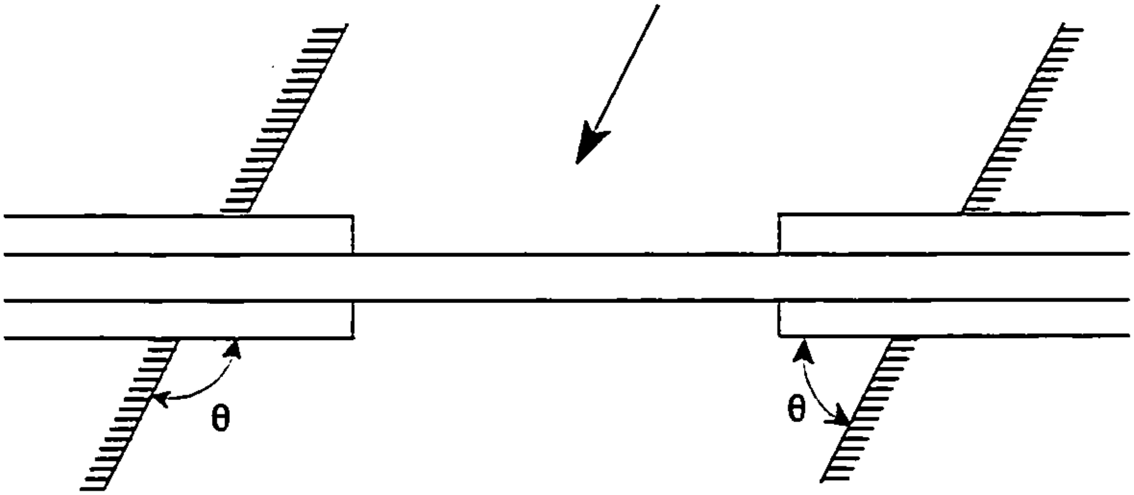

Case 7: Abutments set at an angle θ to the flow

Figure 1.5- Abutment cases (Cont'd)

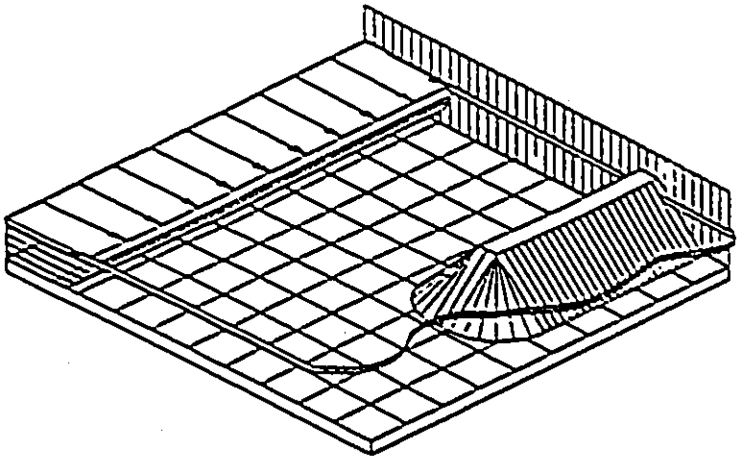

Figure 1.6- Typical laboratory condition for abutment scour tests (Richardson and Richardson, 1993a)

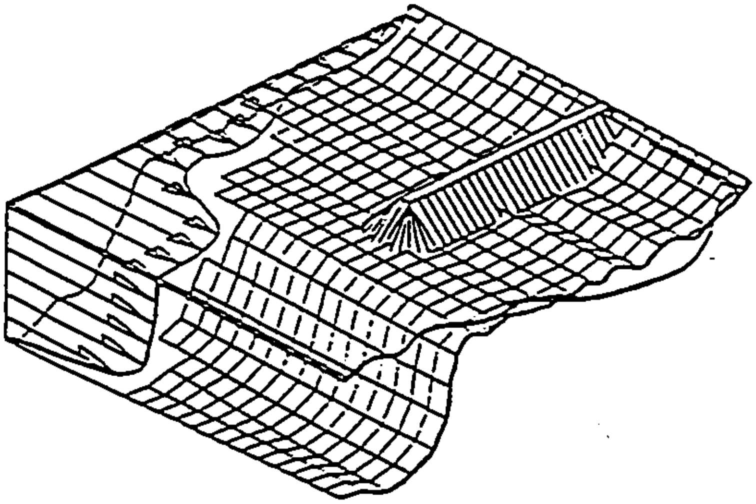

Figure 1.7- Typical field condition (Richardson and Richardson, 1993a)

CHAPTER TWO

LITERATURE REVIEW

2.1- INTRODUCTION

Scouring around spur-dikes (bank protection structures in river engineering) has been studied since the early 1950's (Ahmad, 1953). The scour process around a bridge abutment bears similarity to that of spur-dikes, hence, scouring formulae were interchangeably used in both cases. During the last decade the failure of many bridges in the United States and other parts of the world because of scouring problems motivated researches into the causes of bridge failures. Since very limited data relating to bridge abutment scour were available, the subject has been given priority since the early 1980's (Wong, 1982) and many research programs on this particular topic were initiated.

However, almost all such research has been performed in flumes having *rectangular* cross sections. This general arrangements simulates an abutment set in the MC of a watercourse (Ahmad, 1953; Garde et al., 1961; Gill, 1972; Cunha, 1975; Rajaratnam and Nwachukwu, 1983a, 1983b; Zaghloul, 1983; Kwan, 1984, 1988; and Kandasamy, 1985, 1989). In practice, bridge abutments are usually set in the FP of a river and most often terminate there, i.e. they are usually not long enough to encroach on the MC. Extensive literature has been published on the local scour associated with bridge piers and to a lesser extent with bridge abutments. Yet, there is a lack of studies on bridge abutment scour that properly simulate the field situation, i.e. bridge abutments set and terminating in the FP zone.

The advancements put forward in the field of the local scour at bridge sites are reviewed in this chapter. In cases where information on bridge abutment scour were missing, special attention was paid to aspects of bridge pier scour that bear similarity to that of bridge abutment. The mechanics of local scour at bridge piers and abutments and the influence of governing factors on the local scour are covered in the following sections. Abutment scour depth prediction formulae are also included. Since the present study deals with certain aspects of compound channel flows, relevant materials regarding the flow interaction phenomena (between the MC and the FP zones) are reviewed in the last section of this chapter.

2.2- MECHANISMS OF LOCAL SCOUR AT BRIDGE SITES

In general, the local scour depth around an abutment is a function of many parameters, which may include: fluid properties, flow conditions, sediment characteristics, abutment and channel geometry, and time. Since most of the relevant parameters are inter-related, the influence of a specific parameter on the scour depth might be eclipsed by other ones.

2.2.1- Scour types

Three types of scour, called *general scour*, *constriction scour* and *local scour* might be observed in a watercourse (Simons and Senturk, 1992; Raudkivi, 1984). *General scour* is a natural process and occurs in a stream irrespective of the presence of man-made hydraulic structures, however, it might strongly be affected by these structures. In other words, the rate of the natural process of long-term aggradation or degradation might be dramatically changed when a structure is introduced in a stream (Simons and Senturk, 1992).

Contraction scour, on the other hand, is brought about by accelerated flow due to a natural or man-induced contraction in a watercourse. This kind of scour involves bed material movement from across all or most of the channel width. Finally, *local scour* might be defined as the abrupt decrease in the bed elevation due to a sharp change in the flow pattern originated by a structural element.

The sum of the *general scour*, *constriction scour*, and *local scour* equals the *total scour*. Among the mentioned scour types, the *local scour* depth is generally 5 to 10 times greater than the depth of other types of scour. Long-term bed elevation changes ,however, might exceed the other two scour components when major changes (such as dams) are induced in stream conditions (Simons and Senturk, 1992).

2.2.2- Local scour classification

Introducing a bridge abutment, or any other kind of flow obstructing structure into a watercourse, dramatically changes the flow pattern of the stream in the vicinity of the structure. Highly three-dimensional and rotational in nature, the generated flow structure locally increases the bed shear stress to a value higher than the critical one and initiates the scour process. The temporal development of the scour hole can be expressed as:

$$\frac{dV}{dt} = (Q_s)_o - (Q_s)_i \tag{2.1}$$

in which V = volume of scour hole, t = time, and $(Q_s)_o$ and $(Q_s)_i$ are respectively the volumetric rate of sediment going out of and coming into the scour hole.

According to the conditions of bed material movement, the local scour process is generally classified as *clear-water* scour or *live-bed* scour (Laursen, 1952; Raudkivi and Sutherland, 1981). When the approach flow velocity of a stream does not exceed a critical value, above which bed particles move, no general bed material movement is observed. In such flow conditions $(Q_s)_i = 0$ and no bed material enters the scour hole, therefore, the local scour process is classified as *clear-water* scour.

Live-bed scour, however, occurs in streams having general bed movement. In this case, the bed shear stress is higher than the critical value at every point of the streambed. Therefore, the removed particles from the scour hole are replenished by the moving bed materials, i.e. $(Q_s)_o \geq (Q_s)_i > 0$. Since no such replacement for the removed material takes place in a *clear-water* condition, the scour hole is generally deeper in *clear-water* conditions than in *live-bed* conditions. Accordingly, the *clear-water* scour depth is recommended for design purposes (Melville, 1992; Melville and Sutherland, 1988)

2.2.3- Flow field around bridge piers and abutments

During the last three decades the flow field and the scouring mechanisms around a circular bridge pier have been studied extensively by many researchers (Shen et al., 1966; Melville, 1975; Ettema, 1980; Dargahi, 1987). Different experimental setups and bed configurations were used in these studies. On the other hand, only a few studies have investigated the flow field in the vicinity of bridge abutments. Nevertheless, some researchers postulated that the scouring mechanisms at abutments, to some extent, might be considered analogous to those associated with pier scour (Kandasamy, 1985). Consequently, a review of the main conclusions of the previous pier scour studies will facilitate a better understanding of the complex flow field around bridge abutments as well.

Based on the results of previous studies, Breusers and Raudkivi (1991) separated the flow pattern around a bridge pier into four components, namely: the *downflow* in front of the pier, the *horseshoe vortex*, the *cast-off* vortices and the *wake*, and *bow* waves. Figure 2.1 shows these characteristic components around a cylindrical bridge pier.

Similar to the bridge pier case, dividing the bridge abutment flow field into its main components makes it easier to recognize the main scouring agents of this complex flow field.(Kwan, 1984, 1988; Wong, 1982; Tey, 1984; Kandasamy, 1985). Kwan (1988) summarized the main components as: downflow, primary vortex, secondary vortex, and wake vortices. Figure 2.2 shows the flow structure at a semi-circular ended bridge abutment.

2.2.3.1- Downflow feature

Acting like a vertical jet, the downflow erodes a hole in front of a bridge pier (Figure 2.1). In a stream, the velocity distribution in the vertical direction (depth) is not uniform (Figure 2.1); it decreases from the surface downwards. Coming to rest at the front of the pier, a fluid particle at any elevation produces a stagnation pressure which is bigger than that generated at a lower elevation. Thus a downwards pressure gradient occurs which initiates a downflow velocity in front of the pier. When a scour hole develops, the maximum downflow velocity at any depth occurs at $0.02b$ to$0.05b$ (b= pier diameter) upstream of the pier and the maximum of the downflow strength occurs just below the bed level (Figure 2.3), (Ettema, 1980). Within the scour hole, the maximum downflow velocity might reach values as high as 0.8 times the mean approach velocity at one diameter below the original bed level and under the action of the horseshoe vortex may also move closer to the pier at lower elevations (Raudkivi, 1986).

Although all components of the flow field contribute in the development of the scour hole, Chiew (1984) considered the downflow component to be the main cause of local scour around bridge piers. Earlier studies assumed scour initiation right at the *stagnation plane*. Later studies, however, indicated different points at which the scour hole is initiated. Studying the *clear-water* local scour around a bridge pier, Nakagawa and Suzuki (1975) separated the scour process into four stages and attributed the scour near the side of the pier to the first stage. They observed that the maximum scour started near the side of the pier at the early stage of the scour process and moved towards the stagnation plane at the upstream face thenceforth. Melville's (1975) studies, however, showed initiation of scour at 100°. Aside from the issue of the starting point of scour, the *equilibrium* scour depth at a cylindrical pier occurs at the *stagnation plane*.

The factor responsible for the downflow at bridge piers also accounts for the downflow at bridge abutments. Within the scour hole but close to the bed the downflow at bridge abutment joins the primary vortex and becomes a part of it (Figure 2.4). Since published data of the downflow velocity at abutments are scarce, the magnitude of the maximum downflow can not be determined precisely. Although Kwan (1988) believes in similarity between the downflow velocity profile at piers and abutments, he measured different downflow velocities at a wing-wall abutment for different flow depths. Kwan (1988) found that the maximum downflow velocities were 0.75 U_o and 0.6 U_o (U_o=average flow velocity) at flow depths of 0.15 m and 0.075 m respectively. The results, however, are not conclusive; velocity measurements at different flow depths for different abutment shapes need to be made in order to draw a general conclusion.

2.2.3.2- Horseshoe vortices

In the case of a bridge pier, the *downflow* starts excavating the scour hole and, as the result of flow separation at the rim of the excavated hole, the *horseshoe* vortex develops. In other words, although it is important in the sense of transporting material away from the scour hole, the *horseshoe* vortex should be considered the consequence of the scour hole and not the cause of it (Breusers and Raudkivi, 1991). Passing the sides of the pier, the *horseshoe* vortex extends downstream for a few pier diameters, then it loses its identity and becomes a part of general turbulence thereafter. Hence, the *downflow* and the *horseshoe* vortex are the dominant scouring mechanisms and hence they are primarily responsible for the development of the scour hole.

In the case of a bridge abutment, the so-called *primary vortex* (analogous to the horseshoe vortex) system is developed. A blunt-nose obstacle introduced in a stream generates a strong pressure field which separates the boundary layer of the approaching flow (Shen et al., 1966). The boundary layer rolls up to form the *primary vortex* system (Figure 2.5).

As mentioned earlier, it is commonly believed that the accelerating flow initiates local erosion around an obstacle by generating local shear stress higher than the required value to move the bed materials (Melville, 1975; Ettema, 1980; Chiew, 1984; Kwan, 1984). Also, researchers generally agree that, although the development of the scour hole is mainly attributed to the *primary vortex* (abutment case) or the *horseshoe vortex* (pier case), this vortex is generated as a consequence of the scour hole

(Melville, 1975; Baker, 1980; Breusers and Raudkivi, 1991). Figure 2.6 shows the flow pattern within a scour hole according to velocity measurements by Shen et al. (1966). Also, the alignment of the primary vortex as it passes the constriction is shown in Figure 2.7. Looking along the axis of the vortex in the downstream direction, Kwan (1988) described the sense of the vortex rotation as *anti-clockwise* for an abutment installed in the *left* FP.

2.2.3.3- The secondary vortex

A series of *grooves* in the upstream part of the local scour hole was observed by Kwan (1984), Tey (1984), and Kandasamy (1985) during their abutment scour studies. The primary scour hole exists next to the abutment but the grooves occurred at a higher elevation within the scour hole (Figure 2.8). Similar observations lead researchers to a general conclusion that the *primary* vortex induces a *secondary* vortex with counter-rotational direction. This *secondary* vortex accounts for the presence of the observed grooves (Kwan, 1988).

2.2.3.4- The wake

Raudkivi (1986) considered the flow acceleration around a pier as a second consequence of the stagnation pressure. He attributed the generation of the *wake* and the *cast-off* vortices to the flow separation at the cylinder sides. The mean flow bends the axes of these vortices while conveying them downstream. Closer to the bed, the *cast-off* vortices interact with the *horseshoe* vortex. This leads to lateral and vertical oscillation in the trailing part of the vortices. According to Breusers and Raudkivi (1991), the frequency of vortex shedding, n, might be estimated using the Strouhal relationship, $nb/U_o \approx 0.2$.

Having a low-pressure centre, the *cast-off* vortices act as small tornados that lift sediment from the bed (Breusers and Raudkivi, 1991). Unlike the *horseshoe* vortex system, generally, minor sediment removal occurs as a result of the *wake* vortex system (Chiew, 1984). The *wake* vortices might affect bridge abutments in the same way that they do bridge piers. Figure 2.9 shows the *wake* vortex system at a semi-circular (SC) abutment. Kwan (1984), and Kandasamy (1985) also observed vortices in the so-called *dead water* region, however, little significance was attributed to them.

2.3- INFLUENCE OF GOVERNING FACTORS ON LOCAL SCOUR

As mentioned earlier, while numerous parameters affect the process of local scour, the influence of some of these are difficult to quantify (Breusers et al., 1977). The influence of a specific parameter is usually affected by other parameters, which further complicates the situation. In general, the *equilibrium* scour depth at an abutment, y_{se}, might be considered as a function of many parameters including: fluid properties, flow conditions, sediment characteristics, abutment and channel geometry, or time. The important parameters include:

(a)- sediment characteristics
- -density of bed material, ρ_s
- -median grain diameter, D_{50}
- -grain size distribution, $\sigma_g = \sqrt{D_{84}/D_{16}}$
- -angle of repose of material, φ
- -critical shear stress, τ_c, or critical shear velocity, u_{*c}
- -other parameters such as cohesiveness, c, particle shape factor, ψ, and fall velocity, ω

(b)- flow conditions
- -approach flow depth, y_o
- -approach flow velocity, U_o

-bed shear stress, τ_o, or shear velocity, u_*

-flow angle of attack, α

(c)- fluid properties

-density of water, ρ

-kinematic viscosity, ν

(d)- abutment and channel geometry

-abutment length, L

-abutment shape, K_s

-opening ratio, $\alpha_o = \frac{B-L}{B}$, or contraction ratio, L/B

-surface roughness

(e)- acceleration due to gravity, g

(f)- time

-time since the scour starts

A complete list of important parameters is very long. Situations having additional influencing factors might be observed in other cases such as those including: unsteady flow, stratified bed material, unique structures, and any scour protection devices. The influence of certain parameters on the scour process was investigated thoroughly by others; a summary of the relevant work is presented herein.

2.3.1- Effect of approach flow

The effects of the flow characteristics, namely: α, U_o, y_o, and τ_o were considered of primary importance in the local scour process and were studied in detail for bridge piers. An empirical coefficient, $K_{\alpha L}$, which accounts for the effects of the flow angle of attack on the local scour depth at rectangular bridge piers was proposed by Laursen and Toch (1956) (Figure 2.10). Their proposed coefficient has been generally applied for design purposes in the interim (Melville and Sutherland, 1988). Kwan (1984) and Kandasamy (1985) studied the effect of skewed abutments on y_{se}. According to their data the deepest y_{se} was observed at an abutment perpendicular to the flow, i.e. $\theta=90^{o}$ (Figure 2.11). In other words, even abutments aligned upstream ($\theta>90^{o}$) generated scour depth less than that generated by abutments having $\theta=90^{o}$. This result contradicts previous findings by other researchers (Ahmad, 1953; Laursen, 1958).

Kandasamy (1985) and Kwan (1984) attributed the difference between their findings and that of others to the equilibrium state. The reason, however, can be attributed to the generation of the secondary hole upstream the abutments. In other words, the development of the secondary scour hole at the final stage of the scour process replenishes the main scour hole with sediment. If the bed material is supplied to the main scour hole with the same rate as the scoured one, there will be no increase in the scour depth. This might erroneously be considered as the equilibrium stage.

Recently, Melville (1992) analysed the available abutment data of other researchers and proposed a coefficient, based on an envelope drawn to the available data, which incorporates the influence of abutment alignment on the scour depth (Figure 2.11). The influence of other flow characteristics, such as U_o, τ_o, and y_o on the equilibrium scour depth have been extensively studied; a summary of the related findings is presented.

To study the influence of the approach flow velocity on the scour process, usually, the velocity ratio, U_o/U_{oc}, or the shear velocity ratio, u_*/u_{*c}, was considered by many researchers. In these ratio, U_{oc} and u_{*c} are respectively the critical velocity and critical shear velocity corresponding to the initiation of sediment motion. Generally, the shear velocity ratio is used to determine the stability of the bed material and to classify the local scour process, i.e. whether a clear-water or live-bed condition governs. Pier scour studies indicated that no scour occurs if $U_o/U_{oc} < 0.5$. Also, the local scour around a cylindrical pier at $U_o/U_{oc}=0.5$ is negligible (Ettema, 1980; Melville, 1984). Further increase in this ratio up to $U_o/U_{oc} \leq 1$ results in a linear increase in the equilibrium scour depth (Ettema, 1980; Liu et al., 1961; Laursen and Toch, 1953)

Considering Manning's roughness coefficient, n, as a function of the grain size of the bed materials, Manning's formula for a fixed-bed *wide* open channel takes the form

$$\frac{U_o}{u_*} = 7.66\left(\frac{y_o}{k_s}\right)^{1/6} \tag{2.2}$$

in which k_s = equivalent sand roughness height. At the threshold condition, Equation 2.2 becomes:

$$\frac{U_{oc}}{u_{*c}} = 7.66\left(\frac{y_o}{k_s}\right)^{1/6} \tag{2.3}$$

Since during a clear-water condition the bed roughness does not change, k_s might be considered as a function of D_{50}. Therefore, considering a constant value for $y_o\ /k_s$ and equating Equations 2.2 and 2.3 yield:

$$\frac{u_*}{u_{*c}} = \frac{U_o}{U_{oc}} \tag{2.4}$$

Equation 2.4 shows that in a clear-water condition the velocity ratio and the shear velocity ratio might interchangeably be used. During live-bed conditions, however, the roughness of the channel is no longer constant. The latter depends on both the bed material and the bed features. Therefore, the shear velocity ratio and the velocity ratio can not be held equivalent in live-bed conditions.

For $U_o/U_{oc}>0.5$, the depth of equilibrium scour increases and reaches a peak value at around $U_o=U_{oc}$. After this peak, according to Shen et al. (1969), further increase in the flow velocity decreases the equilibrium scour depth in the order of about $0.1(y_{se})_{max}$ (Figure 2.12). Based on Shen et al.'s (1969) findings, some researchers ascribed the maximum equilibrium scour depth to a flow condition just before the threshold (Shen et al., 1969; Breusers et al., 1977; Cunha, 1975). However, Raudkivi (1984) was probably the first to suggest that the scouring process can include a second peak. Subsequent studies, applying higher velocities, exposed the second peak and showed that two maxima do exist (Chiew, 1984). The first peak, called the *threshold peak*, was attributed to the threshold condition of bed movement and the second one, called the *transition flat bed*, was associated with the transition flat bed condition (Melville, 1984). Of these two peaks the first is the higher when coarse non-ripple-forming sand is used, while the second peak is higher in the case of ripple-forming sand ($D_{50}<0.6$ to 0.7 mm) (Figure 2.13).

According to Breusers and Raudkivi (1991), for experiments with non-ripple-forming sands, an undisturbed upstream bed can still be observed even when u_* approaches $0.95u_{*c}$. A flat bed can not be maintained at this flow condition with finer sands. Using ripple-forming sands, when $u_*>0.6u_{*c}$ usually bed material moves and ripples develop. Ripple formation transports bed material into the scour hole and prevents the equilibrium scour depth reaching the same peak of scour depth that occurs for non-ripple-forming sediment (Figure 2.13). However, if the geometric standard deviation of the bed material falls in the range $1.3 < \sigma_g$ ($\sqrt{D_{84}/D_{16}}$)< 1.5, coarser grains armour the bed surface but they are not large enough to armour the scour hole where the turbulence agitations are higher. In this case a clear water scour depth of the same order as observed with non-ripple forming sediments can be reached in laboratory tests. The dotted line in Figure 2.13 indicates the fluctuation in the scour depth associated with the passage of bed features.

2.3.2- Effect of flow depth

Since $u_* = \sqrt{g y_o S_o}$, assuming constant values for S_o and g, an increase in the flow depth increases the shear velocity ratio. The effects of this aspect of the flow depth were considered earlier. The influence of the flow depth on scour hole development, assuming a constant u_* / u_{*c}, are presented here.

Observations of the scour process for bridge piers in a shallow flow range indicate that an increase in the flow depth increases y_{se}. According to Raudkivi and Ettema (1982), for a constant value of u_* / u_{*c}, a limit between 1 to 3 for y_o/b was reported, beyond which further increase in the flow depth will have negligible effects on y_{se}. Based on Bonasoundas' (1973) data (reported by Breusers et al., 1977) y_{se} depends on flow depth if $y_o/b<2$ (Figure 2.14a). The same trend is seen in Basak's (1975) data (Reported by Ettema, 1980) which were collected using $u_*/u_{*c}>1$ (Figure 2.14b).

Ettema (1980) reported the flow depths range that influences the scour process. Courser sediments require higher flow velocities to maintain a constant shear velocity ratio, u_*/u_{*c}. Higher surface flow velocities evidently produce higher stagnation head, consequently the downflow influences a deeper zone. Ettema concluded that flow depth ratios up to y_o/b=6 might affect y_{se} if coarse sand is used, while, for fine sediment the scour depth becomes independent of the flow depth at $y_o/b=1$ (Figure 2.14c).

According to Raudkivi and Ettema (1982) the horseshoe vortex at the base and the surface roller at the free surface were a consequence of the pier presence in a stream. Because these two rollers have opposite senses of rotation, the scour depth will not be sensitive to flow depth if they do not interfere with each other. The surface roller becomes more dominant by decreasing the flow depth and eventually eliminates the horseshoe vortex for small flow depth. Also, at shallow flow depths a reduction in the downflow as well as the formation of a bar downstream of the pier account for the reduction in the scour depth.

Studying live bed scour at bridge piers, Chiew (1984) observed the presence of both surface rollers and horseshoe vortices at a very shallow flow depth. He came to the conclusion that in shallow flow, the reduction in the downflow strength mainly accounted for the reduction in the equilibrium scour depth.

Similar to pier scour, in the case of a bridge abutment there might exist a limiting value of y_o/L beyond which the scour depth becomes independent of the flow depth. However, because only a limited amount of abutment data are available for large y_o/L, a general conclusion regarding the magnitude of the limiting value of y_o/L might not be drawn.

2.3.3- Effect of abutment configuration

Field and laboratory studies clearly indicate that bridge abutment length and shape have significant impact on the local scour depth. Different shapes strongly influence the local flow field. Streamlined shapes, for example, intuitively produce less disturbance (and hence less scour depth) than blunt shapes. The influence of abutment shape on the magnitude of the scour depth has usually been expressed through a shape factor, whose value depends on a reference abutment shape. Different abutment shapes were selected as a reference shape by various researchers. Wong (1982) chose a semi-circular end abutment, while Melville (1992) selected a vertical plate as a reference shape for his shape factor, which varied between 1 (vertical plate) and 0.45 (spill-through).

Different methods have been proposed to account for abutment length in scour depth-formulae. Laursen (1962a), Ahmad (1953), Garde et al. (1961), Gill (1972), Cunha (1973), and Rajaratnam and Nwachukwu (1983b) gave equal importance to the abutment length and the flume width. They reviewed the opening ratio, $\alpha_o = (B-L)/B$, (or the contraction ratio, L/B) as a suitable parameter to represent both factors.

For a short abutment installed in a wide uniform channel flow, Neill (1973) argued that the scour depth can not be analysed in terms of contraction ratio if the flume is very wide. Also, it is unlikely to observe significant difference in the scour depth at an abutment of a constant length if the channel width is enlarged while the shear velocity ratio and the flow depth are kept constant. Declaring his agreement with Neill's conclusion for short abutments, Gill (1974), however, believes that the channel width (or opening ratio) becomes an important parameter for long abutments.

Cunha (1973) believes that the spur length has two consequences on the flow:

concentration of vorticity and contraction of flow. Generally, these two factors overlap and the scour depth is affected by both. Presenting a criterion to determine the importance of the opening ratio, Cunha (1973) asserted that the contraction of the flow has no effect on the scour depth in a live-bed condition, unless the scour hole covers the entire width of the channel. Also, in a clear-water condition the effects of contraction scour on the local scour vanish if $\alpha_o > 0.9$. However, smaller opening ratios such as 0.55 (Kandasamy, 1985), 0.425 (Kandasamy, 1989), 0.42 (Kwan, 1984), and 0.7 (Kwan, 1988) were used in laboratory studies without affecting the local scour depth by the contraction scour. Therefore, further studies are required to draw a general conclusion defining the limit of α_o that does not affect the local scour depth with contraction scour.

The mechanisms of local scour and contraction scour are different, therefore, differentiating between the effects of each mechanism, where both are significant, seems necessary. However, this is very difficult in most situations. Hence, the effect of α_o on the local scour depth might be neglected provided that neither a small opening ratio, α_o, is considered nor the generated scour hole covers the entire width of the channel. In such a case, of the two factors the abutment length affects the scour process the most.

Another group of researchers (Kwan, 1984, 1988; Kandasamy, 1985, 1989; Melville and Raudkivi, 1984) consider the length of the abutment as the main *geometrical* parameter that affects the scour hole the most. The analysis, in this case, was primarily based on normalizing the abutment length by another parameter such as the flow depth.

Abutment scour studies (Kwan, 1984; Kandasamy, 1989) suggest that there exists a limited abutment length beyond which y_{se} becomes independent of L. Also, a similar conclusion was drawn for the effect of the flow depth on y_{se} for bridge pier studies (Ettema, 1980; Kwan, 1988). These conclusions led researchers to consider the scour depth as a function of the flow depth and the abutment length, i.e. $y_{se}=f(y_o,L)$ (Kwan, 1988; Melville, 1992). Accordingly, based on the abutment data of other researchers, Melville (1992), proposed the limits $1 \leq L/y_o \leq 25$ within which both factors affect the local scour depth. For $L/y_o \leq 1$ and $L/y_o > 25$, he respectively related the local scour depth to only the abutment length and the flow depth.

Some other researchers (Richardson and Richardson, 1993a, 1993b; Sturm and Janjua, 1993, 1994; Karaki, 1959, 1960) believe that a discharge ratio might be a more reasonable parameter to consider than abutment length. However, different definitions for the discharge ratio were applied. For example, in their analysis, Sturm and Janjua (1994) used the ratio of the proportional discharge (associated with the bridge opening width) to the total discharge. Richardson and Richardson (1993), on the other hand, suggested the ratio of the flow intercepted by the abutment that returns to the MC to that portion of the MC flow which belongs to a width equal to the width of the scour hole to be used.

2.3.4- Effect of pier and sediment sizes

The effects of sediment characteristics on y_{se} has been the subject of studies by, among others, Shen et al. (1966), Ettema (1980), and Chiew (1984). Considering other researchers' piers data in addition to their own data, Shen et al. (1966) came to the conclusion that the maximum scour depth is independent of sediment size when D_{50}<0.52mm.

Extensive studies conducted at the University of Auckland investigated different aspects of the scour process and determined the relative importance of the contributing factors. The effects of sediment size and gradation on the maximum scour depth were studied by Ettema (1980). Based on laboratory data of both ripple-forming and non-ripple-forming sediment for six pier sizes, b, and sediment sizes in the range $0.24 < D_{50} < 7.8$ mm, Ettema established a graphical relationship between the relative size of the pier, b/D_{50} and the relative equilibrium scour depth y_{se}/b (Figure 2.15). With non-ripple-forming sediment his data indicate that sediment size has no influence on y_{se}/b as long as $b/D_{50} > 25$. With ripple-forming sediment, however, the scour depths were lower and the results were more scattered. Lower depths arise because ripples invariably occur near threshold conditions, creating a small amount of sediment transport which replenishes the scour hole.

Chiew (1984) extended Ettema's work to observe the effects of pier and sediment sizes on the equilibrium scour depth under live-bed conditions. Using the same parameters as Ettema's, Chiew showed that for live-bed conditions the relationship between y_{sa} and b/D_{50} follows the same trend as it does for the clear-water condition (Figure 2.16). The family of curves illustrated in Figure 2.16 show that, at a constant value of u_* /u_{*c}, the relative equilibrium scour depth y_{sd}/b increases almost linearly with increasing b/D_{50}. Also, in both clear-water and live-bed conditions, y_{sd}/b might be considered independent of sediment size as long as the relative pier size $b/D_{50} > 50$.

It seems that the effect of sediment size validated for the case of pier scour might also apply in the case of abutment scour (Kwan, 1988). Assuming that an abutment of size $2L$ was equivalent to a pier of diameter, b, Melville and Raudkivi (1984) considered scour depths at abutments in most practical situations independent of the sediment size, since $2L/D_{50} \leq 50$ is unlikely to occur in practice.

2.2.5- Effect of sediment grading

Raudkivi and Ettema (1977) investigated the effect of grain size distribution on the local depth of scour at a bridge pier. They found that the maximum scour depth for coarse grained, non-ripple-forming sediment (D_{50}>0.6 to 0.7 mm) of a single grain size ($\sigma \to 0$) reaches $y_{se}/b \approx 2.1$ to 2.3 and it is independent of the grain size (Figure 2.17). However, a flat bed cannot be maintained near threshold conditions when uniform ($\sigma \to 0$) sand having D_{50}<0.7 mm is used. Ripples develop and a small amount of general sediment transport reduces the maximum scour hole to $(y_{se}/b)_{max}$=1.4 to 1.5 (Raudkivi and Ettema, 1977).

As the normal standard deviation of the grain size distribution increases, an armour layer on the upstream bed develops and prevents the development of ripples. There exists a critical value of σ/D_{50} in which armouring can just be achieved on the bed and not in the scour hole, consequently, the scour hole depth will be maximized (Breusers and Raudkivi, 1991). Grading also affects the maximum value of y_{se}/b, but not the time taken to reach equilibrium (Raudkivi and Ettema, 1977). In practice, the possible maximum value of the equilibrium depth of clear-water scour $y_{se}(\sigma)/D_{50}$ can be estimated from the following equation:

$$\frac{y_{se}(\sigma)}{D_{50}}=K_{\sigma}\frac{y_{se}}{D_{50}} \qquad (2.5)$$

in which y_{se} is the equilibrium scour depth in uniform sand, $\sigma_g = 1$. The value of K_σ as a function of σ_g depends on whether the sediment is ripple-forming or not. When u_*/u_{*c}<0.8

The formation of an armour layer on the surface of non-uniform ripple-forming sands prevents the growth of ripples and scour develops as in a non-ripple-forming sediment (Figure 2.18). Figure 2.18 is based on the data of Ettema (1976) for bridge piers and Wong's data (1982) for abutments.

2.4- TEMPORAL DEVELOPMENT OF LOCAL SCOUR

Local scour due to presence of obstacles in an alluvial stream might occur under live-bed or clear-water conditions. The temporal development of the scour hole and the *equilibrium scour depth*, y_{se}, largely depend on the predominant state of the sediment movement. Therefore, it is very important to distinguish between these conditions in any study of local scour.

Although live-bed conditions are usually predominant during floods, the maximum scour depth might occur under a clear-water condition in the field. When a flood starts to recede the bed level of the stream is minimum due to the severe general scour of the earlier stage of the flood. During the early stage of the flood recession the general sediment transport is significantly reduced, i.e. a clear-water condition might prevail. In such a case, it is more likely to observe the maximum scour depth during this period. Usually, the duration of the flood recession period does not last long enough to allow the development of the equilibrium scour depth in the field. Nevertheless, a normal river flow near the threshold state might last a long period, which facilitates the development of y_{se} in the field.

The scour depth under live-bed conditions rapidly increases with time to a maximum value and fluctuates about a mean value thenceforth (Figure 2.19). The mean value of the fluctuating scour depth is usually considered as the equilibrium scour depth in a live-bed state. Primarily, the creeping movement of the bed features generated during a live-bed condition calls for the oscillation of the scour depth. The size and the height of the moving bed features dictate the magnitude of the scour depth fluctuation. Based on laboratory studies of scouring around a cylindrical pier, Shen et al. (1969) came to the conclusion that the live-bed equilibrium scour depth increases and decreases less than one-half of a dune height when the trough and the dune crest respectively pass the pier.

Under live-bed conditions, the required time to reach y_{se} in laboratories is relatively short; it typically takes several hundred minutes (Kwan, 1988). Under a clear-water condition, however, the equilibrium scour depth might be established after a relatively very long period. Nevertheless, required periods as short as 12 hours (Dargahi, 1990; Sturm and Janjua, 1994) and as long as 10080 hours (Blaisdell, 1983) to reach y_{se} are reported in the literature. There is, however, an agreement among researchers that the rate of scour during the initial period is relatively high (Ettema, 1980; Kwan, 1988). The high scour rate of the initial period establishes a significant percentage of the equilibrium scour depth within the first several hours of a test. After this initial period, the rate of scour progressively decreases such that the equilibrium depth is reached asymptotically. Beyond the initial period of a test, careful attention should be paid to the time interval taken between two consecutive measurements. No appreciable difference in the scour depth can be observed within a short time interval, especially during the asymptotical increment of scour depth development. Therefore, if two consecutive measurements are taken within a short period, one might groundlessly assume that the equilibrium state is achieved.

During the last four decades, the temporal development of the scour hole under a clear-water condition was investigated by many researchers (Laursen, 1962a; Shen et al., 1966; Cunha, 1975; Ettema, 1980; Blaisdell et al., 1981; Franzetti et al., 1982; and Kwan, 1984, 1988). Small-scale models of bridge piers, spur-dikes, and abutments were used in these studies. Yet, no simple rule has been established to estimate the necessary test duration to attain the static equilibrium scour depth.

Cunha (1975) reported the time evolution of scour depth around a 0.2-m long spur-dike using two types of bed materials, namely, sand having D_{50} = 1.6 mm and gravel of D_{50} = 5.75 mm. He applied a uniform flow depth, y_o = 0.09 m in his experiments and used this flow depth to normalize the scour depth. Cunha also considered flow velocities as high as 0.38 m/s and 0.7 m/s as critical ones to initiate bed movement respectively in the applied small and large sizes of bed materials.

Cunha claimed that only three of the experiments accomplished with sand under a clear-water condition reached the equilibrium scour depth after about 80 hr (Figure 2.20). However, he applied lower flow velocities than the critical one (0.38 m/s) in these experiments. This implies that the observed scour depths are smaller than the maximum possible because of the application of shear velocity ratios, u_* / u_{*c}, smaller than unity. Using the same bed materials, Cunha (1975) also conducted a series of tests to study the temporal scour development under live-bed conditions. The normalized results plotted in Figure 2.21 clearly show that all experiments reached the equilibrium scour depth after a relatively short period (100 minutes).

Cunha (1975) identified four phases in the temporal development of the clear- water scour hole and classified them in two classes as *transition* and *principal* phases. According to his experiments, the *first transition* phase extends up to the thirtieth minute beyond which the *first principal* phase starts. The *second transitional* phase falls in between the first principal phase and the last one, which constitutes the *equilibrium* stage.

Using four grain sizes and geometric standard deviation, σ_g, in the range $1.17 \le \sigma_g \le 4.55$, Ettema (1980) recorded the temporal scour depth development around a cylindrical bridge pier having a diameter of 101.6 mm. He used the pier diameter to normalize the scour depth and plotted the results versus the product of Reynolds No., Strouhal No., and the relative size of the sediment to the pier diameter. The results are presented as a series of linear logarithmic lines in Figure 2.22.

Ettema recognized three segments of straight lines for each test (Figure 2.22) and attributed them to the predominate condition of the flow field. He attributed the first segment of the rapid scouring to the downflow. The middle segment was related to the development of the scour hole during which the horseshoe vortices move away from the cylinder and grow in size and strength. Finally, the equilibrium scour state was indicated by the third segment.

Kwan (1988), however, described the scouring process in three phases as follows: (*i*) during the initial transition phase, the scour depth rapidly increases while the scouring rate significantly decreases, (*ii*) then, the scour hole steadily widens and deepens over the long period of the principal erosion phase--the second phase, (*iii*) and finally, the equilibrium phase, during which only very little scour occurs over a long period.

Using abutment lengths in the range $0.164 \text{ m} < L < 1.4 \text{ m}$, Kwan (1984) performed tests under a clear-water condition to observe the development of the scour hole around SC abutments. He used sand having $D_{50} = 0.9$ mm and applied a flow depth of 0.05 m which yields a shear velocity ratio, u_* / u_{*c} = 0.95. The temporal development of the normalized scour depth according to Kwan's data are shown in

Figure 2.23. Inspection of Figure 2.23 reveals that the scour rate during the initial phase is higher than that of the principal phase. Therefore, Kwan (1984) concluded that the downflow and the principal vortex system generate less scour than the accelerating flow does. Kwan's conclusion contradicts the pier study results of Ettema (1980), whose data indicated that greater scour depth was produced during the second stage of the scouring process (compare Figures 2.22 and 2.23). Kwan reasoned that the concentration of the downflow and the principal vortex produce strong scouring agents in front of the pier while their distribution over a large area in the abutment case generate a milder scouring rate during the principal phase (see Figure 2.24).

2.4.1- Proposed relationships for temporal scour development

Researchers proposed different empirical relationships to describe the temporal development of a scour hole. These relationships might be classified into three types. It is believed that all are equally valid approximations of the actual process (Kwan, 1988). The first type takes the form:

$$y_s = a\, b^t \tag{2.6}$$

in which y_s = the scour depth at time t, and a and b are parameters whose values depend on bed materials, obstacle geometry, and flow characteristics. Many researchers, among them Laursen (1963), Cunha (1975), and Carstens (1966), suggested this form. The second type adopted by Ahmad (1953), Liu et al. (1961), and Chang and Yevdjevich (1962) takes the form:

$$y_s = a\,(1-e^{-bt}) \tag{2.7}$$

Finally, the third type endorsed by Shen et al. (1966), Gill (1972), Ettema (1980), Nwachukwu and Rajaratnam (1980), Zaghloul (1983), Wong (1982), and Kwan (1984) takes the form:

$$y_s = a \, Log \, b \, t \tag{2.8}$$

Observing the asymptotical clear-water scour depth increment, Franzetti et al. (1982) used dimensional analysis to develop a relationship by which clear-water scour depth at a *circular* bridge pier can be extrapolated to obtain the ultimate scour depth y_{se}. Their proposed relationship takes the form:

$$\frac{y_s}{y_{se}} = 1 - e^{A\tau^B} \tag{2.9}$$

in which $\tau = Ut/B$, U = mean velocity of the undisturbed flow, and A and B are coefficients varying with test conditions. Franzetti et al. showed that experiments need only be carried out for a period of $t_e/6$, where t_e is the required period to reach the equilibrium scour depth. The coefficients A and B should be evaluated using data obtained during $t_{1/6} = t_e/6$, hence, the equilibrium scour depth around a circular pier might be evaluated using this equation.

Also, data from a culvert outlet (cantilevered pipe) were used by Blaisdell et al. (1981) to determine the development time associated with y_{se}. Hyperbolic logarithmic, linear logarithmic, and linear semi-logarithmic methods were evaluated in their studies. They came to the conclusion that the differences in the predicted dimensions of the scour hole using various method might be small. It is necessary to consider a practical time for determining y_{se} using linear logarithmic and semi-logarithmic methods, while the hyperbolic method has the advantage of not being dependent on this factor. They also claimed that the methods are able to determine the limiting extent of scour as characterized by Laursen (1952).

To study the clear-water erosion near groin-like structures, Rajaratnam and Nwachukwu (1983b) conducted experiments using a 3-mm thick, 229-mm long vertical plate and uniform sediment having a D_{50} = 1.4 mm. The variations of the maximum depth of erosion with respect to time, which occurred near the nose of the groin, are shown in Figure 2.25. They normalized their data using the time associated with 75% of the ultimate scour depth (Figure 2.26) and concluded that the scour profiles along the groin for different experiments might be considered approximately similar.

The temporal scour depth was also studied by Nazarul Islam (1986). He analysed data obtained by different researchers and proposed a relationship to predict the temporal development of a scour hole at a bridge pier. His relationship takes the form:

$$\frac{y_s}{y_{se}} = \left[\sin\left(\frac{\pi}{2}\frac{t}{t_e}\right)\right]^m \tag{2.10}$$

in which m is a coefficient that depends on the geometry of the obstacle and the flow conditions.

Equation 2.10 has the advantage of generating the expected initial and final conditions, i.e. $y_s = 0$ at $t = 0$ and $y_s = y_{se}$ at $t = t_e$. However, despite the fact that data for spur-dikes were used in Islam's analysis, the constant m might be evaluated for only *circular bridge piers* of diameter b by the following equation

$$m = 0.135 \left(\frac{y_o}{D_{50}}\right)^{0.087} \left(\frac{b}{y_o}\right)^{0.25} \qquad (2.11)$$

Kothyari et al. (1992) presented a computational scheme to predict the temporal variation of the scour depth. Their model was based on simplifying assumptions which are necessary to quantify the geometric and hydraulic characteristics of the primary vortex. These assumptions might be summarized as follows:

- At the pier nose, before scour begins the shape of the primary vortex is circular and the shear stress is four times as much as the shear stress of the approach flow.
- The diameter of the vortex is approximated by $D_v / y_o = 0.28 \left(b/y_o\right)^{0.85}$, where D_v = vortex diameter.
- The slope of the upstream half of the scour hole equals the angle of repose of the bed material, φ; also its shape might be approximated by the inverted frustum of a right circular cone.
- At any given time the cross-sectional area of the primary vortex equals the cross-section of the scour hole plus its initial cross-sectional area.

According to Kothyari et al. (1992) the model determines the scour depth in front of a *circular* bridge pier placed in uniform, non uniform, and stratified beds under steady and unsteady clear-water scour. However, the simplifying assumptions which form the basis of Kothyari et al.'s model, restrict its application to only *circular* bridge piers.

The temporal developments of the scour depth according to Kandasamy (1985) and Kwan's (1988) data are presented in Figures 2.27 and 2.28 respectively. The data of these researchers were normalized according to the equilibrium scour depth of each test and their results are presented in Figures 2.29 and 2.30 respectively. To compare the results obtained by Kandasamy (1985) and Kwan (1988) the normalized values were plotted in Figure 2.31. This Figure shows that all the data follow a similar trend, especially during the initial and the final periods of the scouring process. However, data for the intermediate stage are distributed over a relatively wider range.

2.5- SCOUR DEPTH PREDICTION FORMULAS

2.5.1- Laursen's equations

Considering the concept of continuity for sediment flow, Laursen (1962a, 1980) proposed an equation to estimate the scour depth at an abutment. He assumed that the *long contraction* approximates the case of the abutment. Laursen considered the scour in the long contraction as a fraction (1/r) of the scour at the abutment ,y_s , (Figure 2.32).

Typically, water in the MC is transporting sediment, and water in the overbank area is relatively free of sediment, i.e. clear water. When these flows mix at the abutment, there is a deficiency of sediment in the mixture. This deficiency is satisfied with material from the abutment scour hole. Laursen realized that the mixing occurred primarily in the zone of flow near the bank. Therefore, diluting the overbank flow with the entire channel flow would not be reasonable because the computed scour depth would decrease directly with the width of the bridge opening. Consequently, Laursen (1962a) defined an influence zone as shown in Figure 2.33 and derived his abutment scour equations based on no mixing outside this zone.

Laursen (1962a) considered the width of the influence zone as wide as 2.75 times the depth of the abutment scour hole, which means that his proposed abutment scour equations are implicit ones. For the typical case where the flow in the influence zone, Q_w, transports sediment and flow from the overbank area, Q_o, is clear-water, Laursen's sediment continuity equation takes the form:

$$\frac{Q_o}{Q_w}\frac{w}{y_w} = 2.75\frac{y_s}{y_w}\left[\left(\frac{1}{r}\frac{y_s}{y_w}+1\right)^{7/6} -1\right] \qquad \textbf{(2.12)}$$

in which y_w is the average depth of flow in the width w (Figure 2.32). Figure 2.34 shows a plot of Equation 2.12 with a recommended value of $r = 4.1$. Also, Laursen experimental data for runs with the approach fill and abutment normal to the flow direction are presented in this figure.

For the special situation in which both the flow in the influence zone and the overbank flow are clear-water, which, according to Laursen (1963) could occur at relief bridges or where abutments are set back far enough on the FP, Laursen's second equation was written as:

$$\frac{L}{y_o} = 2.75\frac{y_s}{y_o}\left[\frac{\left(\frac{1}{r}\frac{y_s}{y_o}+1\right)^{7/6}}{\left(\frac{\tau'}{\tau_c}\right)^{1/2}} - 1\right] \qquad \textbf{(2.13)}$$

$$\frac{\tau'}{\tau_c} = \frac{U_o^2}{120\ D_{50}^{2/3}\ y_o^{1/3}}$$

in which τ' = intensity of shear at boundary associated with sediment particle; r = 4.1 and 11.5 for low and high velocity respectively; and y_s = deepest part of the scour hole, which is assumed at the edge of the abutment.

Laursen's r-value essentially distributes the scour in a triangular hole. The larger the r-value, the larger the ratio of the deepest scour depth y_s to the average scour depth in the influence zone (Jones, 1984).

2.5.2- Garde et al.'s equation

Garde et al. (1961) investigated the maximum scour depth at a spur-dike in a laboratory flume shown in Figure 2.35. The following were the conditions applied in their studies:

- The spur-dike was placed perpendicular to the flow direction.
- α_o=0.900, 0.835, 0.667, and 0.530 were applied.
- The influence of the sediment size was investigated using D_{50}=0.29, 0.45, 1.00, and 2.25 mm.
- They applied discharges per unit width, q, in the range $0.002 < q < 0.0127$ m^2/s.

Under the limitations imposed on Garde et al.'s investigations, they concluded that:

1- The sediment has an influence both on the rate of scour and on the maximum scour depth, and the average drag coefficient, $C_D = \frac{4}{3}\frac{(\gamma_s - \gamma)D_{50}}{\omega^2 \rho}$, is a suitable parameter whose variations indicate the role of sediment characteristics on the nature of scour. In the above relationship ω = settling velocity of sediment.

2- The Froude number for the approach channel, $F = U_o/\sqrt{g y_o}$, can be used to reflect the effect of flow characteristics on the maximum scour depth.

3- Representing a significant dimensionless term, α_o characterizes the spur-dike geometry.

4- The dimensionless scour depth $\frac{y_o + y_s}{y_o}$ is given by:

$$\frac{y_o+y_s}{y_o} = K \frac{1}{\alpha_o} F^N \tag{2.14}$$

in which K and N = coefficients whose values are related to C_D in Figure 2.36.

2.5.3- Gill's equations

Based on Straub's long contraction scour equation and experiments with two sizes of sand, namely: coarse sand of D_{50} = 1.52 mm and fine sand of D_{50} = 0.91 mm, Gill (1972) proposed the following equation to evaluate the scour depth around spur-dikes:

$$\frac{y_o+y_s}{y_o}=8.375\left(\frac{D_{50}}{y_o}\right)^{0.25}\alpha_o^{-6/7}\left[\frac{1}{\alpha_o^{-1/N}\left(1-\frac{\tau_c}{\tau_o}\right)+\frac{\tau_c}{\tau_o}}\right]^{3/7} \tag{2.15}$$

$$1-\frac{\tau_c}{\tau_o} = 0 \ for \ \frac{\tau_c}{\tau_o} \geq 1$$

in which N = numerical constant. Based on various well known bed load equations N might take values between 1.5 and 3. When $\frac{\tau_c}{\tau_o}>1$, a clear-water case reveals, i.e. the movement of sand occurs only locally in the vicinity of the spur and Equation 2.15 for this case reduces to:

$$\frac{y_o+y_s}{y_o}=8.375\left(\frac{D_{50}}{y_o}\right)^{0.25}\alpha_o^{-6/7}\left(\frac{\tau_o}{\tau_c}\right)^{3/7} \tag{2.16}$$

In live bed conditions, however, τ_c/τ_o tends to zero and Equation 2.15 takes the form:

$$\frac{y_o+y_s}{y_o}=8.375\left(\frac{D_{50}}{y_o}\right)^{0.25}\alpha_o^{\left(\frac{3}{7N}-\frac{6}{7}\right)} \tag{2.17}$$

At the threshold condition of bed material movement, $\tau_c/\tau_o=1$,the last term of the right-hand side of Equation 2.15 becomes unity. This yields the maximum scour depth which is given by:

$$\left(\frac{y_o+y_s}{y_o}\right)_{\max} = 8.375\left(\frac{D_{50}}{y_o}\right)^{0.25} \alpha_o^{\cdot 67} \tag{2.18}$$

Considering the extreme values of N, i.e., $N=3$ and $N=1.5$, The power of the last term (contraction term) of Equation 2.17 becomes 5/7 and 4/7 respectively

To study the sensitivity of the predicted scour depth to the extreme values of N, Gill (1972) considered a typically large value for the contraction ratio, $\alpha_o=2$, and kept all other conditions constant. Applying the extreme values of N (i.e. 1.5 and 3) to the selected conditions yields only about 10 percent difference in the predicted scour depth. Since the observed difference is for extremely high rates of sediment transport it would still be smaller for moderate and low rates of transport.

According to Gill (1972) the difference in the predicted scour depth using extreme values of N would even be smaller than 4 percent if $\alpha_o \leq 0.733$. Most of his data were collected using this contraction ratio, therefore, he came to the conclusion that any of the presently available sediment transport formulas can be used for the purpose of scour prediction. Also, for the engineering works which are generally designed for worst conditions, Gill suggested the use of Equation 2.18 to determine the depth of the local scour hole. Gill believes that the distinction between clear-water and live-bed conditions in this case is unnecessary, unless, specific prototype conditions are to be reported in a model.

2.5.5- Froehlich's equations

A total of 164 clear-water and 170 live-bed measurements of the maximum depth of local scour at model bridge abutments presented by different researchers were analysed by Froehlich (1989). He used multiple linear regression analysis to determine a quantitative relation between the relative depth of local scour and a set of dimensionless independent variables.

A single regression model for predicting the maximum relative local scour depth at an abutment, y_s/y_o, was developed using all the available data of scour measurements. For clear-water scour conditions, the regression model reduces to:

$$\frac{y_s}{y_o}=0.78\ K_s\ K_\theta \left(\frac{L'}{y_o}\right)^{0.63} F^{1.16} \left(\frac{y_o}{D_{50}}\right)^{0.43} \sigma_g^{-1.87}\ +FS \qquad (2.19)$$

While for live-bed scour conditions it takes the form:

$$\frac{y_s}{y_o}=2.27\ K_s\ K_\theta \left(\frac{L'}{y_o}\right)^{0.43} F^{0.61}+FS \qquad (2.20)$$

in which

y_o = depth of flow at the abutment (not including depth of local scour).

K_s = coefficient for abutment shape (= 1.0 for a vertical abutment that has square or rounded corners, and a vertical embankment, 0.82 for a vertical abutment that has wing walls and sloped approached embankment, and 0.55 for a spill-through abutment and a sloped approach embankment).

$K_\theta=(\theta/90)^{0.13}$, which is a coefficient for the angle of embankment to flow (θ = the angle (in degrees) between the approach embankment and the direction of the main flow. It is less than 90° if the embankment points downstream).

$L' = A_a / y_o$, the projected length of abutment normal to the flow.

A_a = flow area of an approach cross-section which is obstructed by a roadway embankment.

$F = U_o / \sqrt{g y_o}$, is the Froude number of the approach flow upstream of the abutment, $U_o = Q_a / A_a$, and Q_a = flow obstructed by an approach embankment, and

FS = safety factor.

All dimensional variables used in these equations need to have the same unit of length.

According to Equation 2.19 increasing D_{50} decreases y_s/y_o. For a larger sediment size, however, a higher shear velocity is required to satisfay the threshold condition. In such a case one would expect to observe larger y_s/y_o. Moreover, extensive studies by the FHWA indicated that all traditional equations (including Froehlich's equations) predict excessive scour depth (Richardson et al., 1991a)

2.4.6- Melville's equations

Several studies of abutment scour were performed at Auckland University (Melville, 1992). Most experimental data were obtained for $0.9 < u_* / u_{*c} < 0.95$ and $D_{50} = 0.8$ mm (without general bed load).

The data were analysed by Melville (1992). He described y_{se} at an abutment as a function of parameters mentioned in the following equation:

$$y_{se} = f(\rho, \nu, U_o, y_o, \rho_s, D_{50}, \sigma_g, L, Sh, Al, G, g) \quad (2.21)$$

in which Sh and Al = parameters describing the shape and alignment of the abutment; G = parameter describing the effects of lateral distribution of flow and cross-sectional shape of the approach channel.

Assuming constant relative density of sediment and the absence of viscous effects, Melville (1992) normalized y_{se} with the abutment length and flow depth as shown in Equations 2.22 and 2.23. He asserted that Equation 2.22 is more applicable to short abutments while Equation 2.23 is better for long abutments.

$$\frac{y_{se}}{L}=f\left(\frac{U_o^2}{gD_{50}}, \frac{y_o}{L}, \frac{D_{50}}{L}, \sigma_g, Sh, Al, G\right) \tag{2.22}$$

$$\frac{y_{se}}{y_o}=f\left(\frac{U_o^2}{gD_{50}}, \frac{L}{y_o}, \frac{D_{50}}{y_o}, \sigma_g, Sh, Al, G\right) \tag{2.23}$$

Equations 2.22 and 2.23 can be evaluated using laboratory data by writing them in the form:

$$\frac{y_{se}}{L} = K_I\, K_y\, K_D\, K_\sigma\, K_s\, K_\theta\, K_G \tag{2.24}$$

$$\frac{y_{se}}{y_o} = K_I\, K_L\, K_D\, K_\sigma\, K_s\, K_\theta\, K_G \tag{2.25}$$

in which K-factors = expressions describing the influence of each parameter in Equations 2.22 and 2.23, K_I = flow intensity, K_y = flow depth, K_D = sediment size, K_σ

= sediment gradation, K_L = abutment length, K_s and K_θ = abutment shape and alignment respectively, and K_G = approach channel geometry.

Equations 2.24 and 2.25 form the basis of the design recommendation suggested by Melville (1992). Most of the data presented are derived from experiments conducted at threshold conditions, which as previously stated produce the largest scour depths over the range of flow velocities investigated to date. Because insufficient information is presently available to quantify some of the K factors Melville (1992) suggested a value of unity for them.

Melville scaled the scour depth for long and short abutments with flow depth and abutment length respectively. He recommended the use of Equations 2.26 to 2.28 according to the abutment condition L/y_o.

$$y_{se} = 2\ K_s\ L\ ; \quad \frac{L}{y_o}<1 \tag{2.26}$$

$$y_{se} = 2\ K_s^*\ K_\theta^*\ (y_o L)^{0.6}\ ; \quad 1\le\frac{L}{y_o}\le 25 \tag{2.27}$$

$$y_{se} = 10\ K_\theta\ y_o\ ; \quad \frac{L}{y_o}>25 \tag{2.28}$$

These equations give conservative values because the method assumes uniform distribution of flow and depth across the river channel, (Melville, 1992).

Melville's equations were based on data obtained in rectangular channels at or close to threshold conditions of particle movement. In cases with abutments sitting in the FP (which is usually the case) flow in the FP is slower than the MC flow. Therefore, the shear velocity ratio is an important factor that largely governs the scour process in that region and should be incorporated in the formulation of the process. Equations 2.26 to 2.27, therefore, are not reliable for abutments terminating in the FP. Furthermore, in the field, long abutments are usually provided with relief bridges which decrease the diverted flow at the abutment end. In such cases, Equation 2.28 cannot be applied since it predicts unrealistic scour depth.

Melville (1995) defined the geometry factor, K_G, in a compound channel by the following equation:

$$K_G = \sqrt{1 - \frac{L^*}{L}\left[1 - \left(\frac{y_a}{y_o}\right)^{5/3} \frac{n}{n_a}\right]} \tag{2.29}$$

in which L^* = the width of the flood channel, y_a and y_o = the depths of the approach flow in the FP and in the MC respectively, and n and n_a are Manning roughness coefficients of the MC and the FP respectively.

He also introduced the *equivalent length*, L_e, as an alternative approach to estimate the scour depth at an abutment sited in a compound channel (Figure 2.37). Determined by Equation 2.30, the equivalent length, L_e, is defined as the length of an abutment which would induce the same scour depth in a rectangular channel as the actual abutment (of length L) when sited in the compound channel. These channels, termed by Melville (1995) as *corresponding channels*, have both identical overall width and identical flow depths.

$$L_e = L\sqrt{1-\frac{L^{*}}{L}\left[1-\left(\frac{y_a}{y_o}\right)^{5/3}\frac{n}{n_a}\right]} \tag{2.30}$$

Melville (1995) compared the results obtained using K_G with Dongol's data (Figure 2.37) and concluded that the approach channel geometry factor K_G defined by Equation 2.29 is in good agreement with the experimental data. However, it tends to slightly overestimate actual scour depths. He also asserted that the equivalent length of abutment given by Equation 2.30 can be used for design prediction of local scour depth at an abutment sited in a compound river channel, as shown in Figure 2.37. Equations 2.29 and 2.30 were obtained only for abutments long enough to encroach on the MC. This situation, however, is unlikely to be considered in practice without the provision of relief bridges.

Recently, when emphasizing the need for additional abutment scour research, Melville and parola (1995) categorized bridge abutments under three cases (Figure 2.38). He stressed the major deficiencies that exist in the data sets of cases II and III and recommended further studies to investigate the effects of the channel geometry on the scour phenomena for these cases.

2.5.7- Sturm and Janjua's equation

Sturm and Janjua (1993) proposed a prediction equation for clear-water scour at an abutment which terminates in the FP of a compound channel. Their experiments were conducted in a compound flume having insignificant MC width (0.3 and 0.2 m) and a relatively large FP width (2.49 and 2.59 m) (Figure 2.39). They assumed that the effect of the compound channel geometry on the scour can be consolidated into the approach FP velocity, U_a, and the discharge contraction ratio, M, and proposed the following functional relation.

$$\frac{y_s}{y_a} = f\,(F_a,\ M,\ D_{50}) \tag{2.31}$$

in which y_a and F_a = approach flow depth and Froude number in the FP upstream of the end of the abutment, M=Q_o /Q is the discharge contraction ratio, Q_o = that portion of the flow in the approach section with a width equal to the opening width, and Q = the total approach discharge.

Sturm and Janjua (1993) found that the influence of D_{50} /y_a suggested by Equation 2.31 was insignificant. Also, previous studies suggest that sediment size does not affect the maximum clear-water scour depth around bridge piers if b/D_{50} >50, which was the case for their experiments. Consequently, in a later study they related D_{50} to the critical value of the approach Froude number for initiation of motion, which can be evaluated using the following equation:

$$F_c = 2.27\left(\frac{D_{50}}{y_o}\right)^{1/3} \tag{2.32}$$

Furthermore, instead of using average values of U_a and y_a, they suggested that both the flow velocity and the flow depth in the FP upstream of the end of the abutment be used in the evaluation of F_a. Therefore, Equation 2.31 takes the form:

$$\frac{y_s}{y_a} = f\,(F_a,\ M,\ F_c) \tag{2.33}$$

The scour data according to Storm and Janjua (1994) are plotted in Figure 2.40 based on the dimensional analysis of Equation 2.34 with F_a /(M F_c) as the independent variable. They performed a least-squares regression analysis on the data (Figure 2.40) and proposed the following best-fit linear equation as:

$$\frac{y_s}{y_a} = 7.7\left(\frac{F_a}{M\,F_c} - 0.35\right) \qquad (2.34)$$

Sturm and Janjua (1993) compared their experimental data to Froehlich's equation in Figure 2.41. The scour depth is over-predicted by approximately 50%. They also suggested that: 1) the direct measurement of the approach velocity upstream of the end of the abutment is a better measure of approach conditions for a compound channel; and 2) that flow interaction between the MC and FP in the contracted section reduces the scour from that which would be expected in earlier studies using rectangular cross sections.

Sturm and Janjua's (1994) data were obtained in a laboratory flume having insignificant MC width. In other words, the ratio of FP width/MC width was relatively large (2.49/0.3, and 2.59/0.2) and the effects of the MC flow on that of the FP was negligible. consequently, a uniform flow velocity pattern was observed in the FP of their channel. In the field the flow distribution is not uniform. Sturm and Janjua's data (1994) were not collected at a specific value of u_*/u_{*c}, rather a relatively wide range of shear velocity ratio ($0.3<u_*/u_{*c}<0.9$) applied in their tests. Probably the fixed horizontal flume bed did not allow them to establish the desired flow depth and u_*/u_{*c} simultaneously. Consequently, due to the limitation of Sturm and Janjua's data and the restrictions of their experimental set-up, further studies are required to provide the necessary data with higher certainty to prepare an appropriate base for estimating scour depth at an abutment set in the FP with an acceptable degree of accuracy.

2.6- FLOW INTERACTION IN A COMPOUND FLUME

Watercourse cross-sectional geometry has long been recognized as an important parameter which governs the pattern of velocity distribution, boundary shear stress, momentum transfer, and secondary circulations in an open channel flow (Myers, 1991). Compound cross-sections, which are common in natural watercourses, consist of a deep central MC and one or two side FP. The effects of the cross-section geometry of compound channels on the flow characteristics are usually more pronounced. Flow in the FP is generally slower than the MC flow, because of the high resistance coefficients associated with the former. At small FP depths, the difference between the (high) MC flow velocity and (low) FP velocity initiates a relatively strong momentum transfer mechanism in the transverse direction. Therefore, when compared with *in-bank* values, MC discharge and flow velocity decrease as a consequence of the momentum flux from the MC to the FP, while these flow characteristics increase in the FP. Careful attention must therefore be paid to the cross-section shape effects on the flow characteristic, especially when dealing with channels having compound cross-sections.

The value of the shear stress τ, or the shear velocity, $u_*(= \sqrt{\tau/\rho})$, and their distribution along the wetted perimeter of a channel are critically important in regard to loose-boundary hydraulics. Most physical modelling studies of the local scouring phenomenon around bridge piers (Laursen and Toch, 1956, 1962; Karaki, 1959; Liu et al., 1961; Shen, 1966; Melville, 1975; Ettema, 1980; Chiew, 1984; Dargahi, 1987; and Kothyari et al. 1992) and abutments (Ahmad, 1953; Garde et al., 1961; Gill, 1972; Cunha, 1975; Rajaratnam and Nwachukwu, 1983a, 1983b; Zaghloul, 1983; Kwan, 1984, 1988; and Kandasamy, 1985, 1989) were conducted in laboratory flumes of rectangular cross-section in which the effects of lateral momentum transfer were not considered.

In a compound flume, however, the aforementioned momentum transfer mechanism and its impact on both velocity and boundary shear stress distribution cannot be ignored. The phenomenon of interaction between flow in the MC and that over the FP of a compound channel has been studied extensively (Zheleznyakov, 1965, 1971; Sellin, 1964; Townsend, 1968; Myers, 1975, 1977; Knight, and Demetriou, 1983; Knight and Shiono, 1990). Sellin (1964) and Zheleznyakov (1965, 1971) observed a bank of vortices having vertical axes along MC/FP junctions. These vortices transfer momentum between the deep section of the MC and the shallow FP by their continuous emergence and decay. Therefore, as a consequence of flow interactions the MC flow velocity and discharge are decreased immediately above bankfull depth, while those FP values are increased. Zheleznyakov (1965, 1971),however, showed that as the depth increases further, MC velocity and discharge begin to increase again towards bankfull values.

Myers and Elsawy's (1975) study of the interaction phenomenon quantified the effects of the lateral momentum flux on both the value and the distribution shape of the boundary shear in the MC and FP of an asymmetric compound flume. They compared measured values of shear stress obtained under an *interaction* condition with those for an *insulated* flow, i.e. the FP flow was isolated from the MC flow using a vertical plate at the MC/FP junction. They observed a symmetrical boundary shear pattern in the FP under the non-interaction condition, while, the presence of *interaction* increased FP shear stress values and altered the distribution shape significantly.

Under an *interaction* condition, the MC supplies energy to the FP, which increases the shear stress in that region. According to Myers and Elsawy's data, for the shallowest depth in the FP considered, the average FP shear was doubled and its maximum value was increased by a factor of 2.6 under an interaction condition (Figure 2.42). However, since the intensity of the phenomenon decreases as the FP flow depth increases, the changes in the shear stress (value and distribution) become smaller at higher FP flow depths. Nevertheless, Figure 2.42 shows that even at a relatively high ratio of FP depth, y_a to total flow depth, H, $\frac{y_a}{H}=0.38$, a considerable increase in the average (50%) and the maximum (30%) FP boundary shear still exists.

Although based on a limited experimental investigation in an asymmetric small-scale compound flume having vertical walls, Myers and Elsawy's results indicate that lateral momentum transfer has significant impact on the boundary shear stress (value and distribution) in compound flume flow. Failure to account for the existence of such a mechanism might result in an erroneous analysis.

Using a symmetrical compound channel having vertical walls and considering a relative flow depth ratio in the range $0.1 \leq \frac{y_a}{H} \leq 0.5$, Knight and Demetriou (1983) studied the discharge characteristics, the shear stress and shear force distribution acting on the MC and FP boundaries. Using ratios of $\frac{B}{b}$ = 1, 2, 3, and 4 (in which B = total width and b = MC width), they presented relationships to estimate apparent shear forces acting on the vertical interface between the MC and one FP, ASF_V, and acting on the horizontal plane at the bankfull elevation, ASF_H, as a percentage of the total shear force, i.e. $\rho g A S_o$. The results of Knight and Demetriou indicate that the value of the apparent shear force acting on the vertical interface between one FP and the MC is highly depth dependent, especially for large ratios of total width to MC width, B/b. As B/b increases the percentage of ASF_V values systematically increase for $y_a/H<0.3$ and systematically decreases for $y_a/H>0.3$. The apparent shear force acting on the vertical interface is always positive, which indicates that the FP flow retards the MC flow (Knight and Demetriou, 1983). While the apparent shear force acting on the horizontal interface varies with B/b and y_a/H, it might take positive or negative values, simulating both acceleration or retardation effects.

The interaction between MC and FP flows was also studied by Rajaratnam and Ahmadi (1979). In their studies a 1.22 m wide straight compound channel was modified to a symmetrical compound cross-section having a MC width of 0.203 m and two FP zones each 0.507 m in width. Reporting the effects of flow interaction and momentum transfer on both longitudinal and transverse velocity distributions in the MC and FP, Rajaratnam and Ahmadi concluded that the FP and MC velocity profiles above the bankfull level (FP level) are approximately similar if they reviewed with respect to the undisturbed FP velocity. To draw a more general conclusion, the same study was performed by Rajaratnam and Ahmadi (1981) using a compound channel having a wider MC than that of the former study in order to eliminate the effect of the interaction on a narrow mid-MC strip of the flow. They found that the apparent shear stress at the vertical plane of the MC/FP junction is mainly a function of H/y_a and the variation across the mixing region of the FP is significant. They also indicated that, even in the mixing region of the FP, the velocity profiles in the vertical direction follow the logarithmic law provided that the local shear velocity is used.

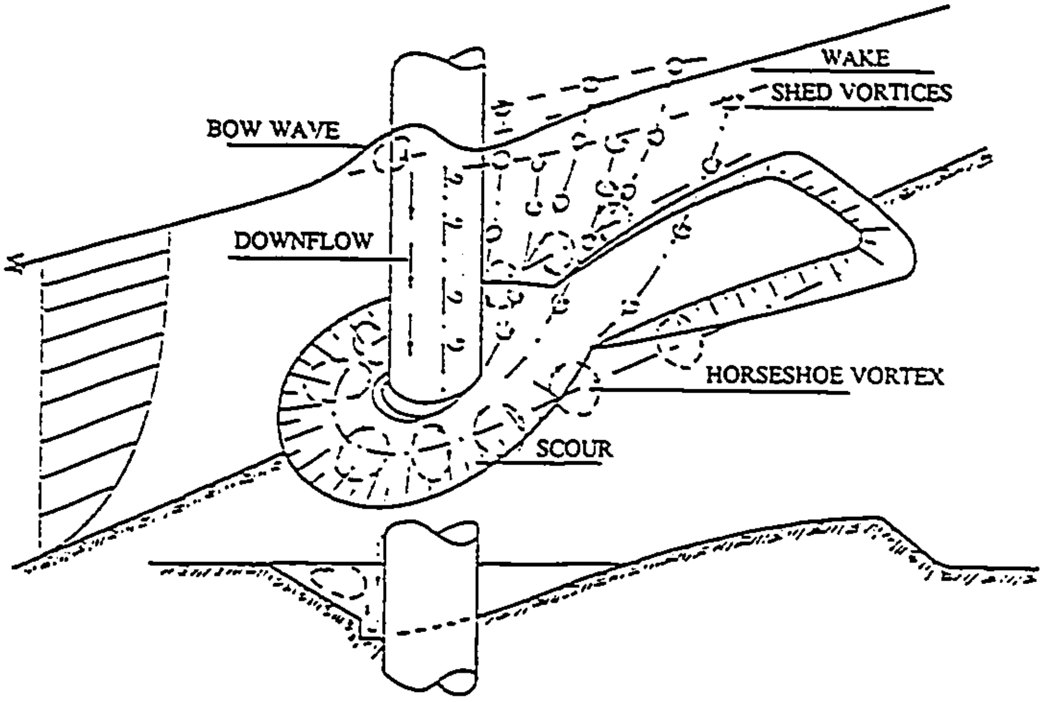

Figure 2.1- Diagrammatic representation of the flow pattern adjacent to a cylindrical pier (Raudkivi 1991)

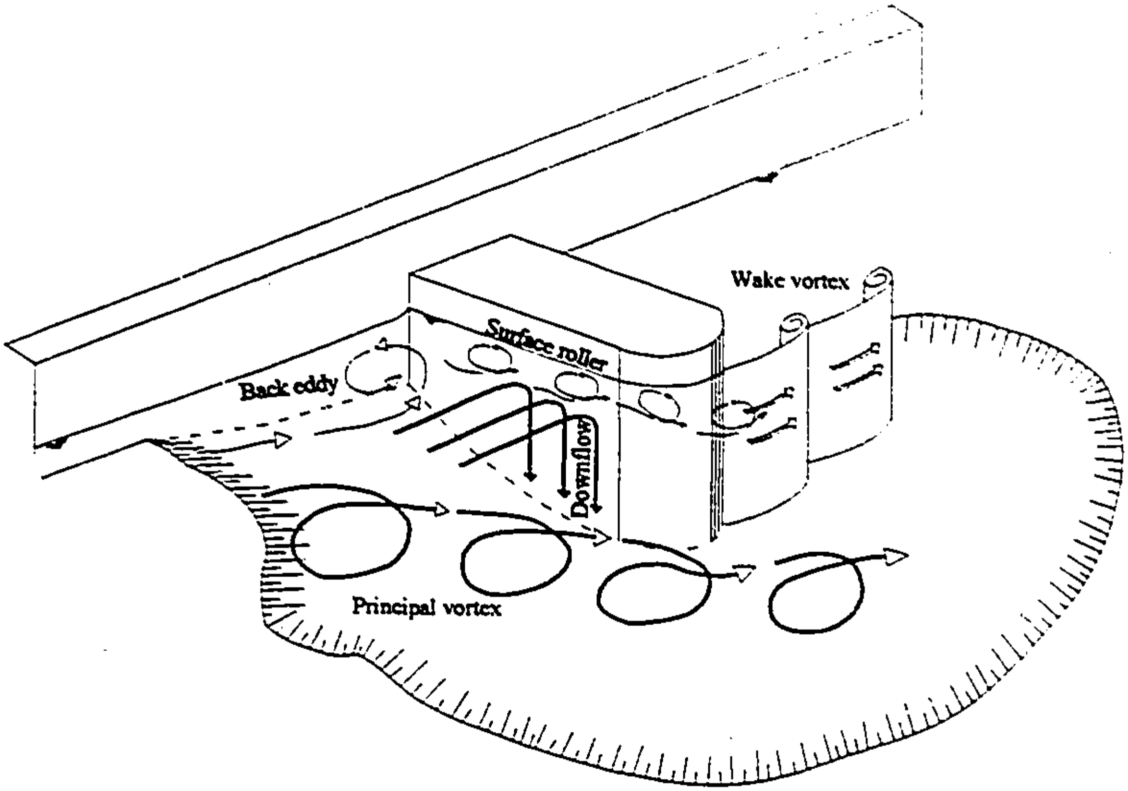

Figure 2.2- Flow structure around a semi-circular (SC) abutment

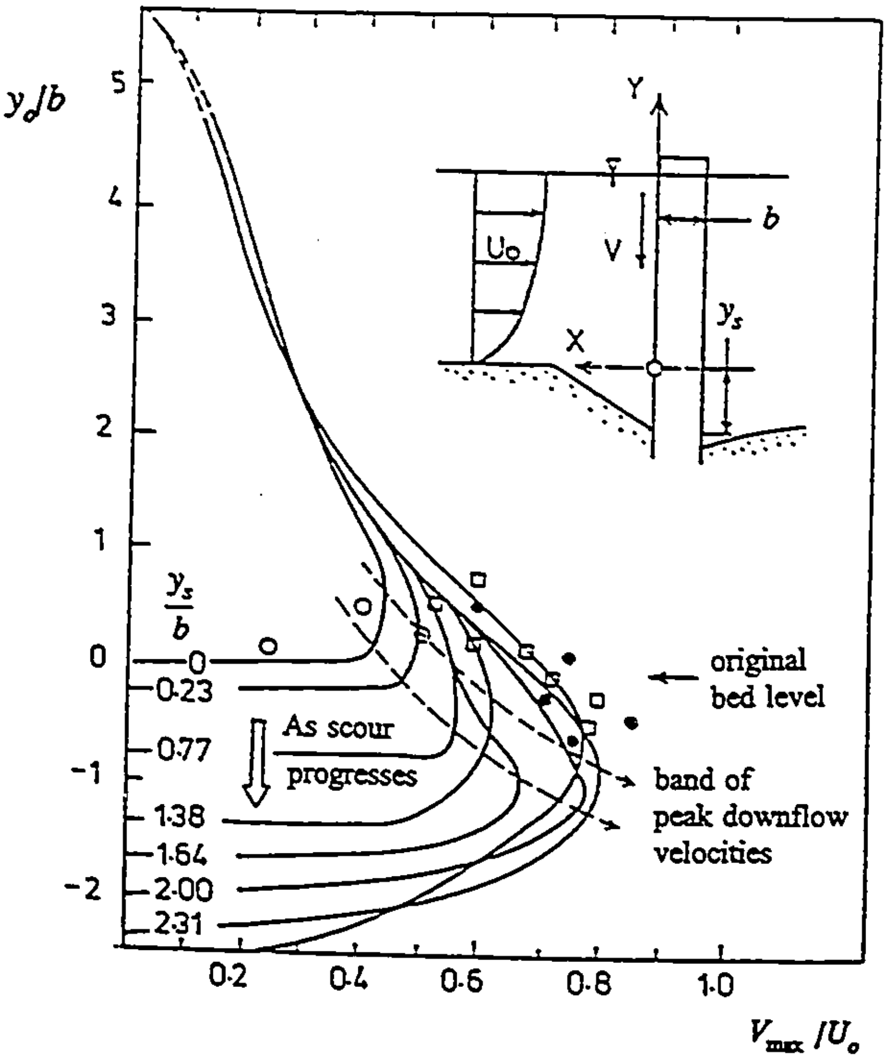

Figure 2.3- Pier downflow velocities at different stages of scour Melville's (1975) and Ettema's (1980) data

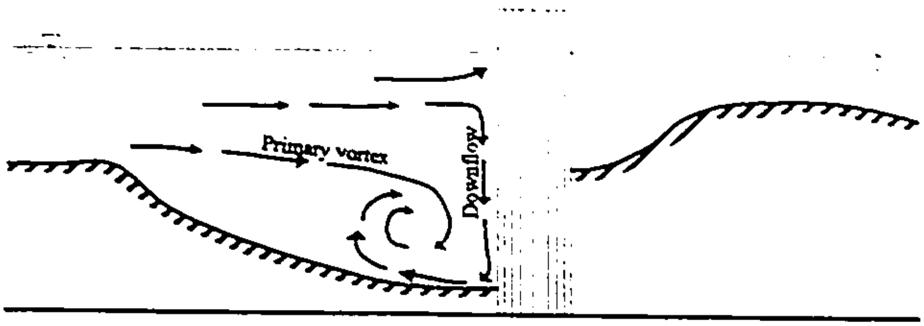

Figure 2.4- Downflow and primary vortex

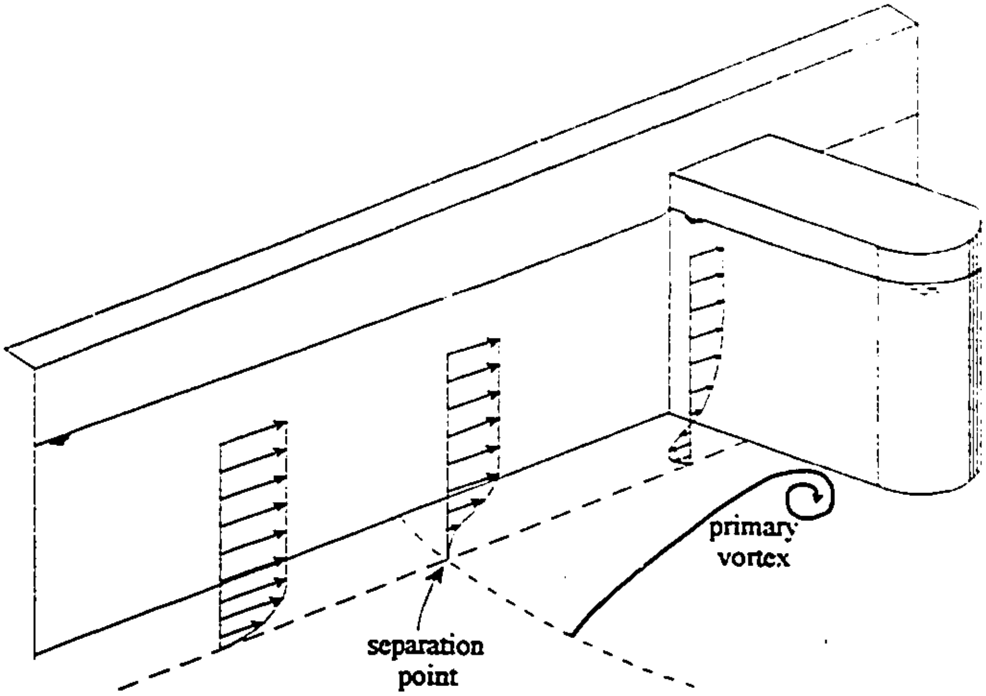

Figure 2.5- Separation of boundary layer and primary vortex formation

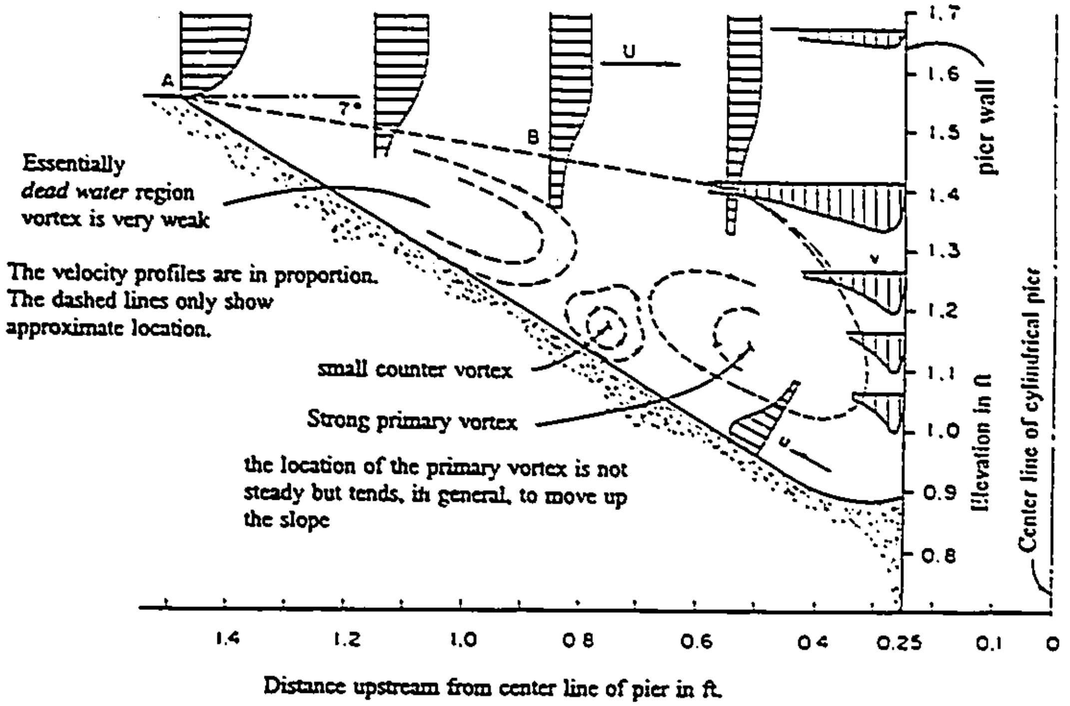

Figure 2.6- Flow pattern in a scour hole according to velocity measurements of Shen et al (1966)

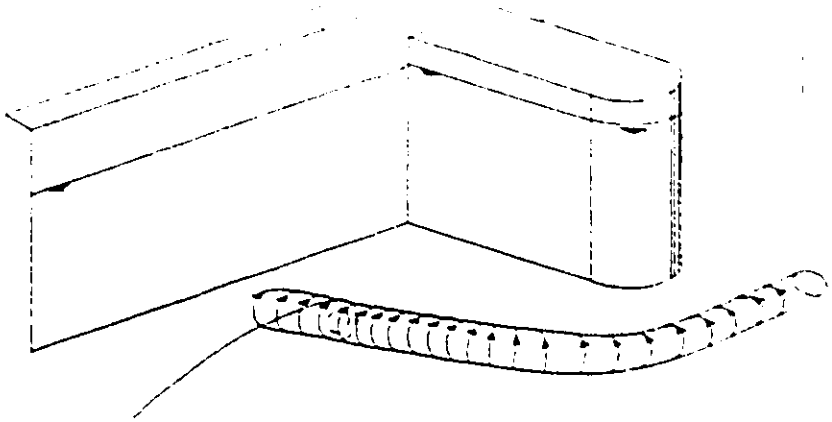

Figure 2.7- Skewed primary vortex around an abutment

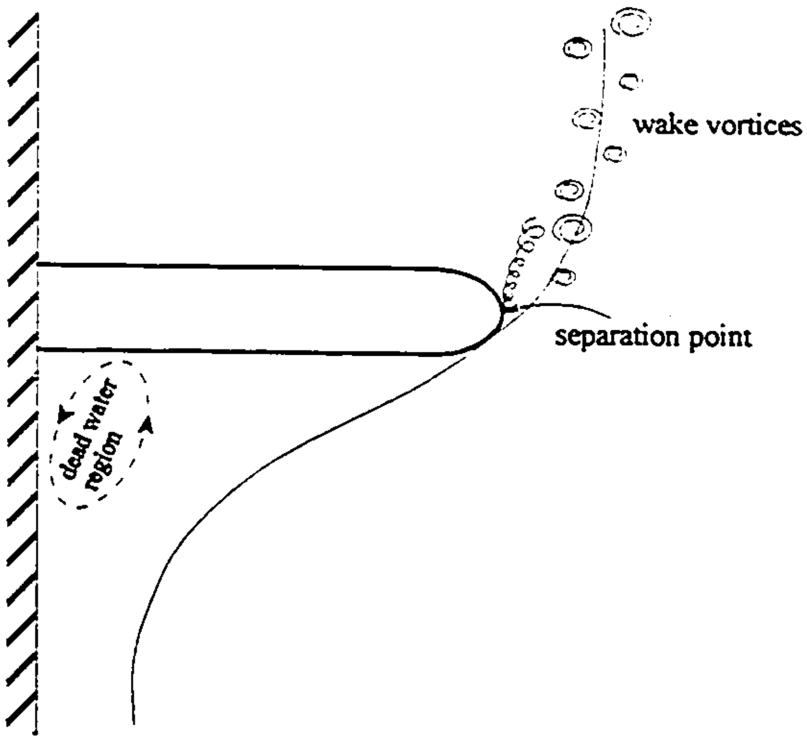

Figure 2.9- Flow separation and wake vortices around SC abutment

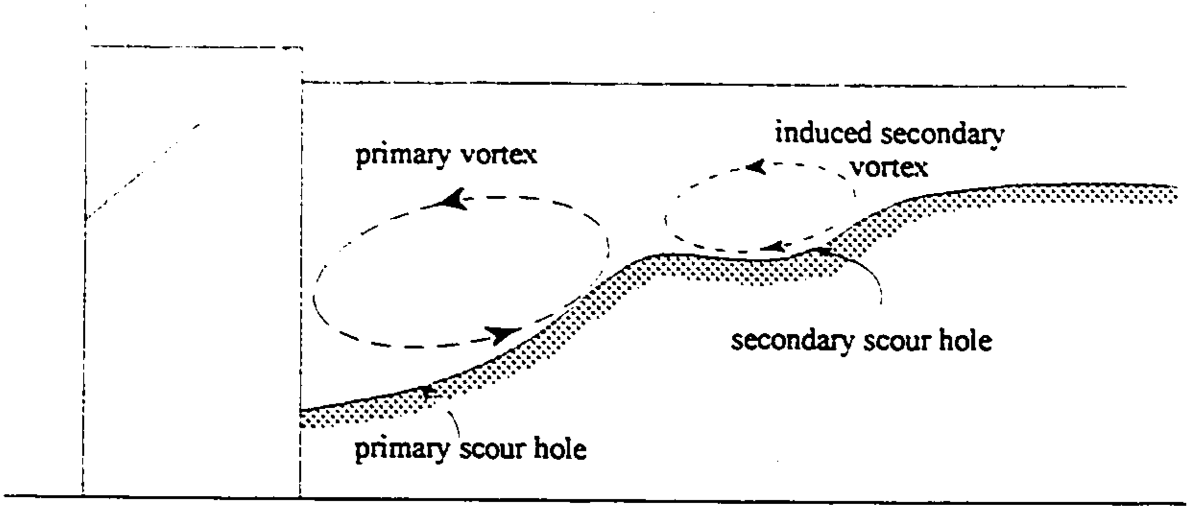

Figure 2.8- Conceptualised model of secondary vortex formation (Kwan 1988)

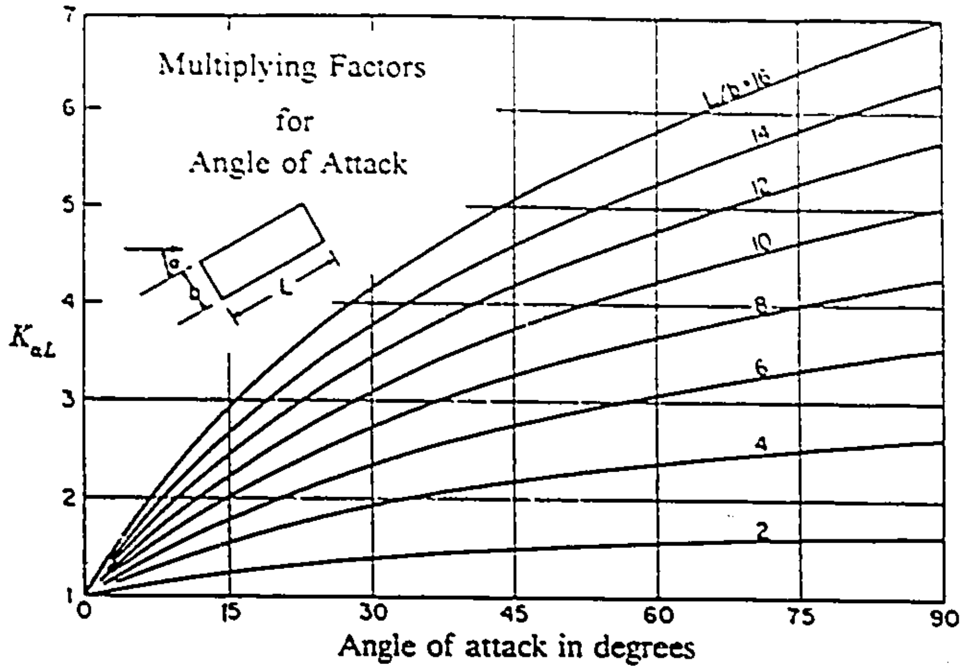

Figure 2.10- Design factors for piers not aligned with flow (Laursen and touch 1956)

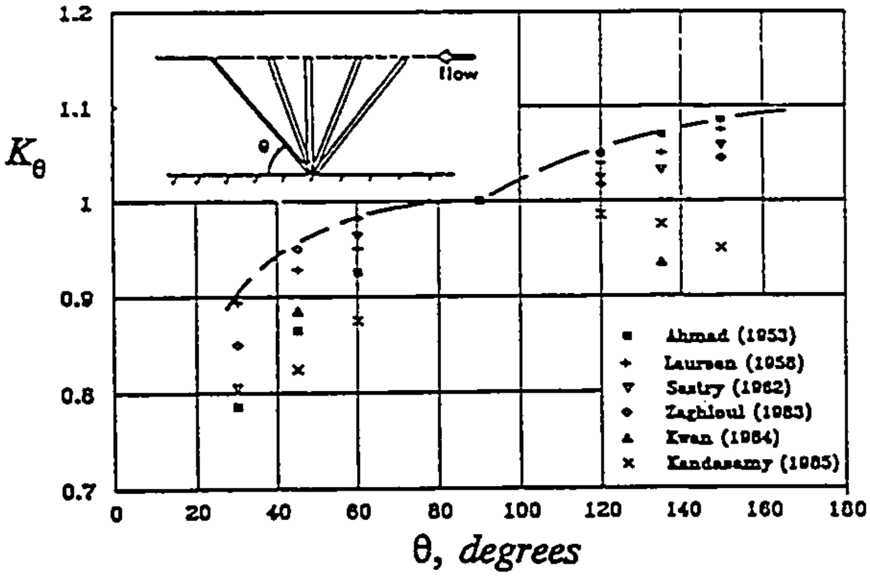

Figure 2.11- Influence of abutment alignment on scour depth (Melville, 1992)

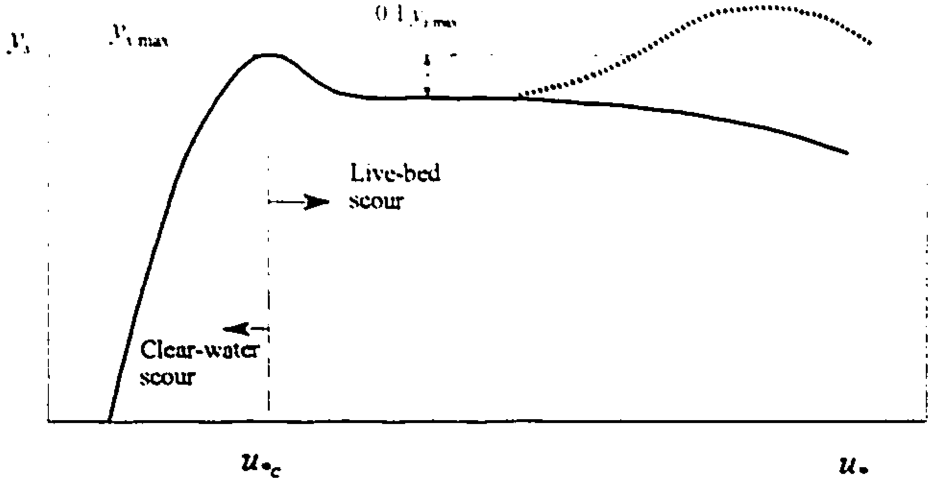

Figure 2.12- Scour depth as a function of shear velocity or approach velocity (Raudkivi, 1986)

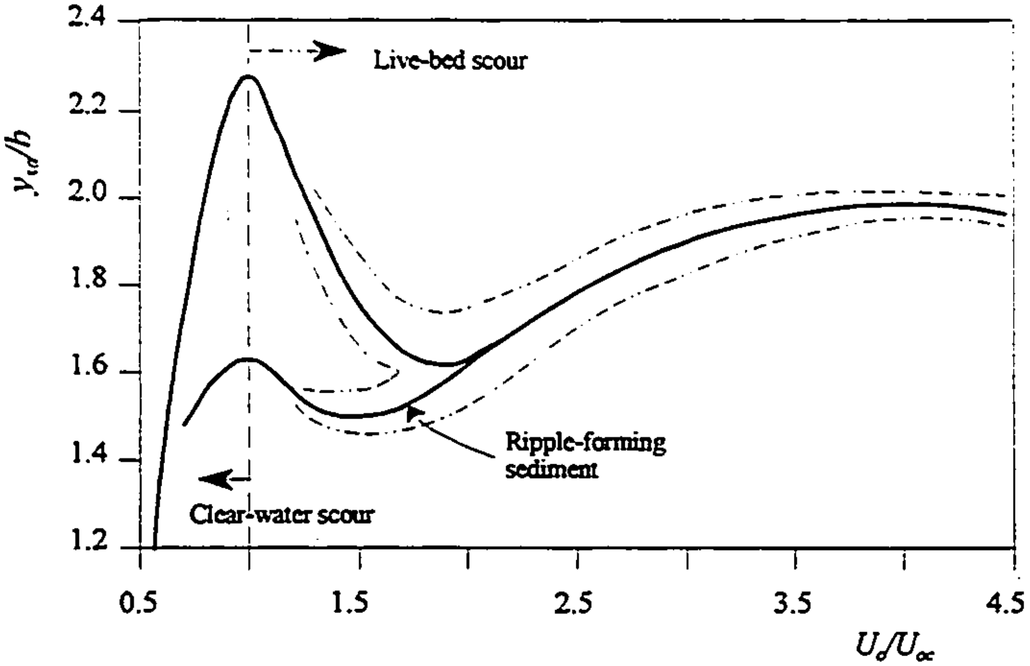

Figure 2.13- Diagrammatic illustration of scour depth at a cylindrical bridge pier in a uniform sediment (Raudkivi, 1986)

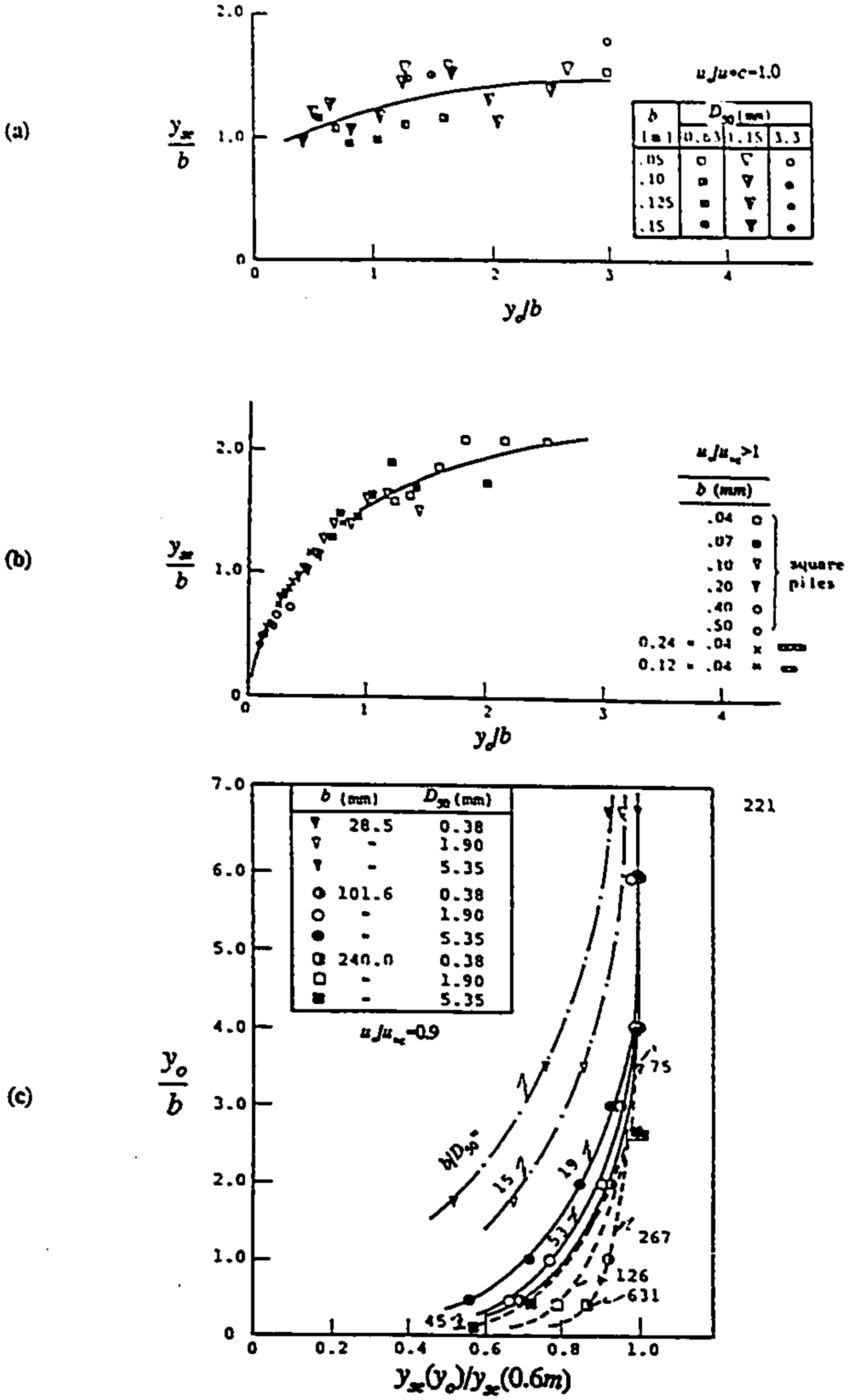

Figure 2.14- Relative equilibrium scour depth versus y_o/b

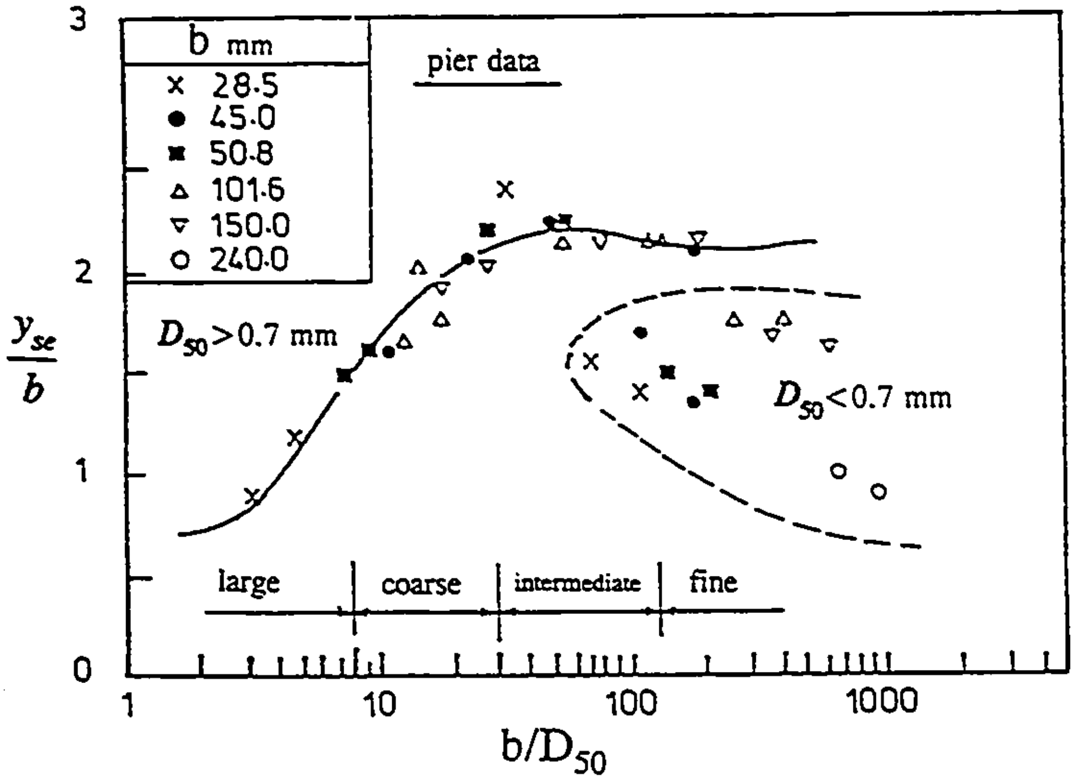

Figure 2.15- Scour depth as a function of the parameter b/D_{50} (Ettema 1980)

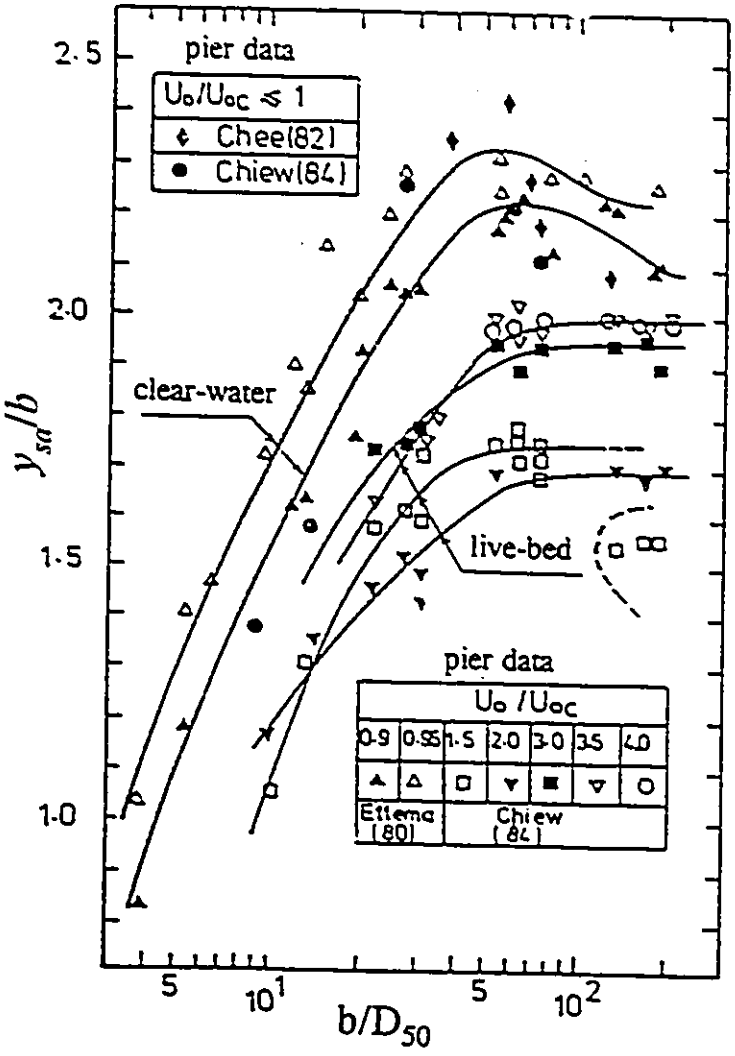

Figure 2.16- Relative equilibrium scour depth versus b/D_{50} at various values of U_o/U_{oc} (Chiew 1984)

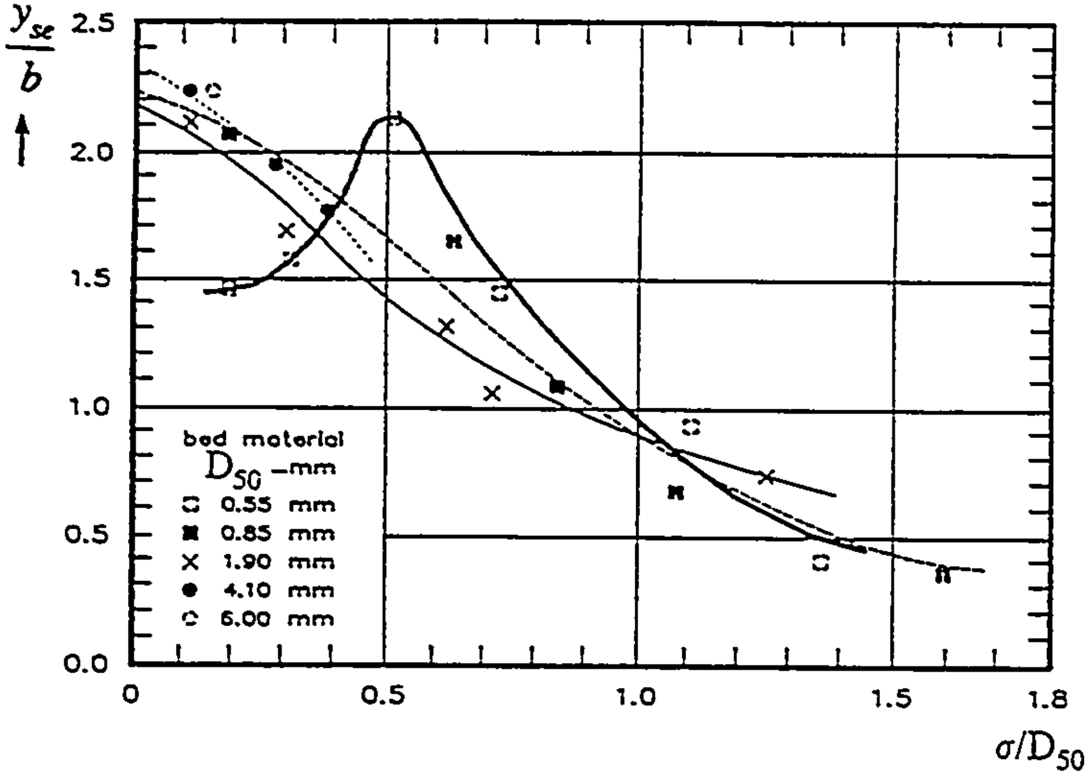

Figure 2.17- Equilibrium clear-water scour depth divided by pier diameter, y_{se}/b, as a function of the sediment grading, $u_*=u_{*c}$ (Raudkivi and Ettema 1977)

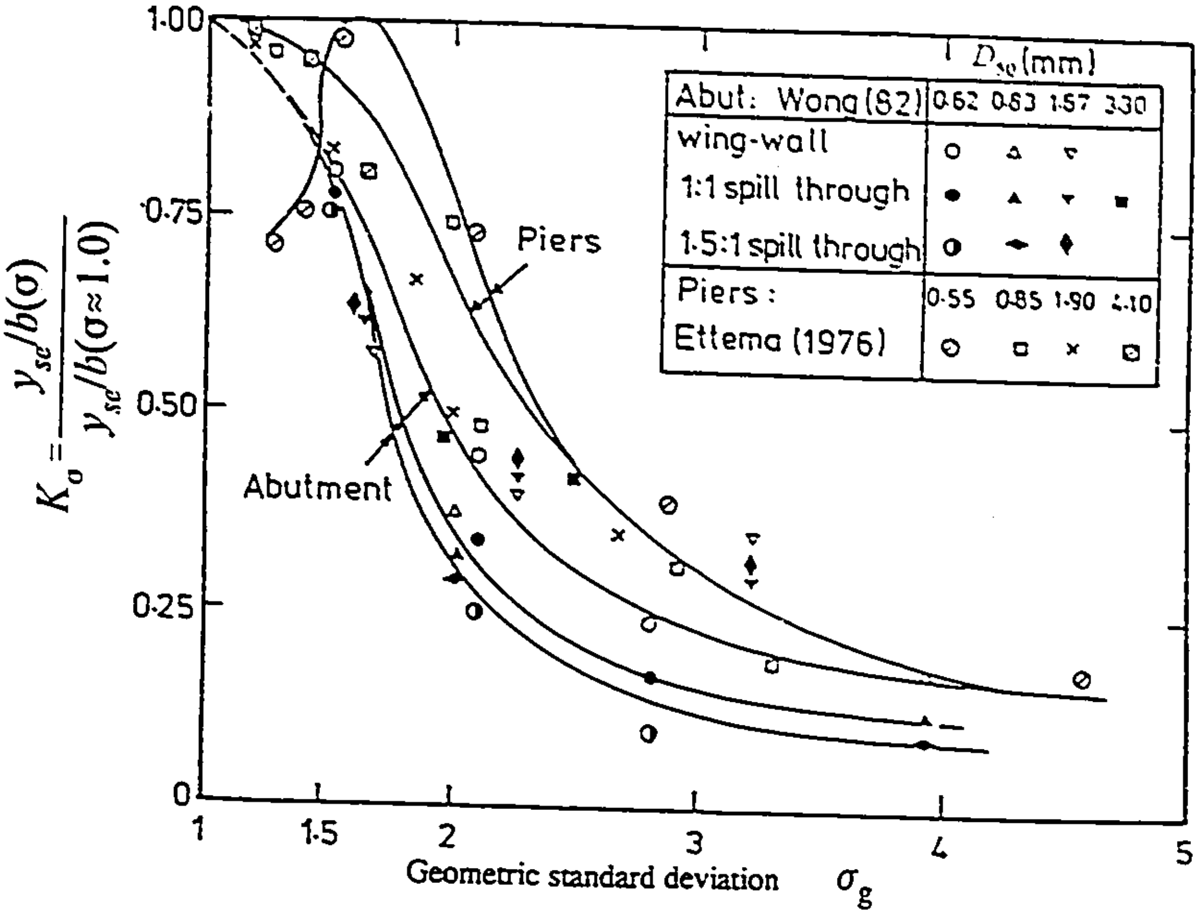

Figure 2.18- Values of K_σ coefficient with σ_g at $u_* / u_{*c} = 0.95$ (data of Ettema 1976 and Wong 1982)

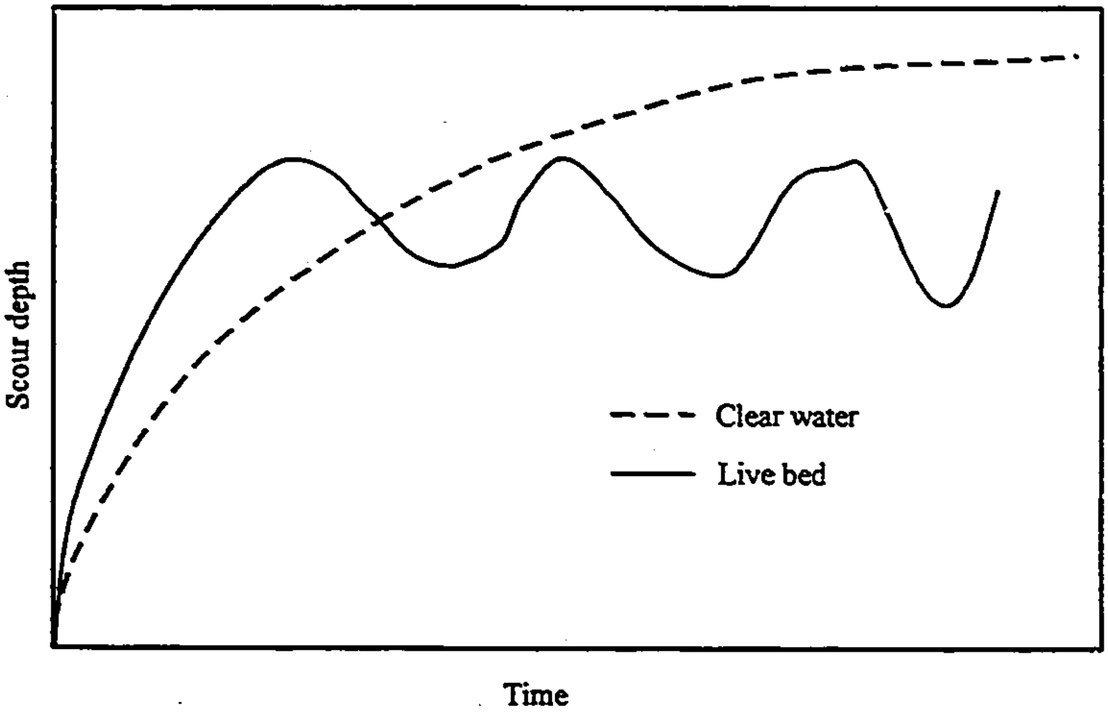

Figure 2.19-Temporal scour depth development in live-bed and clear-water conditions

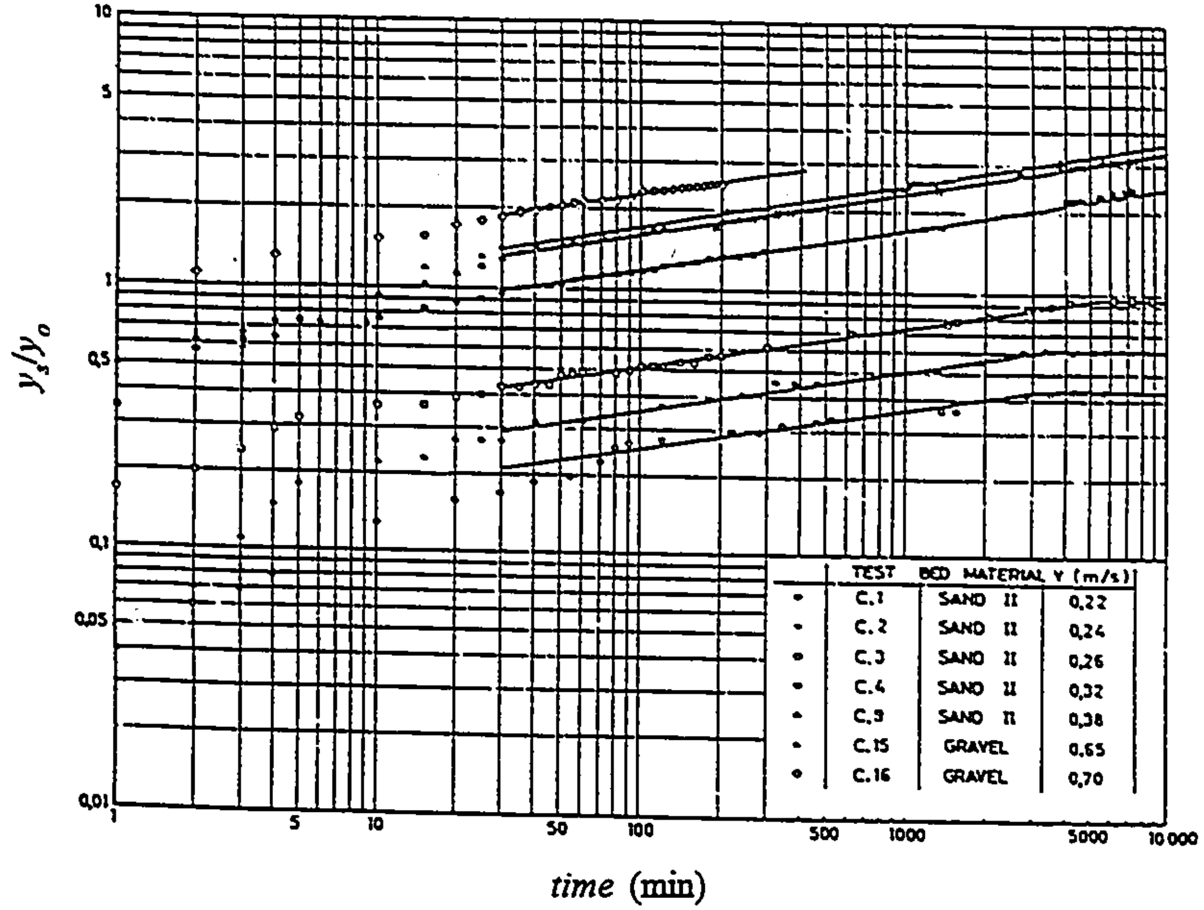

Figure 2.20- Temporal development of clear-water scour depth according to Cunha's (1975) data

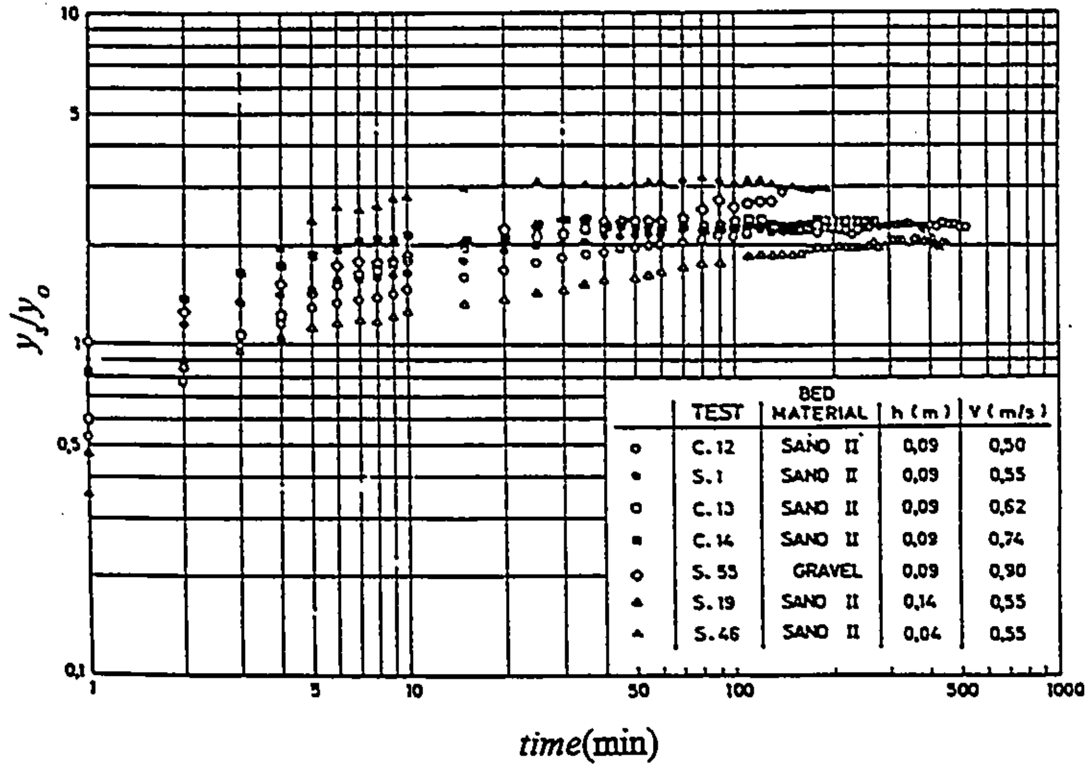

Figure 2.21- Temporal development of live-bed scour depth according to Cunha's (1975) data

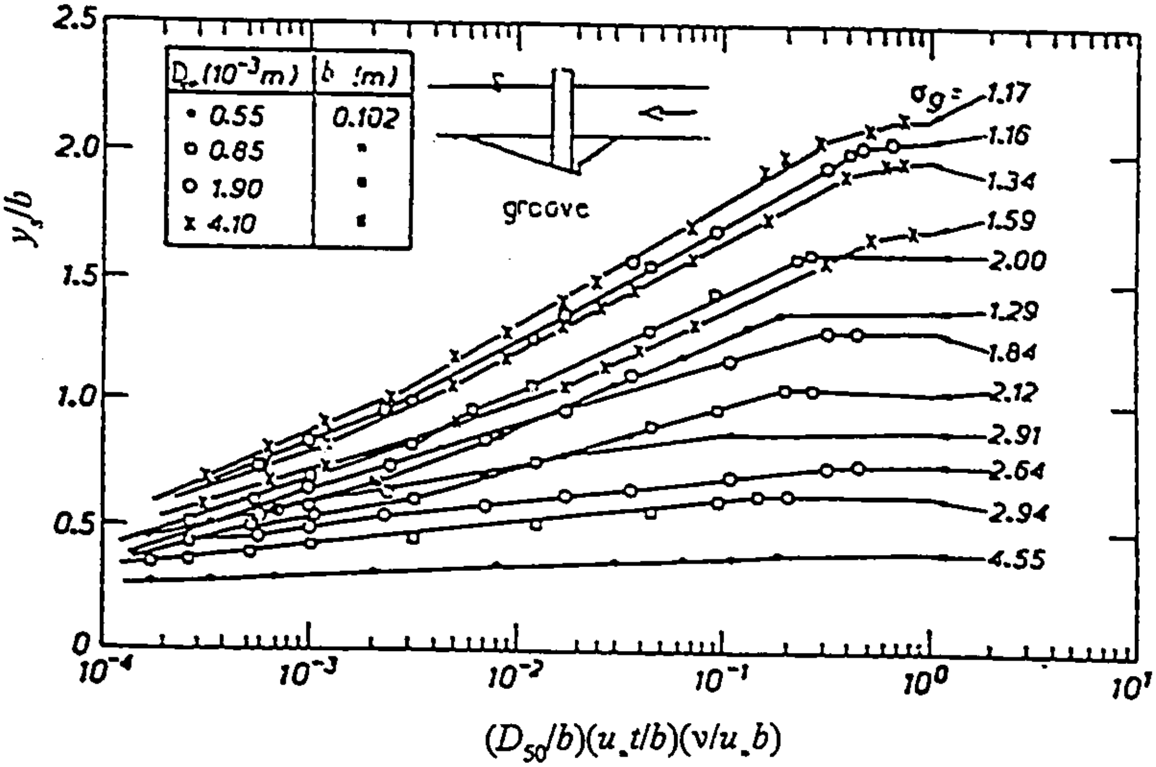

Figure 2.22- Normalized scour depth at a circular bridge pier as a function of time in nonuniform bed sediment (Ettema and Raudkivi, 1982)

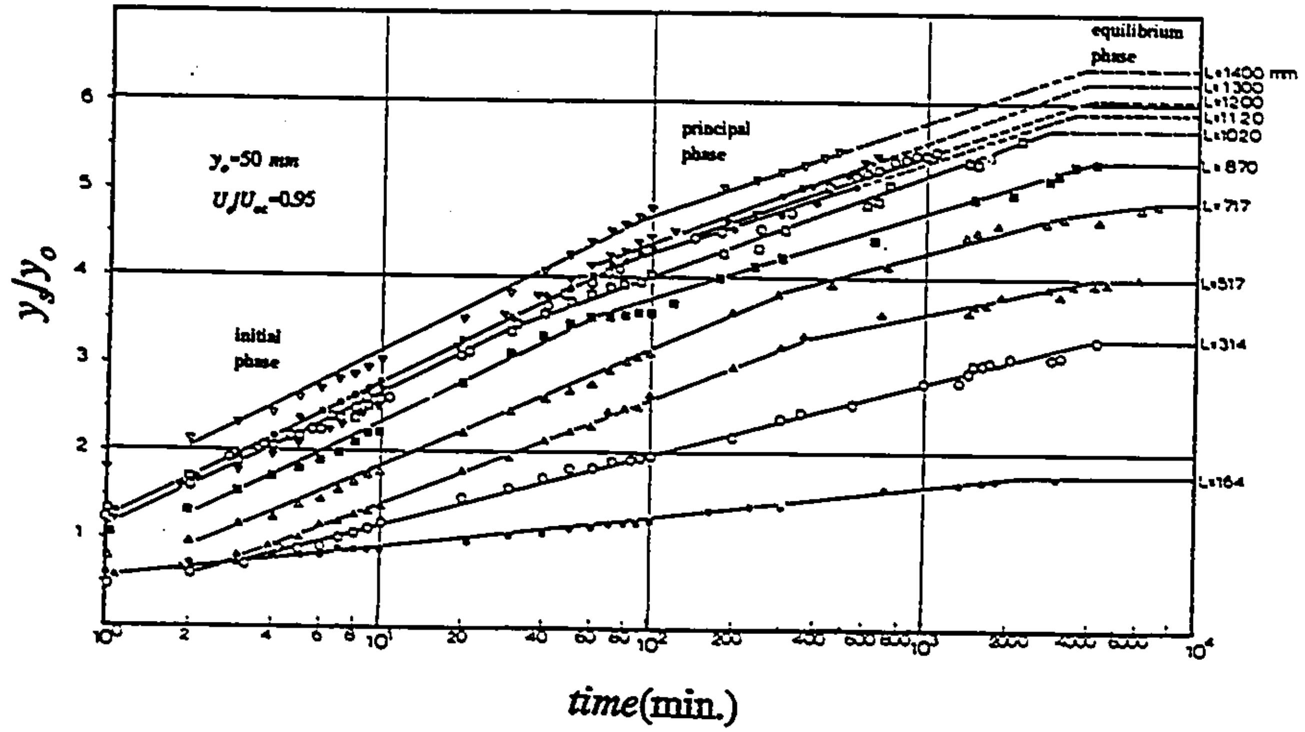

Figure 2.23- Temporal scour development around abutments of various lengths according to Kwan's (1984) data

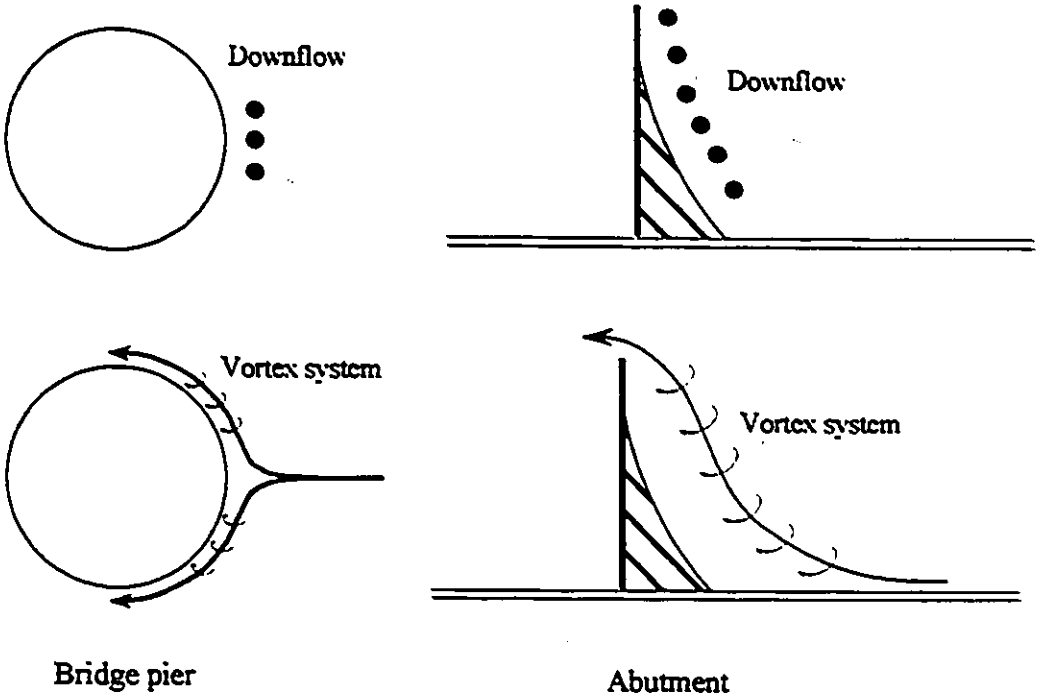

Figure 2.24- Downflow and vortex system at bridge piers and abutments (Kwan 1984)

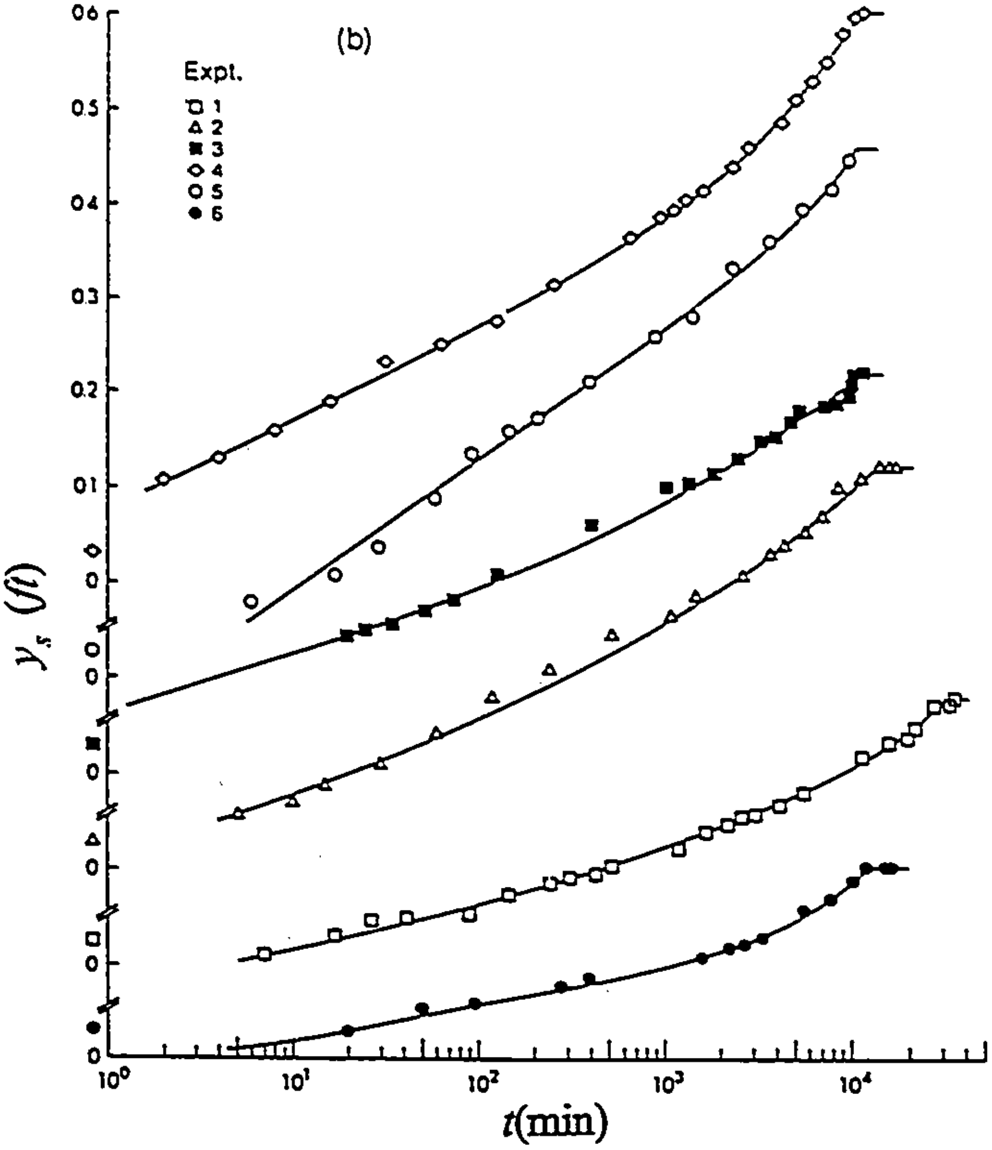

Figure 2.25- Erosion development with time according to spur-dike study of Rajaratnam and Nwachukwu (1983)

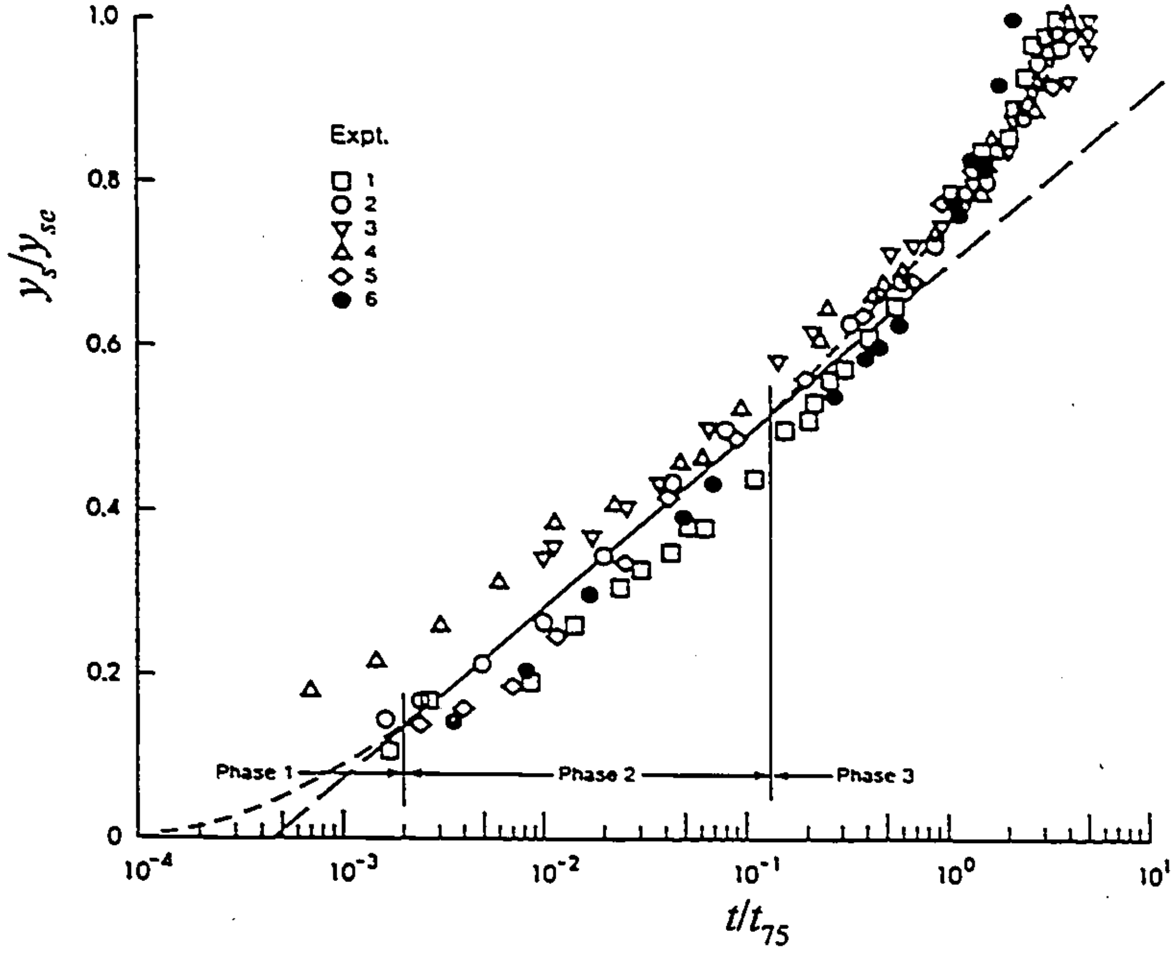

Figure 2.26- Similarity of scour hole development according to Rajaratnam and Nwachukwu's(1983) data

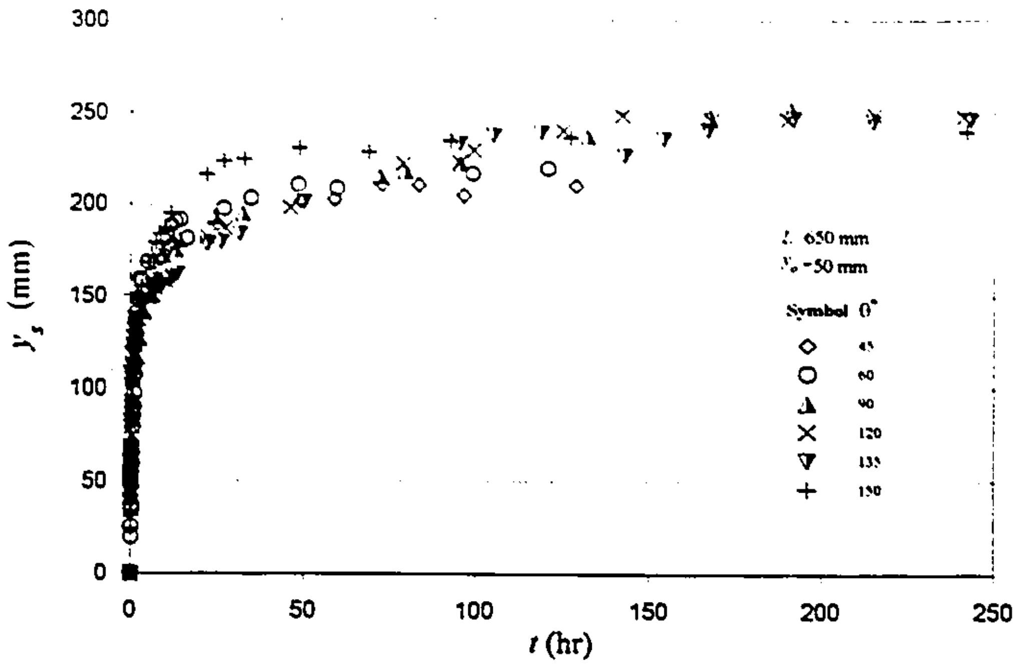

Figure 2.27-Temporal scour development according to data of Kandasamy (1985) for skewed abutments

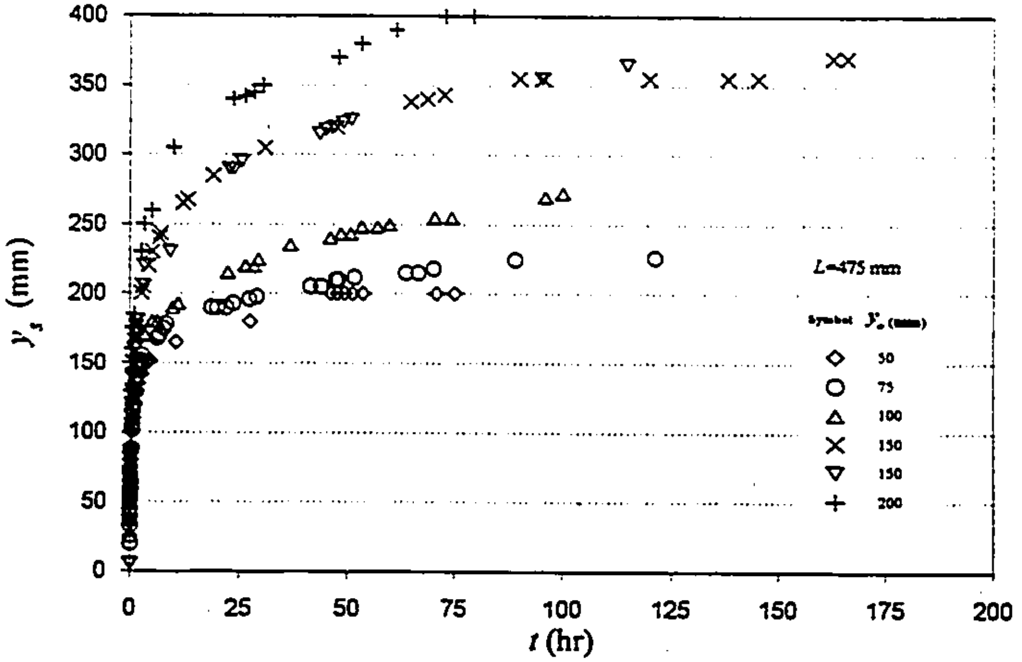

Figure 2.28-Temporal scour development according to data of Kwan (1989)

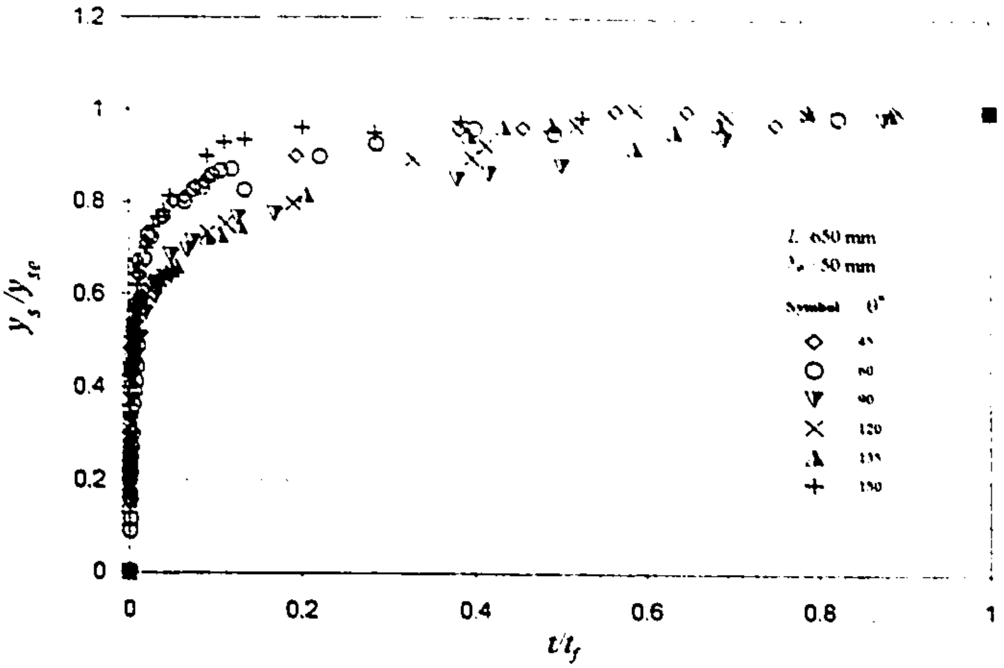

Figure 2.29-Normalized data of Kandasamy (1985) of temporal scour development for skewed abutments

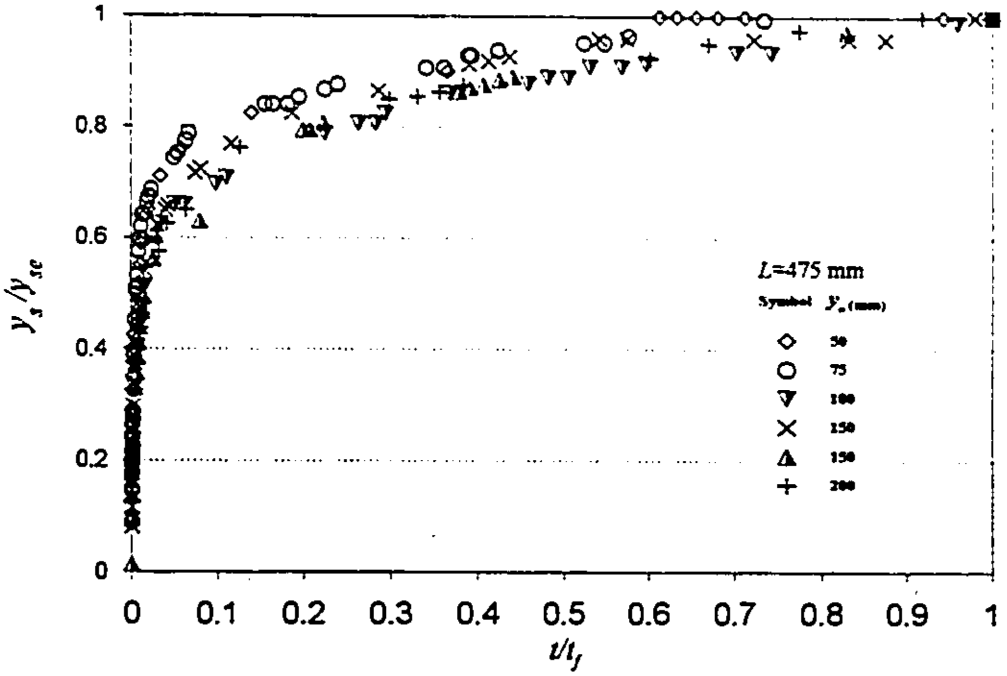

Figure 2.30- Normalized data of Kwan (1989) of temporal scour development at abutments

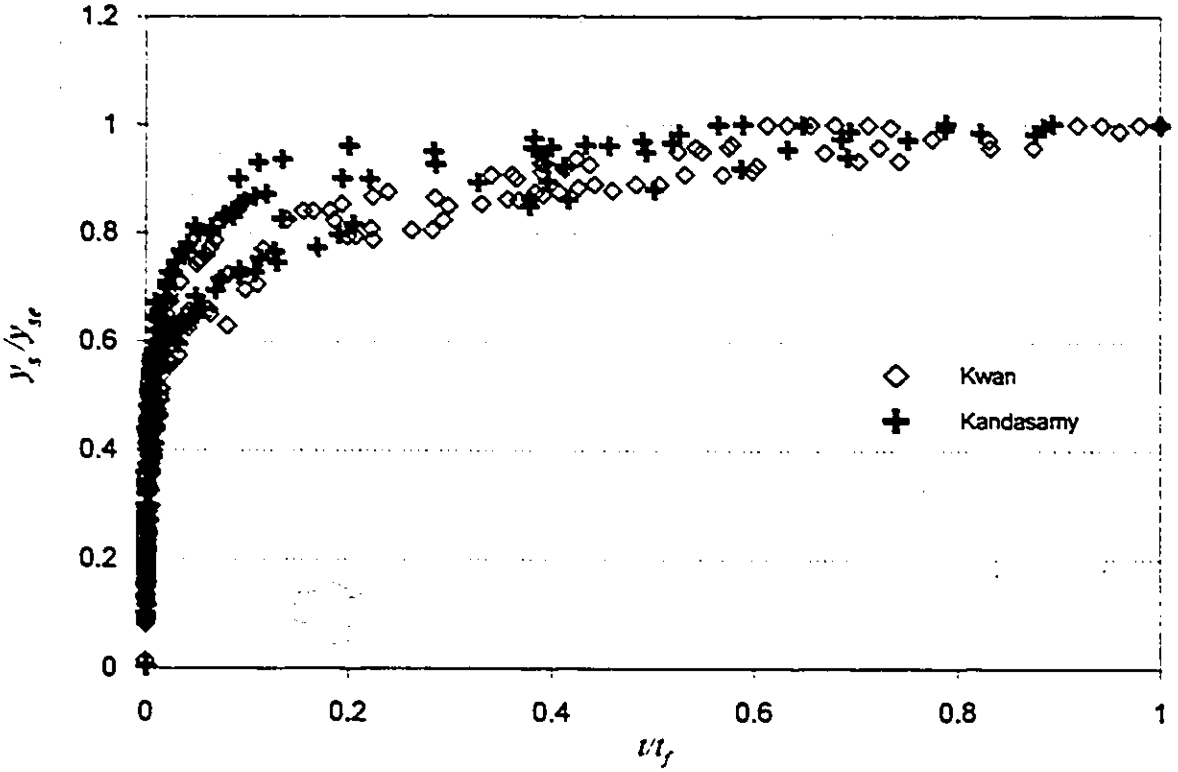

Figure 2.31-Normalized temporal scour development data of Kandasamy (1985) and Kwan (1989)

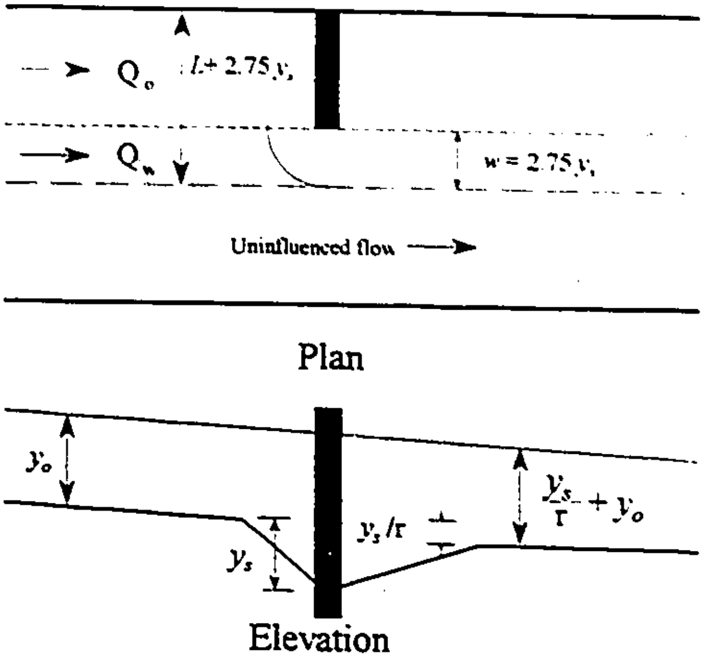

Figure 2.32- Definition sketch of overbank constriction (Laursen, 1962)

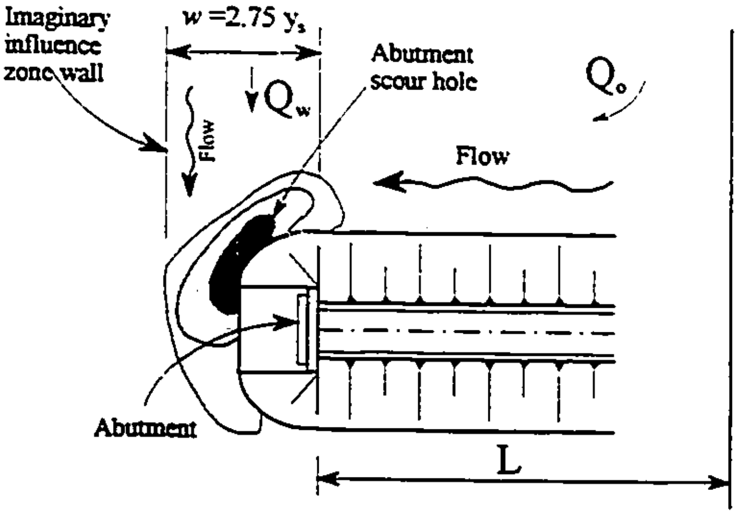

Figure 2.33- Typical scour at an abutment

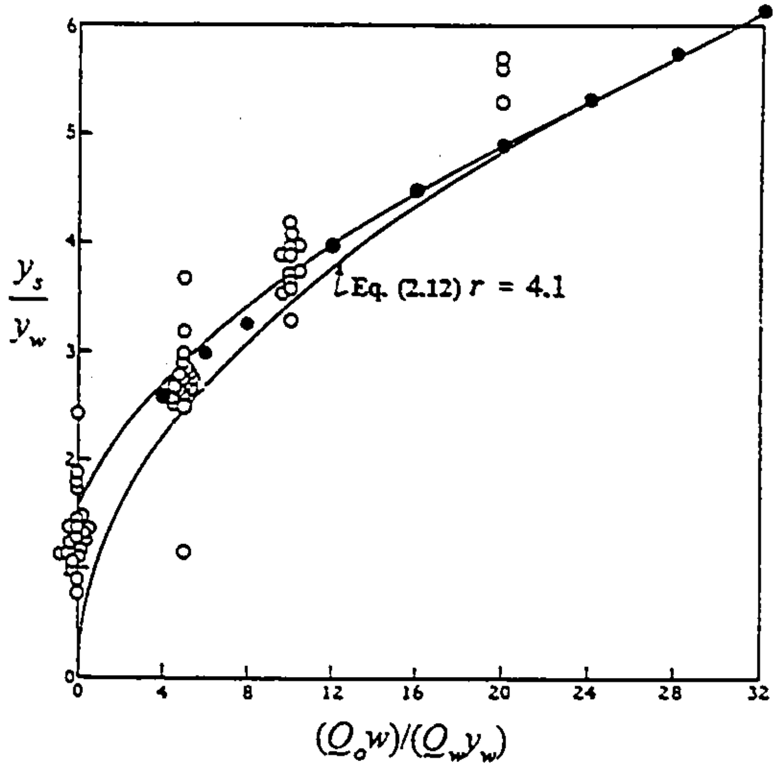

Figure 2.34- Scour at an overbank constriction

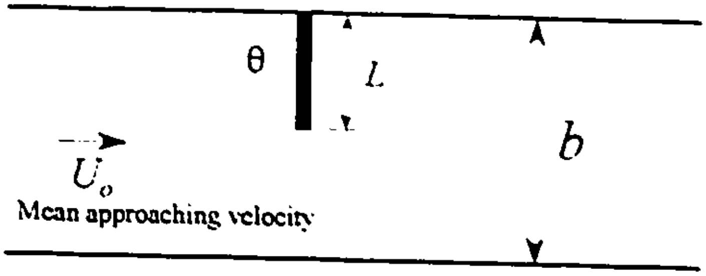

Plan

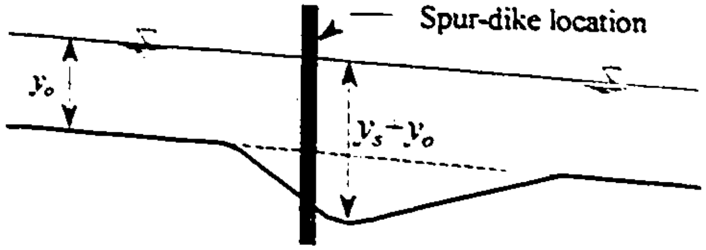

Elevation

Figure 2.35- Definition sketch of typical spur-dike

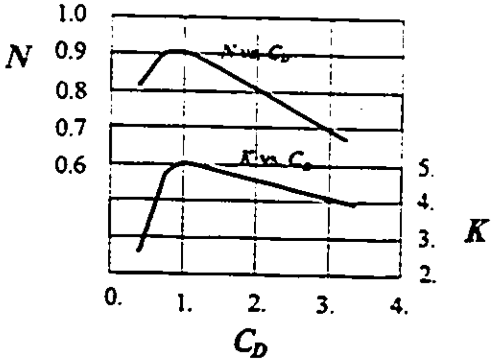

Figure 2.36- Variation of N and K with C_D (Garde et al. 1961)

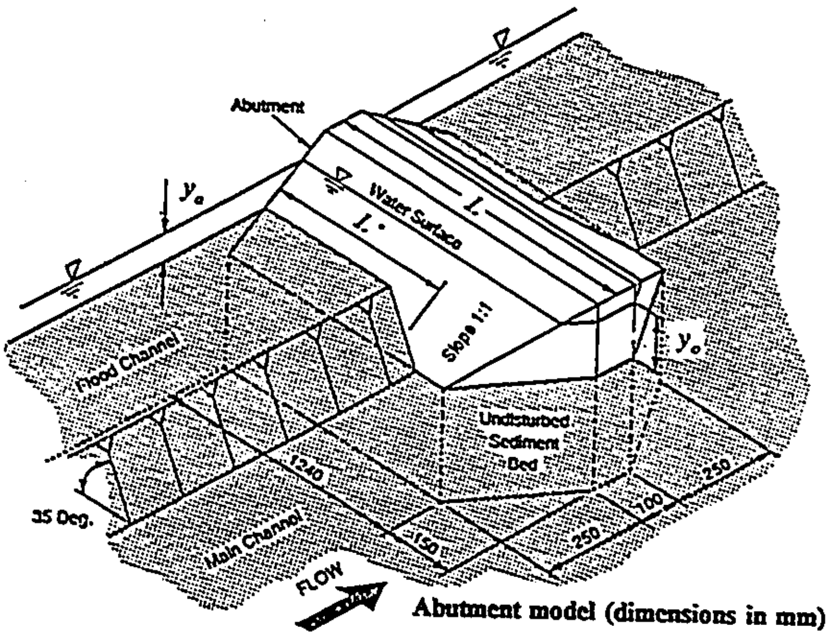

Abutment model (dimensions in mm)

Figure 2.37- The abutment model and approach channel geometry (Melville, 1995)

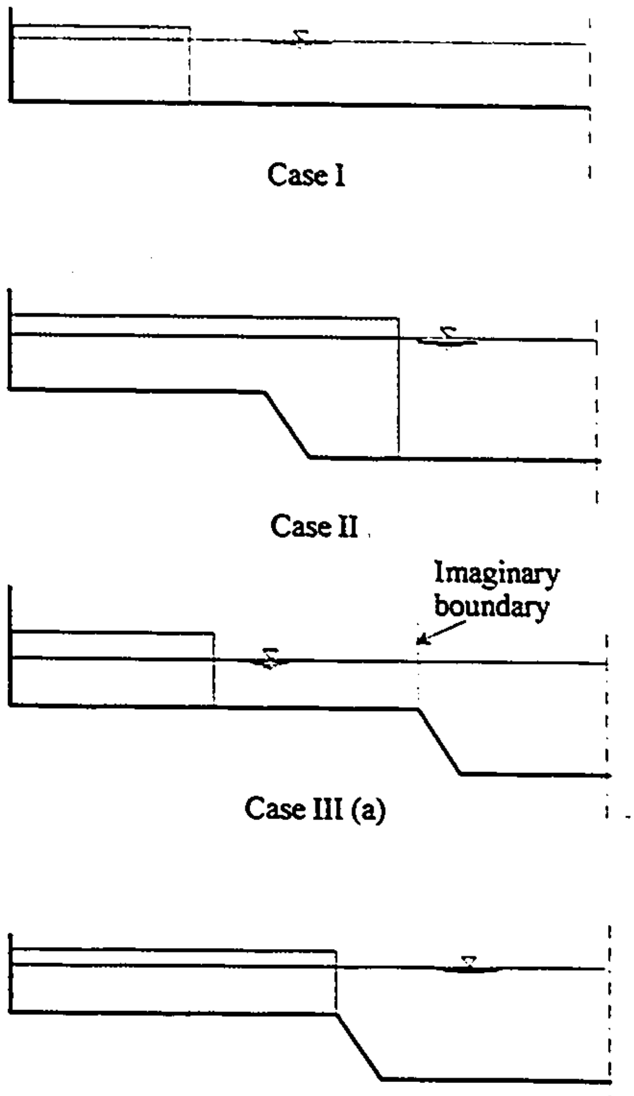

Figure 2.38- The three cases of bridge abutment scour (Melville, 1995)

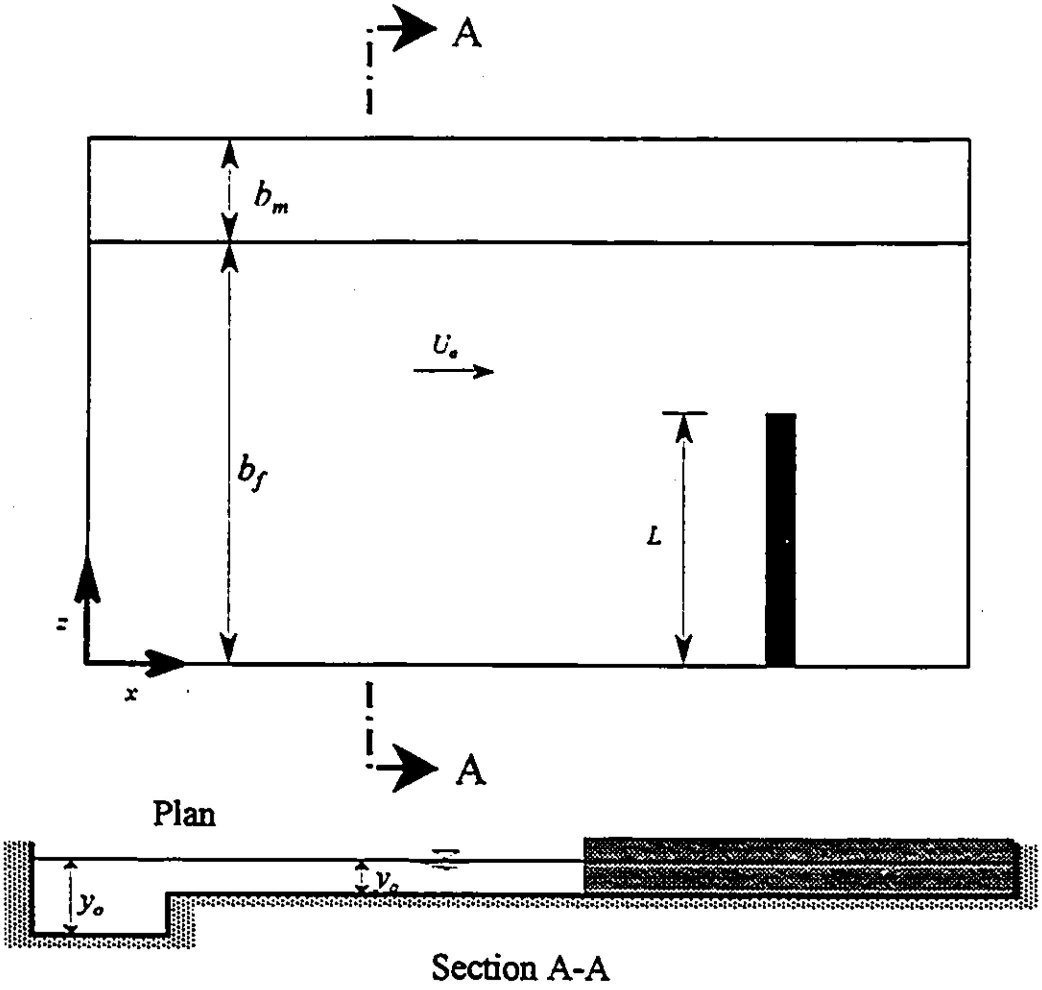

Figure 2.39- Definition sketch of Sturm and Janjua's (1993) laboratory flume

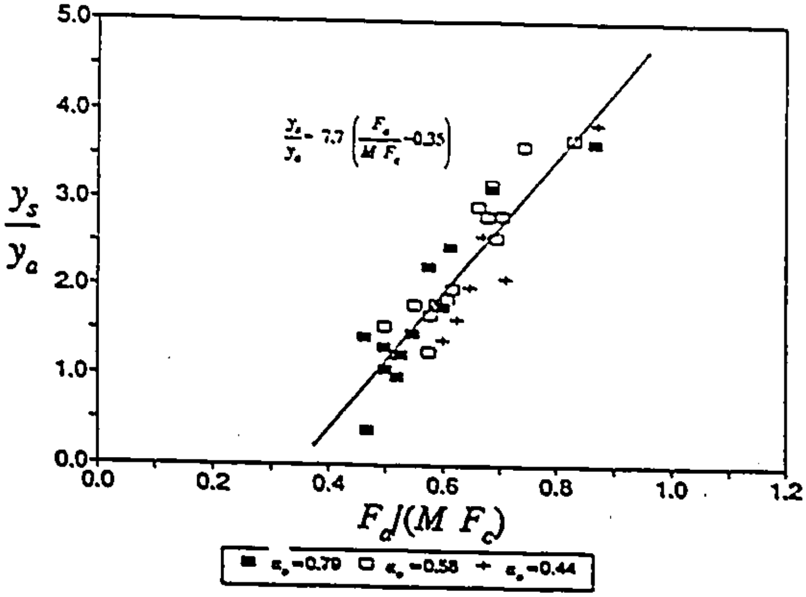

Figure 2.40- Correlation of y_s/y_a with $F_d/(MF_c)$ for sturm and Janjua's data (1994)

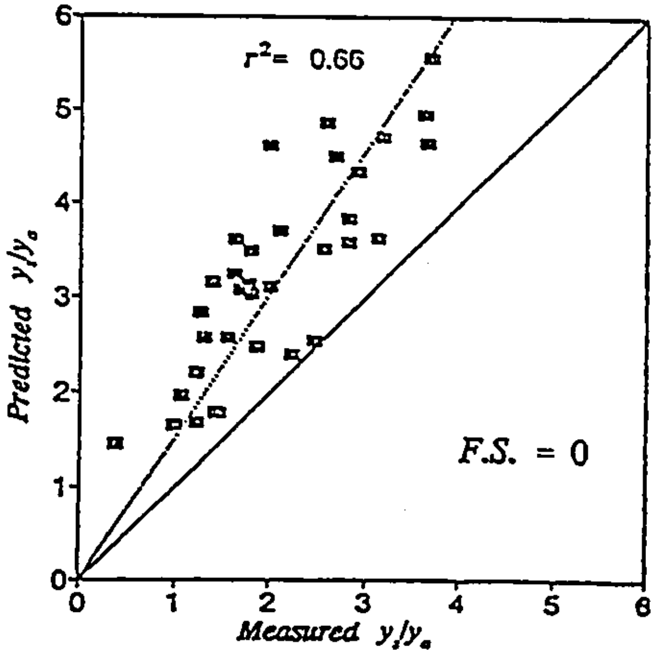

Figure 2.41- Comparison of sturm and Janjua's data (1993) with Froehlich's equation

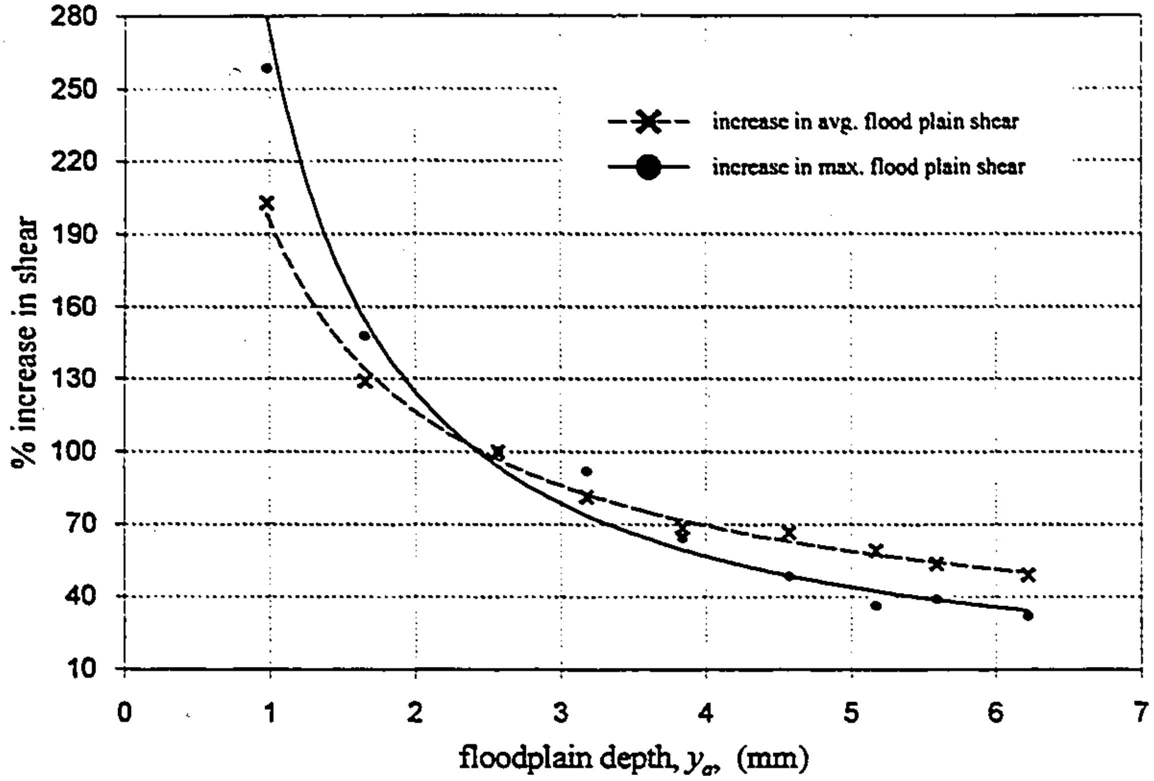

Figure 2.42- Increase in average and maximum floodplain shear due to MC/FP interaction, expressed as percentage of isolated floodplain value (Myers and Elsawy, 1975)

CHAPTER THREE

THEORETICAL CONSIDERATIONS

3.1- INTRODUCTION

Flowing liquid exerts hydrodynamic forces upon the wetted perimeter of any kind of conveyance system (open channel or closed conduit). If the bed materials consist of loose cohesionless particles of a given size, then a certain magnitude of the exerted hydrodynamic forces causes bed particles to move. However, particles of a given size move neither instantaneously nor universally. In fact, at any given hydraulic condition only some of the particles move.

The theoretical basis describing the threshold condition of particle movement is covered in the first section of this chapter. The second section reviews the universal velocity distribution law and the method by which the equivalent sand roughness can be evaluated. The third section deals with the dimensional analysis related to the scour phenomena considered in this study.

3.2- PARTICLE MOVEMENT

The equations describing the initial movement of bed particles were founded on several principles: the critical velocity (fluid impact on particles), the critical shear stress (the frictional drag of the flow on the particles), and the lift force criteria (the pressure differences due to the velocity gradient). Although the approaches seem to be different, it can be shown that they are not entirely dissimilar.

3.2.1- Critical velocity equations

Considering the angle of repose, φ, and the forces acting parallel, F_t, and normal, F_n, to it (Figure 3.1), it is shown (Appendix A) that the critical bottom velocity for initiating movement in a mass of cohesionless, loose, and solid particles can be expressed by:

$$\frac{u_{b_c}^2}{(\rho_s/\rho - 1)\, gD} = \frac{2k_3\,(\tan\varphi\,\cos\alpha - \sin\alpha)}{C_D\,k_1 + C_L\,k_2\,\tan\varphi} \tag{3.1}$$

in which u_{b_c} is the critical bottom velocity at which incipient sediment motion occurs, C_D, C_L = drag and lift coefficient, respectively, D = particle diameter, k_1, k_2, and k_3 = particle shape factors. The right-hand side of Equation 3.1 is termed the *sediment coefficient* A':

$$A' = \frac{2k_3\,(\tan\varphi\,\cos\alpha - \sin\alpha)}{C_D\,k_1 + C_L\,k_2\,\tan\varphi} \tag{3.2}$$

Equation 3.2 shows that the *sediment coefficient* is a function of: (*i*) the bed material (grain size, size distribution, shape, texture, etc.), (*ii*) the flow characteristics which determine C_D and C_L, (*iii*) the channel slope, and (*iv*) the angle of repose, which depends on particle properties.

3.2.2- Critical shear stress equations

Based on the relation between τ_o and u_b (Appendix A), Equation 3.1 can be written in terms of the critical shear stress, τ_c, at the incipient particle motion to take the form:

$$\frac{\tau_c}{(\gamma_s - \gamma)D} = A'' \qquad (3.3)$$

in which A''= a sediment coefficient. The threshold condition of particle motion might be presented as follows (Simons and Senturk, 1992):

$$\frac{\tau_c}{(\gamma_s - \gamma)\, D_s} = f\left(\frac{u_{*c}\, D_s}{\nu}\right) \qquad (3.4)$$

The left term of Equation 3.4, is the ratio of the drag force to the gravitational force, i.e., it is a type of Froude number expressed in terms of the shear velocity ratio and the grain size. The right hand side, however, is the particle Reynolds number, which is usually referred to as the *shear Reynolds number*, R_{e*}.

Field data for a wide range of grain sizes, from fine to coarse noncohesive materials were studied by Lane (1953) to establish the limiting tractive force diagram (Figure 3.2). The diagram, which has been used for design purposes, clearly shows that considerably lower critical shear stress is allowed for clear water than for water carrying sediment.

Leliavsky (1955) believed that a simple relationship such as:

$$\tau_c = 166\ D \qquad g/m^2 \qquad (3.5)$$

satisfactorily relates the critical shear stress to the grain size. In this equation the mean particle diameter, D, is expersssed in millimetres and should be smaller than 3.5

mm. Figure 3.3 is a plot of Equation 3.5 along with the data of different researchers. Equation 3.5 is simple in form. Graf (1971), however, declared that it apparently applies to most of the data.

Many experimental programs have been conducted by researchers to establish an explicit solution of the functional relationship, as given in Equation A.18. The first was that of Shields (1936) (reported by Vanoni, 1975) who proposed a graphical solution, which was later modified by Rouse (1939) to take the form given in Figure 3.4. On this graph a number of interesting facts can be observed. For a particular value of R_{e*}, the corresponding value of F_* falling on the curve indicates the threshold condition of particle movement, while lower and higher values correspond to no bed motion and general bed motion respectively. Also, the curve is very similar to the friction diagram for artificially roughened pipes and the drag coefficients relationship for a sphere or a cylinder, which might indicate that these phenomena are fluid related (Graf, 1971).

3.2.3- Lift force mechanisms

Lift forces were incorporated in the derivation of the basic equation of scour (Equation A.2). However, its quantitative effect has not been stressed yet. Assuming a potential flow over a long, circular cylinder with its major axis perpendicular to the flow, Jeffreys (1929) presented a criterion for the occurrence of lift force. He showed that lift takes place if Equation 3.6 is satisfied.

$$(\frac{1}{3}+\frac{1}{9}\pi^2)u_\infty^2 > \frac{\rho_s-\rho}{\rho}ga \tag{3.6}$$

In this equation u_∞ = the free-stream velocity, and a = the radius of the particle ($a = D/2$). Flow passing a grain is a 3-D flow, however, Equation 3.6 was derived for a 2-D flow which behaves differently from a 3-D flow. Therefore, consideration of a modifying factor in this case is essential. Also, the shortcoming of Jeffreys' model is that drag forces are altogether disregarded. The qualitative functional relationship in the Shields diagram (Figure 3.4) can also be derived with a model for lift forces rather than for shear forces. This fact, however, only adds further confidence in the Shields diagram.

3.3- LOG VELOCITY LAW

The velocity and shear stress distributions play key roles in any *loose boundary* hydraulics study. Although deviating from the undisturbed floodplain and main channel values, the velocity distributions in these regions still follow the universal log-law. The theoretical basis of the velocity distribution is presented in Appendix A and the approach by which the bed roughness is evaluated is presented in the next section.

3.3.1- Equivalent sand roughness

In order to apply the universal velocity-distribution equation with a constant chosen based on Nikuradse's experiments, the roughness should be evaluated so as to present a comparable behaviour with Nikuradse's roughness. To determine a relationship between the equivalent sand roughness and the apparent roughness (in terms of D_{50}) of a movable sand bed of an open channel flow, Equations A.33 and A.34 will be equated for a specific point of a velocity profile to yield:

$$B_s - \frac{1}{\kappa} \ln k_s = B - \frac{1}{\kappa} \ln k + B \tag{3.8}$$

$$\frac{1}{\kappa} \ln \frac{y}{k_s} + B_s = \frac{1}{\kappa} \ln \frac{y}{k} + B \tag{3.7}$$

and

$$\frac{k_s}{k} = e^{\kappa(B_s - B)} \tag{3.9}$$

Knowing the value of k (=D_{50} in the case of a movable sand bed), B is evaluated for a specific velocity profile using Equation A.33 (Appendix A). Equation 3.9, then, gives k_s provided that another relation between k_s and B_s exists. Curve B_s of Figure 3.5 forms the basis for such a relationship (in graphical form). Therefore Equation 3.9, along with this curve, might be used in a *trial and error* procedure to determine the equivalent sand roughness k_s for specific bed and flow conditions. Modifying Equation 3.8 in the following form, however, eliminates the necessity of trial and error procedures for determining k_s:

$$B_s - \frac{1}{\kappa} \ln \frac{k_s u_*}{\nu} = B - \frac{1}{\kappa} \ln \frac{k u_*}{\nu} = B' \tag{3.11}$$

$$B_s - \frac{1}{\kappa} \ln k_s + \frac{1}{\kappa} \ln \frac{u_*}{\nu} - \frac{1}{\kappa} \ln \frac{u_*}{\nu} = B - \frac{1}{\kappa} \ln k \tag{3.10}$$

For any given B_s of Figure 3.5, B' can be evaluated and plotted against $\frac{k_s u_*}{\nu}$. Knowing B' for specific values of B and k, B_s and k_s can simply be evaluated with the aid of the B'-curve of Figure 3.5.

3.4- DIMENSIONAL ANALYSIS OF ABUTMENT SCOUR

Many practical engineering problems in fluid mechanics cannot be solved by analytical procedures alone and the field of open channel hydraulics likely presents such problems more than any other branch of fluid mechanics. The essential difficulty of the problem may lie in the complexity of the boundary condition, or it may lie in the ignorance of the basic nature of the flow phenomenon. In these instances engineers must also rely on interpretation and judgment, based on experimental observations and experiences respectively. Dimensional analysis is a powerful tool in tidying up arguments involving a large number of physical parameters and formulation problems which defy analytical solutions and must be solved experimentally. The methods of dimensional analysis are based on Fourier's *Principle of Dimensional Homogeneity* (1882), which states that an equation expressing a physical relationship among quantities must be dimensionally homogeneous. This principle provides the means of ascertaining the forms of physical equations from knowledge of the relevant variables.

In order to form a usable criterion for analysis of the data and to interpret the phenomenon of local scour at bridge abutments, a dimensional analysis might be considered to form a functional relationship among the governing factors. The interaction between the flow obstructed by the abutment and the flow in the channel adjacent to the abutment affects the scour depth and the ratio of these flows determines the most affective length of the abutment. Considering these facts, for clear-water conditions the equilibrium scour depth at an abutment may be regarded as being a function of the following factors:

ρ_s = density of the sediment particles.

ρ = density of the fluid.

ν = kinematic viscosity of the fluid.

U_a = depth-averaged flow velocity at the abutment end.

H = total flow depth in the main channel of the flume.

y_a = flow depth in the floodplain.

Q_a = flow intercepted by the abutment and diverted towards the main channel.

Q_w = flow related to a specific width of the channel at the abutment.

D_{50} = median size of the bed material.

L = abutment length.

g = acceleration due to gravity.

σ_g = geometric standard deviation of the sediment particle size distribution, and

Sh = abutment shape factor.

The functional relationship in a mathematical notation takes the form:

$$y_{se} = f(\rho_s, \rho, \nu, U_a, H, y_a, Q_a, Q_w, D_{50}, g, L, \sigma_g, Sh) \qquad (3.12)$$

Since the submerged weight of the sediment particles $\gamma_s'(=g(\rho_s-\rho))$, gives an indication of the buoyancy forces acting on the particles, it is more significant in the sediment transport phenomena than the dry weight. Therefore, substituting γ_s' for ρ_s, Equation 3.12 can be non-dimentionalized in the following form:

$$\frac{y_{se}}{y_a} = f\,(\frac{\rho U_a}{\gamma_s' D_{50}}, \frac{U_a y_a}{\nu}, \frac{D_{50}}{y_a}, \frac{H}{y_a}, \frac{L}{D_{50}}, \frac{U_a}{\sqrt{g\, y_a}}, \frac{Q_a}{y_a\, U_a^2}, \frac{Q_w}{y_a\, U_a^2}, \sigma_g, Sh) \tag{3.13}$$

in which $(\rho\ U_a^2\ )/(\gamma_s'\ D_{50})$ = the sediment number, which is related to incipient bed movement with the substitution of flow velocity for shear velocity. It is also referred to as the densimetric Froude number, F_D.

Applying certain modifications acceptable within the dimensional analysis to Equation 3.13 it becomes:

$$\frac{y_{se}}{y_a} = f\,(\frac{\rho U_a}{\gamma_s' D_{50}}, \frac{U_a y_a}{\nu}, \frac{D_{50}}{y_a}, \frac{H}{y_a}, \frac{L}{D_{50}}, \frac{U_a}{\sqrt{g\, y_a}}, \frac{Q_a}{Q_w}, \sigma_g, Sh) \tag{3.14}$$

Some of the terms of Equation 3.14 are redundant, are kept constant in this study, or have negligible influence on the scour phenomena. Therefore, these terms can be eliminated from Equation 3.14. Since water and sand were used as the fluid and the sediment in the current study, ρ and ρ_s are constant. The term $(\rho\ U_a^{\ 2})/(\gamma_s'\ D_{50})$ is the Froude number with a characteristic length D_{50}, i.e. $F_D = U_a / \sqrt{g D_{50}}$. For a given flow condition and particle size, $F_a\ =\ U_a / \sqrt{g\ y_a}$ and F_D differ only by a constant which implies that one of these terms is redundant. Also, in the scour process the influence of viscosity is regarded insignificant and can be eliminated. Therefore, Equation 3.14 reduces to:

$$\frac{y_{se}}{y_a} = f\left(\frac{D_{50}}{y_a}, \frac{H}{y_a}, \frac{L}{D_{50}}, \frac{U_a}{\sqrt{g\,y_a}}, \frac{Q_a}{Q_w}, \sigma_g, Sh\right) \qquad (3.15)$$

The geometric standard deviation of the sand used in this study, σ_g have the value 1.13, which indicates a uniform grain size distribution. Since σ_g was constant throughout the tests, it was eliminated from Equation 3.15. Furthermore, the discharge ratio Q_d/Q_w could be used to better indicate the effective length L of the abutment. On the other hand, the relative floodplain flow depth y_d/H was an indication of the intensity of LMT between the main channel flow and that of the floodplain. Therefore, its effects are implicitly incorporated in the discharge ratio. In other words, LMT alters the flow velocity distribution across the flood plain and the main channel and eventually affects the discharge ratio, since the latter should be determined based on the measured velocity distribution. Therefore, y_d/H and L/D_{50} were eliminated from Equation 3.15 to give:

$$\frac{y_{se}}{y_a} = f\left(\frac{D_{50}}{y_a}, F_a, \frac{Q_a}{Q_w}, Sh\right) \qquad (3.16)$$

The relative size of the sediment, D_{50}/y_a, is considered a measure representing the relative roughness of the channel bed. This parameter might be replaced by the critical Froude number, F_c, for the initiation of bed material movement as described here. Considering the equivalent Nikuradse sand roughness in the logarithmic velocity distribution as a function of the sediment size (k_s=CD_{50}, in which C is a coefficient) the velocity distribution on a rough surface might be written as a function of the relative sediment size. Substituting k_s=CD_{50} in Equation A.41 and applying the critical shear velocity yields:

$$\frac{U_c}{u_{*c}} = 5.75 \log \left(C \frac{D_{50}}{y_a} \right)^{-1} + 6 \tag{3.17}$$

The critical velocity for initiating bed material motion can be determined by substituting the critical shear velocity for a given sediment size from Shields diagram into Equation 3.17. The critical Froude number, F_c can now be calculated according to the computed critical velocity:

$$F_c = \frac{U_c}{\sqrt{g\, y_a}} \tag{3.18}$$

Therefore, substituting F_c for $D_{50}/\, y_a$ in Equation 3.16 yields:

$$\frac{y_{sc}}{y_a} = f\left(F_c,\, F_a,\, \frac{Q_a}{Q_w},\, Sh \right) \tag{3.19}$$

Equation 3.19 is used in the analysis of the data of the current study.

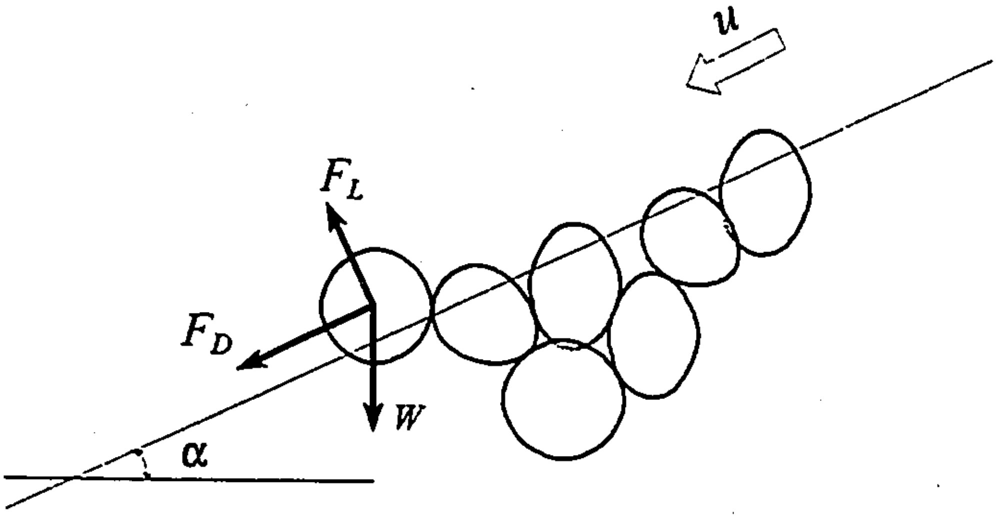

Figure 3.1- Force diagram on particles in a cohesionless loose bed

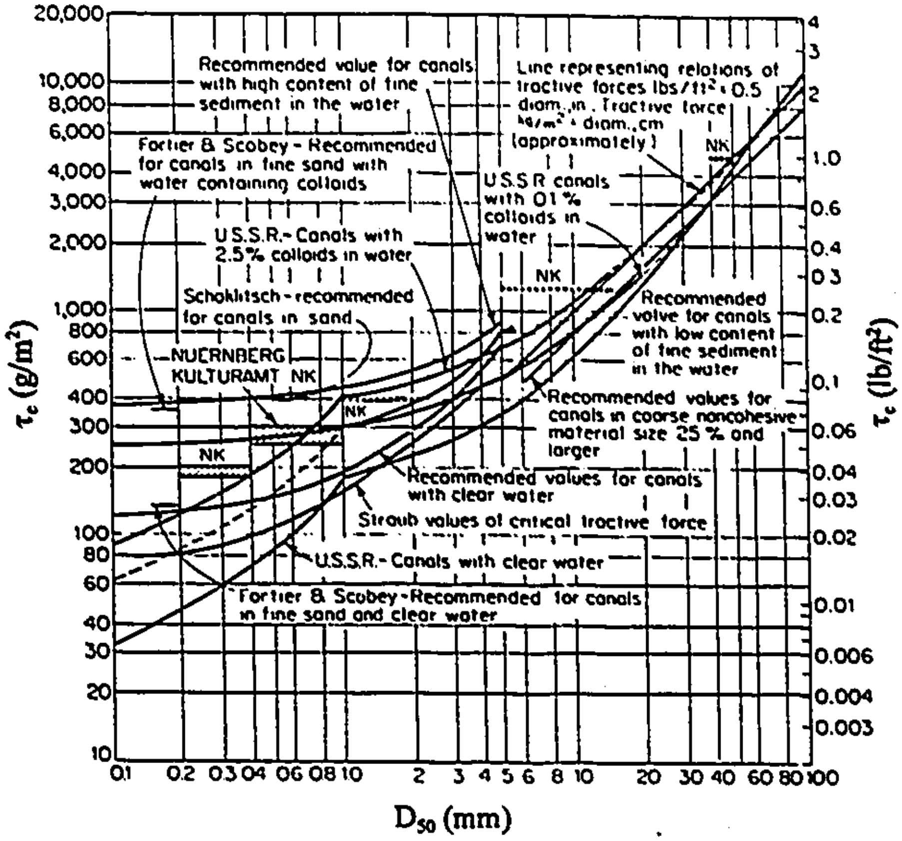

Figure 3.2- Critical shear stress as a function of D_{50} (Lane, 1953)

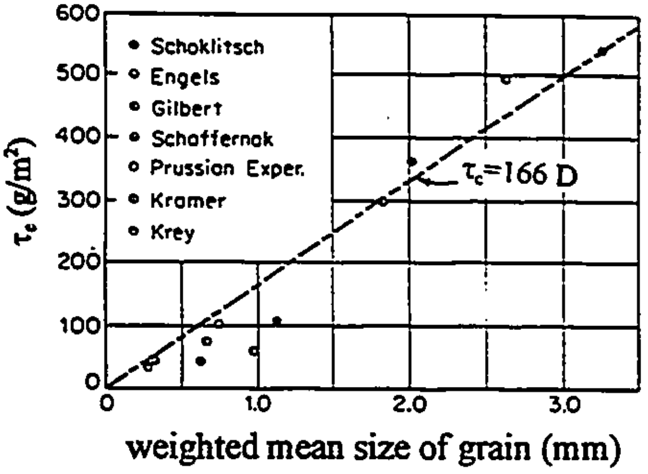

Figure 3.3- Critical shear stress as a function of grain diameter (Leliavsky, 1955)

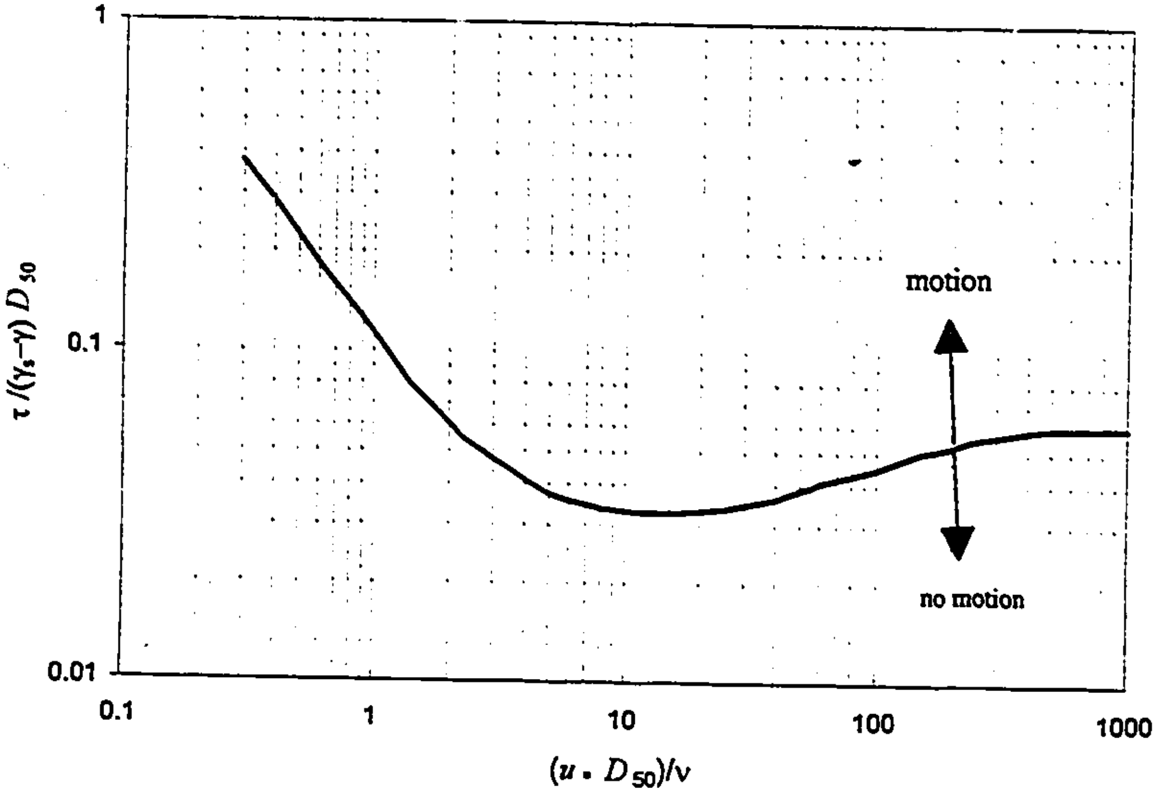

Figure 3.4- Shields' diagram (Vanoni, 1975)

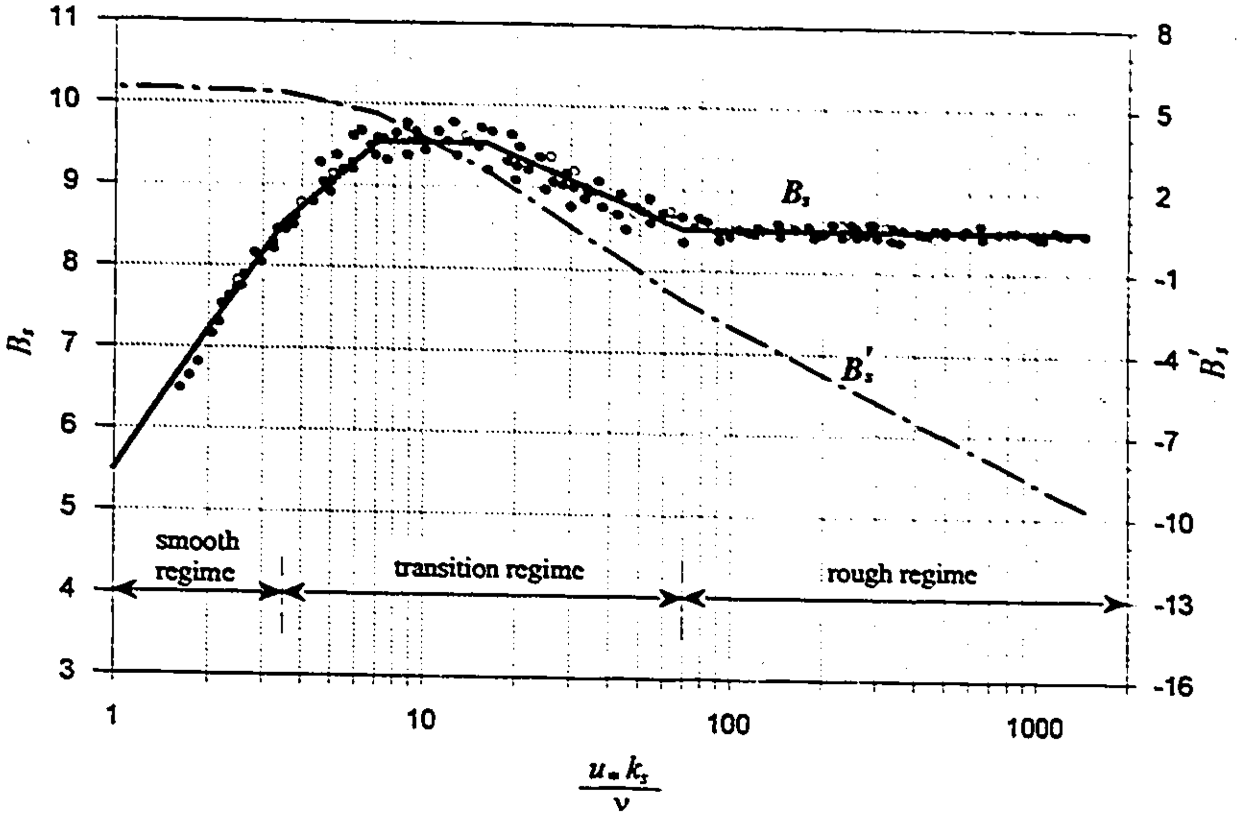

Figure 3.5- B_s and B'_s as a function of $u_* k_s/\nu$, for Nikuradse sand roughness

CHAPTER FOUR

EXPERIMENTAL SET-UP

4.1- INTRODUCTION

Published laboratory data of local scour around bridge abutments and spur dikes were mainly obtained using flumes having rectangular cross sections without FPs (Ahmad,1953; Garde et al., 1961; Gill, 1972; Cunha, 1975; Zaghloul, 1983; Rajaratnam and Nwachukwu, 1983a, 1983b; Kwan, 1984, 1988; Kandasamy, 1985, 1989; Melville, 1992) . Sturm and Janjua (1994) provide the only data set for an abutment installed in a FP zone. Sturm and Janjua used a compound channel with rectangular sections for both the MC and the FP zones. As yet, no published data of scour around an abutment terminating in the FP of a compound non-rectangular cross section have been reported in the literature.

The aim of this study was to experimentally investigate the local scouring process in the vicinity of bridge abutments terminating in the FP of a compound channel having a trapezoidal MC. This chapter provides details on the experimental flume used and the special data acquisition system designed for the study. The original compound flume and the modified test section required for this study, the pump, the flow and scour depth measurement devices, and the velocity measurement devices are described in the first part of this chapter. The second part deals with the procedures followed in designing and testing a data acquisition system for recording flow velocities.

4.2- EXPERIMENTAL SET-UP

4.2.1- The flume

The experiments were performed in the compound flume of the Hydraulics Laboratory of the Civil Engineering Department, University of Ottawa. The flume had been originally built for fixed-boundary compound flow studies and was modified to suit the present studies. The original fixed-boundary (plexiglass) compound flume had an overall length and width of 12.192 and 1.168 m respectively (Figure 4.1). The MC of the compound flume is trapezoidal in shape with a bottom width 0.304 m and side slopes 0.5H:1V. The rectangular FPs, on each side of the MC, are each 0.381 m wide. The depth of the MC from the invert to the bed level of the FP is 0.104 m and the total depth of the flume is 0.205 m. To facilitate installation of modified test sections, the flume's overall length was constructed in five 2.438 metre-long sections. The entire flume rests on a wooden platform supported on two I beams. The beams are pivoted close to the upstream end and supported close to the downstream end with two manually-driven screw-type jacks. Vertical movement of the jacks allows longitudinal slope adjustments of the flume. Plate 4.1 shows an overall view of the flume.

The third section of the flume was replaced with a new section designed and built to accommodate movable bed material in its left FP (Figures 4.2 a, b, and c). The new test section's modified FP contained a recessed section to accommodate the bed material and the model abutments. The recessed part of the test section is 0.266 m deep, while its length and width at the bed level of the FP were kept unchanged, i.e. 2.438 and 0.381 m respectively. A perspective view of the test section and the recessed part is shown in Figure 4.3.

The inlet section of the flume consists of a large tank equipped with two screens containing hair-like material to dissipate large eddies and to remove air bubbles from the water supply. Water is supplied to the tank through a 194 mm-diameter pipe. A *perforated-T* end section to this pipe distributes the flow evenly and minimizes turbulence within the inlet tank. Leaving the inlet tank, the flow passes underneath a wave suppressor (1.168 m long and 0.4 m wide) installed across the flume at the entrance section to suppress any residual surface waves. Plate 4.2 shows the inlet section of the flume with the wave suppressor in place.

The original (Plexiglass) material determined the roughness of the MC; the FP roughness on the other hand was artificially increased so as to more closely simulate *field* conditions. This was achieved by applying *roughness modules* onto the FP invert. Each *roughness module* is 2.438 m long and 0.318 m wide. It consists of wire mesh, having a wire diameter of 0.5 mm and 3.17 mm square patterned openings soldered onto strips of metal sheets with the above mention dimension. All experiments were performed with these *roughness modules* placed on the FP section, except for the recessed section which accommodated the movable bed material.

The flume had twelve tapping points on the invert of the MC to measure the piezometric head. The water surface elevation along the flume was recorded using ordinary manometers connected to these tappings. Spacing between the tappings is 0.762 m and the first tap was installed at a distance 0.609 m from the upstream end of the flume. A total distance of 8.991 m from the entrance of the flume is covered by these manometers.

The downstream end of the flume is equipped with an adjustable tailgate used to control the flow profiles generated in the flume (Plate 4.3). Passing over the tailgate, the flow enters into a flow measurement tank which is equipped with baffled plates to reduce the turbulence and to ensure a tranquil water surface within the measurement well of the tank. A sharp-edge rectangular weir (0.508 m long) was installed at the end of the discharge measurement tank to record the flowrate. Prior to its installation, the weir was calibrated using a weighting tank. After spilling over the rectangular weir, water enters an underground sump and is then recirculated by means of a constant rotational speed (870 RPM) pump. The pump is capable of delivering a maximum flowrate of 0.315 m^3/s with a total head of 18.28 m.

4.2.2- Depth measurement device

During the course of this study flow depth and local scour depth were measured by means of a point gauge installed on a carrier (Carrier I) shown in plate 4.4. The scale of the point gauge had a ten-part vernier which permits depth measurements as small as 0.1 mm. To establish near-uniform flow depth in the flume a second carrier (Carrier II), equipped with a similar point gauge (Plate 4.5), was stationed on the flume well upstream of the first gauge. Carrier II was also used to attach a miniature current meter (propeller-type) and a Pitot tube (Plate 4.5).

4.2.3- Velocity measurement devices

4.2.3.1- Mini-propeller

Flow velocity in the channel was primarily measured using the a *Streamflo-Series* velocity meter manufactured by Nixon Instrumentations Ltd. Originally designed by the British Department of Scientific and Industrial Research, the standard low-speed velocity probe (a mini-propeller) is capable of detecting flow velocities as low as

0.025 m/s. Plate 4.6 shows the model 403 velocity probe used in this study. The overall length of the probe is 0.468 m and the measuring head of the *sensing probe* consists of a fine-bladed PVC rotor (11.6 mm in diameter) mounted on a hard stainless steel spindle. An insulated gold wire is contained within the tube of the probe and terminates 0.1 mm from the rotor blades' tips. When the rotor revolves by the movement of a conductive liquid, the measurable impedance between the gold wire and the tube changes slightly each time a rotor blade passes over a specific point on the tube. This variation is used by an indicator to show the rotational speed in terms of frequency (hertz).

In the current study the sensing probe was connected to the Analogue Indicator (AI) model 401 (Plate 4.7). A battery operated instrument, the AI is supplied with an analog display that can show a 0 to 50 hertz signal. To record higher frequencies, the AI is also equipped with a scale-5 switch that allows an extended range display of 0 to 250 hertz. The AI device sees a pulse for each blade encounter. The internal circuitry, then, converts these pulses which have proportional widths to the speed of the blades into a 0 to 200 μA current. The current is displayed as frequency in the range of 0 to 50 hertz on the front panel. Since this AI displays the rotational speed of the mini-propeller in hertz, specific calibration curves supplied by the manufacturer must be used to obtain actual flow velocities. The maximum error in the measured velocity associated with this device is about ± 1.5% of the true velocity.

4.2.3.2- Pitot tube

When the flow depth in the FP was too small to use the micro-propeller for velocity measurements, a Pitot tube was used instead (Plate 4.8). The Pitot tube used was a 6 mm-diameter unit supplied by United Sensor Corporation. Common manometers were connected to the Pitot tube to record differential head. Manometers were read using a Gaertner Cathetometer (model M911). Having a 20-part vernier, this device permits recording elevation as small as 0.05 mm.

4.3- DATA ACQUISITION SYSTEM

During the preliminary tests it became apparent that the movements of the analog display are too fast to be scanned and recorded manually, making accurate data collection impossible. Moreover, processing velocity measurement in this manner is both time consuming and tedious. High accuracy in recording flow velocity could only be achieved using a computer-based data acquisition system. An appropriate system was designed for this particular application.

A special outlet is available on the rear panel of the AI unit which provides a standard *precision current* with the range 0 to 200 μA. The current is specifically provided to feed a Nixon Instruments graphical recorder and it can not be accepted by a data acquisition board without modification. An analog signal can be recorded by a computer if the computer is equipped with an Analogue to Digital (A/D) conversion board which usually accepts *voltage signals* with a specific range and provides a conversion of the received signals to a digital form. The A/D conversion board model DT 2811 of Data Translation, Inc. was selected for this purpose and the output of the applied AI was modified to match the board requirements.

The DT 2811 board is a 12-bit A/D convertor with three main features: Analogue to Digital (A/D) conversion, Digital to Analogue (D/A) conversion, and Digital Input/Output (I/O) transfer operations. The DT 2811 has three different input modes, i.e. Single-Ended (SE), Differential (DI), and Pseudo-Differential (PDI) inputs.

Furthermore, three input ranges are accepted by this board: ± 5 volts, 0 to +5 volts, and ± 2.5 volts. For this study the A/D conversion board was configured with the first input range (± 5 volt).

The selected DT2811 A/D conversion board of Data Translation Inc. does not accept the precision current output of the Nixon AI. That current must be converted to a ±5 volts, suitable for the A/D card input range. To accomplish that, a new device was designed and built to receive the original *precision current* output of the AI and convert it to an acceptable voltage within the A/D board's range. Termed: *Precision Current to Voltage Current* (PCVC), this device, along with the other components of the whole system (Streamflo Instruments, and the A/D conversion board) went under comprehensive tests (Presented in appendix B) to check overall accuracy prior to application. A summary of the results is presented here.

First the DT2811 A/D conversion board itself was tested to check its accuracy and to examine the possible meed for calibration. The adopted configuration includes SE input mode, ±5 volts input range, and gain of one. An interactive computer program was developed to scan and record the converted data acquired by the first channel of the A/D conversion board. A very constant voltage source was connected to the first channel of the board for a long period. The maximum variations of the recorded data were less than ±0.0015 volts (less than 0.2% of the full scale) which indicate that stable and reliable data were acquired (Figure 4.4). Therefore, further calibration of the A/D conversion board was not necessary.

When the output of the PCVC was connected to the A/D conversion board, the voltage dropped and fluctuated 15 to 35% below the actual value. Numerous observations and tests carried out to detect the cause of this phenomenon led to the detection of 25 to 35 micro Amp of leakage current between the flowing water and the computer's ground. Although the leakage current was small, it represented a significant percentage of the original range produced by the AI and could not be ignored in this case.

Theoretically, no current should be detected between the grounding of the system and the flowing water, therefore, a solution to this problem could not be supplied by the A/D conversion board manufacturer. Many large electrical devices and pumps running in the laboratory seem to produce electrical noise which affects the working condition of the system. Therefore, changing the input mode of the A/D conversion board to the DI mode seemed the only solution to the problem. Testing the A/D conversion board in the DI mode with a constant voltage source, however, showed large instability in the records (Figure 4.5).

Careful supplementary tests indicated that referencing the low end of the used differential input channel through a 1 kΩ resistor to the Analogue Ground of the board entirely eliminated the instability from the records. Figure 4.6 shows the recorded data using the full scale (compare with Figure 4.5), while Figure 4.7 shows the deviation of each data point from the original voltage. It should be mentioned that each data point of these figures is the average of eighty readings accomplished within eight seconds (ten records per second).

Changing the input mode to the DI did not resolve the problem of the drop in recorded voltage, therefore, isolating the computer ground was the only solution. By designing a Ground Isolation Device (GID) and installing it between the PCVC and the A/D conversion board direct connection was avoided and accurate data were captured and converted by the board.

The idea behind the GID is the deployment of a matched pair of photo voltaic optical isolators working in harmony on both sides of the isolation barrier to produce two equal voltages. An infrared beam is emitted on the PCVC side forcing a voltage to a pear on the computer side. Likewise, the computer side will emit a beam proportion to voltage it received back to PCVC side to ensure solid and repeatable results. Implementing the system with the GID removed the drop in the recorded voltage and reliable data were acquired thereafter. A schematic sketch of the complete data acquisition system is shown in Figure 4.8. Also, Figure 4.9 shows the acquired velocity measurements using the implemented system during a prolonged period (7000 seconds). The fluctuations in the recorded data are related to the turbulence structure.

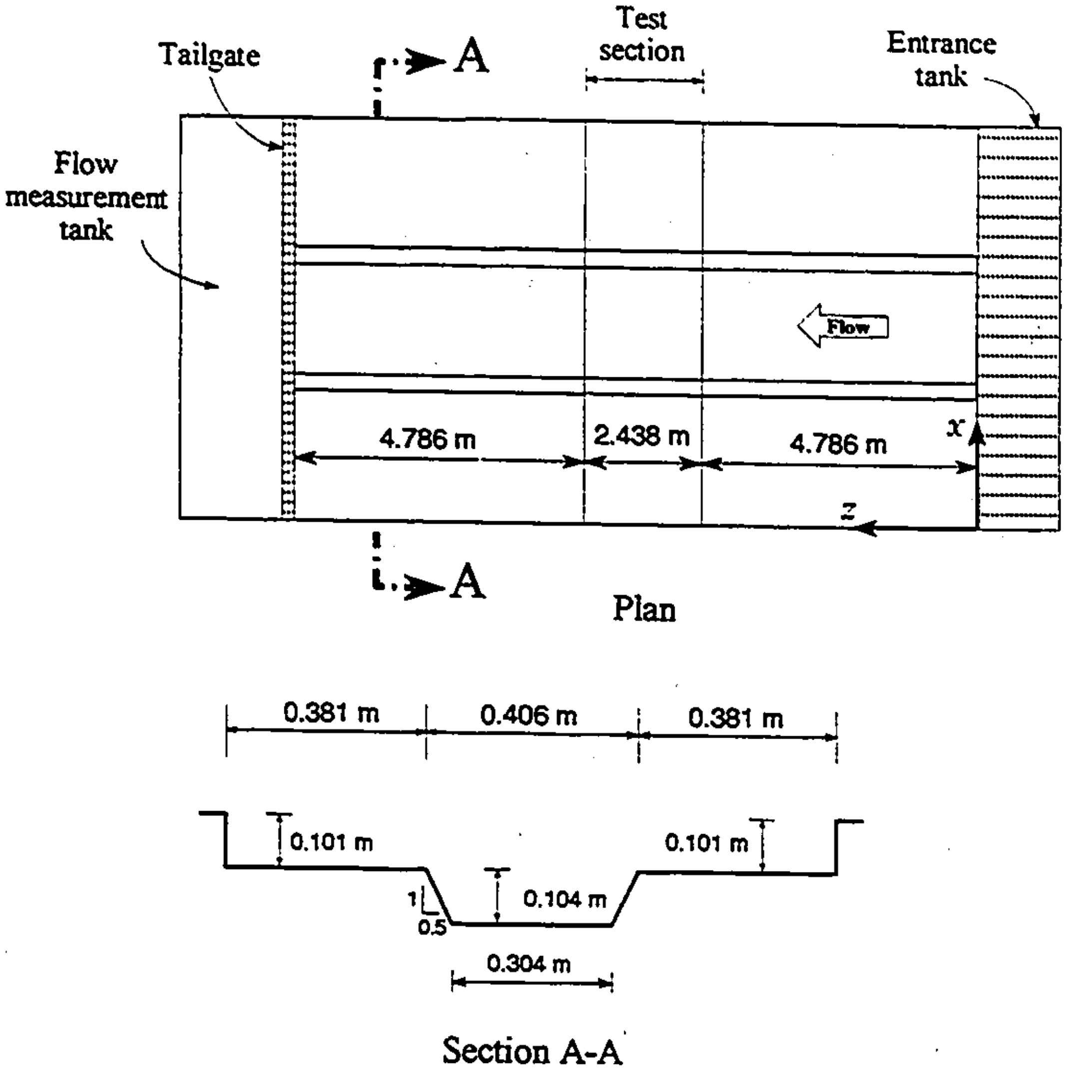

Figure 4.1- Schematic presentation of the compound flume

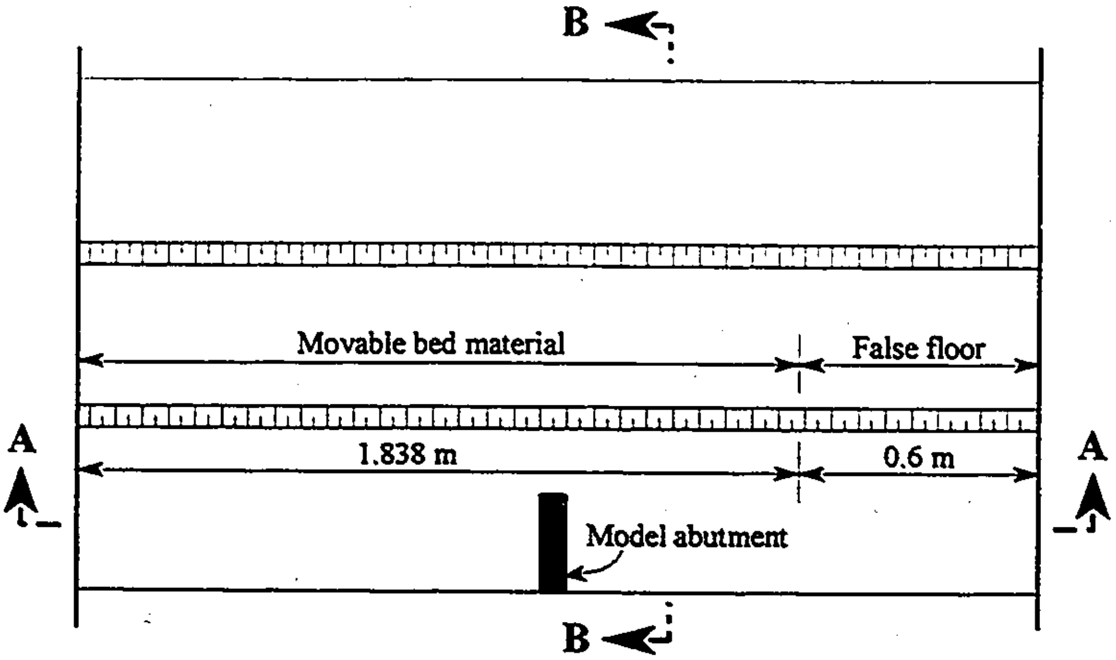

a- Plan view of the test section

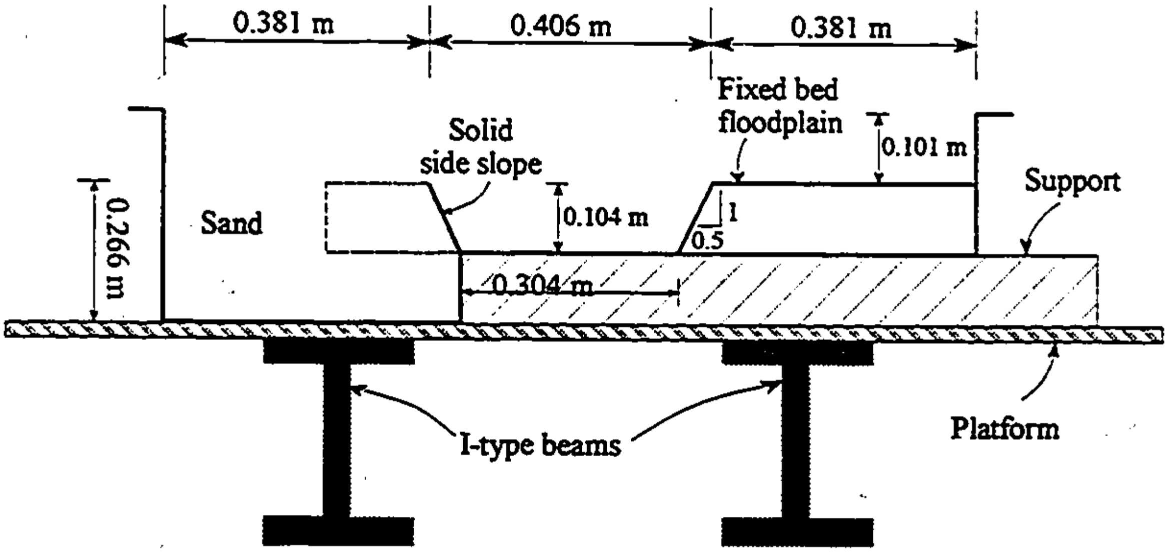

b- Section B-B

Figure 4.2- Schematic presentation of the modified test section (cont.)

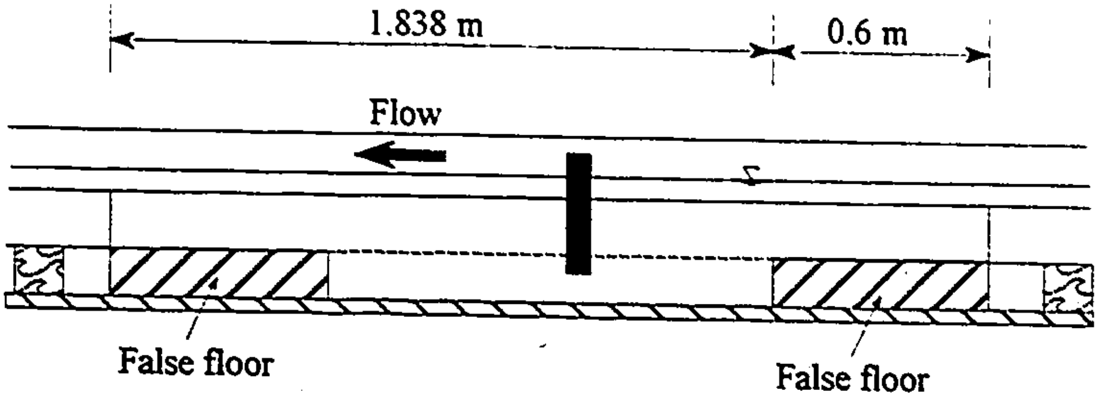

C- Section A-A

Figure 4.2 (cont.)- Schematic presentation of the modified test section

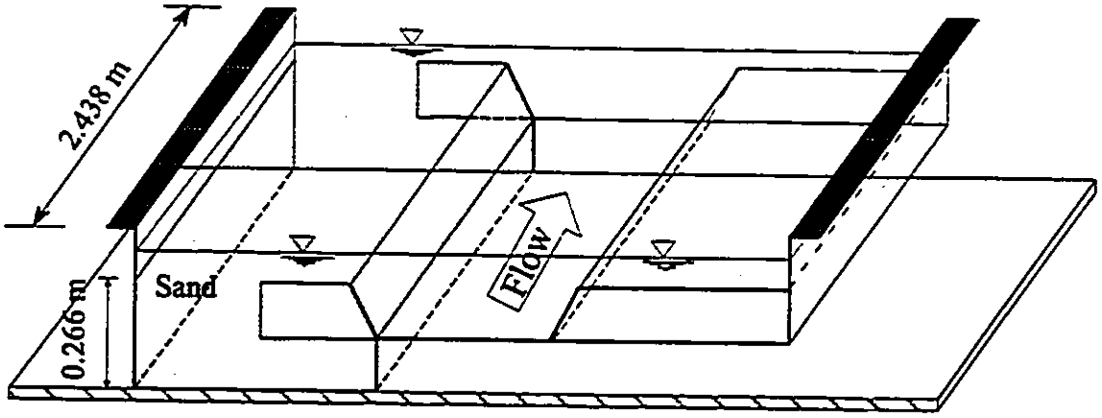

Figure 4.3- Perspective view of the test section

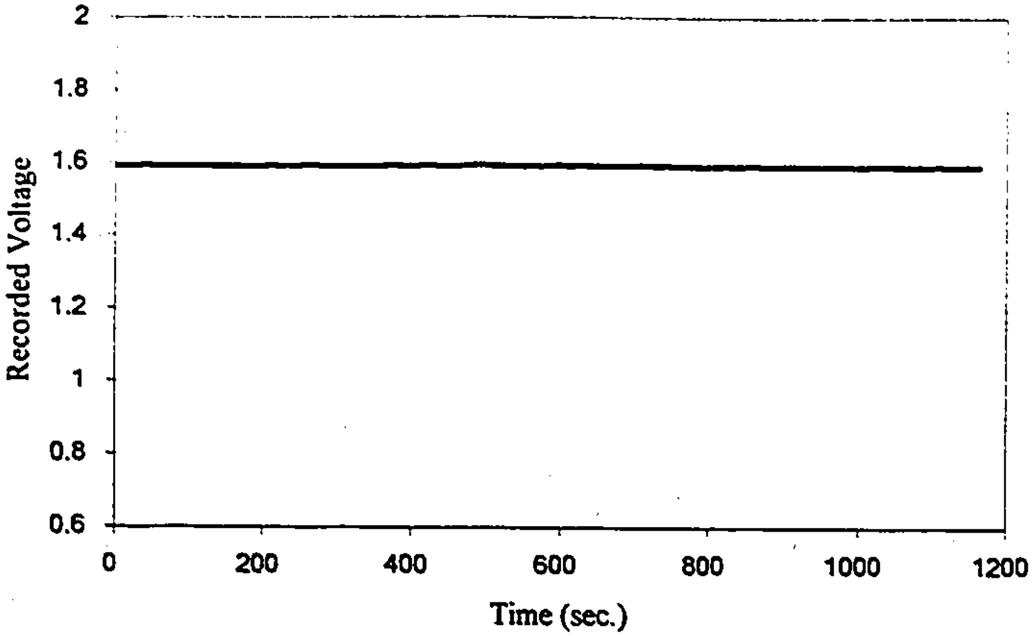

Figure 4.4- Recorded values of a constant voltage source using SE input mode

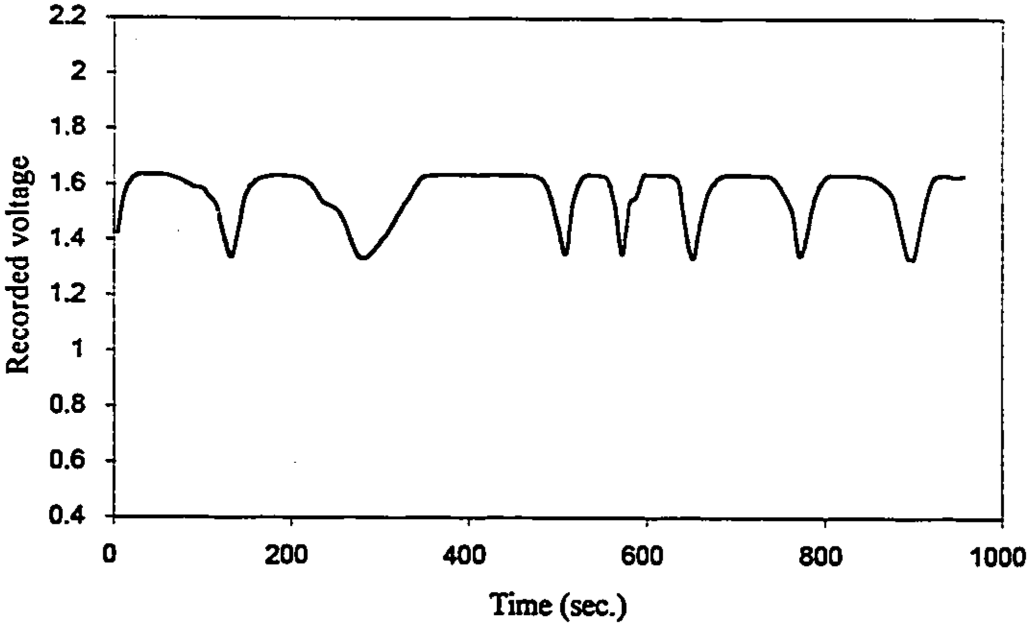

Figure 4.5- Recorded data of a constant voltage source using DI input mode

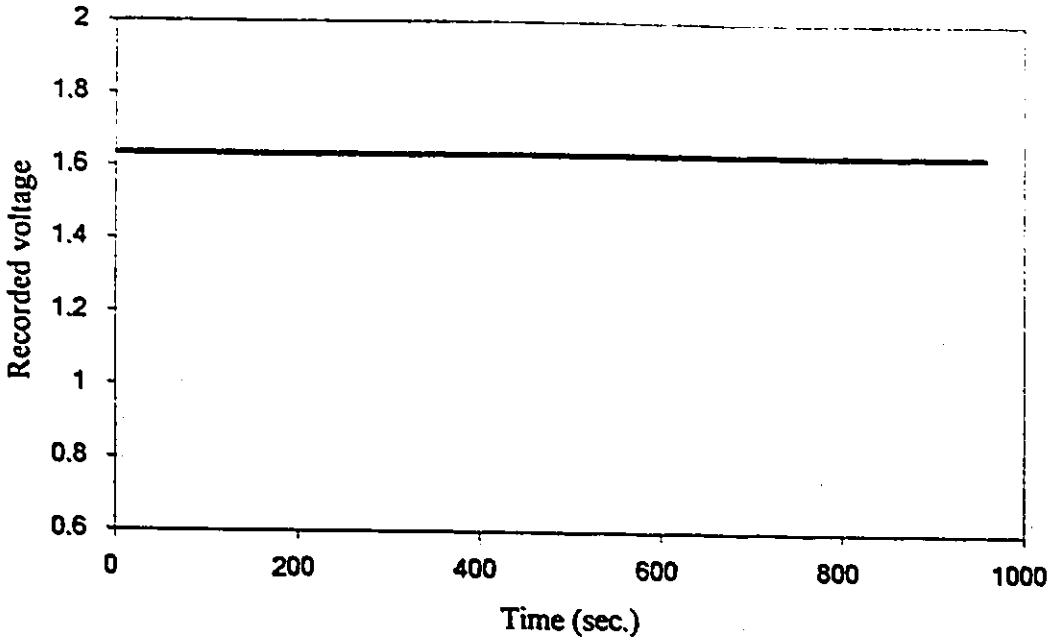

Figure 4.6- Recorded data of a constant voltage source using DI input mode and applying 1 kΩ resistor

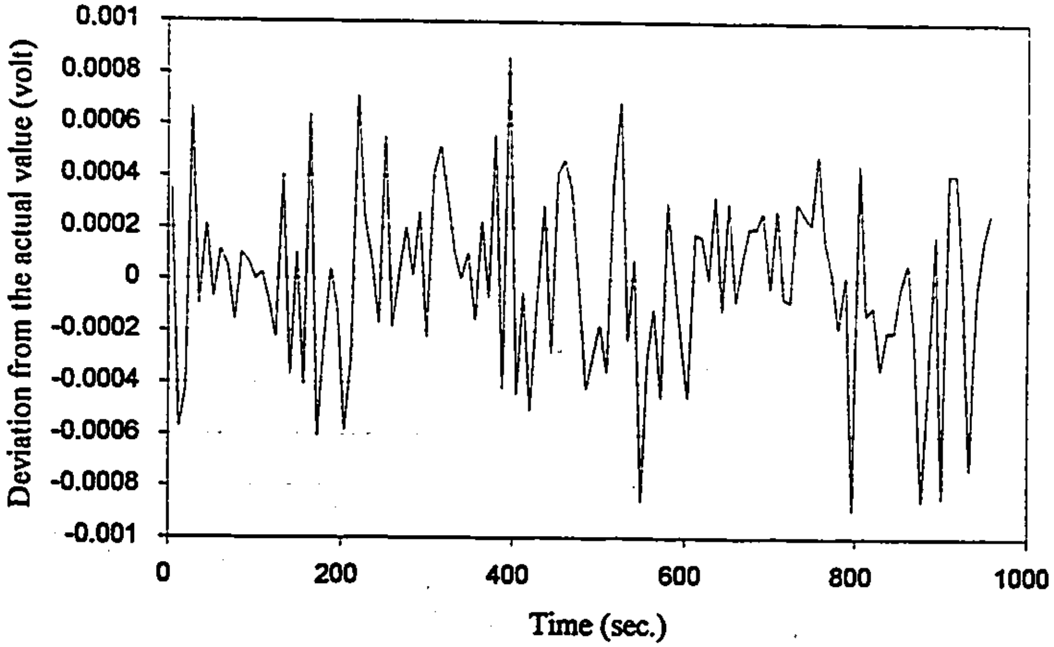

Figure 4.7- Deviation of the recorded voltage from the actual values using DI input mode and applying 1 kΩ resistor

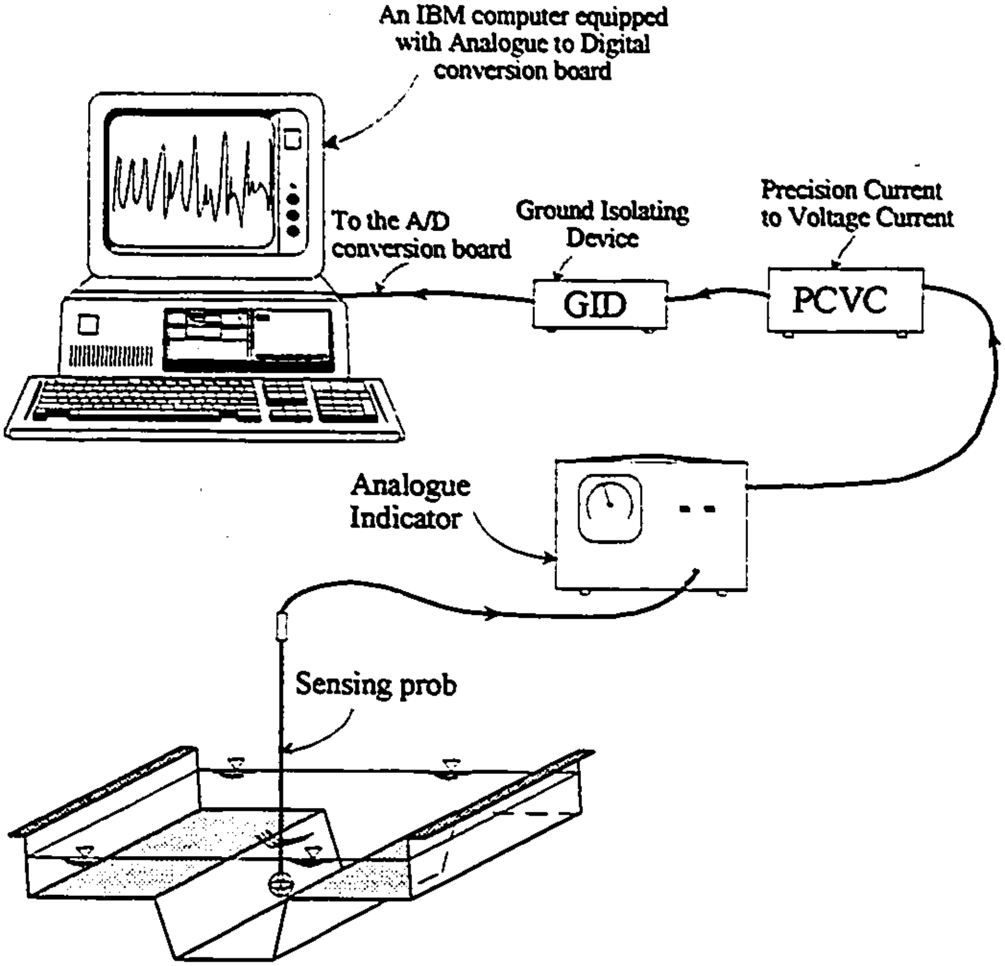

Figure 4.8- A schematic presentation of the complete data acquisition system

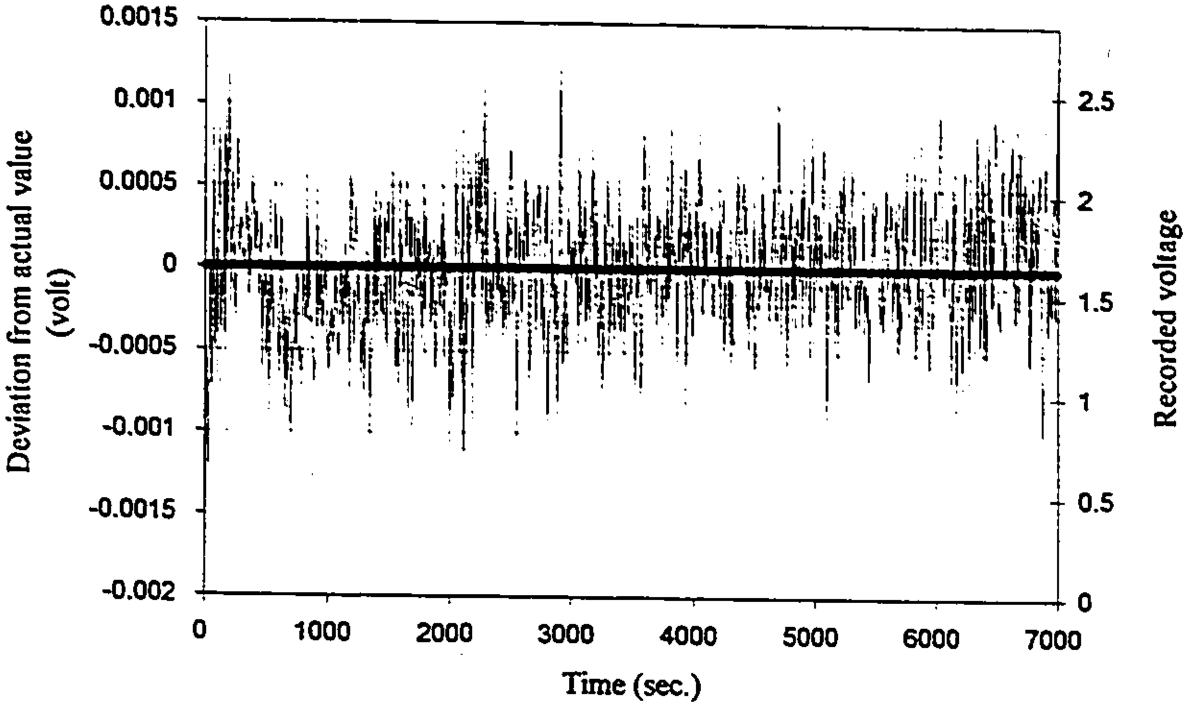

Figure 4.9- Deviation from the actual value along with the recorded voltage of a prolonged test using DI input mode and applying a 1kΩ resistor

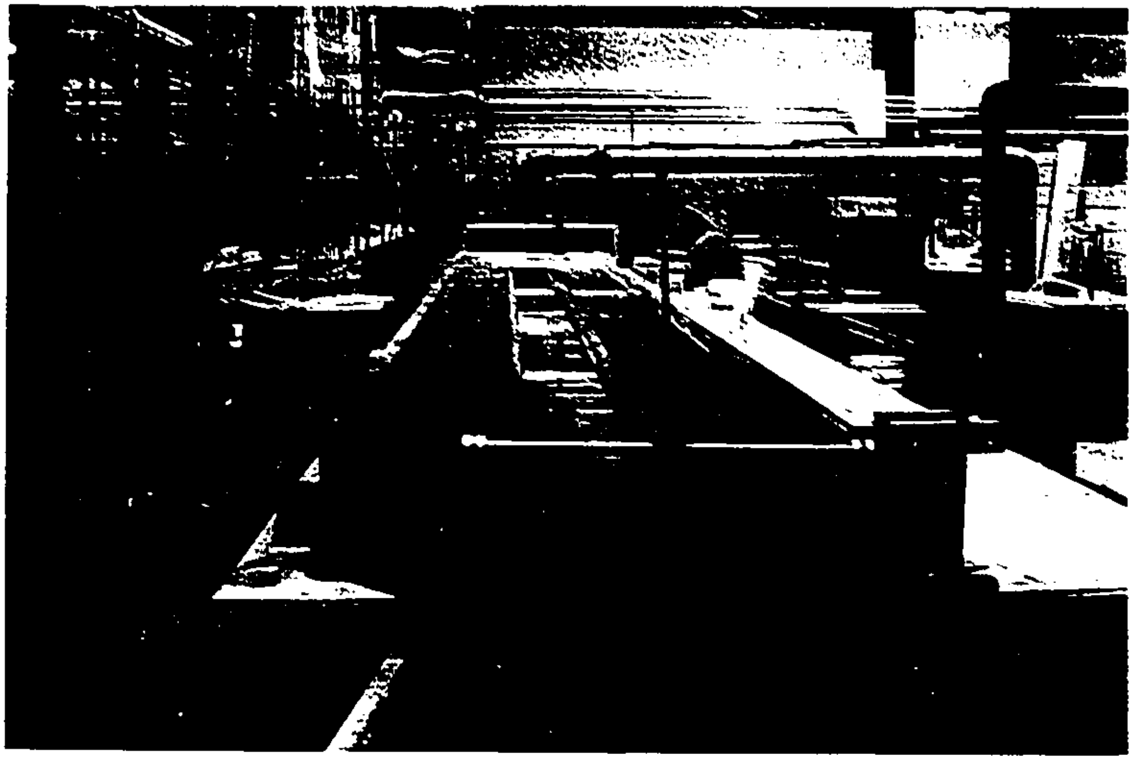

Plate 4.1- Upstream view of the compound flume of the Hydraulics Laboratory of the University of Ottawa

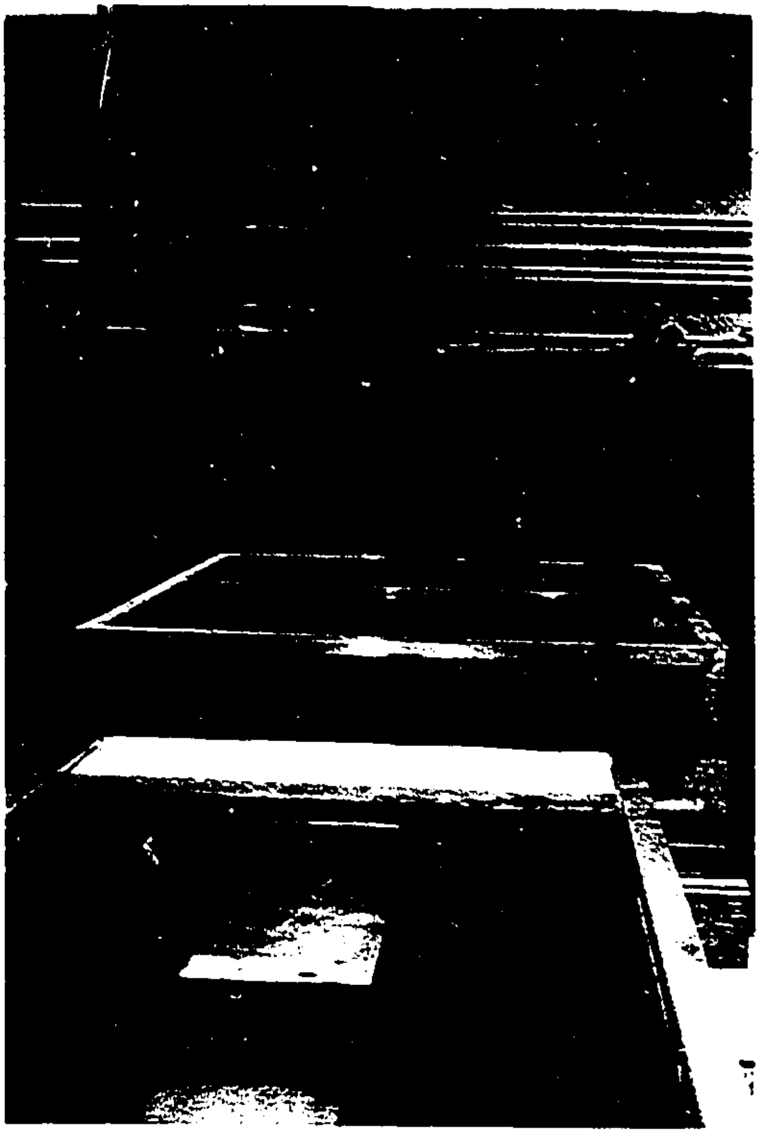

Plate 4.2- Inlet tank and the entrance part of the flume

Plate 4.3- Outlet section of the compound flume

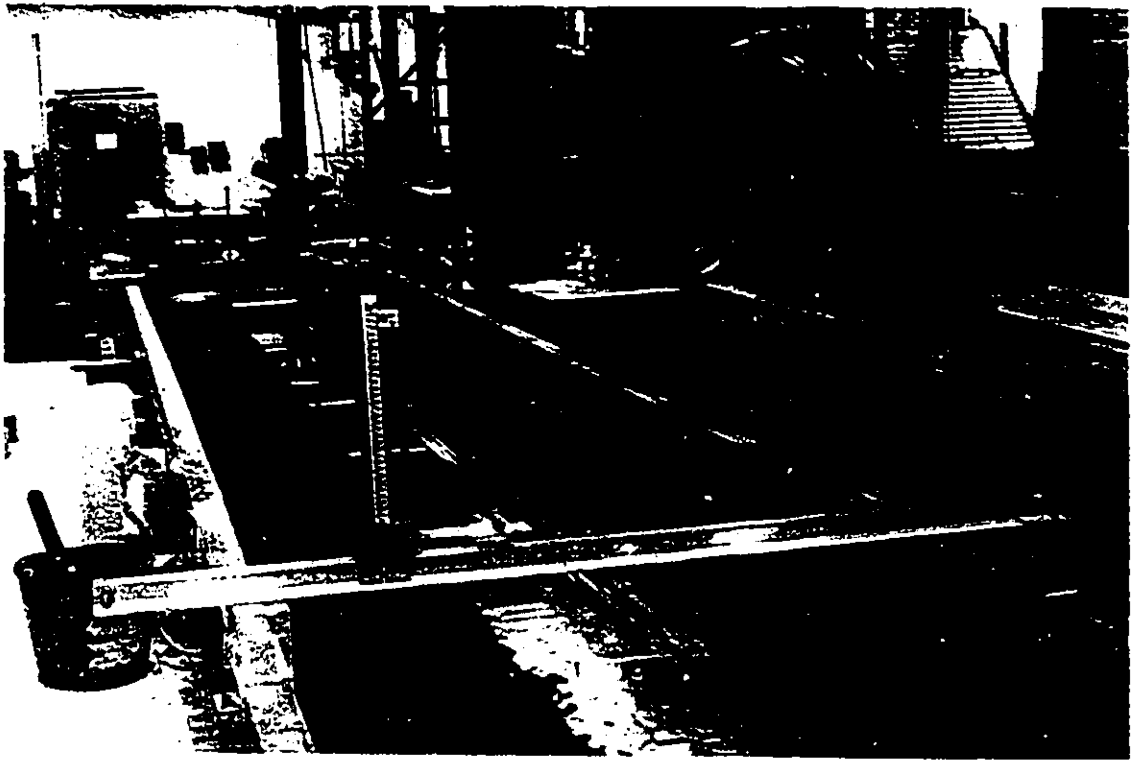

Plate 4.4- Carrier I along with the point gauge used to measure flow depth and scour depth

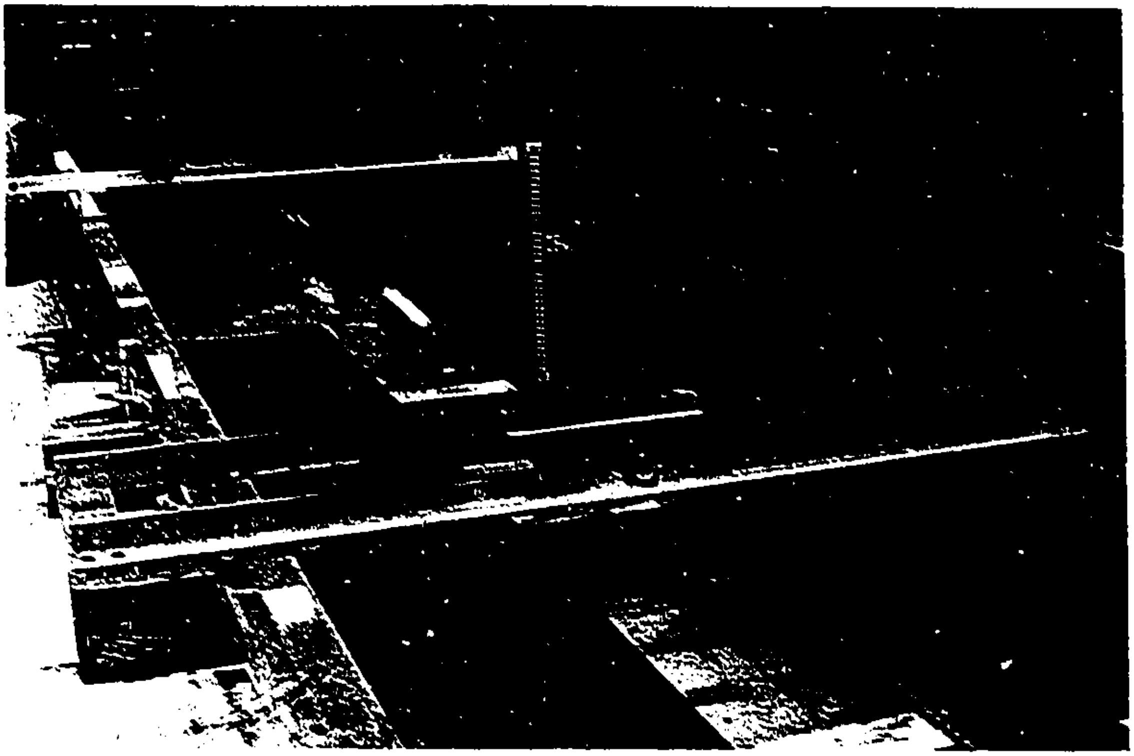

Plate 4.5- Carrier II along with the point gauge applied to measure flow depth and to hold flow velocity probe

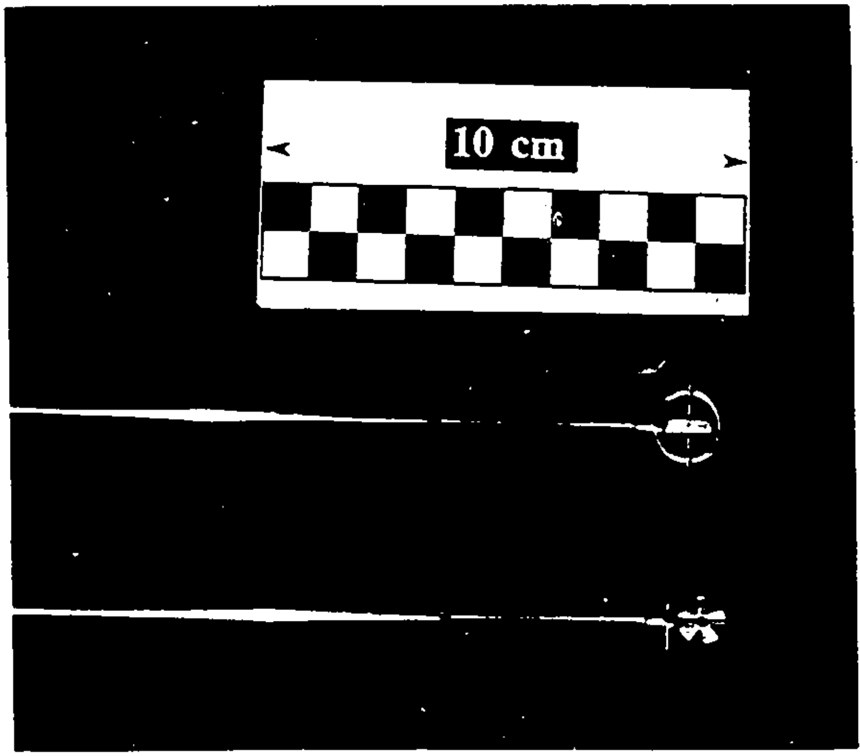

Plate 4.6- Nixon low speed velocity probe model 403

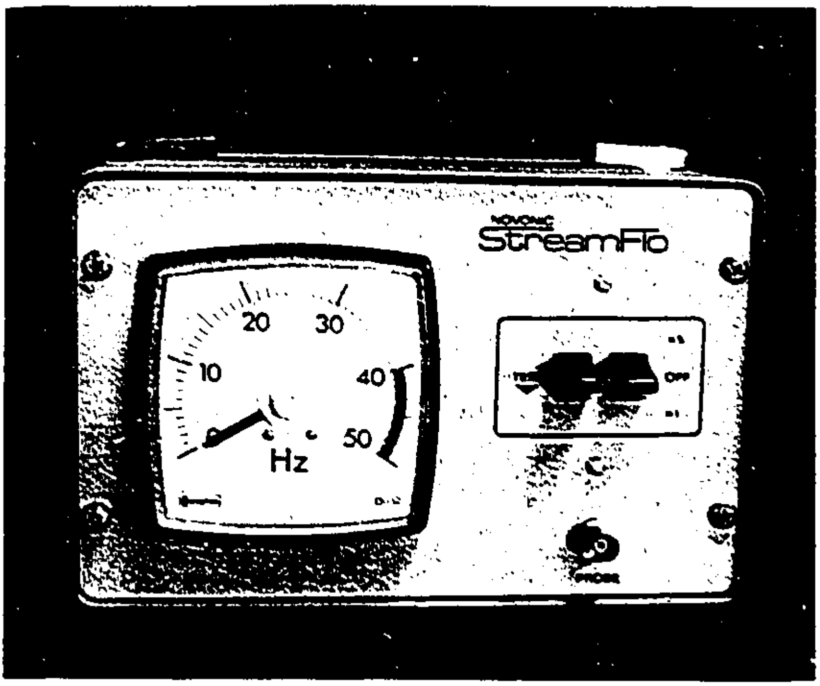

Plate 4.7- Nixon Analogue Indicator (AI) model 401

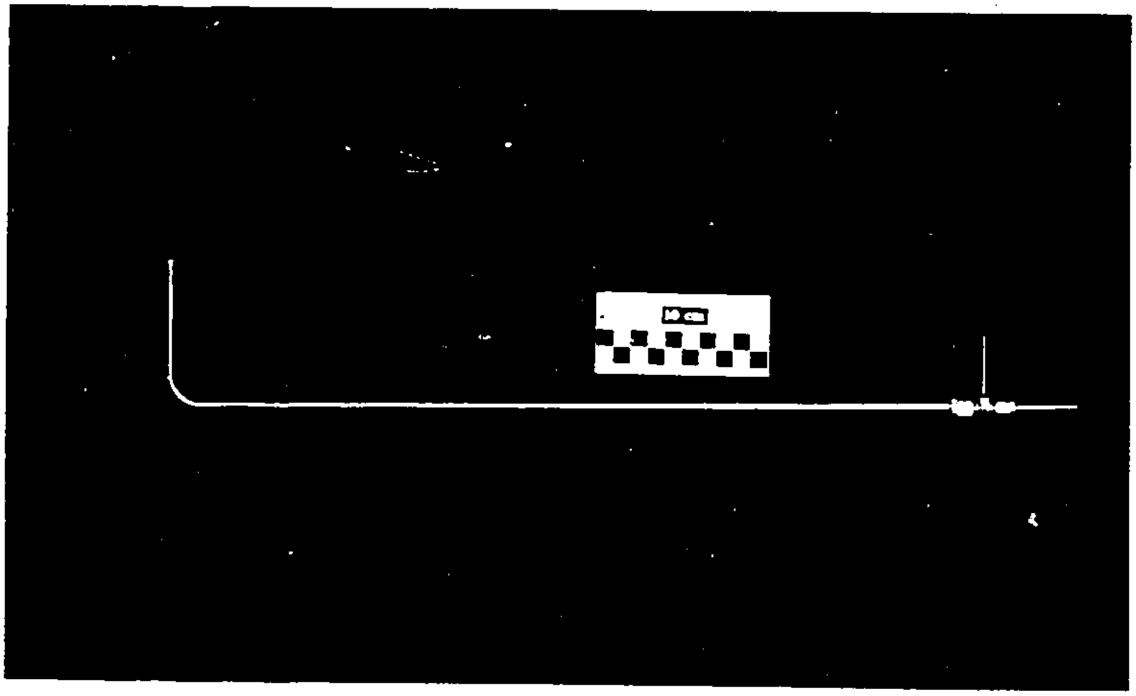

Plate 4.8- United Sensor Corp. Pitot tube applied during the study

CHAPTER FIVE

EXPERIMENTAL PROGRAMME— BOUNDARY CONDITIONS

5.1- INTRODUCTION

Certain experimental parameters, such as: longitudinal channel bed slope, discharge range, required flow depth in the FP, and model bridge abutment length largely depend on the experimental set-up as well as other controlling factors. Controlling factors were thoroughly investigated in a series of preliminary tests so as to select the most appropriate channel-bed material and other important parameters for the main tests. The results of these preliminary tests led to selection of appropriate bed material size, channel longitudinal slopes, required FP flow depths, model bridge abutment lengths, and the discharge range required to generate the near-normal flow depth. In addition to presenting the results of the preliminary tests, the methods by which the controlling factors were investigated are also described in this chapter.

5.2- LONGITUDINAL BED SLOPE

5.2.1- Applicable bed slope range

Generally the *discharge-critical slope* curve for the laboratory channel is an appropriate guide to facilitate selection of a suitable bed slope range for the planned experiments. Figure 5.1 is the *discharge-critical slope* curve for the MC of the compound flume. This figure shows that for discharges up to 0.035 m^3/s, slope values beyond 0.003 tend to produce supercritical conditions. Therefore, longitudinal channel slopes steeper than 0.002 should be avoided. In this study three longitudinal bed slopes (0.0006, 0.00075, and 0.0009) were adopted.

5.2.2- Bed slope settings

Since a laboratory flume generally has a short length, accurately setting the longitudinal slope of a flume requires care and considerable effort. A relatively small error in setting the flume's bed elevation results in a significant error in the longitudinal slope and, in turn, in the computed shear velocity. Hence, to achieve the required accuracy, a precise level (model N3 manufactured by Wild Corp.) was used in our study. This device permitted level adjustments as small as 0.1 mm which, considering the length of our flume, resulted in an error of between ±1% to ±1.5% considering the channel bed slope setting.

The flume level in the transverse direction was also of critical importance, (an irregular or skewed FP in the transverse direction would generate undesirable secondary currents in the flume). To assure properly-levelled FPs, a comprehensive levelling was performed, along the edges of the FPs and the MC, as well as at the centre line of the MC. The results indicated the need for substantial level modifications to achieve the desired condition.

More than 200 points were measured repeatedly during flume bed level adjustments and eventually the flume was entirely levelled in the transverse direction. Having been levelled in the transverse direction, identical longitudinal slopes along the floodplains and the MC are assured when the bed slope settings are accomplished based on only adjusting the centerline of the MC. Figure 5.2 shows the final cross elevations of 15 cross sections along the flume.

Since the flume rests on a wooden platform, it was recognized that the platform allows vertical displacement along the flume when water runs in it, (i.e. the flume settles and changes the preset longitudinal slope). Measurements indicated that dry-bed slope adjustments should be avoided and, to achieve the desirable accuracy, the bed slope setting was accomplished while water was running in the flume. This procedure was followed for setting the aforementioned longitudinal bed slopes and the results are plotted in Figure 5.3. Measured bed elevations are compared with the perfect lines of S_o=0.0006, 0.00075, and 0.0009. As indicated in the figure very close agreement between the bed slope setting and the perfect lines was achieved.

5.3- DEPTH- DISCHARGE RELATIONSHIP

One of the main characteristics of a compound channel is the unique *depth-discharge* (Q-y_o) relationship or the *rating curve*, which depends on flume longitudinal slope, bed roughness, and the geometry of the cross section. Therefore, in studies dealing with compound flumes, the Q-y_o relationship should be specified based on the selected test conditions. To prepare a Q-y_o relationship for a laboratory flume it is essential to establish near-uniform flow conditions first. For a given discharge, a uniform flow in the laboratory channel may be closely approximated by adjusting the tailgate of the flume to a specific height so that the slope of the water surface profile along the flume and the flume's longitudinal slope are essentially the same. The process of tailgate adjustments for establishing uniform flow for a specific discharge is tedious and time consuming. To establish the Q-y_o relationship for a given longitudinal slope, the uniform flow condition should be approximated for different discharges. These Q-y_o curves can then be utilized to determine the required discharges associated with the near-uniform flow depths for various experiments.

In a particular experiment the water surface profile along the channel was recorded via the twelve manometers connected to tapping points located along the MC of the compound flume. The aforementioned procedures of tailgate adjustments were followed to produce a water surface slope close to the preset longitudinal slope of the flume. Manometers were read by a Gaertner Cathetometer, which provides vertical displacement readings at intervals of 0.05 mm. The error associated with this value for the bankfull discharge is about ±0.05% and it is even smaller for the selected flow depths. When the required water surface profile was established, the corresponding near-uniform flow depth, y_o, was measured at different points along the channel using a vernier point gauge. The vernier of the gauge provides for depth readings at intervals of 0.1 mm; the water surface, however, can only be measured to an accuracy of ±1.0 mm due to the presence of water-surface disturbances. This introduces an error in the flow depth measurements around ±0.7% of the total flow depth.

The process of tailgate adjustment was repeated for discharges within the selected discharge range and the observed near-uniform flow depths associated with these discharges were then used to prepare the Q-y_o relationship for the pre-set channel slope. Figures 5.4 to 5.6 show the Q-y_o curves prepared for the selected longitudinal channel slopes: 0.0006, 0.00075, and 0.0009 respectively. These curves were used to determine the necessary flow rate for establishing the near- uniform flow condition required in a particular test. The curves indicate that the discharge range $0.02 < Q < 0.03$ m^3/s produces the required range of flow depths in the FP zones.

The observed water surface profiles associated with those flow conditions applied during the main sets of experiments are presented in Figures 5.7 to 5.10. Also indicated on these figures are the channel bed profiles and the ideal longitudinal slope for each case. The average of the vertical distances between the channel bed and the water surface in these figures represents the FP flow depth in each case. Figures 5.7 to 5.10 clearly indicate that in every case the water surface is essentially parallel to the channel bed, which confirmed that near-normal flow conditions were established in the flume.

5.4-SEDIMENT CHARACTERISTICS

The main experiments should be run at or close to the *threshold* condition of bed material movement, i.e. the shear velocity ratio, u_*/u_{*c}, should be kept close to unity. Therefore, the grain size of the sediment should be selected to satisfy this condition according to the governing parameters induced by the experimental set-up. Accordingly, studying the general relationship, between sediment characteristics and the flow conditions, facilitates selection of the most appropriate grain size for the experiments. In this regard, Shields' diagram is considered the criterion for developing such a relationship among the grain sizes of uniform sediments, the flow depths, and the longitudinal slopes of the channel at the threshold condition of bed material movement.

The procedures followed herein determine, based on Shields' diagram, the grain size that correspond to the threshold condition for a given longitudinal slope and flow depth. The procedure, which requires iteration for each condition (S_o and y_o), is tedious and time consuming. Therefore, to facilitate selection of the most appropriate bed material a computer program was developed which accurately and rapidly establishes the general relationship among the aforementioned parameters.

According to Shields' diagram (Figure 3.4) the uniform sediment grain size, D_s, the sediment Reynolds number, R_{*c}, and the dimensionless shear stress, F_* are related through:

$$R_{e*} = \frac{u_* D_s}{\nu} \tag{5.1}$$

and

$$F_* = \frac{\tau_c}{(\gamma_s - \gamma)\, D_s} \tag{5.2}$$

Substituting $\sqrt{\tau/\rho}$ for u_* in Equation (5.1) and solving for τ_c yields:

$$\tau_c = \frac{(R_{*e}\nu)^2\, \rho}{D_S^2} \tag{5.3}$$

Substituting Equation (5.3) in Equation (5.2) and solving for D_s yields:

$$F_* = \frac{(R_{e*}\ \nu)^2\, \rho}{(\gamma_s - \gamma)\, D_s^3} \tag{5.4}$$

and

$$D_s = \left(\frac{(R_{e*}\ \nu)^2\, \rho}{F_*\ (\gamma_s - \gamma)} \right)^{1/3} \tag{5.5}$$

Knowing the physical characteristics of the sediment and the water, the uniform sediment grain sizes, D_s, for the threshold condition of bed movement can be calculated for each point of Shields' diagram using Equation (5.5). The critical shear stress associated with the computed grain size can be obtained by either using Equation (5.3) or solving (5.2) for τ_c:

$$\tau_c = F_* (\gamma_s - \gamma) D_s \tag{5.6}$$

Using the aforementioned procedure the computer program was developed based on a flowchart shown in Figure 5.11. The program determines the grain size required to establish the threshold condition for the predefined flow depths and longitudinal slopes of the channel. A sample of the output file is presented in Appendix C and the graphical relationship among grain sizes, flow depths, and the selected longitudinal slopes, for the shear velocity ratio u_* / u_{*c}=0.95, is presented in Figure 5.12. This figure will be referred to in the next sections.

5.5- SELECTION OF SEDIMENT SIZE

The Q-y_o curves (Figures 5.4 to 5.6) indicate that any depth in the FP greater than five centimetres produces a relatively high ratio of FP depth to total depth. In such circumstances the effect of the FP becomes insignificant, i.e. the *compound flume* acts as a *single* channel (Bhowmik 1982). This then limits flow depths in the FP in the range of 10 to 50 mm, which corresponds to total flow depths of between 110 and 150 mm.

Figure 5.12 shows for the specified longitudinal slopes the relationship between grain sizes and flow depths at the near-threshold condition of bed material movement. The curves of this figure are based on Shields' diagram and indicate that a selected grain size, D_s, dictates the depth of the flow for each longitudinal slope if the threshold condition of bed material movement is to be maintained. For example, flow depths y_o = 42, 33, and 28 mm establish the threshold condition of bed material movement for D_s =0.5 mm if the longitudinal slopes are S_o=0.0006, 0.00075, and 0.0009, respectively.

5.5.1- Selected sand sample

According to the specified range of both y_o and S_o, grain sizes in the range of 0.3 to 0.6 mm were considered appropriate for the planned experiments. Commercial beach sand was selected for this study. The grain size distribution (based on a sieve analysis of several samples of this sand) appears in Figure 5.13. The following characteristics were determined for this material: D_{84}=0.653 mm, D_{50}=0.47 mm, D_{16}=0.314 mm, and the geometric standard deviation of the sand $\sigma_g=\sqrt{D_{84}/D_{16}}=1.44$

Since $\sigma_g < 1.5$, this sand could be classified as *uniform*, however, its geometric standard deviation approaches the upper limit reported for sand uniformity. According to Figure 5.12, to establish the threshold condition of bed material movement, a flow depth of 42 mm should be maintained in the FP for a longitudinal slope of 0.0006.

Sand having D_{50} < 0.6 to 0.7 mm is classified as a *ripple-forming* one (Ettema 1980). Bogardi's (1959) diagram, however, suggests that for our flow conditions no bed forms should be observed. Hence, to observe the general behaviour of the selected sand under the proposed flow conditions, a series of preliminary tests were performed using VW-abutments of different lengths and a flume longitudinal slope 0.0006. These tests demonstrated that localized bed movement occurred in the FP (in the vicinity of the MC/FP junction) to form a *trough-like* bed feature there. However, no general *ripple* formation was observed along the test section. This local scouring feature is largely the result of a combination of the following: (*i*) the relatively high velocities at the edge of the FP next to the MC (Figure 5.14), and (*ii*) the sand's high geometric standard deviation (which implies that the threshold conditions for smaller fractions are being exceeded in this region).

As mentioned earlier, although the sand used was classified as *ripple-forming* sediment (Ettema, 1980), no ripples formed in the vicinity of the MC in spite of partial bed material movement there. It seems that a weak *armoured* layer forms and prevents ripple formation in this region. The results of the preliminary tests indicated that this sand could not be used without removing, at least, the unusually large-size grains which appeared occasionally during the tests. However, without major modification to the grain size distribution of the sand, the bed material in the vicinity of the MC must be fixed and hardened prior to running any test. Nevertheless, if the weak *armoured* layer prevents ripple formation in the test section, it is very likely to form within the scour hole too and might affect the scour depth as well.

5.5.2- Modification of the sand sample

Given the above problems, it was necessary to modify the test section sand in order to achieve a more uniform grain size distribution without changing, significantly, the original D_{50}. Highly uniform sand will certainly eliminate the risk of *armouring* effects on the bed and within the scour hole and should decrease the movement of smaller particle sizes in the vicinity of the MC. On the other hand, this might encourage ripple formation along the test section during long-term runs.

To obtain the desired sand characteristics, grain sizes greater and smaller than specific values should be removed as much as possible from the original sand bed sample. The original sand sample was removed from the recessed flume section to eliminate the undesired particle sizes. Using a large-scale Gibson sieve shaker, the original sand sample was separated into three samples, namely grain size larger than 0.6 mm, between 0.381 and 0.6 mm, and smaller than 0.381 mm. The third sample was disposed of because of the fine sediment size. The grain size distributions of the first two sand samples were analysed and the results are presented in Figures 5.15 and 5.16, and also in Table 5.1. The angle of repose reported for the dry sand was based on Simons and Albertson's (1960) diagram. According to this diagram φ varies between 29° to 33° for *very rounded* and *very angular* sediments respectively in the size range used in our experiments.

Table 5.1- Characteristics of the sand samples

sand sample	D_{84} (mm)	D_{50} (mm)	D_{16} (mm)	σ_g —	φ (degree)	ρ_s/ρ —
1st	0.794	0.7	0.586	1.16	31	2.65
2nd	0.530	0.500	0.416	1.13	31	2.65

According to Table 5.1 the median size, D_{50}, of the second sand sample is essentially the same as that of the original sand, however, the σ_g of this sand assures a uniform grain size distribution since its value is closer to unity than that of the original sand sample. Accordingly, the second sand sample was selected for the main experimental program (the first sand sample, however, was also used to perform a limited series of experiments).

The recessed part of the test section was refilled with the 2nd sample sand mixture (D_{50}=0.5 mm) and prepared for the tests. The flow condition required to establish the threshold condition was now determined for D_{50}=0.5 mm. Initially a relatively long-term run, with a plain bed and without a model abutment, was performed at the computed near-threshold condition to investigate the behaviour of the improved bed material. It was observed that bed material movement and *trough* formation along the FP in the vicinity of the MC significantly decreased. However, ripples started forming after the third hour of the test. These ripples developed and propagated relatively rapidly in the downstream direction. Therefore, since this grain size was identified as being otherwise appropriate, vis-a-vis general boundary conditions various means of preventing ripple formation were examined.

The application of a thin layer of fast-acting cement on the sand surface stabilized the bed material upstream of the test section and significantly decreased the possibility of ripple formation in the movable-bed part upstream of the test section portion that would contain the model abutments. The hardened sand surface started at the entrance to the test section and extended 0.6 m into the test section (Figure 5.17). A thin layer of the same sand was applied on top of the cement to maintain the same surface roughness along the test section. Repeating the long-term run with a plain bed and without a model abutment indicated that ripple formation could be avoided if the sand bed was prepared with extreme care to produce an even sand surface throughout. For each test, after placing the model abutment, the surrounding hole was filled with 50 mm-thick sand layers. Each layer was compacted in a consistent manner and for a specified period of time to ensure consistent density of material throughout the testing programme. To achieve sand bed levelling as perfect as possible, a special scraper was designed and built (Plate 5.1, a). Almost perfect bed level was attained by installing the scraper over the edge of the flume wall (Figure 5.1, b) and smoothly and continuously moving it in one direction, from one end of the test section to the other end.

5.6- ABUTMENT LENGTHS

A criterion set by Melville (1992) to categorize abutment lengths was applied to determine model abutment lengths for the tests. Melville classified abutment lengths as follows:

$L/y_o < 1$	Short-length abutments,
$1 \le L/y_o \le 25$	Intermediate-length abutments, and
$L/y_o > 25$	Long-length abutments,

With regard to the chosen lower and upper limits of FP flow depth (15 and 50 mm), the range of the model abutment lengths were as follows:

$L/15 < 1 \rightarrow L < 15$ mm

$L/50 > 25 \rightarrow L > 1250$ mm

Considering 75% of the FP width of the experimental set-up as the upper limit for the abutment length, a preliminary series of tests was performed using VW-abutments and vertical sheets of plexiglass. Abutment lengths of 60, 120, 180, and 240 mm were used in these tests. The results indicated that model abutment lengths up to 210 mm can be used in the current study. The scour hole edges produced by larger model abutments rapidly approach the MC side slope which might affect the local scour depth. Accordingly, abutment lengths of 90, 150, and 210 mm were adopted for the main experiments.

5.7- ABUTMENT SHAPES

To investigate the effect of abutment shape on scour depth four different abutment shapes were considered: (*i*) VW-, (*ii*) SC-, (*iii*) WW-, and (*iv*) ST-abutments. These shapes are representative of common shapes used in practice. A side slope of 1 Horizontal:1.75 Vertical was adopted for the WW- and the ST-abutments. Also, based on the flow depth range used and the side slope adopted for the WW- and ST-abutments, a model width of 90 mm was applied. The model abutments were constructed from solid plexiglass blocks. Two-sided tape was used to attach different pieces of the plexiglass units to form the required model abutment shape and length. A schematic of the model abutments used in the study is shown in Figures 5.18 and 5.19. Also, plate 5.2 shows the actual models for the 210 mm length version.

5.8- ESTABLISHING THE DESIRED FLOW CONDITION

The required flow condition depends on the longitudinal channel slope and grain size selected. According to section 5.2.1 the longitudinal slopes selected are S_o=0.0006, 0.00075, and 0.0009. Also, based on section 5.5.1, the sand sample that had its D_{50}=0.5 mm is the most suitable for the study. Knowing the sediment size and the longitudinal slopes, the required flow depth in the FP can be determined according to Figure 5.12. Since Figure 5.12 was based on Shields' diagram, applying the flow depth given by this figure ensures the establishment of the near-threshold condition.

Table 5.2- Depths applied in the current study, for D_{50}=0.5 mm

S_o —	y_* (mm)	H (mm)	y_*/H —
0.0006	42	146	0.29
0.00075	33	137	0.24
0.0009	28	132	0.21

The required flow condition can only be established by setting the appropriate discharge so as to produce the desired flow depth in the FP. With D_{50}=0.5 mm, for each longitudinal slope the required FP flow depth is determined from Figure 5.12. The discharge associated with the selected flow depth can now be determined using the prepared Q-y_o curves (Figures 5.4 to 5.6). The same procedures were also followed to determine the required flow condition for S_o=0.0009 and D_{50}=0.7 mm. Tables 5.2 and 5.3 summarize the results.

Table 5.3-Depths applied in the current study, for D_{50}=0.7 mm

S_o —	y_* (mm)	H (mm)	y_*/H —
0.0009	38	142	0.27

5.9- SELECTION OF TEST DURATION

An appropriate duration for the experiment can only be selected after studying the time variations of the local scour development for the test conditions. Therefore, the first tests were initially run for different periods so as to examine the progression of the local scouring process over time. The experiments were performed for a constant channel slope setting of 0.0006, with flow conditions selected to establish the threshold condition of bed movement for sand with D_{50}=0.5 mm. The procedures given in section 5.8 indicated that a FP depth of 42 mm establishes the desired condition. The same flow conditions were applied to all the tests performed with this bed slope setting. This series of tests consisted of fourteen experiments run for periods of 9.3 hours to a duration exceeding the time required to reach y_{se}. Table 5.4 summarizes the abutment shapes and the total durations applied in each test.

The variations of local scour depth with time for these tests, according to selected abutment end shape and length are presented in Figures 5.20 to 5.23. Figures 5.24 to 5.26, on the other hand, show the impact of different end shapes on scour rate of a specified model abutment length. These two sets of figures show the effect of both length (Figures 5.20 to 5.23) and shape (Figures 5.24 to 5.26) of abutments on the temporal development and final local scour pattern.

Table 5.4- Total test duration applied in each test (hr)

Abutment length (mm)	model abutment shape			
	ST	SC	WW	VW
90	85.0 & 11.7	11.4	10.0	46.8
150	142.0 & 15.0	17.0	16.0	16.5
210	12.0	12.3	9.3	11.0

The first observation one can make is that the scour depth increases with increasing abutment length (Figures 5.20 to 5.23). Also, more of the approach flow is redirected by longer abutments towards the abutment end. This results in increased flow at the end of longer abutments, which accelerates the scouring process towards the equilibrium state. However, the effect of abutment shape on temporal scour development decreases as their length increases (Figures 5.24 to 5.26). Figure 5.24 shows that VW- and WW-abutments produce practically the same effects on the temporal development of the scour hole during the twelve-hour tests. Also, for the same hydraulic conditions the lowest rate of scour was associated with the ST-abutment, whereas the highest rate was associated with the VW-abutment (Figure 5.24). Since the temporal variations of the scour depth are measured at one designated point during a test, the maximum scour depths noted in these figures are not necessarily absolute values. The shape and the length of an abutment have a large impact on the complexity of the flow field generated around an abutment. Hence, the magnitude and position of the maximum scour depth eventually depend on the aforementioned factors.

Considering the equilibrium scour depth, y_{se}, and the scour depth at a specified time, y_s, a practical duration for a test might be selected provided a relationship between y_{se} and y_s is defined. A *long-period* test (142 hr) was performed to establish such a relationship. Figure 5.27 shows the temporal variation of the scour depth for this test. Also indicated on Figure 5.27 are the scour depths associated with the time required for achieving 90% (t_{90}) and 95% (t_{95}) of the equilibrium scour depth. The scour depths associated with t_{90} and t_{95} are also indicated. Two other *long-period* tests were also performed using ST- and VW-abutments, each 90 mm in length. Figure 5.28 shows the temporal variations of the scour holes for these two tests.

The data in Figures 5.28 and 5.29 were normalized using t_{90} and the scour depth associated with it (Figure 5.29). The reason for using t_{90} instead of t_{se} (the time associated with the equilibrium scour depth) is that it is not possible to assign a specific time to y_{se} (Figure 5.27). According to Figure 5.27 the magnitude of y_{se} is more reliable than the time associated with it, therefore, t_{90} associated with $0.9y_{se}$ was selected because it is a specific value on the curve. A curve fitted to these normalized data shows that about 65% of y_{se} was developed during the first nine hours of the tests. Figure 5.29 also indicates that, if an experimental period of 5 hr is selected, the scour depth will amount to 60% of y_{se}. Therefore, given the small difference between these two results, a five-hour test period was adopted in this study. The maximum scour depths (for D_{50}=0.5 mm) observed in our study will therefore be adjusted, based on the Figure 5.29 data, to give corresponding y_{se}-values.

To examine the accuracy of this *extrapolation* procedure, based on the results of the fifth hour for the completed tests, a comparison was performed between measured and computed scour depths of the ninth hour. Figure 5.30 shows the results along with the line of perfect agreement and lines of error. Most of the data collapsed close to the line of perfect agreement. Also, the lines of ±6% error form an envelop to the data. The results, therefore, indicate a good agreement between the measured and the computed scour depth.

5.10-SIMULATING *NON-INTERACTING* FLOW CONDITION

The effects of the MC-FP flow interaction on the local scour process in the FP can be better understood if, in addition to the previous experiments, a few series of test are also performed with a non-interacting flow condition. The results of such tests make it possible to observe whether or not a similarity exists between the scour depth obtained in the FP of a compound channel and that obtained in rectangular flumes. To perform these tests, for the same flow conditions as were applied in the main tests, the flow of the MC should be separated from that of the FP. The method by which the non-interacting flow condition was simulated is described herein.

Applying any means to separate the MC flow from the FP flow affects the established normal flow condition for the specific bed slope setting. However, it was necessary to install a long thin metal sheet at the MC/FP junction to separate the main-channel from the FP flow components. A 0.5 mm thick metal sheet 0.202 m wide and 2.438 m long, was formed in an *L*-shape and installed over the test section junction line separating the MC and the left FP zone (Figure 5.31 and Plate 5.3).

5.11-EFFECTS OF THE GRAIN SIZE

To study the effect of grain size on the local scour depth, two series of tests were performed using the D_{50}=0.7 mm sand sample. For a given bed slope setting, this grain size requires larger flow depth than the smaller sediment size (D_{50}=0.5 mm) to achieve the threshold condition. For D_{50}=0.7 mm the flow depths required to initiate motion at bed slope settings of 0.0006 and 0.00075 produce FP depth to total depth ratios higher than 0.3. Therefore, only a longitudinal bed slope of 0.0009 was adopted for the tests involving this particular sand.

If a larger grain size is employed the corresponding threshold condition requires a higher flow velocity. This is well demonstrated in Figure 5.12. The curves of this figure relate flow depth to grain size to maintain a near-threshold condition for a given longitudinal bed slope. According to this figure, considering two differing grain sizes and a constant flow depth, larger grain size must lie on a higher curve if the threshold condition is to be maintained. A higher curve, however, indicates that a steeper slope is required. A steeper slope implies higher flow velocities, which in turn increase the scour rate such that the equilibrium scour is achieved faster. It is, therefore, necessary to determine the relationship between the measured scour depth (after 5 hr) and y_{se} for experiments performed using the larger grain size, (i.e. D_{50}=0.7 mm).

A long-term test using a 150 mm-long ST abutment was performed at the near-threshold condition for D_{50}=0.7 mm. The test continued for a period exceeding 168 hr, i.e. more than 48 hr after the equilibrium scour depth had been achieved. The results of this test are presented in Figure 5.32. Also indicated on this figure are the scour depths associated with t_{95} and t_{90}. To make a comparison of the results possible, the model abutment chosen for this test was the same as that applied in the long-term test performed with D_{50}=0.5 mm. The results of these two experiments are plotted together in Figure 5.33. It indicates that the scour rate for the coarser sand during the first few hours of the test is higher than the scour rate for the finer sand.

An enlarged view of the lower left corner of Figure 5.33 (presented in Figure 3.34) clearly indicates the difference in the scour rates. Having a higher scour rate at the beginning of the experiment obviously results in a higher y_s/y_{se} ratio for the measured scour depths. To determine y_s/y_{se} for this grain size, the Figure 5.32 data were normalized using t_{90} and the scour depths associated with it are plotted in Figure 5.35. According to Figure 5.35 the observed scour depths amount to 65% of y_{se}. Therefore, the maximum scour depth observed in experiments performed with D_{50}=0.7 mm were adjusted using the aforementioned y_s/y_{se} ratio to give corresponding y_{se}-values.

5.12- SCOUR RATE IN *NON-INTERACTING* FLOW CONDITIONS

Separating the MC flow from the FP flow (by means of a thin metal sheet as discussed in section 5.10) induces unique flow and geometric conditions in the test section which might affect y_s/y_{se}. Therefore, a long-period test was performed for the *non-interacting* flow conditions using D_{50}=0.7 mm and the 150 mm-long ST model abutment. The test data are presented in Figure 5.36. The data for the first 12 hr of two similar tests, i.e. one for an *interacting* condition and the other for an *non-interacting* condition and D_{50}=0.7 mm, are compared in Figure 5.37. The results clearly show that, during the initial stages of the scouring process, a higher scour rate was observed for the *non-interacting* condition, than was observed for the *interacting* condition. This indicates that although identical scour depths were recorded at the end of the fifth hour of both experiments, the scour depth for the *non-interacting* condition represents a higher value of y_s/y_{se} than than for the *interacting* condition. This difference can be attributed to the modified flow condition in the FP. The flow diverted by the abutment is forced to pass only through the opening width bounded by the flow-separating wall and the abutment head; there is no possibility for the diverted flow to be conveyed in the MC. This induced higher flow acceleration at the abutment end which, in turn, increased the rate of scour during the initial stage of the erosion process.

To determine y_s/y_{se} for *the non-interacting* condition, the data of Figure 5.36 were normalized according to t_{90} and the scour depth associated with it. Presented in Figure 3.38, the results indicate that y_s/y_{se} for the *non-interacting* condition is 5% higher than for the *interacting* case. This value was adopted to adjust the scour depth measured in all the tests performed under *non-interacting* conditions.

5.13- FLOW VISUALIZATION TECHNIQUES

The presence of a model abutment in the FP obstructs the approaching flow and redirects it towards the MC/FP junction. A flow-visualization technique is required to determine the angle, β, by which the diverted flow combines with the rest of the FP and MC flow. Although the two flows combine at the abutment end, the adjacent flow fields are also affected. Accordingly, the visualization technique used should be capable of demonstrating the zone of influence of this particular flow feature.

Different means were examined for visualizing the surface flow pattern in the vicinity of the model abutment end. Dusting small bright particles (confetti) on the water surface and photographing their paths (using an extended shutter speed and different lighting conditions) gave results similar to those shown in Plates 5. 4 and 5.5. These plates indicate that, although the white confetti produced reasonable results, increasing the colour intensity of the channel bed would improve the contrast. In a particular experiment using the 210 mm long VW-abutment, the scoured bed was fixed using a thin layer of fast-acting cement and then painted. The required flow condition was then re-established and photographs were taken of the confetti paths using extended shutter speeds with different lighting conditions. Some of the results are presented in plate 5.6 (for the *non-interacting* condition) and in plates 5.7 to 5.9 (for the *interacting* condition). The plates clearly show the direction of the deflected flow and the extent of the adjacent flow fields affected by the deflected flow.

While providing good detail of the general flow pattern, this flow-visualization method is , however, very time consuming (takes a few days) and therefore was not applied in every test. As an alternative to the *surface confetti* technique a *floating strings* method (Plate 5.10) was examined. While ignoring the small-scale flow structures, the method of *floating strings* detected the same general flow pattern as that detected by the white confetti. Therefore, it was used in the present study. Plate 5.10 shows the flow pattern, using *floating strings*, prior to installing a model abutment, and Plates 5.11 and 5.12 show the flow pattern for the *interacting* and *non-interacting* conditions respectively for the same model abutment used in plates 5.4 to 5.9.

The strings were attached to a carrier at a spacing of 25 mm between strings. To photograph the surface flow pattern, the carrier was located in specific locations on the flume walls (to maintain the same relative references in the photographs). Plates 5.13 and 5.14 show the installation method of the floating strings in *interacting* and *non-interacting* conditions respectively.

The *floating strings* method has the advantage over the *surface confetti* method of being capable of capturing the extent of the lateral movements in a single photograph. Such a photograph shows the extent of the influence of the model abutment on the adjacent flow field. The surface flow patterns for long-period test for *interacting* and *non-interacting* conditions using D_{50}=0.7 mm and S_o=0.0009 are shown in plates 5.15 and 5.16. These plates were photographed using 1/60-sec exposure. The same conditions were also photographed using prolonged shutter speeds (4 and 8-sec exposure) to examine the extent of the lateral movements of the *floating strings* (plates 5.17 and 5.18). Plates 5.17 and 5.18 show essentially the same surface flow pattern as that of plates 5.15 and 5.16. Also, comparing the former plates with the latter ones indicates that the minor lateral movements fit within the streamlines bound shown in plates 5.15 and 5.16. Therefore, a shutter speed of 1/30 or higher was adopted for capturing the surface flow pattern of each experiment.

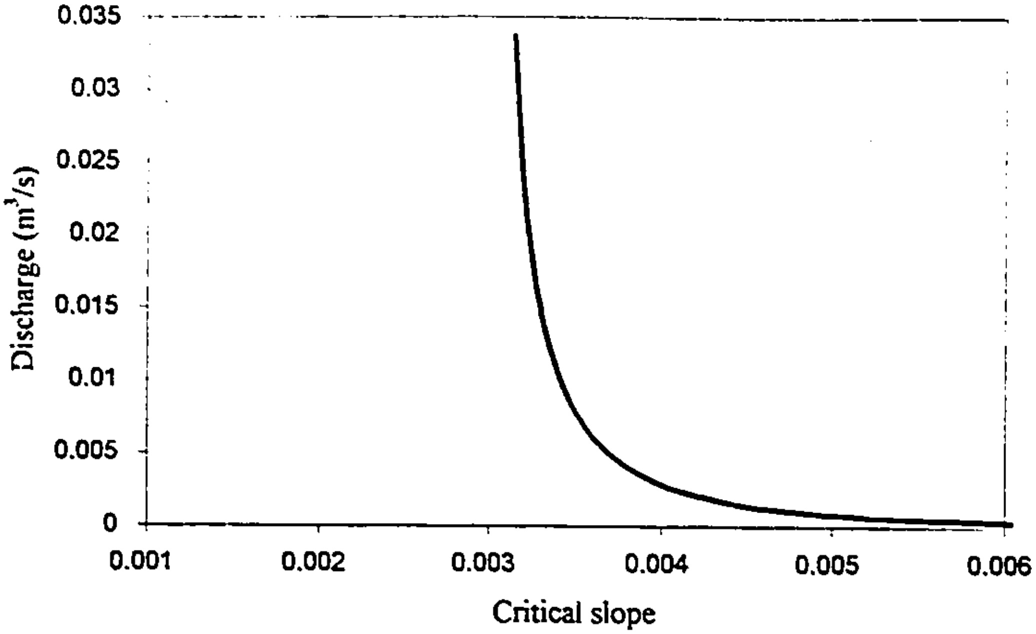

Figure 5.1- Discharge-critical slope curve of the flume's main channel

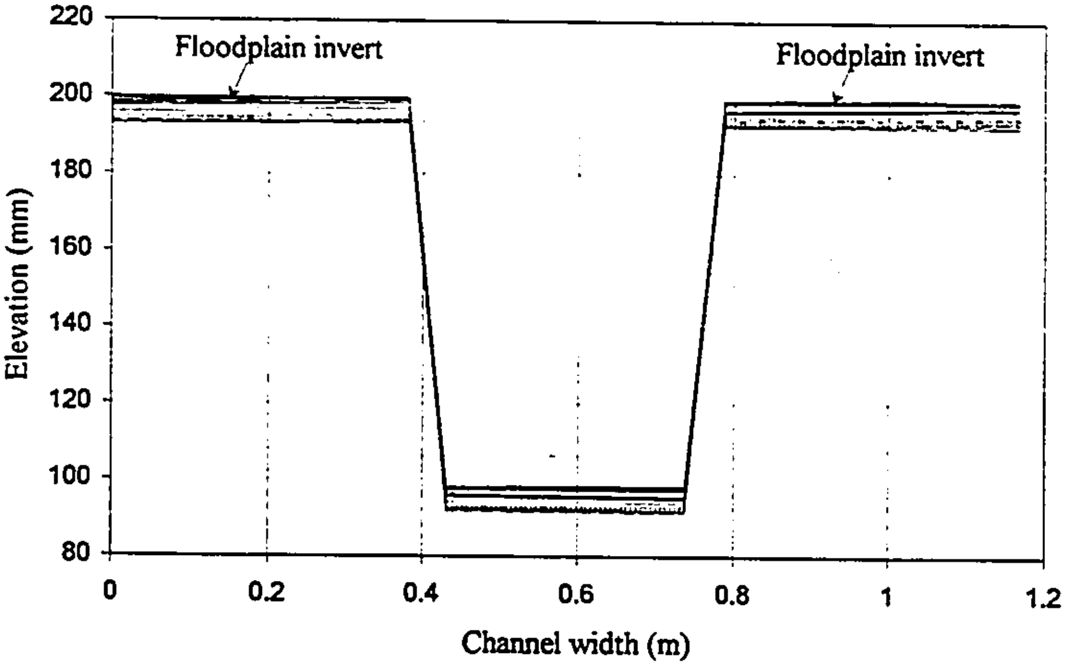

Figure 5.2- Cross-section profiles of the flume at 15 different sections

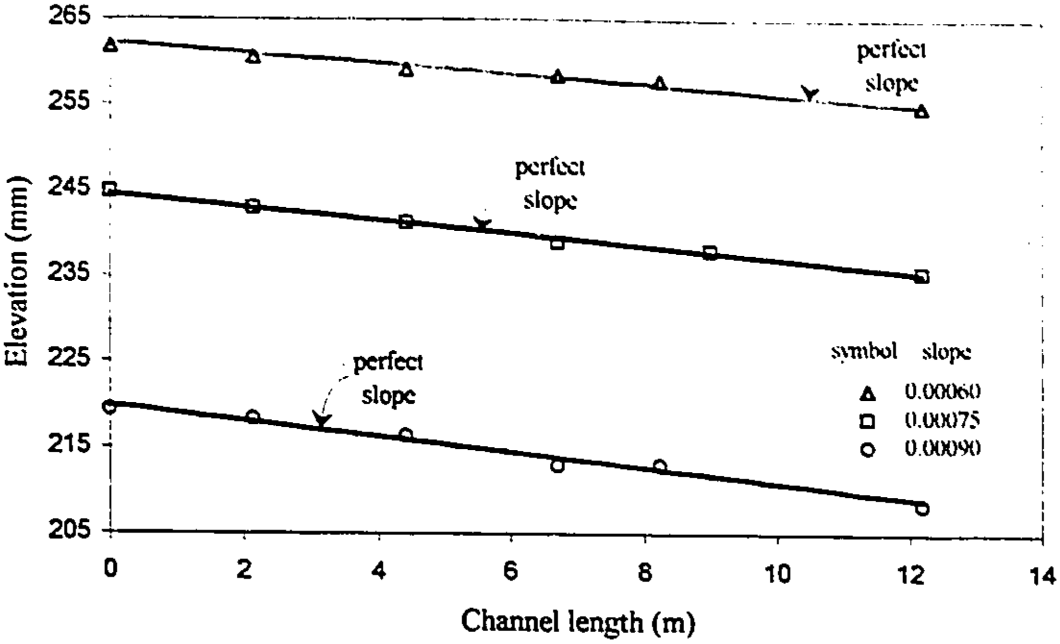

Figure 5.3- Comparison of measured channel bed profiles with the perfect conditions

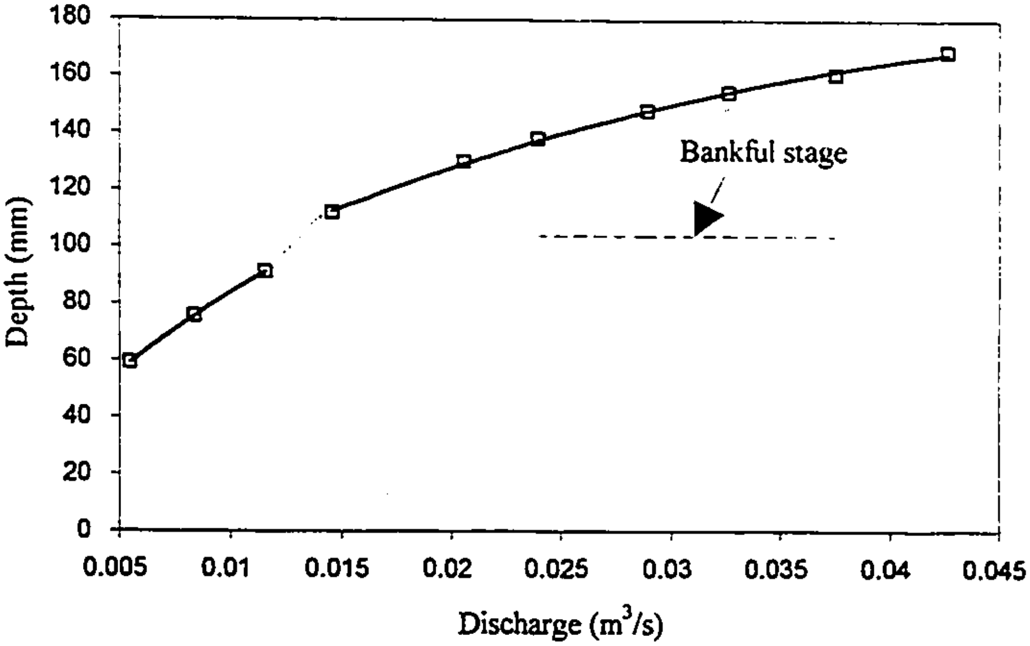

Figure 5.4- Depth-discharge curve of the compound flume for S_o=0.0006

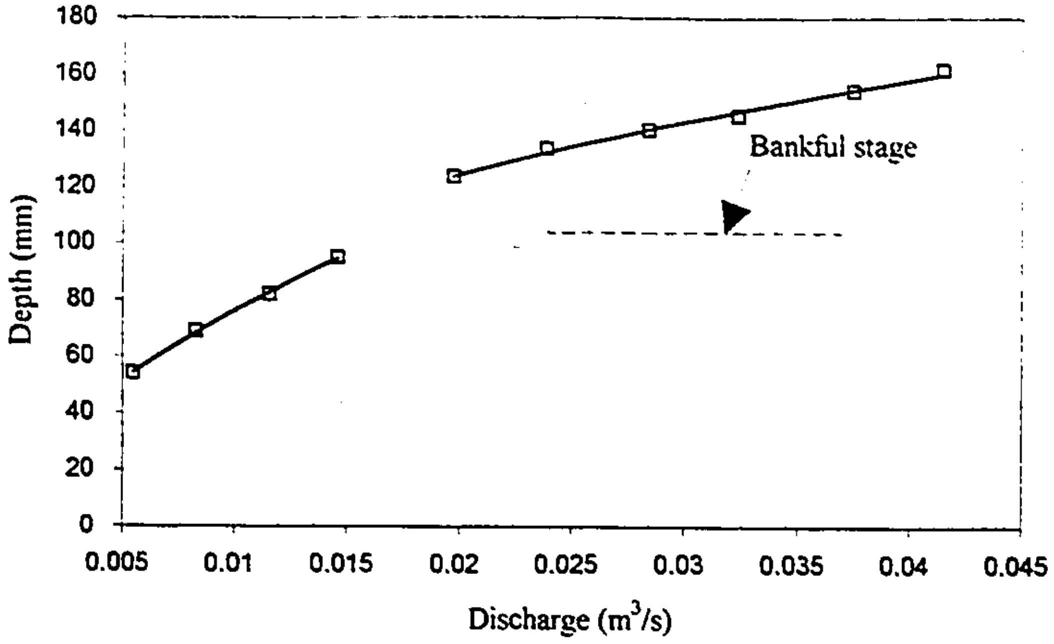

Figure 5.5- Depth-discharge curve of the compound flume for S_o=0.00075

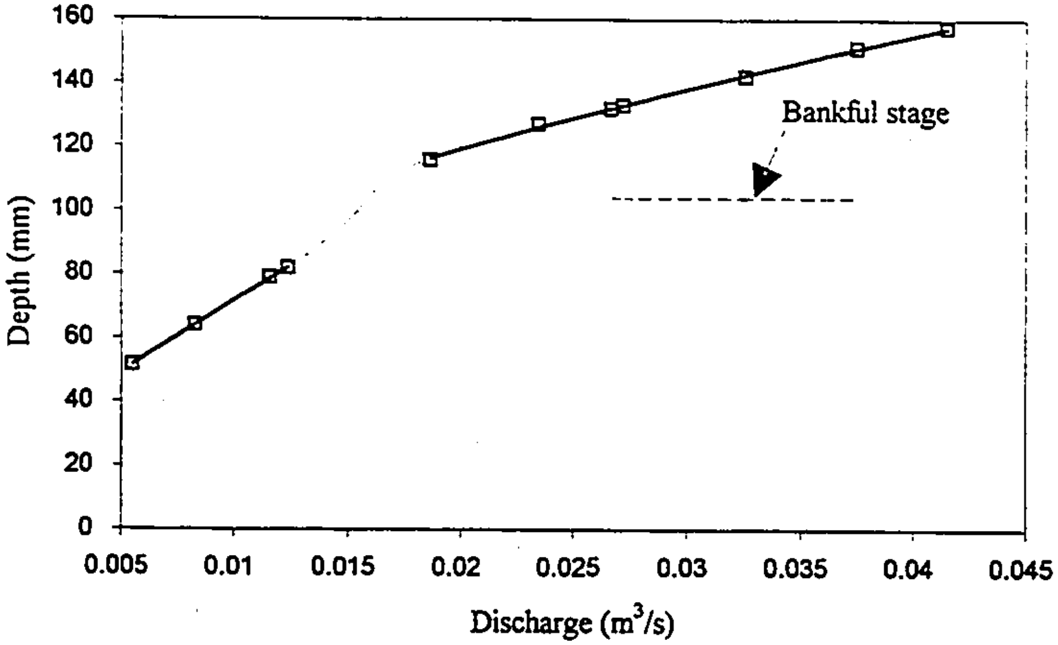

Figure 5.6- Depth-discharge curve of the compound flume for S_o=0.0009

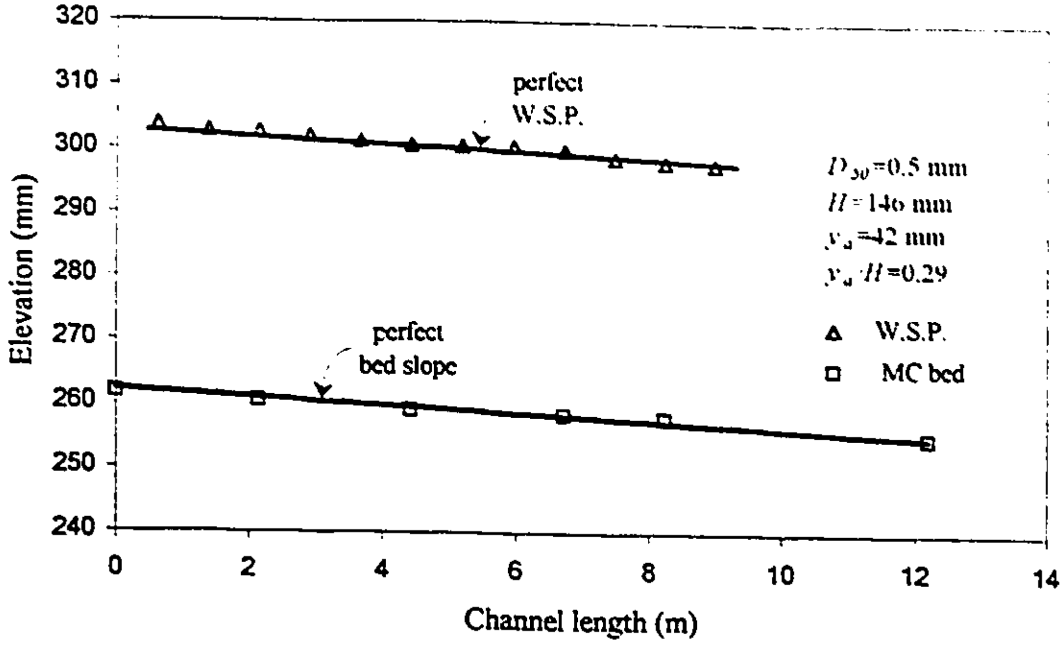

Figure 5.7- Channel bed and water surface profile for S_o=0.0006

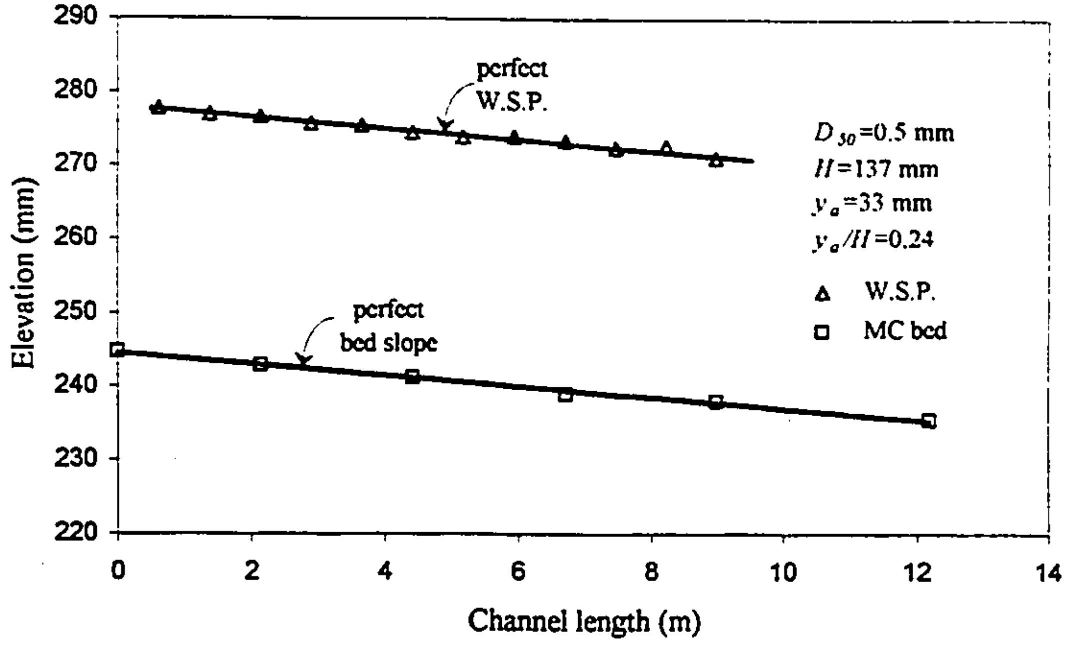

Figure 5.8- Channel bed and water surface profile for S_o=0.00075

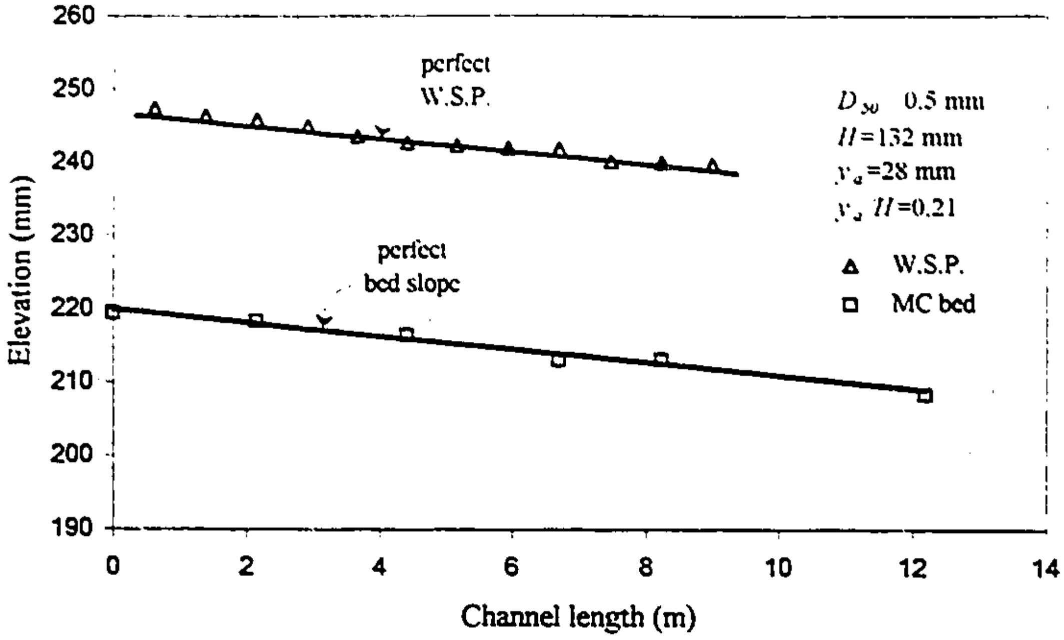

Figure 5.9- Channel bed and water surface profile for S_o=0.0009

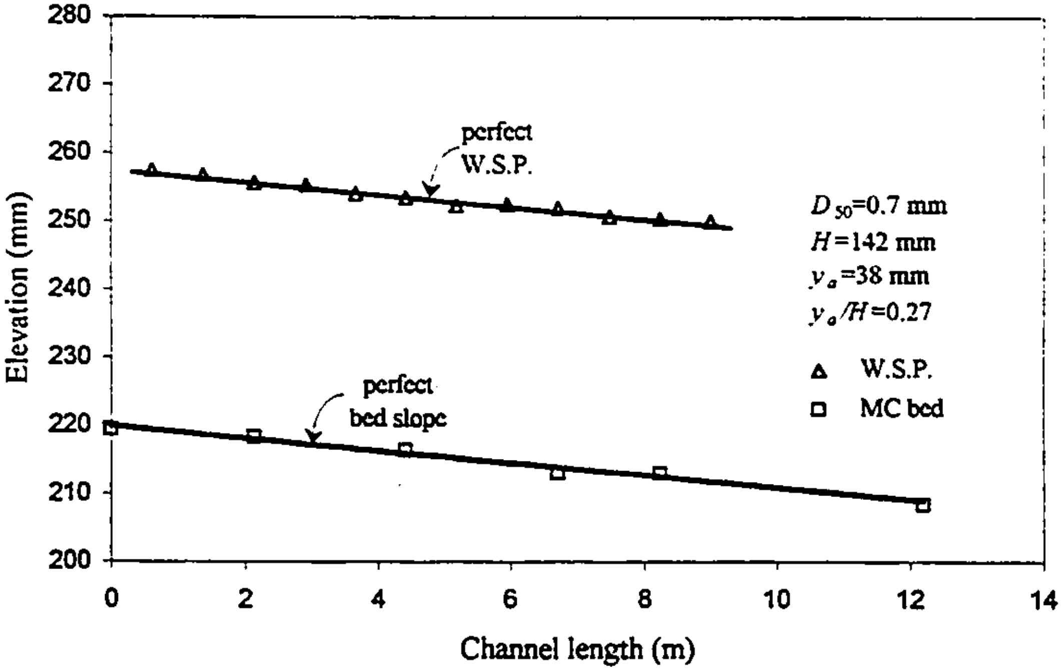

Figure 5.10- Channel bed and water surface profile for S_o=0.0009

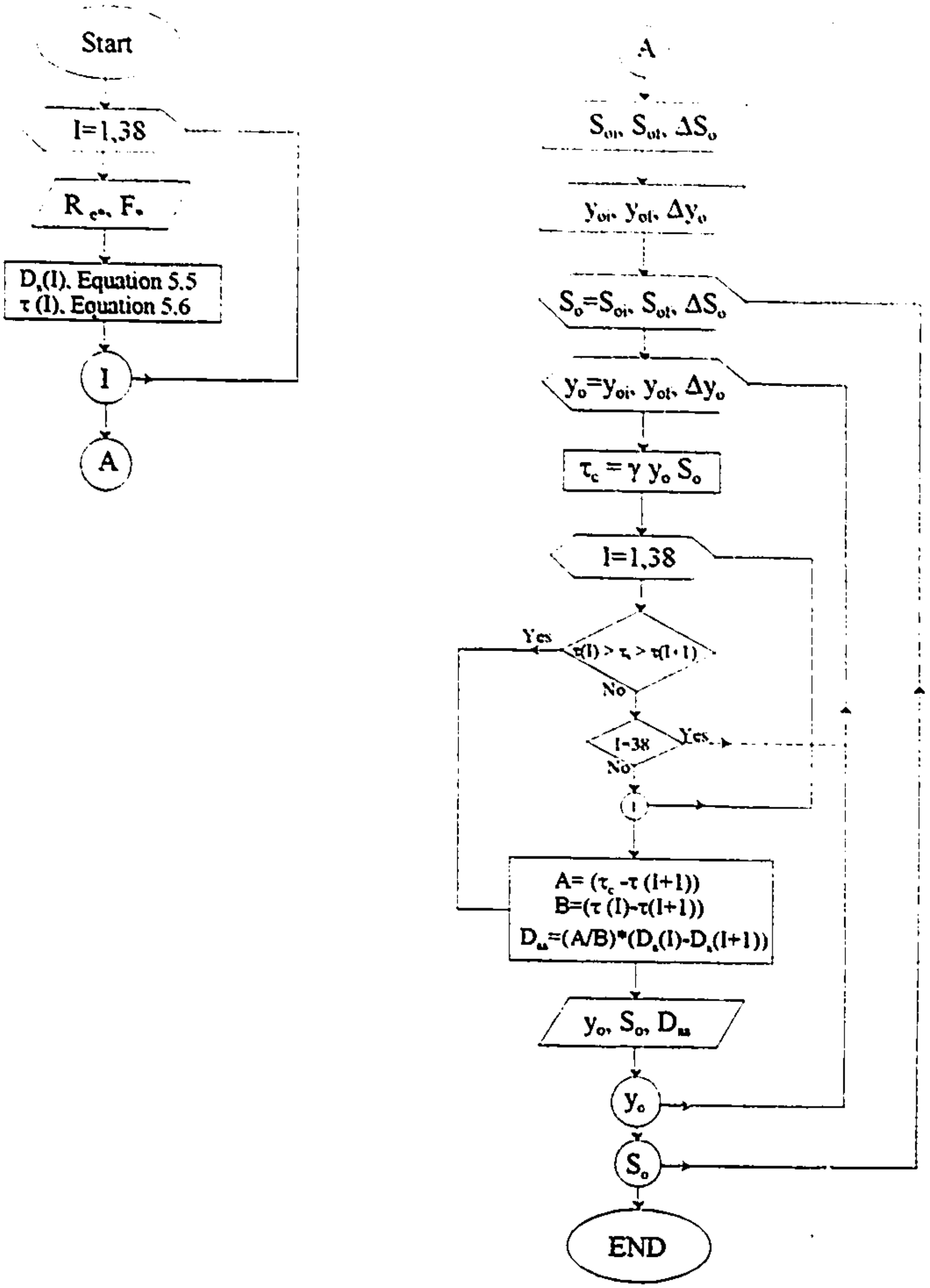

Figure 5.11- Flowchart to determine the relationship between y_o-S_o-D_s for threshold condition

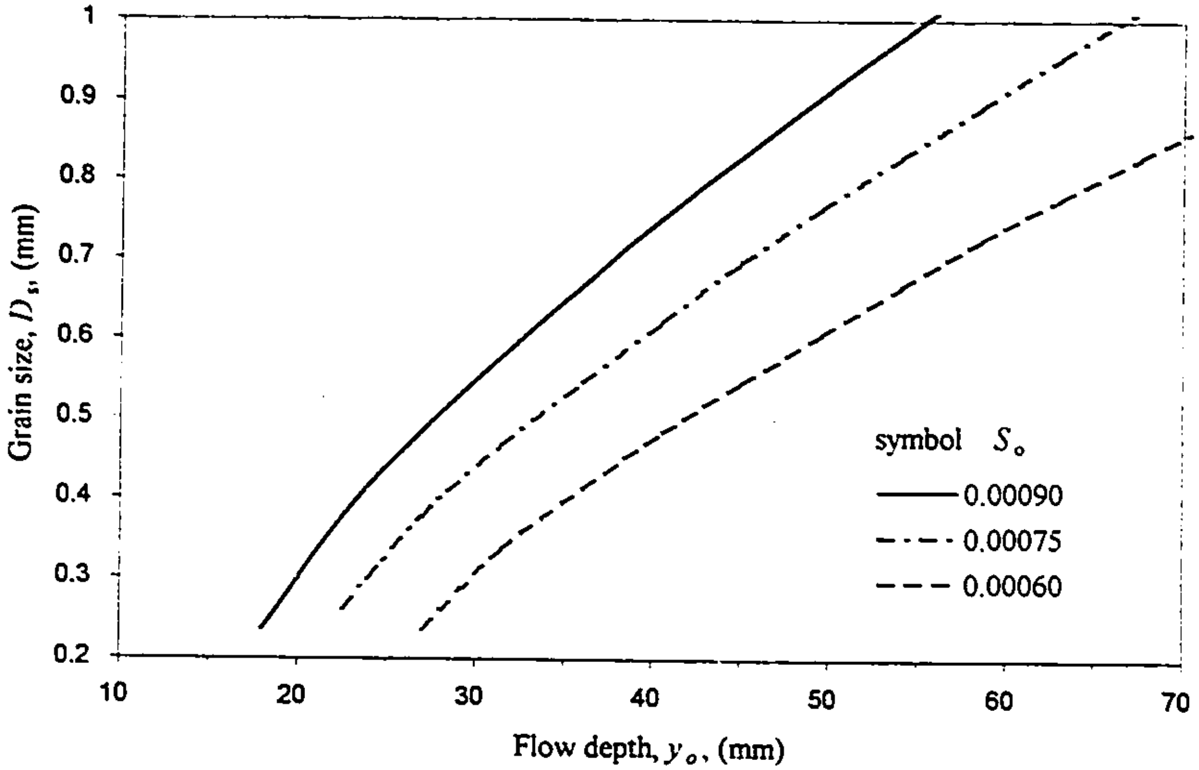

Figure 5.12- y_o-S_o-D_s-relationship for establishing near-threshold condition (u_*/u_{*c}=0.95)

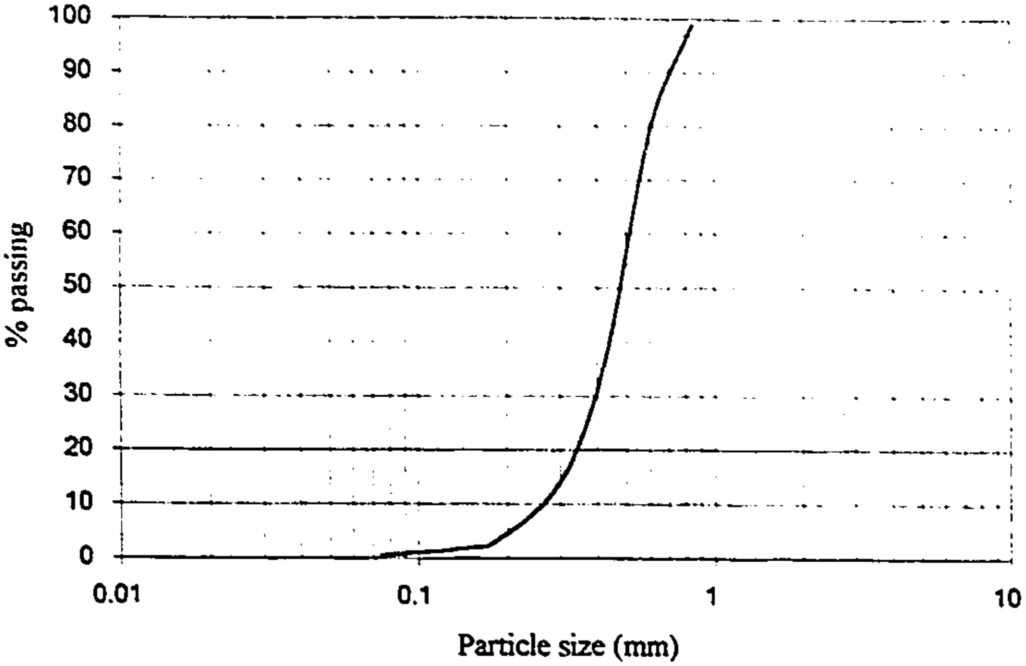

Figure 5.13- Grain size distribution of the original Play sand

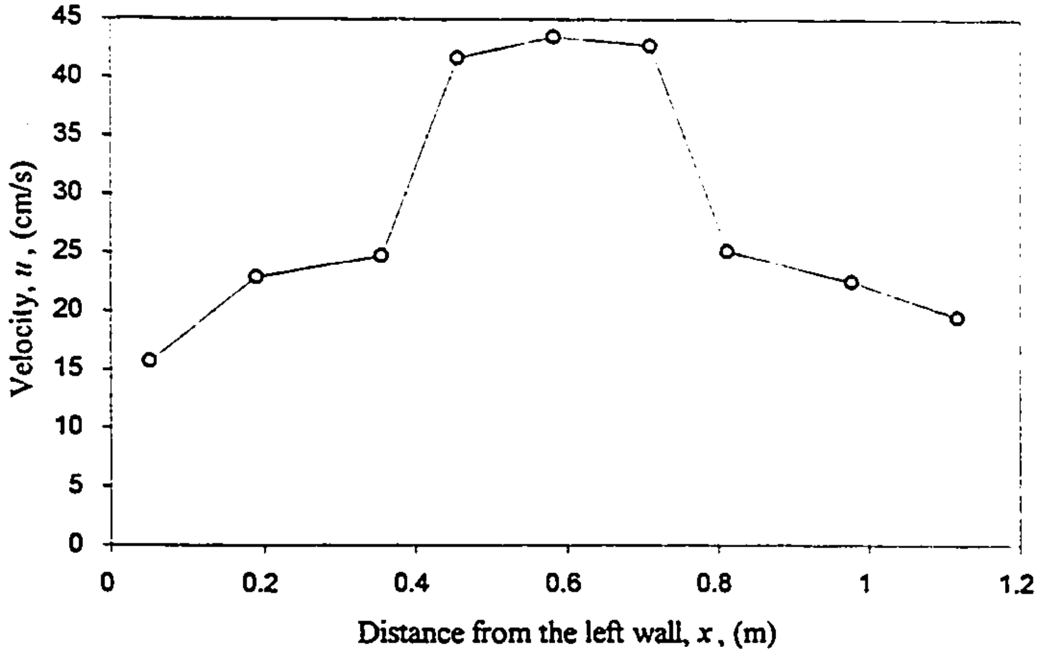

Figure 5.14- Mean longitudinal velocity profile at half-depth of the floodplain

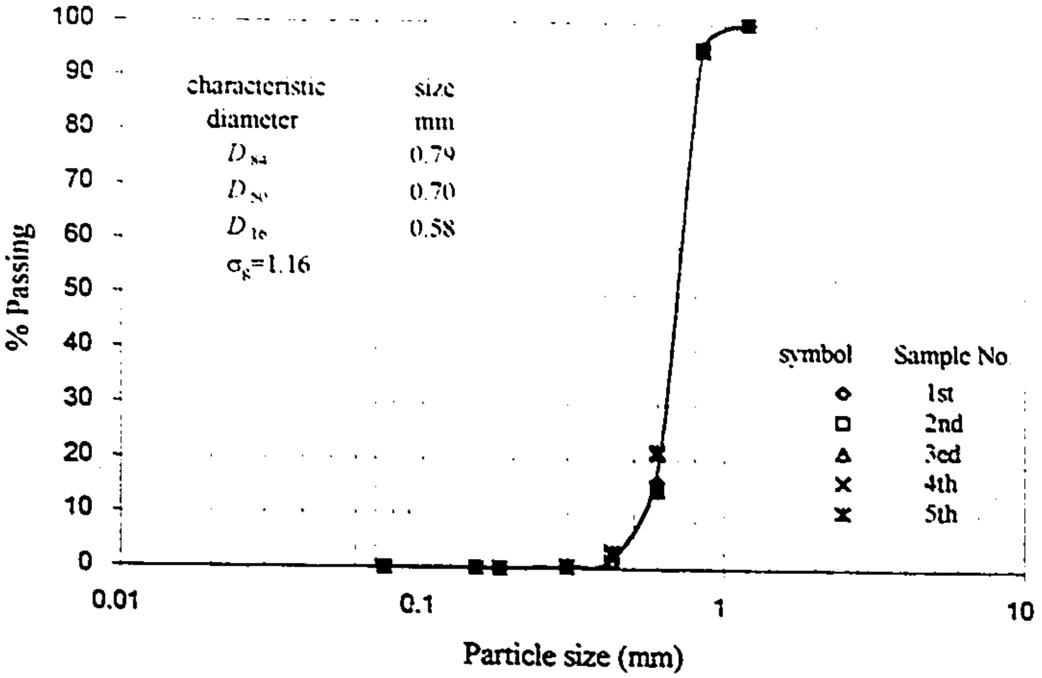

Figure 5.15- Grain size distribution, first sand sample

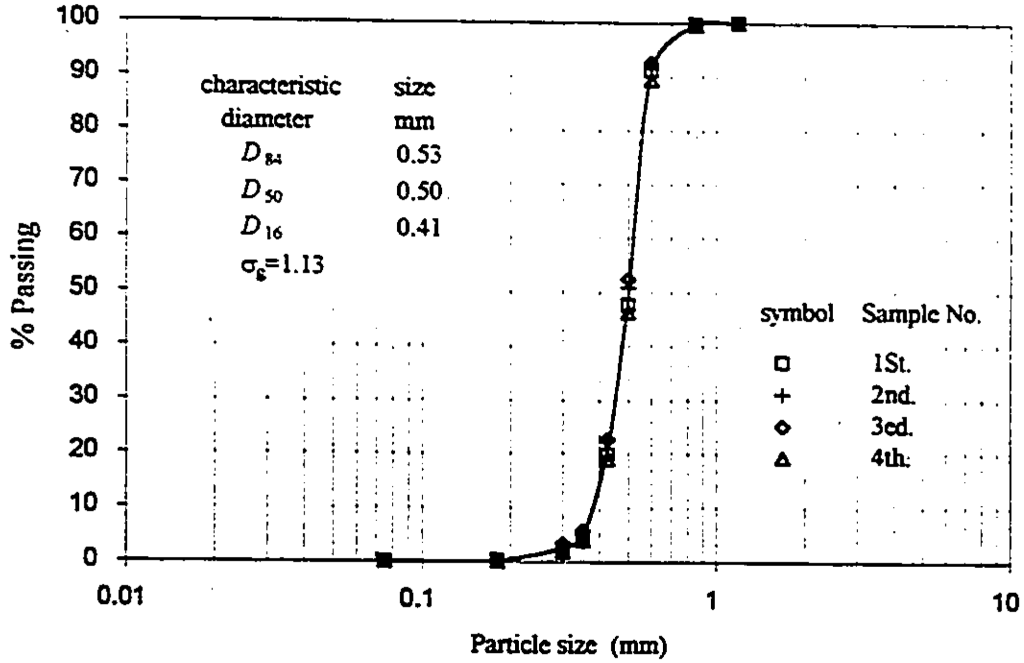

Figure 5.16- Grain size distribution, second sand sample

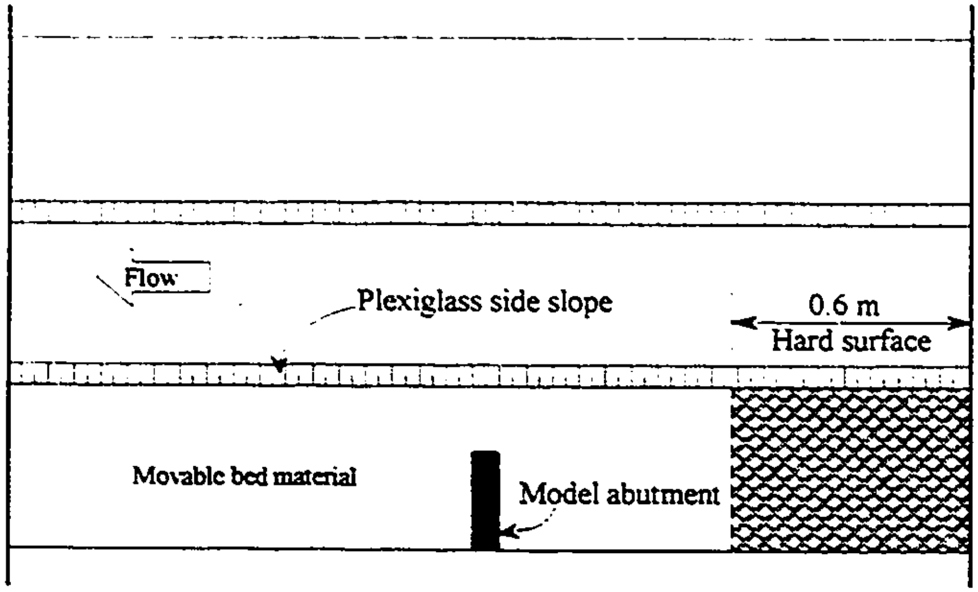

Figure 5.17- Test section arrangement

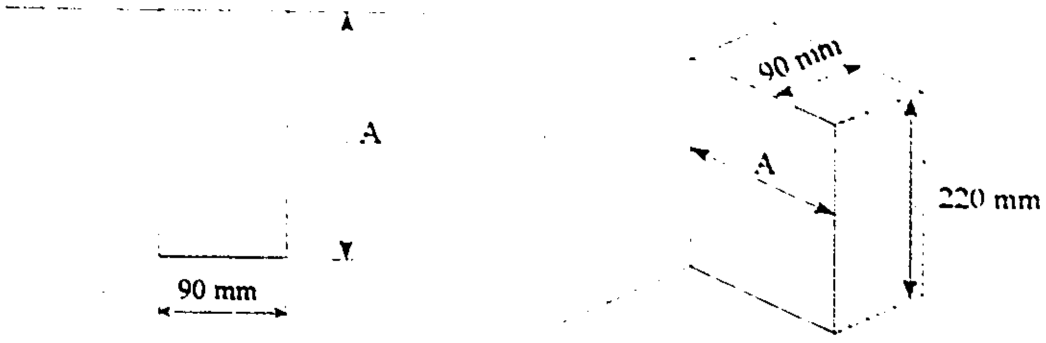

a- Vertical-wall (VW) abutment

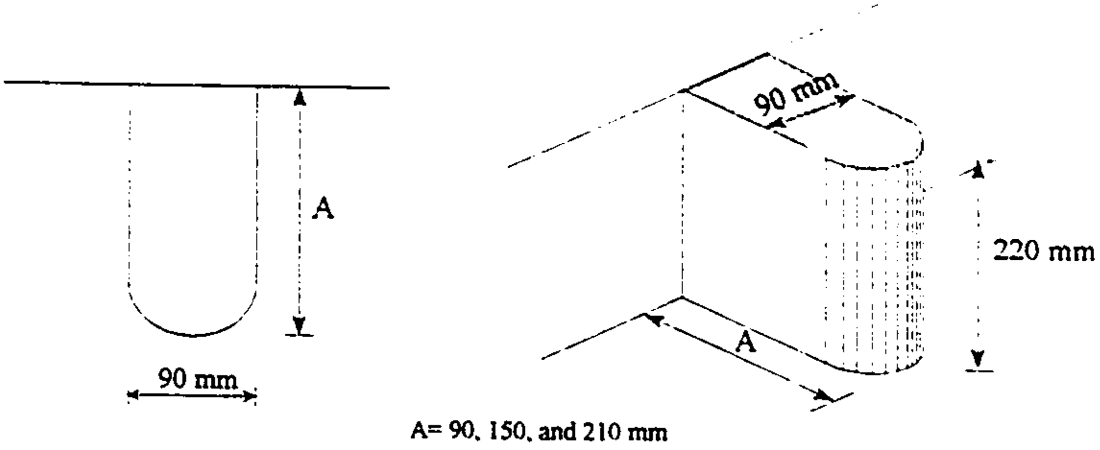

b- Semi-circular (SC) abutment

Figure 5.18- Schematic of the VW and SC model abutments

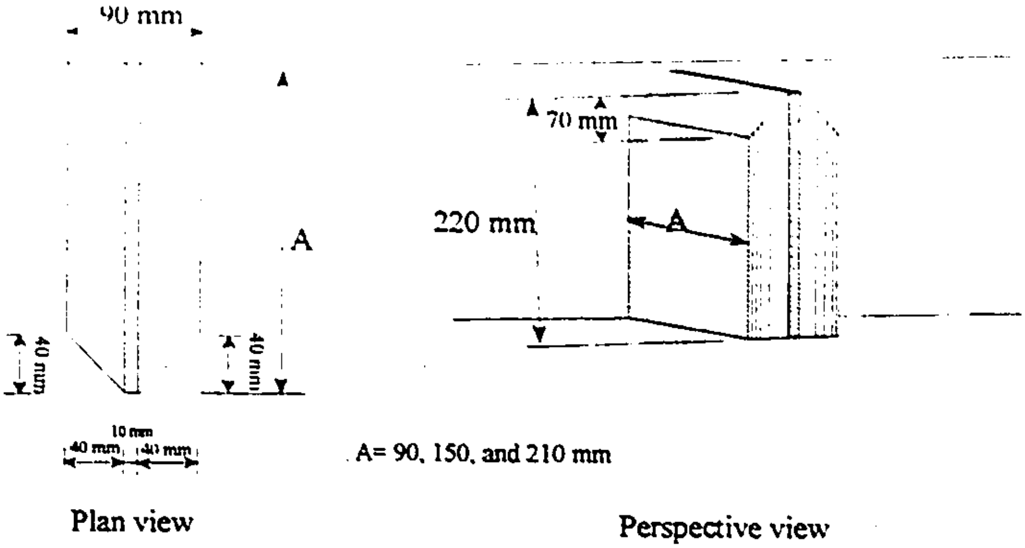

a- Wing-wall (WW) abutment

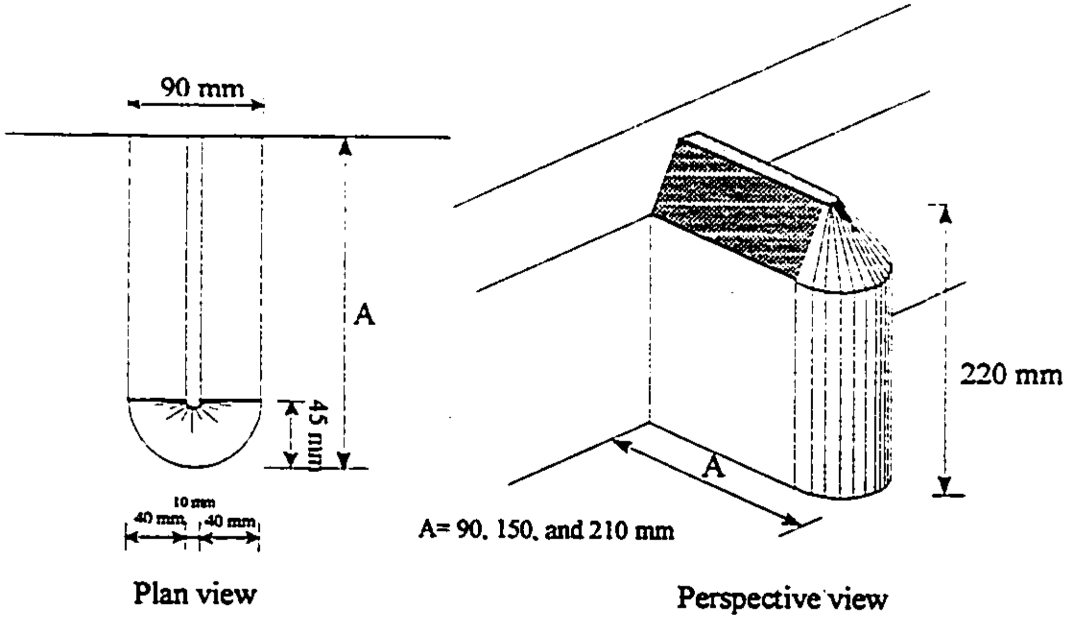

b- Spill-through (ST) abutment

Figure 5.19- Schematic of the WW and ST model abutments

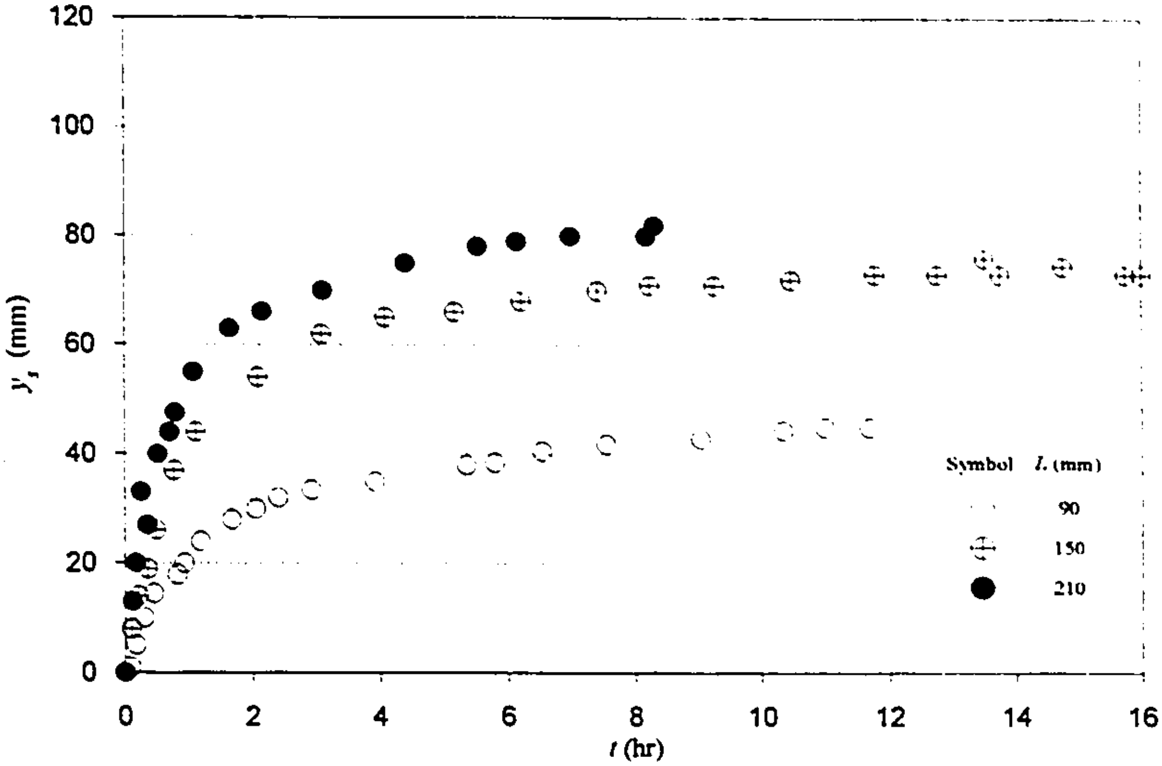

Figure 5.20- Temporal scour development, ST-abutments

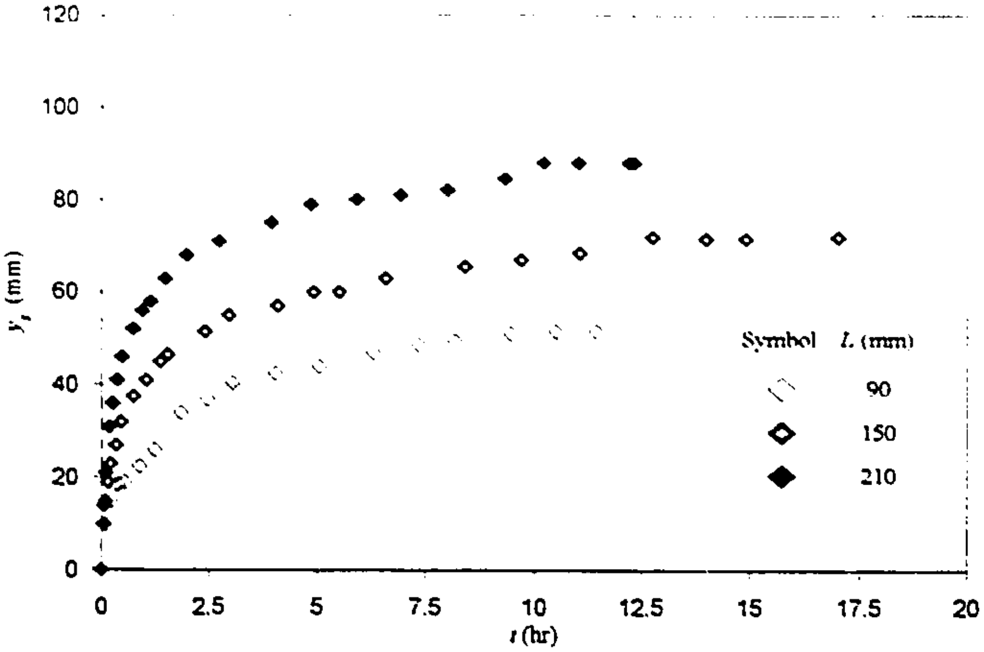

Figure 5.21- Temporal scour development, SC-abutments

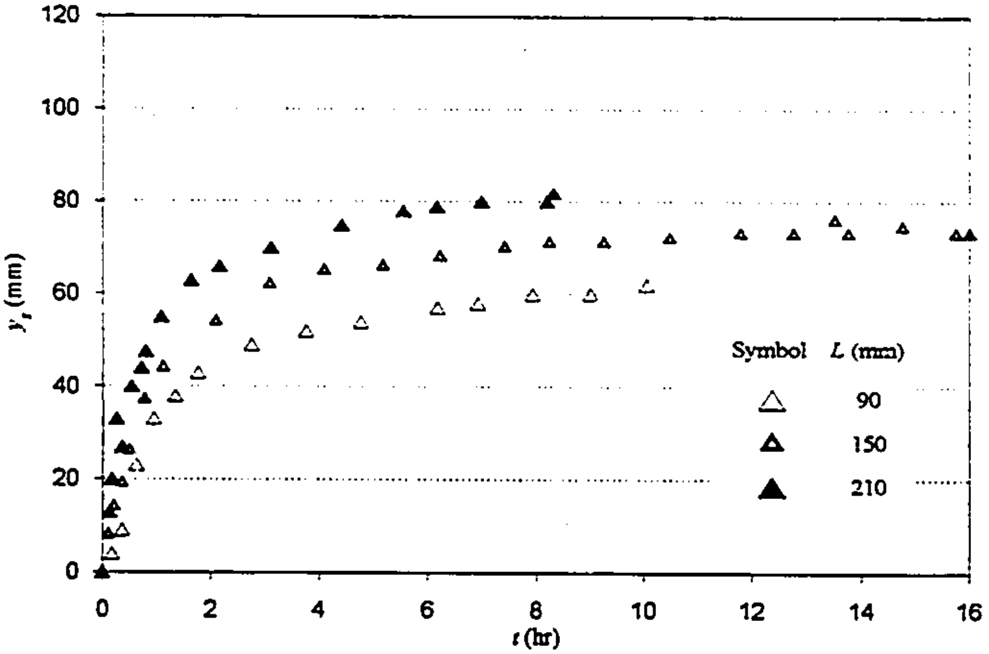

Figure 5.22- Temporal scour development, WW-abutments

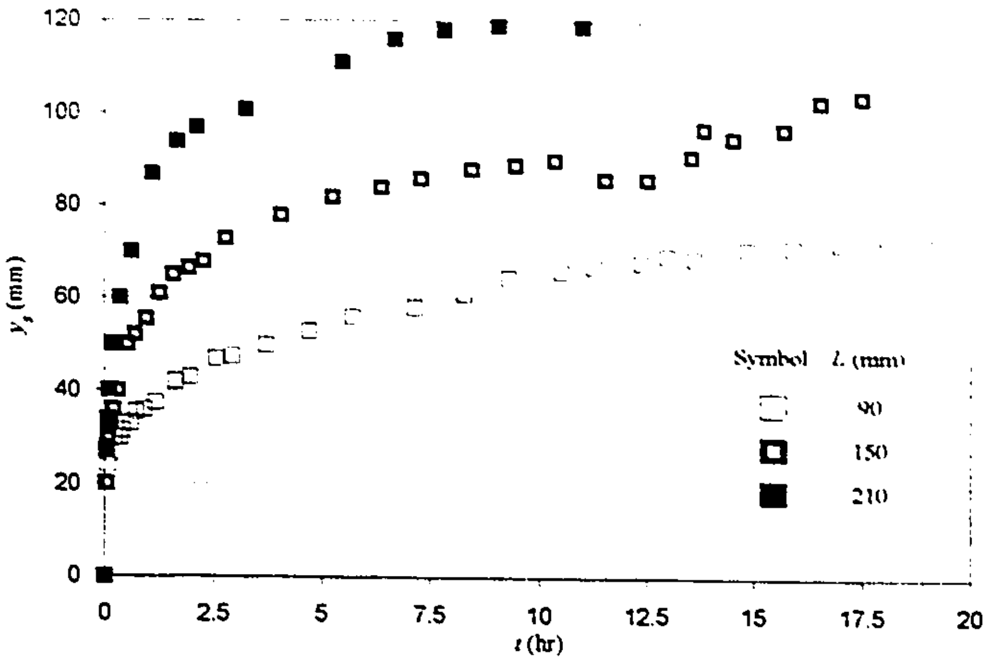

Figure 5.23- Temporal scour development. VW-abutments

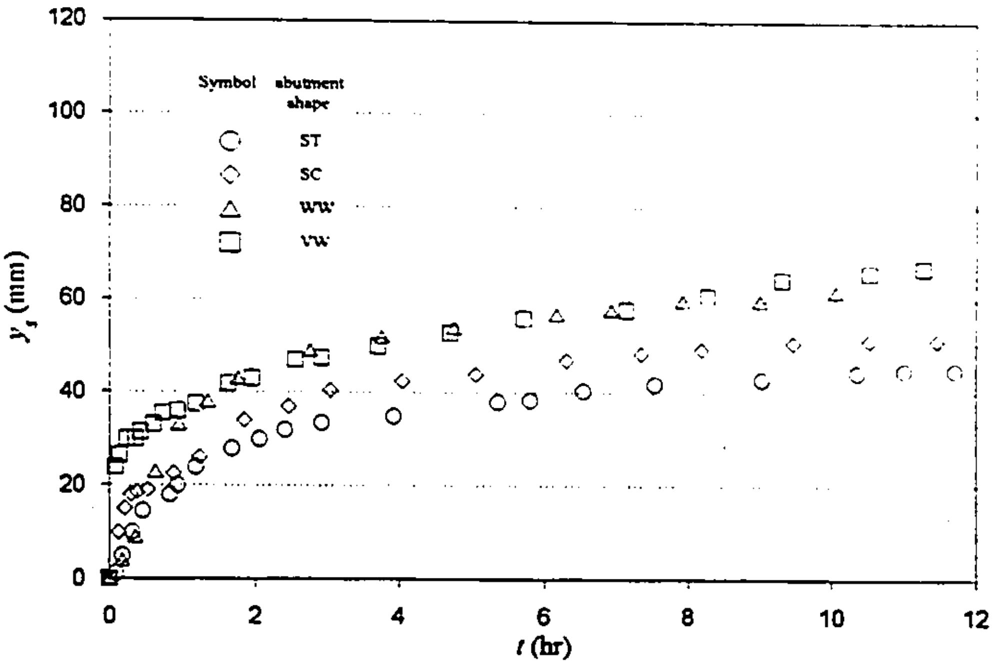

Figure 5.24- Temporal scour development, 90 mm-long abutments

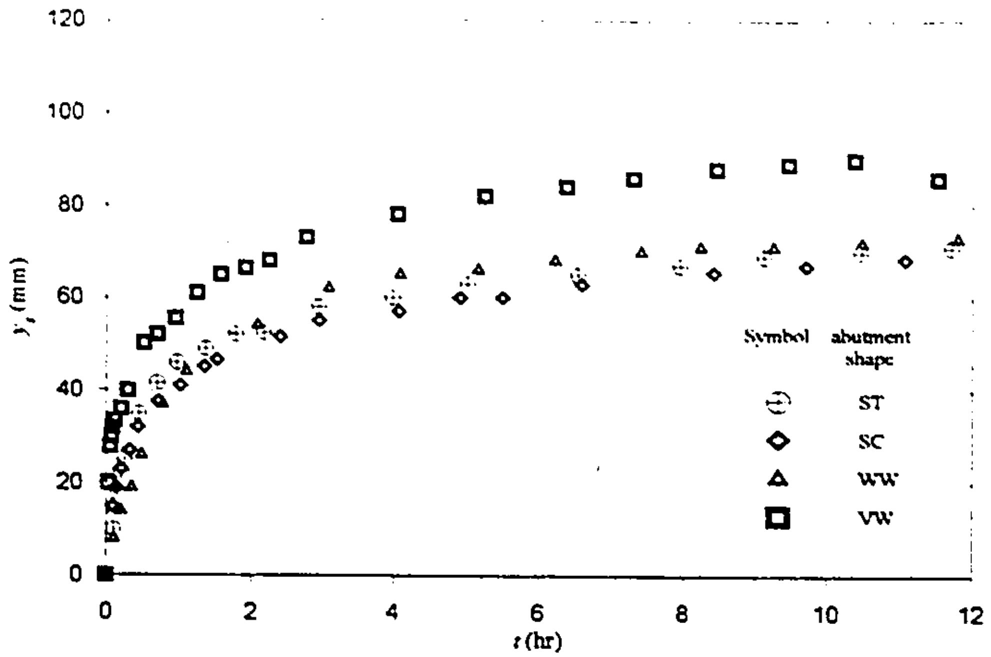

Figure 5.25- Temporal scour development, 150 mm-long abutments

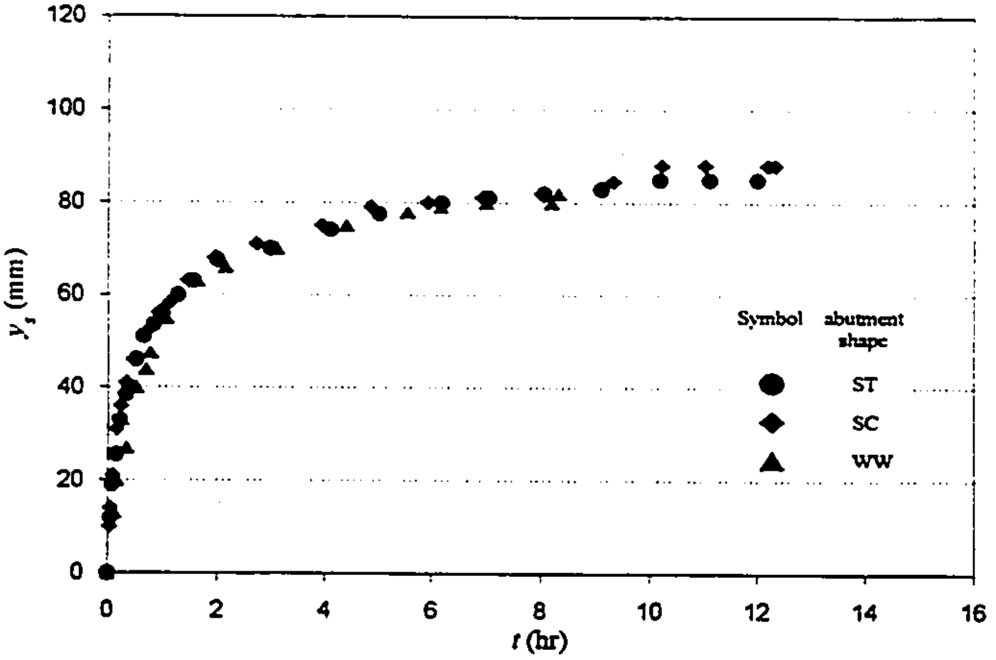

Figure 5.26- Temporal scour development, 210 mm-long abutments

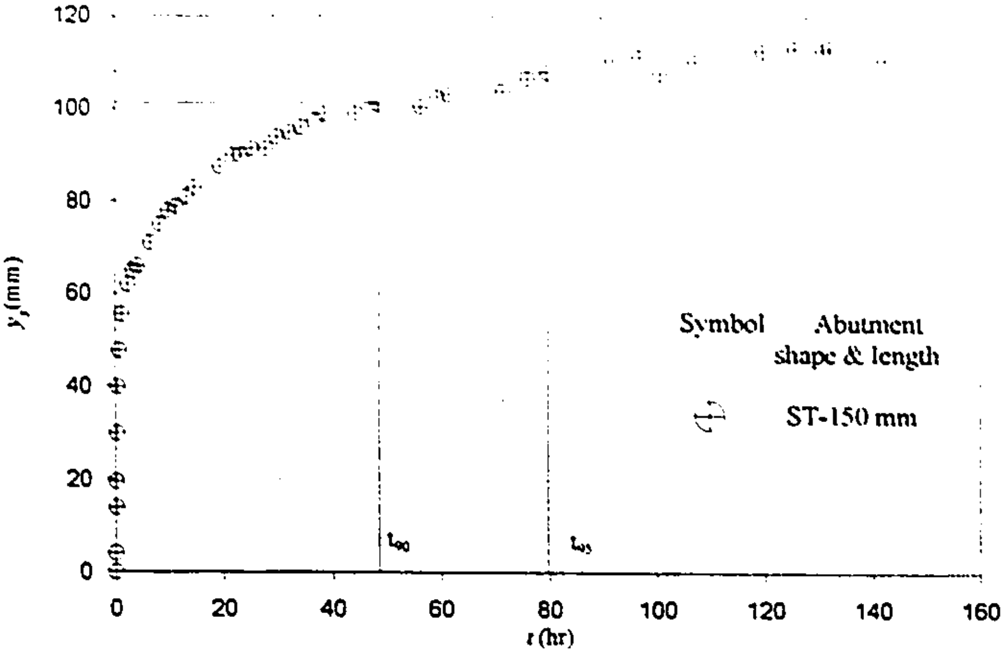

Figure 5.27- Temporal scour development, ST-abutment

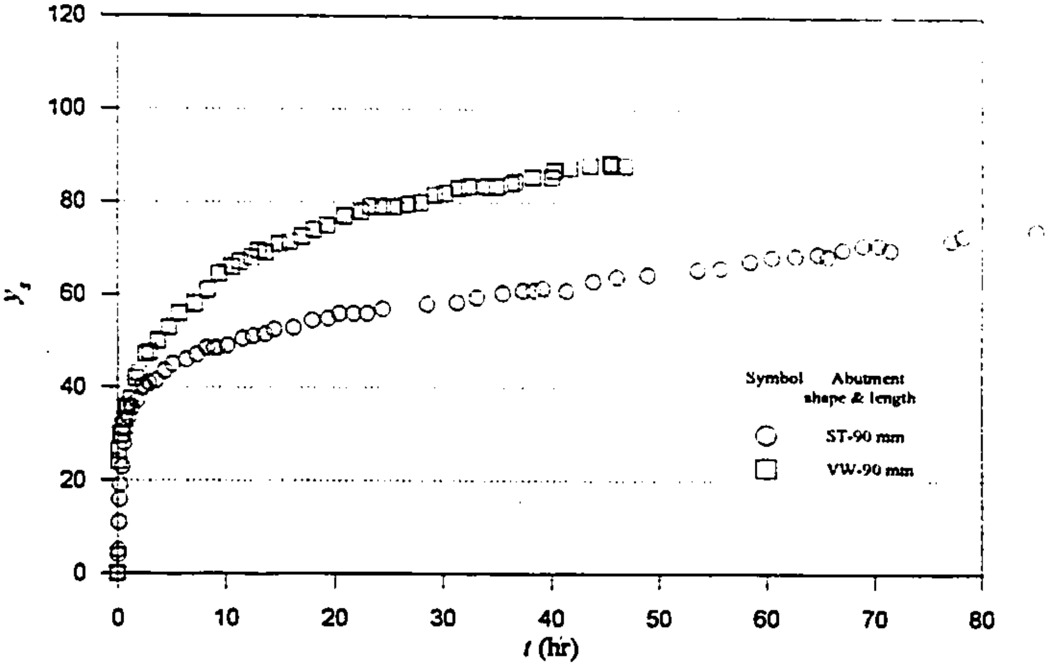

Figure 5.28- Long-term scour development associated with different abutment shapes

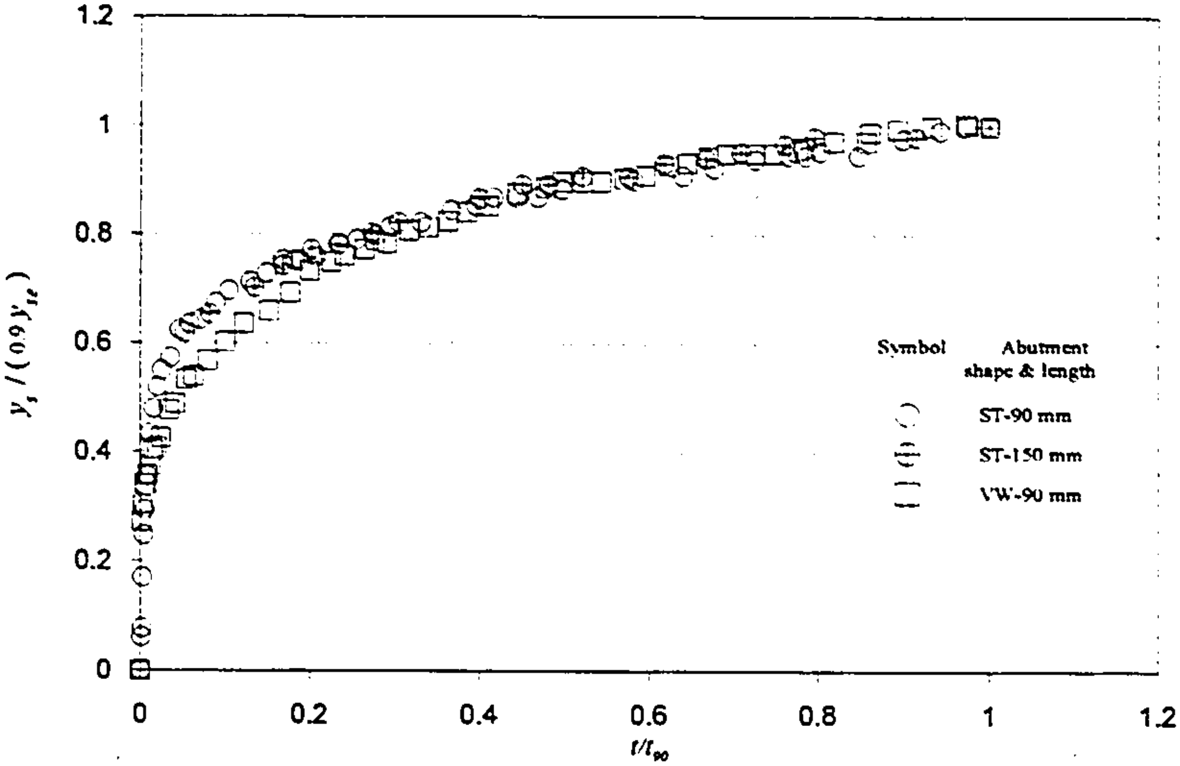

Figure 5.29- Normalized data according to t_{90}

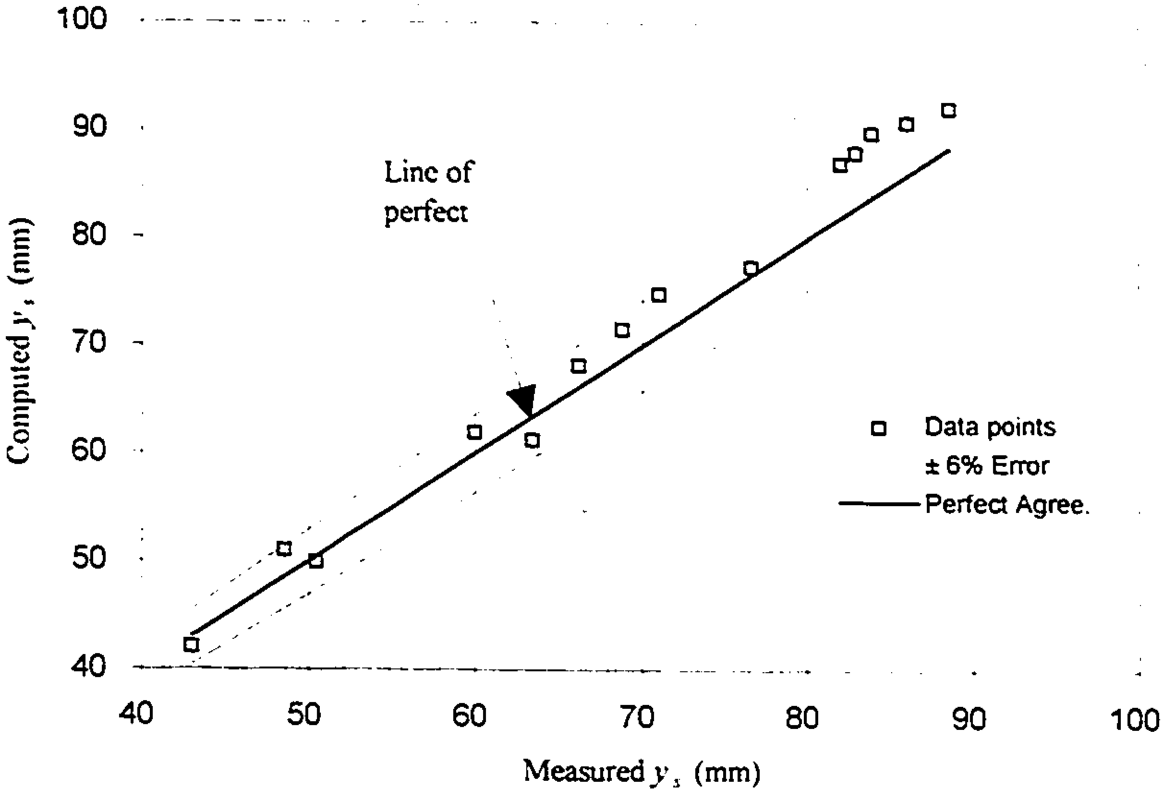

Figure 5.30- Computed vs. measured values of scour depth after nine hours

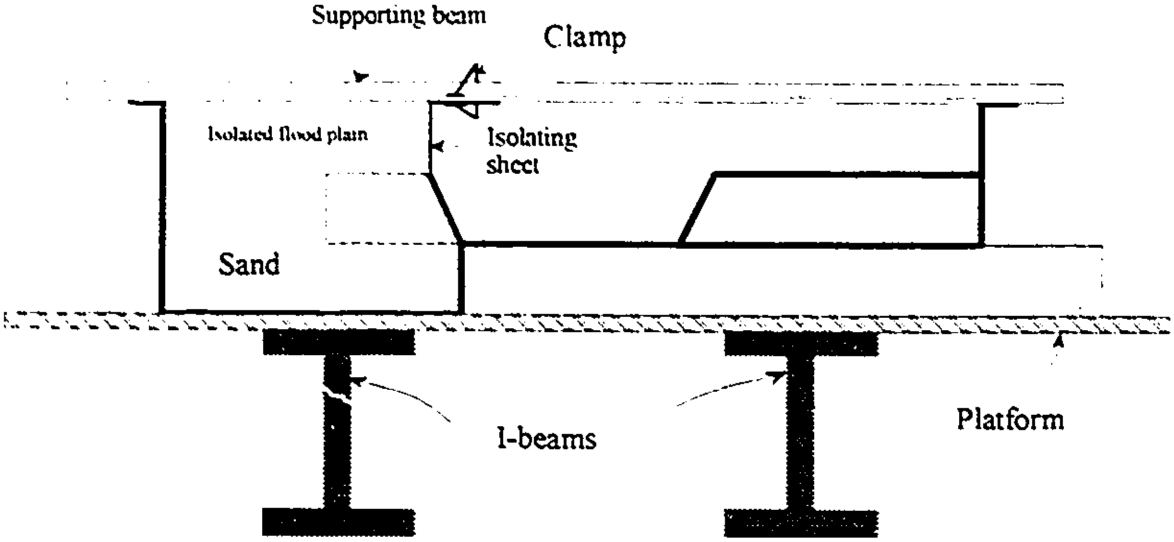

Figure 5.31- Schematic of the flow-isolating sheet

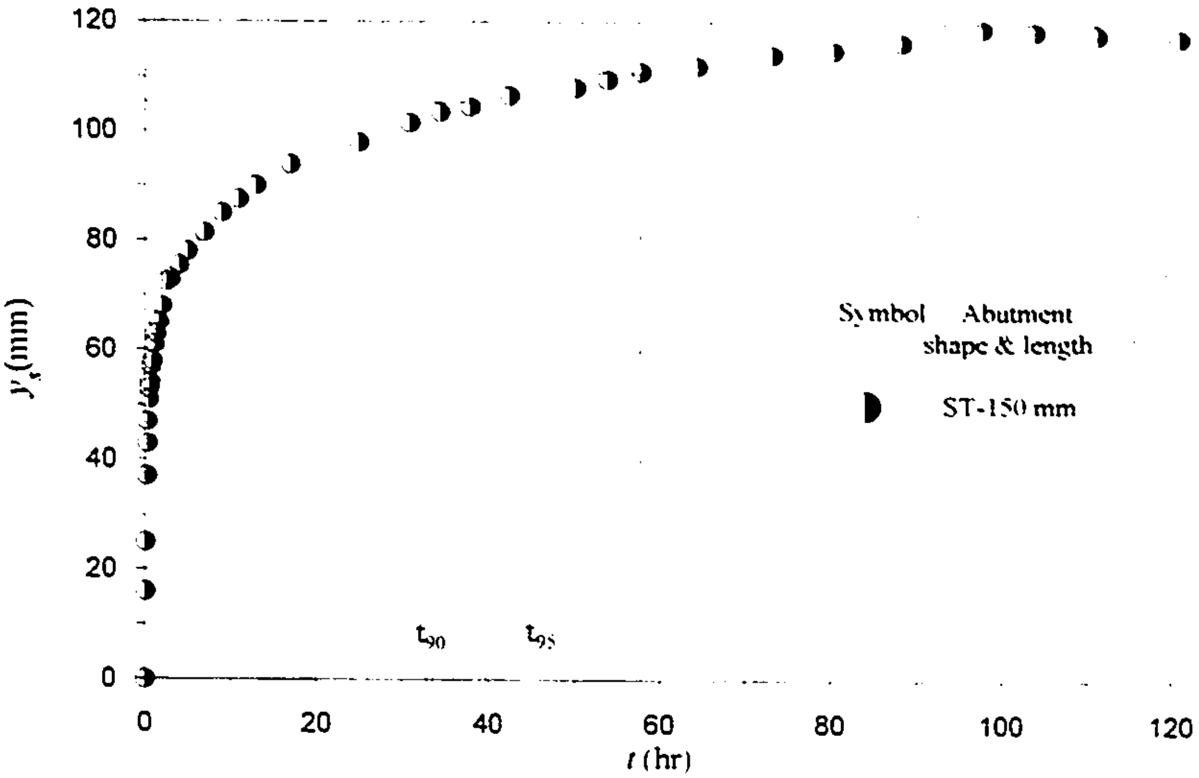

Figure 5.32- Temporal scour development, D_{50}=0.7 mm and ST-abutment

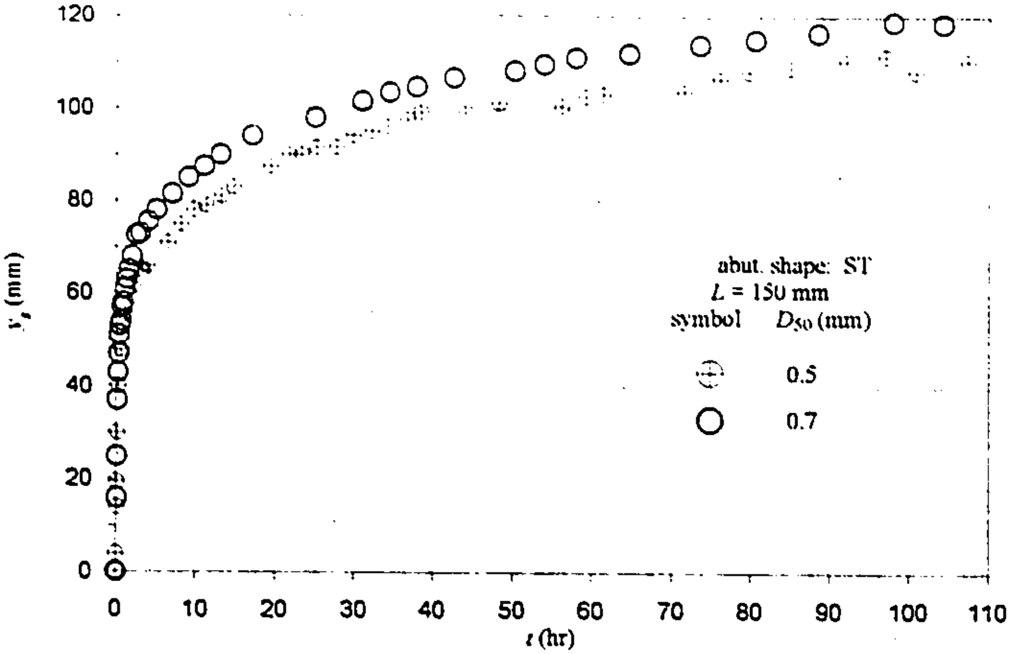

Figure 5.33- Comparison between long-term scour development at threshold conditions and different grain sizes

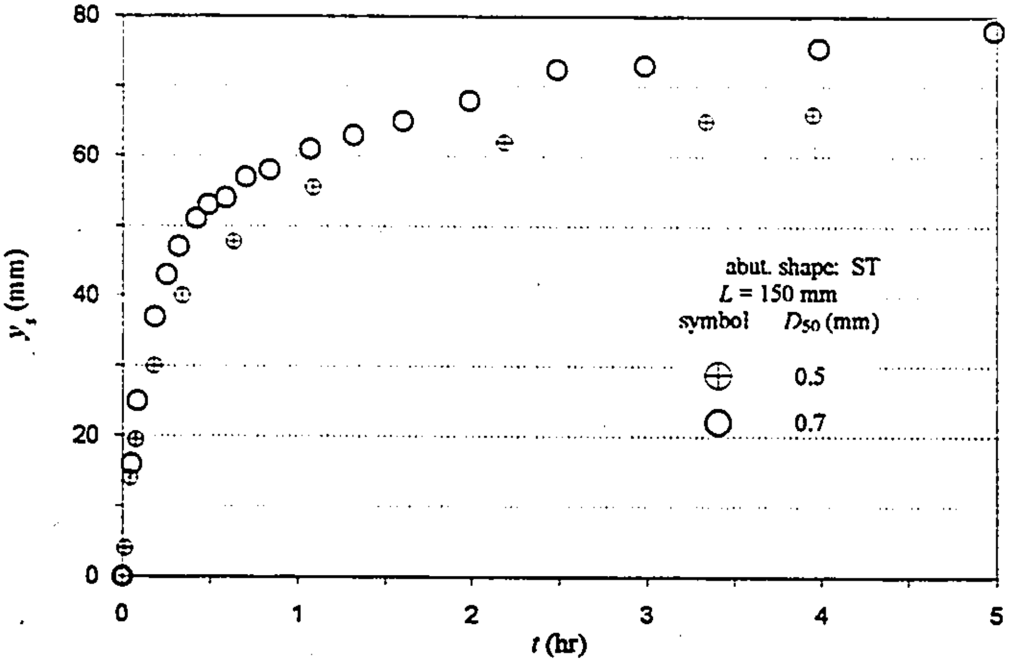

Figure 5.34- Comparison between initial scour development at threshold conditions and different grain sizes

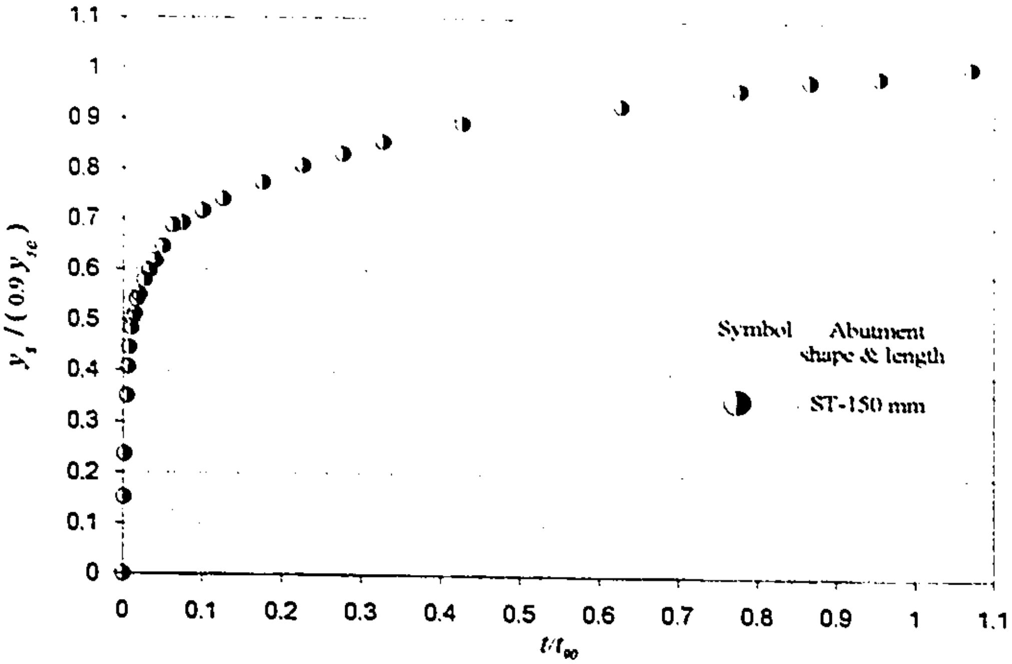

Figure 5.35-Normalized data according to values of t_{90} for D_{50}=0.7 mm and ST-abutment

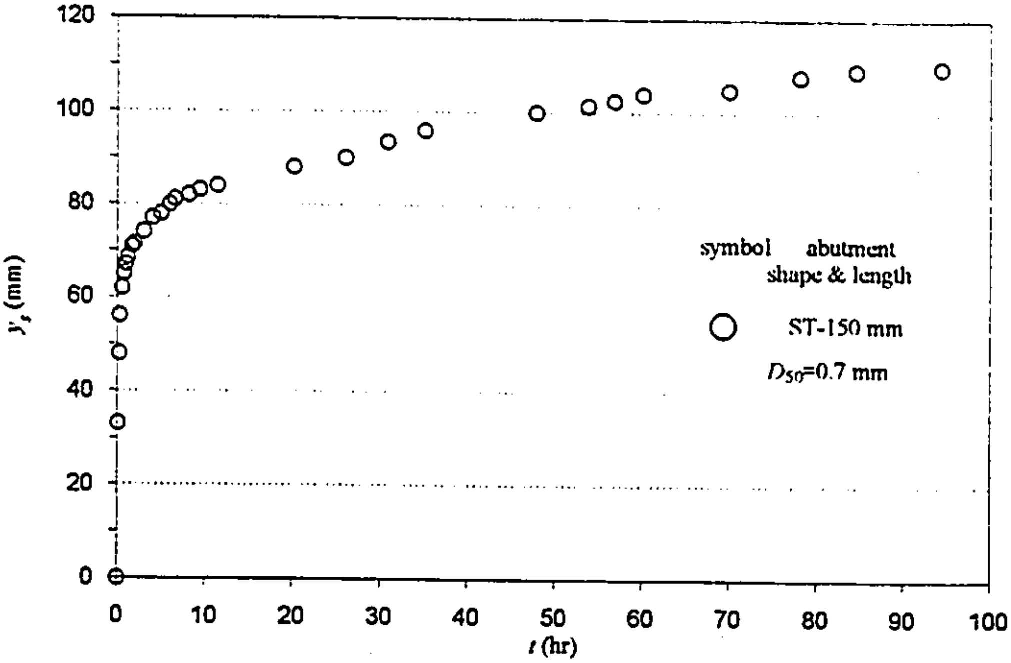

Figure 5.36- Temporal scour development in non-interacting flow condition, ST-abutment

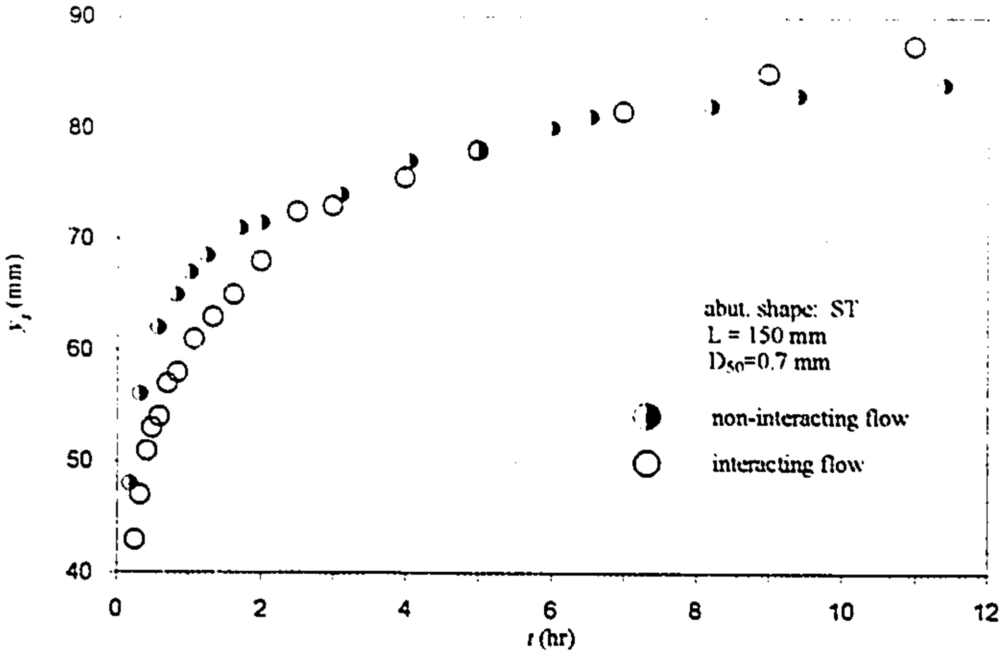

Figure 5.37- Comparison between temporal scour development for interacting and non-interacting flow conditions

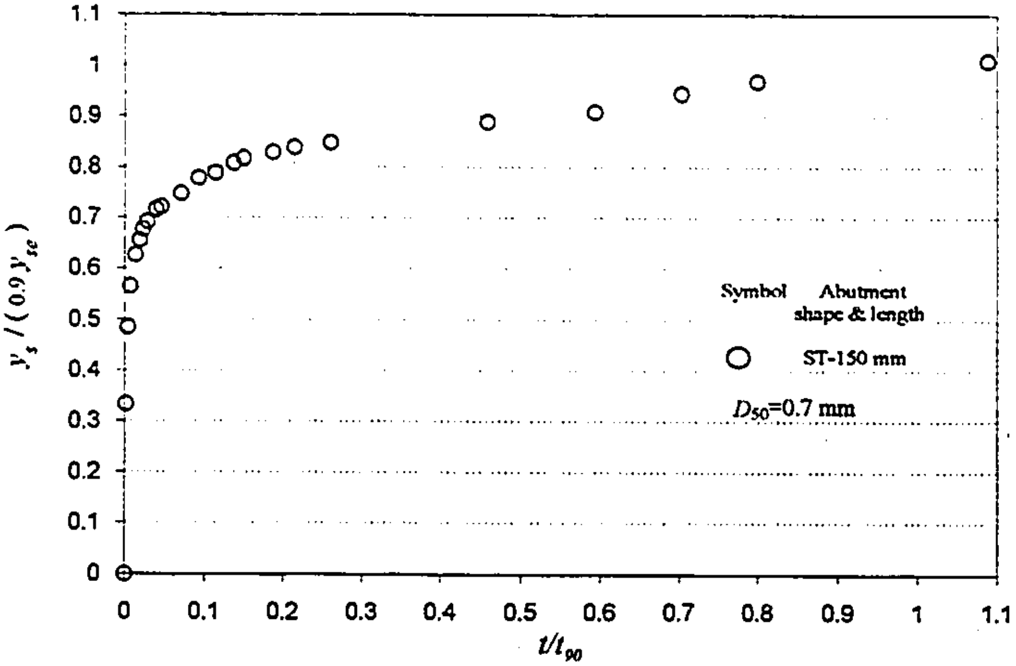

Figure 5.38- Normalized data according to t_{90}, non-interacting flow condition

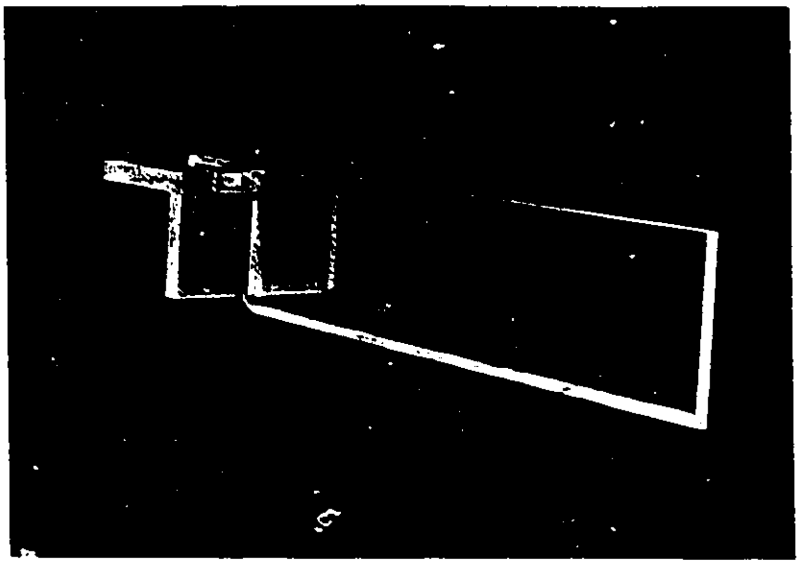

a- Scraper

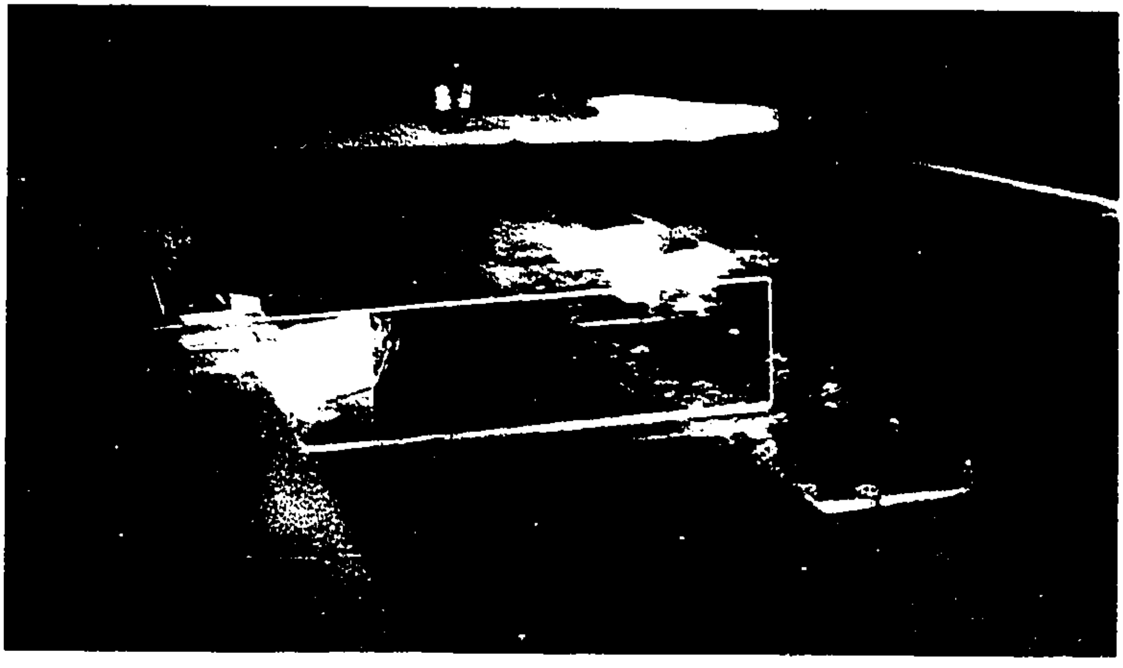

b- Scraper in use

Plate 5.1- Sand bed levelling by scraper

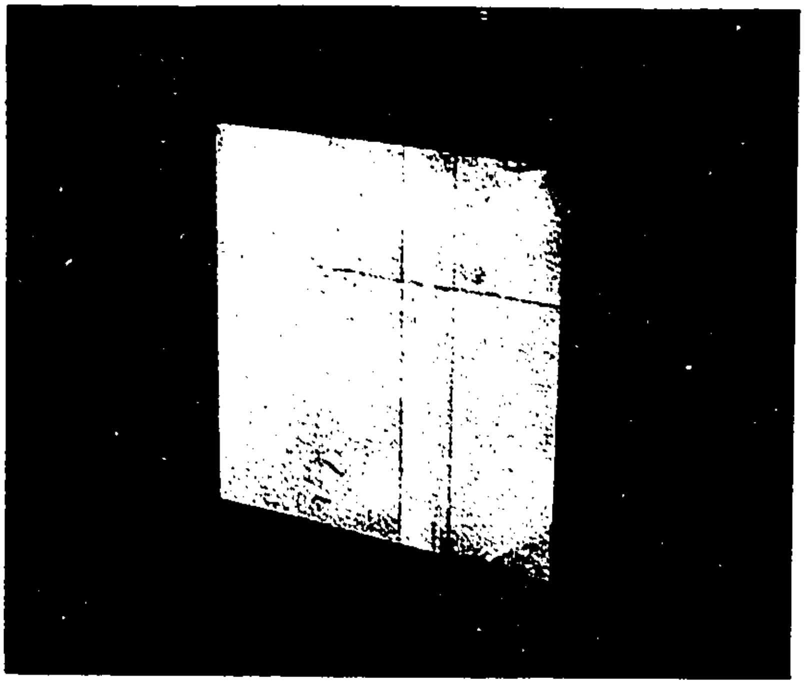

a- Vertical-wall abutment (VW)

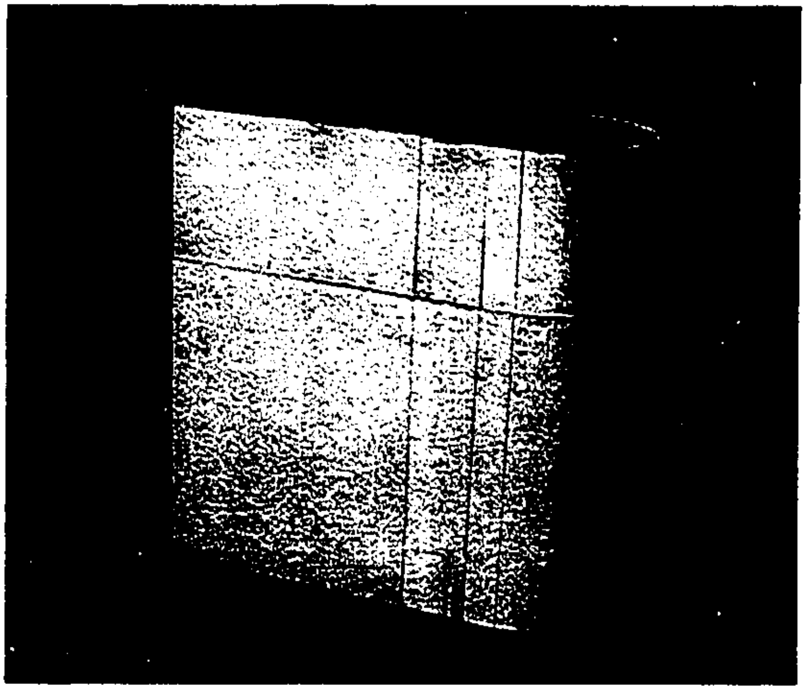

b- Semi-circular abutment (SC)

Plate 5.2- Model abutment shapes

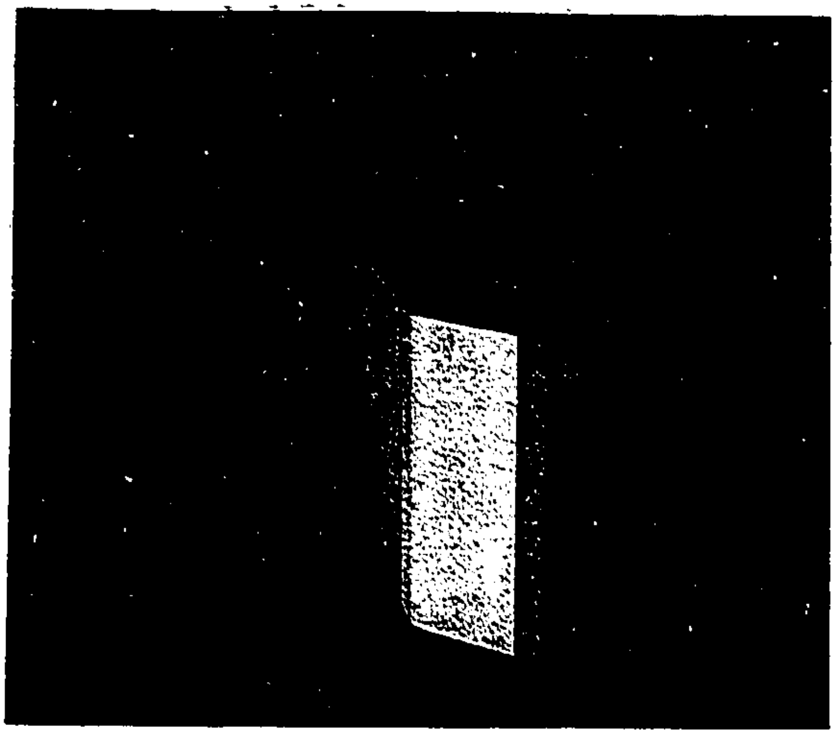

c- Wing-wall abutment (WW)

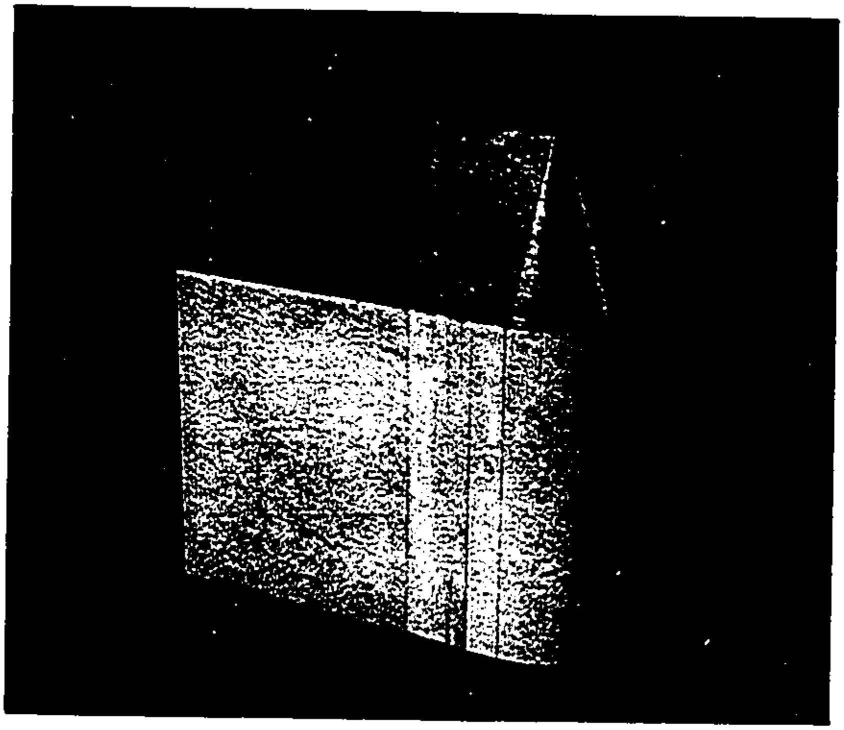

d- Spill-through abutment (ST)

Plate 5.2 (cont.)- Model abutment shapes

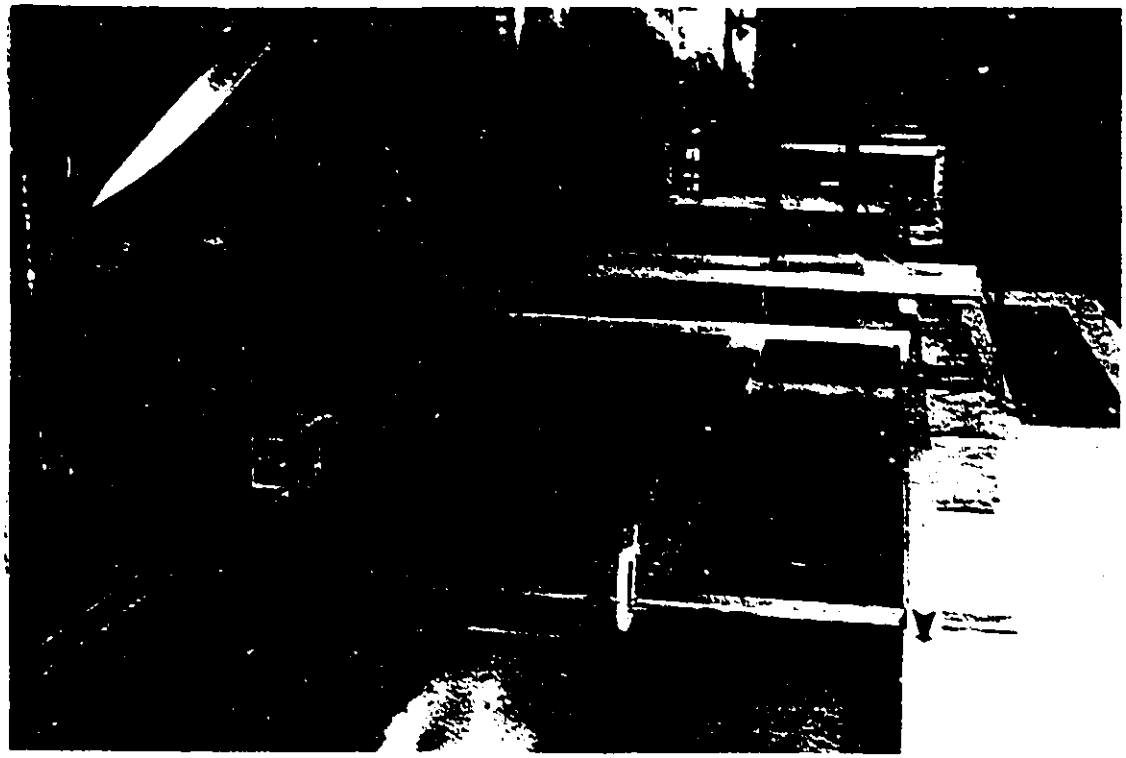

Plate 5.3- Isolating floodplain flow from the main channel flow (non-interacting flow condition)

Plate 5.4- Flow pattern in non-interacting flow condition captured using confetti, 4-sec exposure, and normal lighting condition

Plate 5.5- Flow pattern in non-interacting flow condition captured using confetti, 1-sec exposure, and normal lighting condition

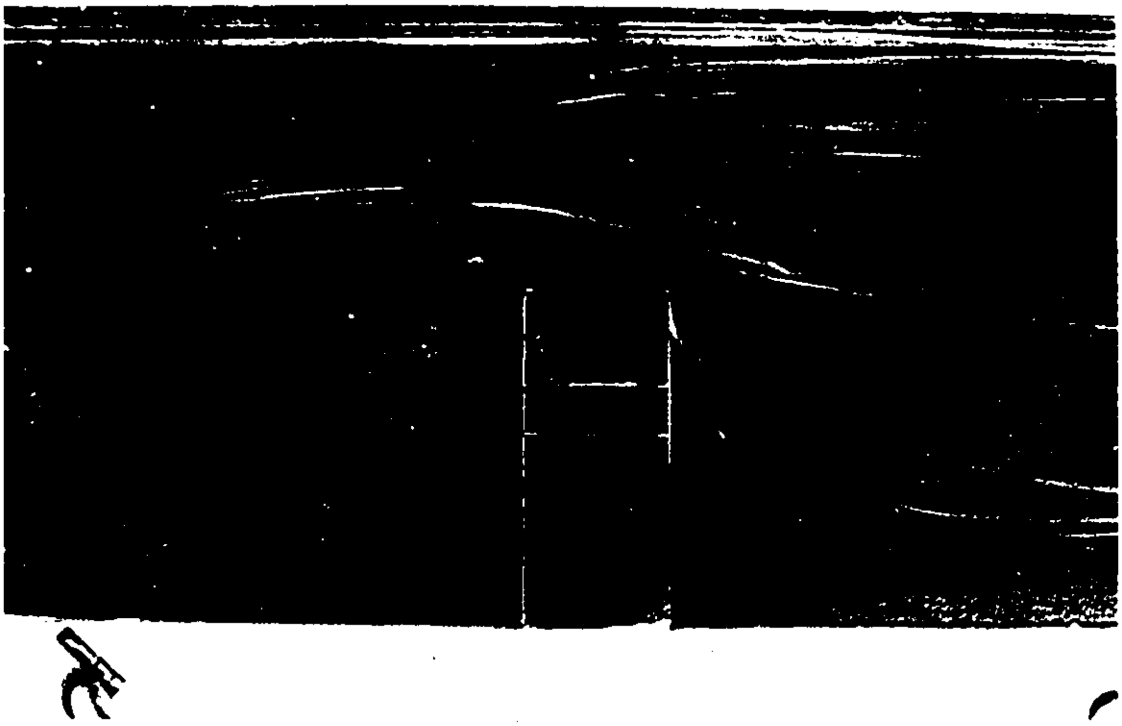

Plate 5.6- Flow pattern in non-interacting flow condition captured using stabilized and darkened bed, confetti, 4-sec exposure, and normal lighting condition

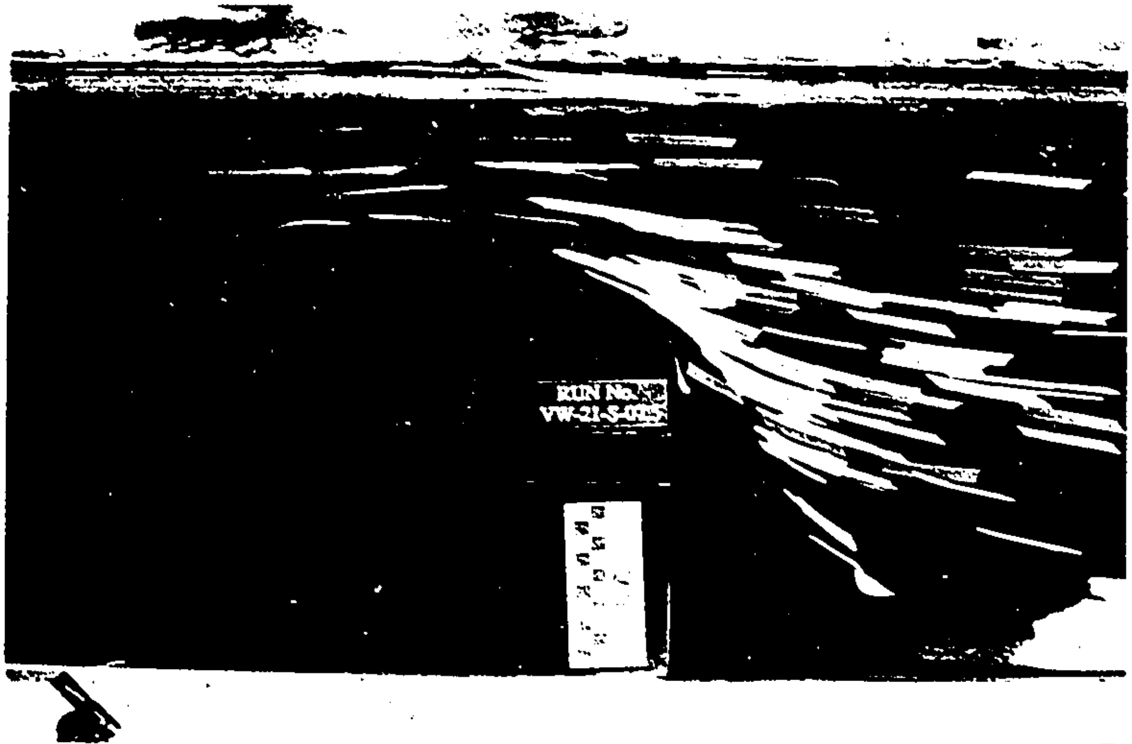

Plate 5.7- Flow pattern in interacting flow condition captured using stabilized and darkened bed, confetti, 1/4-sec exposure, and normal lighting condition

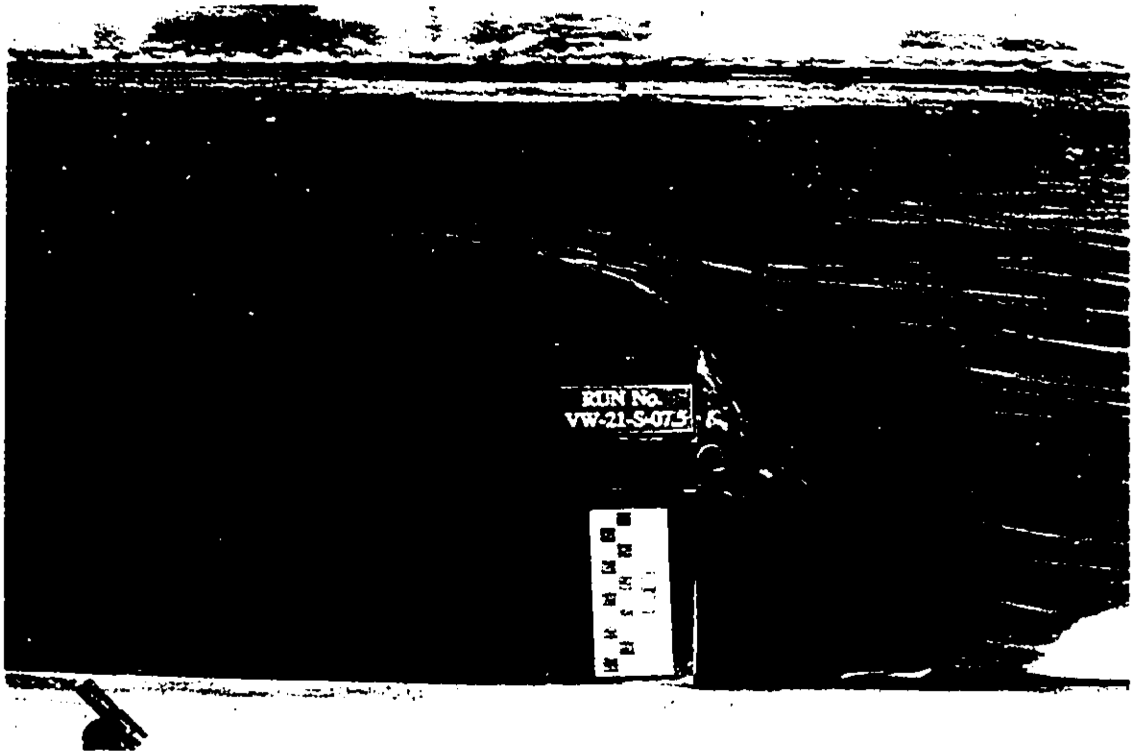

Plate 5.8- Flow pattern in interacting flow condition captured using stabilized and darkened bed, confetti, 8-sec exposure, and normal lighting condition

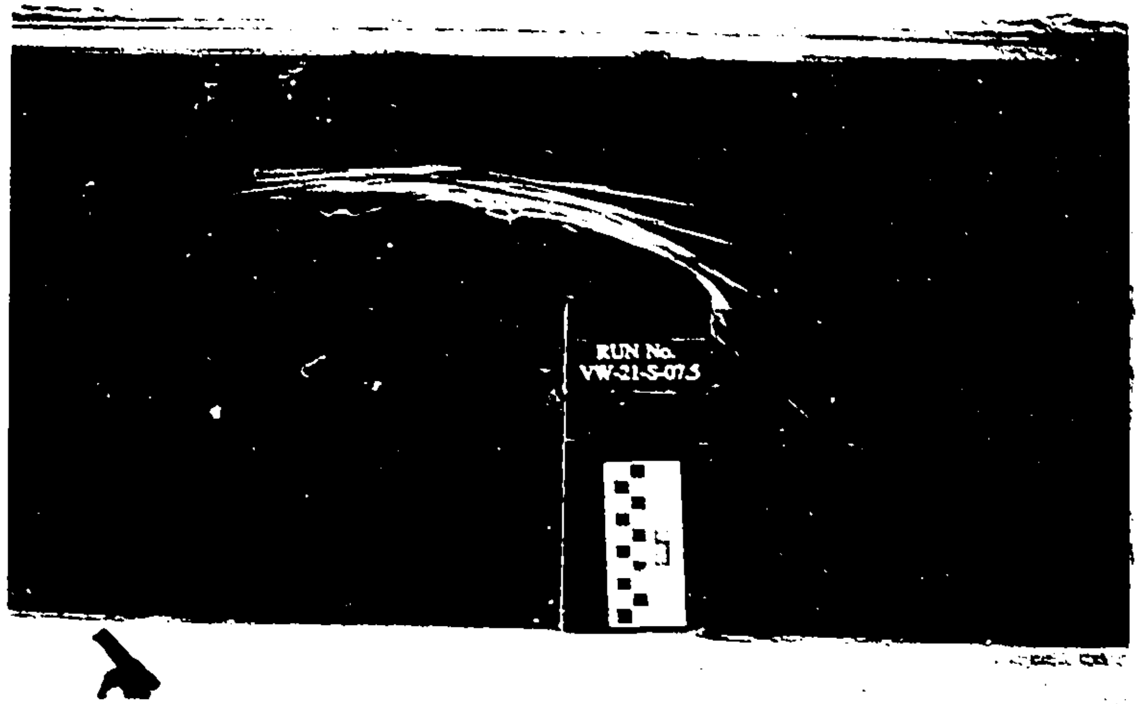

Plate 5.9- Flow pattern in interacting flow condition captured using stabilized and darkened bed, confetti, 8-sec exposure, and fluorescent light

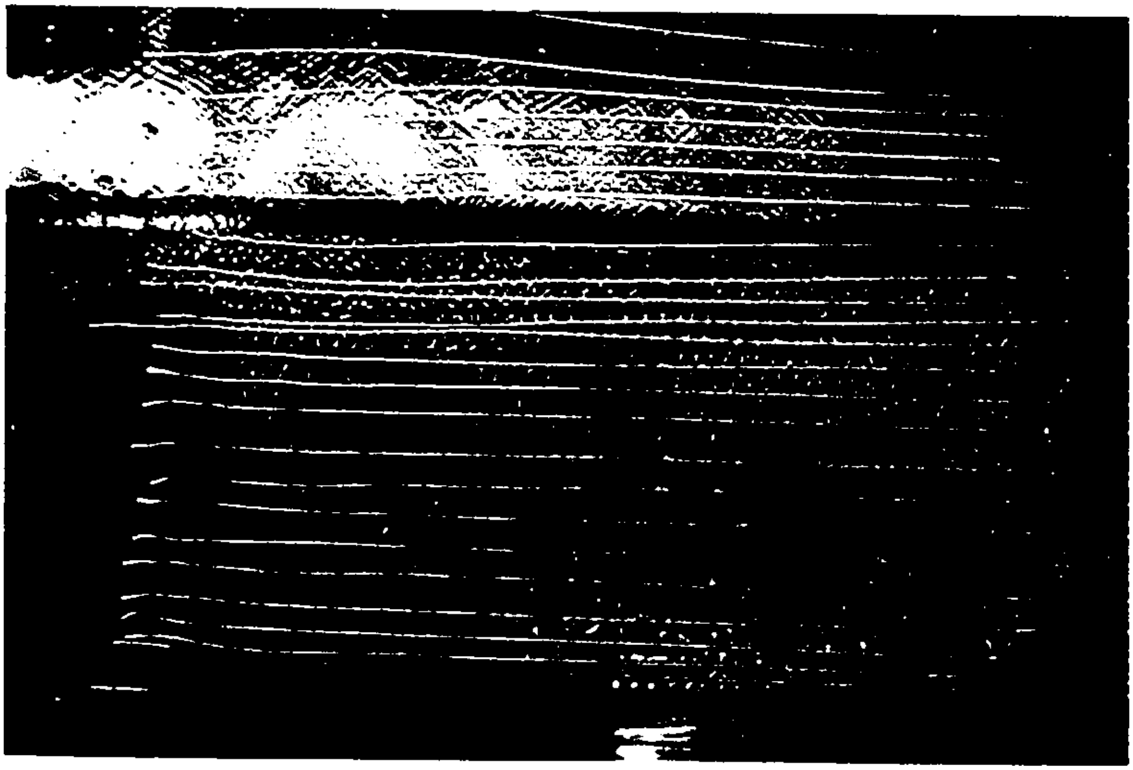

Plate 5.10- Flow pattern in interacting flow condition captured using floating strings prior to installing model abutment

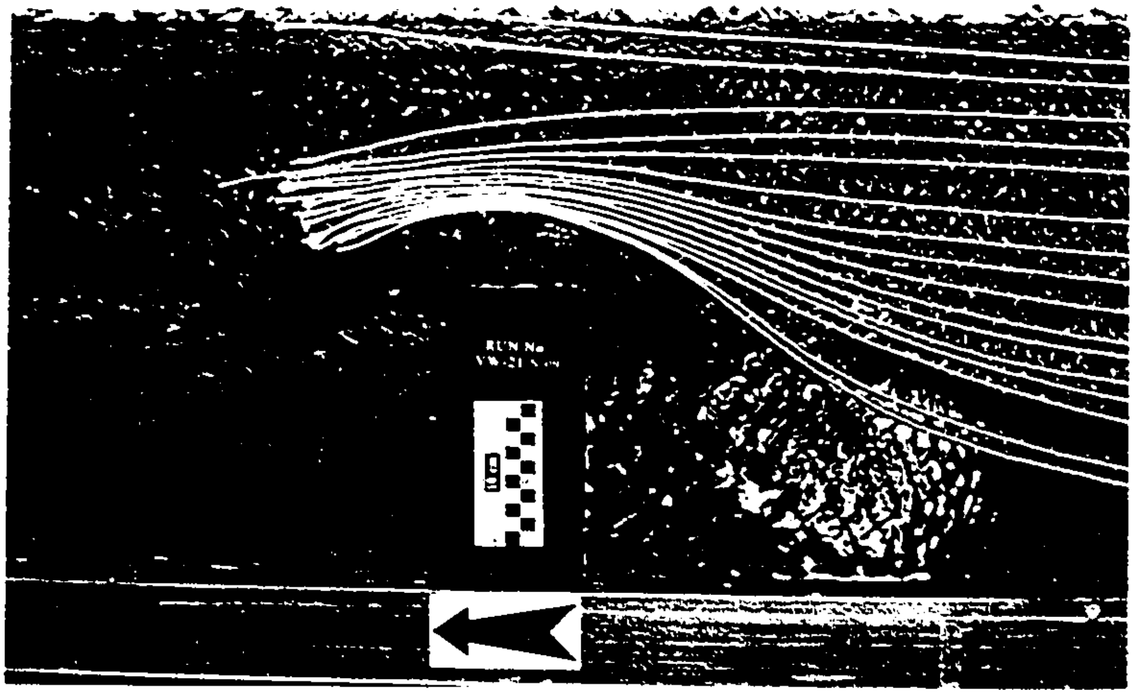

Plate 5.11- Flow pattern in interacting flow condition captured using floating strings, 1/30-sec exposure, and normal lighting condition

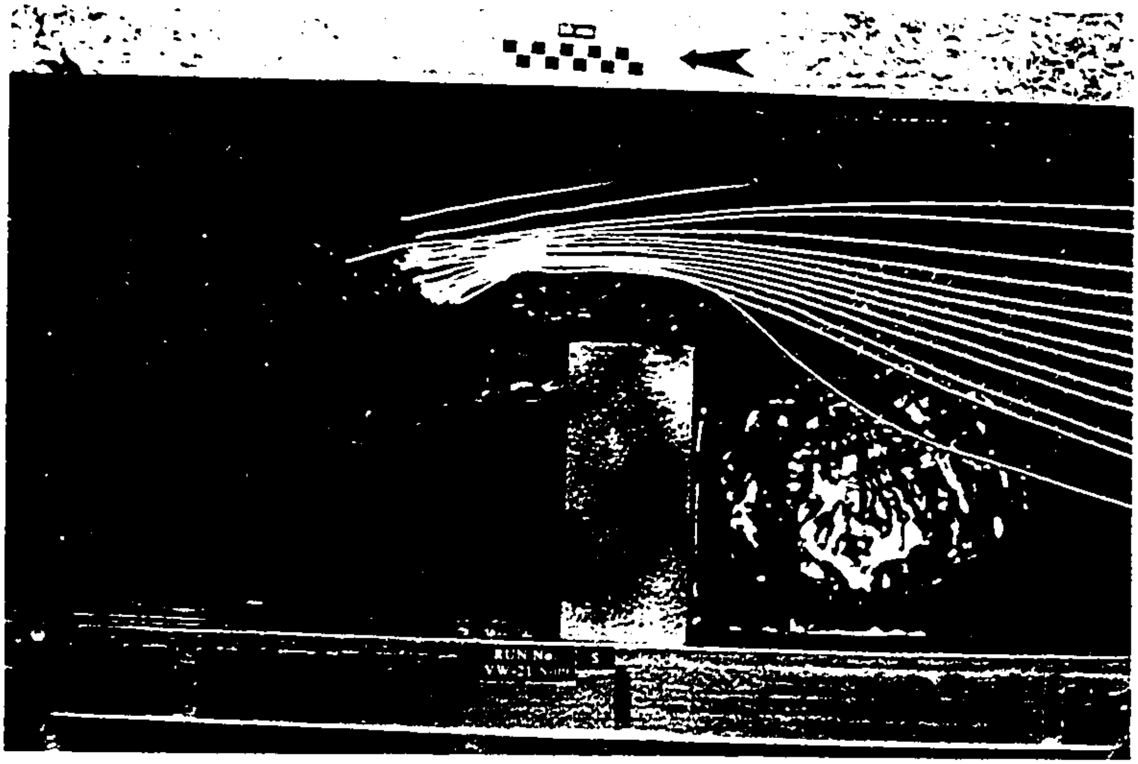

Plate 5.12- Flow pattern in non-interacting flow condition captured using floating strings, 1/30-sec exposure, and normal lighting condition

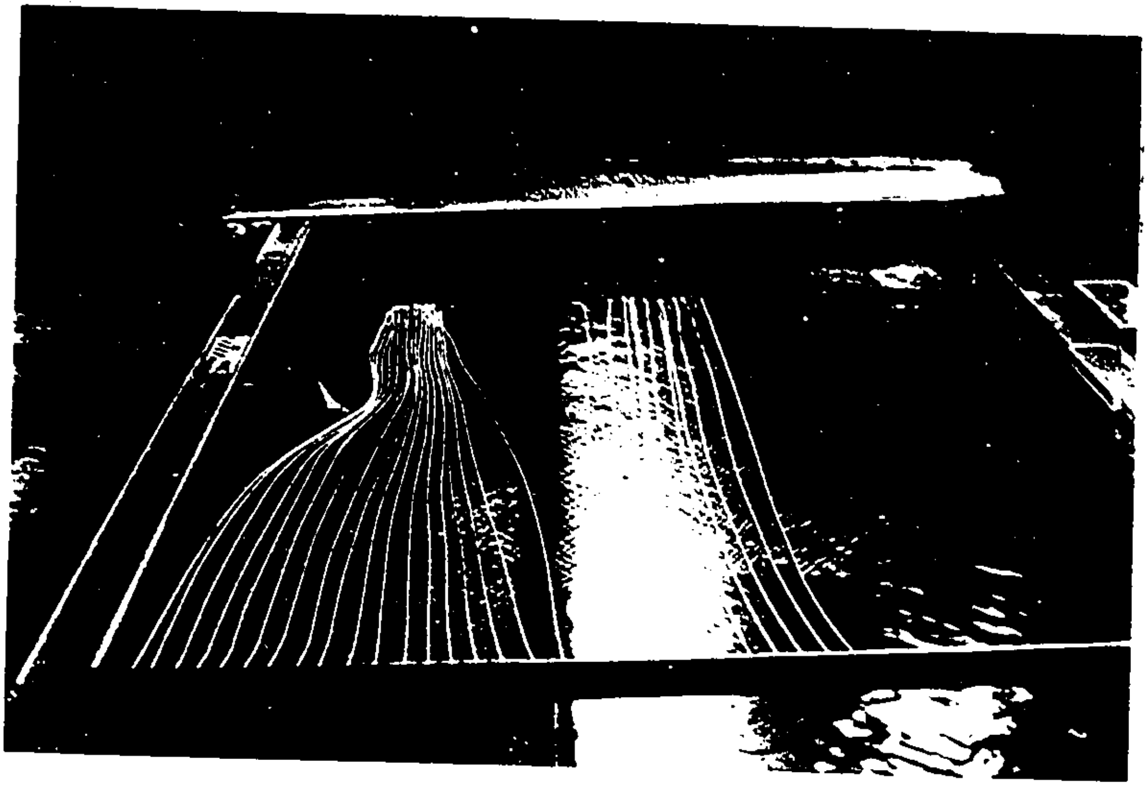

Plate 5.13- Surface flow lines, interacting flow condition

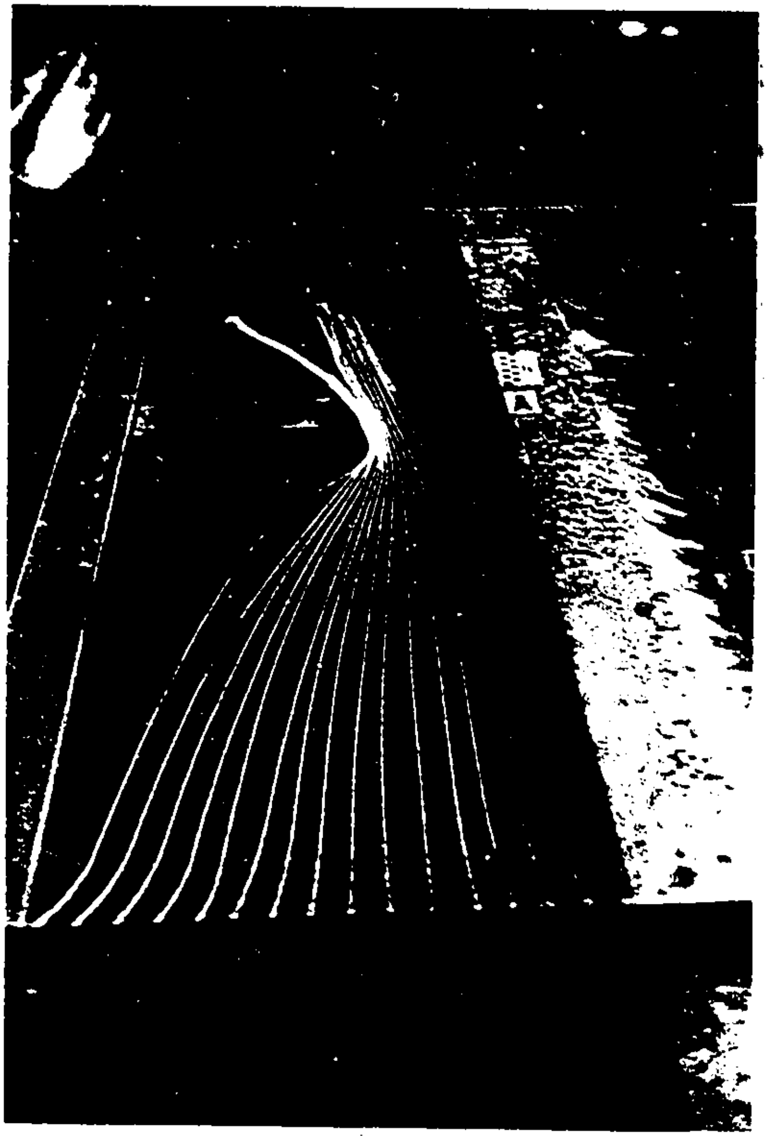

Plate 5.14- Surface flow lines, non-interacting flow condition

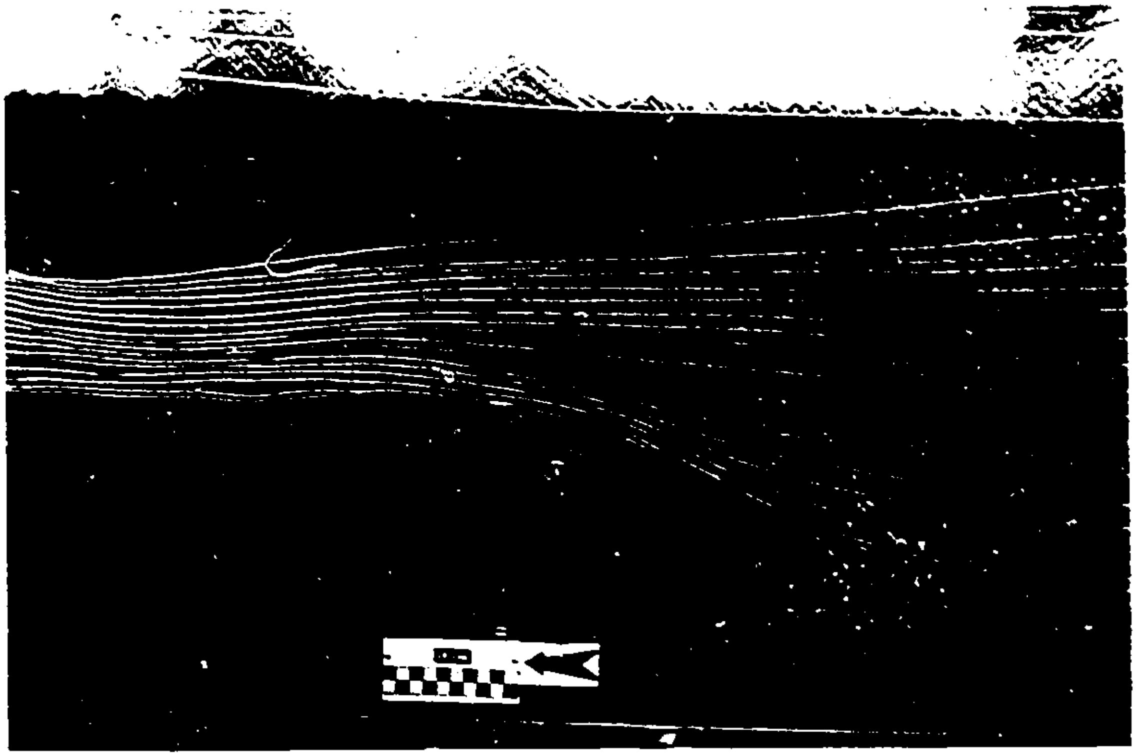

Plate 5.15- Surface flow pattern in long-term test and interacting condition captured using 1/60-sec exposure, and normal lighting condition

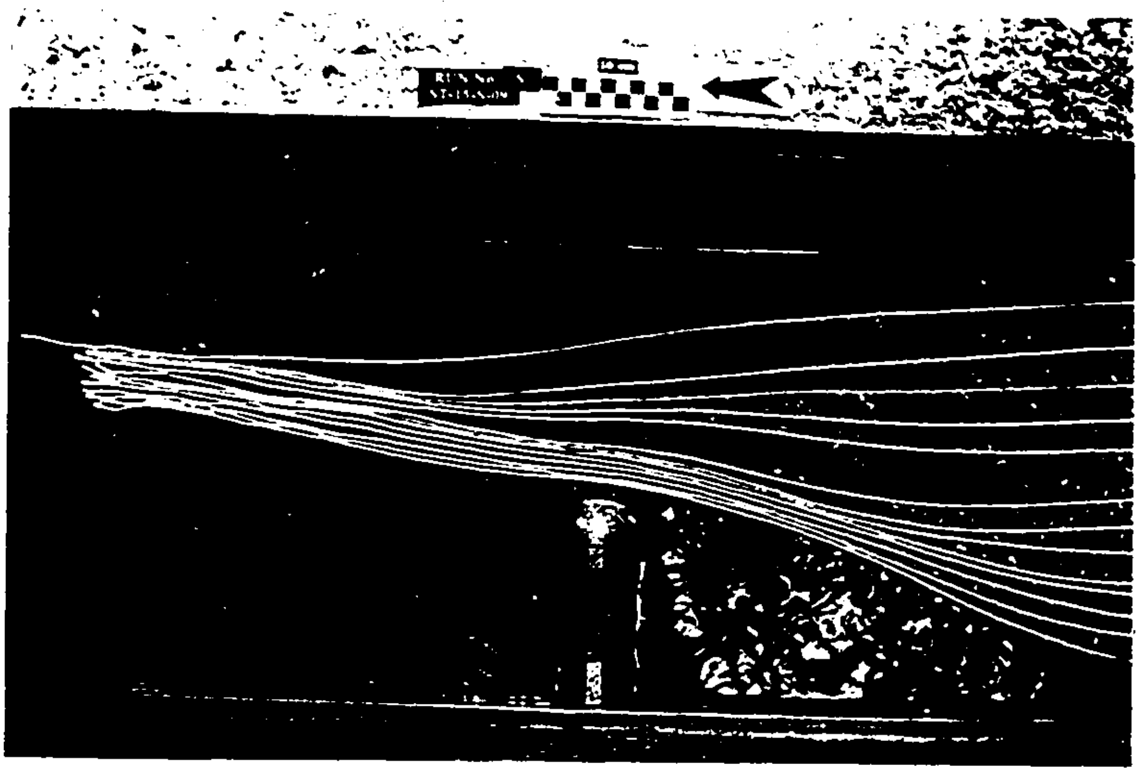

Plate 5.16- Surface flow pattern in long-term test and non-interacting condition captured using 1/60-sec exposure and normal lighting condition

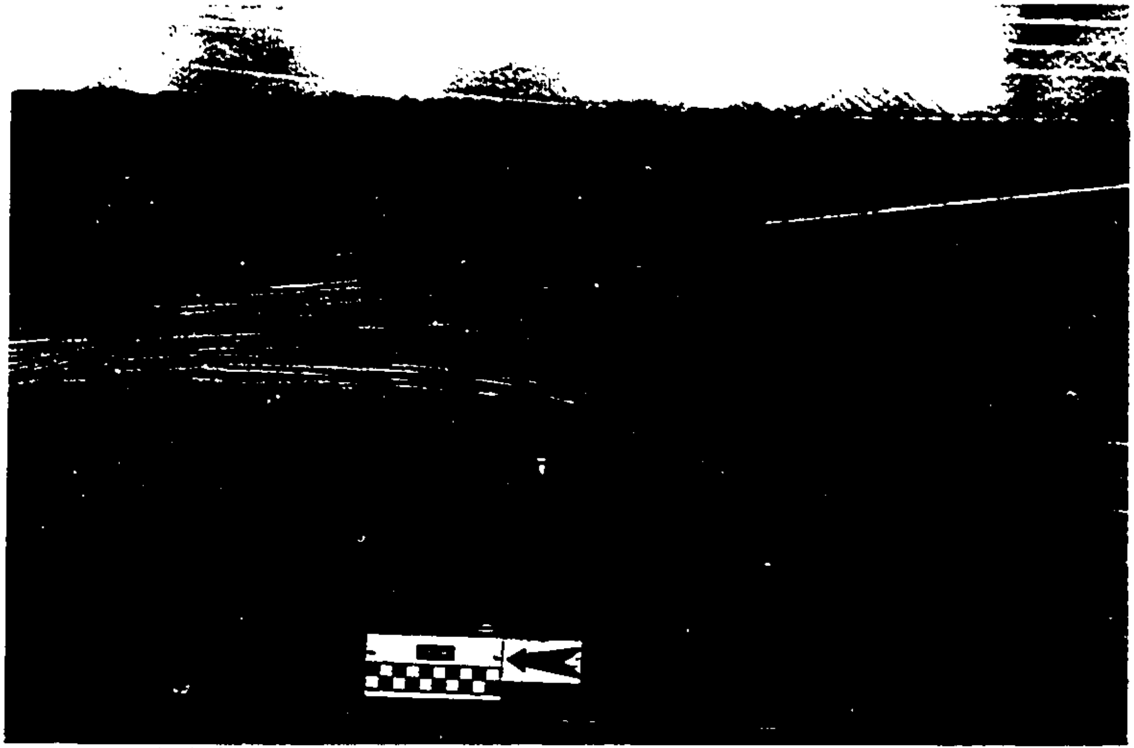

Plate 5.17- Surface flow pattern in long-term test and interacting condition captured using 4-sec exposure, and normal lighting condition

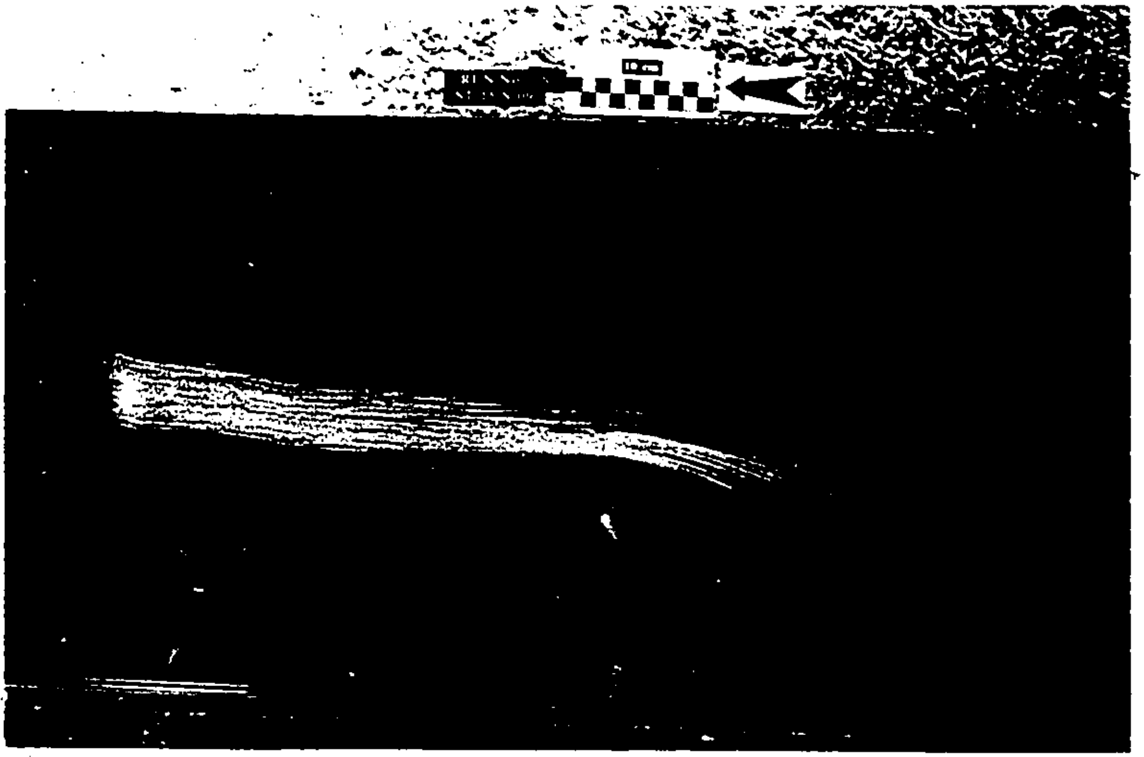

Plate 5.18- Surface flow pattern in long-term test and non-interacting condition captured using 8-sec exposure and normal lighting condition

CHAPTER SIX

DATA ANALYSIS AND DISCUSSIONS

6.1- ANALYSIS OF FLOW DATA

The flow velocity and bed shear stress distribution play key roles in any loose boundary hydraulics study. The distribution of the flow velocity in the longitudinal and transverse direction and the magnitude of *boundary shear stress*, τ, or the *shear velocity*, $u_*(=\sqrt{\tau/\rho})$, are significantly affected by the channel cross section shape. In rectangular laboratory flumes, it is common practice to consider an average value for the bed shear stress and to apply it to the entire width of the flume at the test section. This approach, however, is not applicable to compound channels in which the flow interaction at the MC/FP junction and the momentum transfer phenomenon might significantly affect the flow characteristics. That is, in both the MC and the FP the velocity (value and distribution) and the bed shear stress might deviate significantly from a mean value due to the flow interaction and the momentum transfer. The analysis of the flow velocity data to determine the *bed shear stress* and the *shear velocity* ratio in the FP is presented here.

6.1.1- Velocity profiles in the floodplain

The whole data set of flow velocity measurements for *interacting* conditions can be plotted in dimensionless form (u/u_* versus yu_*/ν) to observe their relative position with respect to the lines of Equations A.30 and A.40. These two equations divide the plane of the plot into three regions (*smooth*, *transition*, and *rough*). The position of the data on such a plot determines the flow regime in the current study. This, however, can only be achieved if u_* is known and Equation A.23 is written in terms yu_*/ν.

Equation A.30 can be written in terms of yu_*/ν if the value of k_s is determined according to the value of $\frac{k_s u_*}{\nu} > 70$ for the *rough* regime. Substituting $k_s = 70\nu/u_*$ for the lower limit of the *rough* regime (Figure 3.5) in Equation A.30, a relationship for the upper limit of the *rough* region is obtained as follows:

$$\frac{u}{u_*} = 5.75 \log\left(\frac{yu_*}{\nu}\right) - 2.11 \qquad \textbf{(6.1)}$$

The form of Equation 6.1 has the advantage of being independent of the equivalent sand roughness and can be used with Equation A.30 to distinguish the various flow regimes.

Plotting Equations A.30 and 6.1 on a semi-log plot divides the x-y plane into the *smooth*, *transition*, and *rough* flow regimes. Since the actual value of u_* is not known, to plot the experimental data on one graph along with Equations A.30 and 6.1, velocity measurements can be non-dimensionalized by $\overline{u}_* = \sqrt{gyS_o}$. Figure 6.1 was prepared according to Equations A.30 and 6.1, based on the approximated value of u_*. In spite of the scatter in the data of Figure 6.1, which is attributed to the application of $\overline{u}_* = \sqrt{gyS_o}$ instead of the actual values of shear velocities, the figure indicates that the flow is essentially in the *transition regime* region.

6.1.2- Determination of shear velocity ratios

6.1.2.1- *Interacting* flow conditions

To determine the actual shear velocity (or the shear velocity ratio u_*/u_{*c}) in the FP, it is necessary that the effective sand roughness, k_s, be evaluated first. The value of k_s is determined according to section 3.3.2 using the velocity profiles measured in the FP. Measured velocities were obtained in the test section at the model abutments' location while they were not in place. The k_s values were then averaged and applied along with the computed value of B_s for the defined flow condition.

Having defined k_s and B_s, the theoretical velocity profiles of different u_*/u_{*c} were fitted to a specific measured velocity profile. The actual u_*/u_{*c} ratios were then determined for the defined positions of the FP, namely at z =6.09 m from the flume inlet and x = 90, 150, and 210 mm from the left flume wall (Figure 4.1). For the series of experiments conducted using S_o=0.0006 and D_{50}=0.5 mm, the measured velocity (along with the fitted theoretical lines) are plotted in Figures 6.2 to 6.4. They clearly indicate that u_*/u_{*c} increases in the FP as the distance x increases towards the MC/FP junction. According to the fitted theoretical lines of Figures 6.2 to 6.4, mean values of u_*/u_{*c} were considered as actual local values at x =90, 150, and 210 mm. The local shear velocities were then determined based on the adopted u_*/u_{*c} values.

The procedure followed for determining the local shear velocity ratio might be evaluated by comparing dimensionless plots of the measured velocities non-dimensionalized by $\overline{u}_* = \sqrt{gyS_o}$ and local u_*. The results obtained utilizing the former value are plotted in Figure 6.5 and show considerable deviation from the theoretical line. The scatter in the data, however, was removed and the data collapsed on the theoretical log-law velocity distribution when the latter values of shear velocities were used (Figure 6.6). The concordance between measured velocities and the theoretical line of Figure 6.6 shows that the velocity distribution in the FP might be considered to follow the universal log-law provided that the local shear velocity is considered.

To determine the local u_*/u_{*c} for flow conditions considered in the present study, the above procedures were repeated for different longitudinal slope settings. Figures 6.7 to 6.10 show the flow velocities measured for uniform flow conditions established using S_o=0.00075 and D_{50}=0.5 mm. The theoretical log-law velocities are also included on these figures. The measured flow velocities, for the uniform flow condition established using S_o=0.0009 and D_{50}=0.7 mm, are presented in Figures 6.11 to 6.14. Finally, the results of flow velocity measurements using S_o=0.0009 and D_{50}=0.7 mm are presented in Figures 6.15 to 6.18.

Figures 6.10, 6.14, and 6.18 show dimensionless plots of the log-law velocity distributions along with the measured velocity profiles. The measured values on these figures were non-dimensionalized by the corresponding local u_*. The agreement between the measured and theoretical values confirms the conclusion that the velocity profiles in the FP follow the log-law provided that the local shear velocities are applied.

The data in Figure 6.1, is now replotted in Figure 6.19 utilizing local u_* instead of $\overline{u}_* = \sqrt{gyS_o}$ to non-dimensionalize the measured velocity values. This figure shows that using local u_* substantially removes the scatter observed in Figure 6.1. All the data obtained with *interacting* conditions at z =6.09 m, x =90, 150, and 210 mm (which were used to prepare Figures 6.2 to 6.18) are included in Figures 6.1 and 6.19.

The adopted values of the local shear velocity ratios, based on the comparison between the theoretical log-law and measured velocities, are summarized in table 6.1

and 6.2. Figures 6.20 to 6.23 show the variations of the local shear velocity ratio in the FP for different test conditions.

Table 6.1- u_*/u_{*c} for *interacting* flow and D_{50}=0.5 mm

x	S_o		
(mm)	0.0006	0.00075	0.0009
90	0.95	0.91	0.94
150	1.01	0.97	1.00
210	1.06	1.01	1.02

Table 6.2- u_*/u_{*c} for *interacting* flow
and D_{50}=0.7 mm

x	S_o
(mm)	0.0009
90	0.90
150	0.95
210	1.00

6.1.2.2- *Non-interacting* flow conditions

In *non-interacting* conditions the FP flow was separated from the MC flow by means of a vertical plate. In such circumstances one expects substantial changes in flow conditions at the MC/FP junction. As a result of the new flow condition, the distribution of the shear velocity in the FP is different from that of *interacting* conditions. In order to determine the shear velocity ratio for *non-interacting* conditions, the flow velocity were measured across the FP at z=6.09 m.

To determine the local u_*/u_{*c} for the test cases considered for *non-interacting* conditions, measured flow velocities are compared with the theoretical log-law lines using different u_*/u_{*c} values. Figures 6.24 to 6.27 show the results for tests performed using S_o=0.00075, D_{50}=0.5 mm and *non-interacting* conditions. The results obtained using S_o=0.0009 and D_{50}=0.5 mm, and S_o=0.0009 and D_{50}=0.7 mm are shown in Figures 6.28-6.31 and 6.32-6.35 respectively.

The concordance between the non-dimensionalized flow velocity data and the theoretical log-law velocity shown in Figures 6.27, 6.31, and 6.35 clearly indicates that the measured velocities follow the log-law distribution when the local shear velocities are used to normalize the data. The shear velocity ratios determined using the procedures described above are summarized in tables 6.3 and 6.4. Table 6.3 shows the results obtained using sand having D_{50}=0.5 mm and different bed slope settings. The results obtained using sand having D_{50}=0.7 mm and S_o=0.0009 are summarized in Table 6.4.

Table 6.3- u_*/u_{*c} for *non-interacting* flow and D_{50}=0.5 mm

x	S_o	
(mm)	0.00075	0.0009
90	0.85	0.91
150	0.90	0.94
210	0.95	0.96

The variations of the shear velocity ratio for *non-interacting* conditions are presented in Figures 6.36 to 6.38. Isolating the FP flow from the MC flow resulted in a significant drop in the shear velocity ratios in this region. Consequently, the scour depth observed for this condition is affected by the mentioned change in u_*/u_{*c} and should be modified if the maximum scour depth is sought. The magnitude by which the scour depth should be modified for different u_*/u_{*c} is discussed in the following section.

Table 6.4- u_*/u_{*c} for *non-interacting* flow and D_{50}=0.7 mm

x	S_o
(mm)	0.0009
90	0.85
150	0.91
210	0.95

6.1.3- Effects of u_*/u_{*c} on local scour

Pier scour studies have indicated that, when $u_* < \frac{u_{*c}}{2}$ the flow intensity is not strong enough to initiate local scour around a bridge pier. Also, the local scour is negligible around a cylindrical pier at $u_*=0.5u_{*c}$(Ettema, 1980; Melville, 1984). However, increasing the shear velocity ratio from 0.5 to 1.0 (as shown in Figures 2.12 and 2.13), results in a linear increase in the scour depth (Ettema, 1980; Liu et at.,1961; Laursen, 1953).

In compound channels, the approach flow velocity is usually not uniformly distributed across the FP; therefore, one might expect varying shear velocity ratios in the FP region. However, the intensity of u_* variations across the FP (and the extent of its effects on local scour depth) depend on factors such as FP and MC boundary roughness, approach FP flow depth to total flow depth, y_f/H, and the geometry of the compound channel. The above factors govern the intensity of the momentum flux from the MC to the FP, which in turn affect the shear velocity distribution in the FP.

In the abutment case, however, very limited data are available which relate the local scour depth to u_*/u_{*c}. Necessary modifications to observed local scour depths can be determined by examining those data obtained for varying shear velocity ratios. Plotting Gill's (1972) spur-dikes (vertical wall abutment) data in Figure 6.39 confirms the linear variations (obtained for the pier case and shown in Figure 2.13) of the relative scour depth y_s/y_n with the shear velocity ratio for $u_*/u_{*c}<1$. However, contrary to the pier case, substantial local scour depth for $u_*/u_{*c}<0.5$ can be observed in the data of Figure 6.32. The figure also indicates that applying a shear velocity ratio close to unity produces the maximum scour depth. In other words, observed local scour depths using $u_*/u_{*c}<1$ should be modified if the maximum value of the scour depth is sought.

6.1.4- Variations of u_*/u_{*c} in the floodplain

6.1.4.1- *Interacting* flow conditions

The deviations of the local u_*/u_{*c} from the critical value for experiments performed with *interacting* conditions are presented in Figures 6.40 to 6.43. For *interacting* conditions established using S_o=0.0006 and D_{50}=0.5 mm, the local u_*/u_{*c} at the end of the short model abutment (L=90 mm) is about 5% less than the critical value (Figure 6.40). Approaching the MC/FP junction, u_*/u_{*c} increases and reaches the critical value at x=130 mm. At the end of the long model abutment (L=210 mm) the local shear velocity is 6% higher than the critical value.

The results of experiments performed with slope settings S_o=0.00075 and 0.0009, and D_{50}=0.5 mm are presented in Figure 6.41 and 6.42. The variations of local u_*/u_{*c} in these cases follow the general trend observed in Figure 6.40. However, since smaller relative flow depths were applied in these experiments, the maximum variation of the local u_*/u_{*c} at the end of the long model abutment (L=210 mm) is only about 2% higher than the critical value. Figures 6.41 and 6.42 indicate that shorter model abutments (L=90 mm) experience about 9% and 6% less local u_* than the critical value when using bed slope settings of 0.00075 and 0.0009 respectively. Finally, considering the flow condition established for D_{50}=0.7 mm and So=0.0009, at the end of the long model abutments local u_* as high as the critical value was observed while, short abutments experienced $0.9u_{*c}$ at their ends.

6.1.4.2- *Non-interacting* flow conditions

Isolating MC flow from the FP flow, by means of a thin vertical wall, eliminates the lateral momentum transfer from the fast moving MC flow to the slower FP flow. In such a case, significant changes in the FP flow velocity and the local shear velocity ratio are expected. The variations of the local u_*/u_{*c} for *non-interacting* conditions are presented in Figures 6.44 to 6.46. The figures show that the local u_*/u_{*c} are generally smaller than the critical value for all the experiments performed with *non-interacting* conditions. Figure 6.44 shows the deviation of u_*/u_{*c} from the critical value for S_o=0.00075 and D_{50}=0.5 mm. The figures indicate that local u_* at the end of the short abutments is approximately 15% less than the critical value, while long abutments experience smaller decreases of about 4% from u_{*c}. Comparing local u_* for *interacting* and *non-interacting* conditions shows that isolating the MC flow from the FP flow generally reduces the local u_* by about 5%. When *non-interacting* conditions was repeated using S_o=0.0009 and D_{50}=0.5 mm, significant decreases in local u_* were also noted. Approximately the same reduction in local u_* was observed in *non-interacting* conditions performed using S_o=0.0009 and both values of D_{50} (Figures 6.45 and 6.46).

When the maximum scour depth is sought, the observed scour depth should be adjusted if the local u_* deviates significantly from the critical value. Also, data are only comparable if they are adjusted for or obtained within the same range of u_*/u_{*c}. In light of these findings, data having a significant deviation of local u_* from the critical value will, therefore, require adjustment.

6.1.5- Deflection angle β and effective w

Examining the surface flow pattern generated in different tests around various model abutments indicates that a specific *effective width*, w, is associated with Q_w. As the flow approaches the abutment, the obstructed portion of the flow is redirected towards the abutment end where the flow accelerates. As indicated in plate 5.7, as the flow approaches the abutment end captured confetti paths elongate showing flow acceleration and approximately 50% increase in the flow velocity in that zone for given test condition.

In addition to the obstructed flow, a portion of the FP (and MC) flow is also attracted towards the abutment end where the flow acceleration takes places. This was observed in all the experiments irrespective of the abutment shape and other test conditions. The extent of the converged flow, however, varies with test conditions. The variations of β and the magnitude of the effective width, w, associated with Q_w for different test conditions are presented herein.

6.1.5.1- Variations of β

The presence of an abutment obstructs a portion of the FP flow , Q_a, and redirects it toward the abutment end. The flow redirected by the abutment intersects with the approaching flow, Q_v, at a specific angle, β, (Figure 6.47). Streamlines closer to the flume wall make sharper turn (smaller radius) to reach the abutment end. The surface flow pattern for *interacting* conditions using S_o=0.0009, D_{50}=0.5 mm, and the SC-abutment are shown in plates 6.1 to 6.3. The plates indicate that as the abutment length increases the angle of the redirected flow, β, increases toward the abutment end. The redirected flow intersects with the approaching flow of the opening width at the abutment end at approximately the same angle β. The larger the angle of intersection of these flows the stronger the spiralling motion at the abutment end. This flow feature can clearly seen by considering the distance of the floating strings from the abutment end.

The characteristic distance between the abutment end and the closest floating string is generated by the vortices of the flow field. Larger and stronger vortices produce bigger characteristic distance. The presence of the spiralling motion and the characteristic distance between the abutment end and the floating strings are clearly demonstrated in the close-up photographs presented in plates 6.4 to 6.7. These photographs where captured for *interacting* conditions using S_o=0.0009, D_{50}=0.7 mm. VW (L=210 mm) and SC (L=150 mm) abutments were utilized in plates 6.4 and 6.5, whereas plates 6.6 and 6.7 show ST (L=210 mm) and WW (L=210 mm) abutments respectively.

Comparing photographs captured using different grain sizes and bed slope settings indicates that the short model abutments (L=90 mm) redirect the obstructed flow at an angle β approximately equal to 15°, the mid-length model abutments (L=150 mm) redirect the flow at β≈ 30°, and the long model abutments (L=210 mm) redirect the flow at β≈ 40°. The angle of flow deflection increases with the abutment length to a maximum value of 90°. This suggests that there exists a limiting scour depth associated with the maximum value of β.

6.1.5.2- The extent of w

As mentioned earlier, a portion of the approaching flow is attracted toward the abutment end where the flow acceleration takes place. To determine the ratio Q_w/Q_a it is necessary to define width w in which flow Q_w contributes to the scouring process. Using the *floating strings* technique, the surface flow pattern of *interacting* conditions was visualized and photographed; the extent for w was then determined.

The flow pattern in the vicinity of SC abutments of different length for *interacting* conditions, S_o=0.0009, and D_{50}=0.7 mm are shown in plates 6.8 to 6.10. Plates 6.11 to 6.13 show the flow pattern in the vicinity of VW-abutments of different lengths for the same test conditions that applied in the former plates. Finally, plates 6.14 to 6.16 show the flow pattern in the vicinity of ST (L=90 mm), VW (L=150 mm), and SC (L=210 mm) abutments, using S_o=0.0009, D_{50}=0.5 mm, and *interacting* conditions.

As indicated in plates 6.8 to 6.16, when the flow approaches the contracted section of the flume the surface flow lines separate into two portions; one portion converges and concentrates at the abutment end where the flow accelerates, and the other portion moves away from the abutment towards the MC/FP junction. Plates 6.8 to 6.16 generally indicate that a larger number of streamlines concentrate at the end of longer abutments resulting in higher flow velocity and local shear stress and in turn a deeper scour hole.

Comparing flow patterns of plates 6.8 to 6.10 and plates 6.11 to 6.13 indicates no significant influence of the abutment shape on the overall extent of the modified flow field generated around abutments. The same conclusion was drawn regarding the influence of the relative flow depth on the extent of w, by comparing plates 6.8 to 6.13 and 6.14 to 6.16. In other words, the extent of w can be related to the length of the obstructing structure. Based on comparison, of photographs taken of different tests for *interacting* conditions, the extent of w (the width associated with Q_w) is considered approximately equal to 70% of the abutment length in each case.

6.1.6- Discharge ratio Q_w/Q_a

the velocity distribution across the FP of a compound channel is usually not uniform. Because of the high resistance coefficient in the FP flow is generally slower in that region than in the MC. As mentioned in section 2.6 the relative flow depth affects the lateral momentum flux, consequently the velocity distribution in the transverse direction in the FP depends on y_d/H. The variations of the depth-averaged flow velocity across the left FP for *interacting* conditions are presented in Figures 6.48 to 6.51. The figures clearly indicate that the velocity gradient in the lateral direction is steeper for smaller relative depth than for larger ratios. This indicates that lateral momentum transfer (LMT) is stronger for smaller y_d/H ratios.

Since flow velocity in the lateral direction is not uniform, to accurately determine Q_w and Q_a the flow should be integrated along the specified widths of the FP, i.e. w and L respectively. This was accomplished by developing a computer programme which utilizes the co-ordinate method to determine the area associated with any point on the flow velocity curve. The programme determines Q_a and Q_w by integrating the flow associated with L and w respectively. The Q_w/Q_a ratios were then determined for different flow conditions and effective width w.

The variations of Q_w/Q_a across the FP for different flow depths and *interacting* conditions are presented in Figures 6.52 to 6.54. The variations of Q_w/Q_a are shown in Figure 6.52 for *interacting* conditions with S_o=0.0006 and D_{50}=0.5 mm. As indicated in the figure the relative depth for this case (y_d/H=0.29) was close to the limit beyond which the effects of the compound section decrease significantly; in such a case the LMT becomes insignificant. The linear variation of the discharge ratio indicated in Figure 6.52 can be attributed to the decrease in LMT. In other words, smaller LMT produces a flatter velocity gradient in the lateral direction, which results in smaller variations in the discharge ratio.

For smaller relative depth ratios, however, stronger LMT exists which results in significant velocity variations in the lateral direction, especially in the vicinity of the MC/FP junction (Figures 6.49 and 6.50). As a result of stronger velocity gradients one would expect that the discharge ratio would increase as the MC/FP junction is approached. This trend can clearly be seen in Figures 6.53 and 6.54. These figures show the variations of Q_w/Q_a in the FP for *interacting* conditions using D_{50}=0.5 mm and bed slope setting S_o=0.00075 and 0.0009, which produced relative depth ratios equal to 0.24 and 0.21 respectively. Also, for *interacting* conditions with D_{50}=0.7 mm and S_o=0.0009 the variations of Q_w/Q_a in the FP are presented in Figure 6.55

The variations of the discharge ratio with FP flow depth at specific positions in the FP for *interacting* conditions using D_{50}=0.5 mm are shown in Figures 6.56 to 6.58. The LMT effect deceases as the distance from the MC/FP junction to the FP wall increases. Dividing the width of the FP into four quarters, relatively similar flow velocity gradients were observed in the lateral direction close to the FP wall, i.e. $0<x<100$ mm (Figures 6.48 to 6.51). The velocity gradients observed in the next quarter ($10<x<200$ mm) are flatter than the former ones, however, similar trends for different flow conditions were also observed in this region. Closer to the MC/FP junction ($200<x<381$ mm) stronger variations in the velocity gradients for different relative depths were observed (Figures 6.48 to 6.51).

As a result of the variations of the lateral velocity gradient the variations of Q_w/Q_a increase as distance from the MC/FP junction decreases. Also, the variations in Q_w/Q_a with y_d/H become more significant as the distance to the MC/FP junction decreases. In other words, as the FP flow depth increases LMT decreases, resulting in more uniform flow velocity gradients in the FP. Flatter velocity gradient in turn results in smaller discharge ratio (Figure 6.58). Figure 6.58, which shows the variations in Q_w/Q_a with y_a for x=210 mm (the long-model abutment), clearly illustrates that the discharge ratio decreases as flow depth in the FP increases. Figures 6.56 and 6.57 show the variations in the same parameters for the short- and mid-length (90 and 150 mm) model abutments. Similar trends can be observed in Figures 6.56 and 6.57 to that observed in Figure 6.58, however, the variations of Q_w/Q_a in the former figures are smaller.

Since LMT affects the region close to the MC/FP junction the most, the greater the distance from the MC/FP junction the smaller will be LMT. Therefore, the lateral velocity gradient in the region close to the FP wall ($0<x<200$ mm) is less affected by variations in y_d/H. This, in turn, leads to smaller variations in Q_w/Q_a with y_a in this region.

6.2- SCOUR DATA; *INTERACTING* FLOW CONDITIONS

6.2.1- Influences of flow depth and abutment length; D_{50}=0.5 mm

Flow depth and abutment length were utilized in previous studies to propose abutment scour prediction equations. In order to facilitate comparison between the data of the present study and the results of the previous studies, the relationship between scour depth, flow depth and abutment length are presented here.

6.2.1.1- Flow depth factor

The variations of y_{se} with y_a based on D_{50}=0.5 mm and different model abutment shapes and lengths, are presented in Figures 6.59 to 6.62. Figure 6.59 shows the variations of the scour depth for SC-abutments of different length. Considering the curve for the 90 mm-long abutment in Figure 5.69, increasing the flow depth from 28 mm to 33 mm increases y_{se}. For y_a>33 mm, an increase in the flow depth does not affect y_{se} significantly. Different model abutment lengths produced similar trends to that of L=90 mm (Figure 6.58). Figures 6.60 to 6.62 show the variations of y_{se} versus y_a for model abutment lengths L=90, 150, and 210 mm and VW-, WW-, and ST-abutment shapes. Different abutment shapes produced different scour depth; the variations of the scour depth in these figures, however, follow the same trend observed for the SC-abutment shape (Figure 5.59).

The decrease in y_{se} for smaller flow depths can be attributed to a decrease in the downflow strength. Also, in shallower flow depths the surface vortices interfere with the primary vortex at the base and decrease its strength, which in turn results in a shallower scour hole. As the flow depth increases the distance between these vortices increases and eventually at a specific flow depth they do not interfere with each other. For this condition scour depth is independent of the flow depth. The data in Figures 6.59 to 6.62 were non-dimensionalized by L and are presented in Figures 6.63 to 6.67. These figures indicate that an increase in flow depth results in an increase in the scour depth, however, the rate of the scour depth growth is decreasing.

To observe the influence of model abutment shape on scour depth, the variations in scour depth for a given abutment length and different model abutment shapes, are presented in Figures 6.67 to 6.68. In these figures which also show the effects of flow depth on scour depth the non-dimensionalized scour depth and flow depth(y_{se}/L and y_a/L) were utilized. Figure 6.67 shows the variability in the scour depth for 90 mm-long model abutments of different shapes. This figure indicates that different model abutments produced similar trends in the scour depth. The smallest scour depth for a given flow depth was generated by the ST-abutments, while the VW-abutments produced the maximum scour depth. For the smallest flow depth used, the scour depths produced by the WW-abutments were smaller than those produced by the VW-abutments. However, as the flow depth continue to increased these abutment shapes eventually generated the same scour depth. For the range of flow depths used in the experiments the depths of the scour produced by the SC-abutments were larger than those produced by the ST-abutments and smaller than those produced by the WW-abutments.

As the abutment length increased, the effects of abutment shape on scour depth decreased (Figure 6.68). Figure 6.68 presents the data for 150 mm-long model abutments of different shape. This figure shows that the ST- and the SC-abutments produced relatively similar scour depth for y_a=28 and 33 mm and it decreases by approximately 5% for y_a=42 mm. However, for the range of flow depths used the WW-abutments produced approximately 5% deeper scour holes than those generated by the ST-abutments. In this case (L=150 mm) the VW-abutments produced the maximum scour depths which were approximately 20% deeper than those generated by the SC-abutments.

The variations in scour depth for 210 mm-long abutments of different shapes observed in Figure 6.69 are similar to those observed for 150 mm-long abutments (Figure 6.68). The difference in the latter case, however, was between the scour depth produced by the VW-abutments and that generated by other abutment shapes. The scour depth produced by the ST-, SC-, and WW-abutments differ only slightly from each other (between 2 to 5%). VW-abutments, however, exhibit significant differences in the magnitude of the scour depths, which were higher approximately 15 to 35% than scour depths generated by the other abutment shapes.

6.2.1.2- Abutment length factor

The variations of y_{se} with L for different flow depths are plotted in Figures 6.70 to 6.73. These results are for SC-, VW-, WW-, and ST-abutments. Figure 6.70 shows the y_{se} generated for a range of flow depths by SC-abutments having different lengths. The trend of y_{se} with L indicates that the scour depth increases with increasing rate as L increases. Other abutment shapes produced similar trends as that generated by the SC-abutment (Figures 6.71 to 6.73). The data in Figure 6.70 (SC-abutments) were non-dimensionalized by the flow depth and are presented in Figure 6.74. The rate of y_{se}/y_o growth with L/y_o is more pronounced in Figure 6.74 than in Figure 6.70. In other words, for a given flow depth y_{se}/y_o grows with increasing rate as L increases. The data for other abutment shapes (VW-, WW-, and ST-abutments) are also non-dimensionalized and are plotted in Figures 6.75 to 6.77. The increasing rate of y_{se}/y_o also can be clearly observed in these figures.

6.2.2- Influences of abutment length and flow depth; D_{50}=0.7 mm

For D_{50}=0.7 mm and S_o=0.0009, the y_{se} versus L relationships under *interacting* conditions are presented in Figure 6.78 for different abutment shapes. The scour depth generated by the short model abutments (L=90 mm) varies with the abutment shape. The VW-abutment generated the maximum scour depth, which was approximately 20% greater than that produced by the SC-abutment. Also, the scour hole produced by the WW-abutment was about 5% deeper than that associated with the SC-abutment. The smallest scour depth was associated with the ST-abutment. It generated a scour hole about 8% smaller than that produced by the SC-abutment.

Except for the VW-abutment, as the abutment length increased the effect of the abutment shape decreased. For the mid-length (L=150 mm) and long (L=210 mm) model abutments only small variations (1 to 3%) were observed in the scour depth generated by the SC-, ST-, and WW-abutments. However, a significant difference (approximately 20%) was observed between the scour depth produced by the VW-abutments and those generated by other abutment shapes.

6.2.2.1- Abutment length factor

A comparison between the D_{50}=0.7 mm and D_{50}=0.5 mm results is possible if the data are non-dimensionalized by a length scale. The effect of sediment size can be examined if scour depth and sediment size are non-dimensionalized by abutment length, L. The non-dimensionalized data for *interacting* conditions are presented in Figures 6.79 to 6.82. These figures show the variations of y_{se}/L with L/D_{50} for different abutments shape and sediment sizes. Figure 6.79 shows the results for SC-abutments of L=90, 150, and 210 mm, for both D_{50}=0.5 and 0.7 mm. The data indicate that, for a given abutment length, decreasing D_{50} decreases y_{se}/L. The rate of reduction in the scour depth, however, decreases with the an increase in L. In other words, the variations in y_{se}/L with L/D_{50} for 150 mm-long abutments are smaller than those for 90 mm-long abutments and are larger than those for 210 mm-long abutments. Figure 6.79 indicates that, for a given abutment length, increasing the sediment size generally results in deeper scour holes when the threshold condition of bed material movement is maintained.

Figures 6.80 to 6.82 show the variations of y_{se}/L with L/D_{50} for VW-, WW-, and ST-abutments respectively. The data in these figures were obtained using D_{50}=0.5 and 0.7 mm and L= 90, 150, and 210 mm model abutment lengths. The data for VW-, WW-, and ST-abutments show a systematic decrease in y_{se}/L with increasing L/D_{50}. The general trend of y_{se}/L variations with L/D_{50} observed for these abutment shapes are the same as that observed for the SC-abutment (Figure 6.79).

The influence of abutment length on scour depth for *interacting* conditions with D_{50}=0.5 mm and D_{50}=0.7 mm are presented in Figures 6.83 to 6.86. Each figure presents the results for a given abutment shape. Figure 6.83 shows that, for a given L/y_a the relative scour depth generated by SC-abutments is higher for D_{50}=0.7 mm than for D_{50}=0.5 mm. Based on the results presented in Figures 6.79 to 6.82, observing higher y_{se}/y_a for D_{50}=0.7 mm than for D_{50}=0.5 mm would be expected. As indicated in Figures 6.84 to 6.86, the trend of y_{se}/y_a variations observed for VW-, WW-, and ST-abutments for D_{50}=0.7 mm is similar to that observed for SC-abutments. The curves fitted to the data points for D_{50}=0.7 mm envelop the data for D_{50}=0.5 mm.

6.2.2.2- Flow depth factor

The data for *interacting* conditions and using both sediment sizes are presented in Figures 6.87 to 6.90 to show the influence of the relative flow depth, y_a/L, on relative scour depth, y_{se}/L. These curves for a specific abutment shape are presented on each figure. The y_{se}/L versus y_o/L relationships for the SC-, VW-, WW-, and ST-abutments are presented in Figures 6.87 to 6.90 respectively. The data correspond to D_{50}=0.7 mm were indicated by curves line in these figures. They show that for a given abutment length increasing the flow depth results in an increase in the scour depth; the rate of the growth, however, is decreasing. Although the trend of these variations was also observed for D_{50}=0.5 mm, slightly higher y_{se}/L values were observed for D_{50}=0.7 mm.

The decrease in variations of y_{se}/L (Figure 6.79 to 6.82) suggests that there is a limiting L/D_{50} beyond which the scour depth becomes independent of the sediment size. For *circular bridge piers* Ettema (1980) showed that, when $b/D_{50}>50$, the impact of sediment size on scour depth y_{se}/b becomes insignificant. In the abutment case, since $L/D_{50}<50$ is unlikely to be encountered in both laboratory and field conditions on one hand and on the other hand there is a lack of data to evaluate the effects of the sediment size, engineers usually rely on Ettema's (bridge pier) results when considering abutments (Melville, 1992). The results of this study, however, indicate that the limit set by Ettema ($b/D_{50}>50$) for *circular bridge piers* is not appropriate for the abutment case. Further studies are required to draw a more general conclusion regarding the effects of sediment size for the case of bridge abutments.

Comparison of the results obtained using two sediment sizes indicates that, for the case of abutments D_{50} affects scour depth even when $L/D_{50} \gg 50$. Accordingly, more realistic relationships to predict local scour depth at bridge abutments can be obtained if the effects of the sediment size are incorporated in the formulation. The effects of relative size of sediment (section 3.4), can be considered by incorporating

F_c (the critical Froude number for initiating bed material movement) in the formulation.

6.2.3- Scour depth versus discharge ratio

6.2.3.1- y_{se}/y_a versus Q_w/Q_a; D_{50}=0.5 mm

As indicated in section 3.4 the discharge ratio was an important parameter for predicting scour at bridge abutments and should be incorporated in the formulation. The variations of the discharge ratio in the FP for different *interacting* conditions are presented in section 6.1.6. In this section the relation between Q_w/Q_a and y_{se}/y_a is presented for different abutment shapes and flow conditions.

The D_{50}=*0.5 mm* results for *interacting* conditions are presented in Figures 6.91 to 6.94. Figure 6.91 shows how of y_{se}/y_a varies with Q_w/Q_a for the SC-abutments in different y_d/H. As discussed in section 6.1.6, the higher the y_d/H the smaller the LMT, i.e. the velocity distribution tends to be more uniform across the FP. This, eventually, results in smaller Q_w/Q_a. Considering the relative flow depth y_d/H=0.21 in Figure 6.91, higher y_{se}/y_a were observed for this ratio than for y_d/H=0.24 and 0.29. Increasing Q_w/Q_a results in higher y_{se}/y_a, the rate of the growth, however, is decreasing.

The y_{se}/y_a versus Q_w/Q_a relationships are presented in Figures 6.92 to 6.94 for the VW-, WW-, and ST-abutments, respectively. The trend of y_{se}/y_a growth in these figures is similar to that observed in Figure 6.91, i.e. the smallest y_d/H produced the highest y_{se}/y_a.

The y_{se}/y_a versus Q_w/Q_a relationships for different abutment shapes and a given relative flow depth ratio are presented in Figures 6.95 to 6.97. Figure 6.95 shows the results for y_a/H=0.21; the largest and the smallest scour depths for a given Q_w/Q_a value were produced by the VW-abutments and the ST-abutments, respectively. The y_{se}/y_a curve for the SC-abutments is lower than that of the WW-abutments, however these abutment shapes produced smaller y_{se}/y_a than the VW-abutments. Figure 6.95 indicates that, for all abutment shapes, y_{se}/y_a increases with decreasing rate when Q_w/Q_a increases. The figure also shows that the influence of abutment shape on scour depth decreases as Q_w/Q_a increases.

The LMT associated with y_a/H=0.21 is higher than that for larger y_a/H. Higher LMT results in larger Q_w/Q_a which, in turn, produces larger scour depths. The y_{se}/y_a versus Q_w/Q_a relationships for y_a/H=0.24 and different abutment shapes are presented in Figure 6.96. As a result of relatively weaker LMT for y_a/H=0.24, the variations in y_{se}/y_a are smaller than those observed in Figure 6.95. Also, the influence of the abutment shapes decreases as Q_w/Q_a increases. Figure 6.97 shows the results for y_a/H=0.29, which indicates that LMT is smaller than for the former y_a/H values. Smaller LMT results in smaller Q_w/Q_a, which translate into smaller y_{se}/y_a. Smaller LMT generally calls for milder growth in y_{se}/y_a which can clearly be observed through a comparison of the rate of y_{se}/y_a growth in Figures 6.95 to 6.97.

6.2.3.2- y_{se}/y_a versus Q_w/Q_a; D50=0.7 mm

The $D_{50}=0.7\ mm$ results are presented in this section and are compared with those for D_{50}=0.5 mm. To maintain near-threshold condition for D_{50}=0.7 mm the relative depth, y_a/H=0.27 is required for S_o=0.0009. High y_a/H reduces LMT between the MC and the FP. As discussed in section 6.1.7, in these circumstances variations in

Q_w/Q_a decrease across the FP. This, in turn, reduces the variations in y_{se}/y_a (i.e. the trend of y_{se}/y_a tends to flatten).

The y_{se}/y_a versus Q_w/Q_a relationships for the SC-, VW-, WW-, and ST-abutments are presented in Figures 6.98 to 6.101 respectively. These figures indicate that y_{se}/y_a increases when Q_w/Q_a increases, however, the trend in these figures indicates that y_{se}/y_a grows at a decreasing rate. The influence of Q_w/Q_a on y_{se}/y_a for *interacting* conditions for D_{50}=0.5 mm and D_{50}=0.7 mm are compared in Figures 6.102 to 6.105. Each figure presents the results for a given abutment shape. Figure 6.102 shows that, for a given Q_w/Q_a, the relative scour depth generated by the SC-abutments is higher for D_{50}=0.7 mm than for D_{50}=0.5 mm. The same trend is also observed in Figures 6.103 to 6.105, which show the results for VW-, WW-, and ST-abutments. The curves fitted to the data points for D_{50}=0.7 mm envelop the data for D_{50}=0.5 mm.

6.2.4- Comparison with former formulae

In this section scour depths predicted by equations proposed by different researchers are compared with observed scour depths for *interacting* conditions. The data for y_a/H=0.27 are presented in Figures 6.106 to 6.109 for SC-, VW-, WW-, and SC-abutments respectively. The data in these figures were compared with the results of Equations 2.14 (Garde et al., 1961), 2.18 (Gill, 1972), 2.19 (Froehlich, 1989), 2.27 (Melville, 1992), and 2.34 (Sturm and Janjua, 1994).

For the range of relative flow depth used, equations 2.14, 2.18, and 2.34 predicted y_{se}/y_a smaller than the observed values. Garde et al., Gill, and Sturm and Janjua's tests were performed using shear velocity ratios smaller than the critical value. Therefore, their equations underestimate the scour depth significantly if the maximum scour depth is sought. As indicated in Figure 6.106, Melville's equation overestimated scour depth for all the investigated abutment lengths. Froehlich's equation on the other hand overestimated scour depth for the 150- and 210-mm abutments and produced lower values for the 9 cm-abutments (Figure 6.106 to 6.109).

The trends of y_{se}/y_a growth produced by both Melville's equation and Froehlich's equation indicate that these equations are very sensitive to abutment length. In other words, the overestimation of scour depth for longer abutments is higher than for shorter abutments. The results for y_a/H=0.24 and 0.21 are presented in Figures 6.110 to 6.113, and 6.114 to 6.117 respectively. These figures show similar trends to that observed in Figures 6.106 to 6.109.

6.3- SCOUR DATA; *NON-INTERACTING* FLOW CONDITIONS

In this section the scour data for *non-interacting* conditions are presented. The experiments for *non-interacting* conditions were also preformed with the both sediment sizes. The bed slope settings used in the D_{50}=0.5 mm experiments were S_o=0.00075 and 0.0009, whereas in the D_{50}=0.7 mm experiments only S_o=0.0009 was used. The relative influences of abutment length and flow depth on the scour depth are presented first. The patterns of the scour holes generated by the different abutment shapes are also presented. The results for *non-interacting* conditions are then compared with that for *interacting* conditions.

6.3.1- Abutment length effects

The role of abutment length in determining scour depth for D_{50}=0.5 and 0.7 mm is presented in Figures 6.118 to 6.121 for different abutment shapes. Figure 6.118

shows how of y_{se}/y_o varies with L/y_o for different-length SC-abutments. The figure indicates that for a given flow depth y_{se}/y_o increases as L increases. Except for the VW-abutments (Figure 6.119), which generated larger variations in y_{se}/y_o, the WW- and the ST-abutments exhibited similar trends to that generated by the SC-abutments (Figure 6.121).

As abutment length increases, abutment shapes account for only minor variations in y_{se}. The scour hole pattern can be considered to reflect the flow structure at the bed. The scour hole pattern generated by the SC-abutments for D_{50}=0.5 mm and S_o=0.00075 are presented in plates 6.17 to 6.19. A semi-circular scour hole formed upstream of the 90 mm-abutment (Plate 6.17). As the abutment length increases, the scour hole, as a consequence of the larger β, extends towards the MC/FP junction (Plates 6.18 and 6.19).

The scour hole pattern generated by the WW- and the VW-abutments for D_{50}=0.5 mm and S_o=0.00075 are presented in Plates 6.20 to 6.22 and 6.23 to 6.25 respectively. The scour holes upstream of the abutments generated by the WW-abutments are generally similar to those generated by the SC-abutments, in the downstream direction, however, a wider portion of the FP bed was disturbed by the WW-abutments than by the SC-abutments. Compared to other abutment shapes the VW-abutments created a basically different scour pattern. Comparing the scour patterns photographed for the 150 mm-abutments (Plates 6.18, 6.21, 6.24, and 6.26) with those for the 210 mm-abutments (Plates 6.19, 6.22, 6.25, and 6.27) shows that, as the abutment length increases different abutment shapes result in relatively similar scour patterns. Since the scour patterns can be considered indicative of the flow structure close to the bed, the stepwise scour pattern generated by the 210 $_{mm}$-abutments suggest that (except for the VW-abutments) the difference in the abutment shapes calls for minor differences in the flow structure. As a consequence of the similarity in the flow structure, the scour depths generated by longer abutments of different shape differ only by 1 to 3%.

6.3.2- Flow depth effects

The data for *non-interacting* conditions for both sediment sizes are presented in Figures 6.122 to 6.125. These figures present the y_{se}/y_a versus y_{se}/L relationships for the SC-, VW-, WW-, and ST-abutments respectively. The data in these figures show that, for a given abutment length, increasing the flow depth increases the scour depth. Moreover, as was the case for *interacting* conditions, the rate of the growth in scour depth decreases with flow depth.

6.3.3- y_{se} for *interacting* and *non-interacting* flow conditions

As indicated beforehand, earlier bridge abutment studies were conducted in laboratory flumes of rectangular cross-section. Although this arrangement simulates abutments positioned in the MC, the results of these studies were used to predict local scour depths for abutments terminating in the FP. Considering an imaginary boundary at the MC/FP junction, Melville (1995) concluded that abutments terminating in the FP (case IIIa in Figure 2.39) might be regarded as being similar to abutments sitting in a rectangular channel (case I in Figure 2.39). In order to examine the validity of this assumption, our data for *non-interacting* conditions are compared with those for *interacting* conditions.

The comparison is based on examining the corresponding y_{se}/y_a versus L/y_a relationship. Figures 6.126 to 129 show, for D_{50}=0.5 mm and S_o=0.00075, the y_{se}/y_a

versus L/y_a relationship under *interacting* and *non-interacting* conditions for the SC-, VW-, WW-, and ST- abutments respectively. The data in Figures 6.126 to 6.129 indicate that *non-interacting* conditions resulted in 15 to 30% smaller y_{se}/y_a than that generated under *interacting* conditions. Isolating the MC flow from the FP flow eliminates LMT and decreases the flow velocity in the region close to the MC/FP junction. This in turn decreases the shear velocity ratio in the FP. To compare the data for the critical u_*/u_{*c}, the data were modified based on u_*/u_{*c} tabulated in Table 6.3. The modified values for *non-interacting* conditions in Figures 6.126 to 6.129 also show 5 to 15% smaller y_{se}/y_a than for *interacting* conditions. The smallest differences between the y_{se}/y_a for *interacting* and *non-interacting* conditions were observed for the 150 mm-abutments. In other words, isolating the FP from the MC affects the 90 mm-abutments and 210 mm-abutments the most.

The relationships between y_{se}/y_a and L/y_a for D_{50}=0.5 mm and S_o=0.0009 are presented in Figures 6.130 to 6.133. These figures also show that y_{se}/y_a produced under *non-interacting* conditions is smaller than that for *interacting* conditions. The variations in y_{se}/y_a for the given bed slope setting generally follow the trend observed in Figures 6.126 to 6.129. The u_*/u_{*c} in Table 6.3 were used to modify the data; nonetheless, the modified y_{se}/y_a are less than those for *interacting* conditions.

Finally, Figures 6.134 to 6.137 show the y_{se}/y_a versus L/y_a for D_{50}=0.7 mm and S_o=0.0009. The differences between y_{se}/y_a for *interacting* and *non-interacting* conditions was between 10 to 35%. The data for *non-interacting* conditions were also modified based on u_*/u_{*c} tabulated in Table 6.4. Similar to the data in Figures 6.126 to 6.133, the *non-interacting* data for D_{50}=0.7 mm, after being modified for the shear velocity ratio, are still smaller than the *interacting* data.

Comparing the *interacting* and *non-interacting* data shows that isolating the MC flow from the FP flow decreases the scour depth. Under *non-interacting* conditions the 210 mm-abutments obstruct 55% of the FP width. In this instance one would expect to observe an increase in the scour depth, because of the contraction scour that would normally occur as a result of the relatively high contracting ratio, α_{w}. Yet, the resulting scour depths are substantially smaller for *non-interacting* conditions than for *interacting* conditions for the 210 mm-abutments. Therefore, substituting case I in Figure 2.39 for case IIIa (by assuming an imaginary wall at the MC/FP junction) is not valid. Accordingly applying relationships based on data obtained from experiments performed in rectangular channels will result in highly conservative (predicted) scour depths.

6.4- PROPOSED SCOUR PREDICTION MODEL

6.4.1- Shape factors

The data for *interacting* conditions will be used to develop a scour prediction formula for abutments terminating in the FP zone. Since scour depths were obtained for different abutment shapes, the whole data set can be utilized providing that the shape effect is removed from the data. Data obtained for the different abutment shapes exhibit some scatter when plotted in non-dimensional form. Using different non-dimensional parameters the data are presented in Figures 6.138 to 6.140. The influence of flow depth, abutment length, and the discharge ratio on scour depth can be observed in Figures 6.138 to 6.140 respectively. The scatter in the data attributed to the abutment shape can be removed by applying appropriate shape factors.

The shape factors can be determined by trial and error procedures. A particular abutment shape is selected as a reference shape. The scour depths generated by other abutment shapes are then modified by coefficients until the best collapse in the data is attained. The coefficients which produced the best collapse in the data were regarded as the shape factors for the different abutment shapes.

In this study the SC-abutment was selected as the reference shape. An appropriate collapse in the data was obtained by applying shape factors K_s=1.25, 1.08, and 0.95 for the VW-, WW-, and ST-abutments respectively. The data in Figures 6.138 to 6.140 were adjusted by the appropriate shape factors and the modified data are presented in Figures 6.141 to 6.143. The modified data were then used to develop the scour prediction model for abutments terminating in the FP.

6.4.2- Prediction of scour depth

The data for *interacting* conditions (presented in Appendix E) are analysed to develop a scour prediction model based on the functional relationship obtained in section 3.4. First, the data were log-transformed, then a multiple regression model was applied. From the results of the multiple regression analysis the scour prediction model takes the form:

$$\frac{y_{se}}{y_a}=13.5\left(\frac{Q_w}{Q_a}\right)^{3.9} F_a^{1.17}\, F_c^{-0.25} \tag{6.2}$$

The coefficient of determination (r^2) and the *statistical* F-observed of the proposed model are 0.9 and 120.6, respectively. Also, the tabulated F-critical for the corresponding degrees of freedom and 0.005 level of significance is 42.5. Since the F-observed >> F-critical the regression equation is useful in predicting the scour depth.

Scour depths were predicted by applying Equation 6.2 to the various test data, and these were then compared with observed value (Figure 6.144). Figure 6.144 indicates that the model fits the data well and most of the data fall within the ±10% error lines. Since Q_w/Q_a in Equation 6.2 was raised to the power of 3.9, it should be evaluated accurately in order to avoid large errors in estimating scour depth. Also, the model can only be validated for field conditions if field data are available; field data for the case of bridge abutments, however, are very scarce and deficient.

The data in the present study were compiled using $2<L/y_a<7.5$, $0.21<y_d/H<0.29$, and $u_*/u_{*c}\approx 1$. Therefore, Equation 6.2 predicts the maximum scour depth for the given ranges of relative abutment lengths and relative flow depths. Further studies are required to evaluate the scour depth for longer abutments and smaller y_d/H at $u_*/u_{*c}\approx 1$, $u_*/u_{*c}<1$, and $u_*/u_{*c}>1$. Also, non-cohesive bed material was employed in this study. Data showing the impact of cohesive materials on the scouring process are scarce. The local scouring process at bridge abutments should be investigated for the case of cohesive sediments.

Furthermore, when applying Equation 6.2 to field conditions the results should be adjusted to account for gradation of the bed material. The impact of gradation on abutment scour in compound flow fields, however, has not been investigated yet. Ettema's (1980) and Wong's (1982) data indicate that, as σ_g increases to 4, the scour depth decreases to about 1/4 (Figure 2.18). Therefore, in the absence of information concerning the impacts of gradation and armouring on abutment scour in compound flow fields, Figure 2.18 should be used to estimate the impact of gradation on local scouring process.

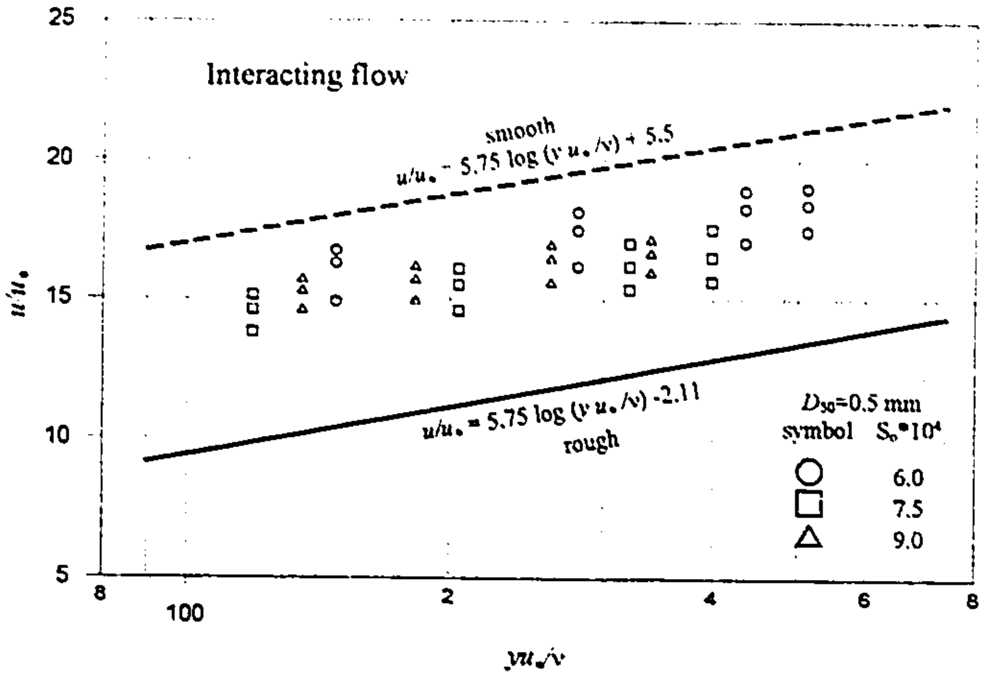

Figure 6.1- Comparison of universal log-law with approach floodplain flow velocity non-dimensionalized by $\overline{u}_*$

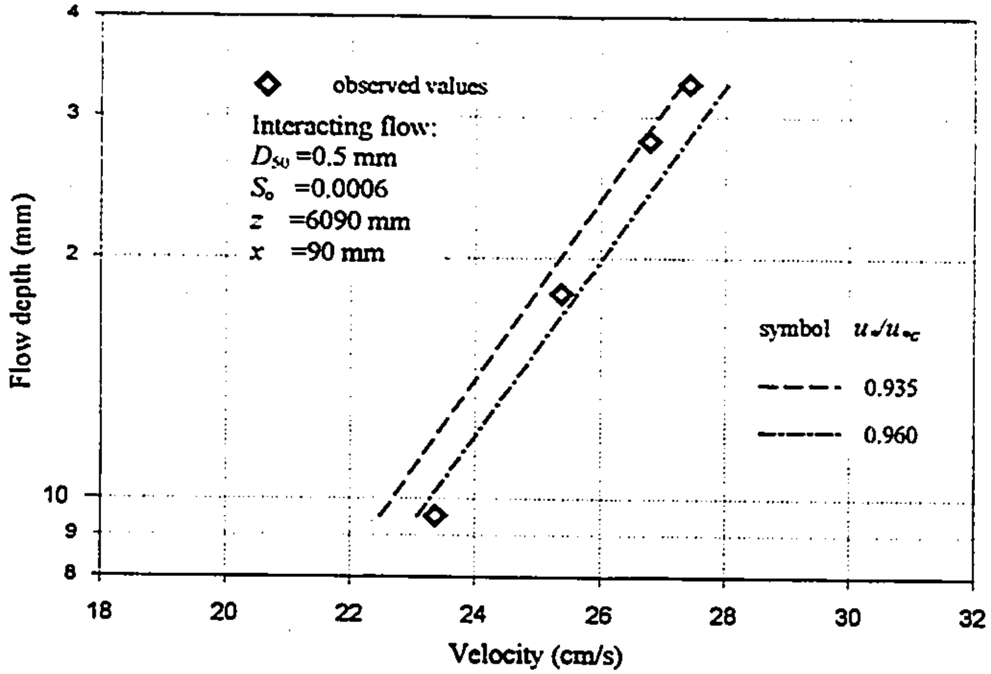

Figure 6.2- Comparison between observed velocity profile and log-law, using different u_*/u_{*c}

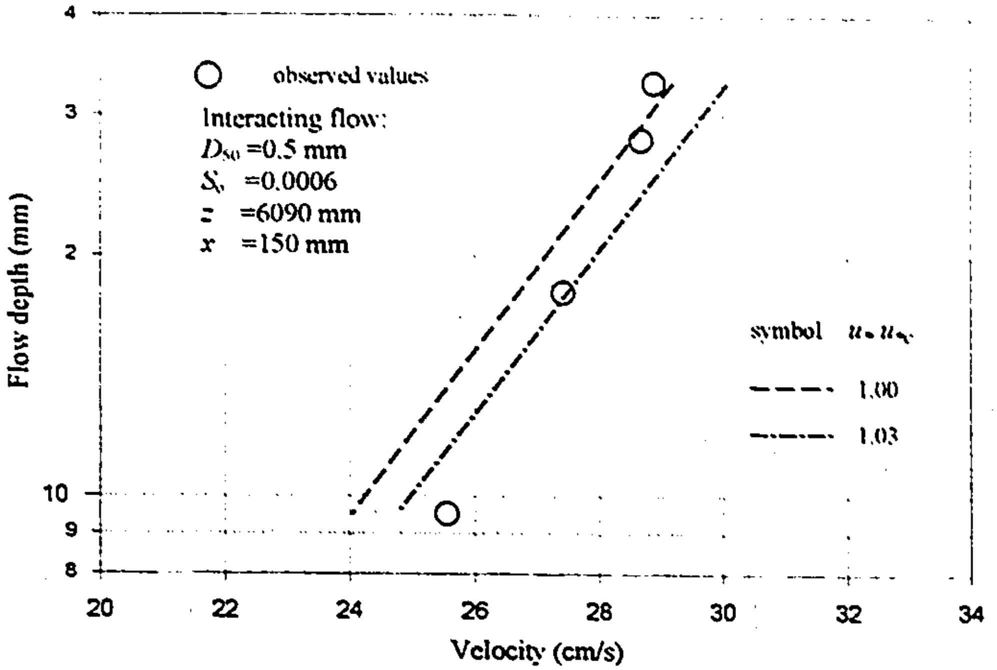

Figure 6.3- Comparison between observed velocity profile and log-law, using different u_*/u_{*c}

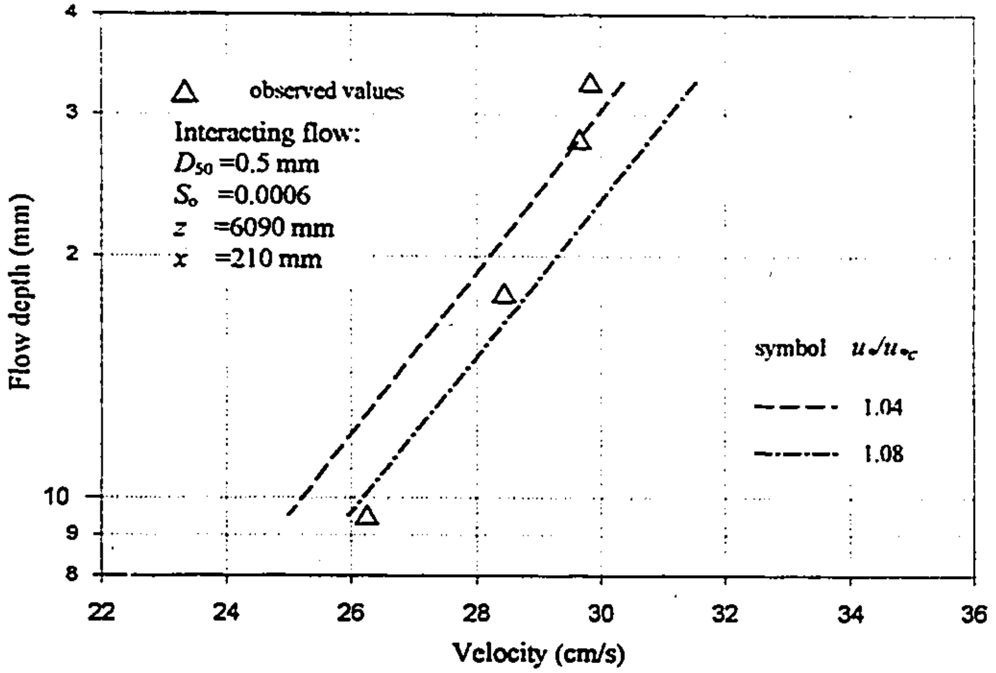

Figure 6.4- Comparison between observed velocity profile and log-law, using different u_*/u_{*c}

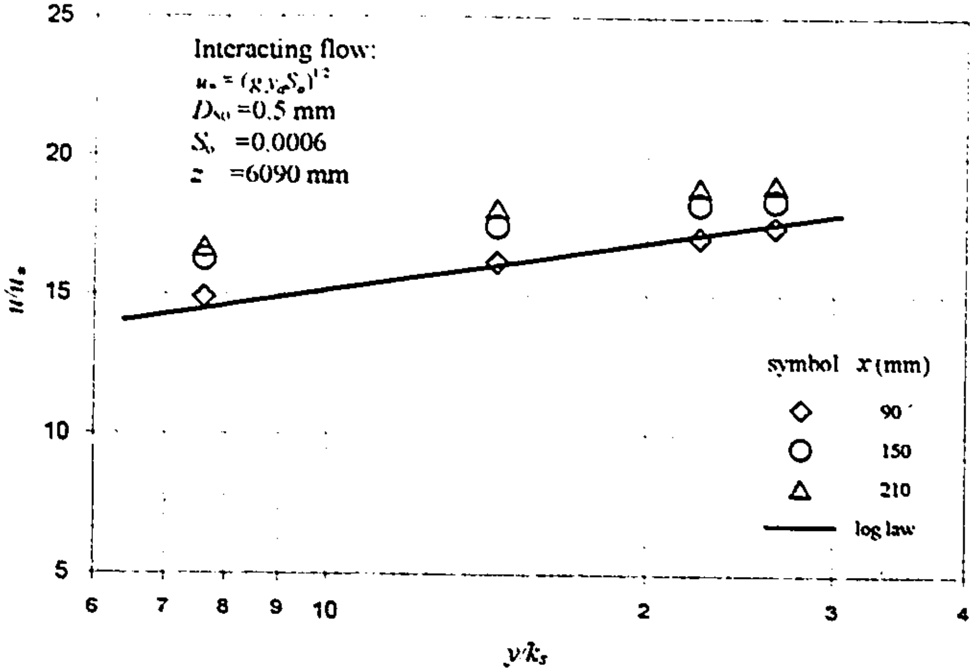

Figure 6.5- Universal log-law and observed velocity profiles

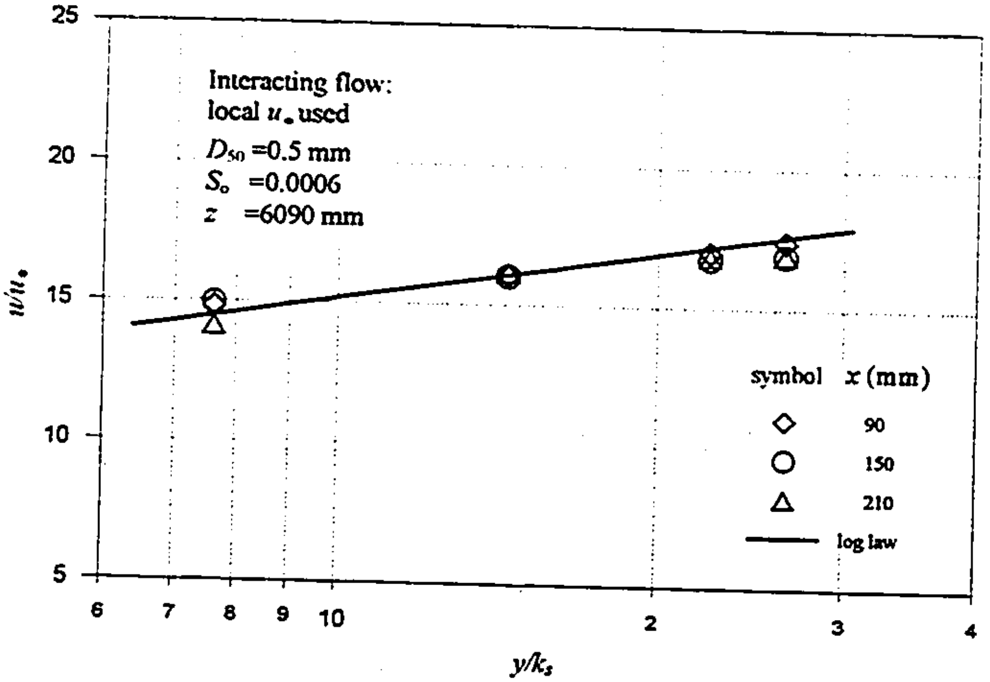

Figure 6.6- Universal log-law and observed velocity profiles

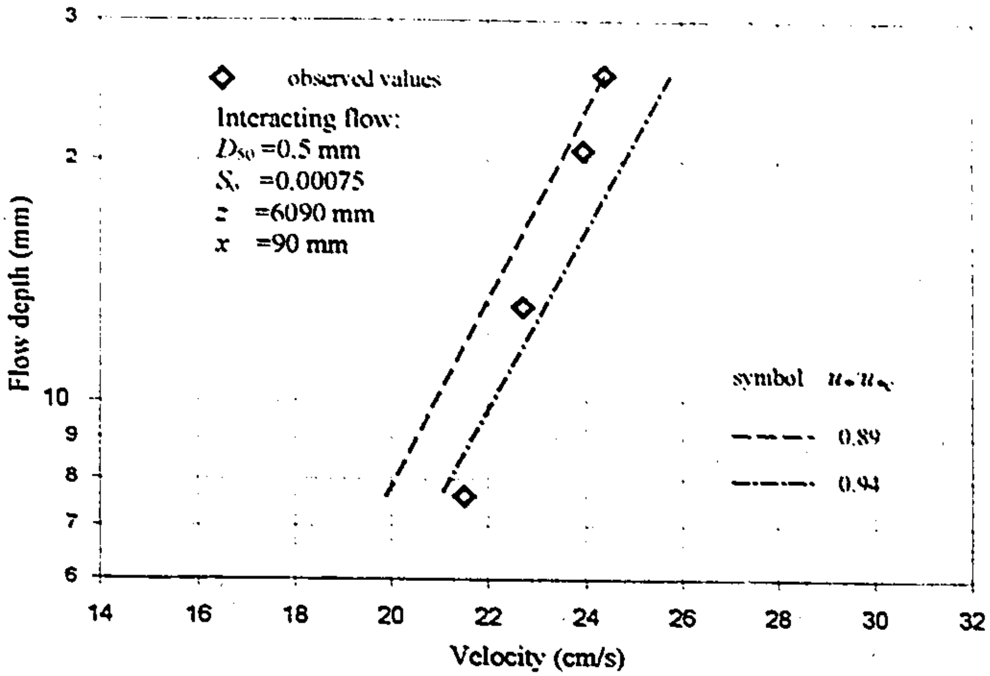

Figure 6.7- Comparison between observed velocity profile and log-law, using different u_*/u_{*c}

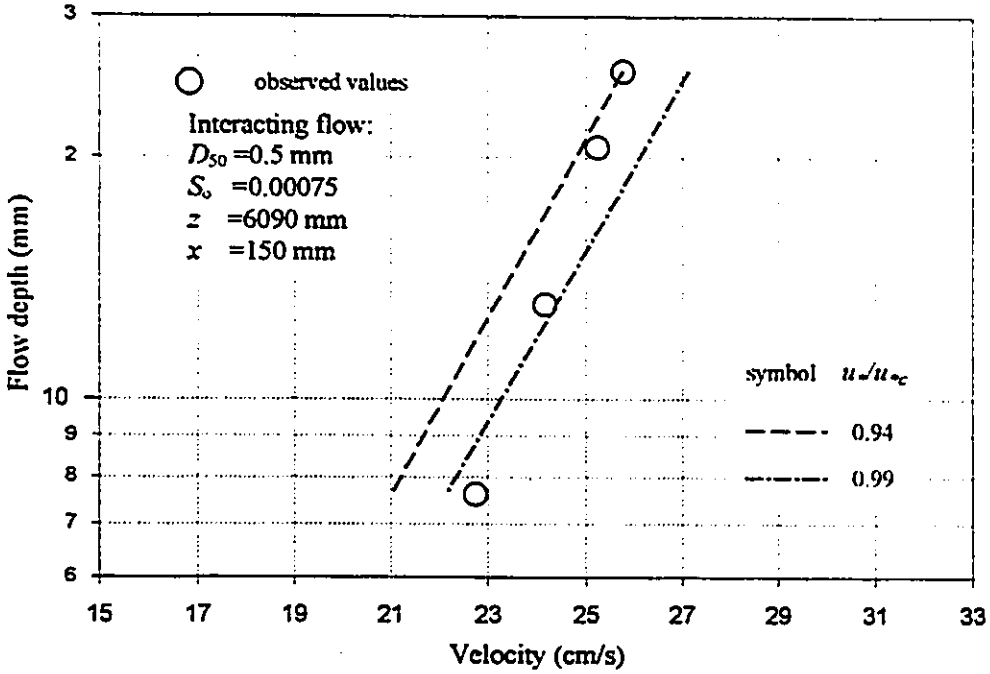

Figure 6.8- Comparison between observed velocity profile and log-law, using different u_*/u_{*c}

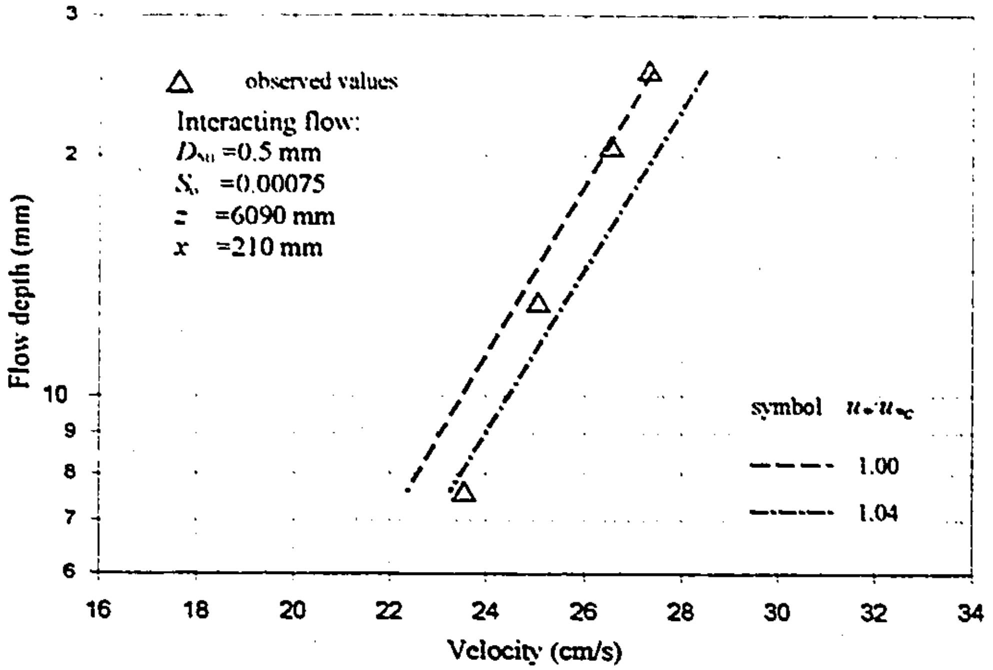

Figure 6.9- Comparison between observed velocity profile and log-law, using different u_*/u_{*c}

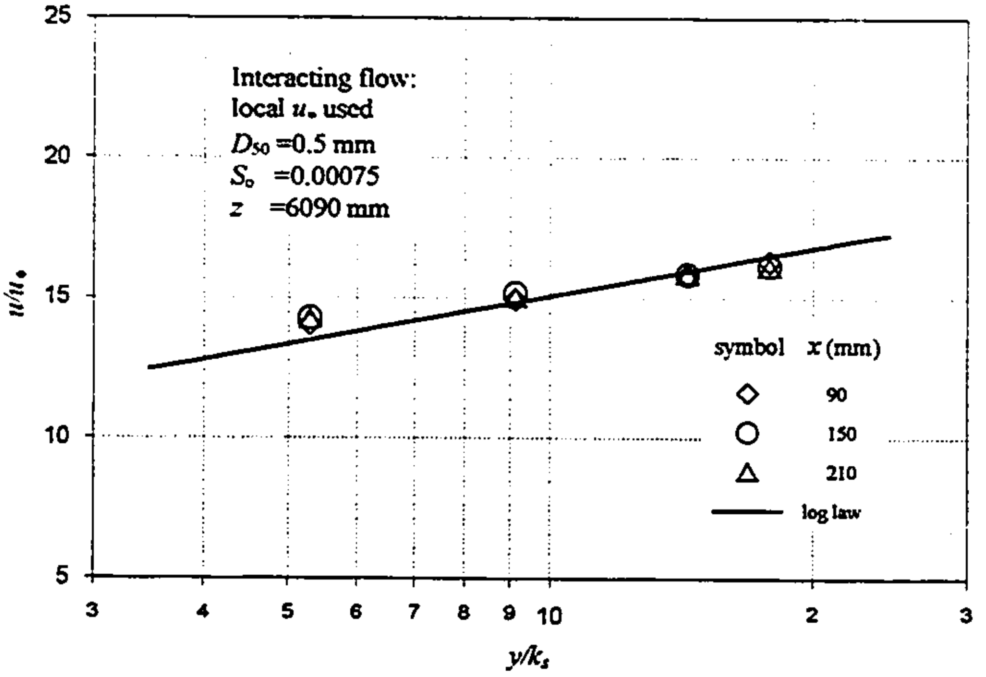

Figure 6.10- Universal log-law and measured velocity profiles

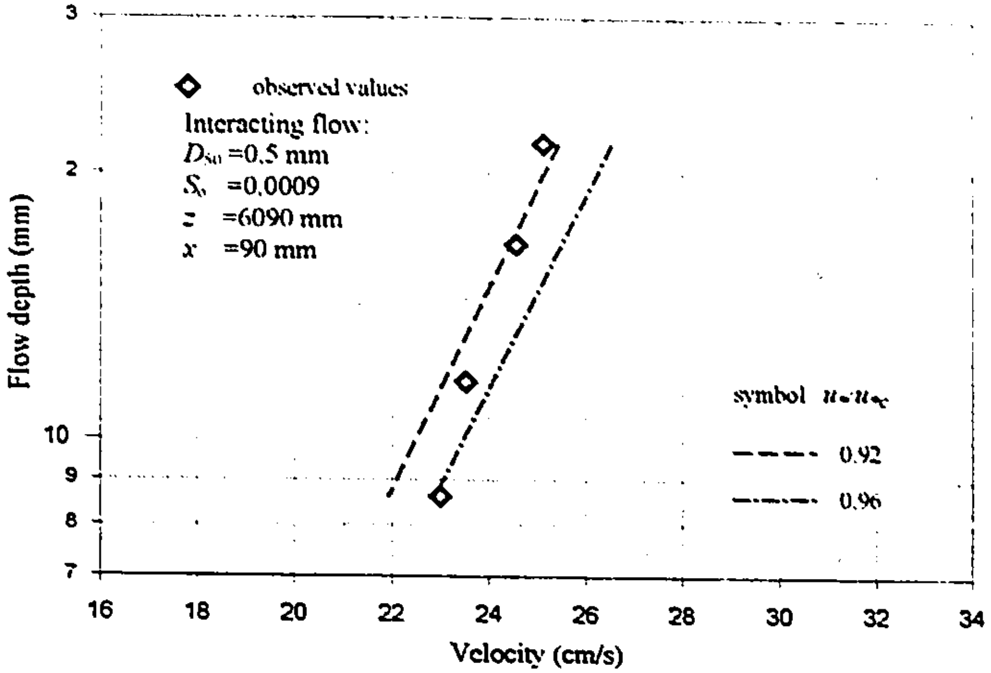

Figure 6.11- Comparison between observed velocity profile and log-law, using different u_*/u_{*c}

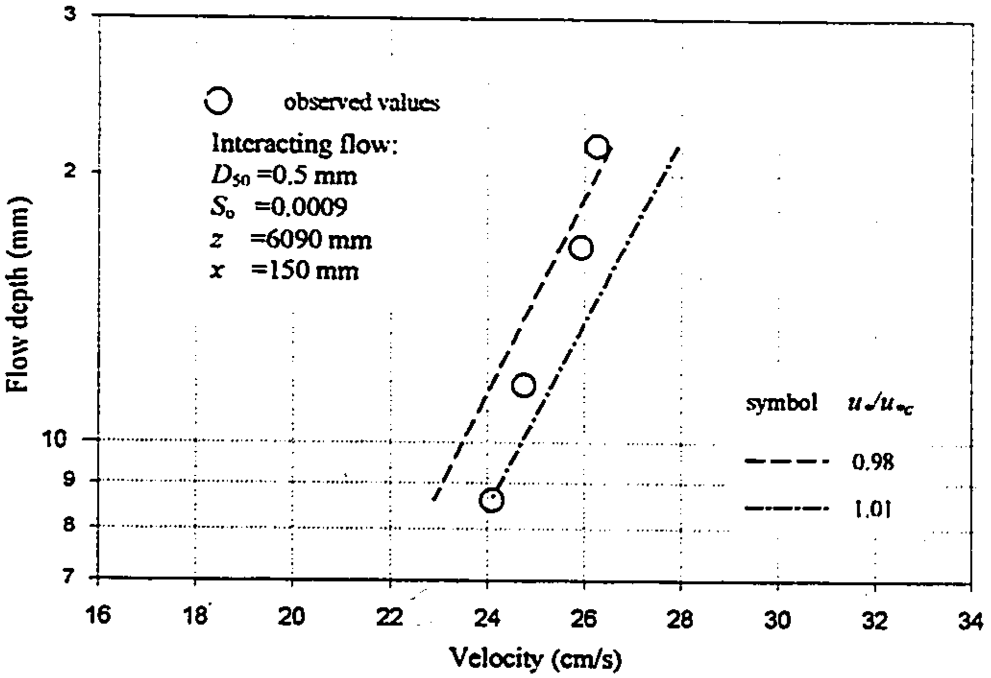

Figure 6.12- Comparison between observed velocity profile and log-law, using different u_*/u_{*c}

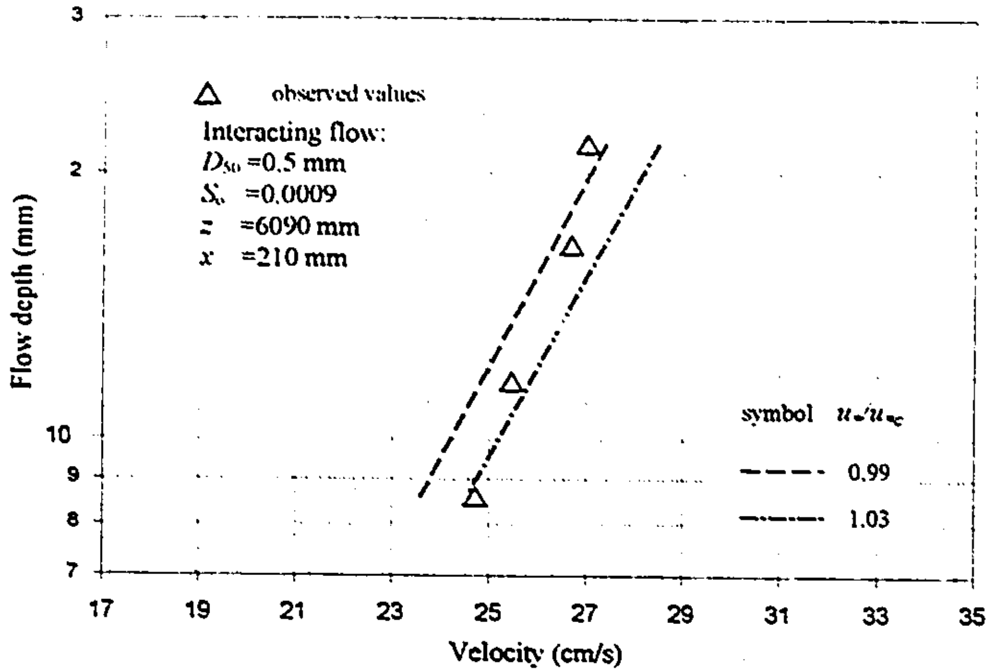

Figure 6.13- Comparison between observed velocity profile and log-law, using different u_*/u_{*c}

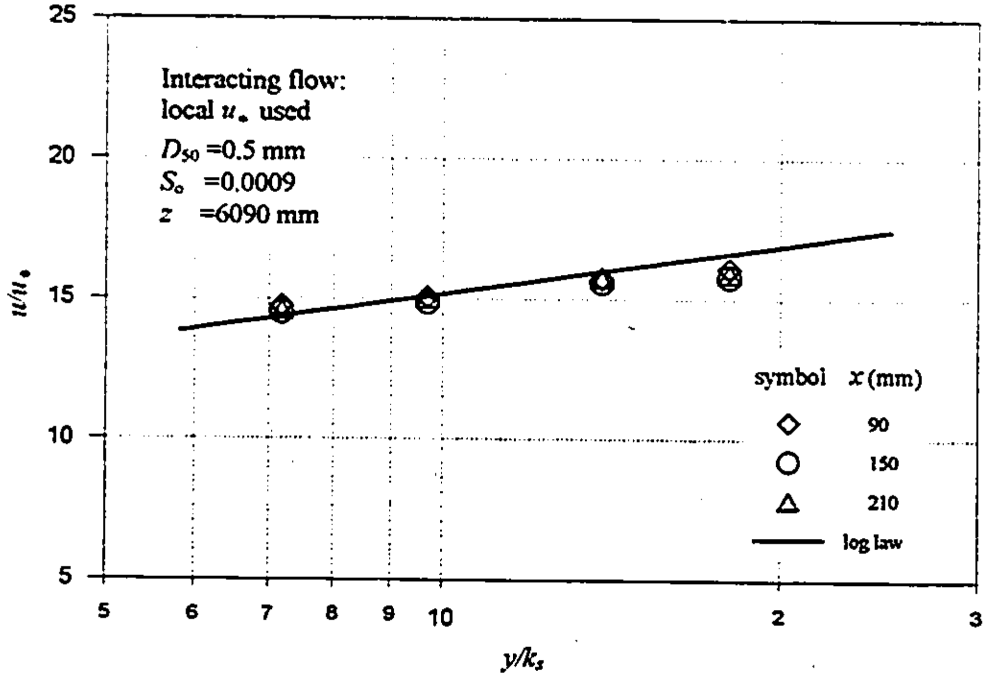

Figure 6.14- Universal log-law and observed velocity profiles

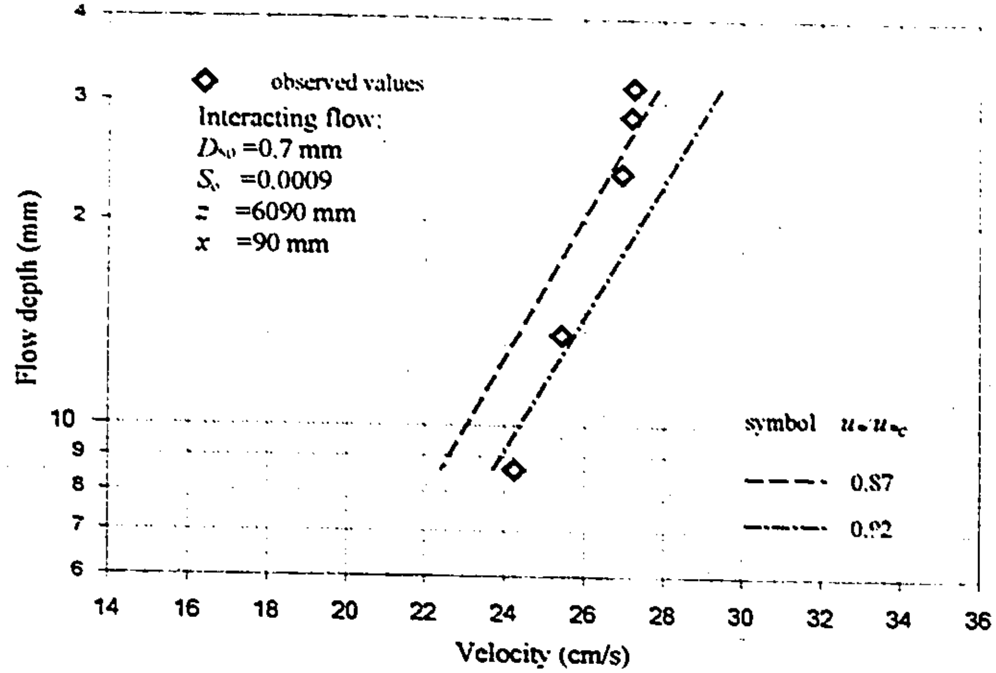

Figure 6.15- Comparison between observed velocity profile and log-law, using different u_*/u_{*c}

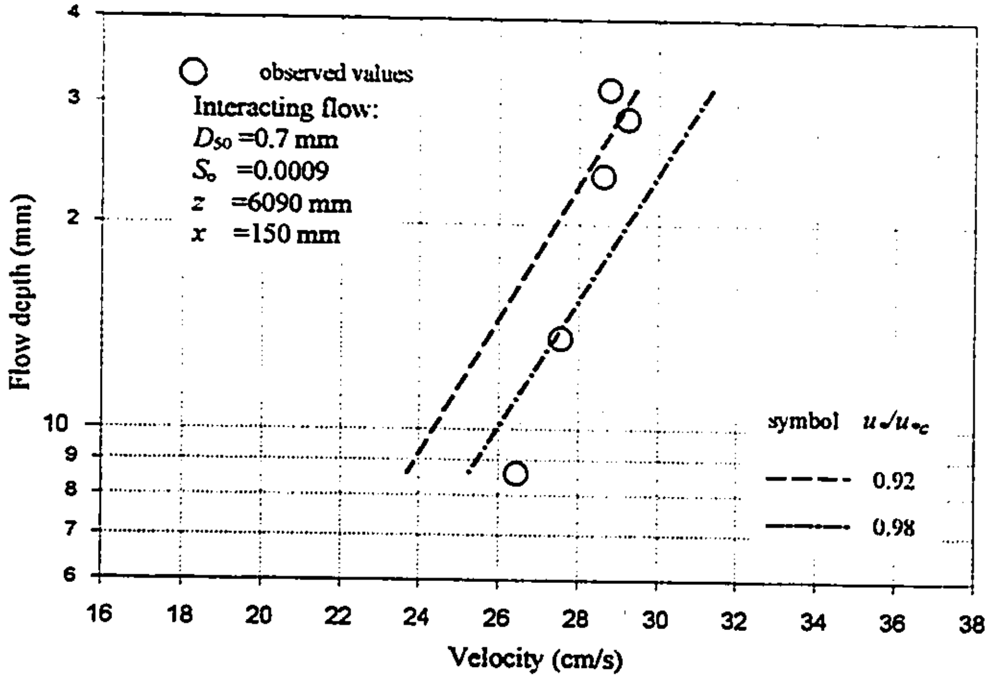

Figure 6.16- Comparison between observed velocity profile and log-law, using different u_*/u_{*c}

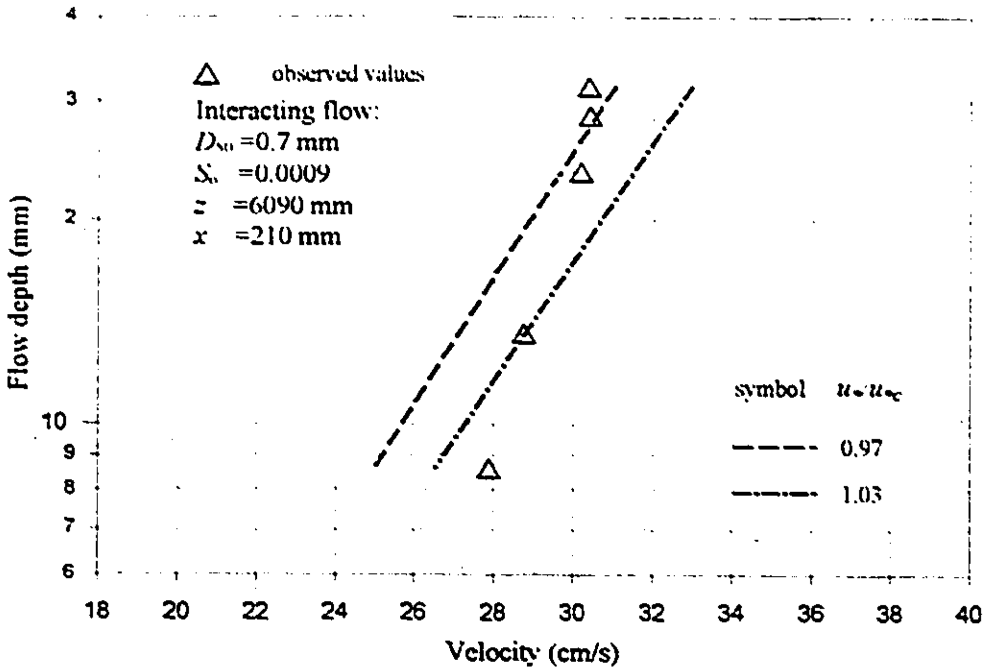

Figure 6.17- Comparison between observed velocity profile and log-law, using different u_*/u_{*c}

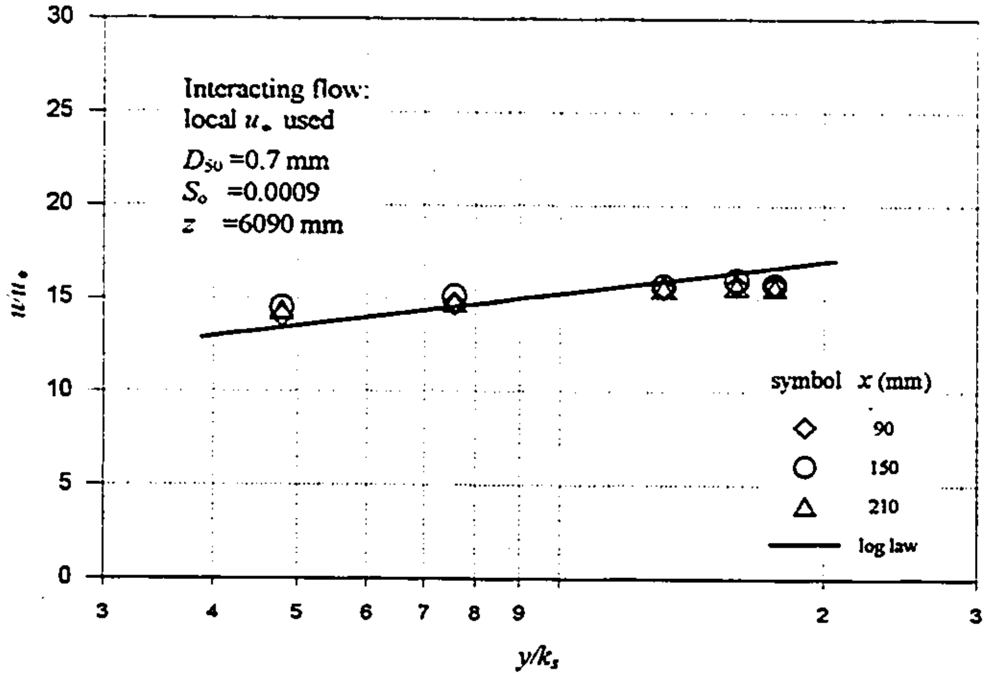

Figure 6.18- Universal log-law and observed velocity profiles

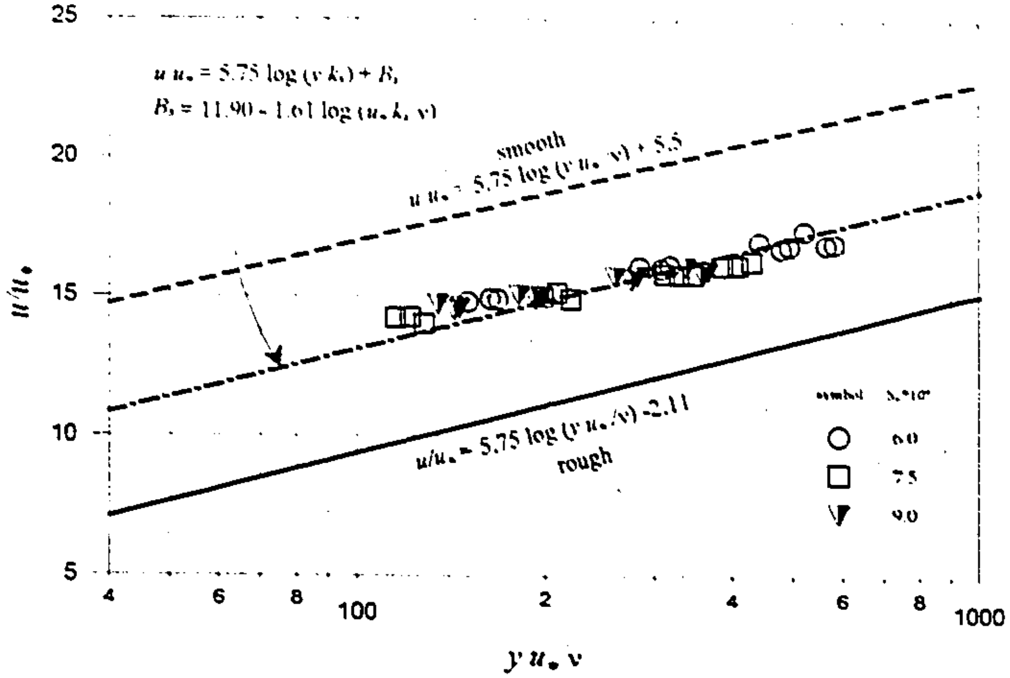

Figure 6.19- Comparison of universal log-law with approach floodplain flow velocity non-dimensionalized by local u_*

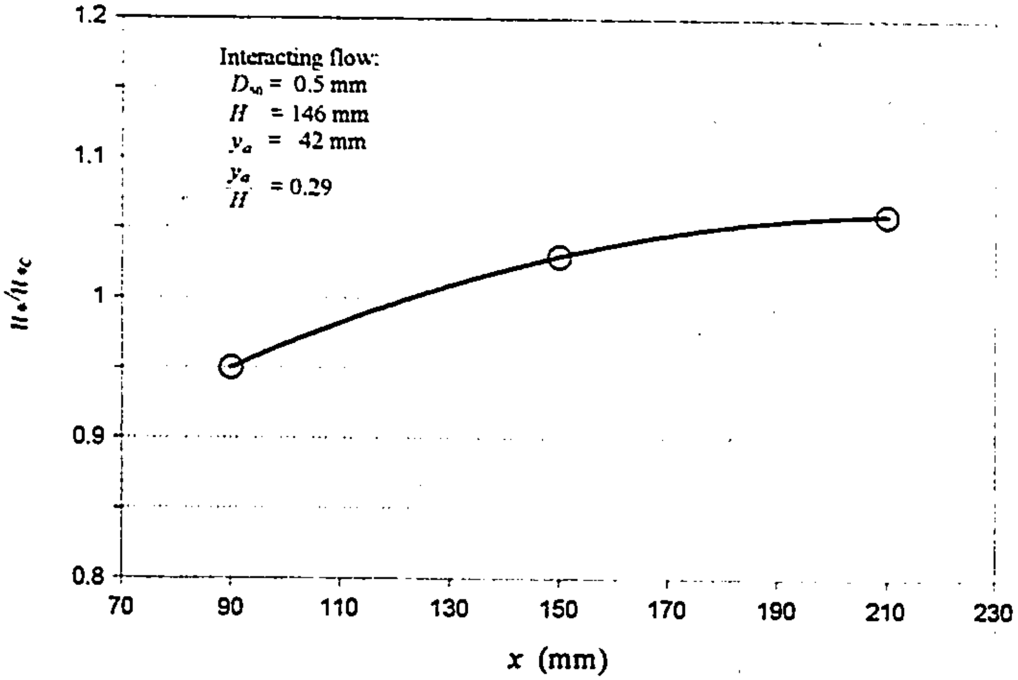

Figure 6.20- Floodplain shear velocity ratio, interacting flow and S_o=0.0006

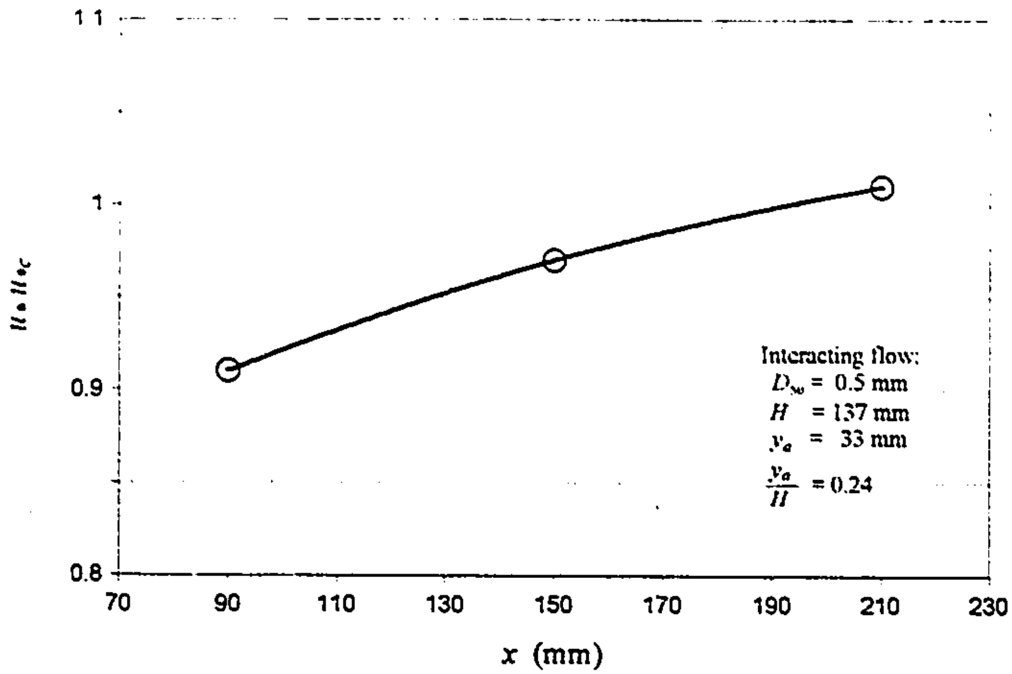

Figure 6.21- Floodplain shear velocity ratio, interacting flow and S_o=0.00075

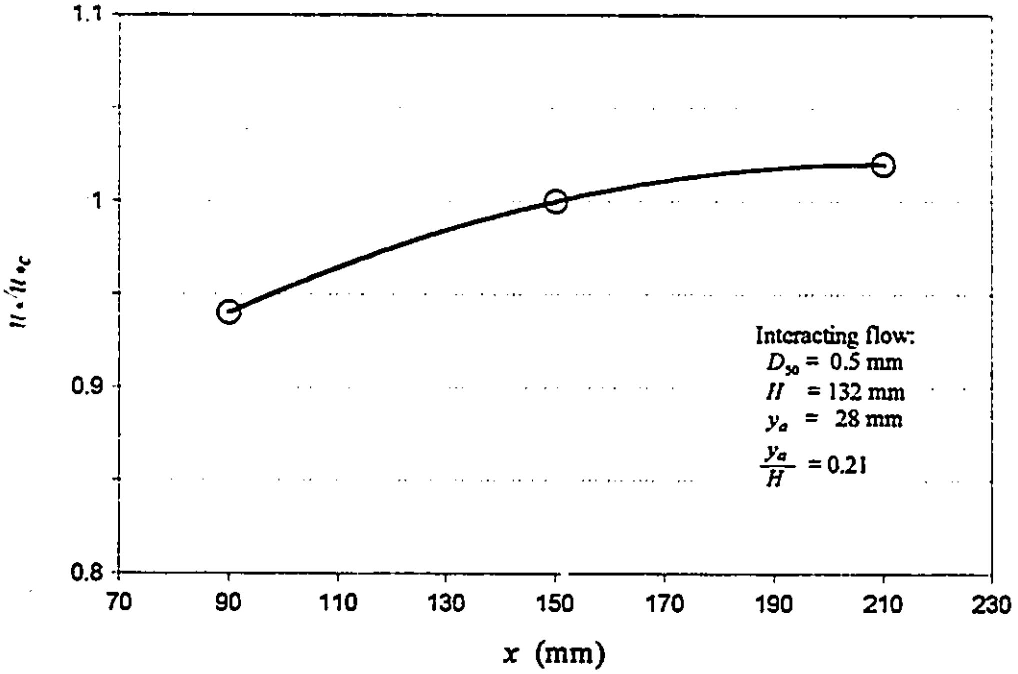

Figure 6.22- Floodplain shear velocity ratio, interacting flow and S_o=0.0009

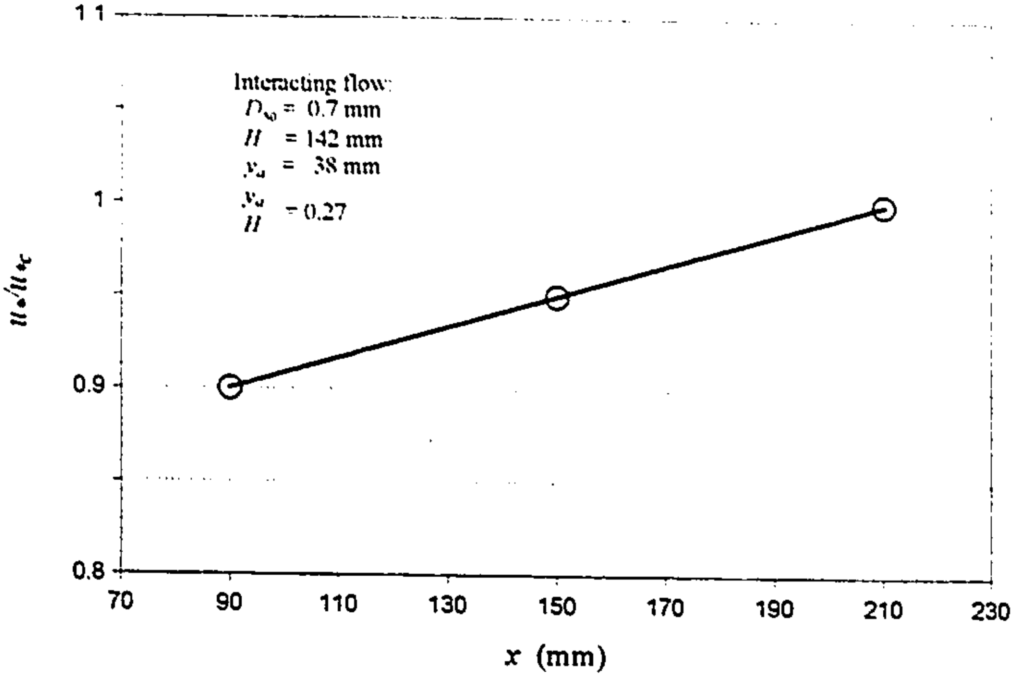

Figure 6.23- Floodplain shear velocity ratio, interacting flow and S_o=0.0009

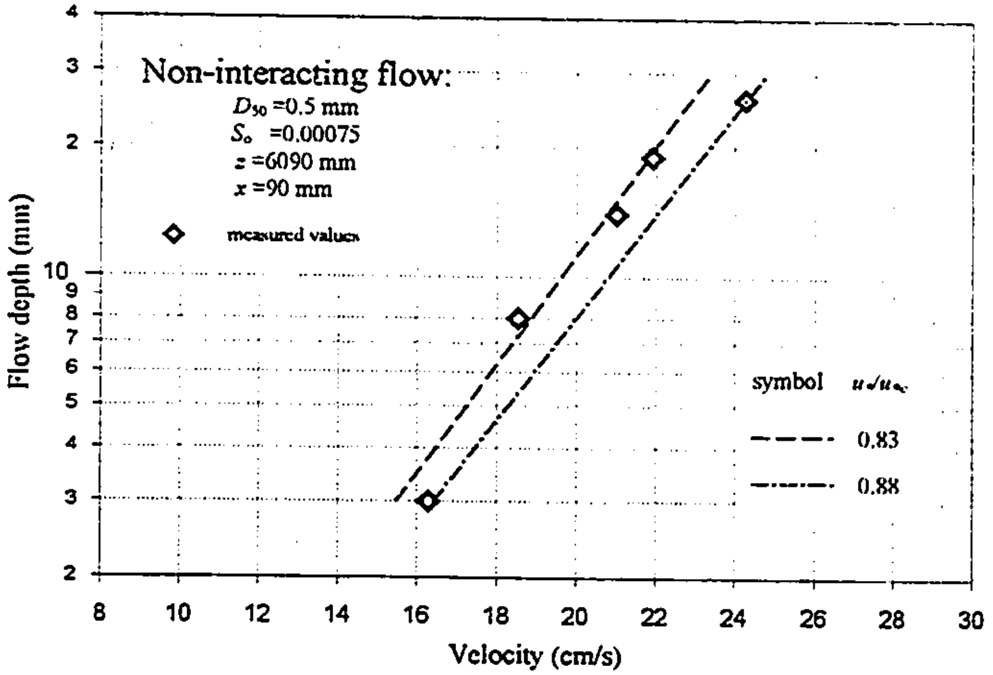

Figure 6.24- Comparison between observed velocity profile and log-law, using different u_*/u_{*c}

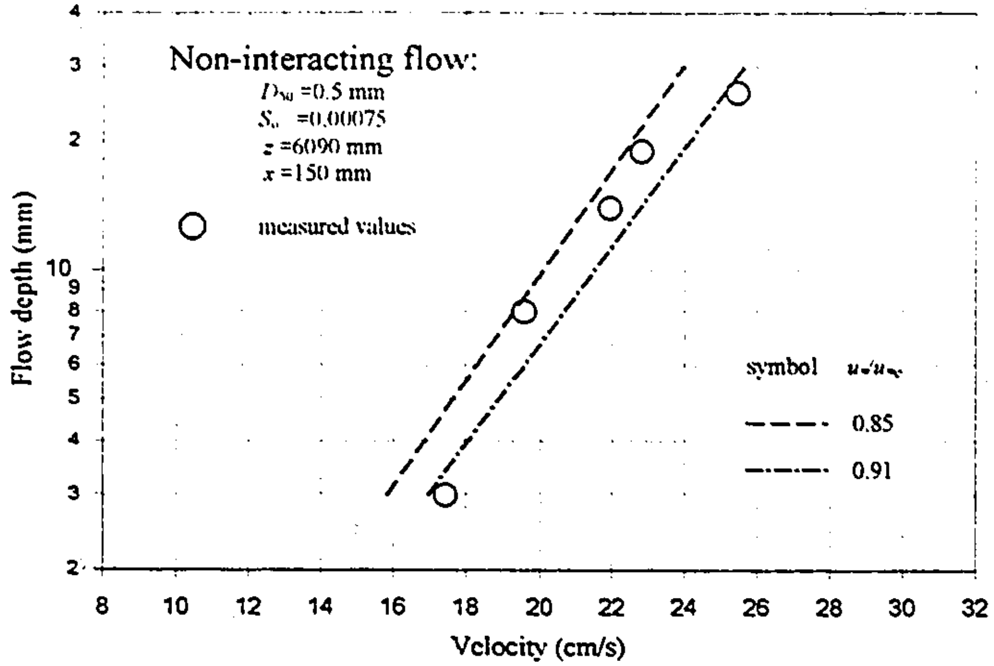

Figure 6.25- Comparison between observed velocity profile and log-law, using different u_*/u_{*c}

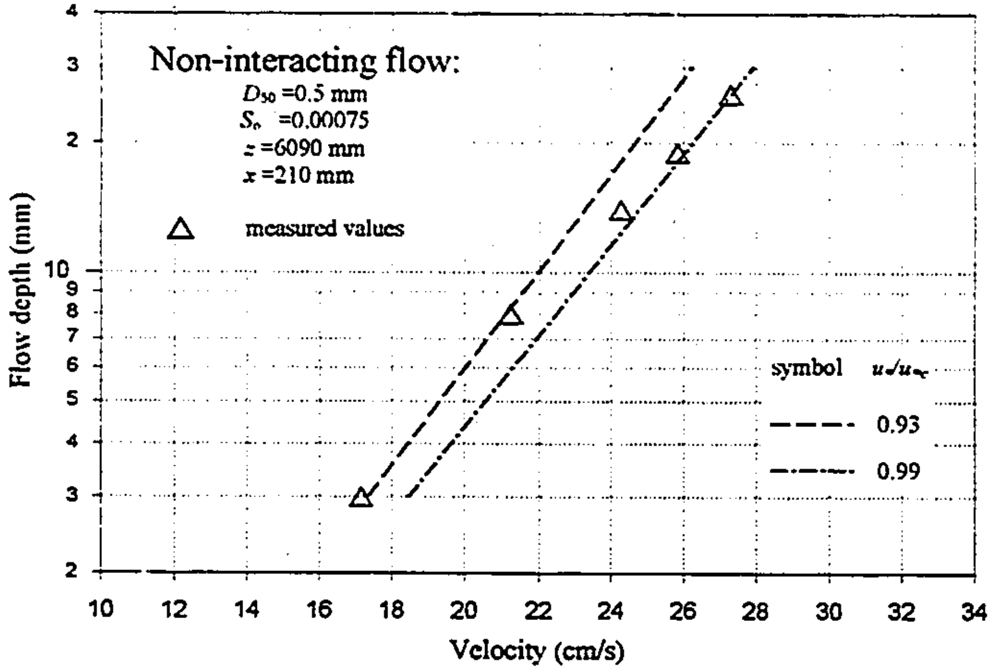

Figure 6.26- Comparison between observed velocity profile and log-law, using different u_*/u_{*c}

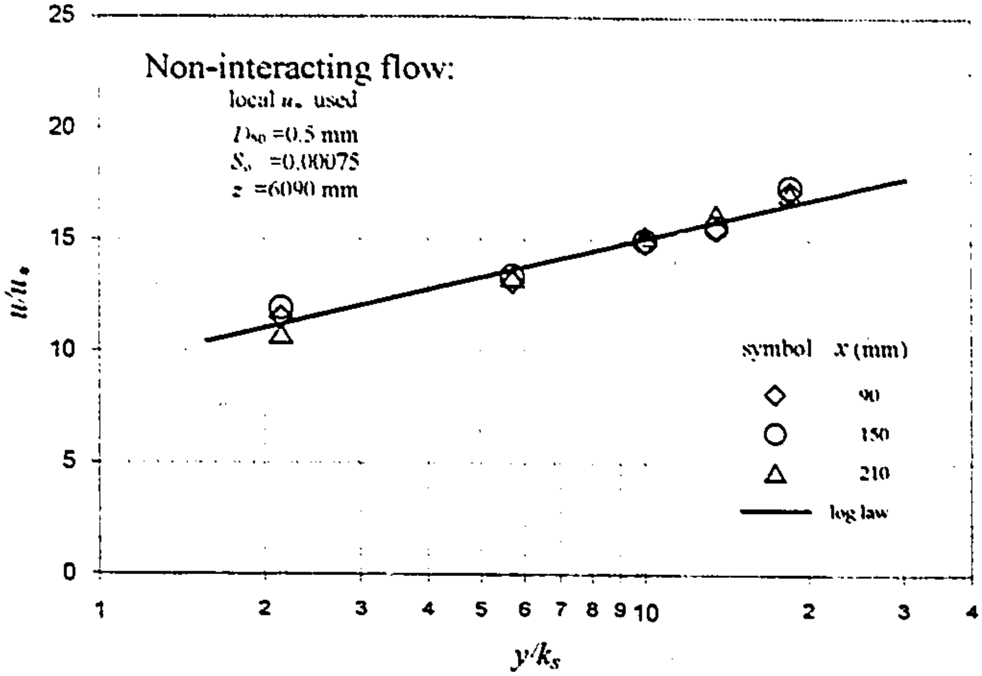

Figure 6.27- Universal log-law and observed velocity profiles

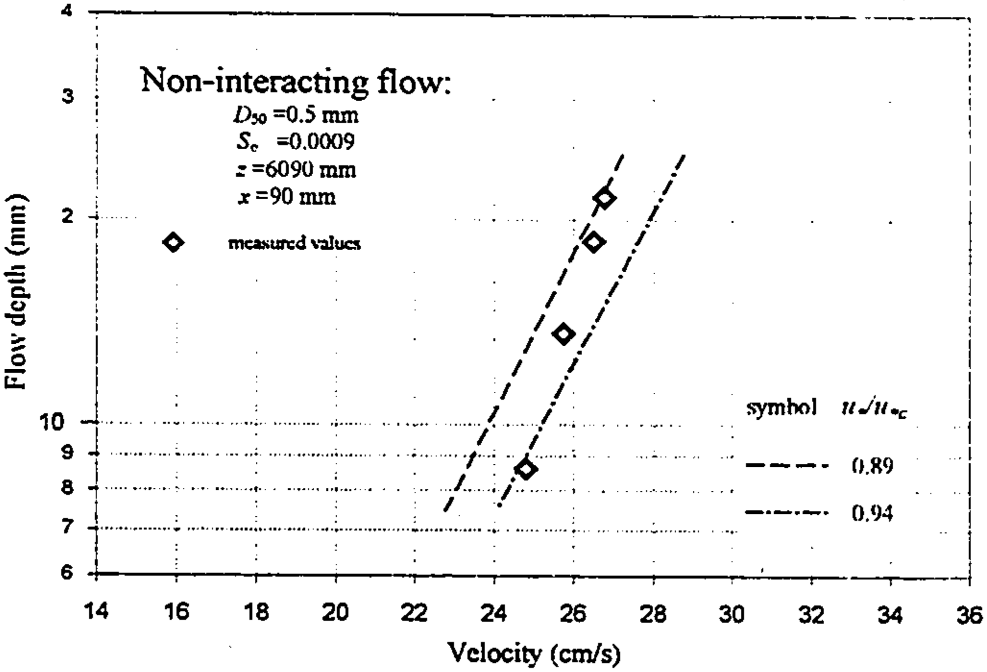

Figure 6.28- Comparison between observed velocity profile and log-law, using different u_*/u_{*c}

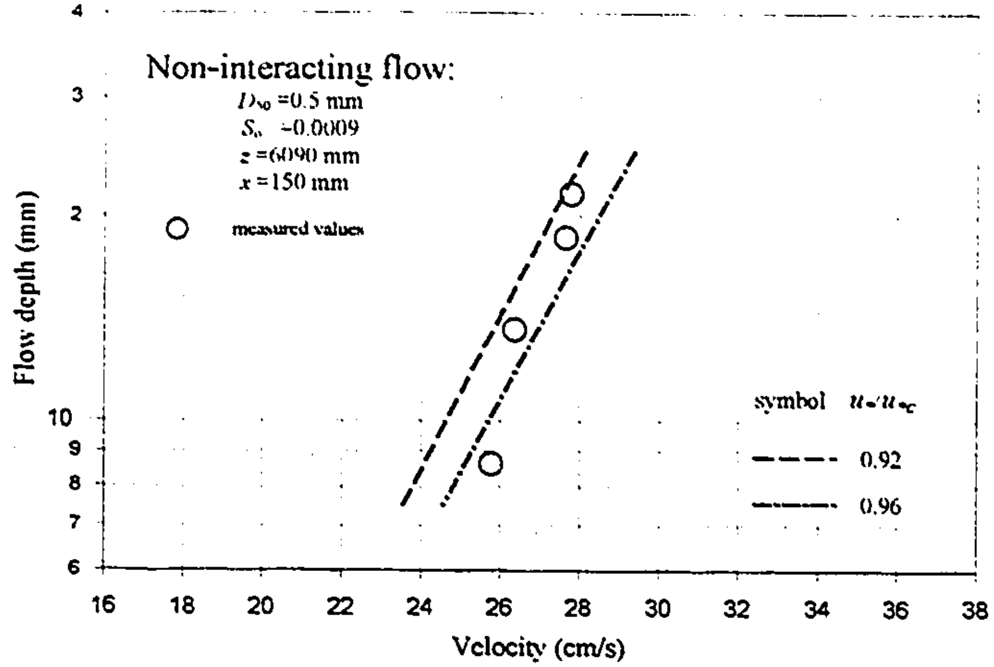

Figure 6.29- Comparison between observed velocity profile and log-law, using different u_*/u_{*c}

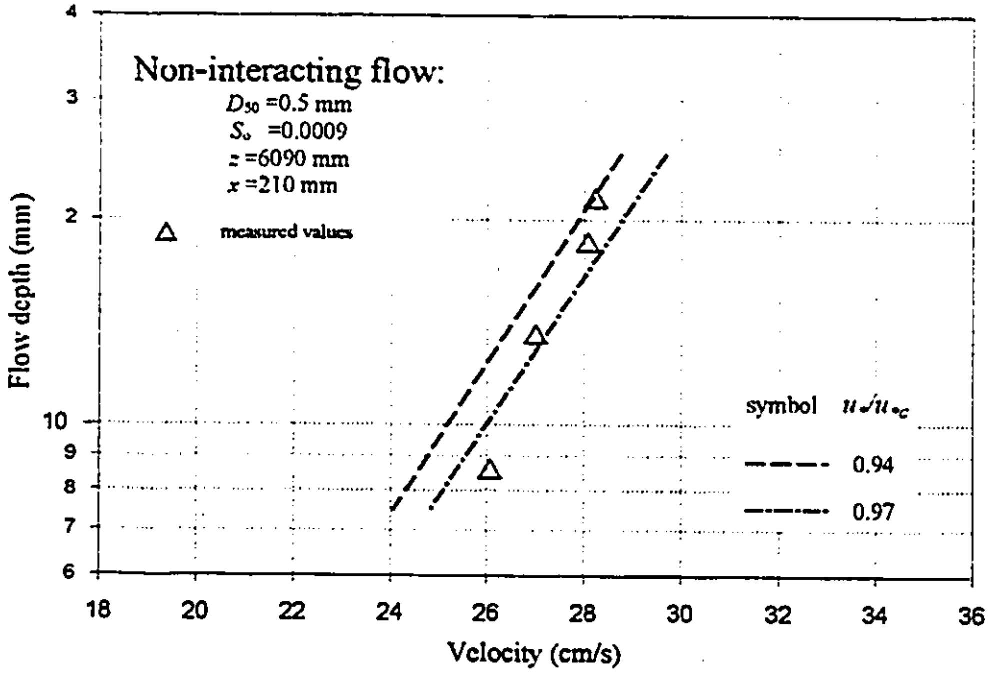

Figure 6.30- Comparison between observed velocity profile and log-law, using different u_*/u_{*c}

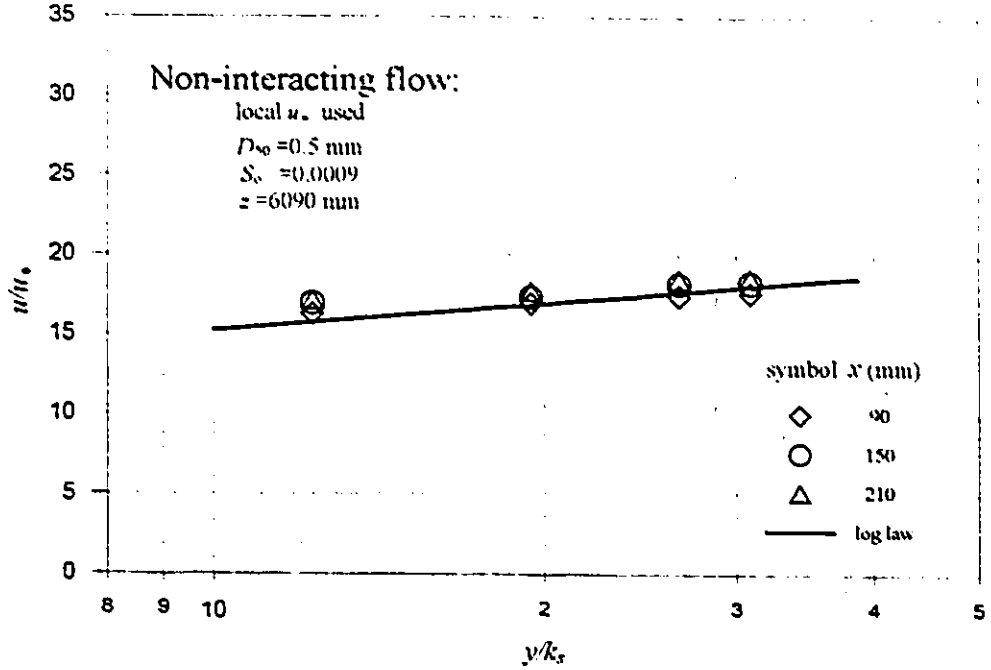

Figure 6.31- Universal log-law and measured velocity profiles

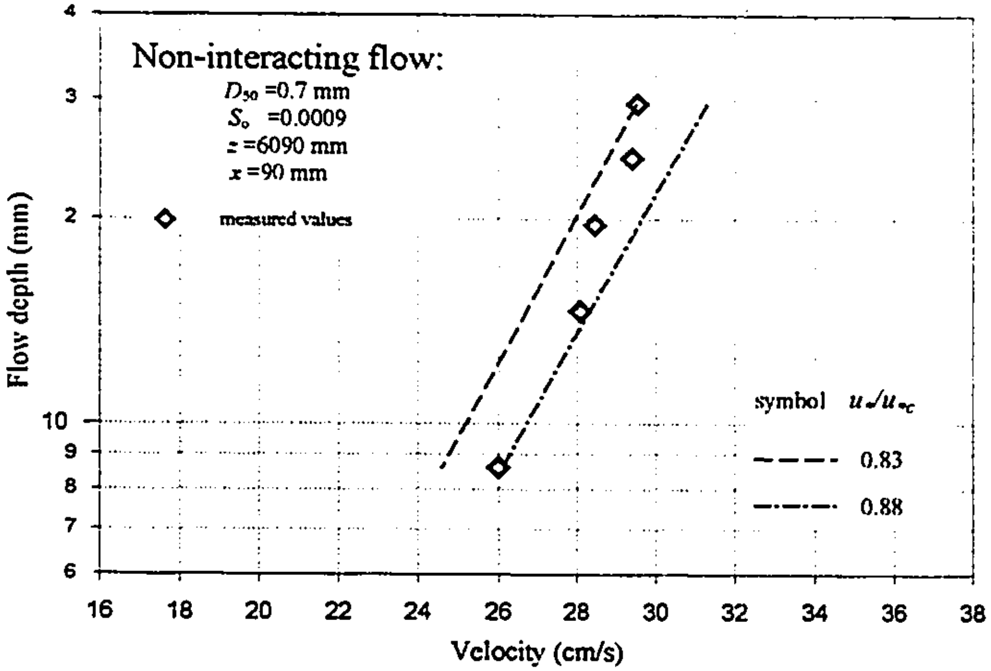

Figure 6.32- Comparison between observed velocity profile and log-law, using different u_*/u_{*c}

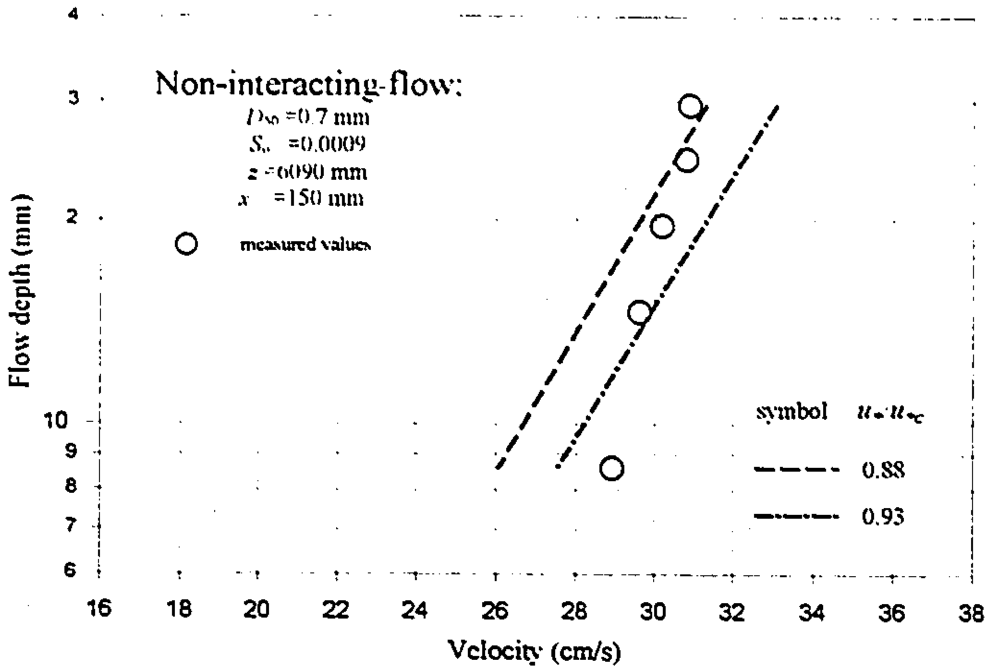

Figure 6.33- Comparison between observed velocity profile and log-law, using different u_*/u_{*c}

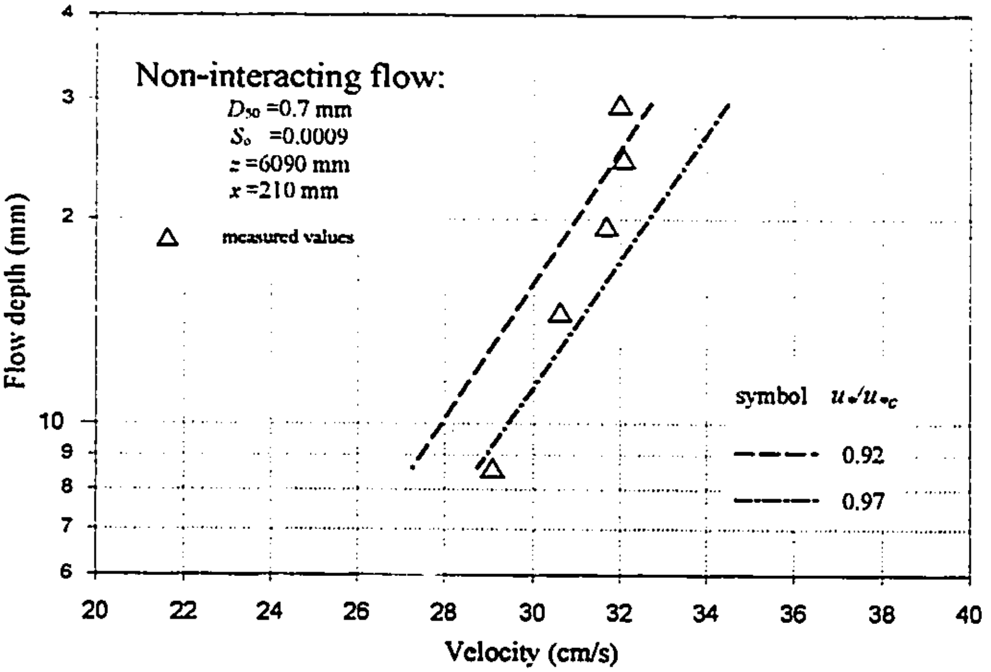

Figure 6.34- Comparison between observed velocity profile and log-law, using different u_*/u_{*c}

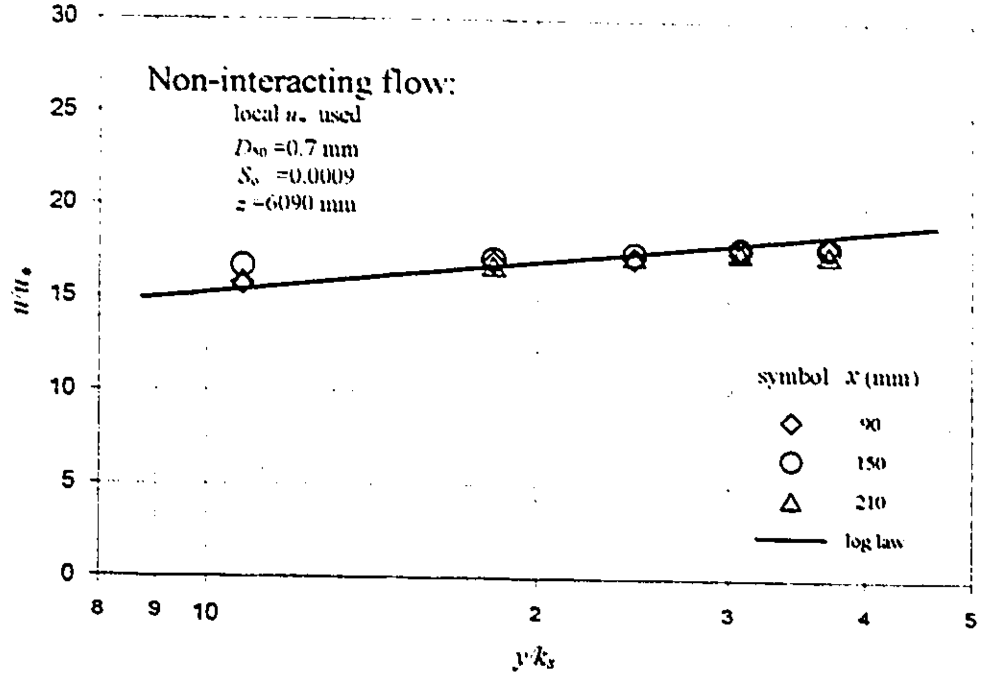

Figure 6.35- Universal log-law and observed velocity profiles

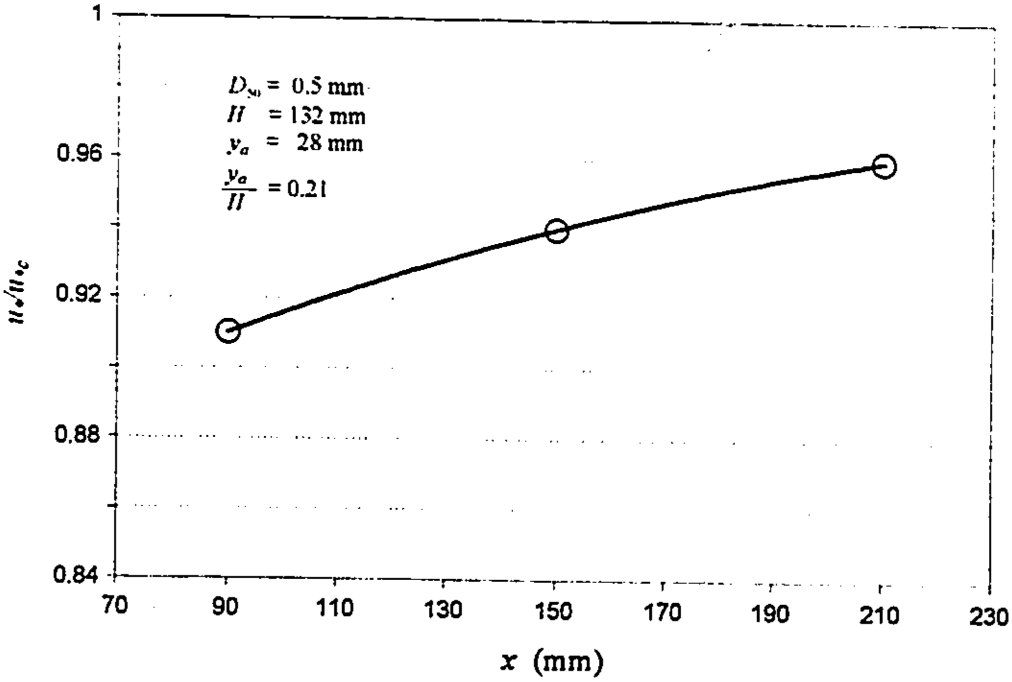

Figure 6.36- Floodplain shear velocity ratio, non-interacting flow and S_o=0.0009

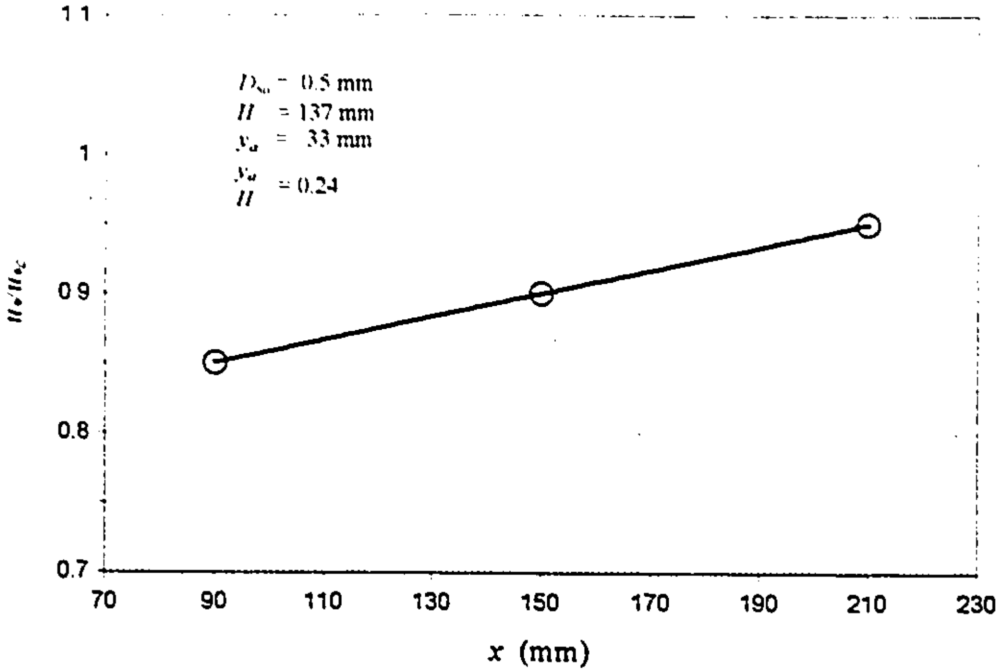

Figure 6.37- Floodplain shear velocity ratio, non-interacting flow and S_o=0.00075

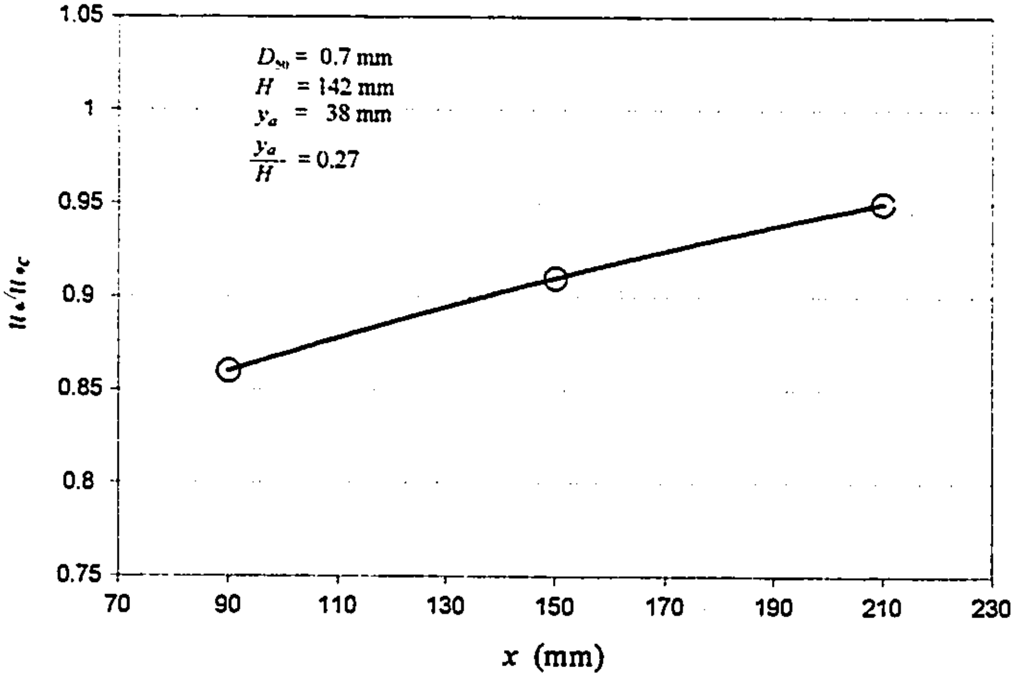

Figure 6.38- Floodplain shear velocity ratio, non-interacting flow and S_o=0.0009

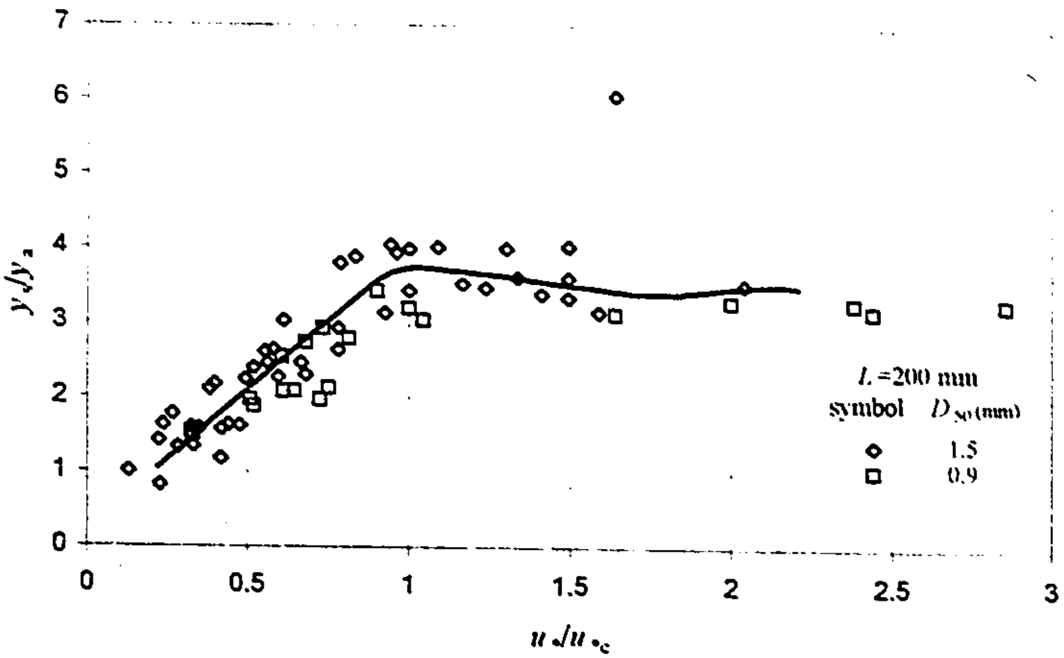

Figure 6.39- Variation of relative scour depth with shear velocity ratio according to Gill's spur-dike data (1972)

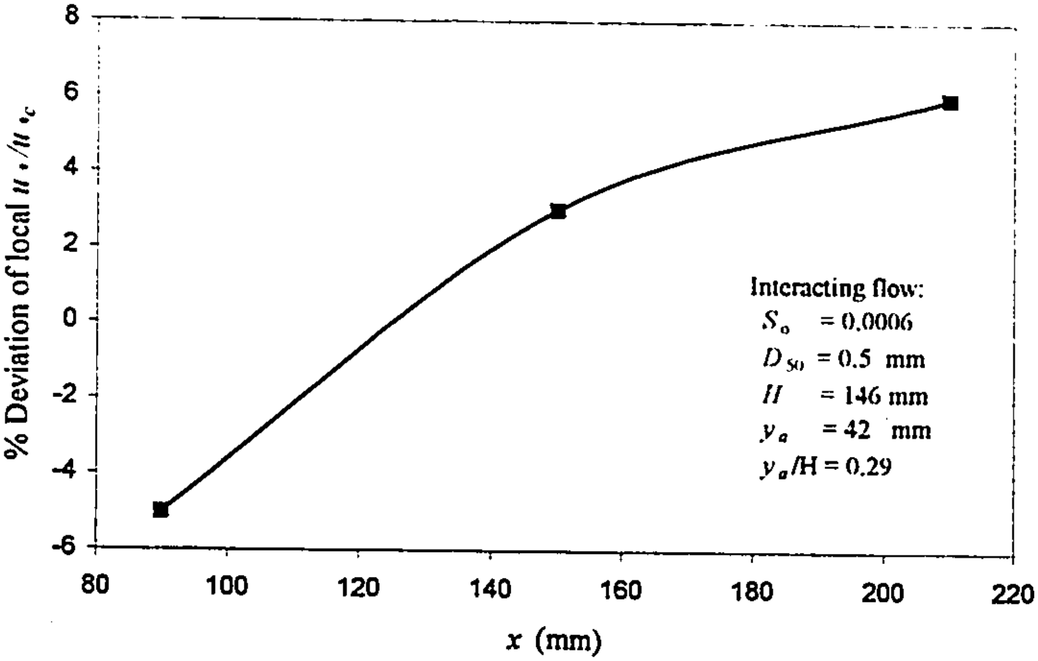

Figure 6.40- Deviation of local u_*/u_{*c} from the critical value, interacting flow

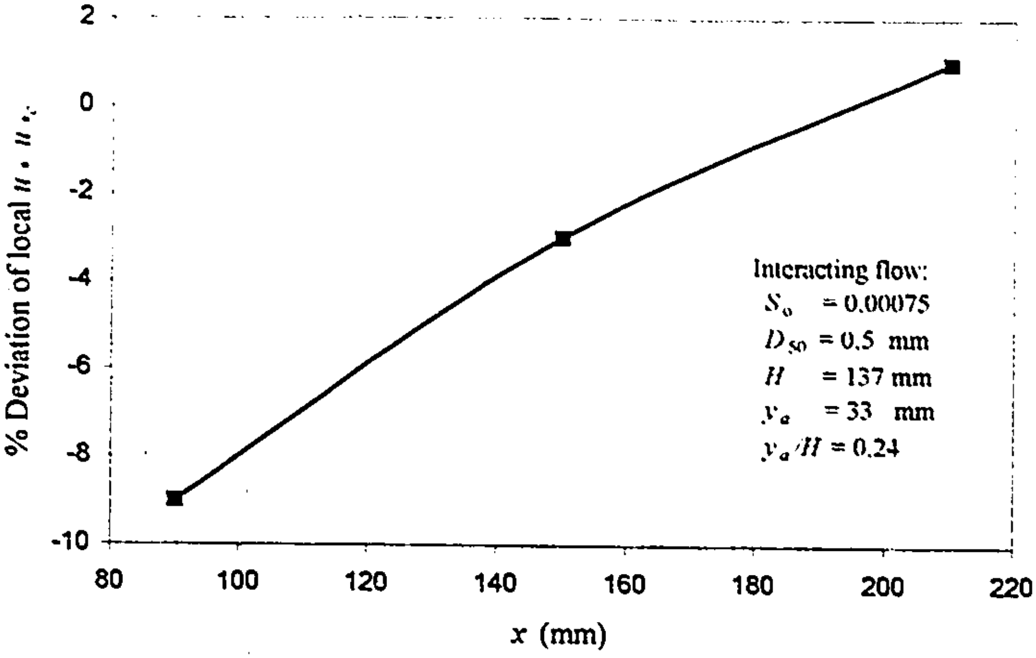

Figure 6.41- Deviation of local u_*/u_{*c} from the critical value, interacting flow

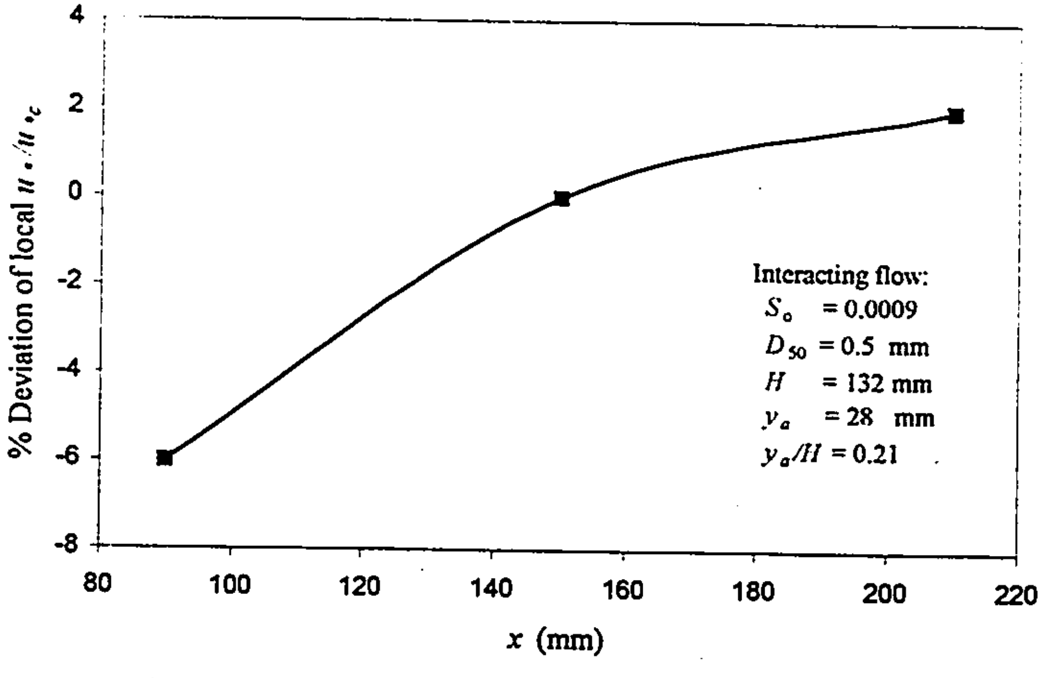

Figure 6.42- Deviation of local u_*/u_{*c} from the critical value, interacting flow

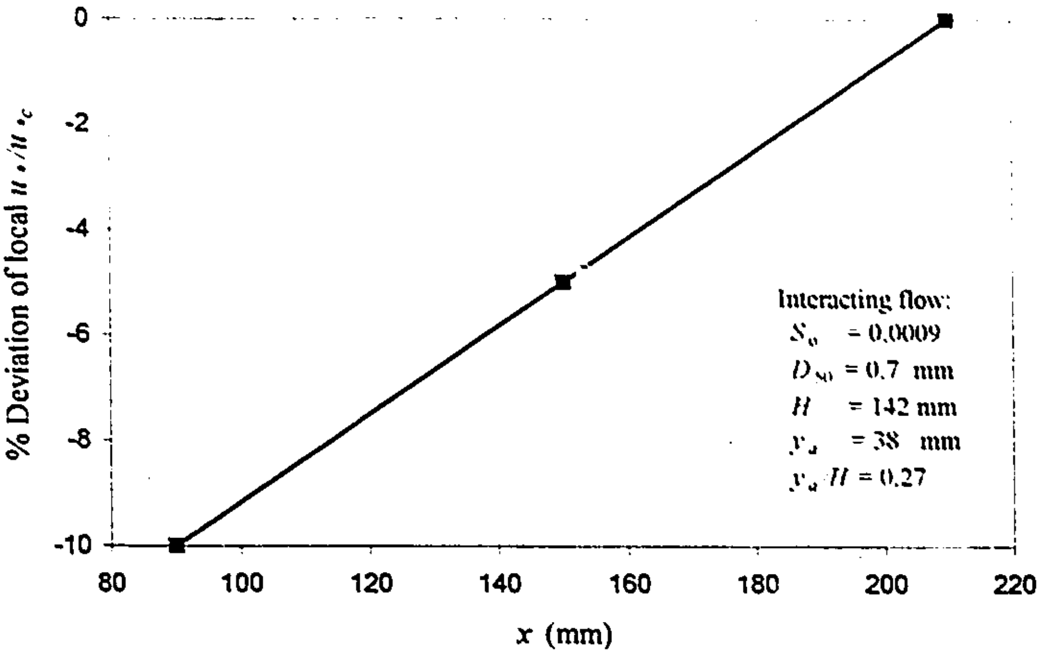

Figure 6.43- Deviation of local u_*/u_{*c} from the critical value, interacting flow

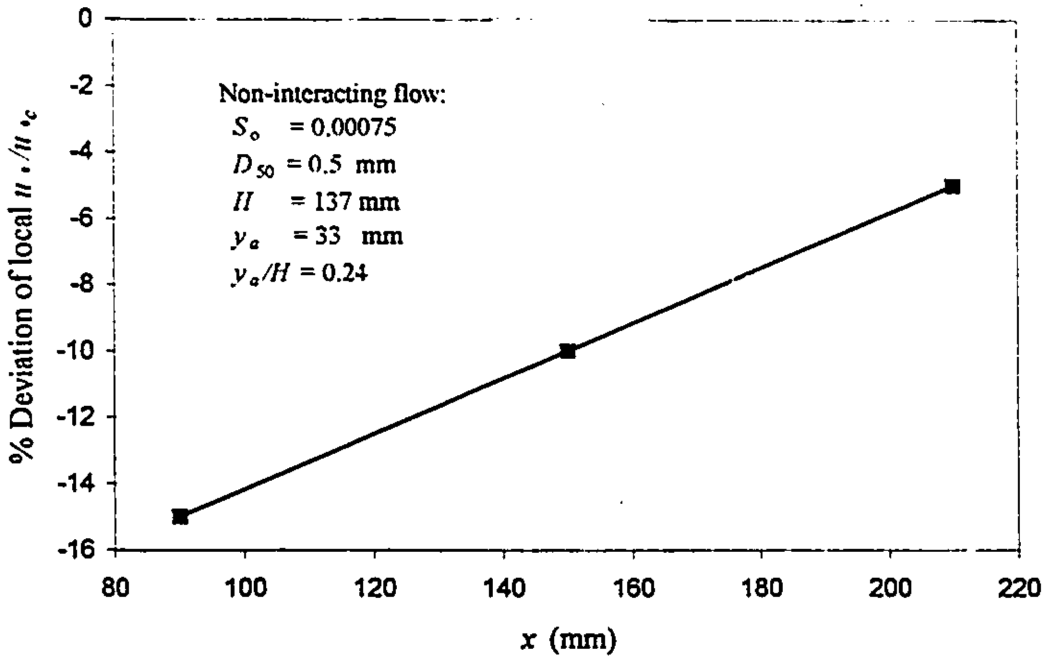

Figure 6.44- Deviation of local u_*/u_{*c} from the critical value, non-interacting flow

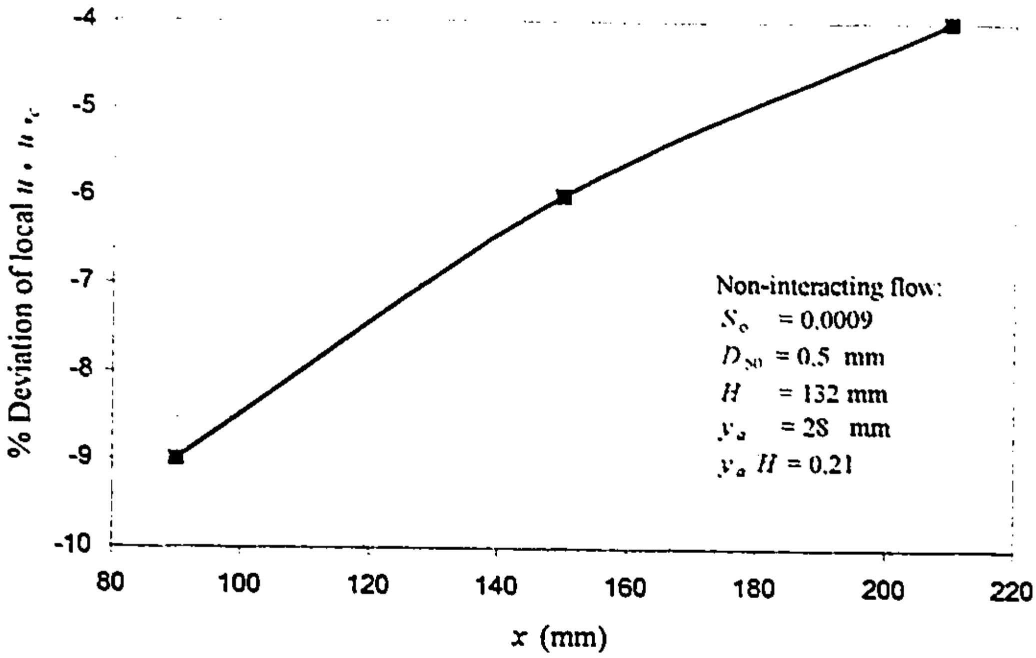

Figure 6.45- Deviation of local u_*/u_{*c} from the critical value, non-interacting flow

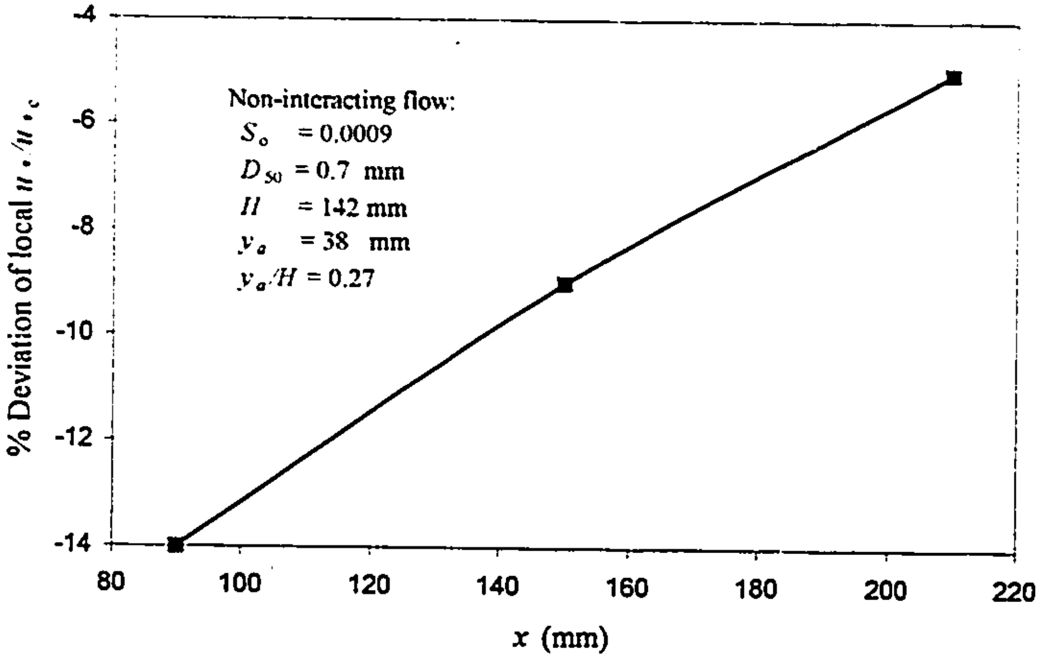

Figure 6.46- Deviation of local u_*/u_{*c} from the critical value, non-interacting flow

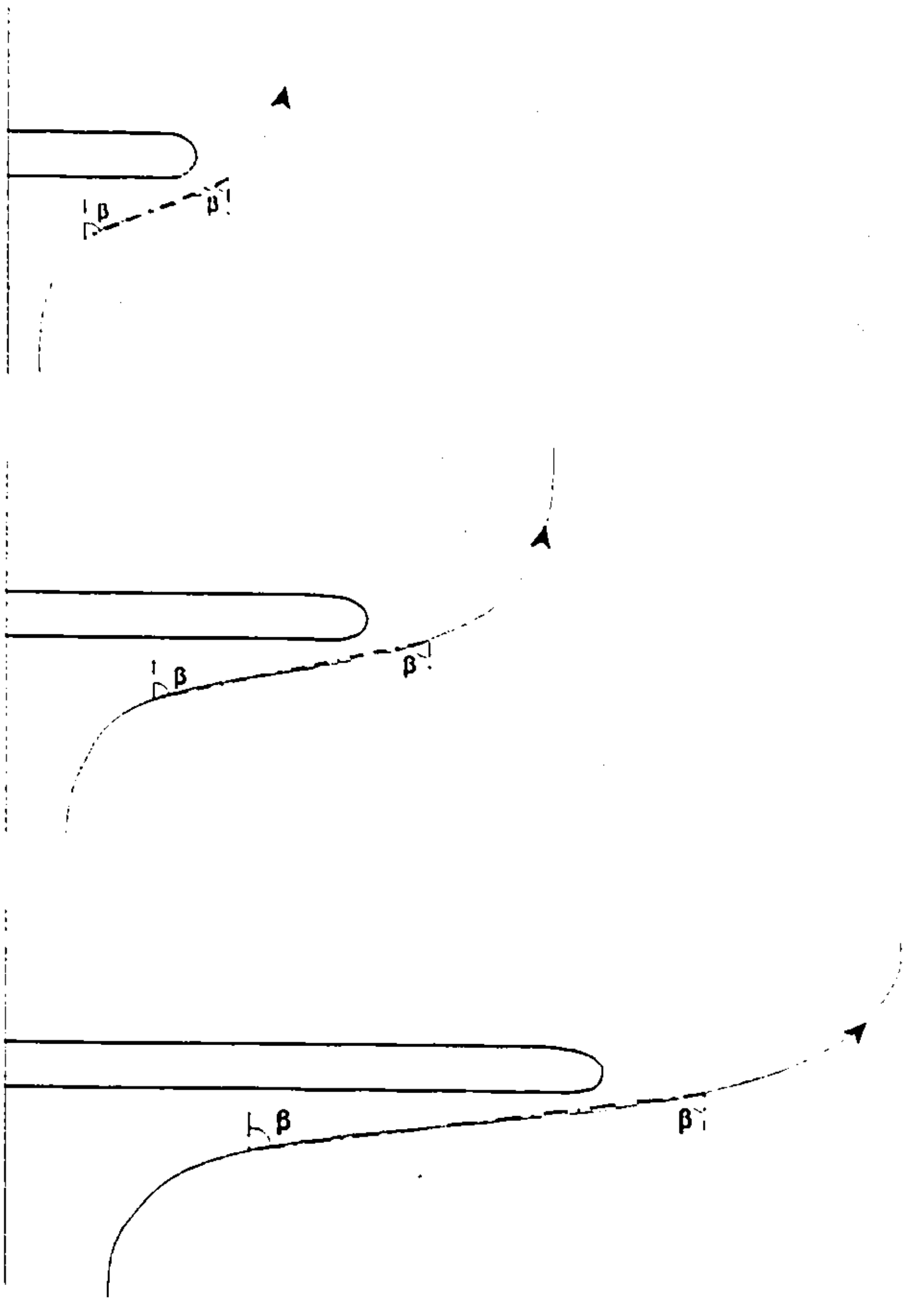

Figure 6.47- Flow deflection angle, β, around SC-abutments

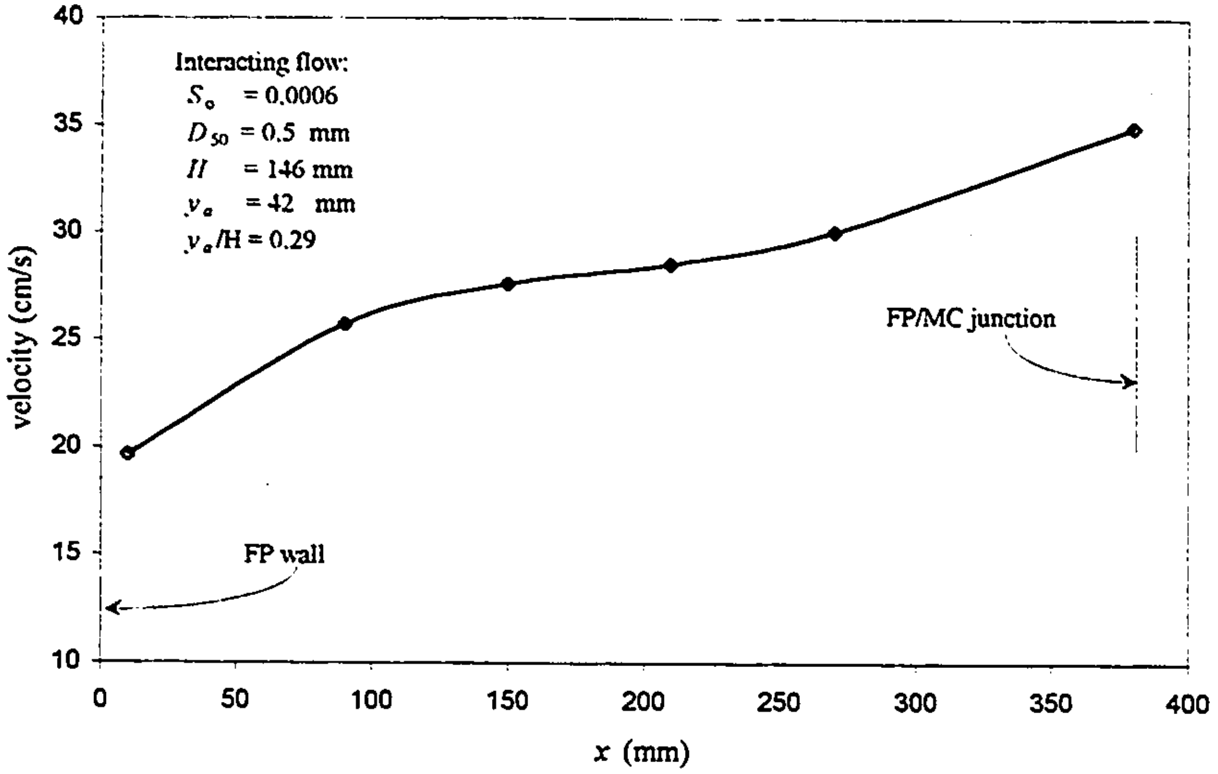

Figure 6.48- Depth-averaged flow velocity in the floodplain, interacting flow

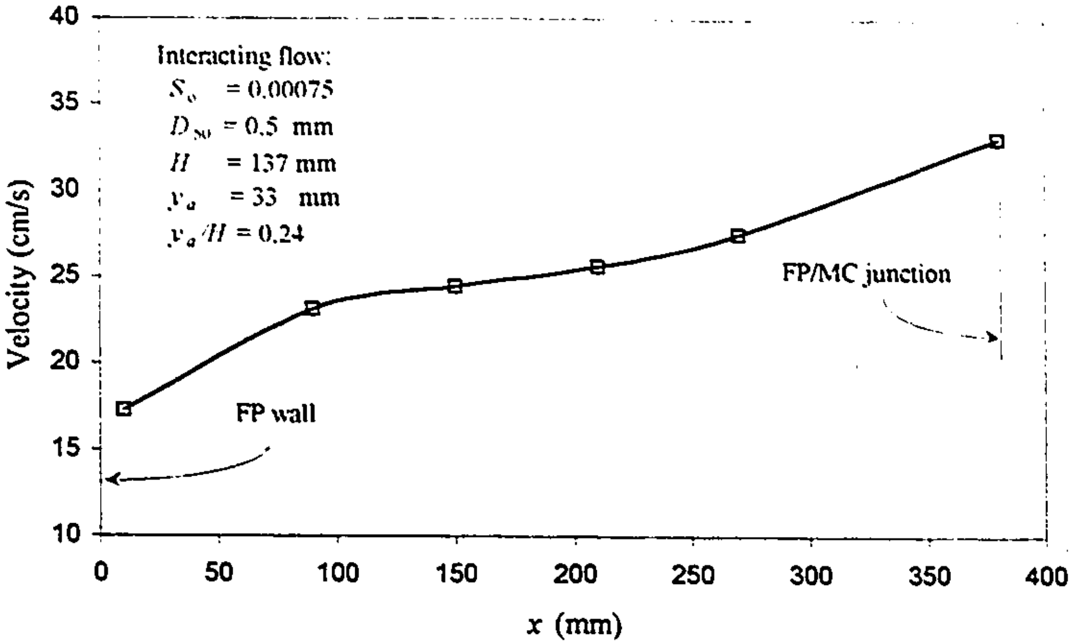

Figure 6.49- Depth-averaged flow velocity in the floodplain, interacting flow

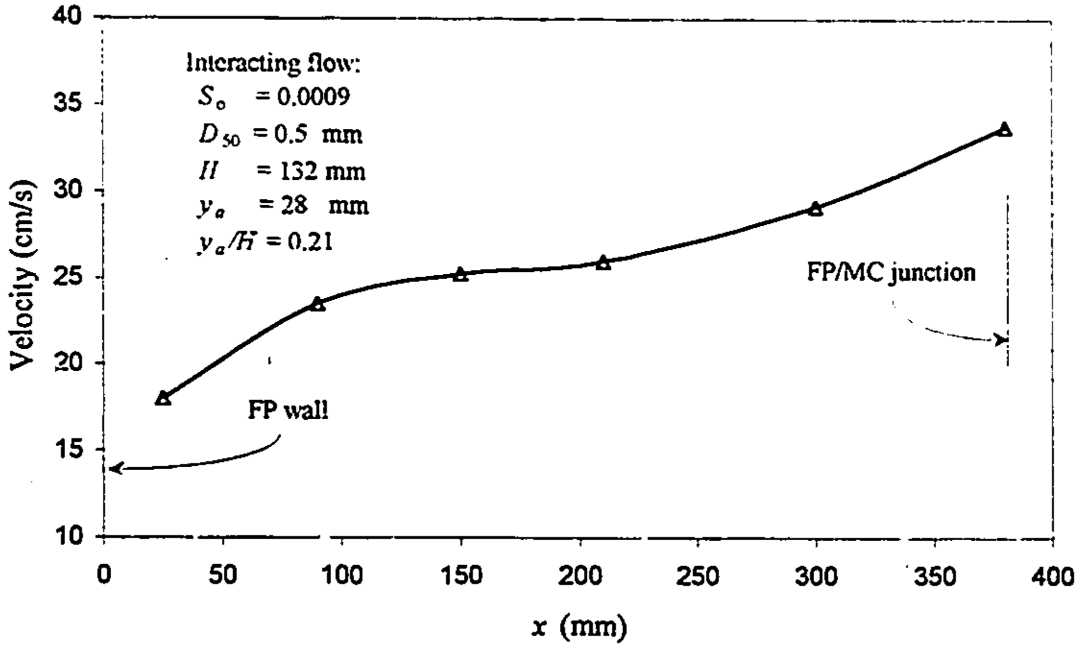

Figure 6.50- Depth-averaged flow velocity in the floodplain, interacting flow

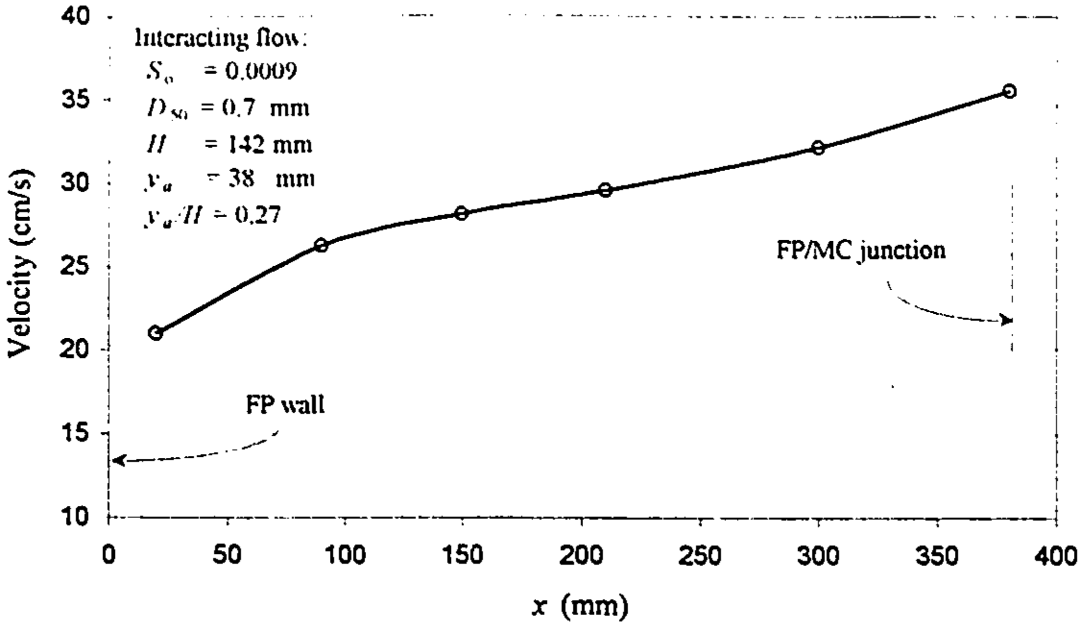

Figure 6.51- Depth-averaged flow velocity in the floodplain, interacting flow

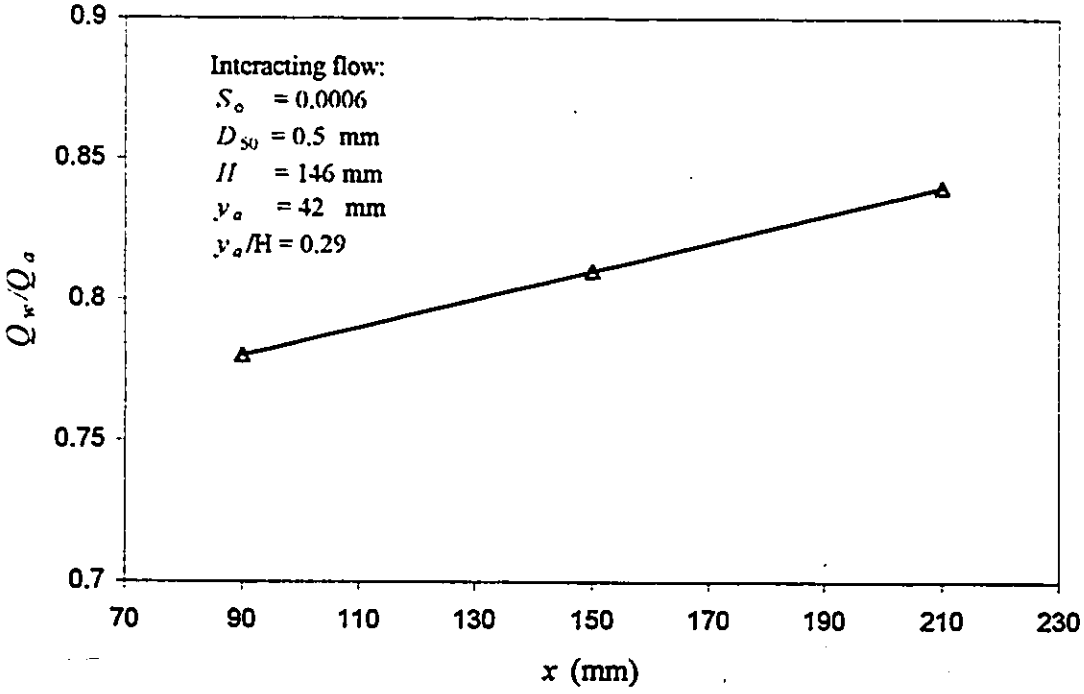

Figure 6.52- Variation of discharge ratio in the floodplain

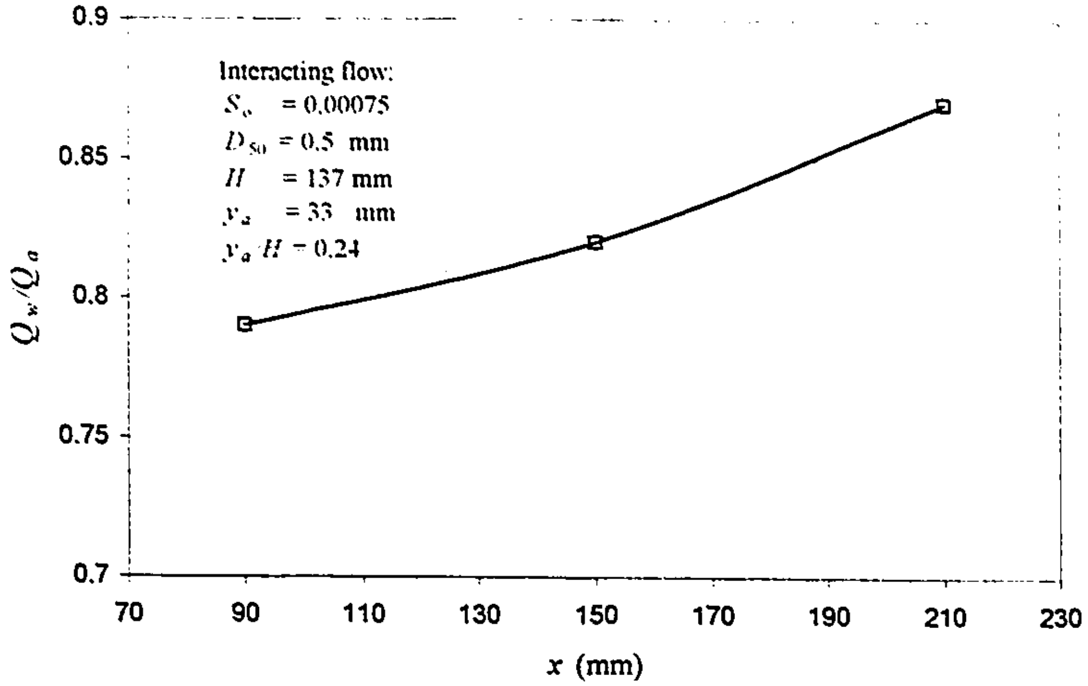

Figure 6.53- Variation of discharge ratio in the floodplain

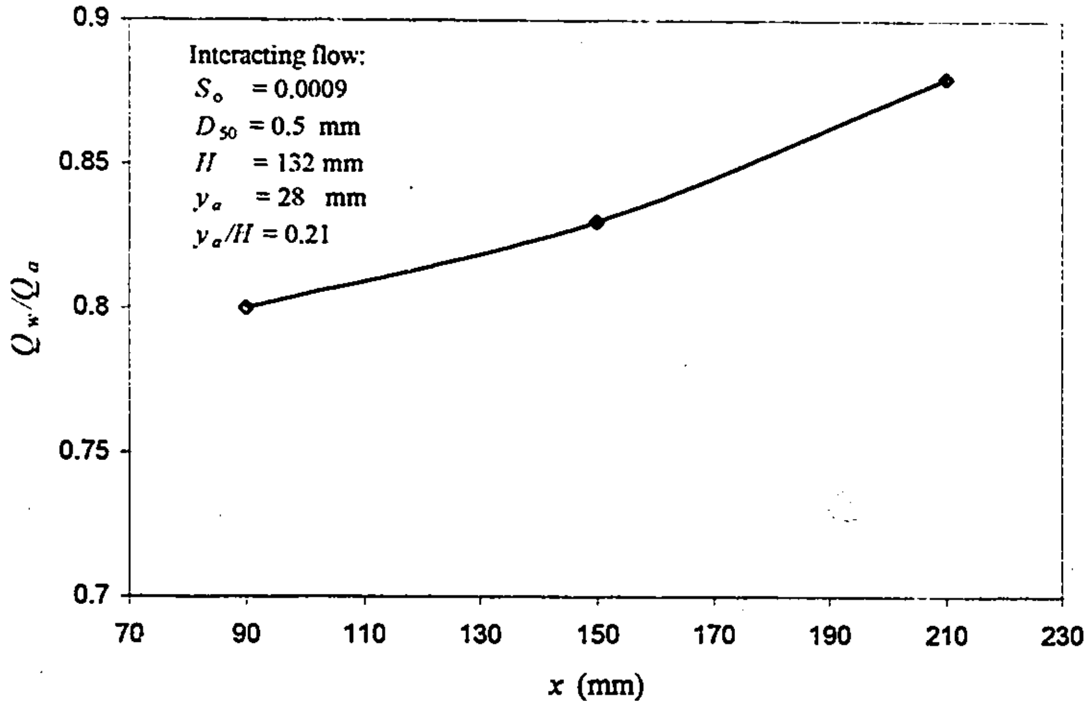

Figure 6.54- Variation of discharge ratio in the floodplain

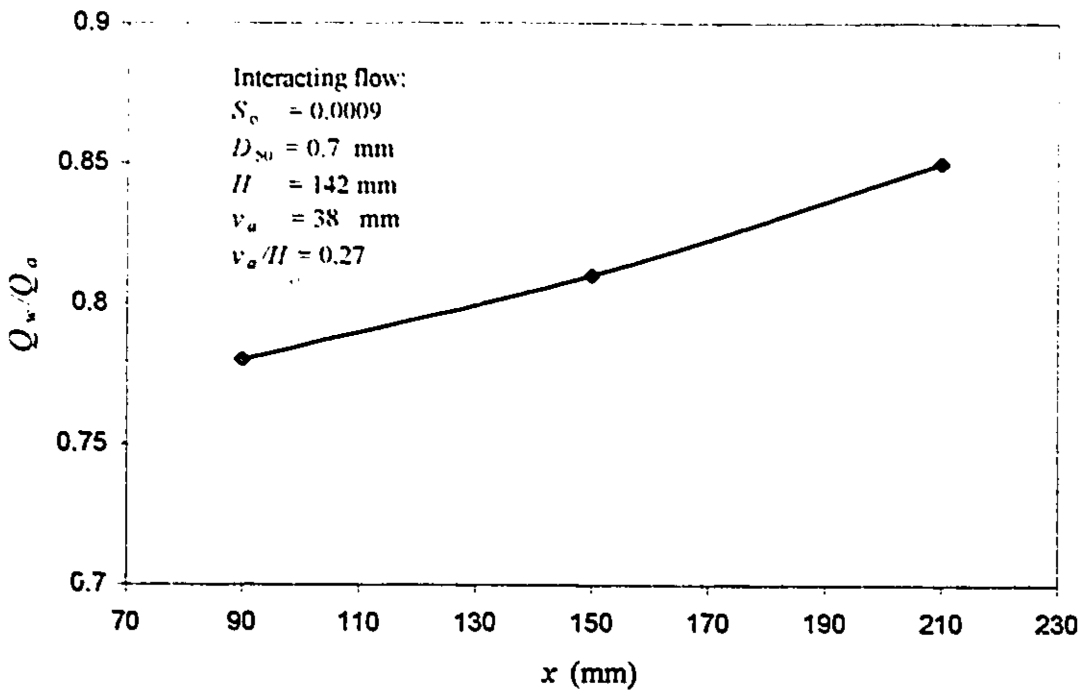

Figure 6.55- Variation of discharge ratio in the floodplain

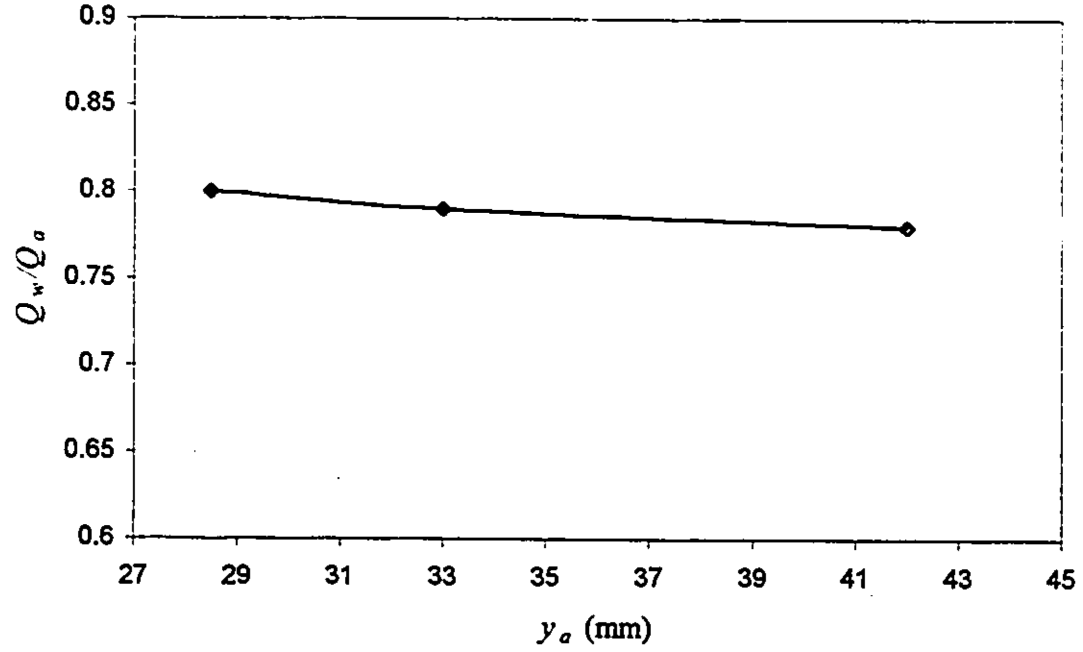

Figure 6.56- Variation of discharge ratio vs. flow depth at x=90 mm

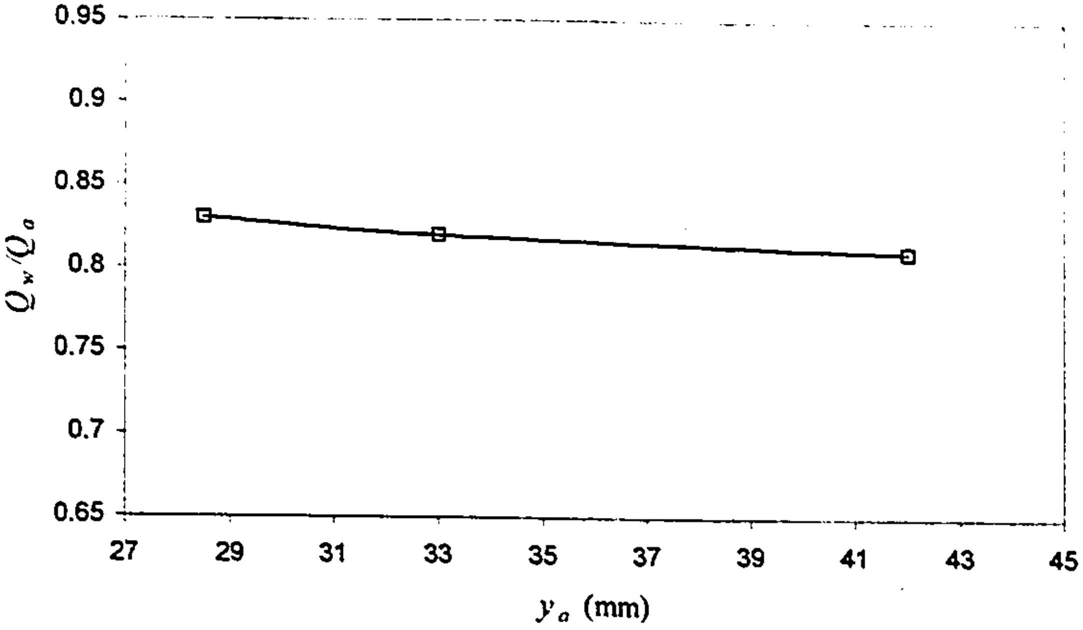

Figure 6.57- Variation of discharge ratio vs. flow depth at x=150 mm

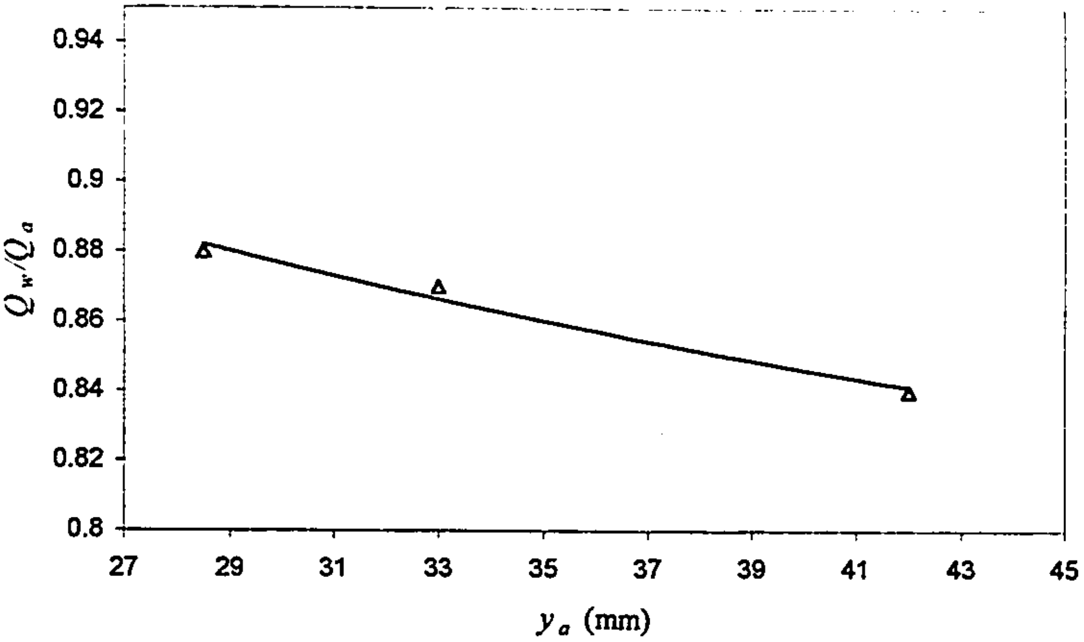

Figure 6.58- Variation of discharge ratio vs. flow depth at x=210 mm

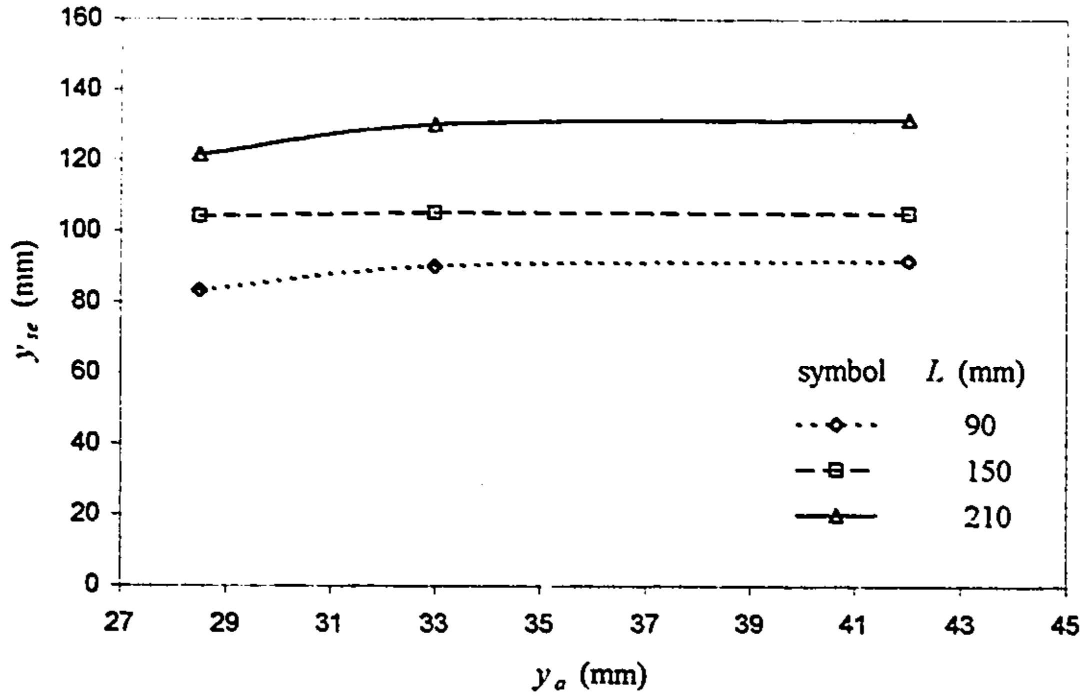

Figure 6.59- Flow depth vs. scour depth, SC-abutment

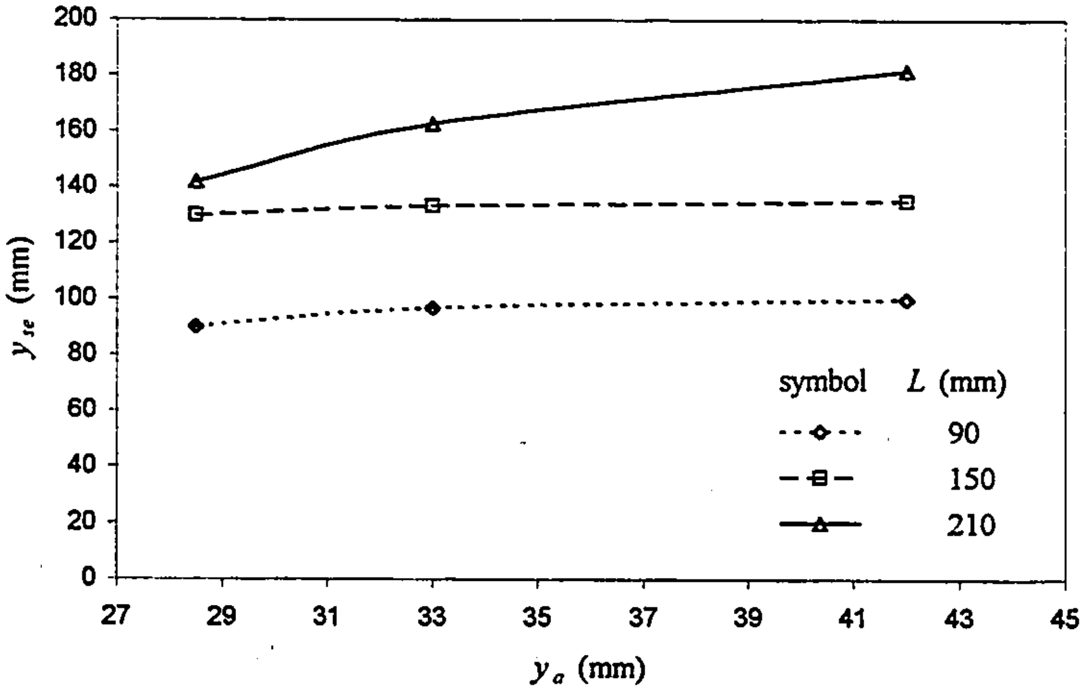

Figure 6.60- Flow depth vs. scour depth, VW-abutment

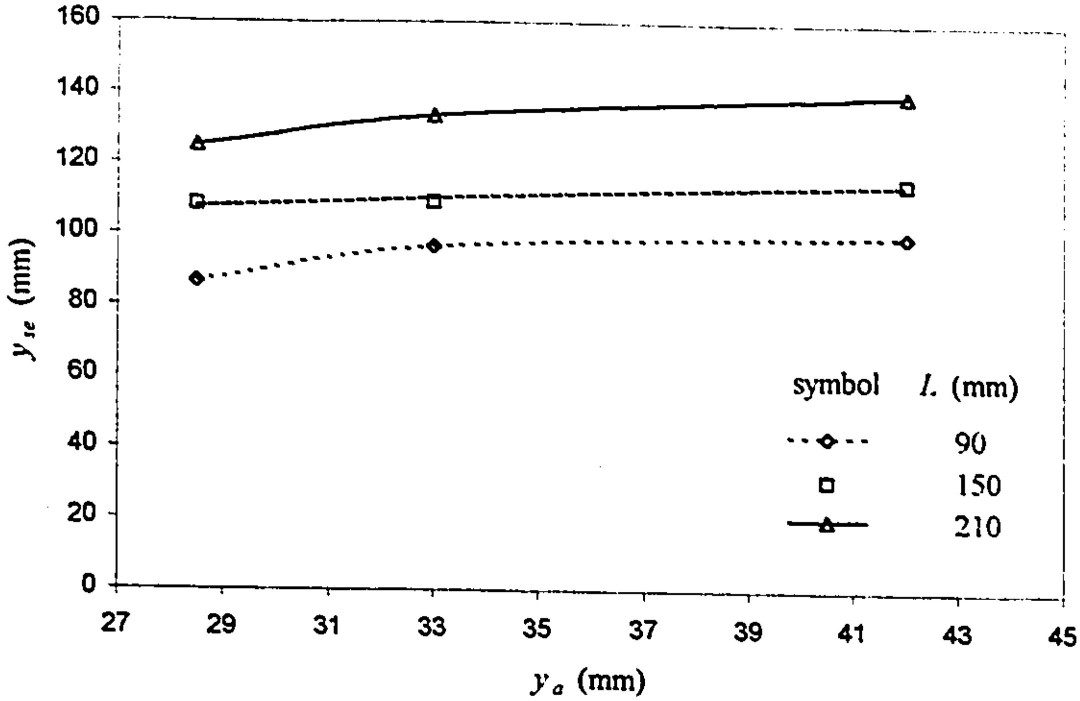

Figure 6.61- Flow depth vs. scour depth, WW-abutment

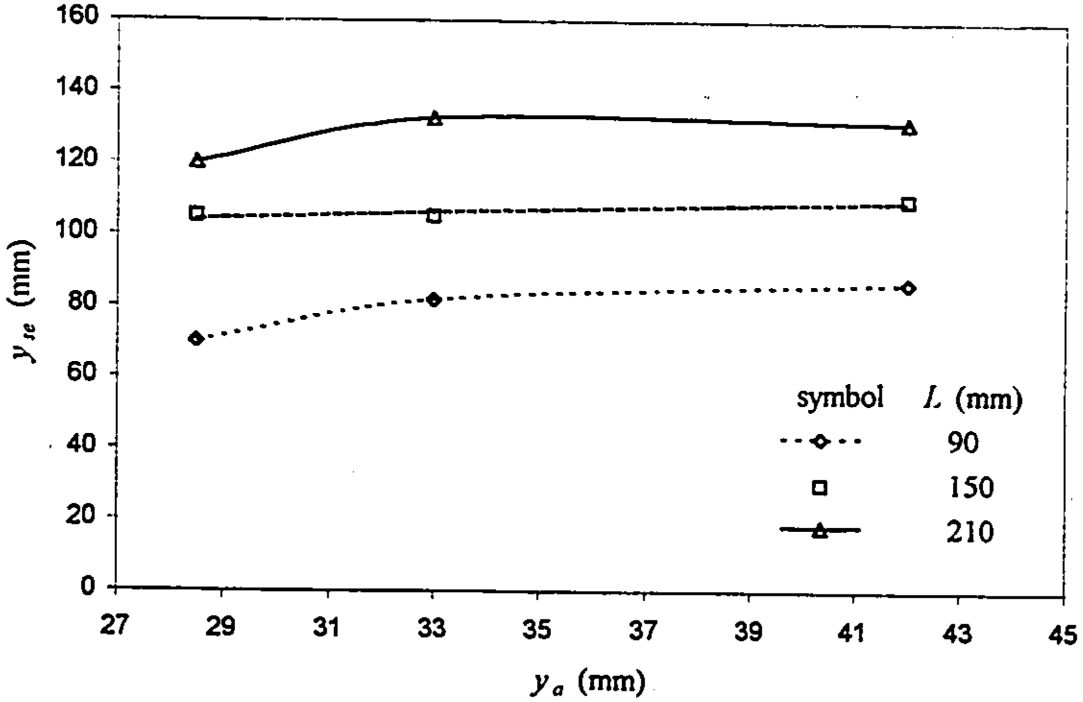

Figure 6.62- Flow depth vs. scour depth, ST-abutment

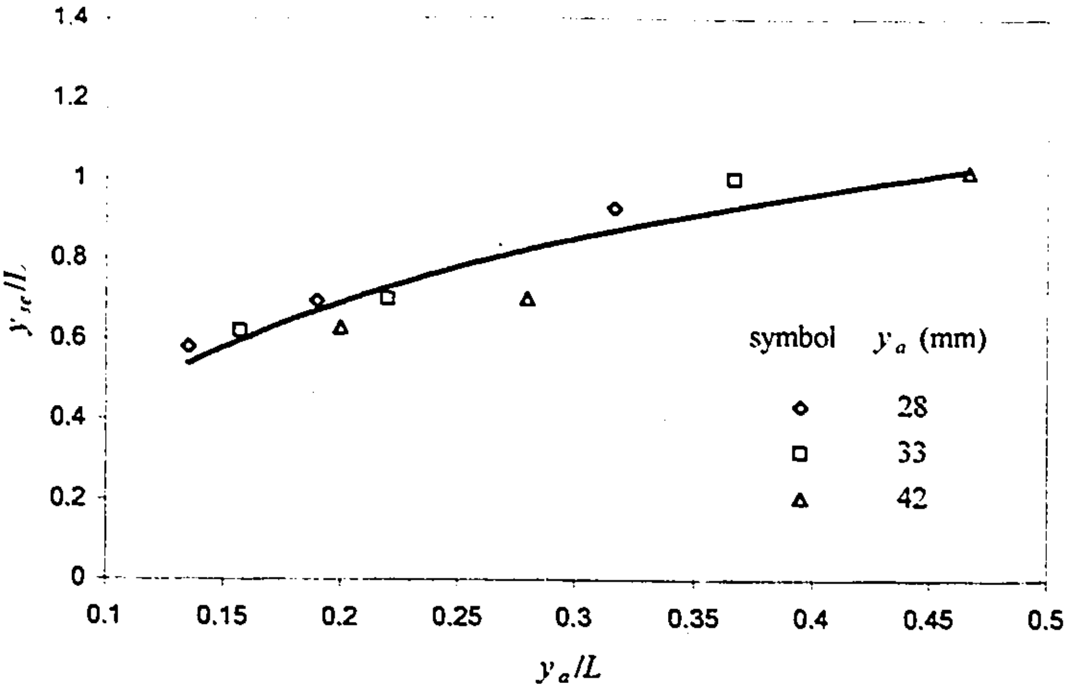

Figure 6.63- Flow depth vs. scour depth, SC-abutment

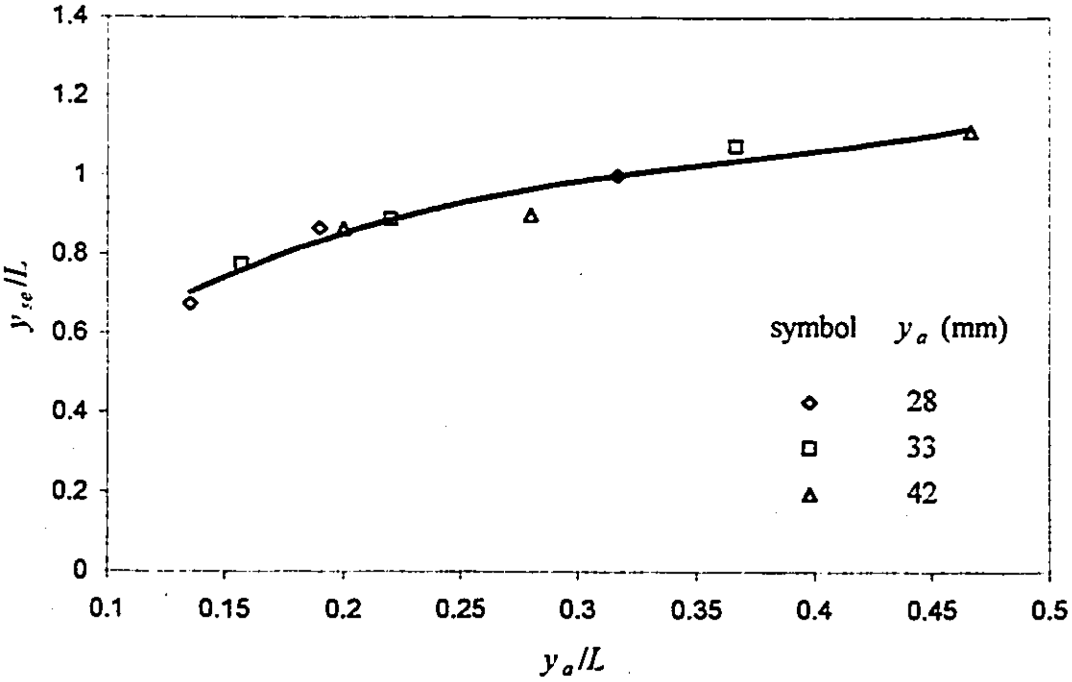

Figure 6.64- Flow depth vs. scour depth, VW-abutment

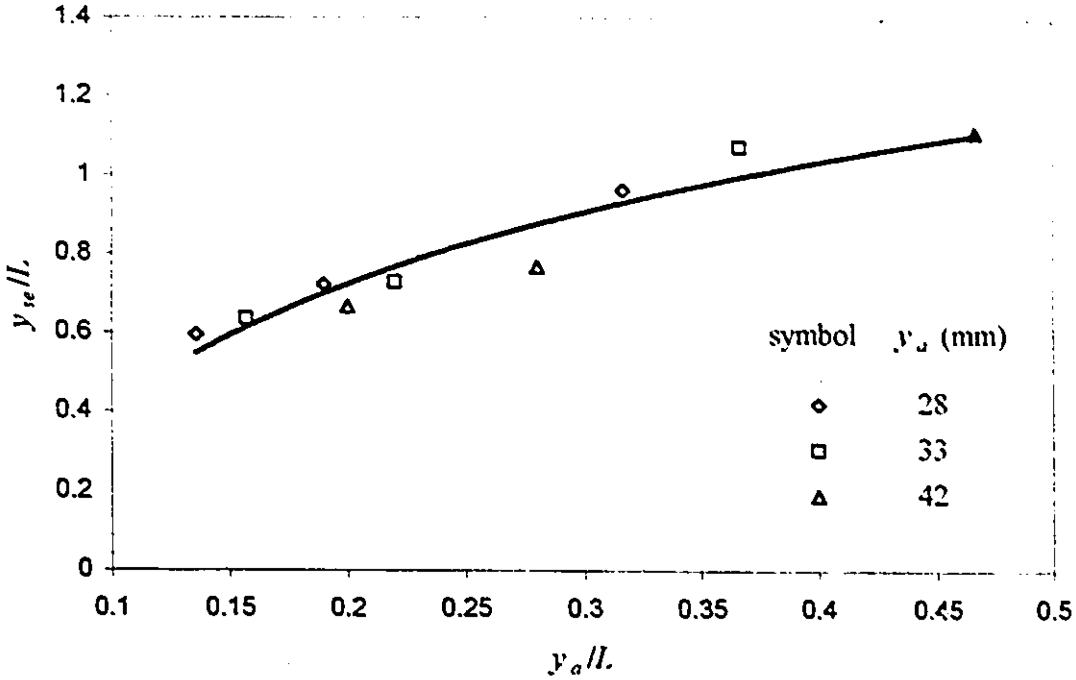

Figure 6.65- Flow depth vs. scour depth, WW-abutment

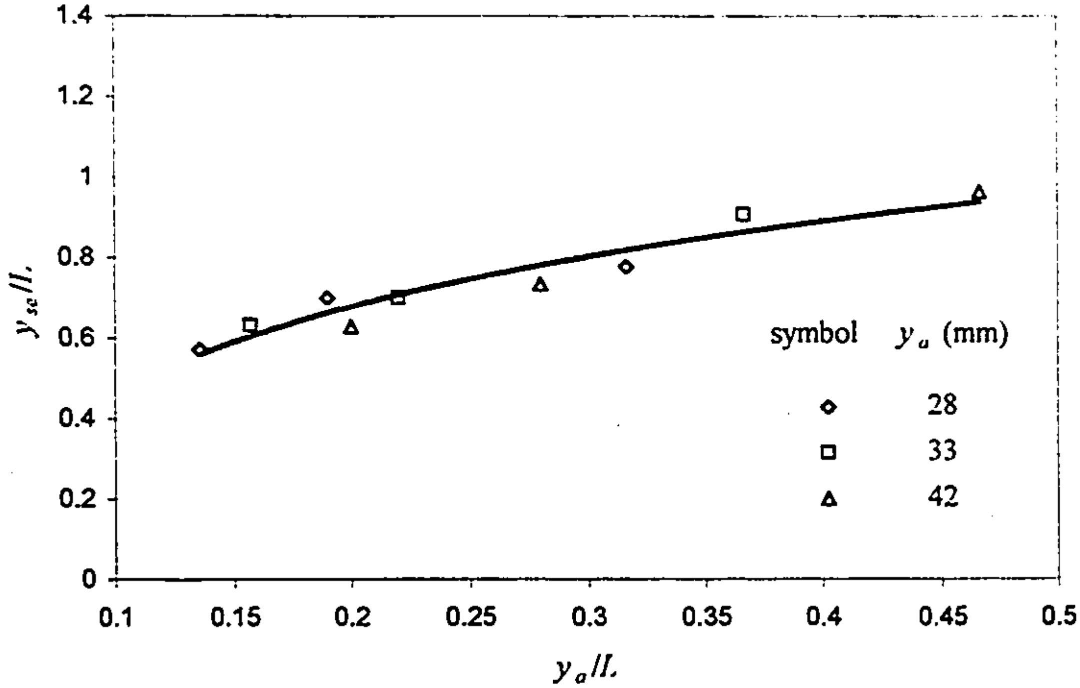

Figure 6.66- Flow depth vs. scour depth, ST-abutment

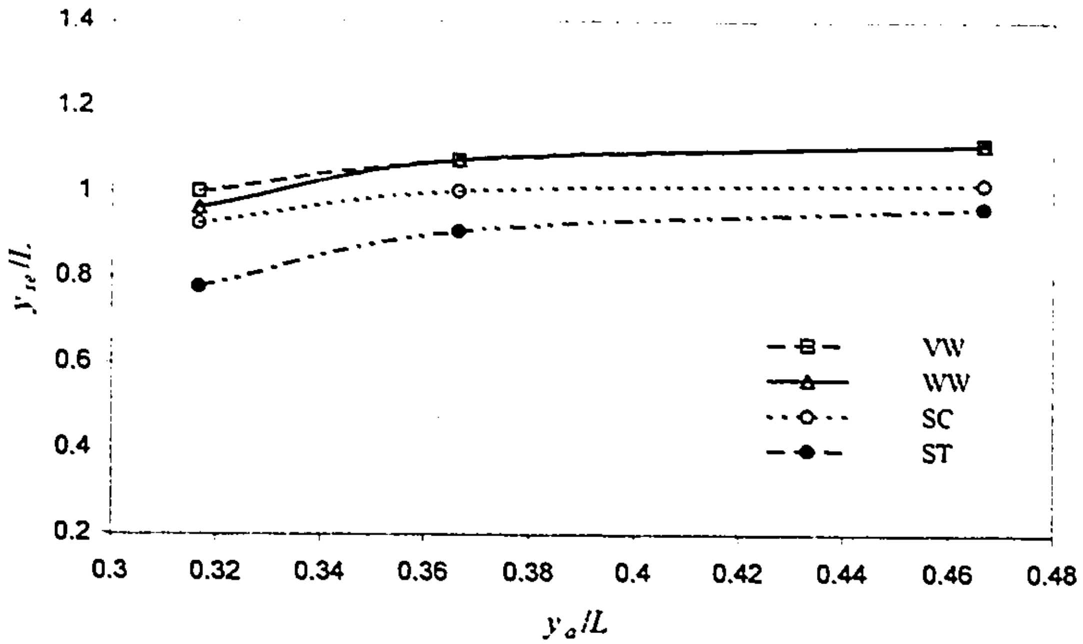

Figure 6.67- Influence of abutment shape and flow depth on scour depth, L=90 mm

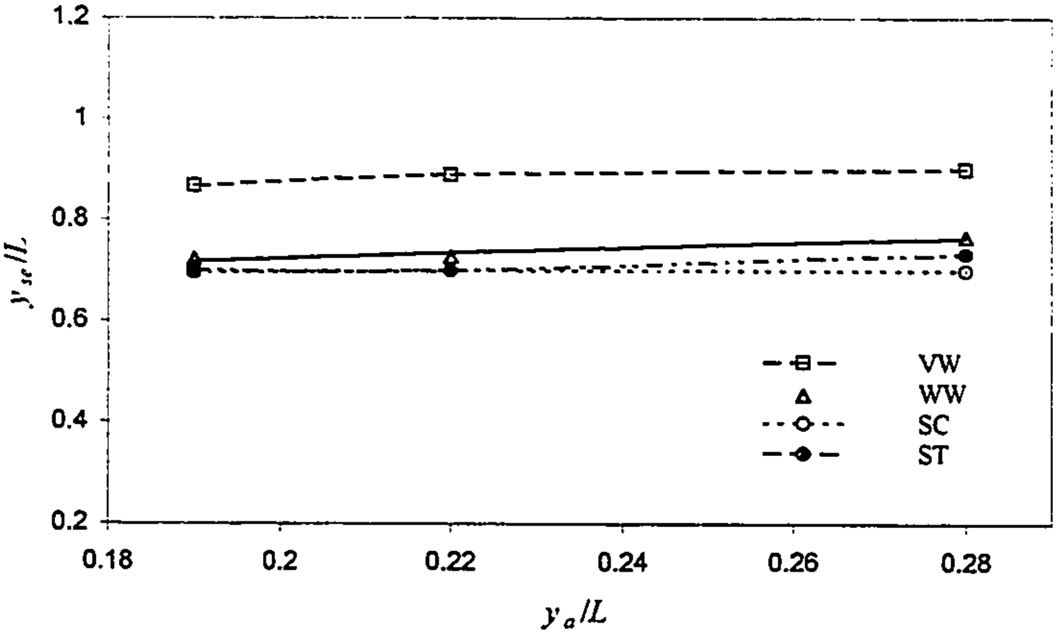

Figure 6.68- Influence of abutment shape and flow depth on scour depth, L=150 mm

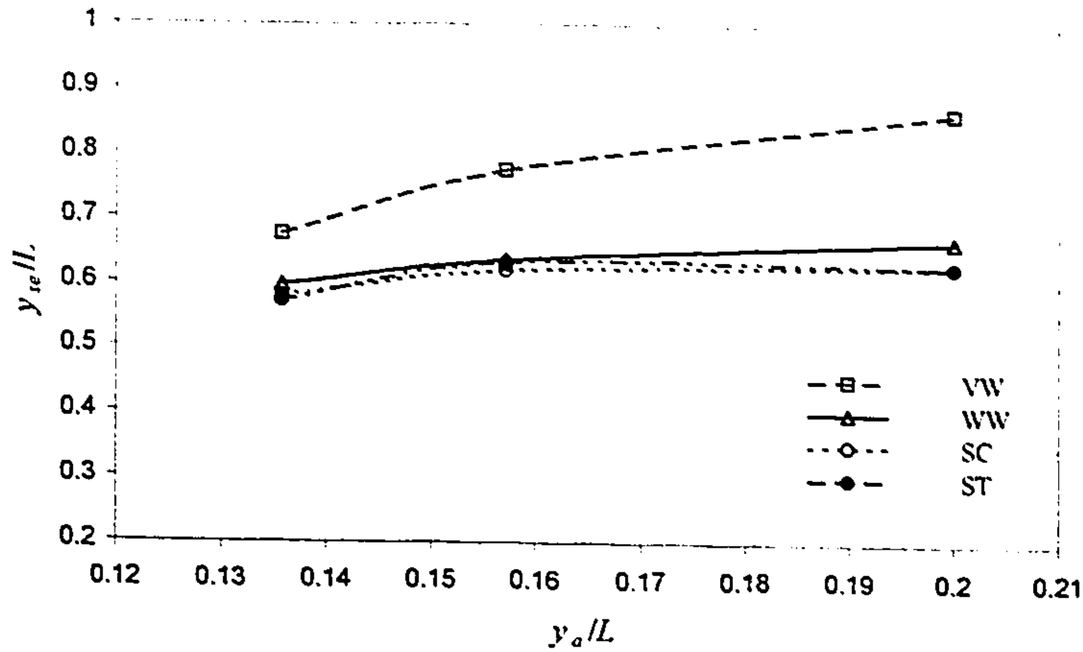

Figure 6.69- Influence of abutment shape and flow depth on the scour depth, L=210 mm

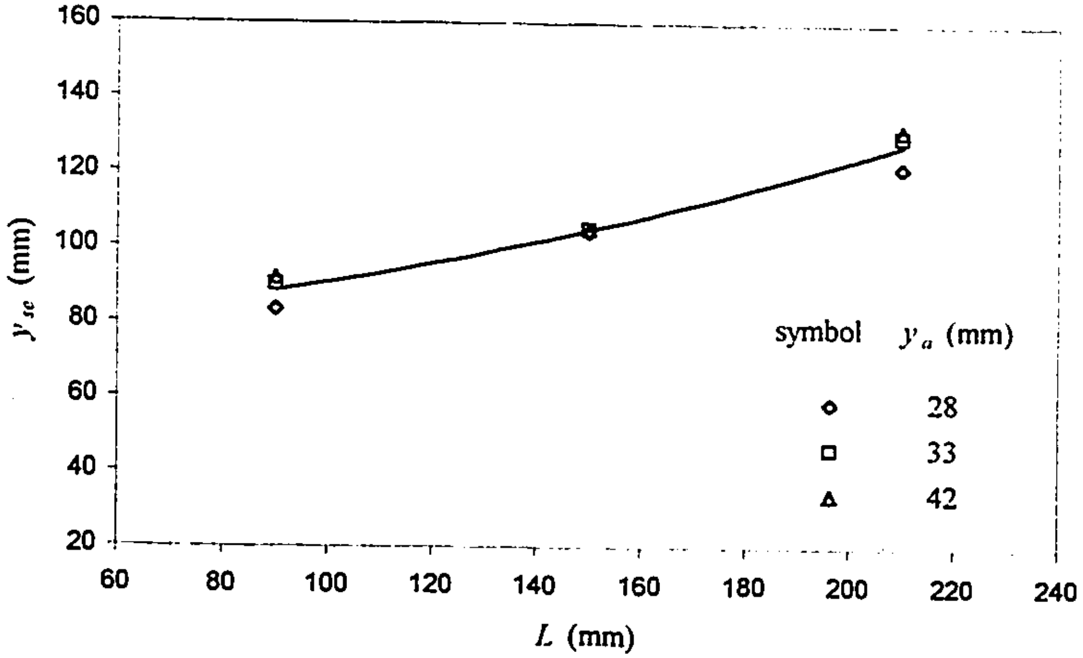

Figure 6.70- Influence of abutment length on scour depth, SC-abutment

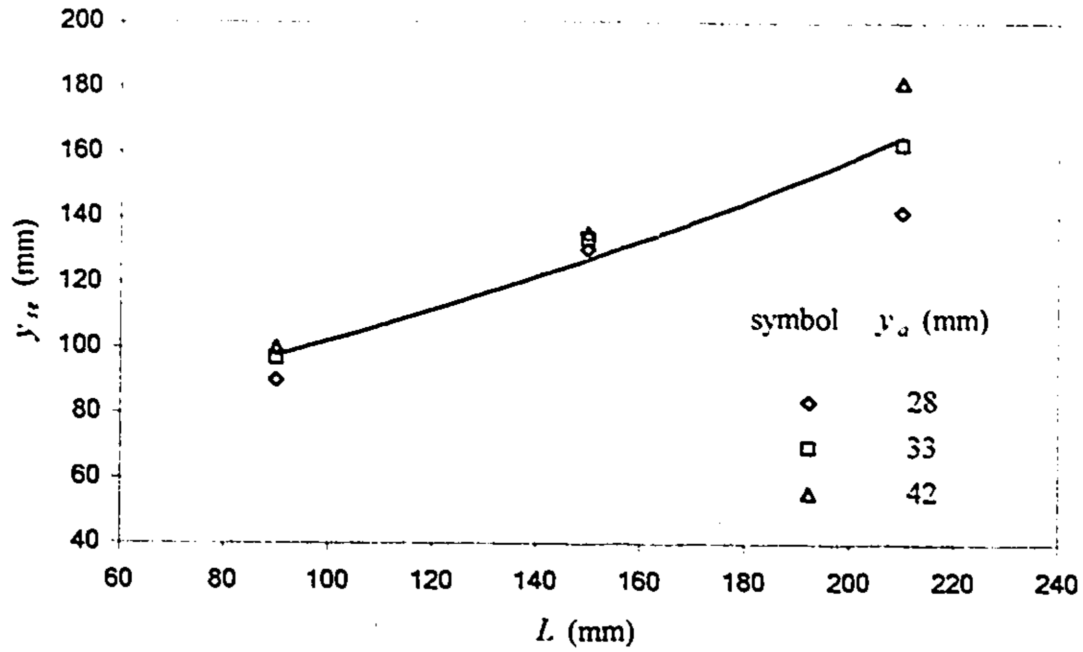

Figure 6.71- Influence of abutment length on scour depth, VW-abutment

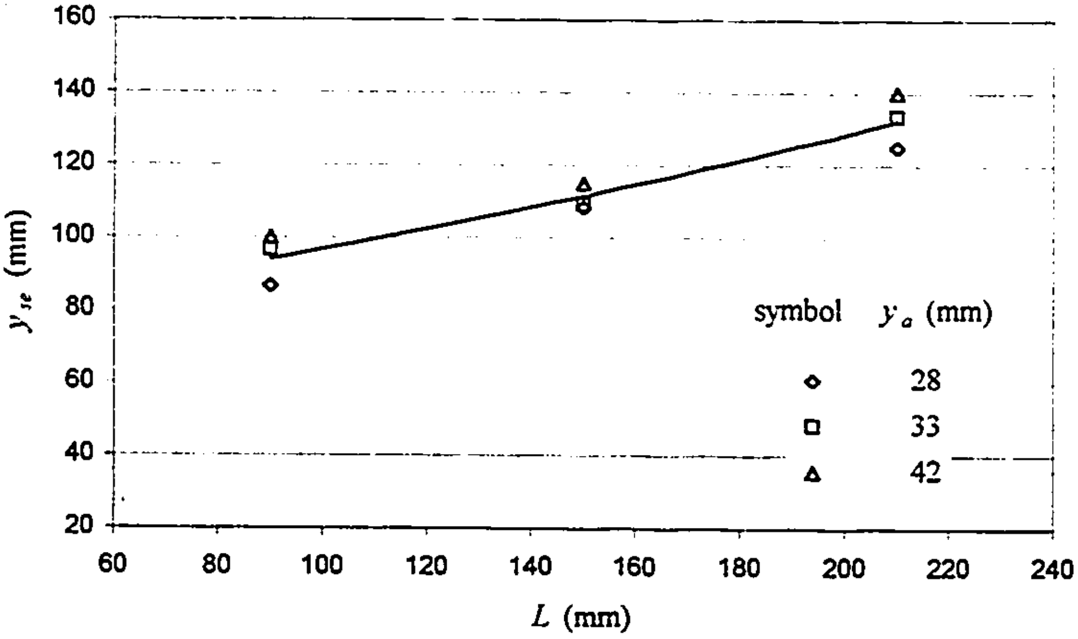

Figure 6.72- Influence of abutment length on scour depth, WW-abutment

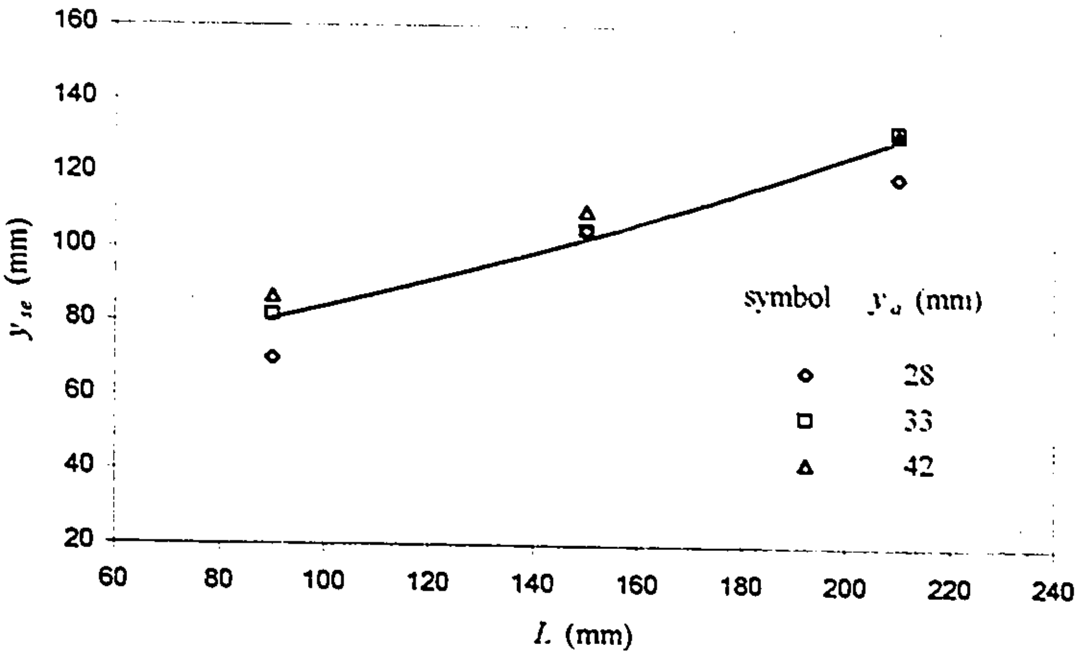

Figure 6.73- Influence of abutment length on scour depth, ST-abutment

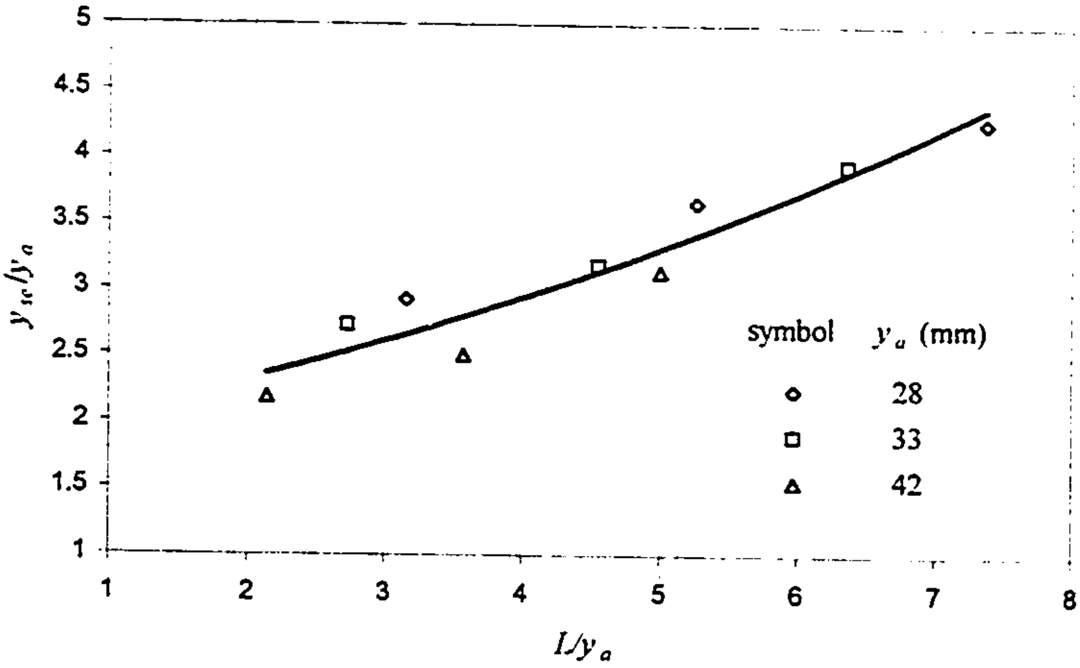

Figure 6.74- Influence of abutment length on scour depth, SC-abutment

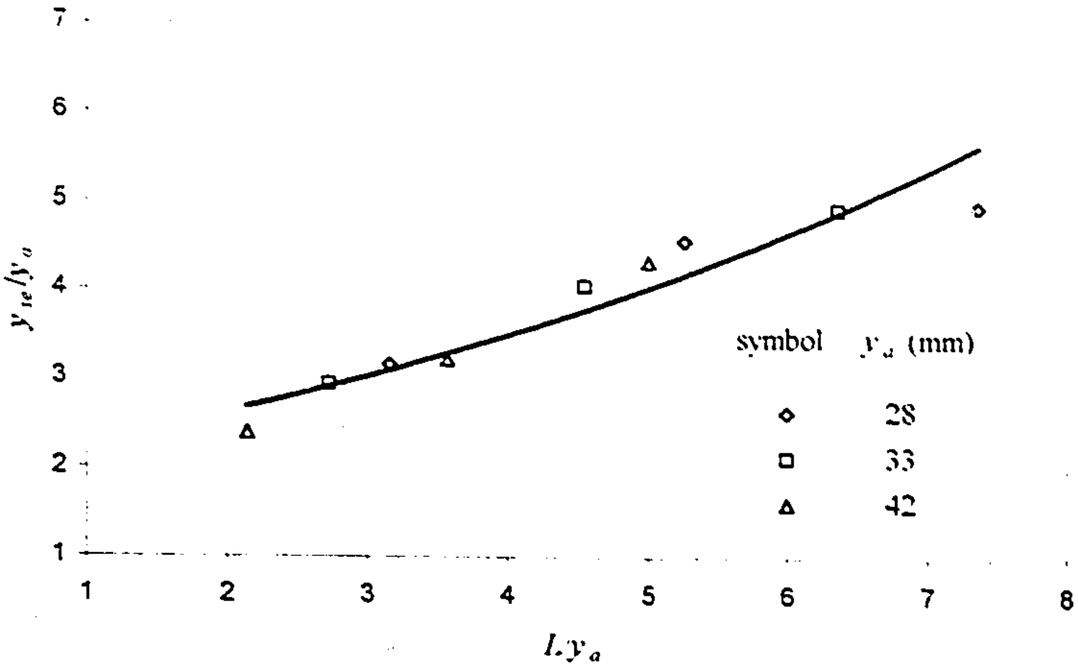

Figure 6.75- Influence of abutment length on scour depth, VW-abutment

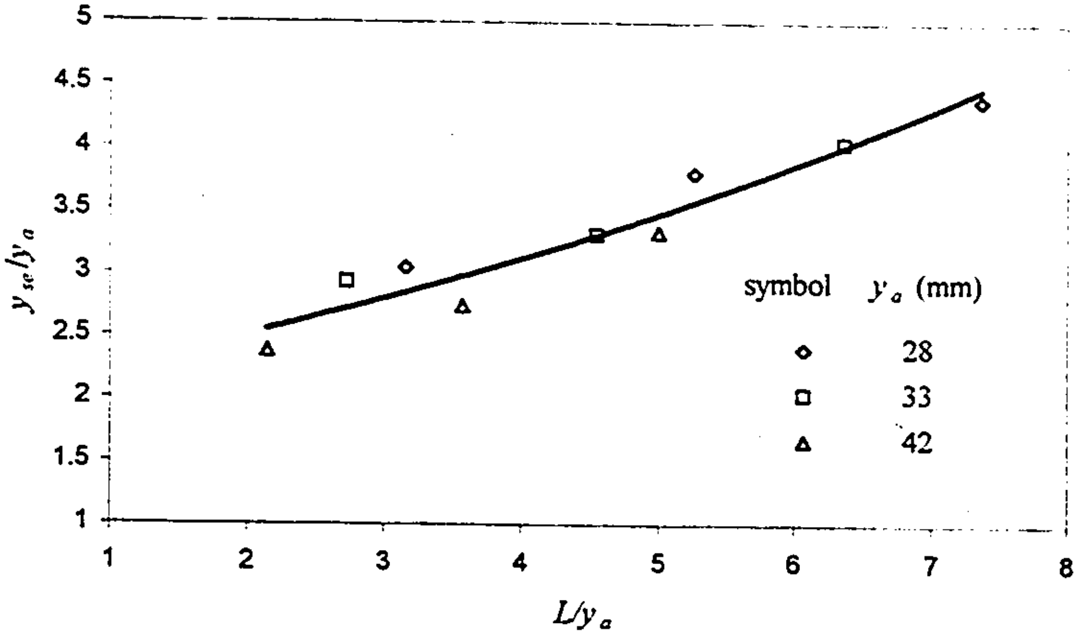

Figure 6.76- Influence of abutment length on scour depth, WW-abutment

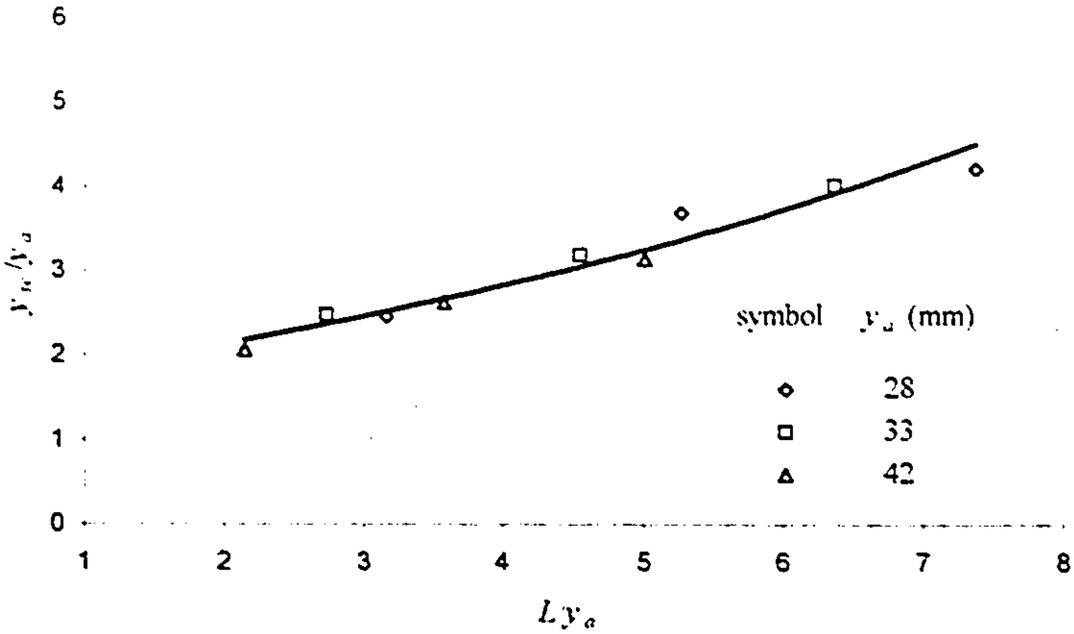

Figure 6.77- Influence of abutment length on scour depth, SC-abutment

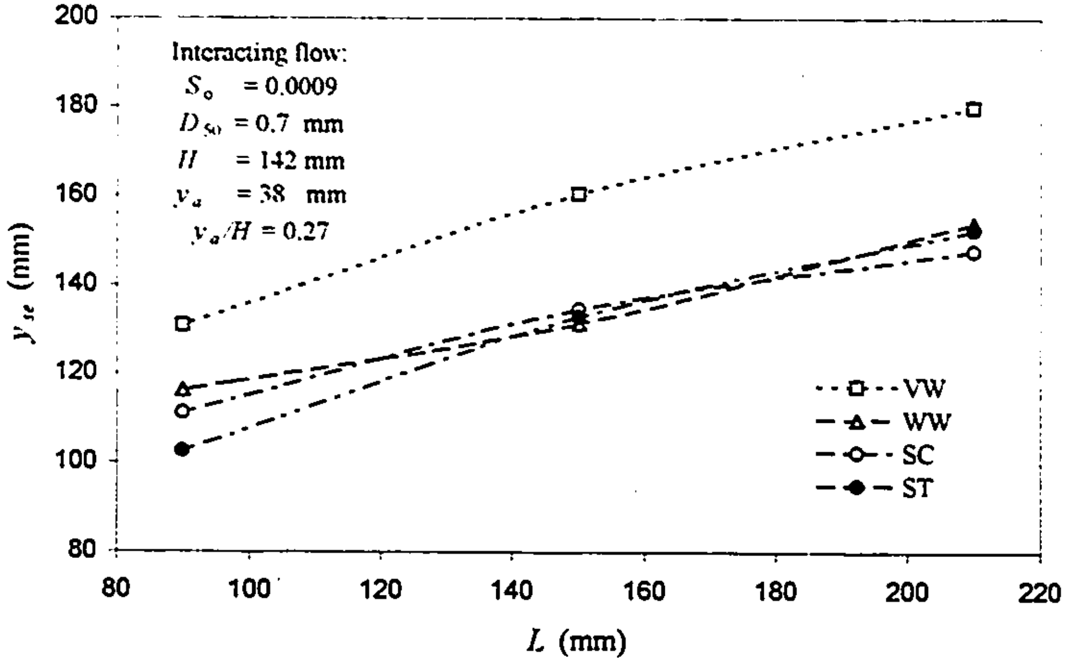

Figure 6.78- Influence of abutment length on y_{se} for different abutment shapes

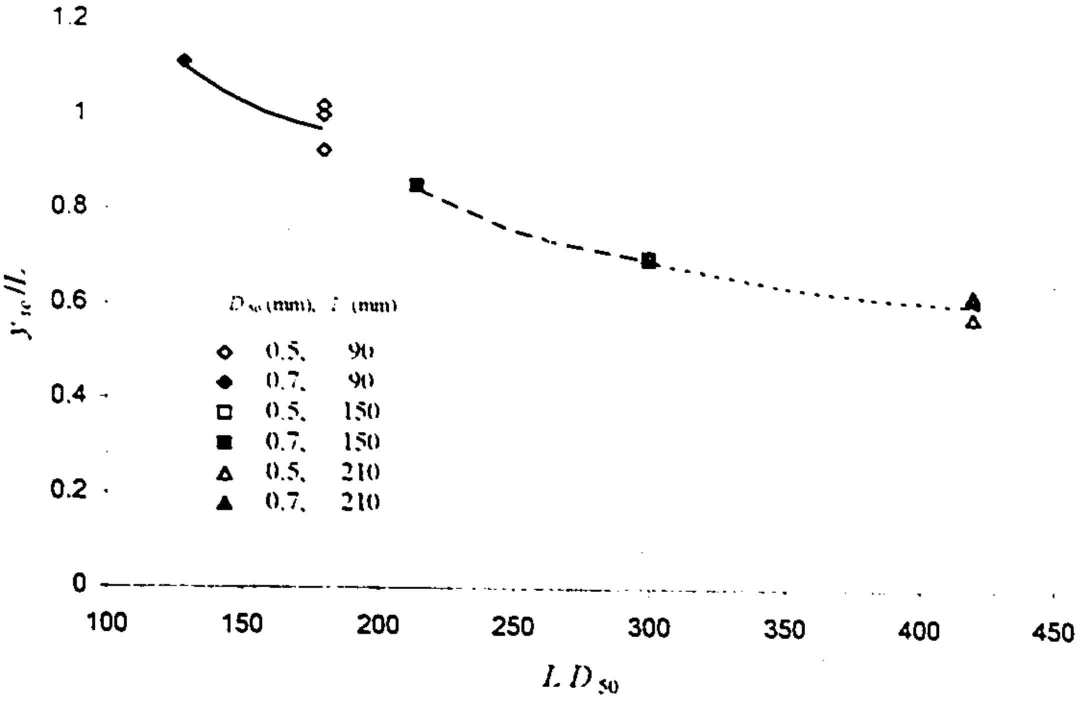

Figure 6.79- Effect of sediment size on scour depth, SC-abutment

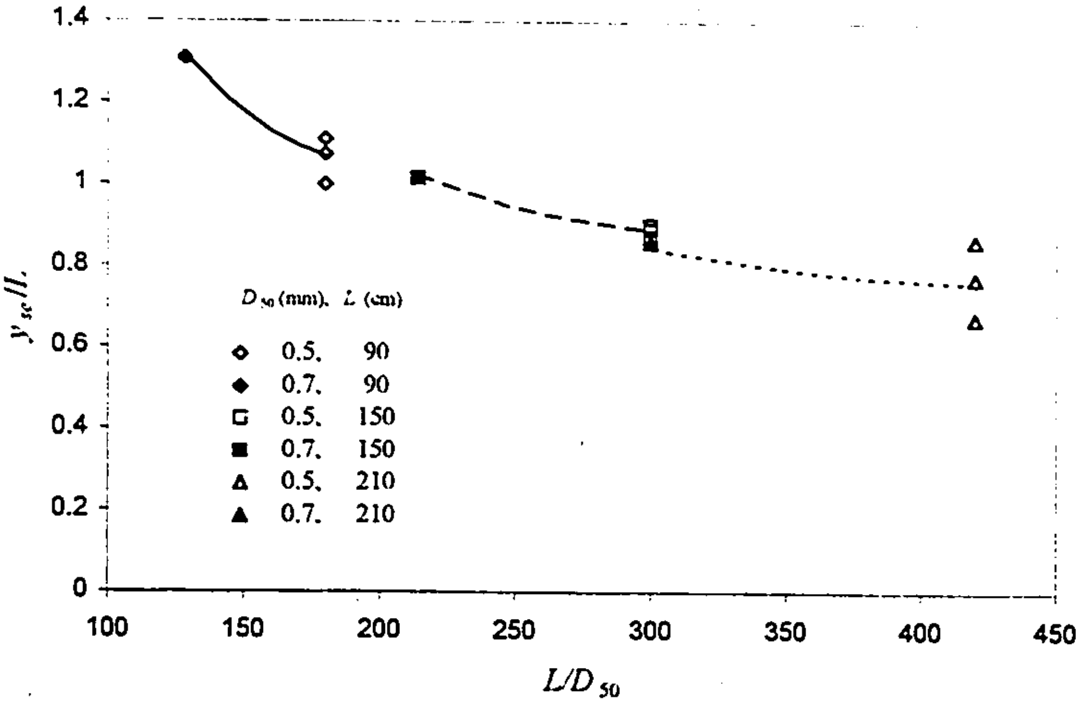

Figure 6.80- Effect of sediment size on scour depth, VW-abutment

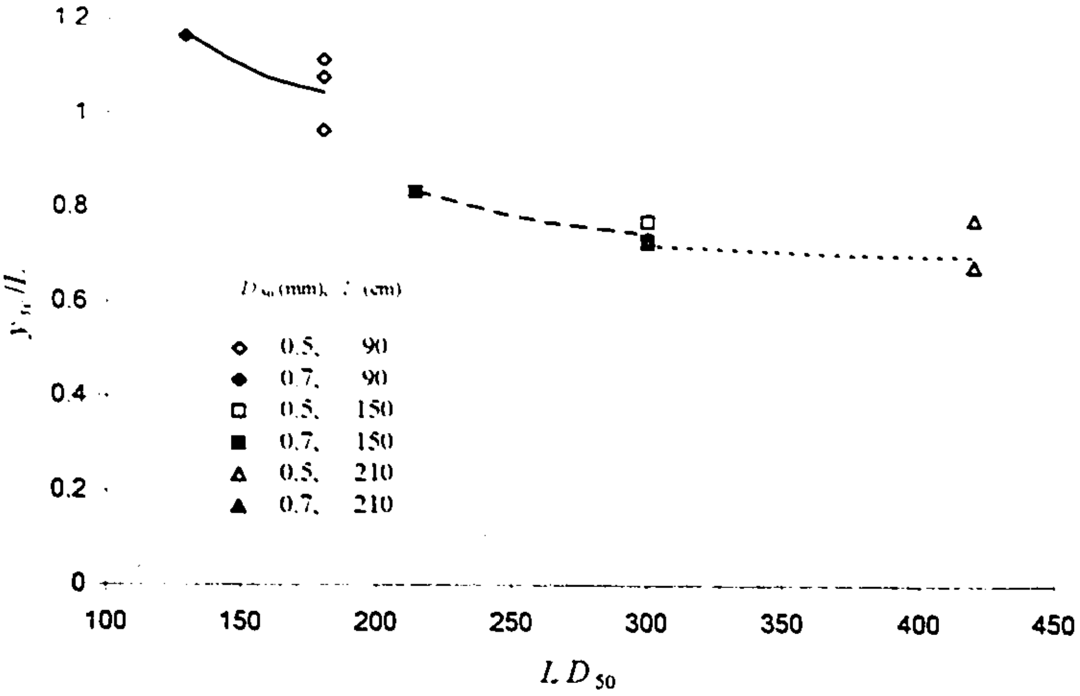

Figure 6.81- Effect of sediment size on scour depth. WW-abutment

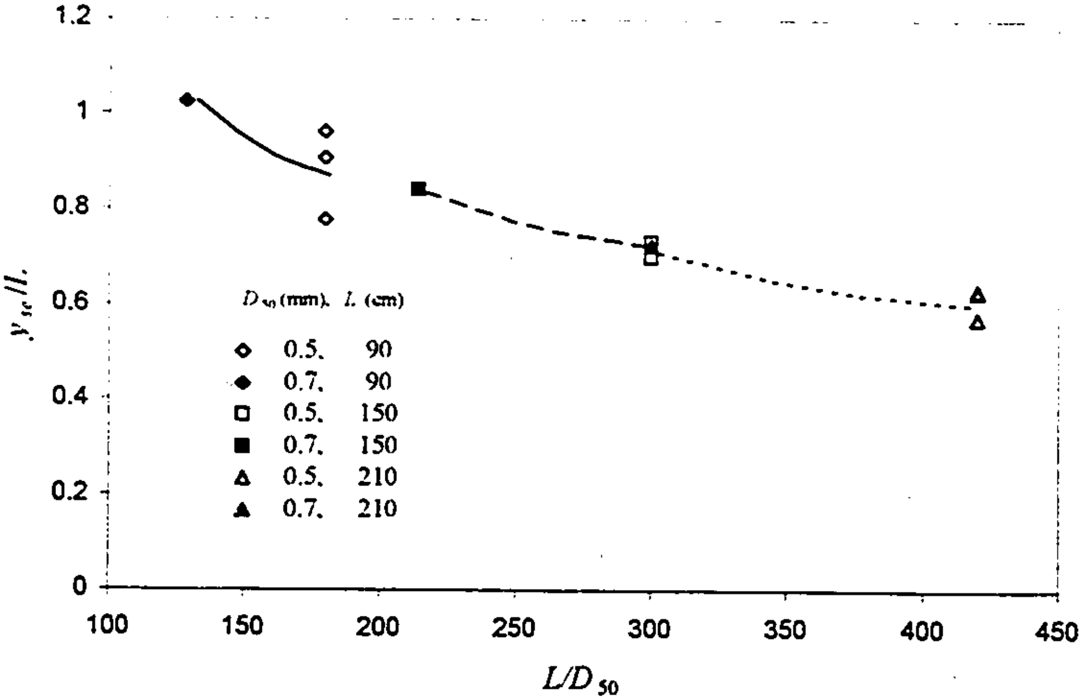

Figure 6.82- Effect of sediment size on scour depth, ST-abutment

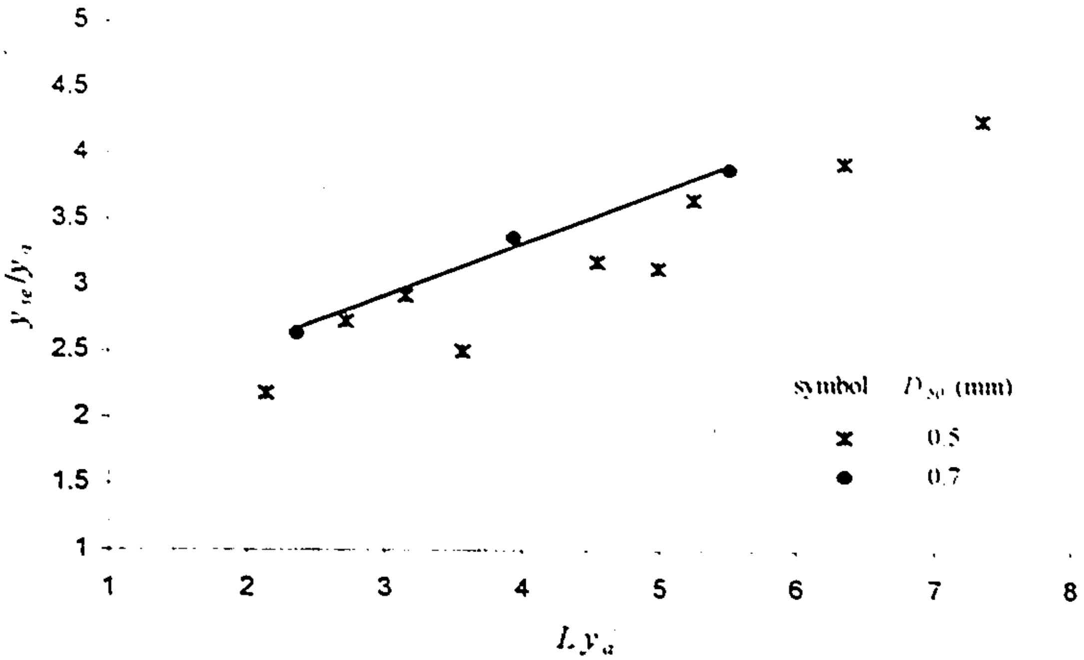

Figure 6.83- Influence of abutment length on scour depth, SC-abutment

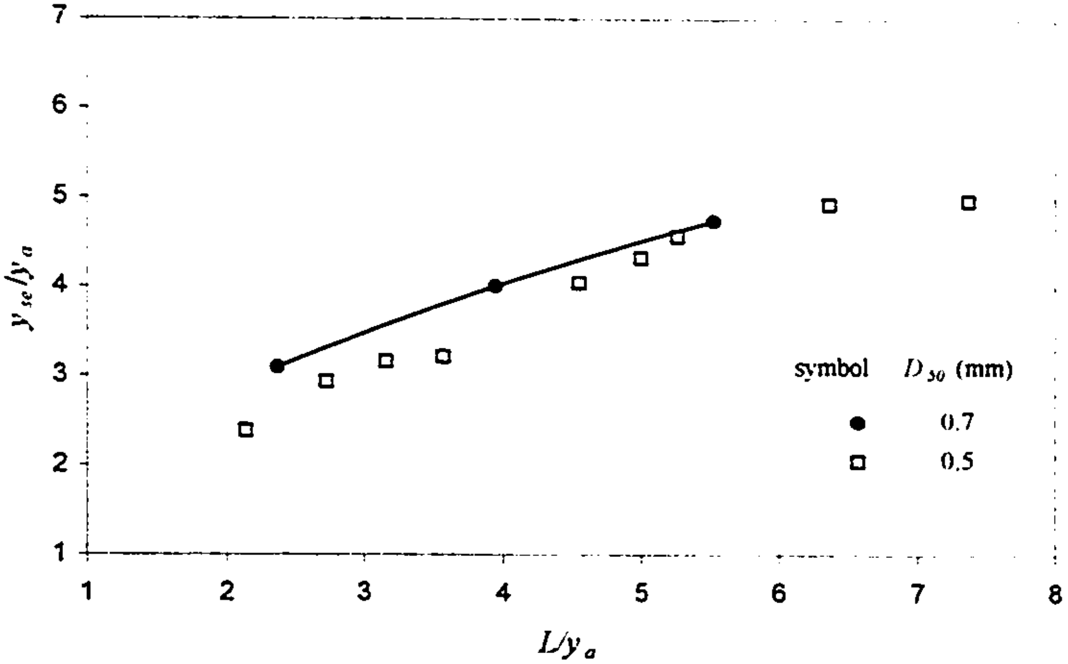

Figure 6.84- Influence of abutment length on scour depth, VW-abutment

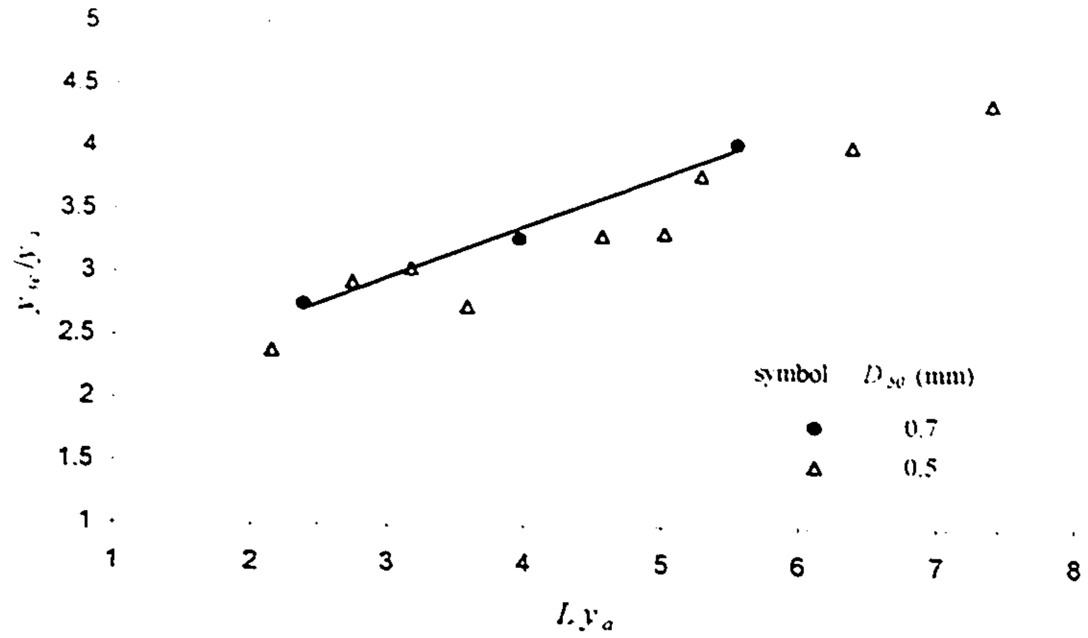

Figure 6.85- Influence of abutment length on scour depth, WW-abutment

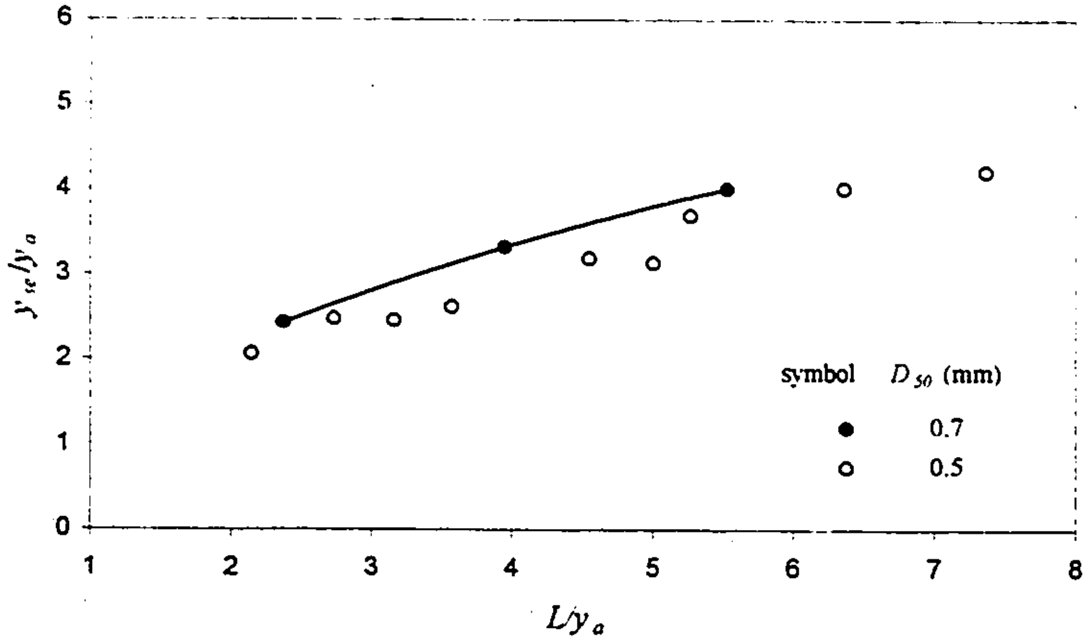

Figure 6.86- Influence of abutment length on scour depth, ST-abutment

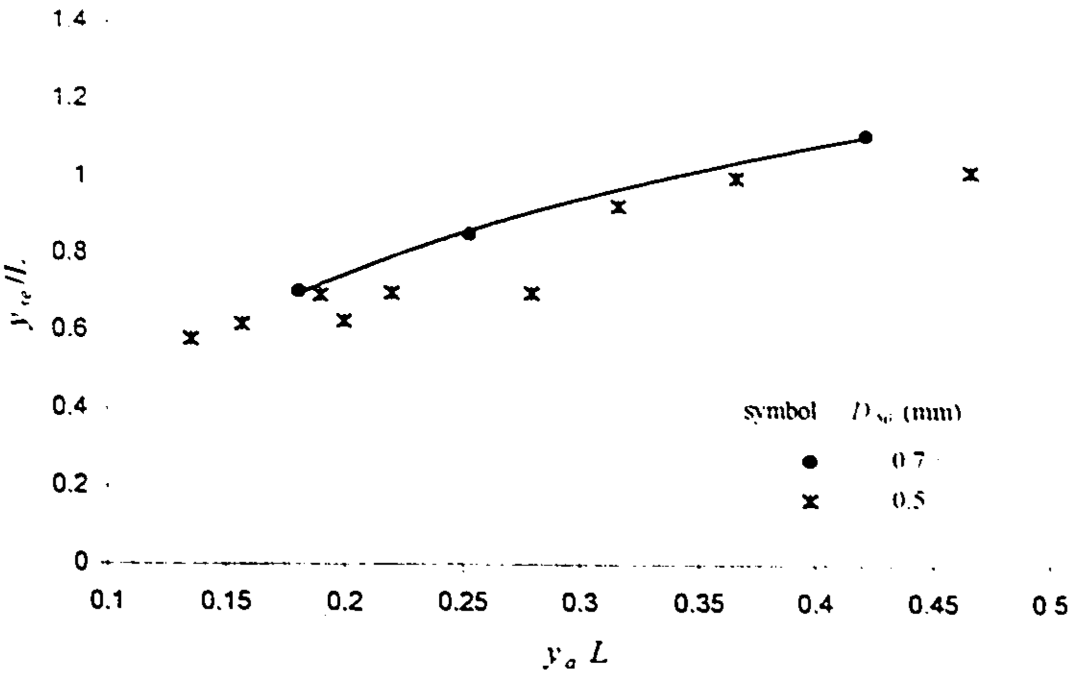

Figure 6.87- Influence of flow depth on scour depth, SC-abutment

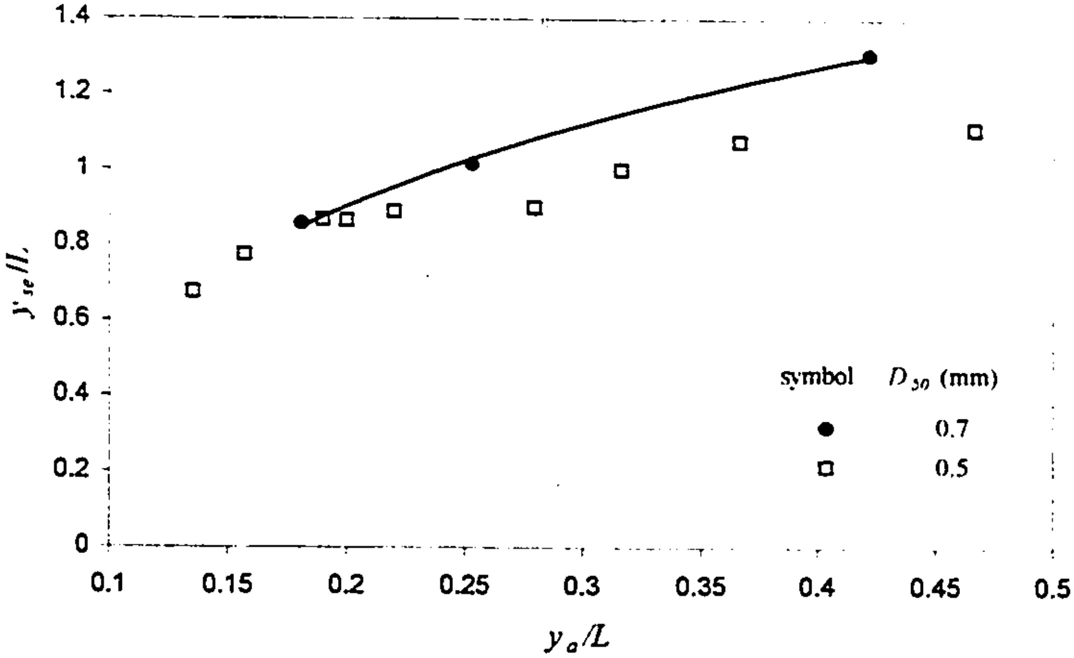

Figure 6.88- Effect of flow depth on scour depth, VW-abutment

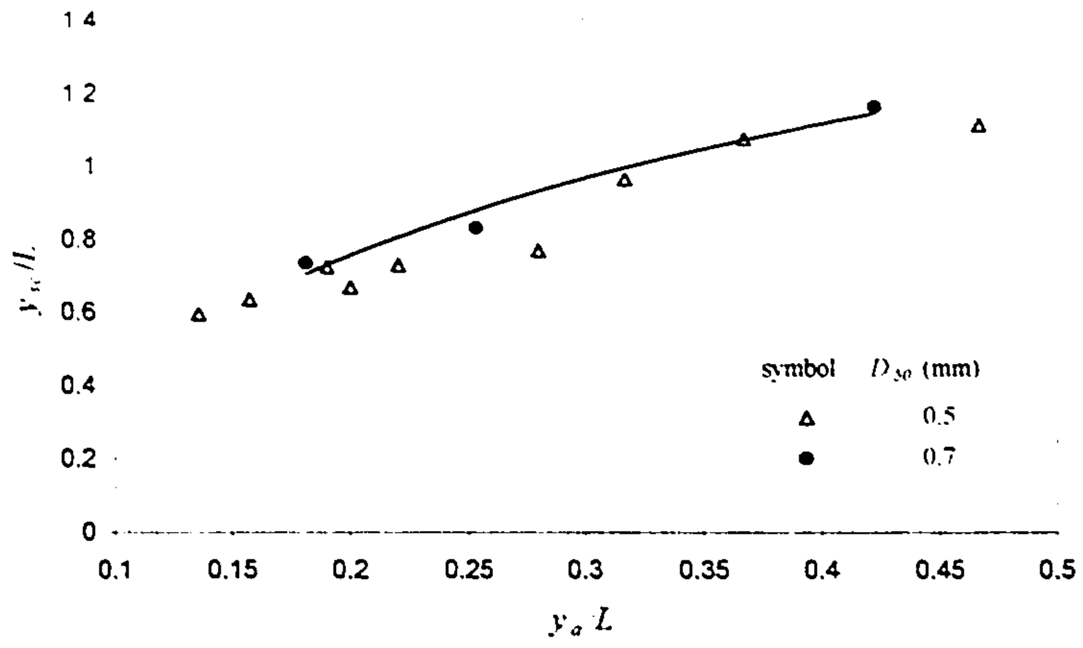

Figure 6.89- Influence of flow depth on scour depth, WW-abutment

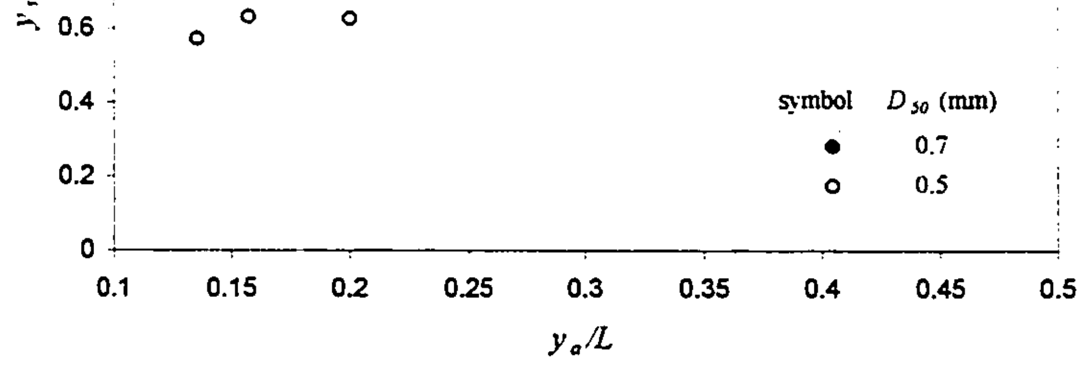

Figure 6.90- Influence of flow depth on scour depth, ST-abutment

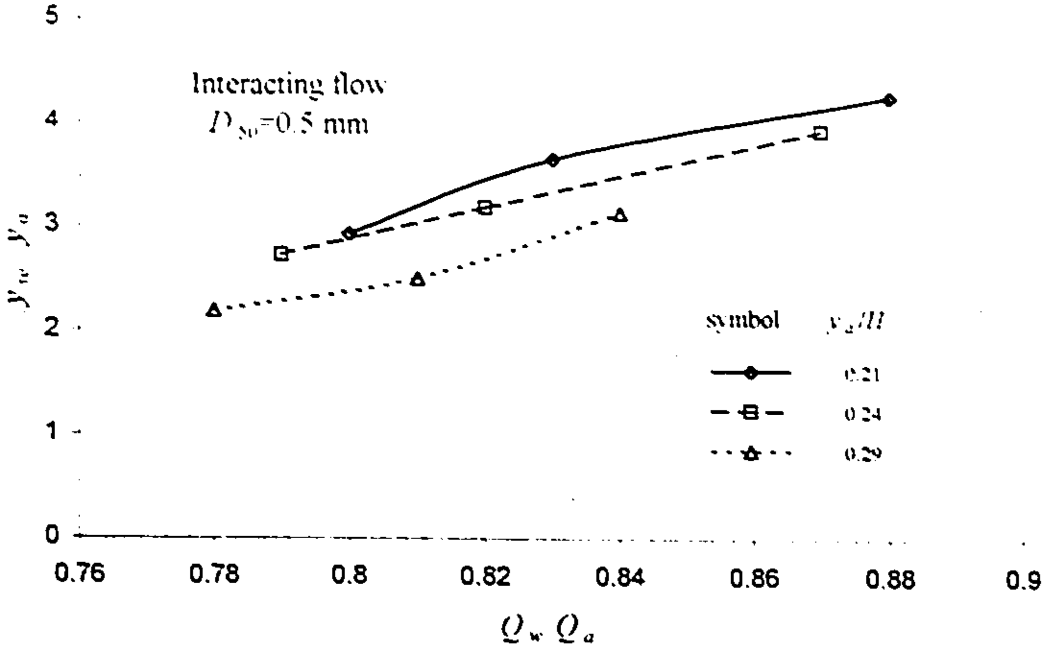

Figure 6.91- Relative scour depth vs. discharge ratio, SC-abutment

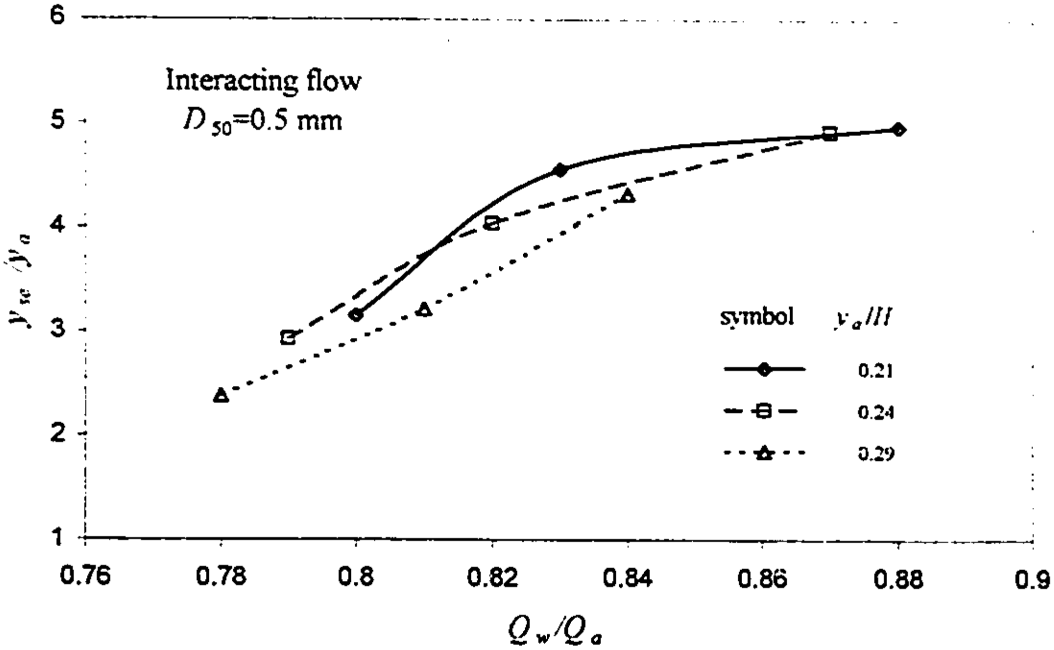

Figure 6.92- Relative scour depth with discharge ratio, VW-abutment

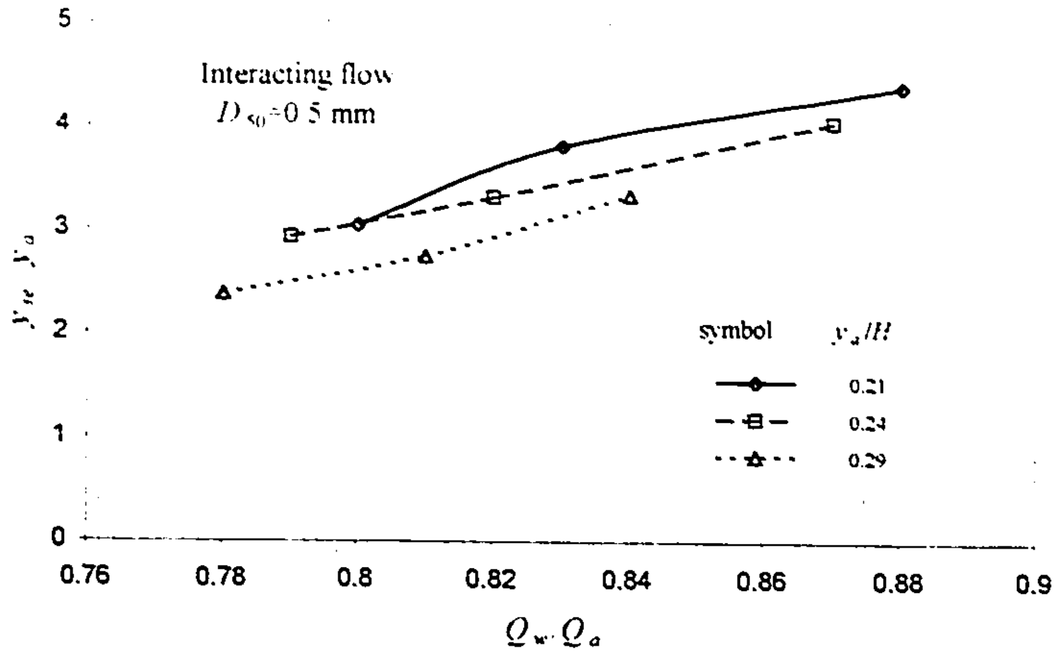

Figure 6.93- Relative scour depth with discharge ratio, WW-abutment

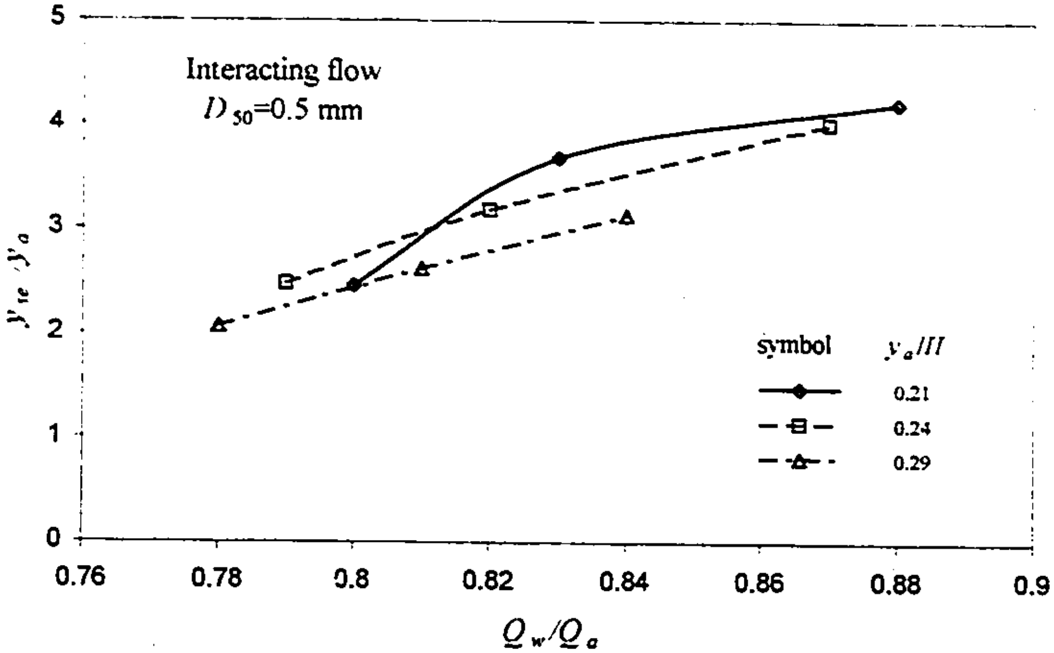

Figure 6.94- Relative scour depth with discharge ratio, ST-abutment

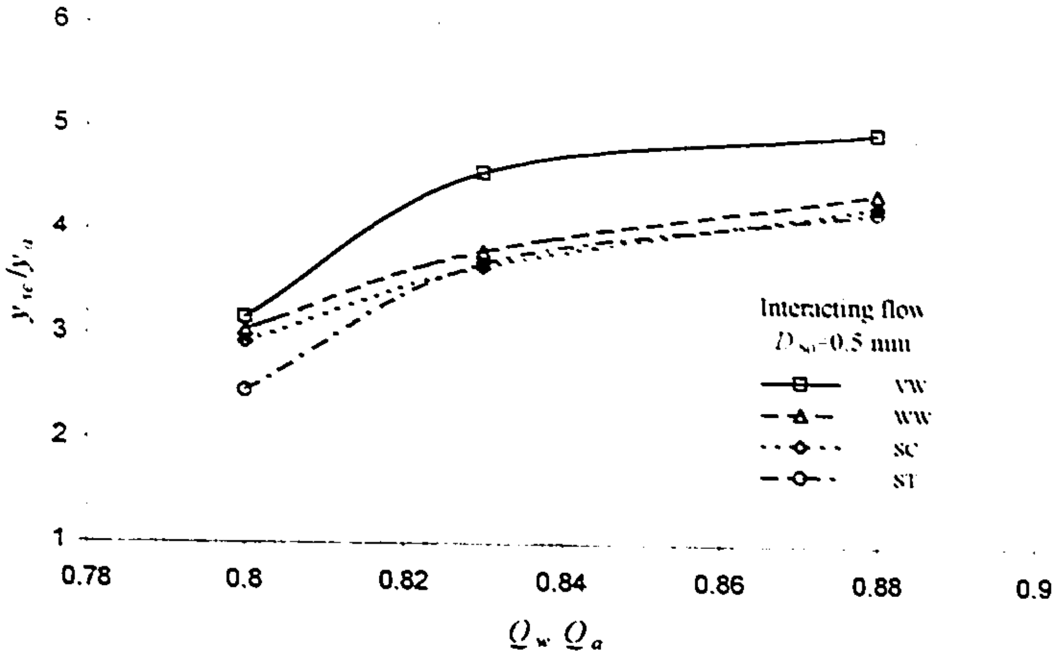

Figure 6.95-Relative scour depth vs. discharge ratio for different abutment shapes, y_a/H=0.21

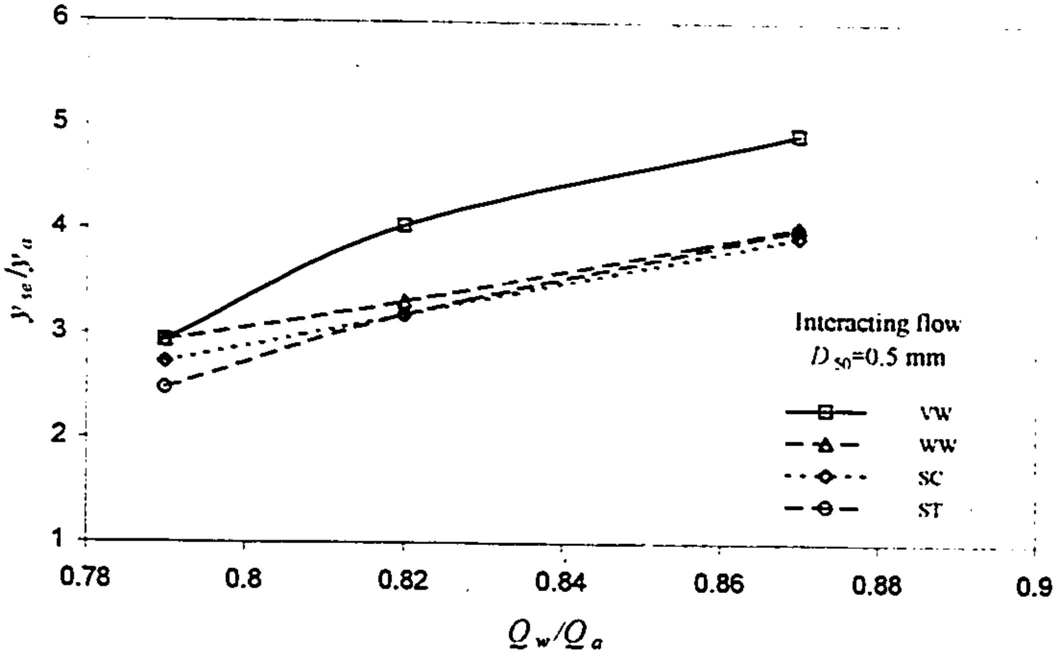

Figure 6.96- Relative scour depth vs. discharge ratio for different abutment shapes, y_a/H=0.24

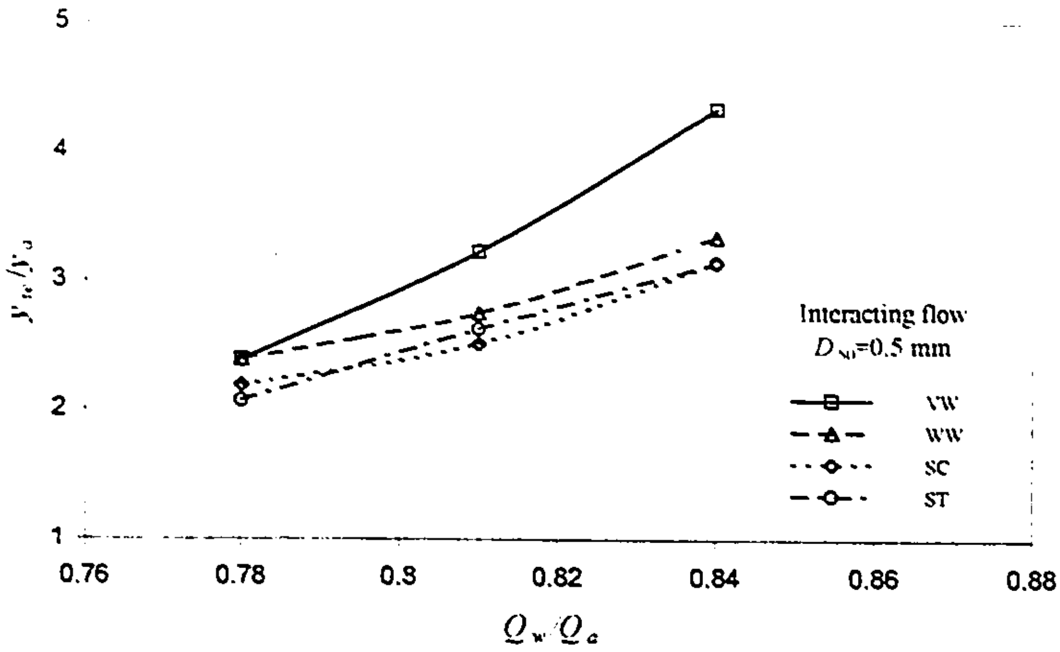

Figure 6.97- Relative scour depth vs. discharge ratio for different abutment shapes, y_a/H=0.29

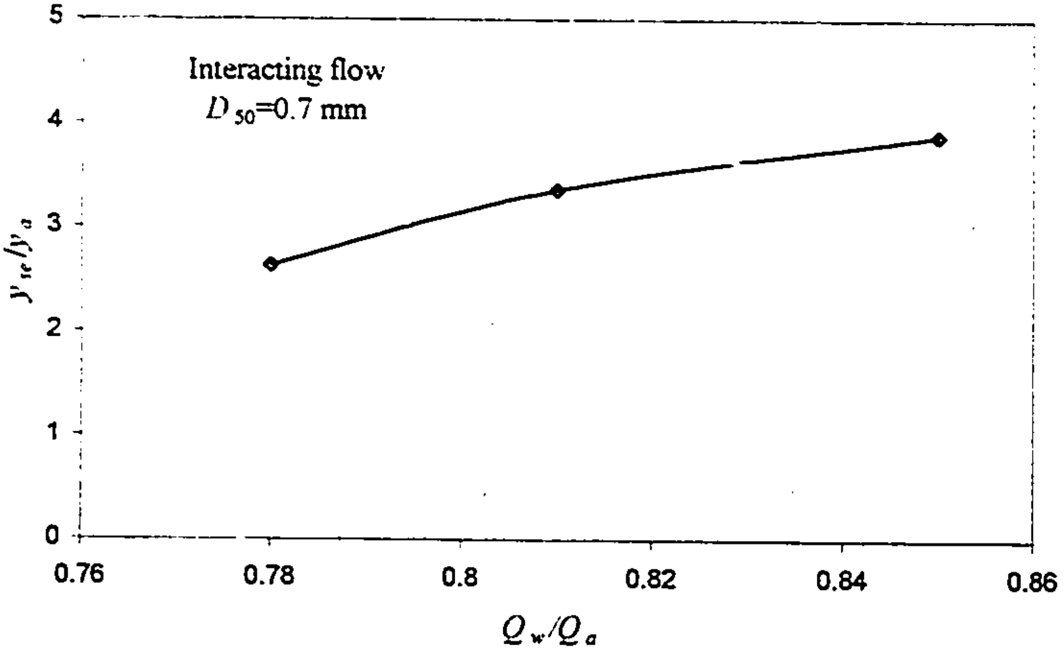

Figure 6.98-Relative scour depth vs. discharge ratio for SC-abutments

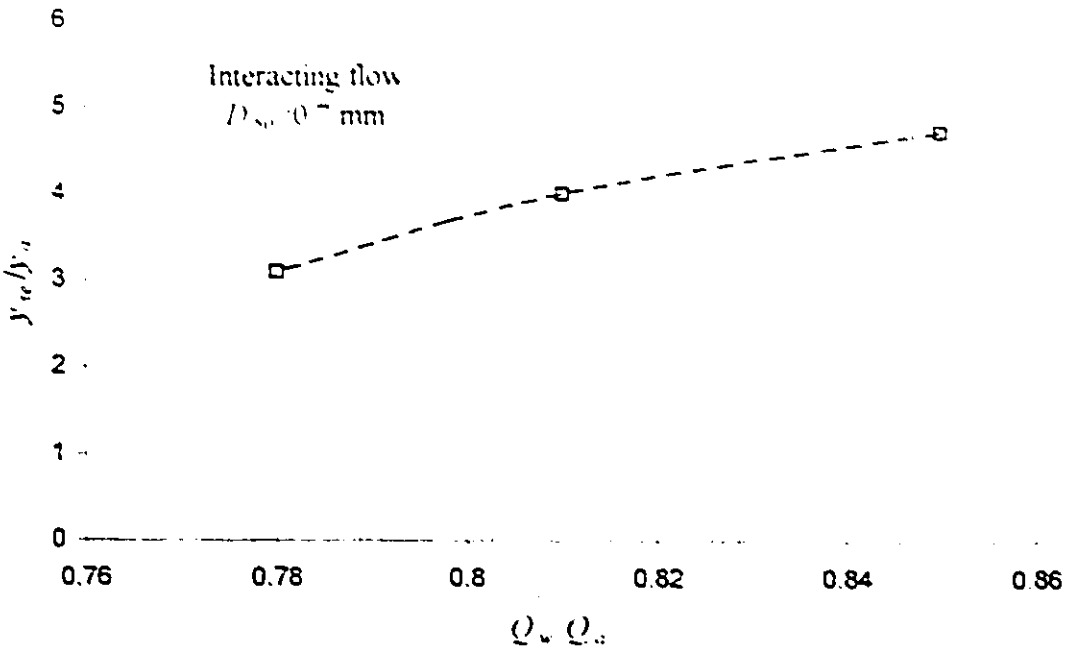

Figure 6.99- Relative scour depth vs. discharge ratio for VW-abutments

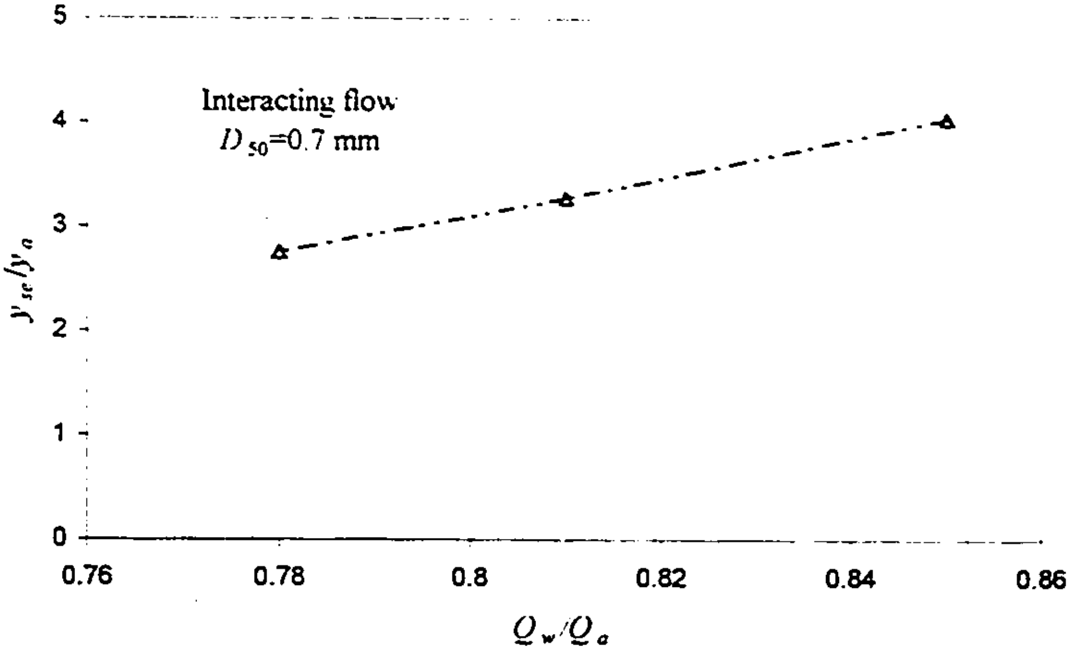

Figure 6.100- Relative scour depth vs. discharge ratio for WW-abutments

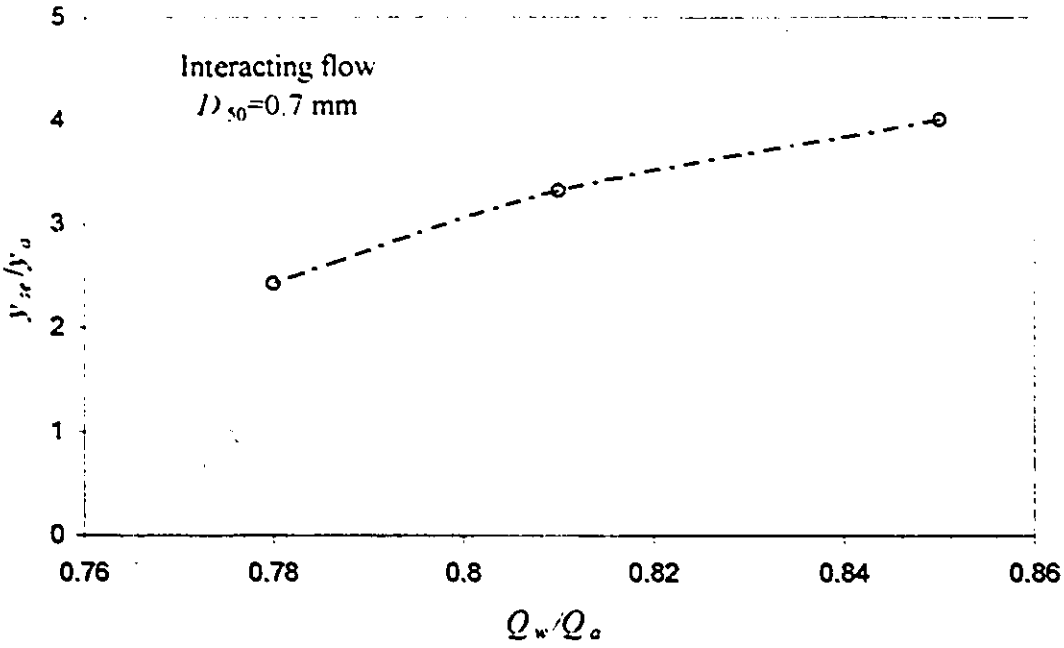

Figure 6.101- Relative scour depth vs. discharge ratio for ST-abutments

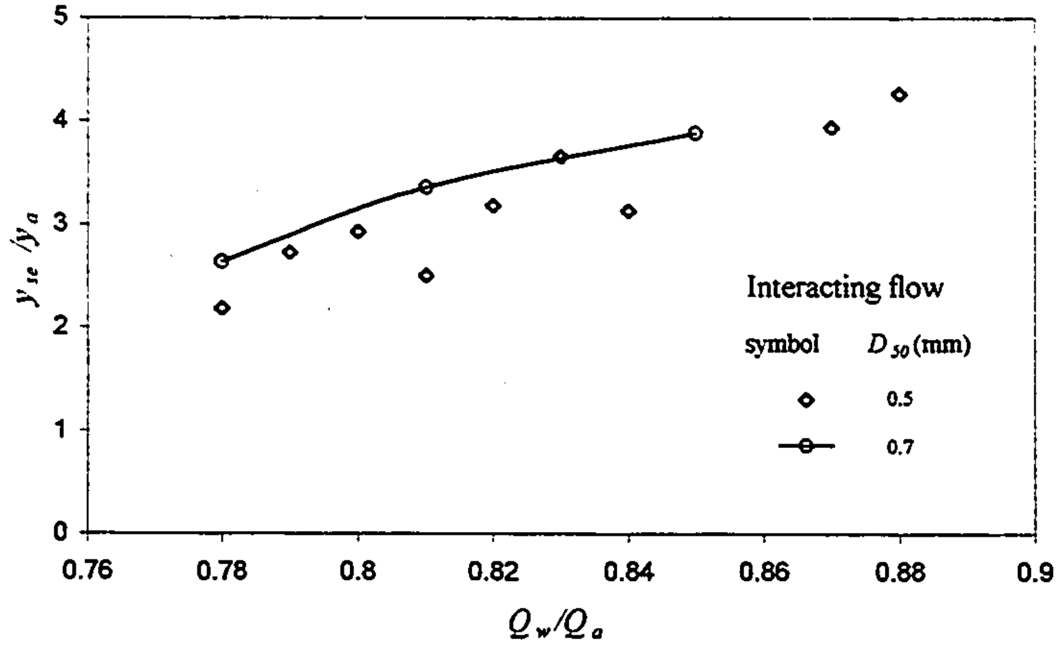

Figure 6.102- Relative scour depth with discharge ratio, SC-abutments

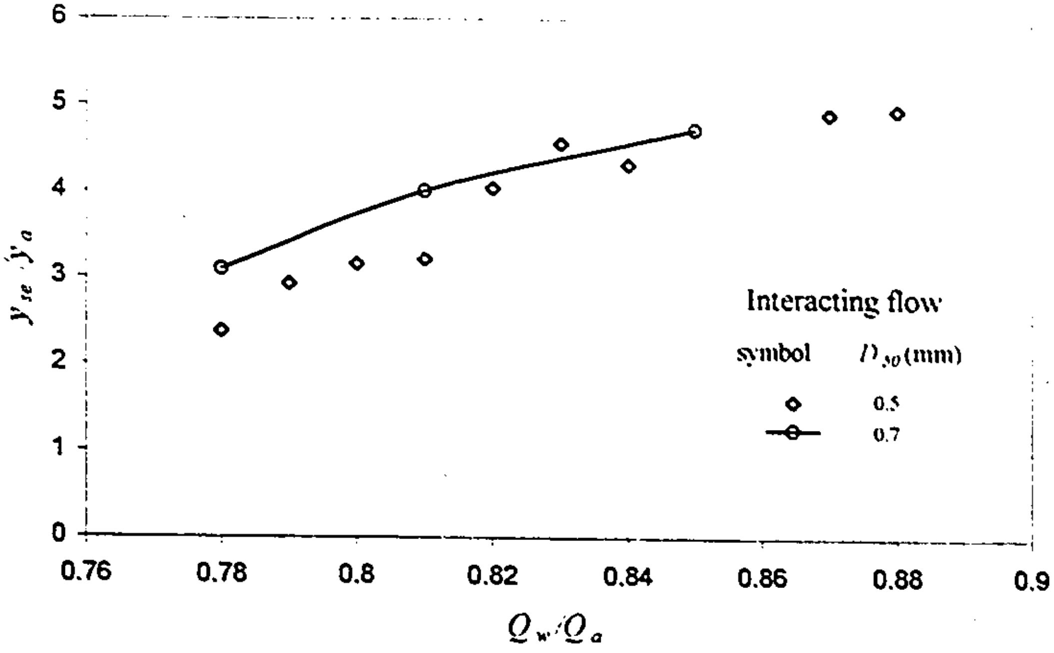

Figure 6.103- Relative scour depth with discharge ratio, VW-abutments

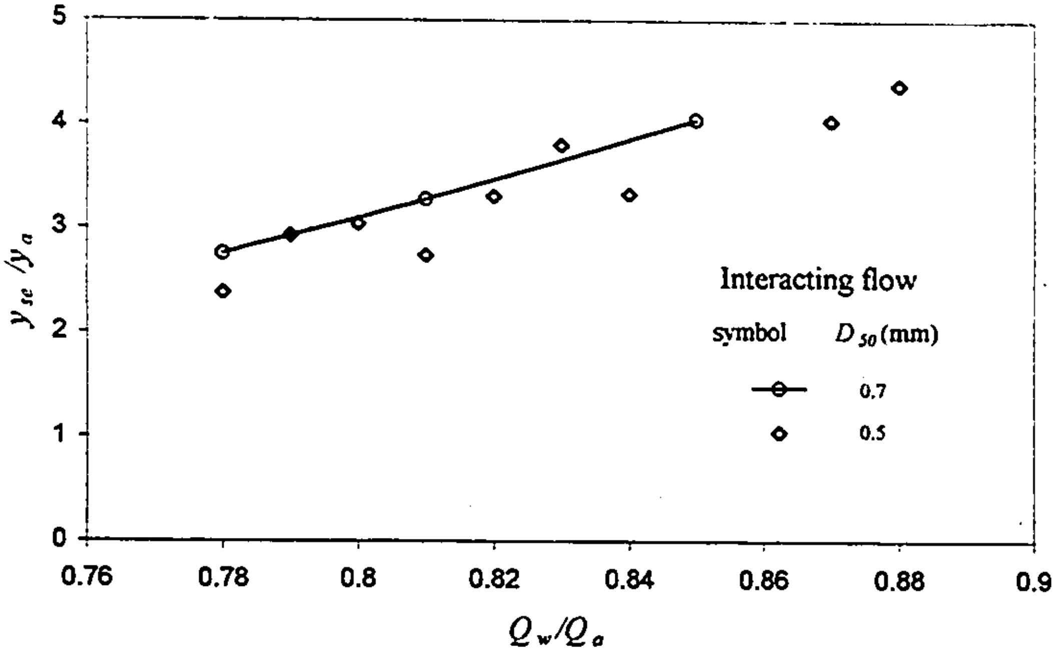

Figure 6.104- Relative scour depth with discharge ratio, WW-abutments

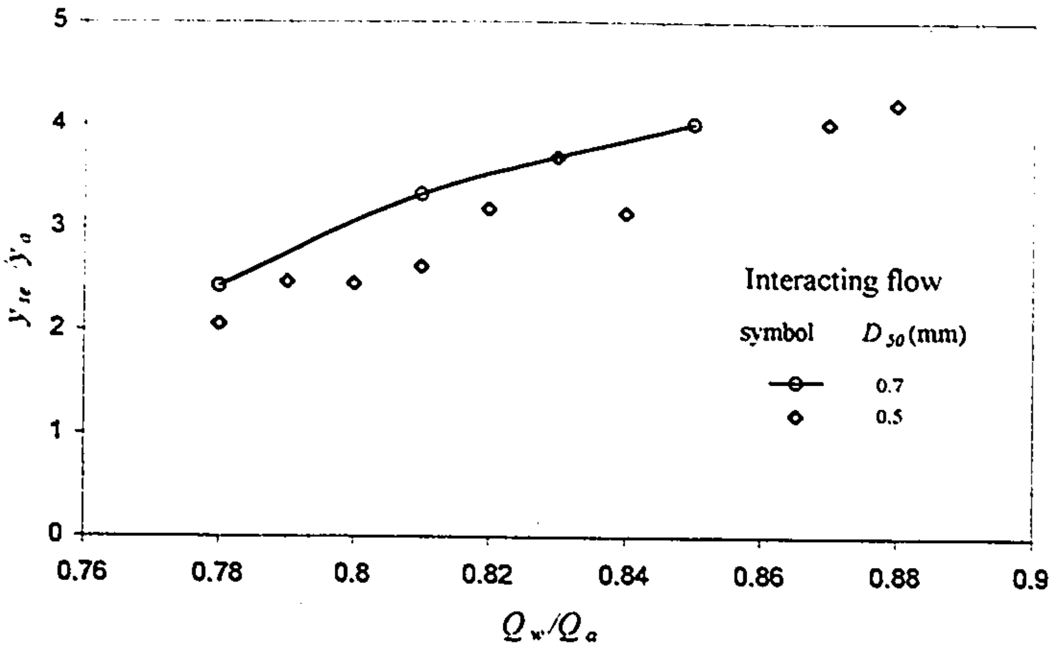

Figure 6.105- Relative scour depth with discharge ratio, ST-abutments

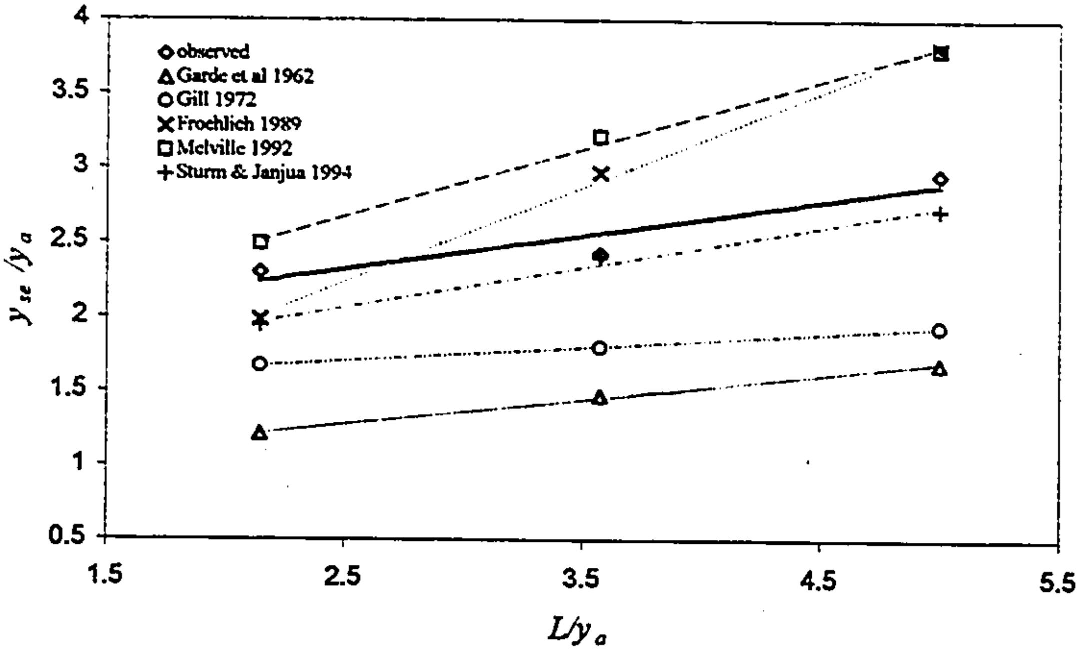

Figure 6.106- Observed and predicted y_{se}/y_a for SC-abutments and y_a/H=0.29

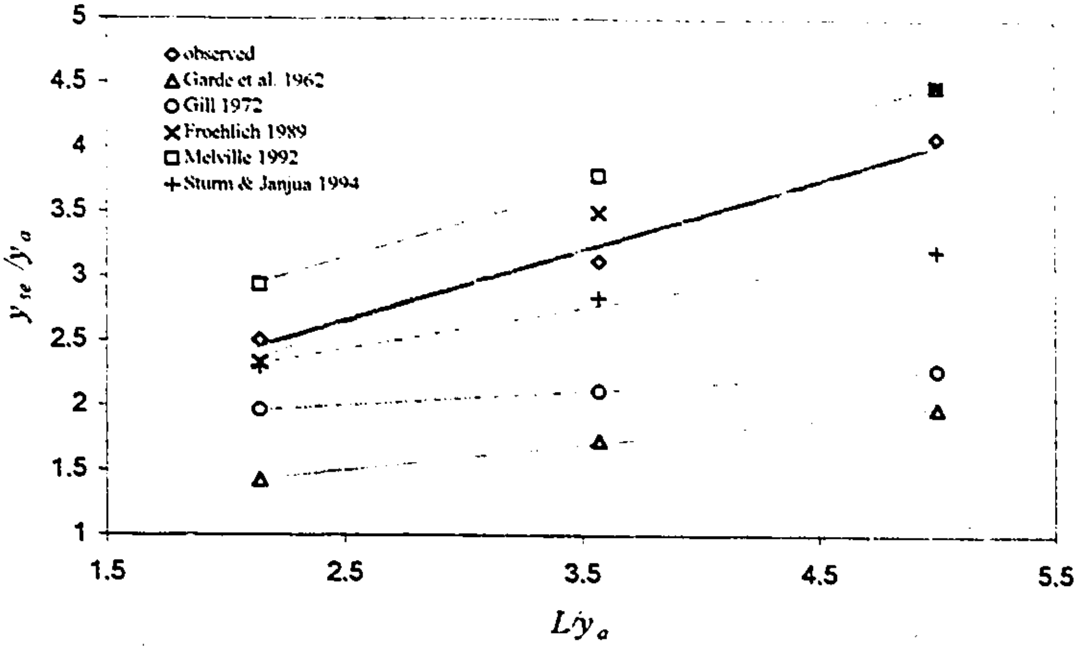

Figure 6.107- Observed and predicted y_{se}/y_a for VW-abutments and y_a/H=0.29

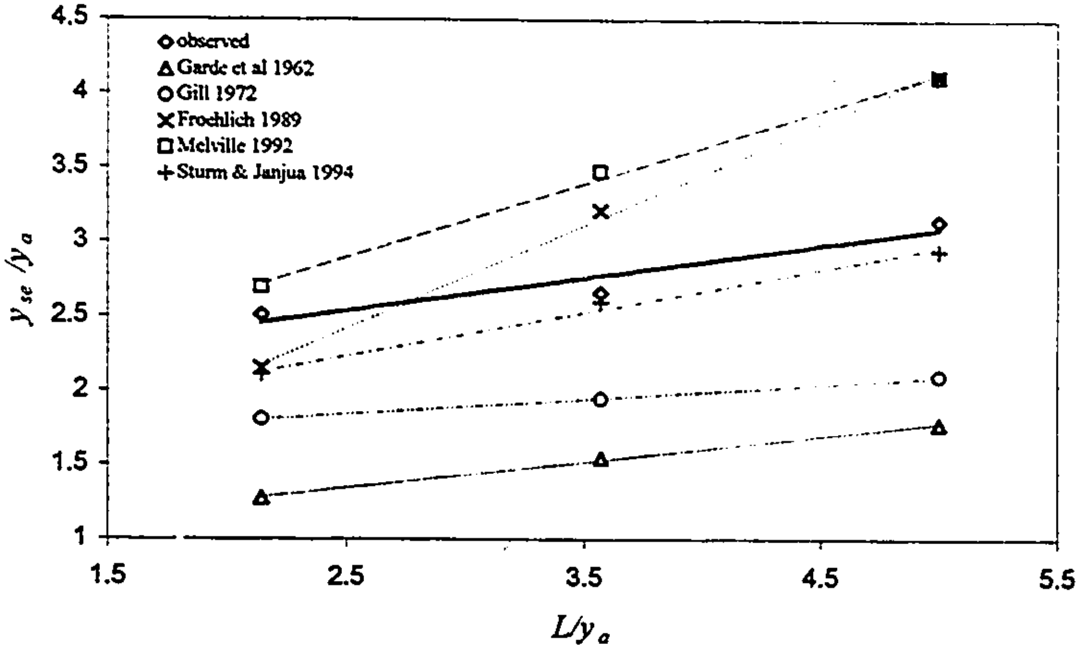

Figure 6.108- Observed and predicted y_{se}/y_a for WW-abutments and y_a/H=0.29

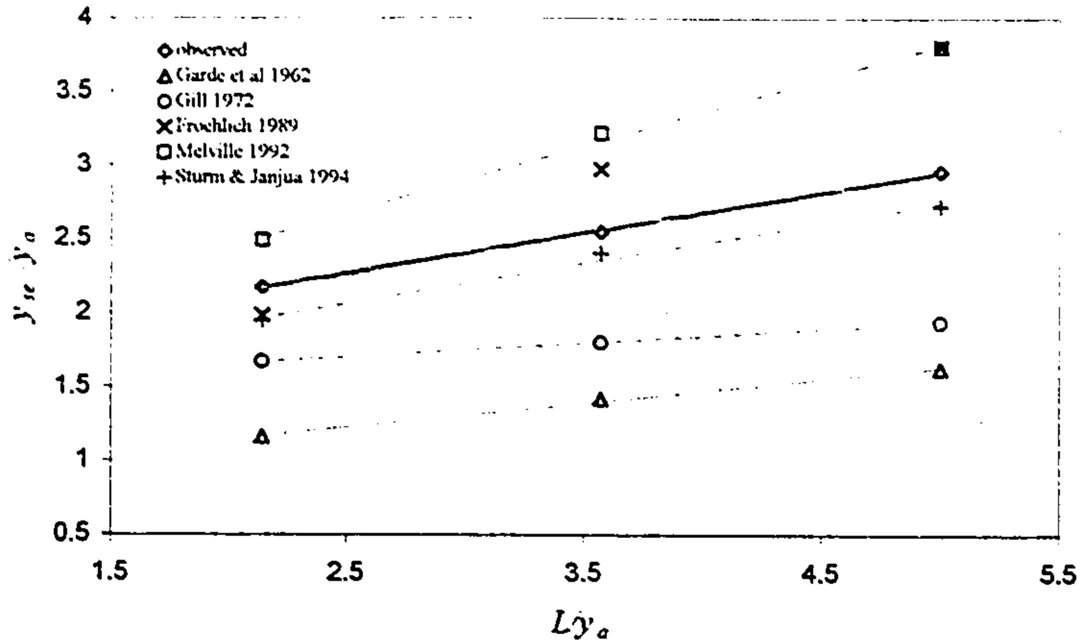

Figure 6.109- Observed and predicted y_{se}/y_a for ST-abutments and y_a/H=0.29

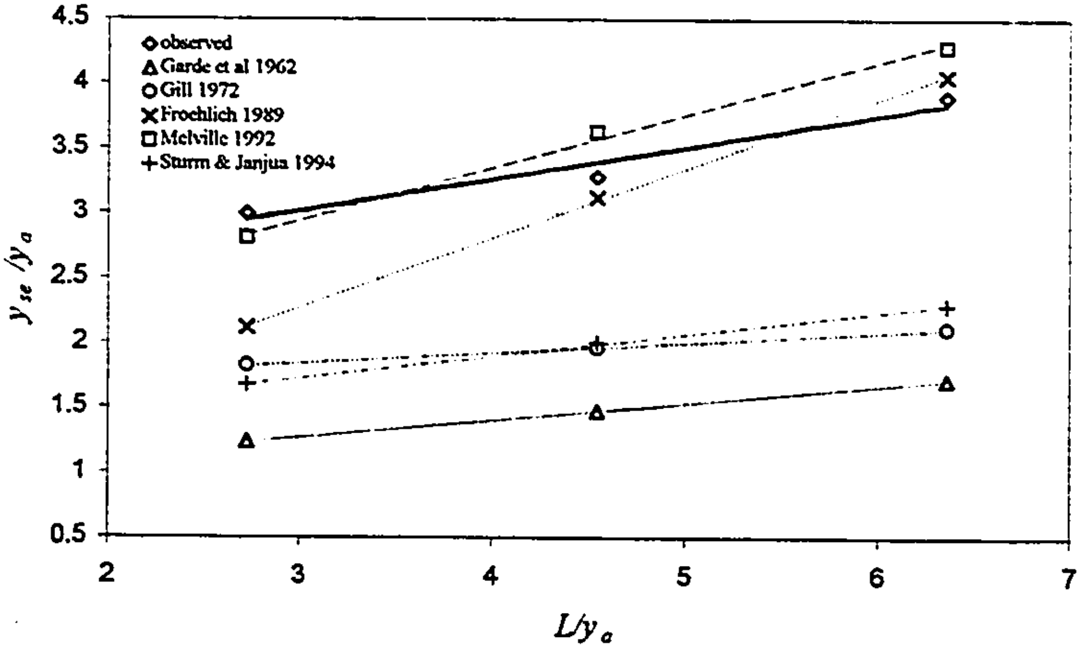

Figure 6.110- Observed and predicted y_{se}/y_a for SC-abutments and y_a/H=0.24

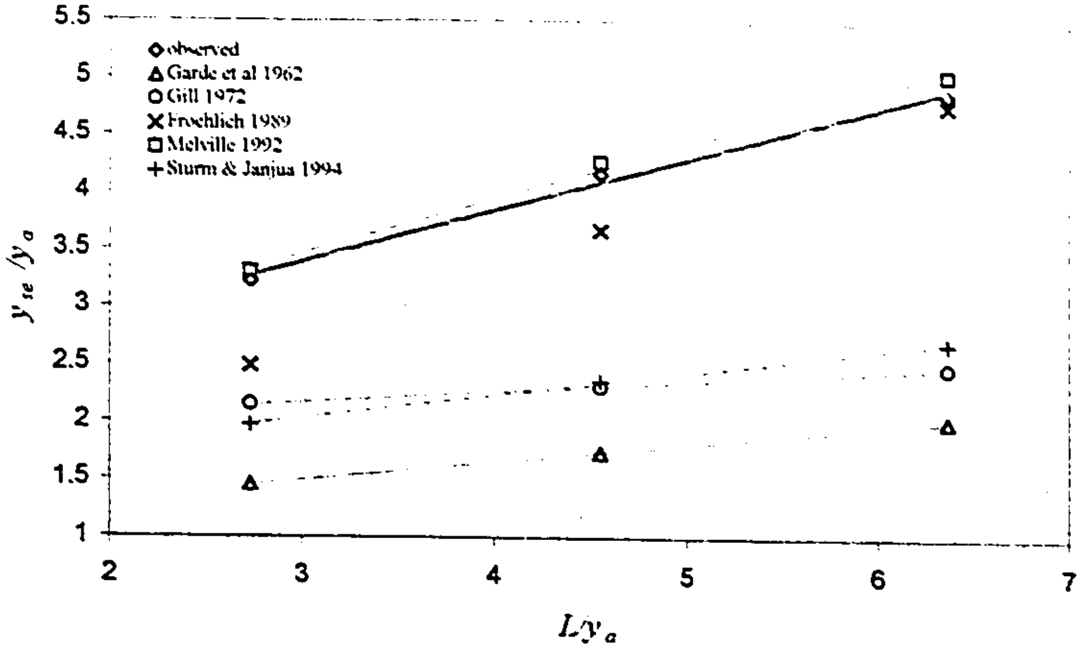

Figure 6.111- Observed and predicted y_{se}/y_a for VW-abutments and y_a/H=0.24

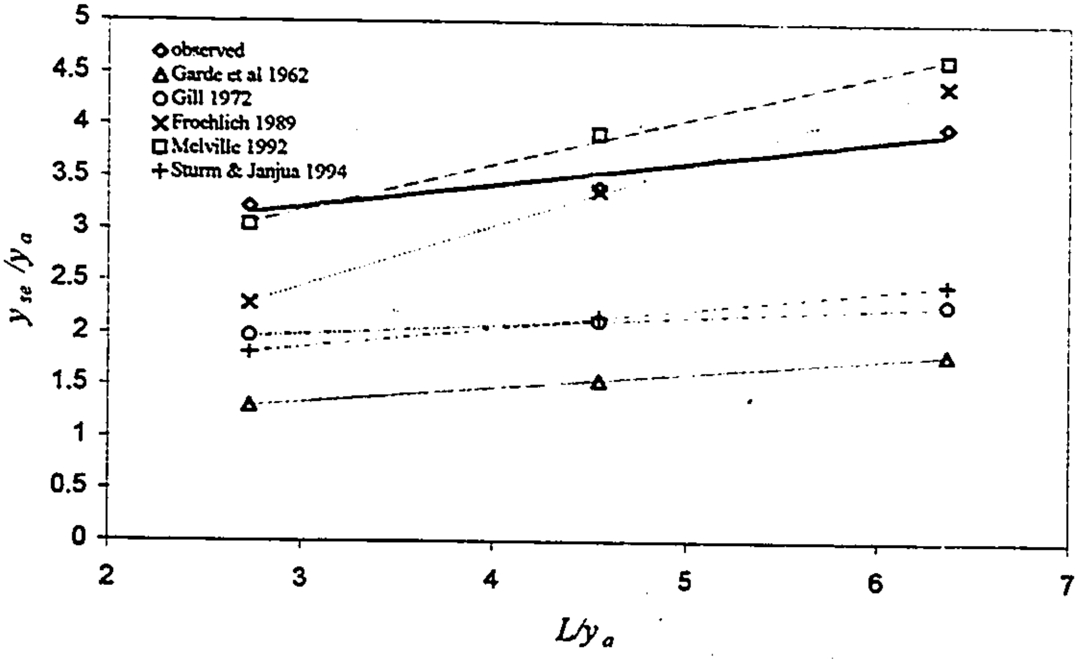

Figure 6.112- Observed and predicted y_{se}/y_a for WW-abutments and y_a/H=0.24

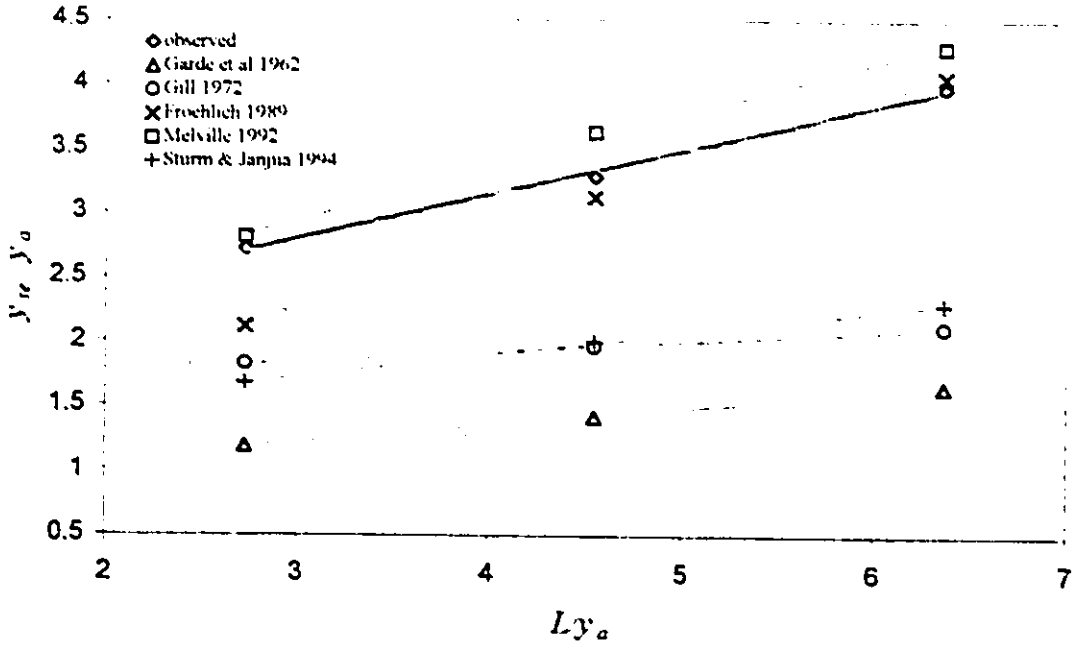

Figure 6.113- Observed and predicted y_{se}/y_a for ST-abutments and y_a/H=0.24

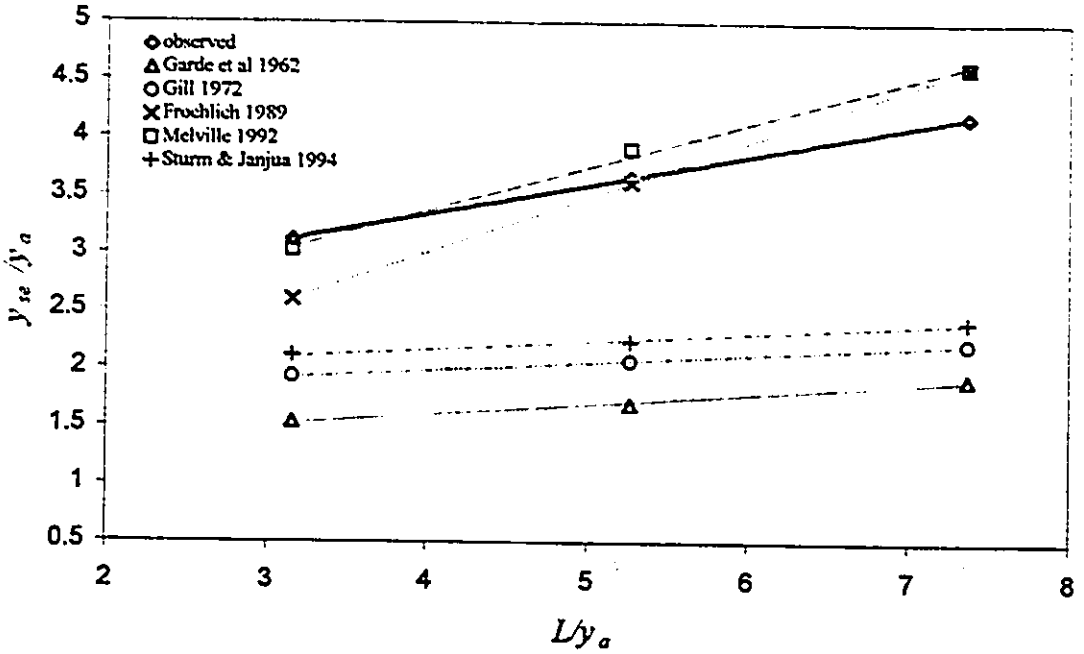

Figure 6.114- Observed and predicted y_{se}/y_a for SC-abutments and y_a/H=0.21

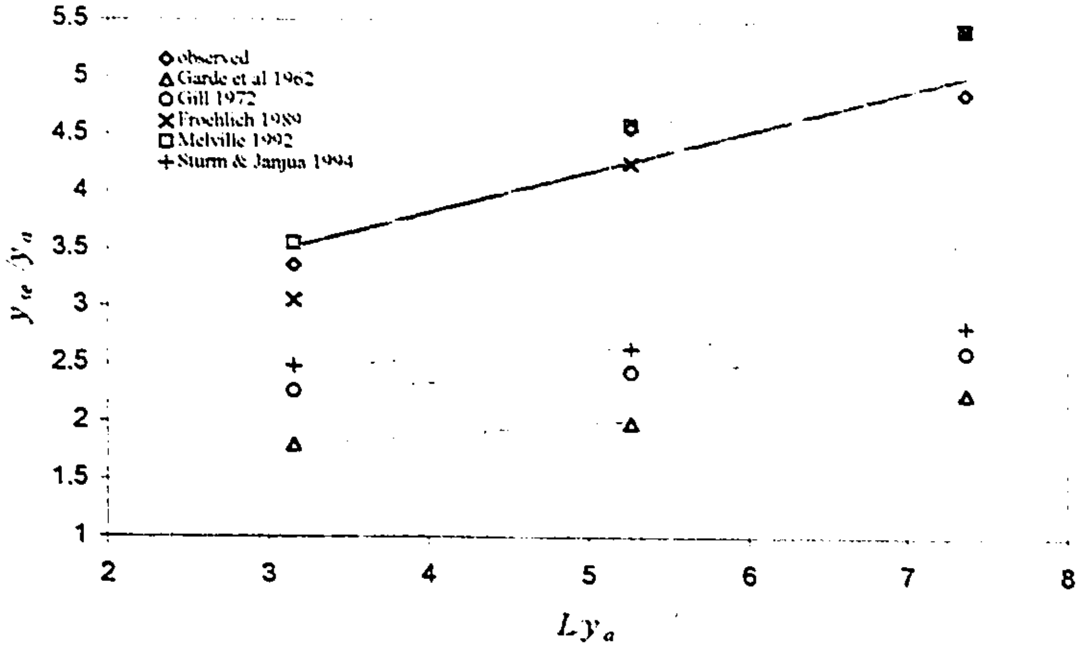

Figure 6.115- Observed and predicted y_{se}/y_a for VW-abutments and y_a/H=0.21

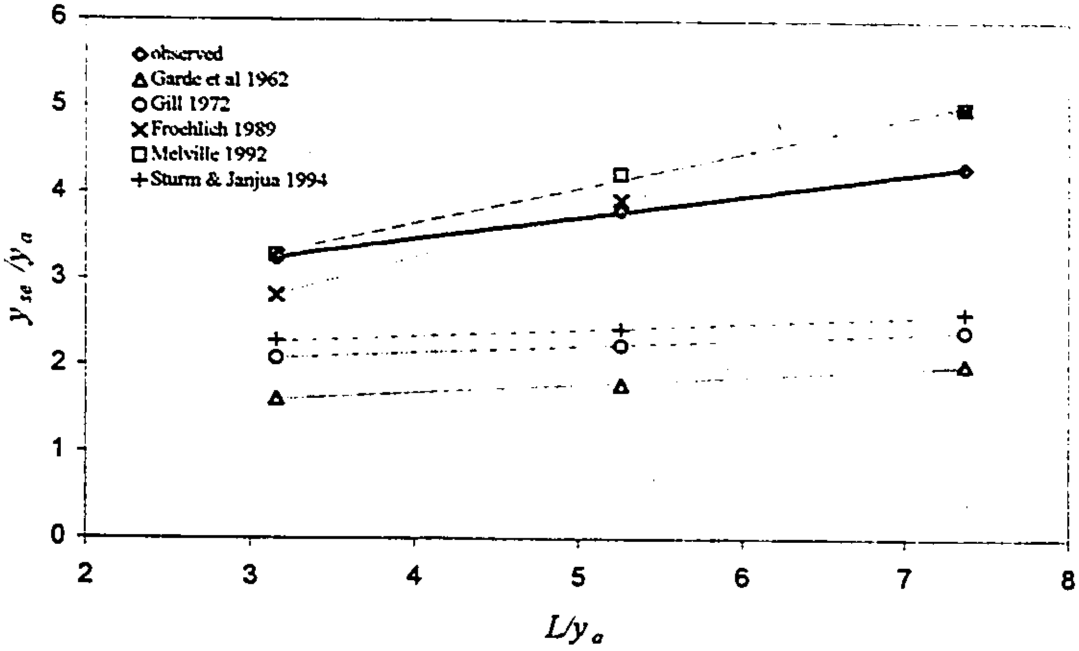

Figure 6.116- Observed and predicted y_{se}/y_a for WW-abutments and y_a/H=0.21

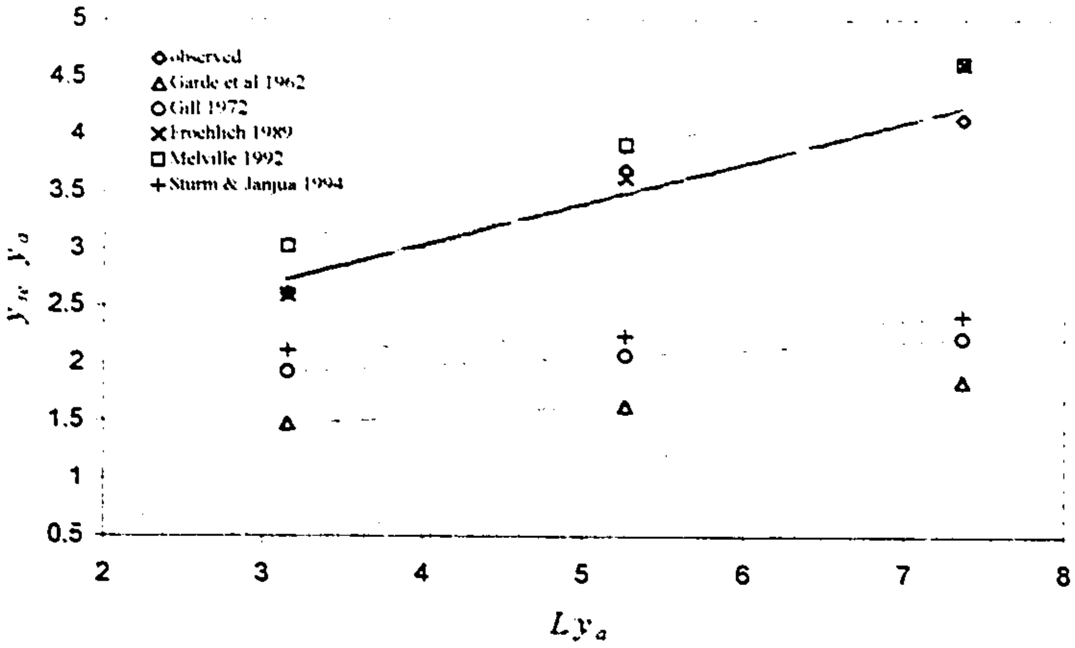

Figure 6.117- Observed and predicted y_{se}/y_a for ST-abutments and y_a/H=0.21

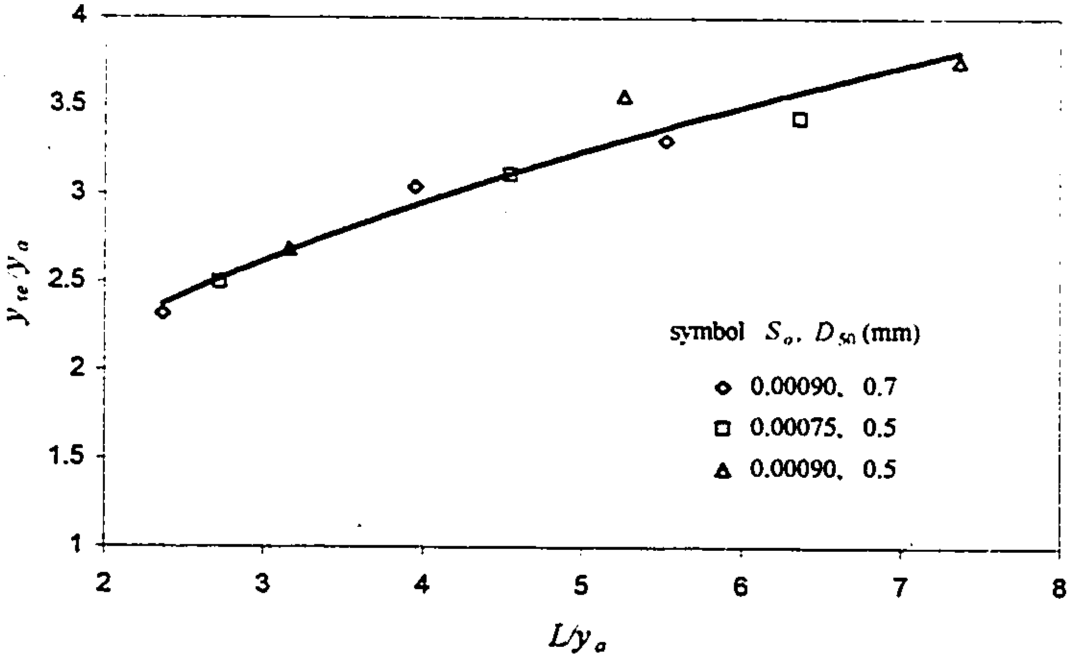

Figure 6.118- y_{se}/y_a vs. L/y_a for non-interacting flow, SC-abutments

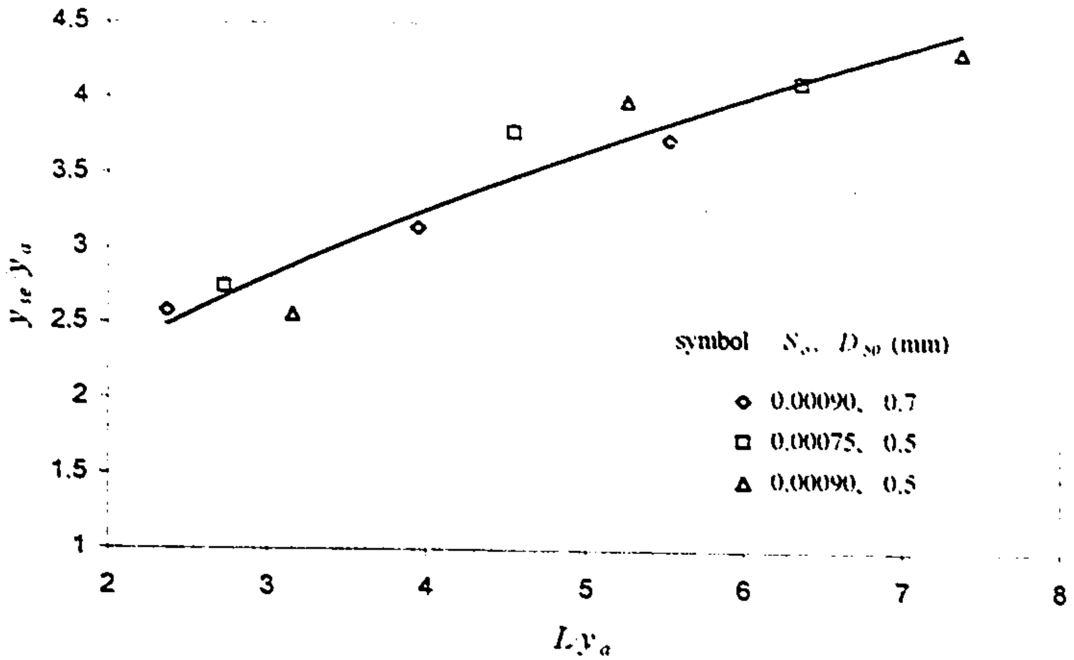

Figure 6.119- y_{se}/y_a vs. L/y_a for non-interacting flow, VW-abutments

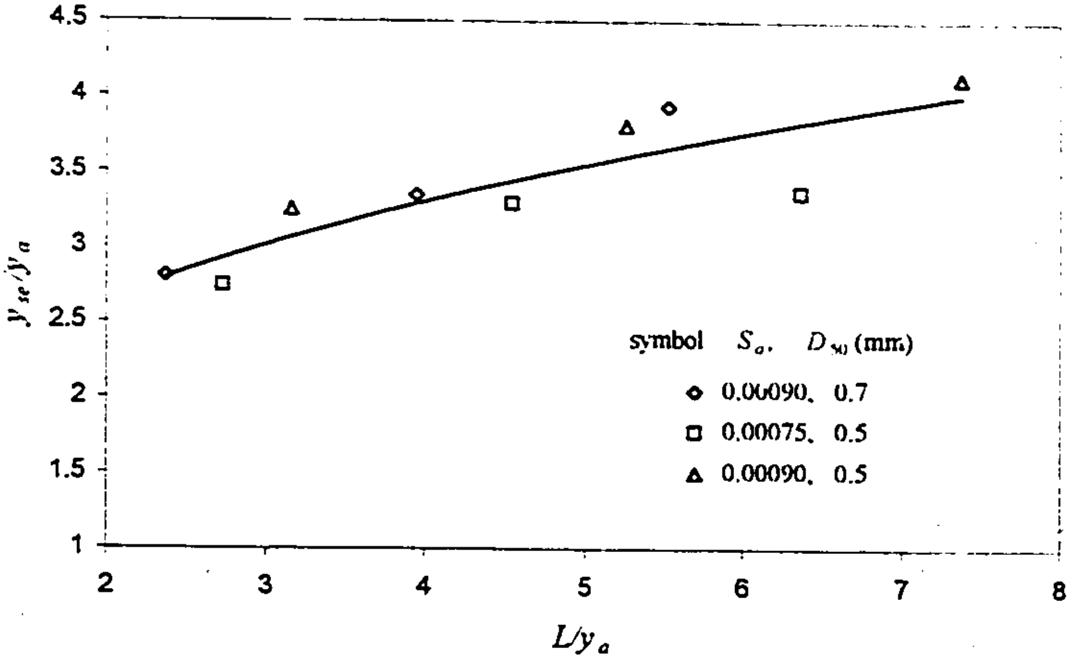

Figure 6.120- y_{se}/y_a vs. L/y_a for non-interacting flow, WW-abutments

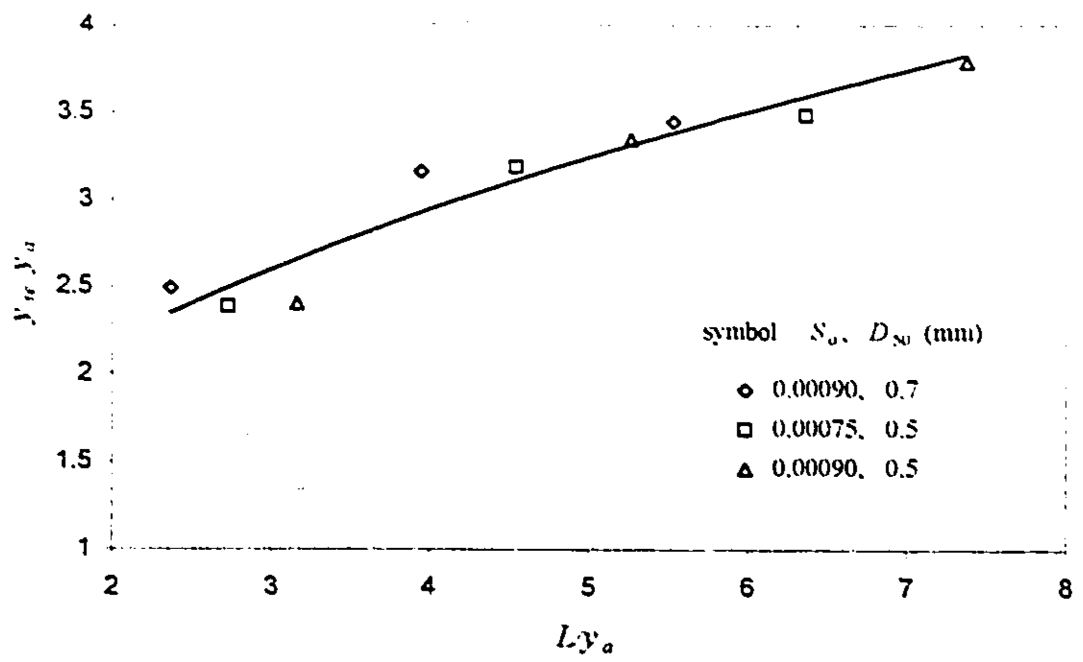

Figure 6.121- y_{se}/y_a vs. L/y_a for non-interacting flow, ST-abutments

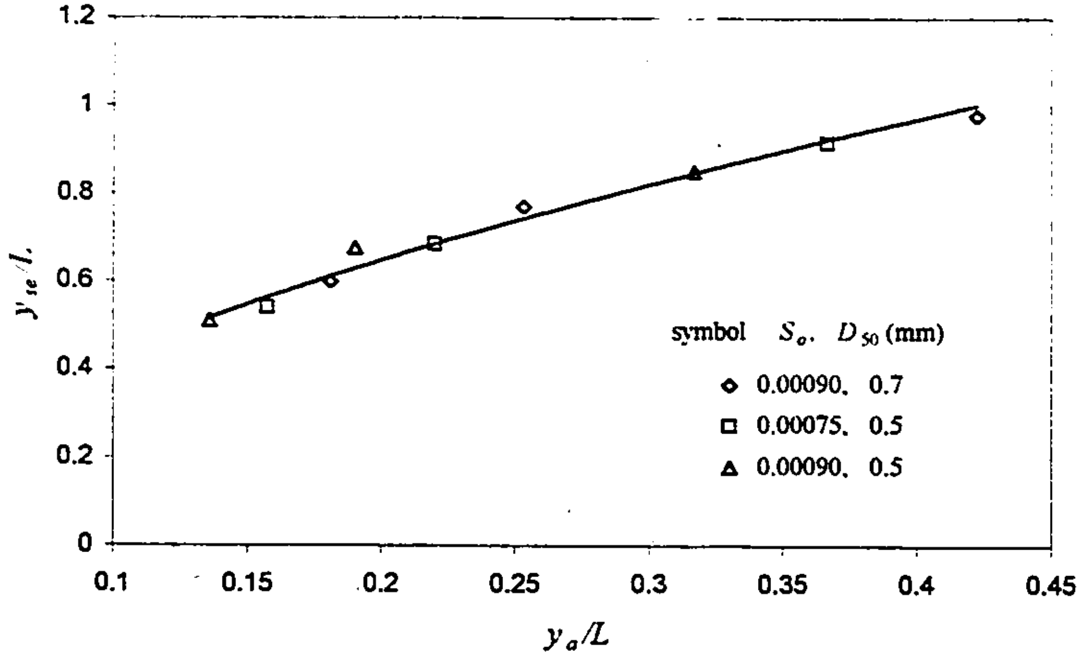

Figure 6.122- y_{se}/L vs. y_a/L for non-interacting flow, SC-abutments

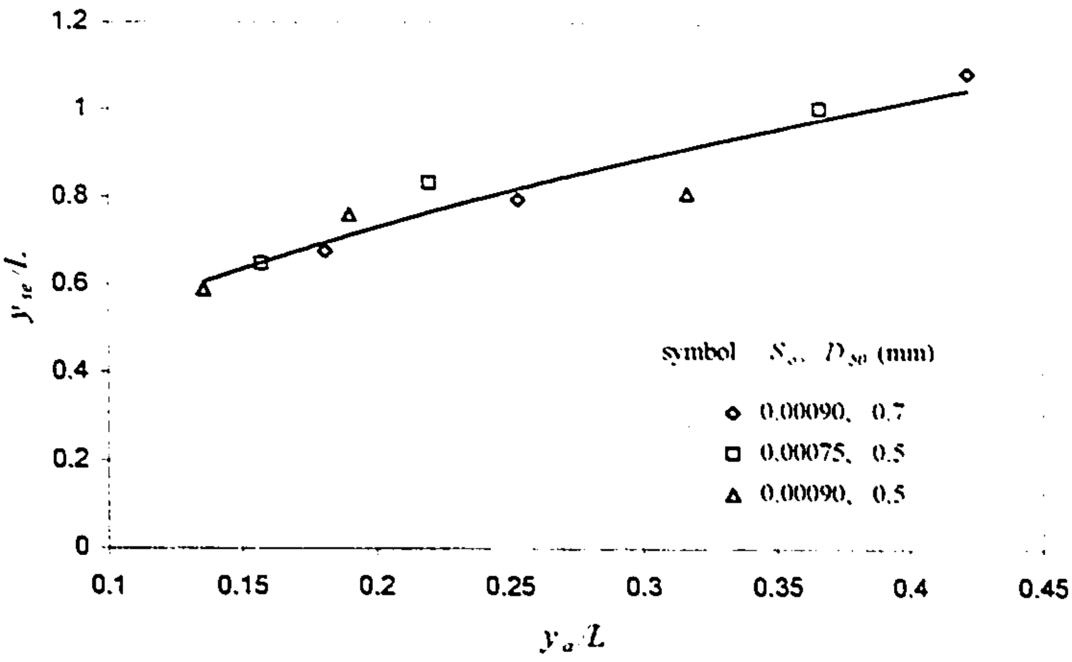

Figure 6.123- y_{se}/L vs. y_a/L for non-interacting flow, VW-abutments

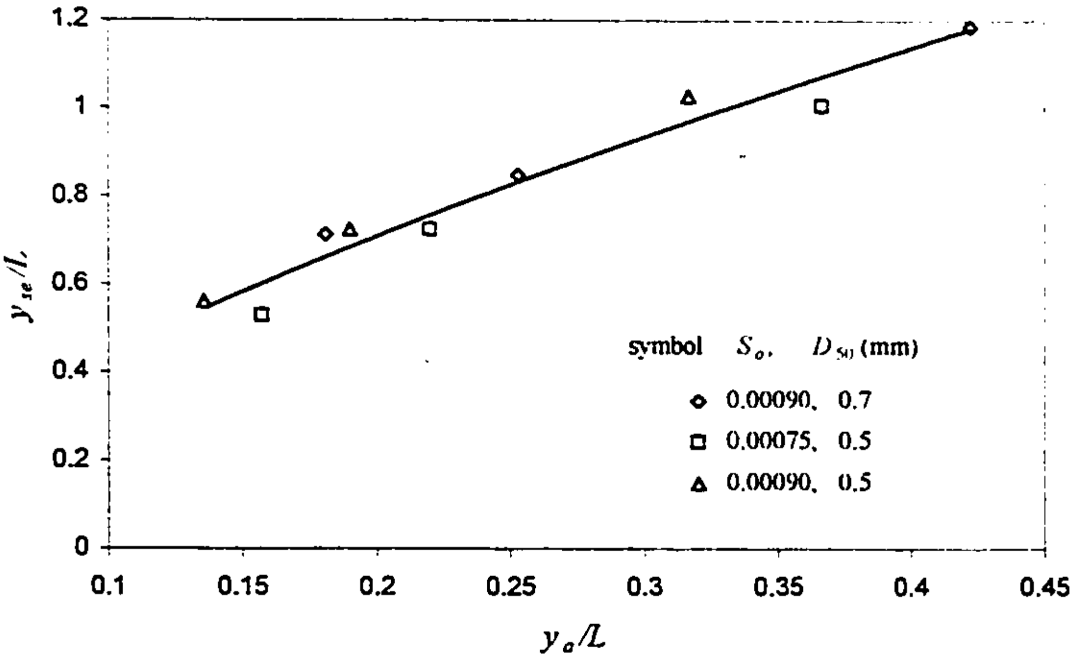

Figure 6.124- y_{se}/L vs. y_a/L for non-interacting flow, WW-abutments

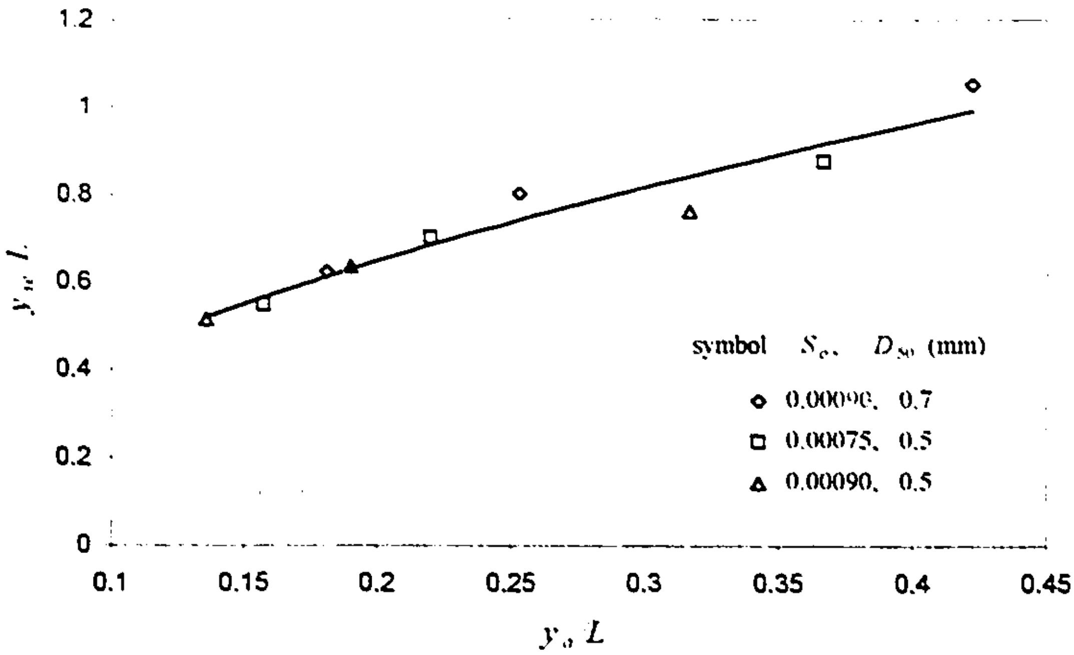

Figure 6.125- y_{se}/L vs. y_a/L for non-interacting flow, ST-abutments

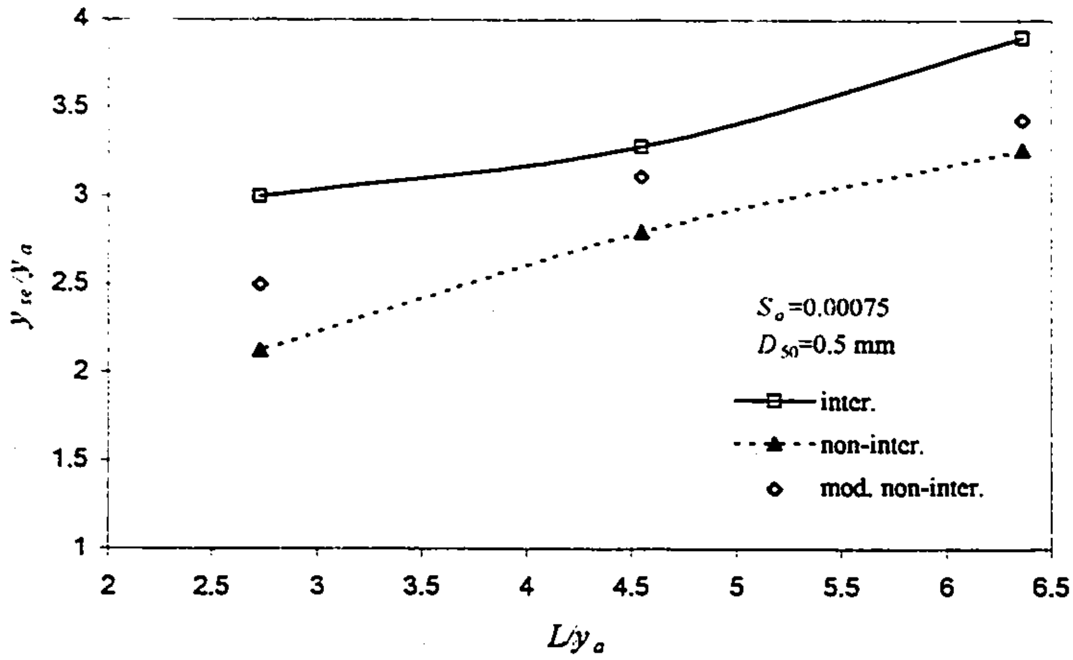

Figure 6.126- y_{se}/y_a vs. L/y_a for interacting and non-interacting flow, SC-abutments

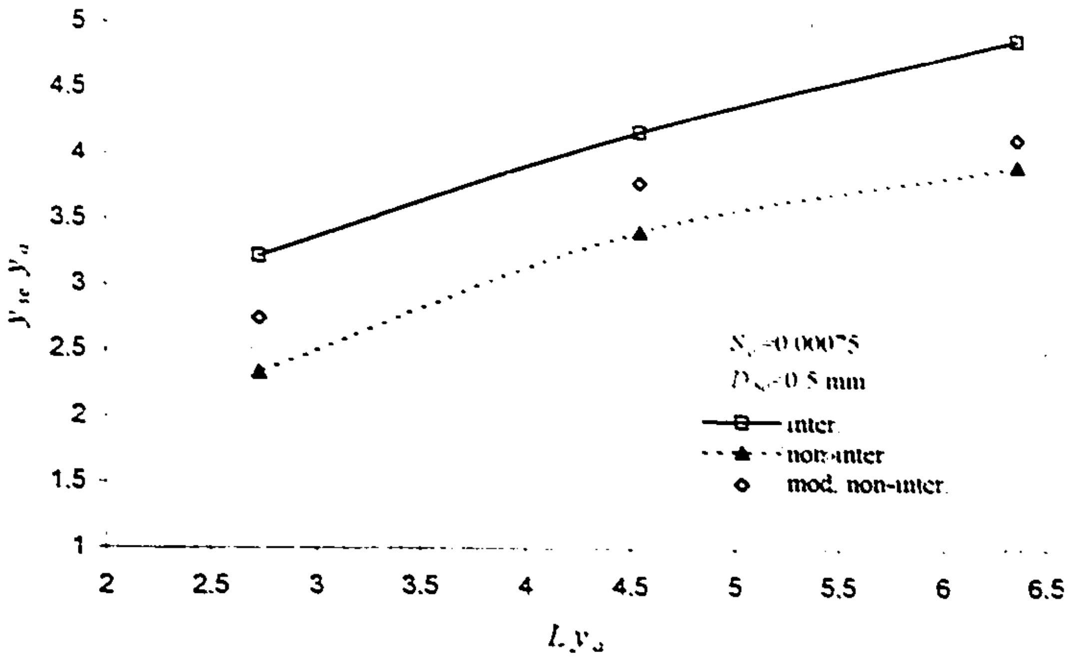

Figure 6.127- y_{se}/y_a vs. L/y_a for interacting and non-interacting flow, VW-abutments

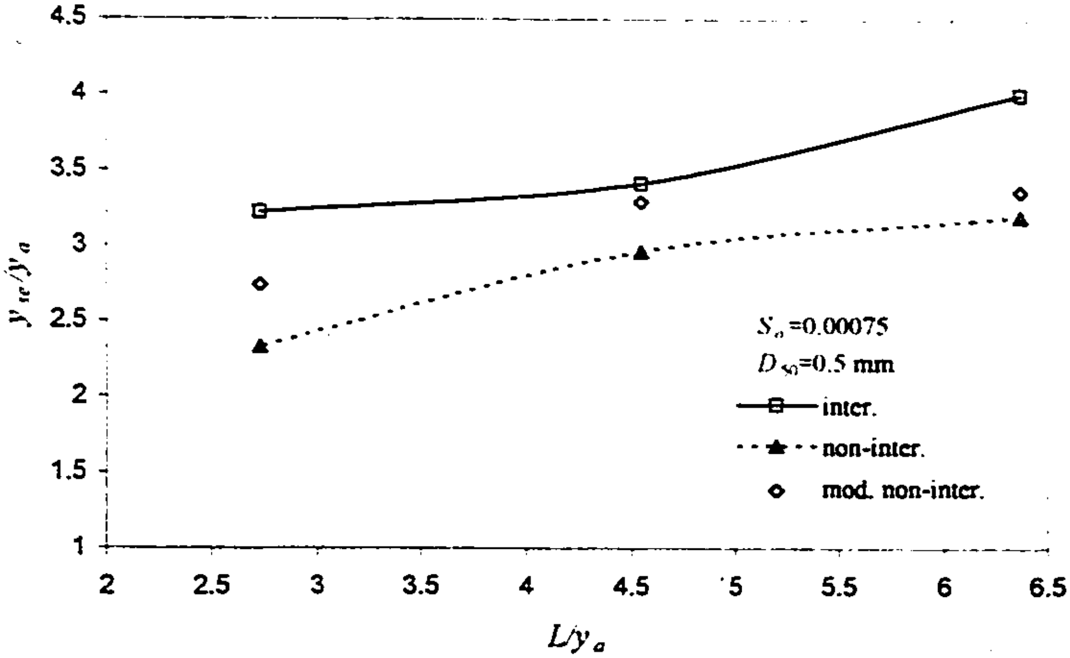

Figure 6.128- y_{se}/y_a vs. L/y_a for interacting and non-interacting flow, WW-abutments

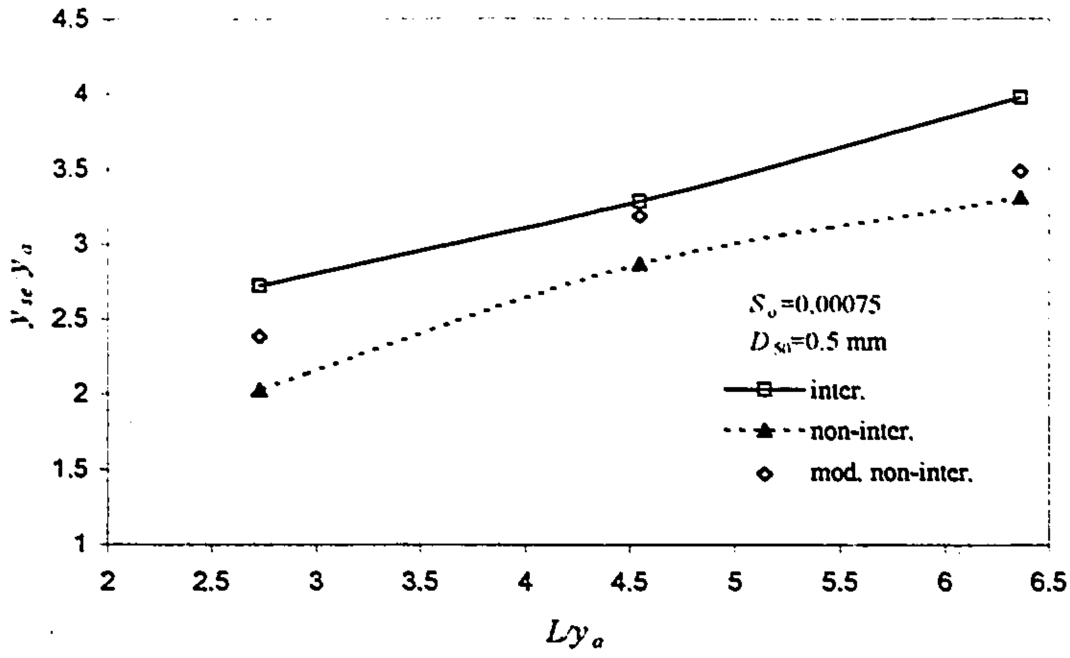

Figure 6.129- y_{se}/y_a vs. L/y_a for interacting and non-interacting flow, ST-abutments

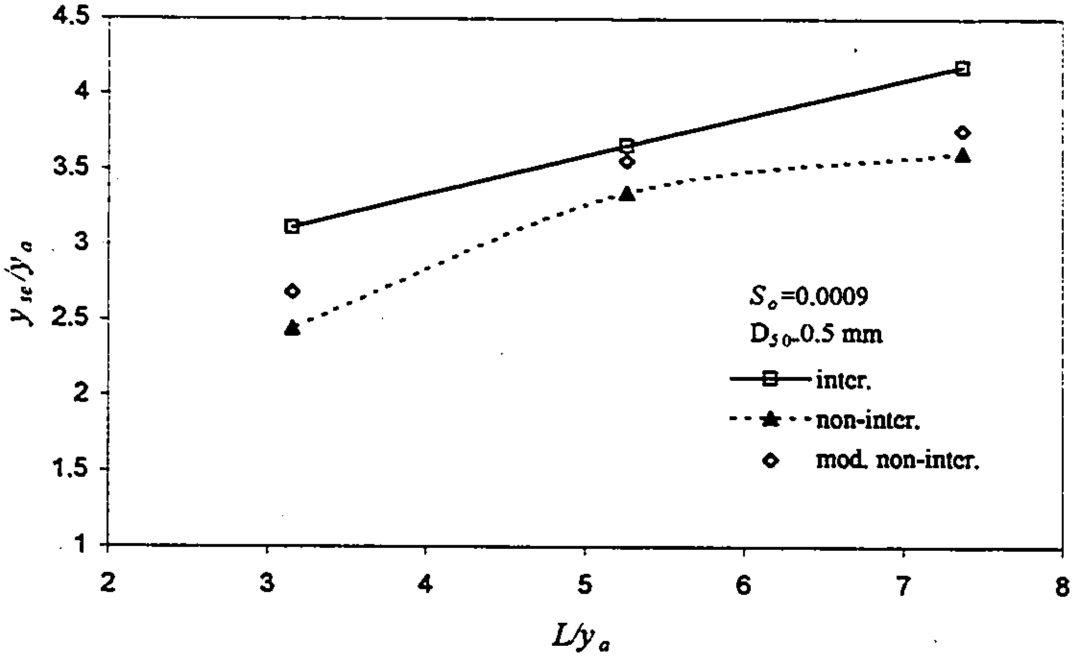

Figure 6.130- y_{se}/y_a vs. L/y_a for interacting and non-interacting flow, SC-abutments

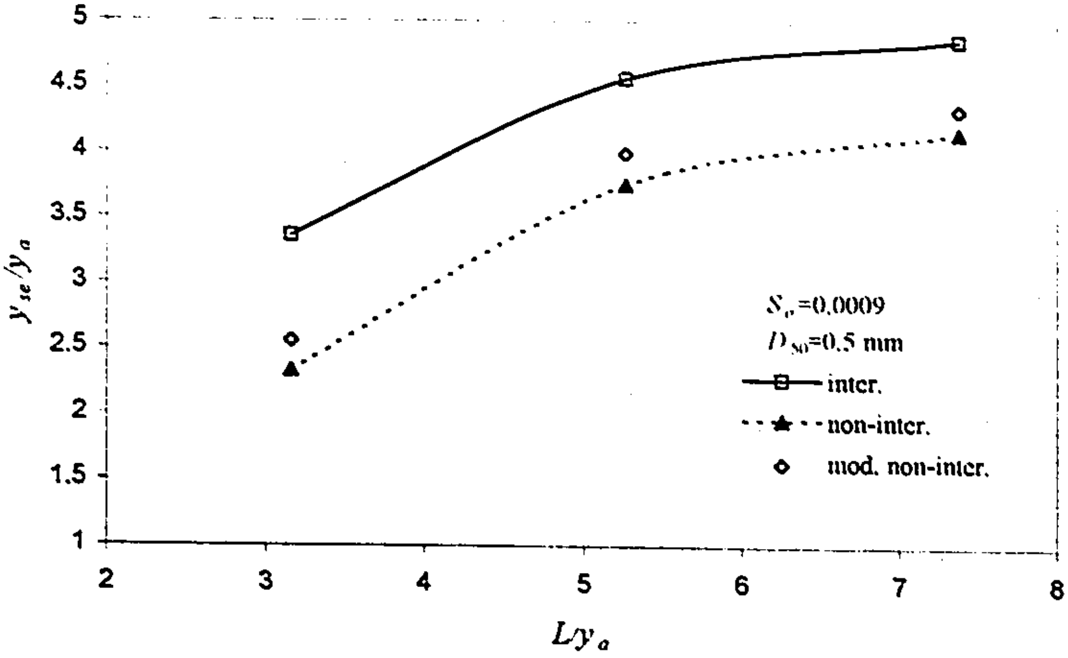

Figure 6.131- y_{se}/y_a vs. L/y_a for interacting and non-interacting flow, VW-abutments

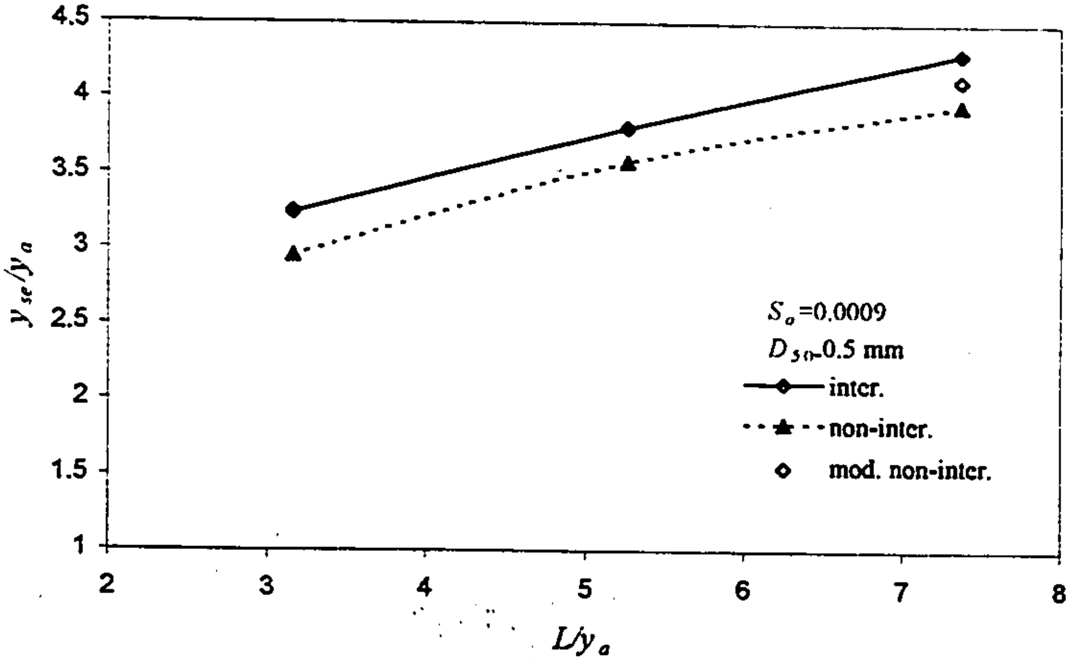

Figure 6.132- y_{se}/y_a vs. L/y_a for interacting and non-interacting flow, WW-abutments

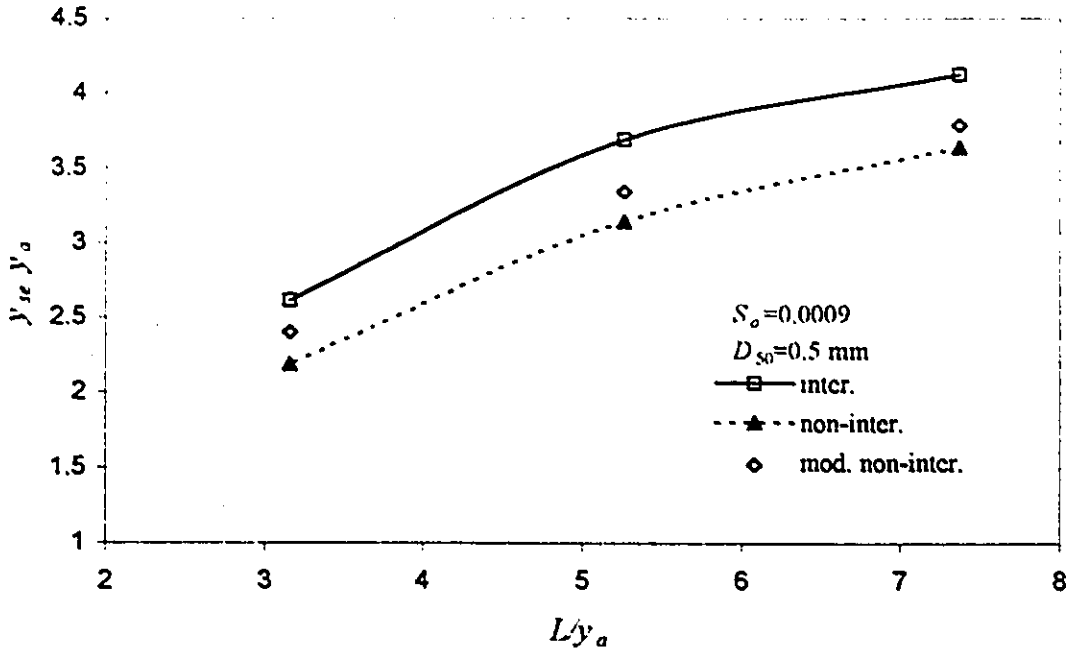

Figure 6.133- y_{se}/y_a vs. L/y_a for interacting and non-interacting flow, ST-abutments

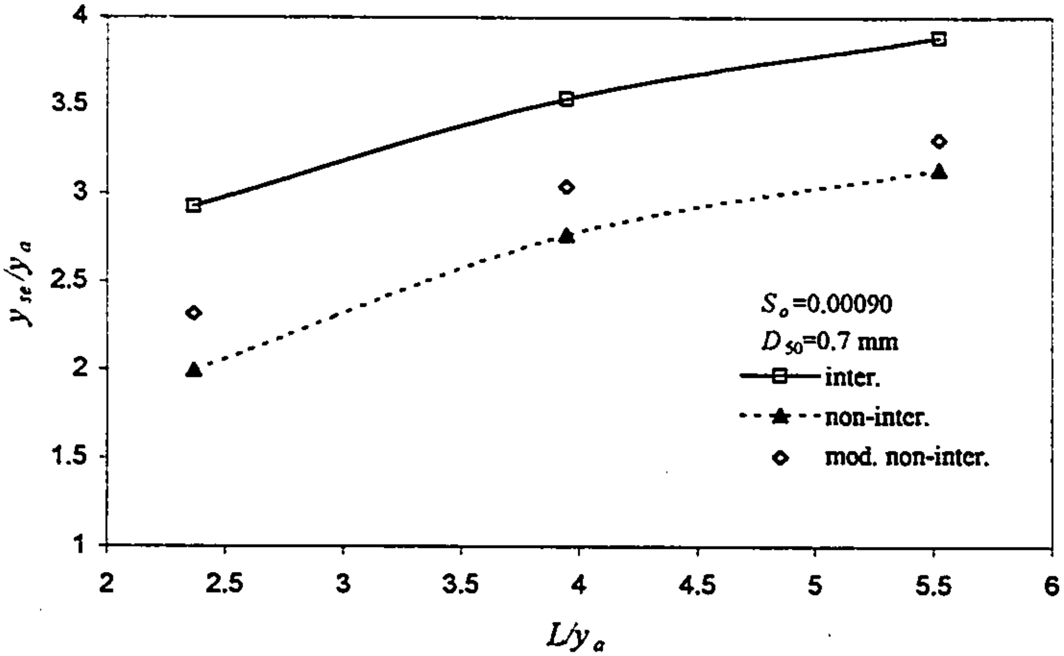

Figure 6.134- y_{se}/y_a vs. L/y_a for interacting and non-interacting flow, SC-abutments

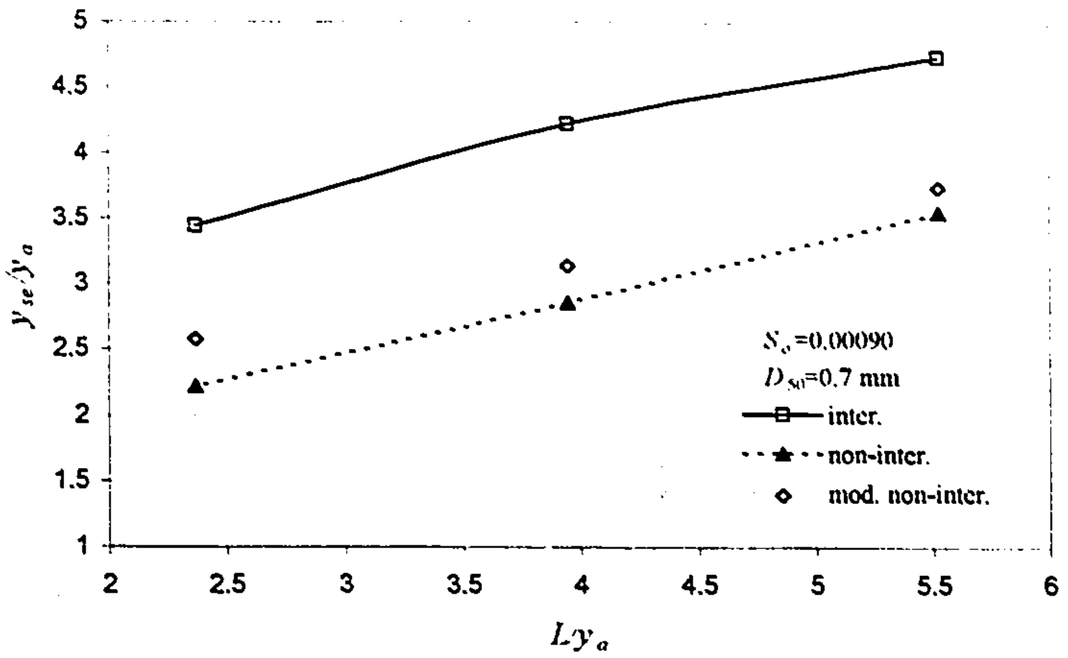

Figure 6.135- y_{se}/y_a vs. L/y_a for interacting and non-interacting flow, VW-abutments

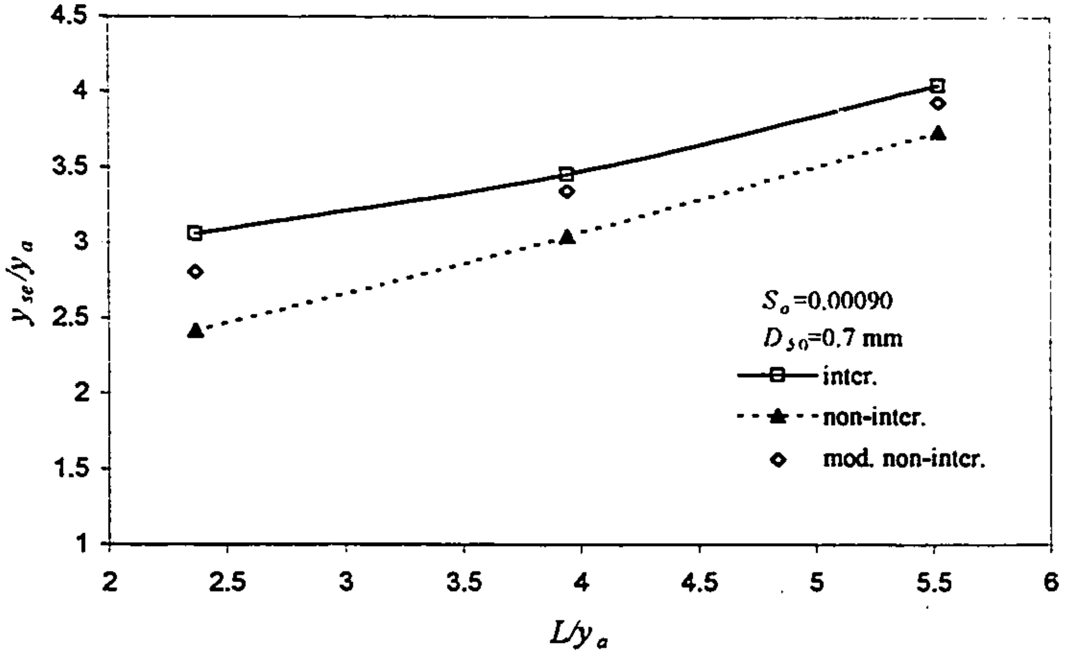

Figure 6.136- y_{se}/y_a vs. L/y_a for interacting and non-interacting flow, WW-abutments

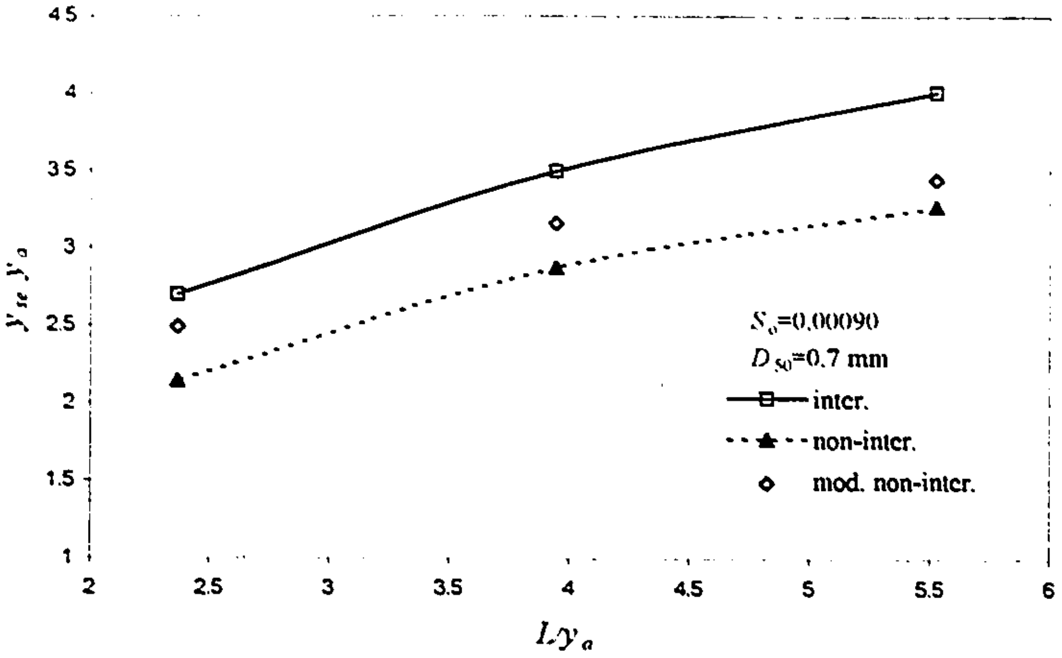

Figure 6.137- y_{se}/y_a vs. L/y_a for interacting and non-interacting flow, ST-abutments

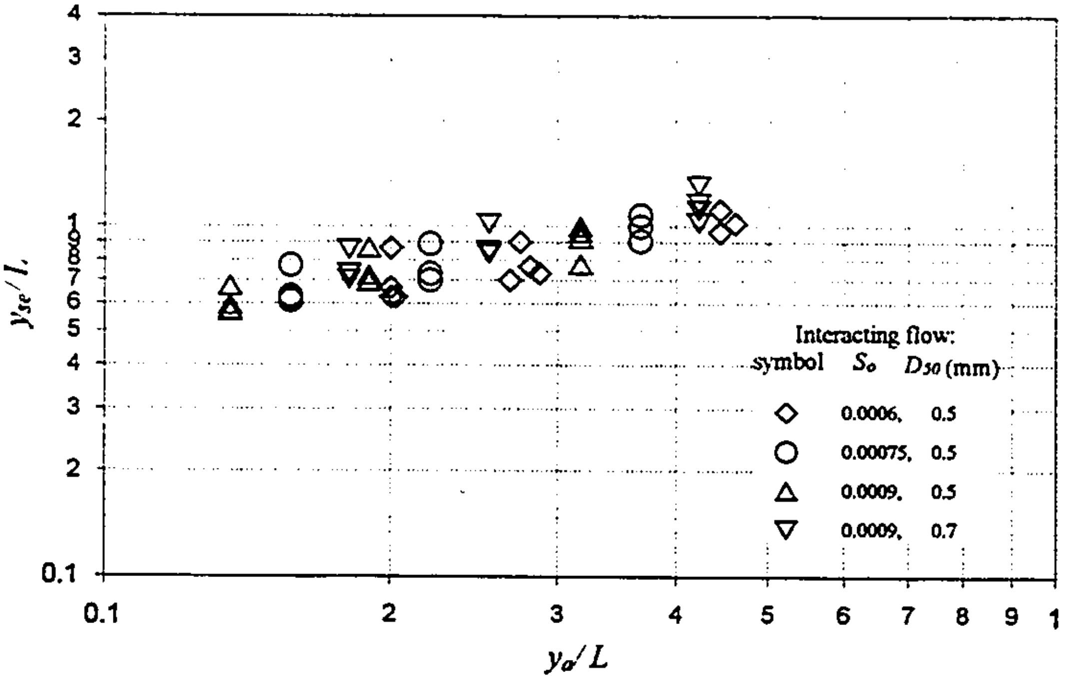

Figure 6.138- Relative scour depth vs. relative flow depth

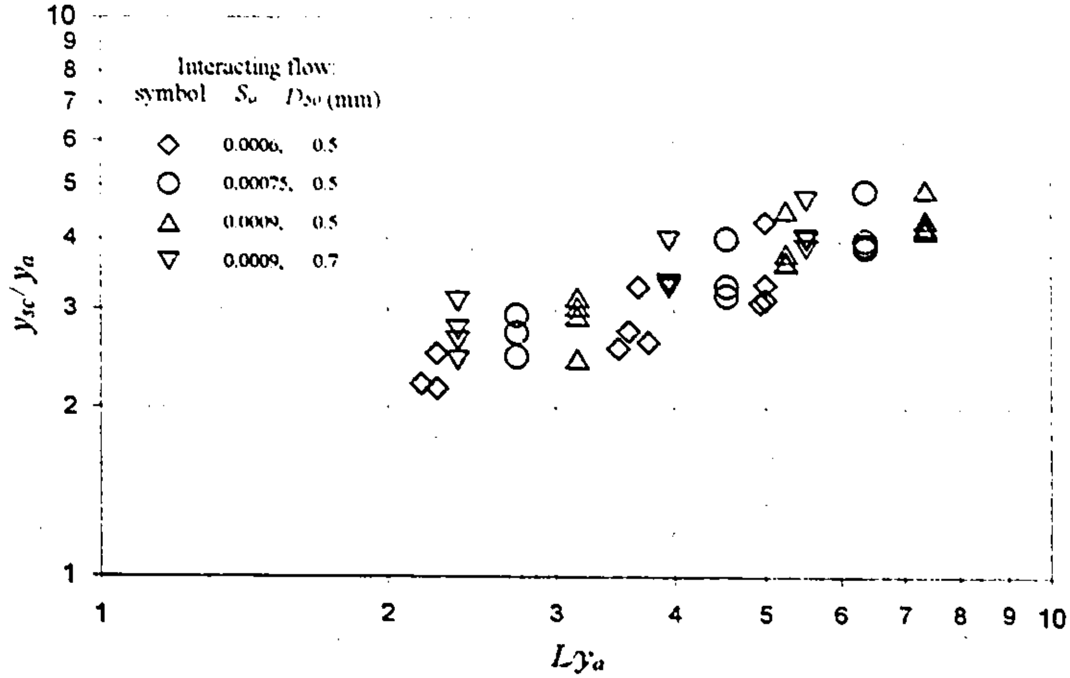

Figure 6.139- Relative scour depth vs. relative flow depth

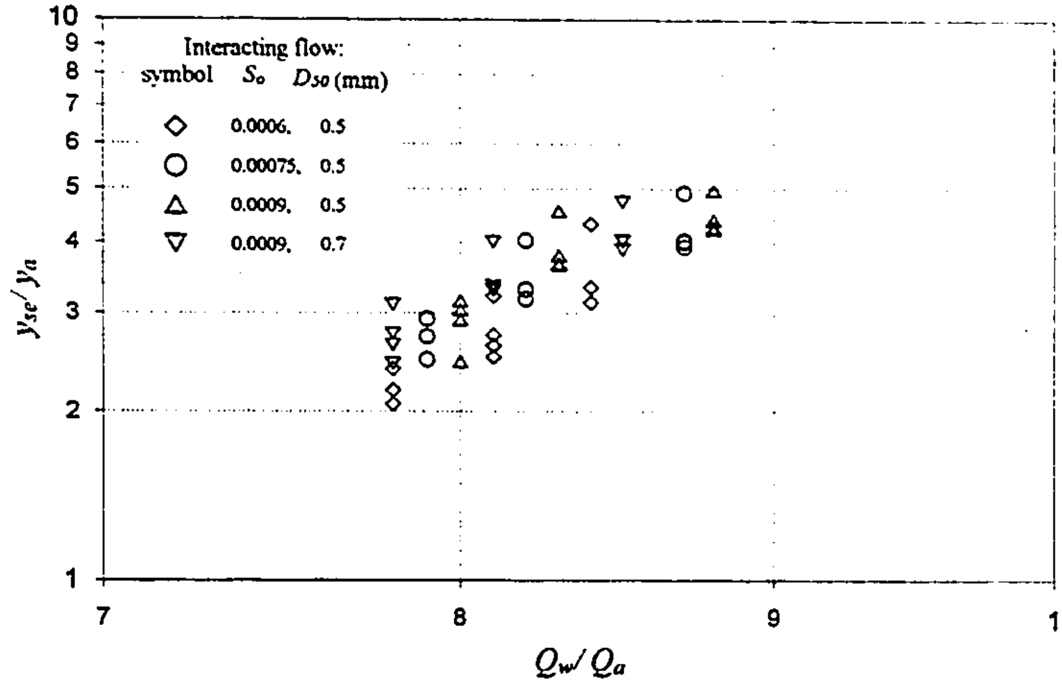

Figure 6.140- Relative scour depth vs. discharge ratio

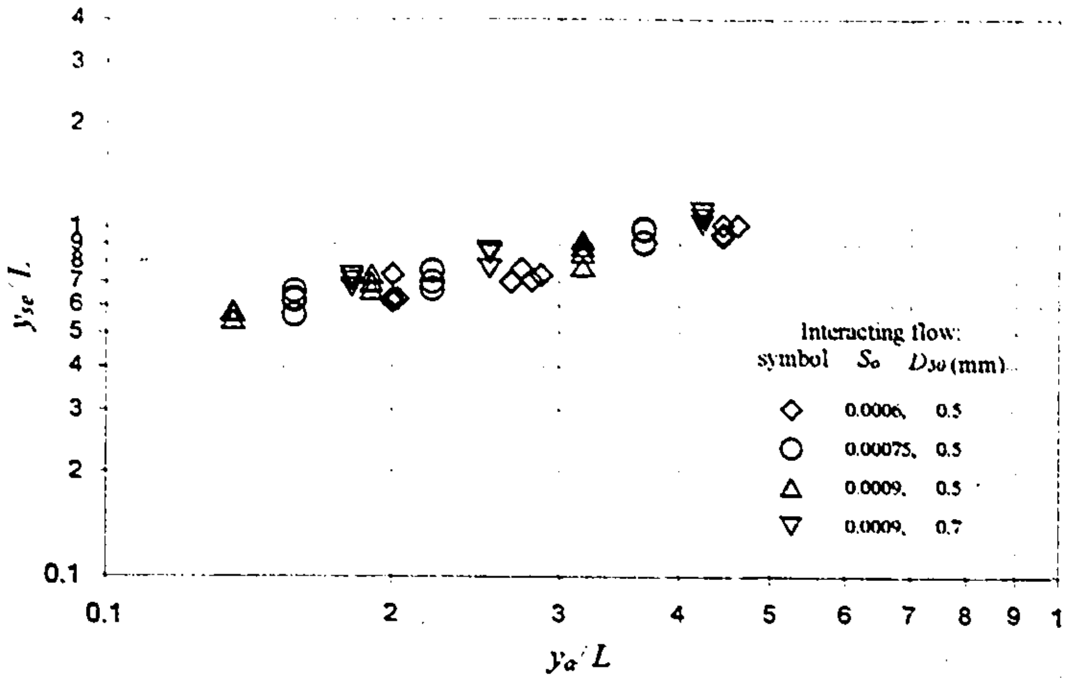

Figure 6.141- Relative scour depth vs. relative flow depth

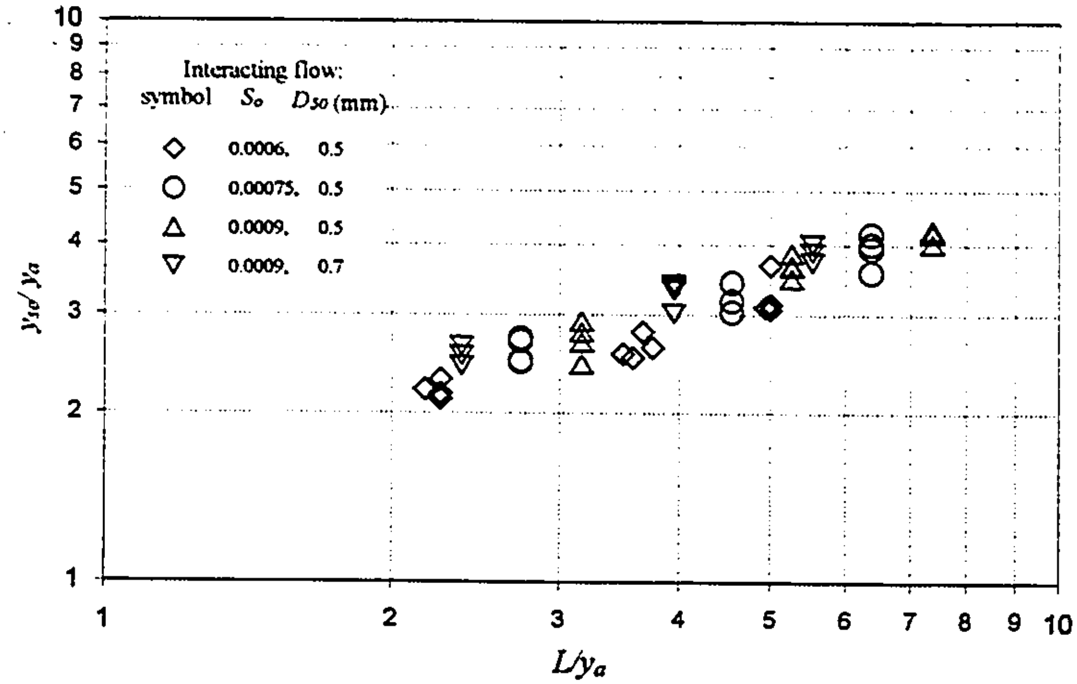

Figure 6.142- Relative scour depth vs. relative flow depth

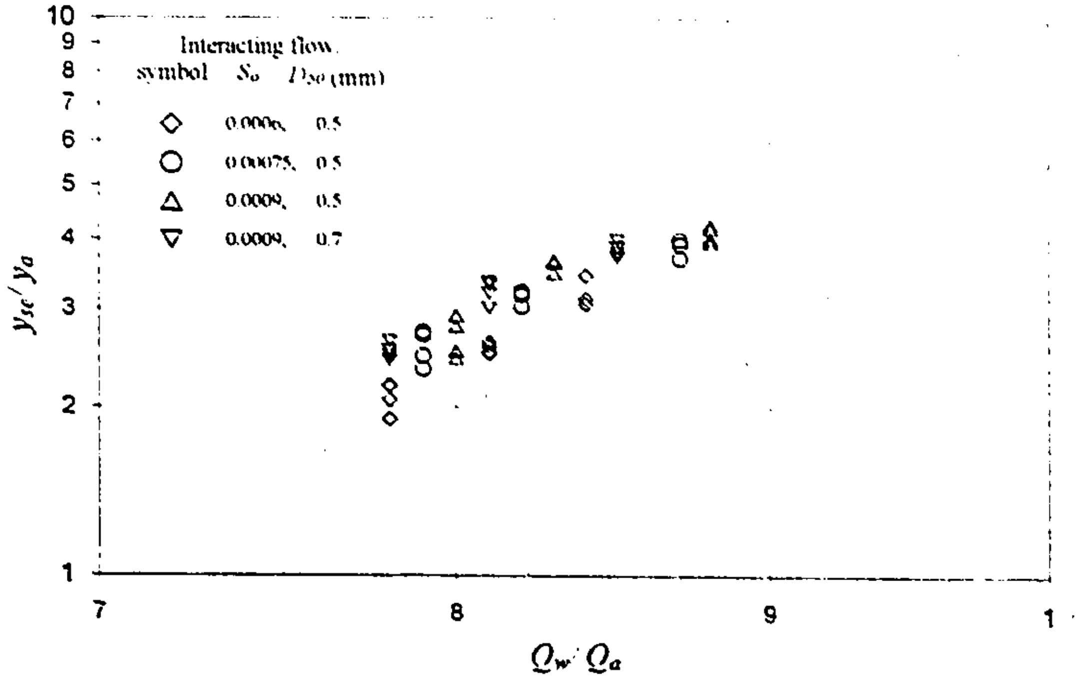

Figure 6.143- Relative scour depth vs. discharge ratio

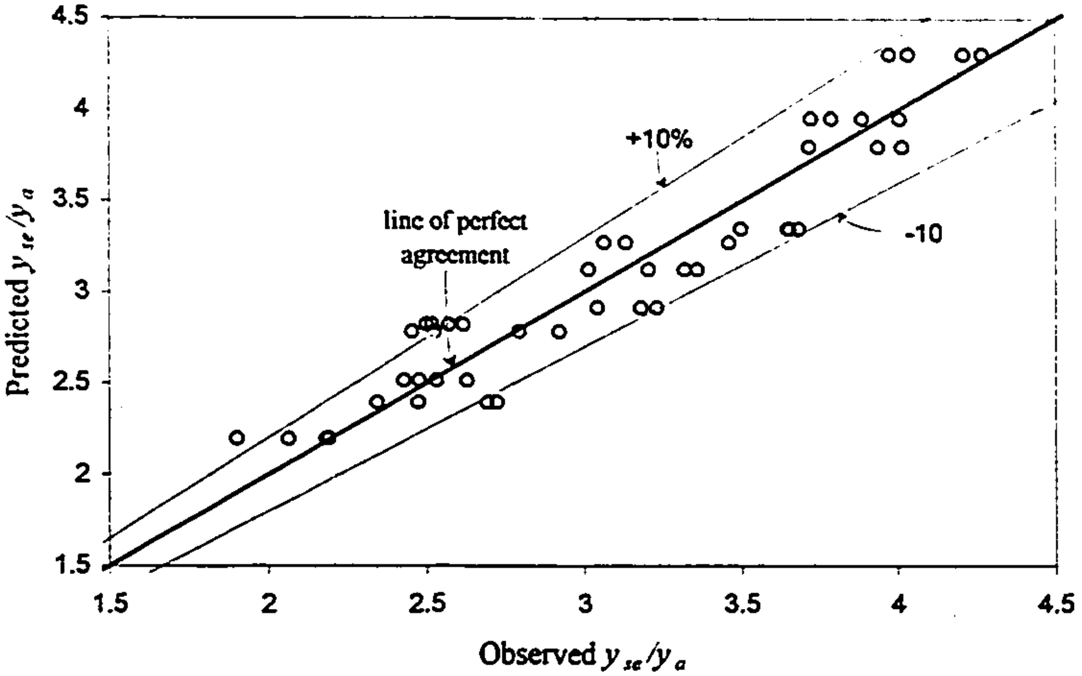

Figure 6.144- Predicted vs. observed y_{se}/y_a

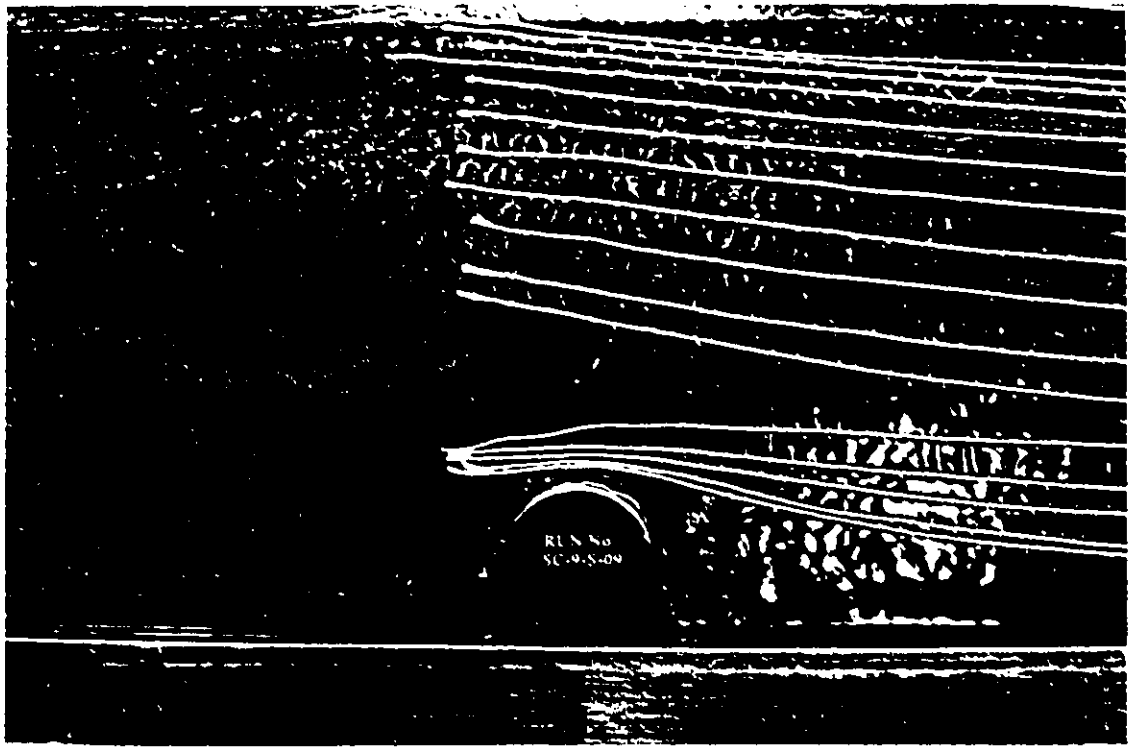

Plate 6.1- Flow deflection around 9 cm-SC abutment for interacting flow, S_o=0.0009, and D_{50}=0.5 mm

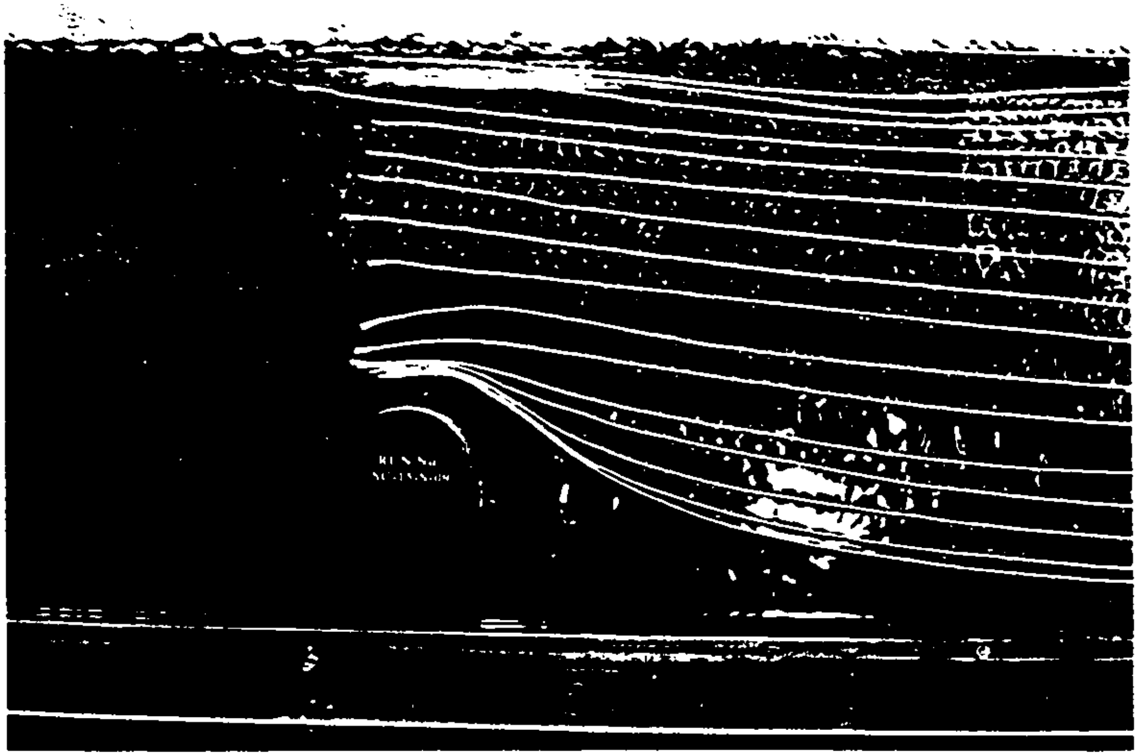

Plate 6.2- Flow deflection around 15 cm-SC abutment for interacting flow, S_o=0.0009, and D_{50}=0.5 mm

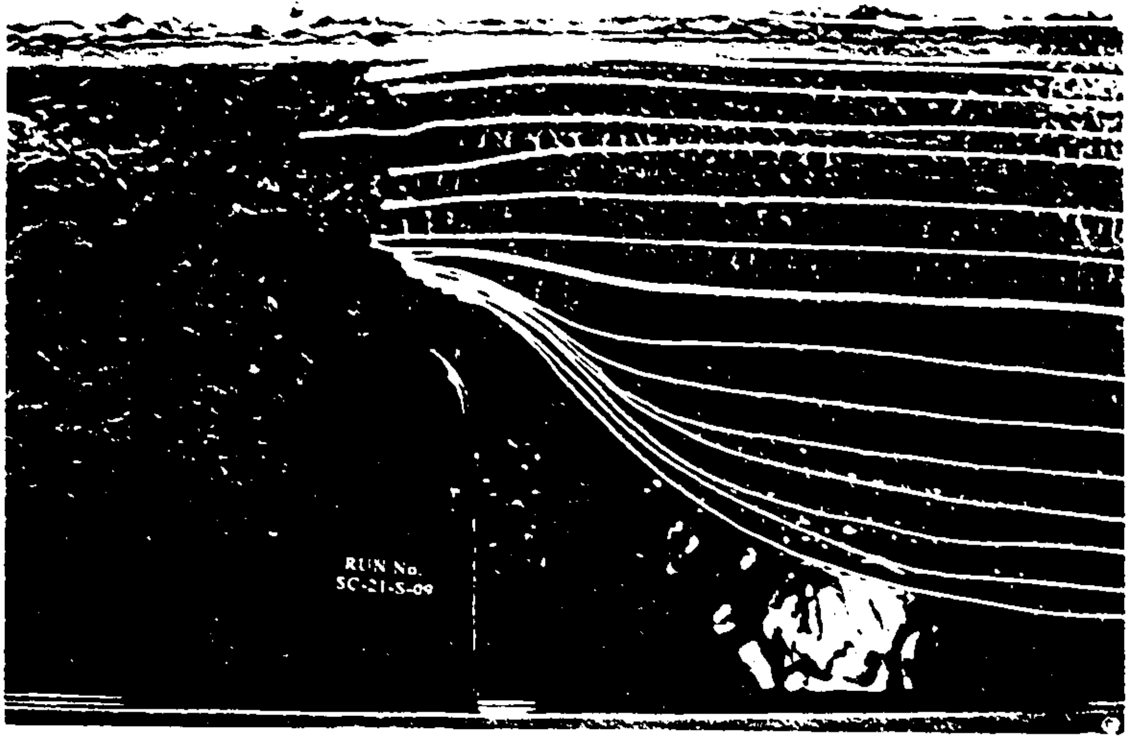

Plate 6.3- Flow deflection around 21 cm-SC abutment for interacting flow, S_o=0.0009, and D_{50}=0.5 mm

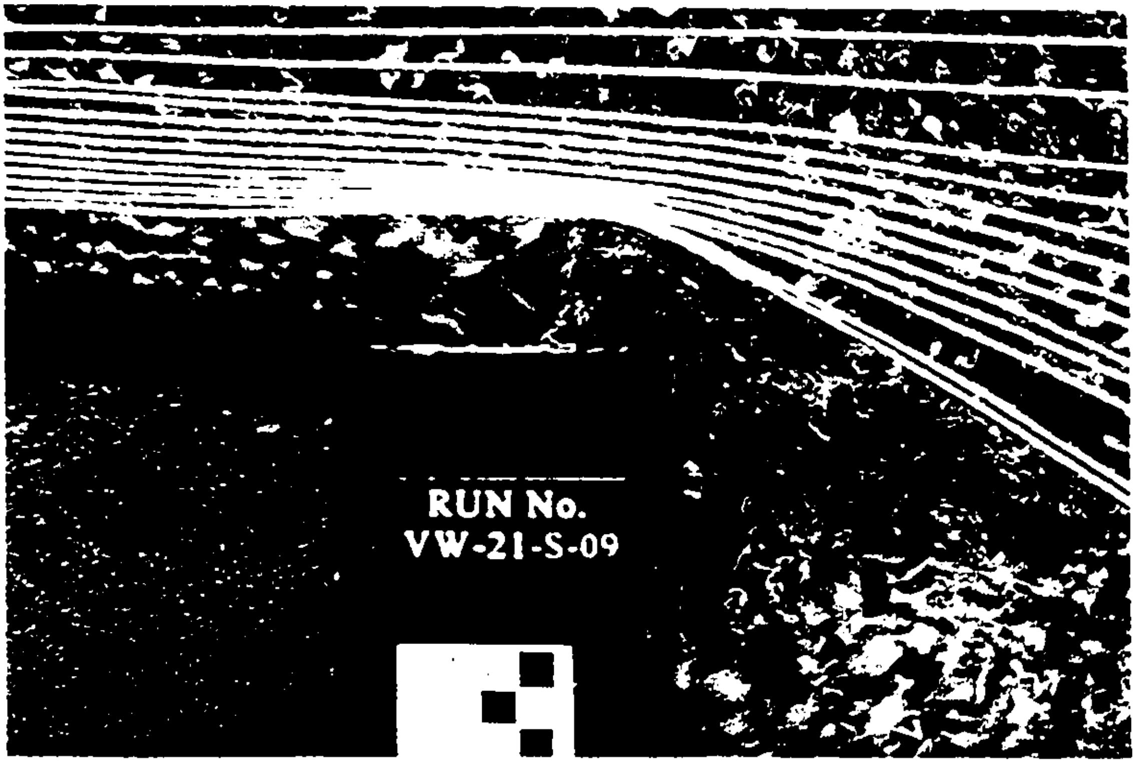

Plate 6.4- Close-up view of the flow pattern around 21 cm-VW abutment for interacting flow, S_o=0.0009, and D_{50}=0.7 mm

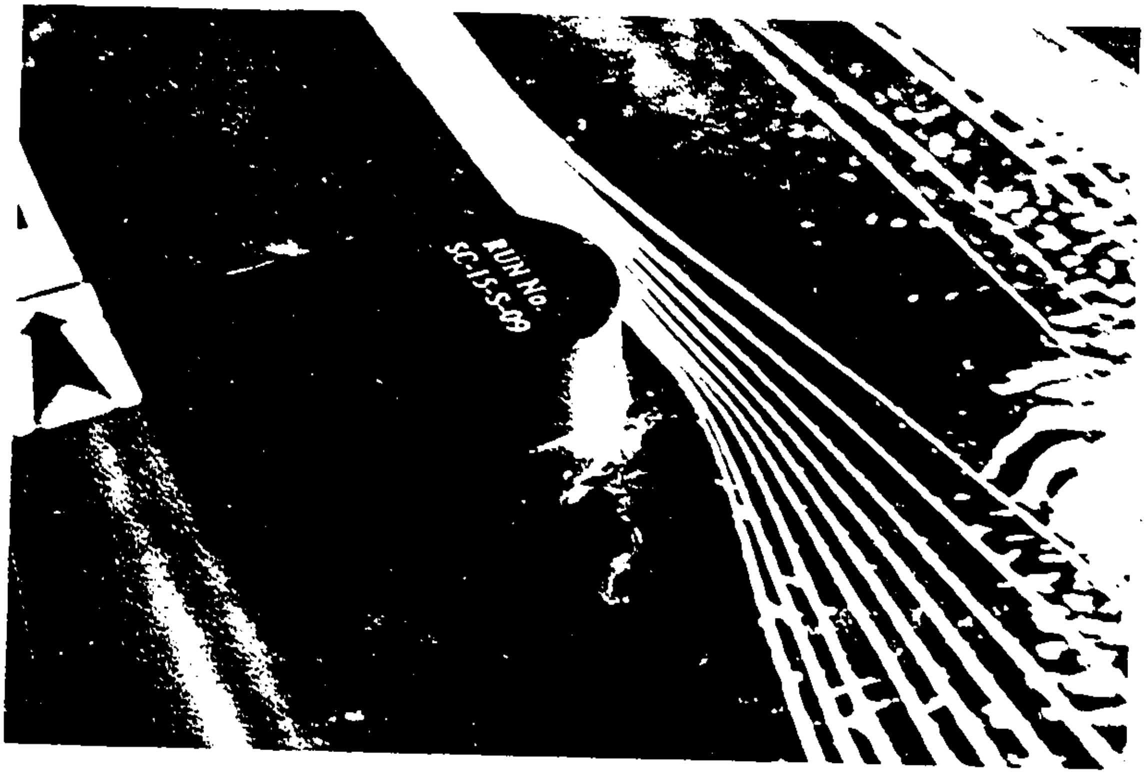

Plate 6.5- Close-up view of the flow pattern around 15 cm-SC abutment for interacting flow, S_o=0.0009, and D_{50}=0.7 mm

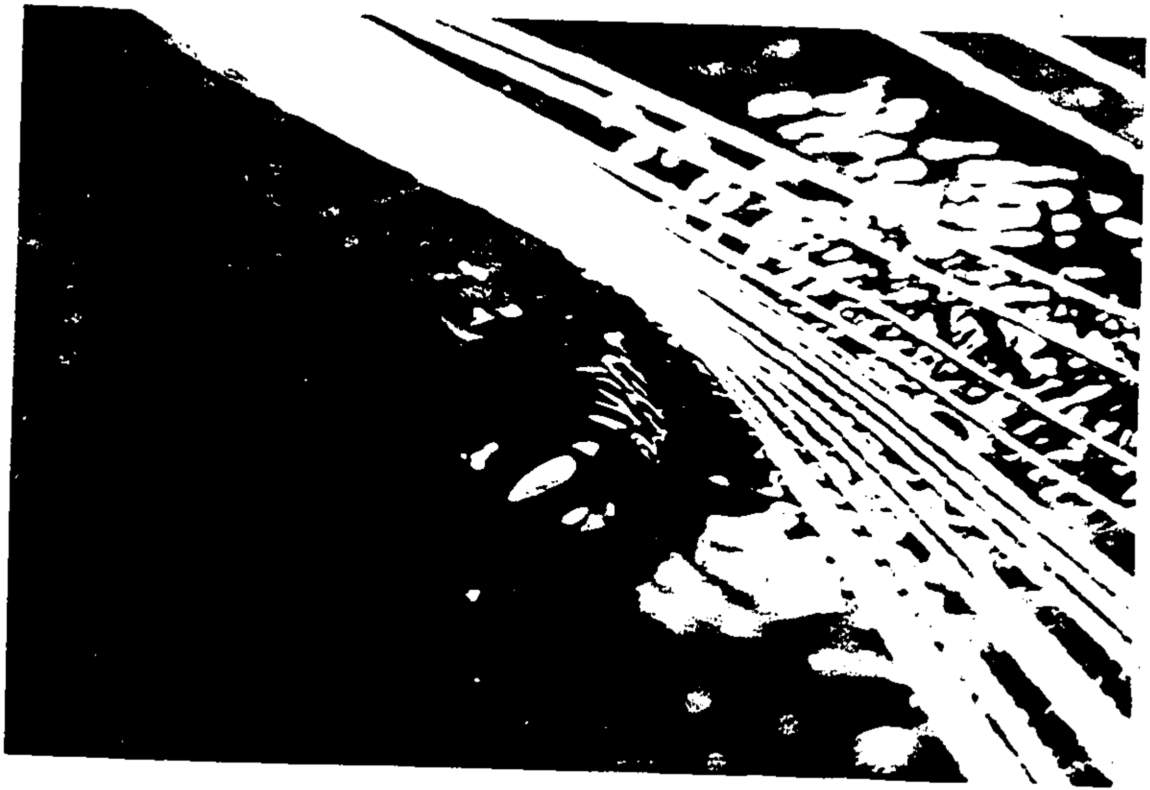

Plate 6.6- Close-up view of the flow pattern around 21 cm-ST abutment for interacting flow, S_o=0.0009, and D_{50}=0.7 mm

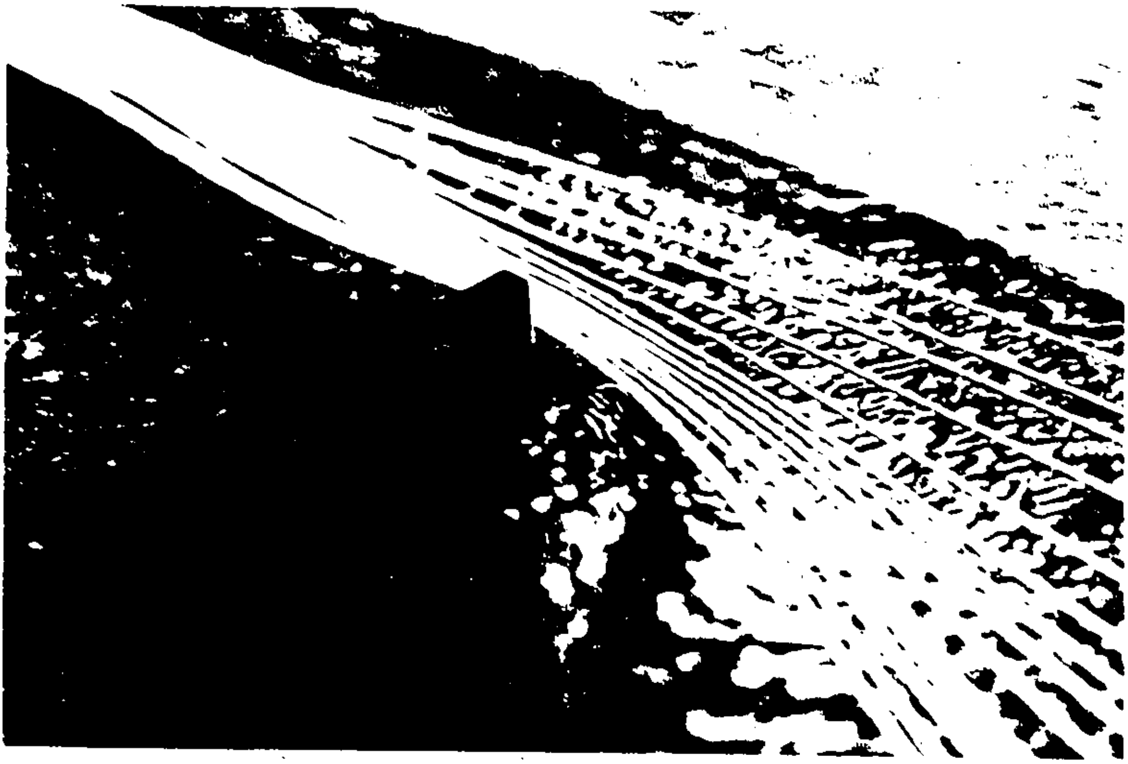

Plate 6.7- Close-up view of the flow pattern around 21 cm-WW abutment for interacting flow, S_o=0.0009, and D_{50}=0.7 mm

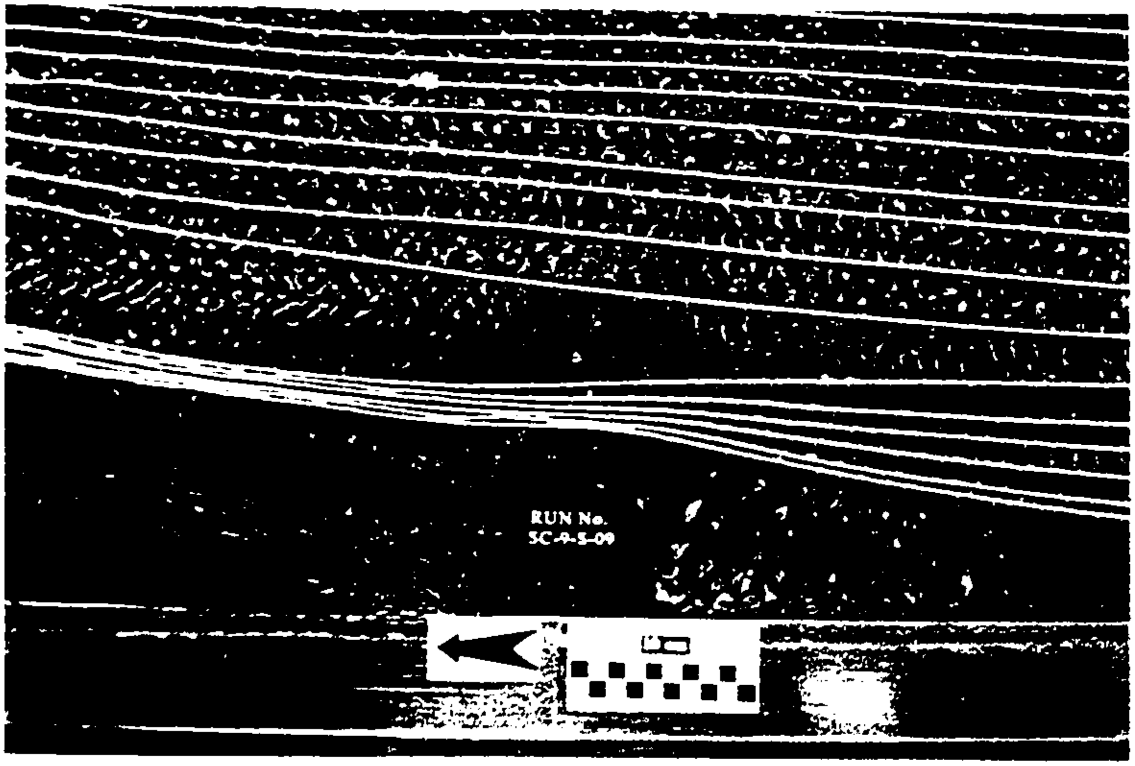

Plate 6.8- Flow convergence around 9 cm-SC abutment for interacting flow, S_o=0.0009, and D_{50}=0.7 mm

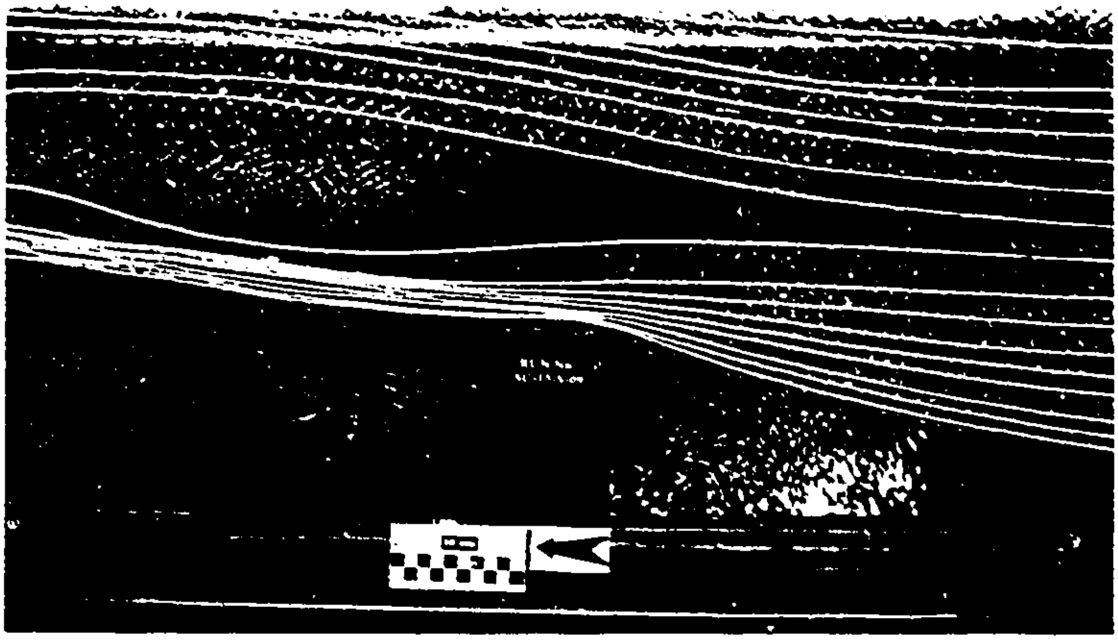

Plate 6.9- Flow convergence around 15 cm-SC abutment for interacting flow, S_o=0.0009, and D_{50}=0.7 mm

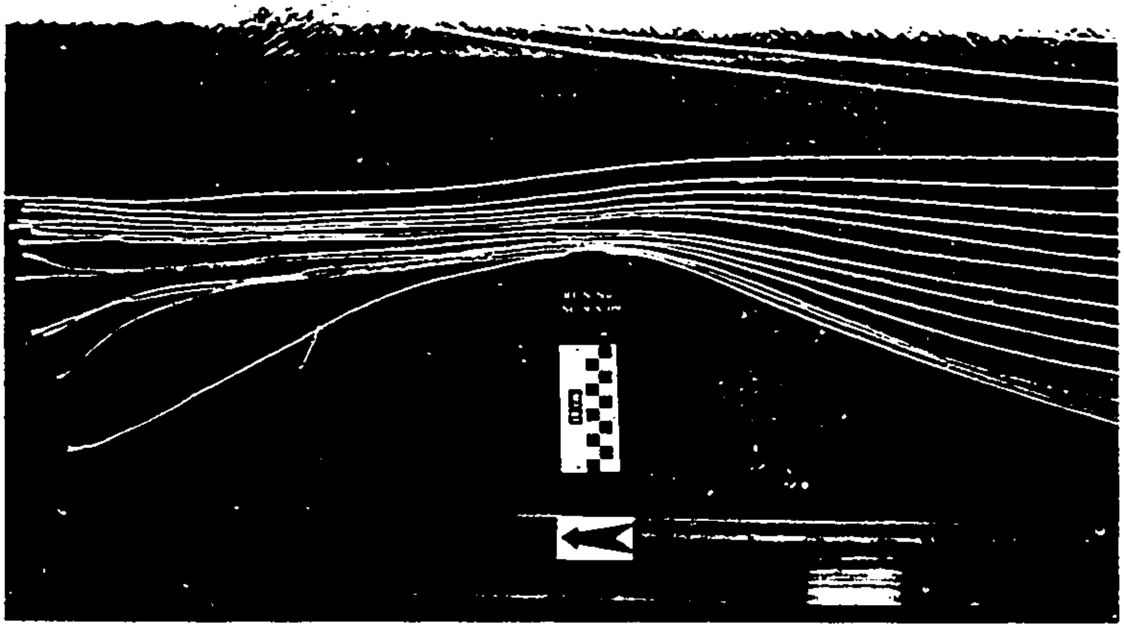

Plate 6.10- Flow convergence around 21 cm-SC abutment for interacting flow, S_o=0.0009, and D_{50}=0.7 mm

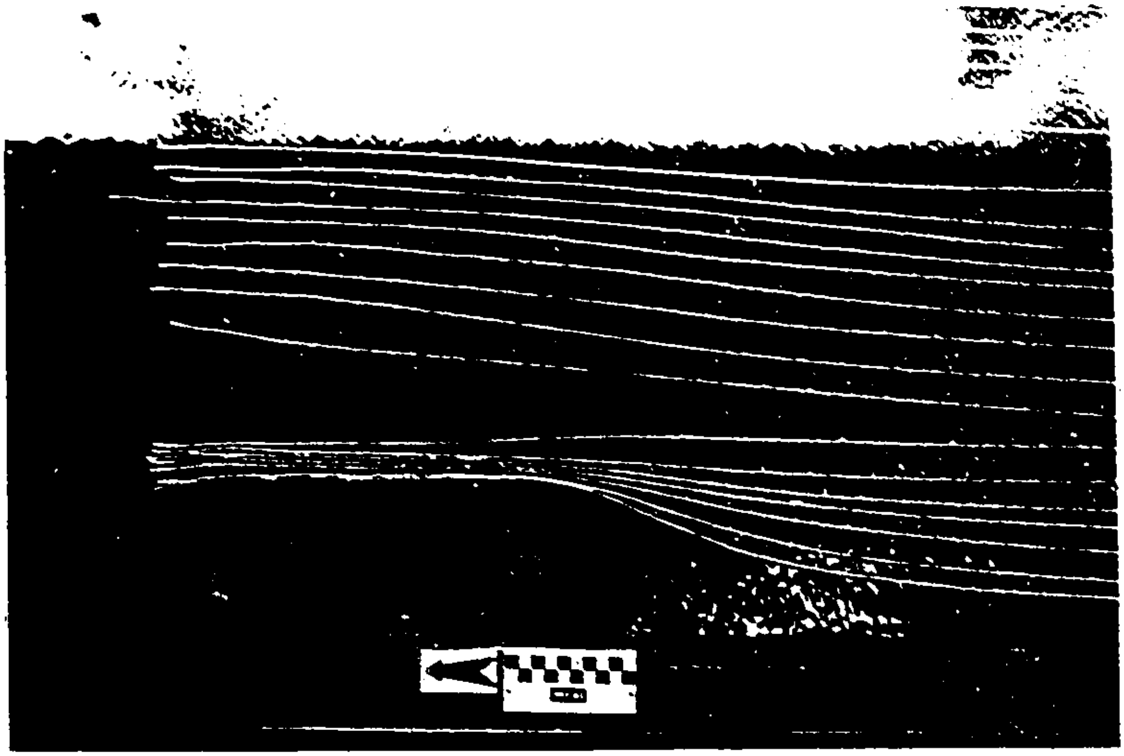

Plate 6.11- Flow convergence around 9 cm-VW abutment for interacting flow, S_o=0.0009, and D_{50}=0.7 mm

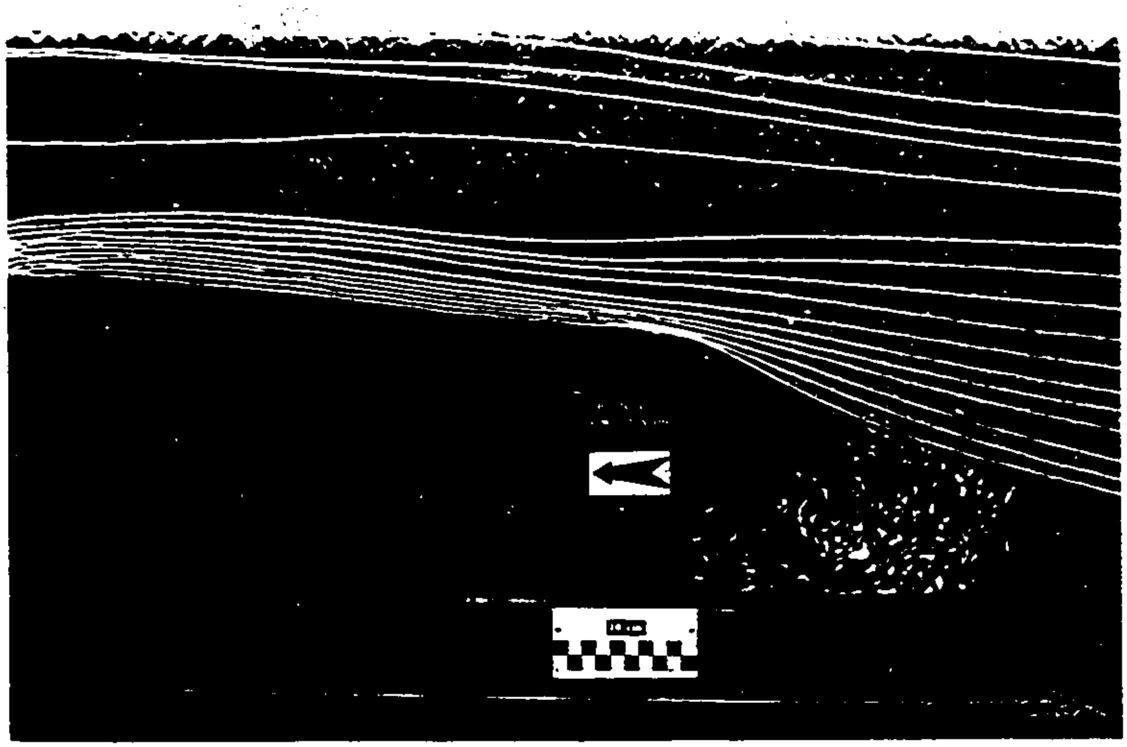

Plate 6.12- Flow convergence around 15 cm-VW abutment for interacting flow, S_o=0.0009, and D_{50}=0.7 mm

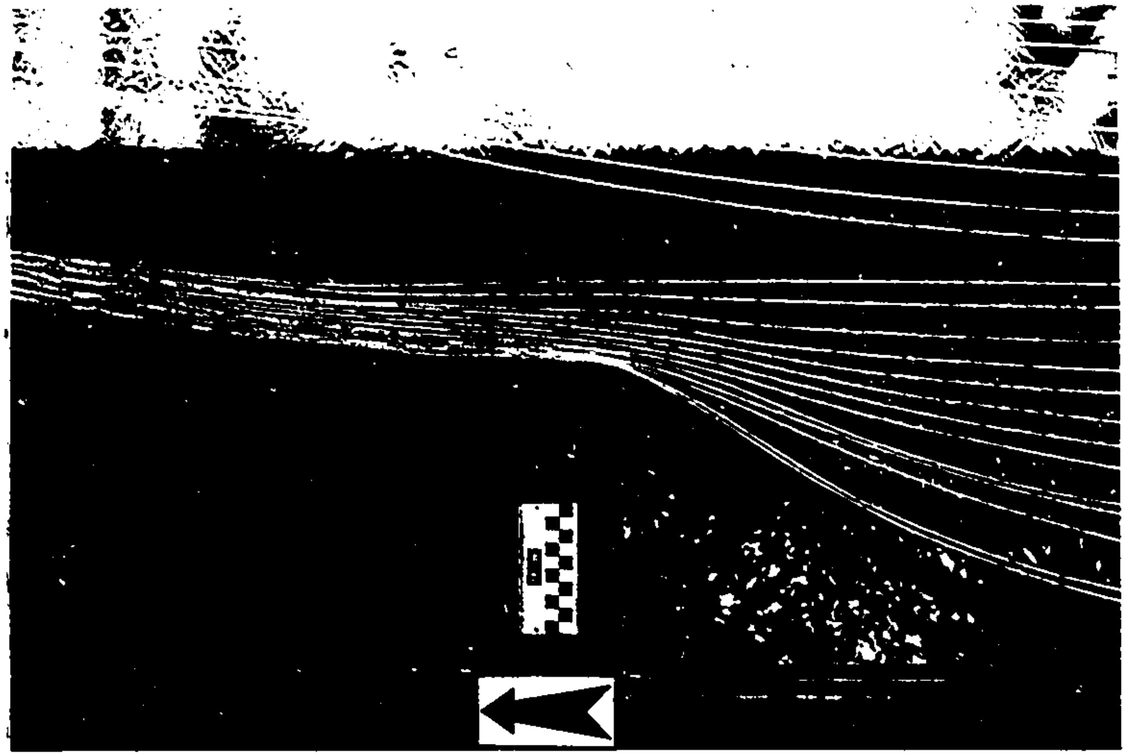

Plate 6.13- Flow convergence around 21 cm-VW abutment for interacting flow, S_o=0.0009, and D_{50}=0.7 mm

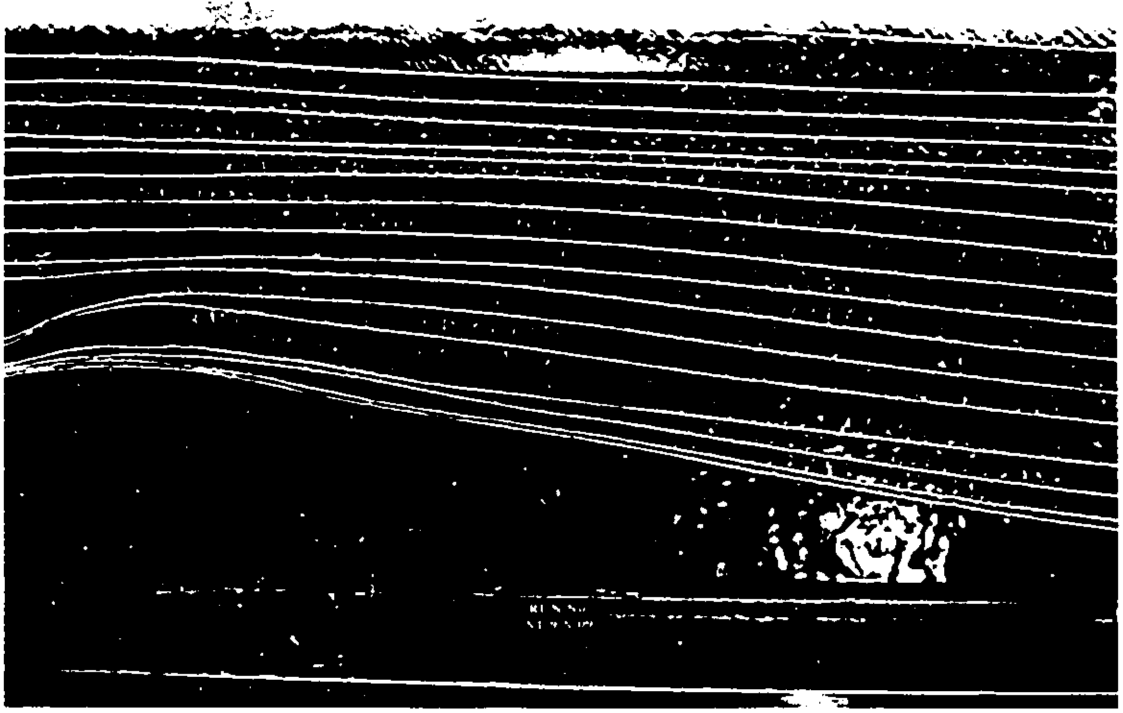

Plate 6.14- Flow convergence around 9 cm-ST abutment for interacting flow, S_o=0.0009, and D_{50}=0.5 mm

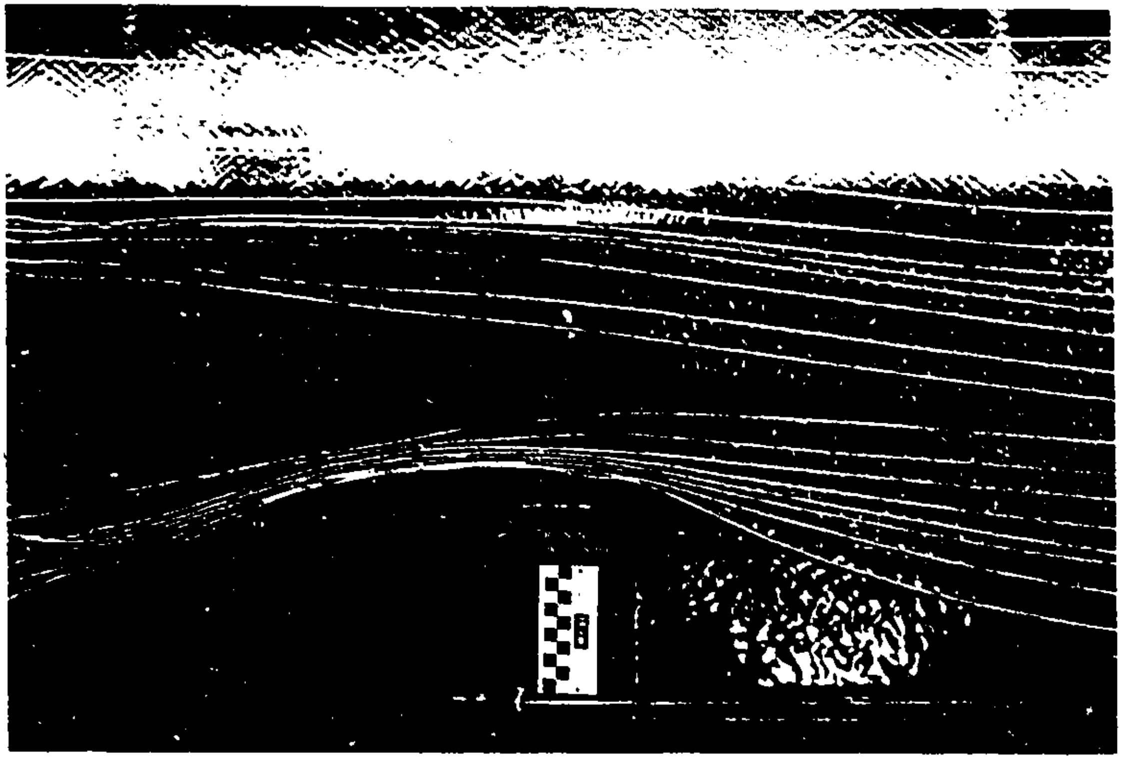

Plate 6.15- Flow convergence around 15 cm-VW abutment for interacting flow, S_o=0.0009, and D_{50}=0.5 mm

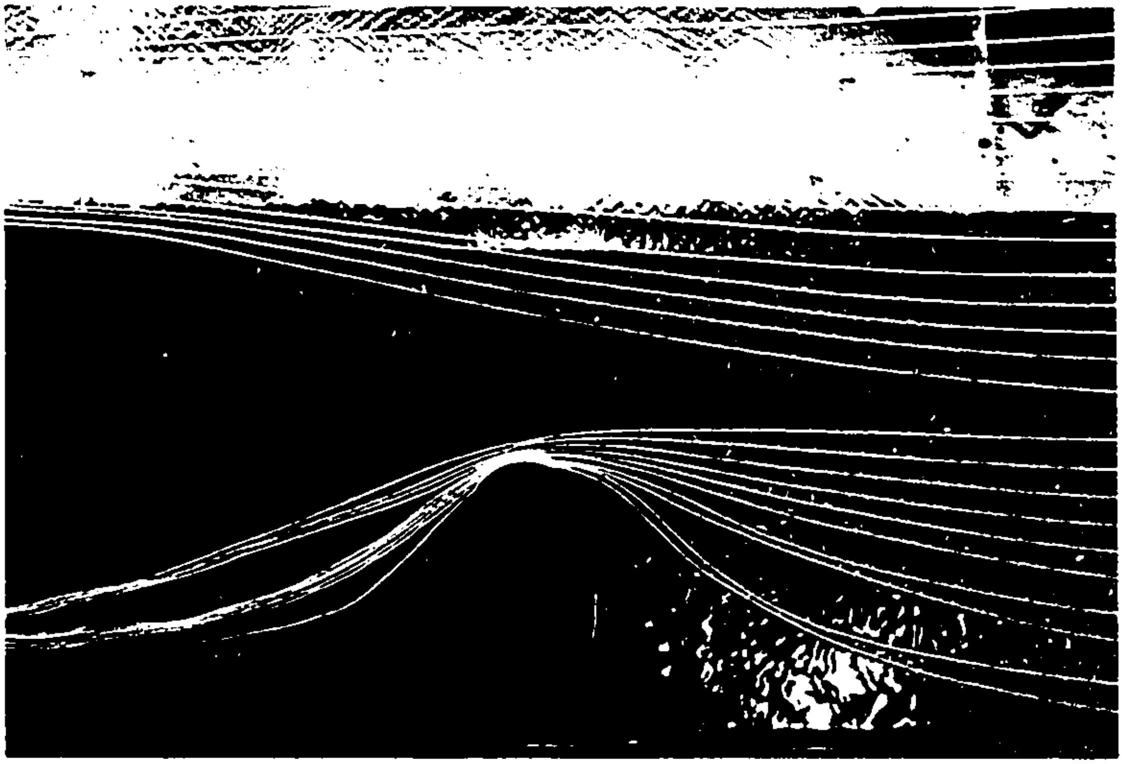

Plate 6.16- Flow convergence around 21 cm-SC abutment for interacting flow, S_o=0.0009, and D_{50}=0.5 mm

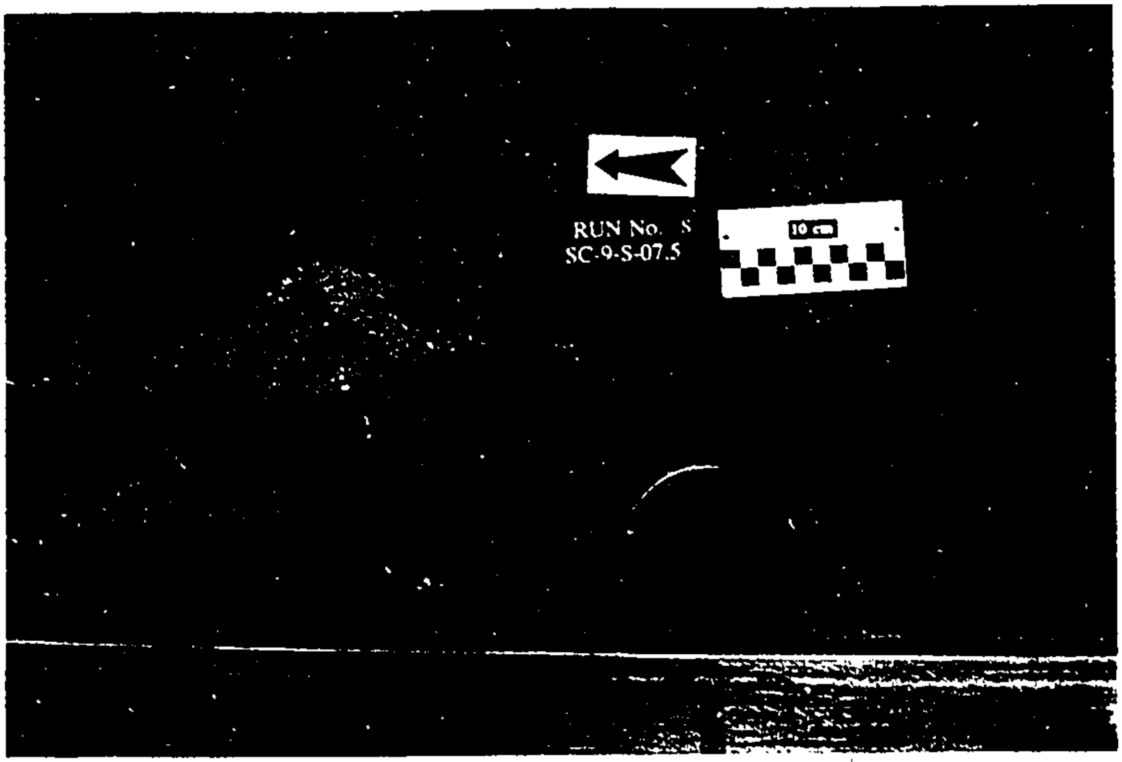

Plate 6.17- Scour pattern around 9 cm-SC abutment for non-interacting flow, S_o=0.00075, and D_{50}=0.5 mm

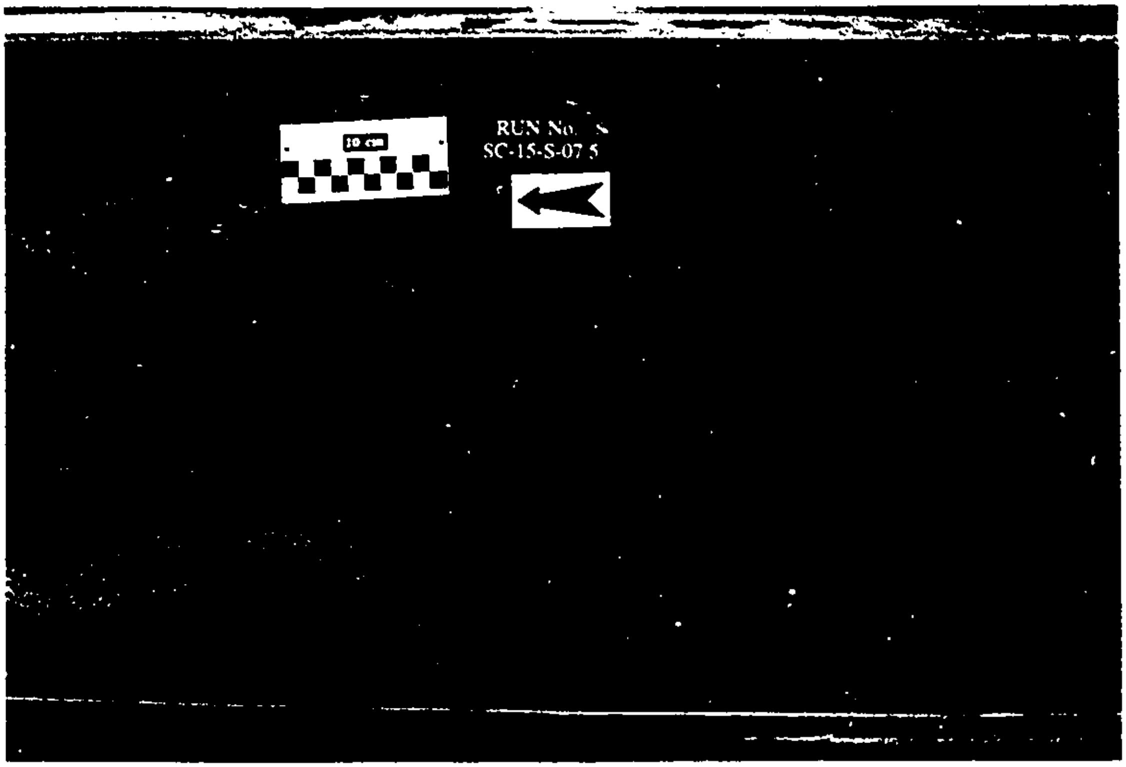

Plate 6.18- Scour pattern around 15 cm-SC abutment for non-interacting flow, S_o=0.00075, and D_{50}=0.5 mm

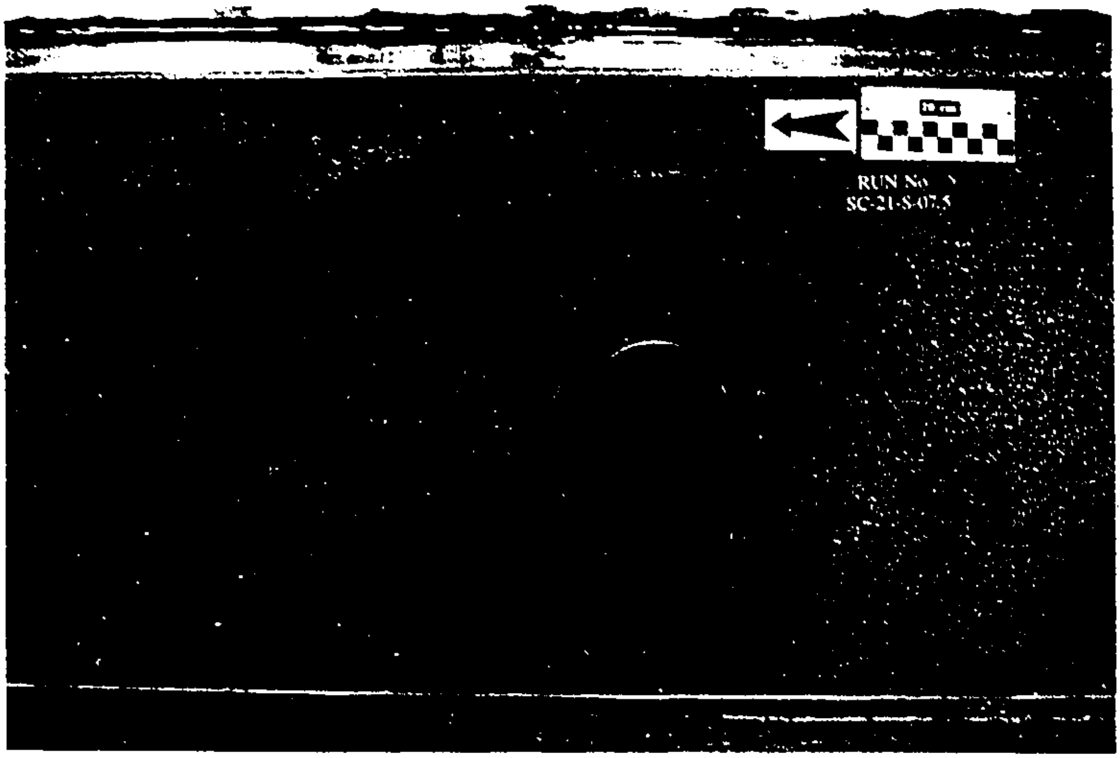

Plate 6.19- Scour pattern around 21 cm-SC abutment for non-interacting flow, S_o=0.00075, and D_{50}=0.5 mm

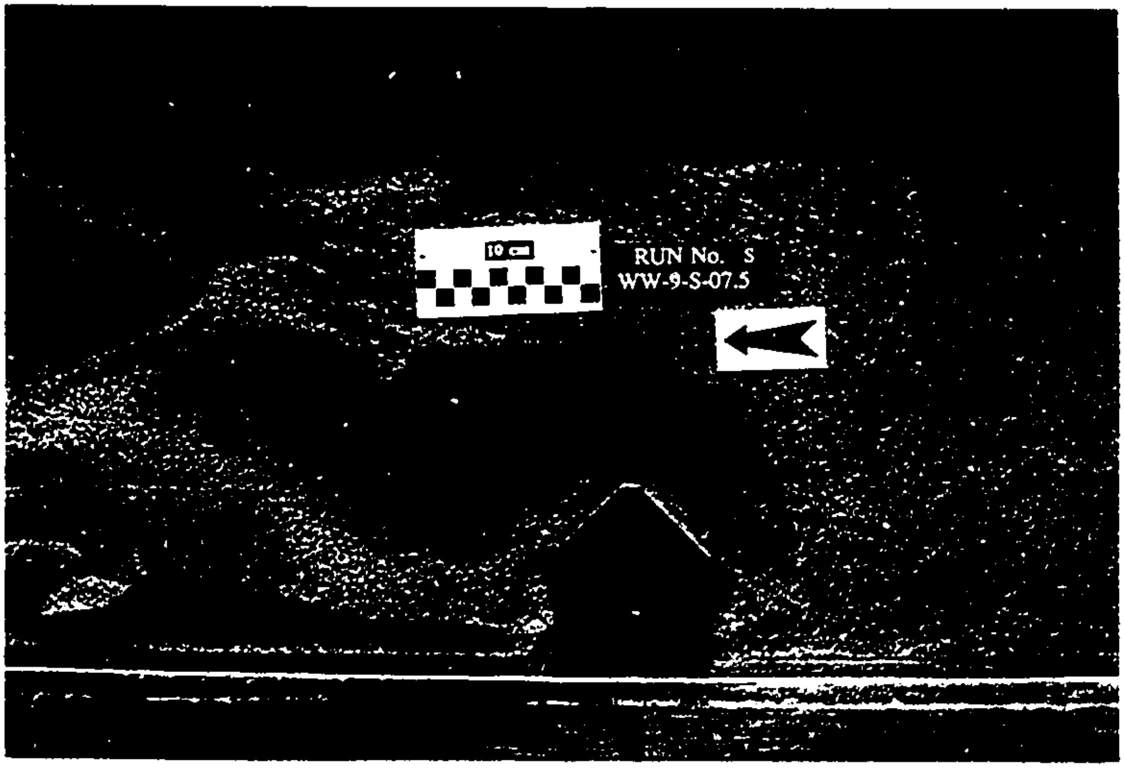

Plate 6.20- Scour pattern around 9 cm-WW abutment for non-interacting flow, S_o=0.00075, and D_{50}=0.5 mm

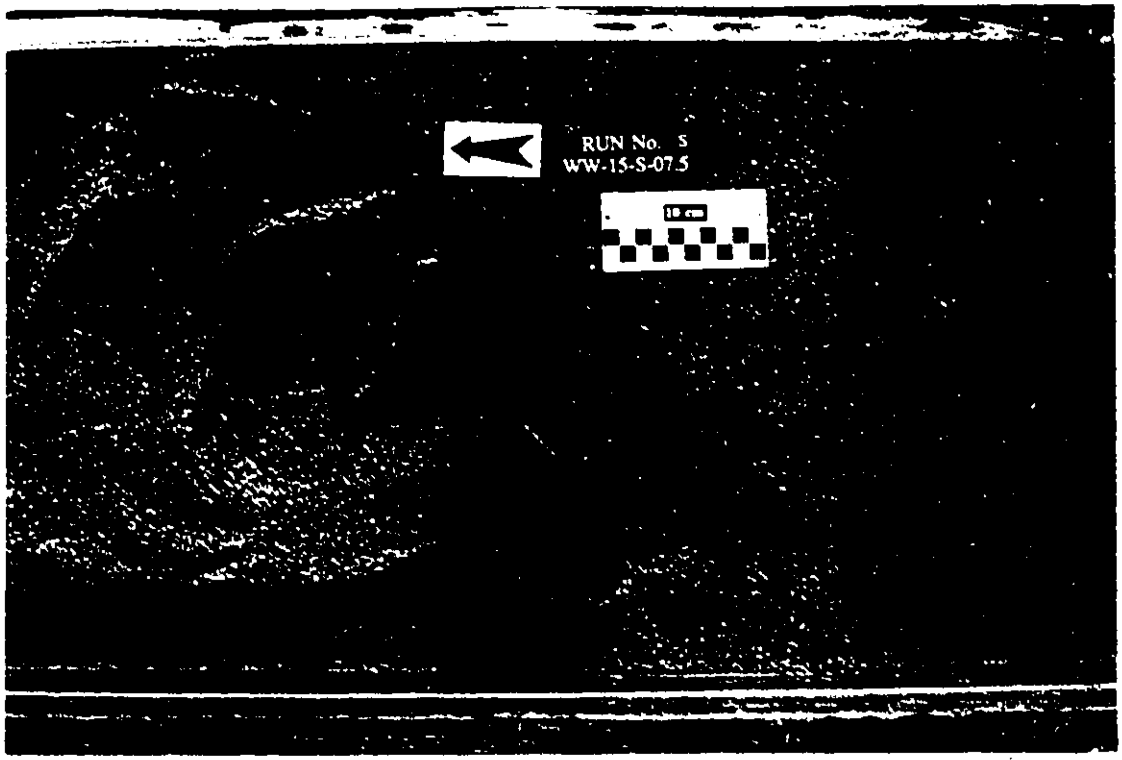

Plate 6.21- Scour pattern around 15 cm-WW abutment for non-interacting flow, S_o=0.00075, and D_{50}=0.5 mm

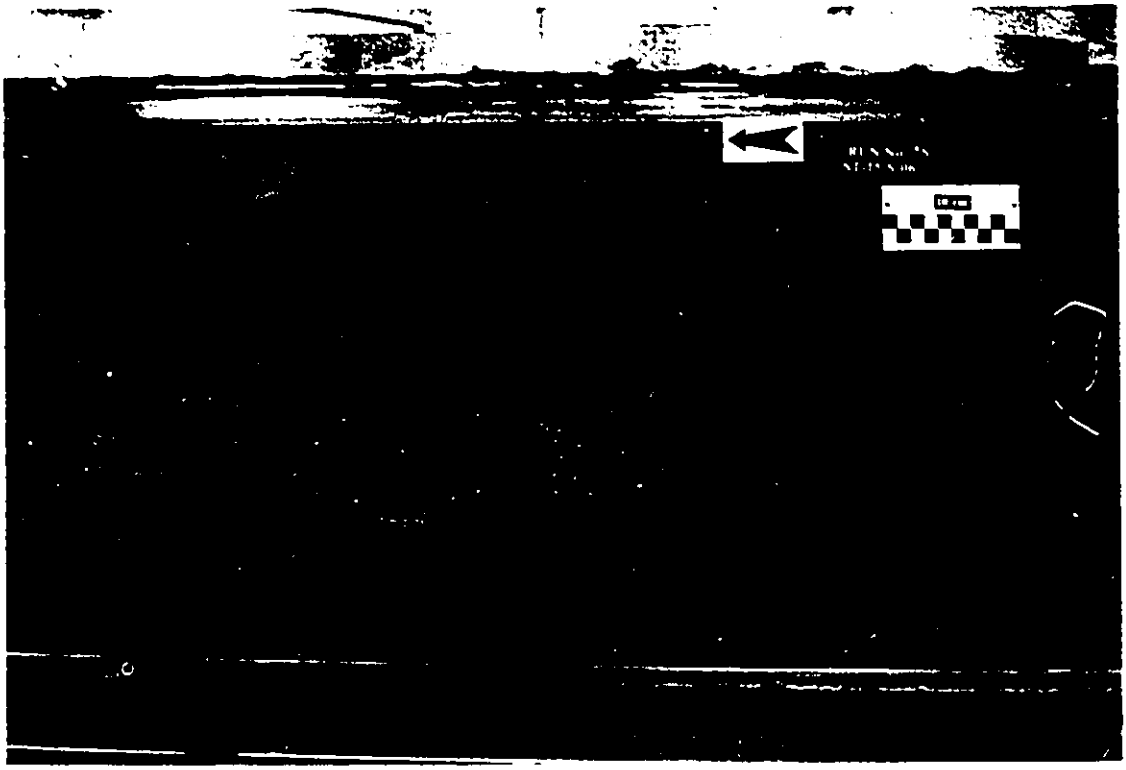

Plate 6.22- Scour pattern around 21 cm-WW abutment for non-interacting flow, S_o=0.00075, and D_{50}=0.5 mm

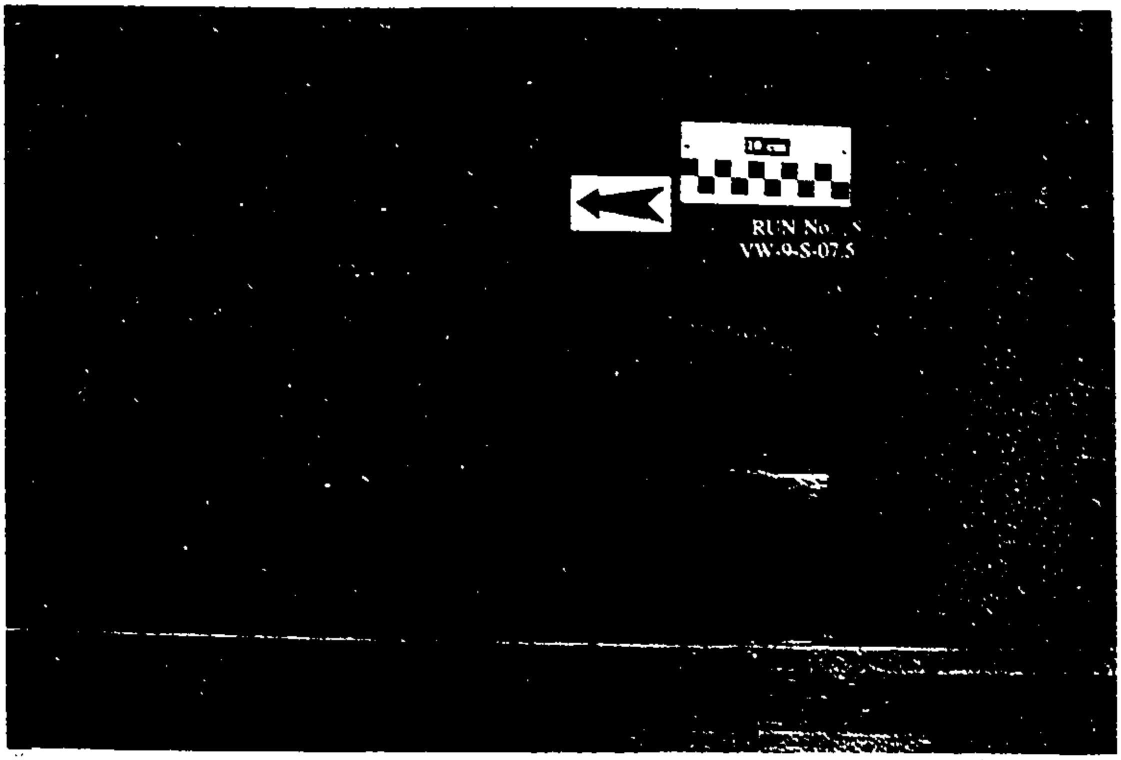

Plate 6.23- Scour pattern around 9 cm-VW abutment for interacting flow, S_o=0.00075, and D_{50}=0.5 mm

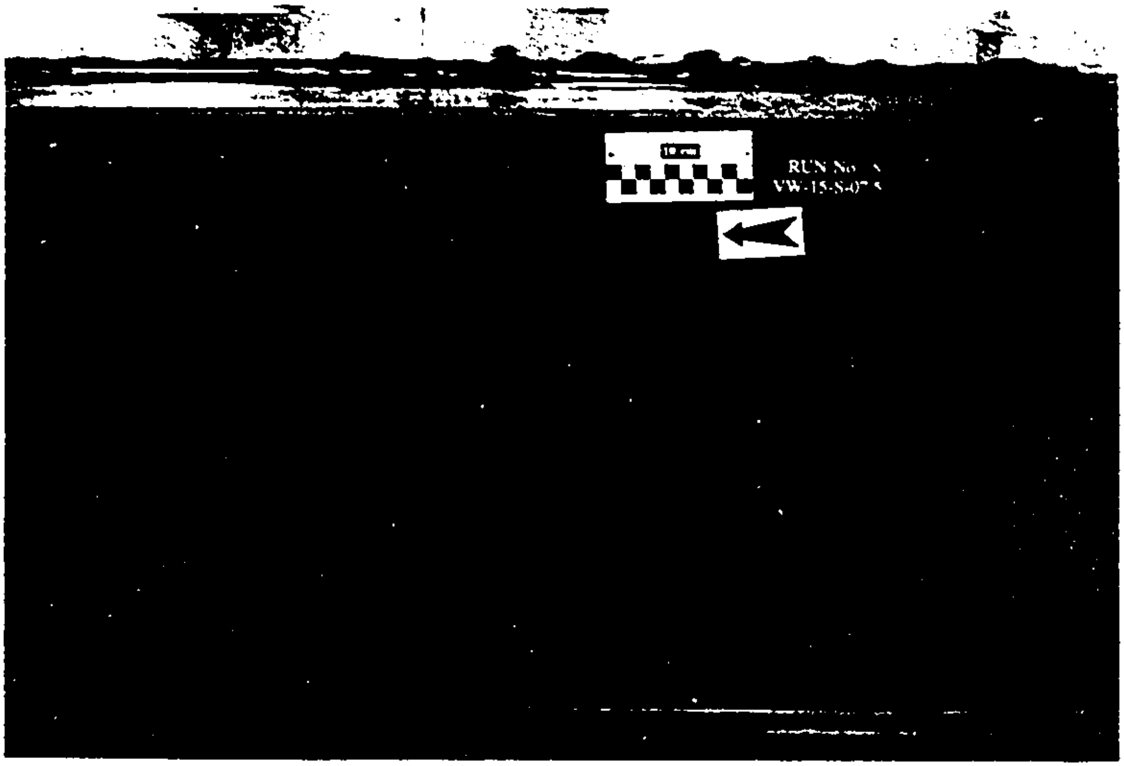

Plate 6.24- Scour pattern around 15 cm-VW abutment for non-interacting flow, S_o=0.00075, and D_{50}=0.5 mm

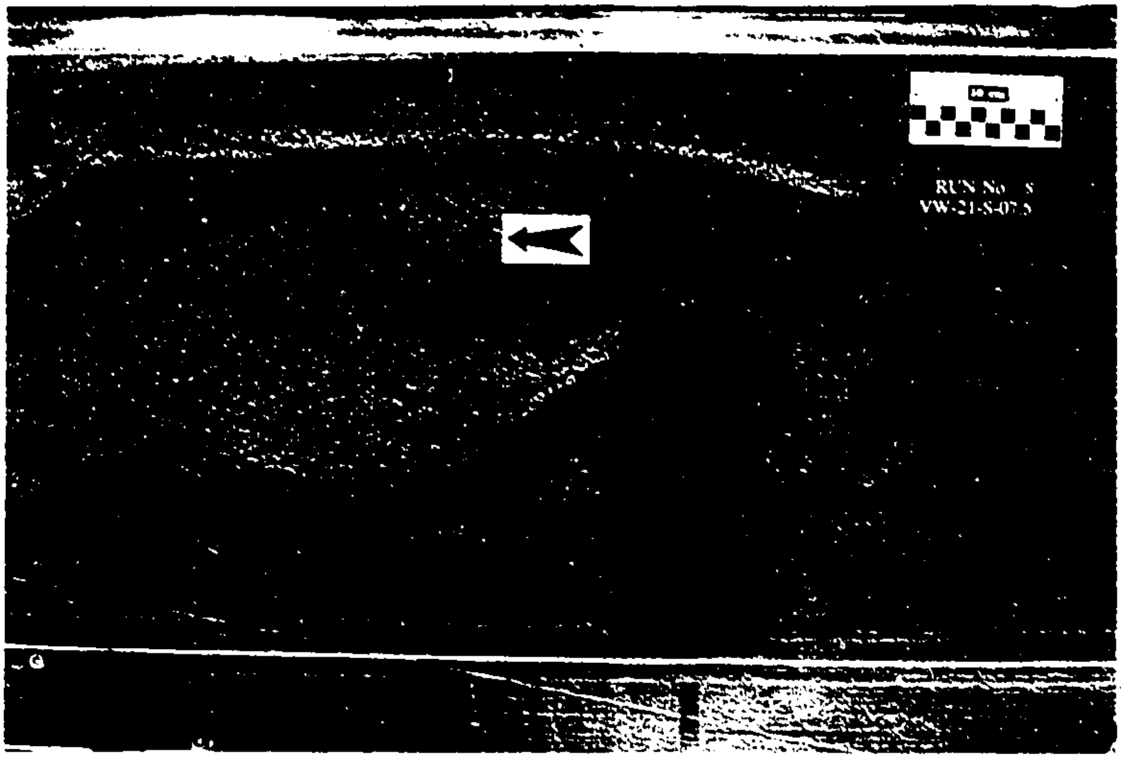

Plate 6.25- Scour pattern around 21 cm-VW abutment for non-interacting flow, S_o=0.00075, and D_{50}=0.5 mm

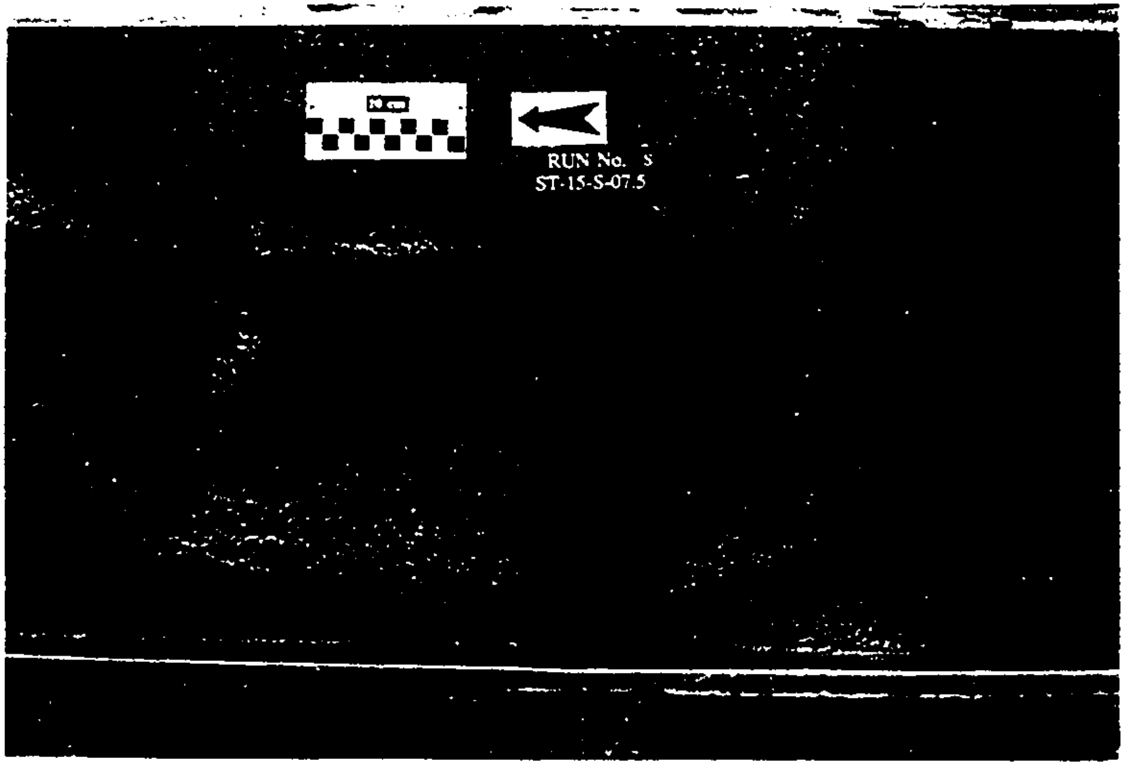

Plate 6.26- Scour pattern around 15 cm-ST abutment for interacting flow, S_o=0.00075, and D_{50}=0.5 mm

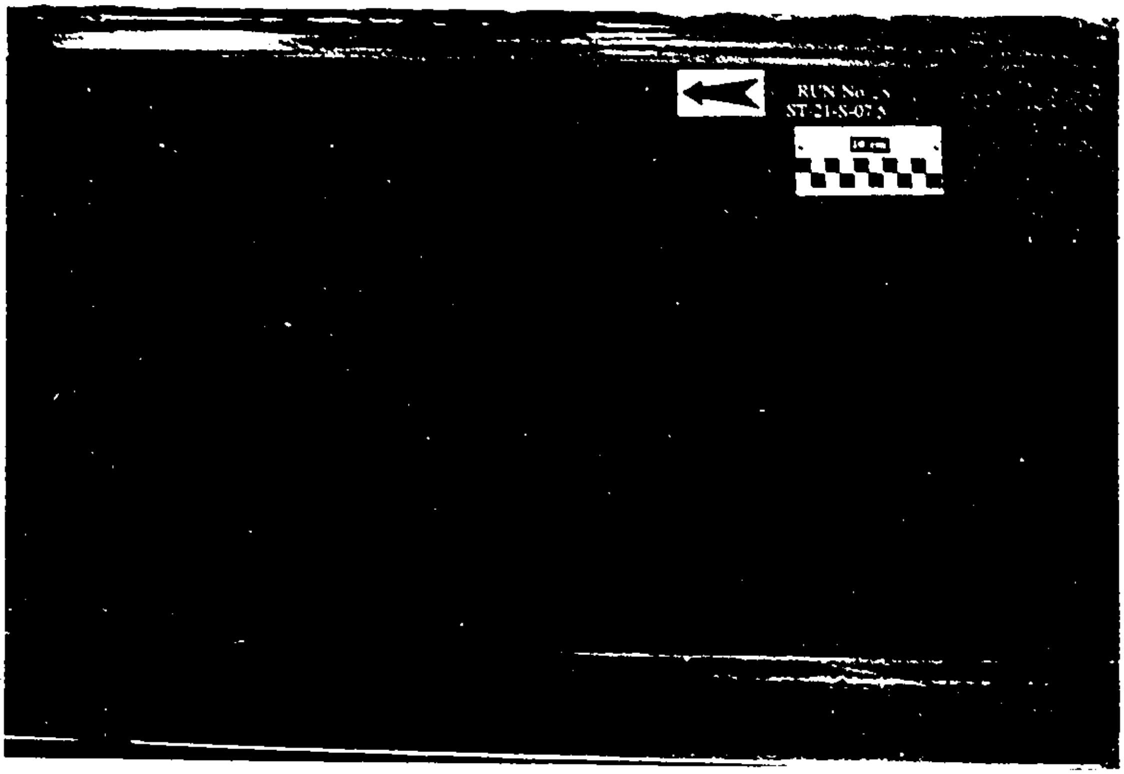

Plate 6.27- Scour pattern around 21 cm-ST abutment for interacting flow, S_o=0.00075, and D_{50}=0.5 mm

CHAPTER SEVEN

SUMMARY, CONCLUSIONS, AND RESEARCH NEEDS

7.1- SUMMARY

Much literature has been published on the local scouring process at bridge sites. Most of these studies have dealt with local scouring in the vicinity of bridge piers and a few with that at spur-dikes and abutments. These studies were almost entirely restricted to laboratory flumes having rectangular cross-sections, which simulated a structure placed in the main channel of a watercourse. While the configuration used might reasonably represent the bridge pier case, it does not properly simulate the abutment case, because abutments are usually set in the FP and most often terminate there. Lack of information on simulating such practical situations has led to the development of abutment scour formulae that predict unrealistic scour depths. The need for further research on this topic has been emphasized by recognized researchers in the field, including Richardson and Richardson, 1993a, 1993b; Melville, 1995; Melville and Parola, 1995, among others.

Melville's (1992) abutment scour prediction equations are the outcome of an extensive research programme performed at Oakland University, New Zealand during 1980-1992. Melville's equations, however, were based on data obtained in rectangular flumes and so they predict excessive scour depth for abutments sitting in the FP. A case study reported by Richardson and Richardson (1993b) indicates that Melville's method determined a scour depth in excess of 50 m for a situation where the actual scour depth was negligible. Recently, Melville (1995) and Melville and

Parola (1995) divided the abutment case into three categories and emphasized the need for more research for abutments that sit and terminate in the FP.

A narrow main-channel width was used in Sturm and Janjua's studies (1993, 1994). The flow condition in the FP was significantly below the threshold condition of bed material movement and it was varied for each test. Due to the limitation of Sturm and Janjua's data, Melville (1995) and Melville and Parola (1995) recommended that further studies should be initiated for abutments terminating in the FP.

Watercourse cross-sectional geometry governs the flow velocity pattern, boundary shear stress, momentum transfer, and secondary circulations in an open channel flow. Since a compound cross-section flume was used in the current study, the LMT phenomenon between the MC and the FP cannot be ignored as it affects the velocity and shear stress distribution in both the MC and FP. According to Myers and Elsawy's (1975) data, even at FP depth/total depth ratio $y_f/H = 0.38$, changes in the FP boundary shear stress are still observed, however these changes are negligible at higher values of y_f/H. Therefore, y_f/H should be limited to 1/3 in any study dealing with LMT in compound-channel flows.

The theoretical basis describing the threshold condition of particle movement was covered in the first section of chapter three. In the second section the universal velocity distribution law and the method by which the equivalent sand roughness can be evaluated were described. The third section dealt with the dimensional analysis related to the local scouring phenomenon examined in the present study. A functional relationship was derived that related scour depth to the discharge ratio, the critical Froude number, the Froude number at the end of the abutment, and the abutment shape factor.

The experimental setup used in the laboratory programme was described in chapter four and details of the procedures followed to establish appropriate boundary conditions were presented in chapter five. A suitable bed slope range was examined and longitudinal bed slopes 0.0006, 0.00075, 0.00090 were selected. Rating curves for the flume were prepared for each bed slope setting . These curves were subsequently used to set the flowrate for the various tests performed. A computer program based on Shields' diagram was developed which related y_o-D_S -S_o for the desired u_*/u_{*c} ratio. In this study u_*/u_{*c} =0.95 was adopted (the corresponding y_o-D_S -S_o relationship is presented in graphical form (Figure 5.12)). A representative grain size D_{50}=0.5 mm was selected for the main experimental programme. Also used in two series of tests was a different sediment sample (D_{50}=0.7 mm) to compare the results with those using D_{50}=0.5 mm.

Based on preliminary tests, model abutment lengths 90, 150, and 210 mm were selected and four different abutment end-shapes, representative of common shapes in practice, were investigated. The required flow conditions for the selected test conditions were determined (Tables 5.2 and 5.3). The first series of the main tests were run for different periods to investigate the temporal variation of the local scour and establish a test duration. Based on the results of the first series of long-term experiments, a test duration of 5 hr was selected for the main testing programme. Also, the ratio y_s/y_{se} was determined. Since *non-interacting* conditions were also investigated, an additional long-term test was performed to determine the effects of the new flow conditions on y_s/y_{se}. This was necessary in order to adjust scour depth. The ratio was also determined for another long-term test performed with D_{50}=0.7 mm. The y_s/y_{se} values obtained were applied to adjust measured scour depth to give corresponding y_{se}-values.

Finally, different techniques to visualize the surface flow pattern in the vicinity of the abutment end-sections were examined. The method of *floating strings* was tested and proved to be an effective and a practical way to visualize the angle at which the diverted (FP) flow combined with the flow component moving in streamwise direction. The method also identified the diverted flow's region of influence on the compound flow field.

The analysis of data and related discussions are presented in chapter six. In compound channels the flow interaction at the MC/FP junction and the momentum transfer phenomenon significantly affect the channel flow characteristics. Therefore, instead of applying an average value for the bed shear stress to the entire width of the FP, the actual velocity distribution should be considered. Velocity measurements indicated that the velocity profiles in the floodplain follow the log-law. Therefore, shear velocity in the floodplain was determined based on a comparison of the actual velocity profile and the log-law velocity distribution.

7.2- CONCLUSIONS

1. Our study data indicate that, for the case of abutments terminating near MC-FP junction regions, under conditions of strong flow interaction, LMT effects can produce a 15-30% increase in local scour depth. Therefore, design relationships for predicting maximum scour depth at bridge abutments should account for LMT.

2. In *interacting* flow conditions, because of the related LMT effects, the long-abutment model experienced 10% more shear velocity than the short-abutment model. Also, isolating the FP flow from the MC flow (i.e. in *non-interacting* conditions) decreased the FP shear velocity by approximately 5%.

3. The data for *non-interacting* conditions were adjusted for critical u_*/u_{*c}. The adjusted values of the relative scour depth, y_{se}/y_a were still 5 to 15% smaller than for *interacting* conditions (Figures 6.126 to 6.129).

4. The discharge ratio Q_a/Q_w is a significant variable in the determimation of abutment scour depth because it accounts for: (*i*) the effective length of the abutment, (*ii*) the effects of FP flow depth to total flow depth ratio, y_d/H, and (*iii*) the effects of LMT. Therefore, it is essential to include the discharge ratio in any abutment scour formulation.

5. Flow deflection angles, β = 15°,30°, and 40° were observed for *short* (L=90 mm), *medium-length* (L=150 mm), and *long* abutments (L=210 mm). The angle β increases with abutment length to a maximum value of 90°. This suggests that there exists a limiting scour depth associated with maximum β.

6. The channel width portion w, associated with Q_w, is a function of the abutment length. In each of the tests performed w was observed to be about 70% of the corresponding abutment length.

7. Since LMT affects the region close to the MC/FP junction the most, the greater the distance from the MC/FP junction the smaller will be the LMT effect. Therefore, the lateral velocity gradient in the region close to the FP wall ($0<x<200$ mm) is less affected by variations in y_d/H. This, in turn, leads to smaller variations in Q_w/Q_a with y_a in this region.

8. Except for the VW-abutment, as the abutment length increases the effect of the abutment shape decreases. For the medium-length (L=150 mm) and long (L=210

mm) model abutments, only small variations (1 to 3%) were observed in the scour depth generated by the SC-, ST-, and WW-abutments. However, a significant difference (approximately 20%) was observed between the scour depth produced by the VW-abutments and those generated by other abutment shapes.

9. The decrease in y_{se}/L variations with L/D_{50} (Figures 6.79 to 6.82) suggests that there is a limiting L/D_{50} beyond which the scour depth becomes independent of the sediment size. The results of our study indicate that the limit set by Ettema (1980) for the impact of b/D_{50} (>50) on the scour depth for *circular bridge piers* is not appropriate for the abutment case. Further studies are required to draw a general conclusion regarding the effects of sediment size for the case of bridge abutments in compound flows.

10. The experimental data for *interacting* conditions were employed to develop a scour prediction model, based on the functional relationship derived in section 3.4. According to the multiple regression analysis the resulting scour prediction model takes the form:

$$\frac{y_{se}}{y_a} = 13.5 \left(\frac{Q_w}{Q_a} \right)^{3.9} F_a^{1.17} \, F_c^{-0.25} \qquad \textbf{(6.2)}$$

Equation 6.2 predicted the scour depth within ±10% error lines (Figure 6.144).

7.3- RESEARCH NEEDS

Bridge engineers believe that traditional abutment scour prediction equations estimate much larger scour depths than are likely to be observed in the field. Generally, the reasons for overestimation of scour depth are attributed to the ways that related laboratory investigations were performed in the past. Approach channel geometry influences the flow field around abutments significantly and must be properly accounted for in research dealing with abutment scour.

A valuable extension of the present work would be to examine the effects on local scour depth of varying the FP width/MC width ratio. The velocity distribution in the FP and the discharge ratio, Q_w/Q_{cr} are affected by the lateral momentum flux, which varies with the FP/MC width ratio. Sediment size and gradation influence the local scour depth generated at abutments and these factors should be investigated further. Circular bridge pier scour studies (Ettema, 1980; Chiew, 1984) have indicated that maximum scour depth is reduced in the case of non-uniform bed material. It is believed, however, for bridge abutments the reduction in scour depth due to non-uniformity in sediment size distribution is different from that for bridge piers and should be investigated. Also, because of the variations in velocity distribution across the FP, and as a result of sediment gradation a different scour pattern to that for bridge piers is anticipated for bridge abutments.

Field sites might consist of stratified soil layers and the FP bed roughness is usually different from that of the MC; it also varies from site to site. When scour-resistant soils are encountered the scour hole progresses laterally. The influence of the complex flow field of compound channels on the scour depth in stratified soil layer would be of great practical interest. To the author's knowledge, no data exist to show how FP roughness impacts on the local scouring phenomenon. FP roughness in the field varies over a very wide range, therefore, such research would also be of great practical interest.

Although it is preferable to orientate the bridge abutments perpendicular to the approaching flow, in some circumstances they might be aligned skew to the main current. Presently, the effect of abutment alignment is considered based on studies of spur-dikes located in rectangular channels. Because of the specific flow characteristics in the FP of compound channels, an abutment located in the FP and aligned to the flow at an angle of attack other than 90° produces different scour depth than a similar abutment located in rectangular flumes. Therefore, it would be of considerable interest to investigate the local scouring phenomenon associated with abutment aligned skew to the main flow direction.

REFERENCES

Ahmad, M. (1953). Experiments on design and behaviour of spur-dikes. Proc. International Hydraulics Convention, Minneapolis, Minnesota, 145-159.

Ahmed, M. (1962). Discussion on "Scour at bridge crossing, Laursen, E. M." Trans. ASCE, Part I, Vol. 127, 198-206.

Baker, C. J. (1980). Theoretical approach to prediction of local scour around bridge piers. J. of Hydr. Res., IAHR, Vol. 18, No. 1, 1-12.

Bhowmik, N. G., and Demissie, M. (1982). Carrying capacity of floodplains. J. of Hydr. Div., ASCE, Vol. 108, No. HY3, 443-452.

Blaisdell, W., Anderson, C. L., and Hebaus, G. G. (1981). Ultimate dimensions of local scour. J. of Hydr. Div., ASCE, Vol. 107 (HY3), 327-337.

Blaisdell, F. W. (1983). Discussion on "Time scale for scour downstream of Hydraulic Jump, Farhoudi, J. and Smith, K. V. H." J. of Hydr. Engrg., ASCE, Vol. 109, No. 8, 1182-1183.

Blench, T. (1962). Discussion on "Scour at bridge crossing, Laursen, E. M." Trans. ASCE, Part I, Vol. 127, 180-181.

Bogardi, J. (1959) (See Garde, R. G., and Ranga Raju, K. G. (1985))

Bradley, J. N. (1962). Discussion on "Scour at bridge crossing, Laursen, E. M." Trans. ASCE, Part I, Vol. 127, 181-183.

Breusers, H. N. C. (1970). Discussion on "Local scour around bridge piers, Shen et al." J. of Hydr. Div., ASCE, Vol. 96, (HY7), 1638-1639.

Breusers, H. N. C., and Raudkivi, A. J. (1991). Scouring. IAHR Hydraulic Structure

Design Manual No. 2. A. A. Balkema Publishers, Old Post Road, Brookfield, VT 05036, USA, 1-143.

Carstens, M. R. (1966). Similarity laws for localized scour. J. of Hydr. Div., ASCE, Vol. 92, (HY3), 13-36.

Chang, F. W. and Yevdjevich, V. (1962). Analytical study of local scour. Colorado State University, Civil Engineering Section, Fort Collins, Co. USA.

Chiew, W. M. (1984). Local scour at bridge piers. Report No. 355, School of Engineering, University of Auckland, Auckland, New Zealand.

Chiew, W. M. (1989). Influence of sediment gradation on scour at bridge piers. Proc. of the 23ed congress of the IAHR, Ottawa, Ontario, Canada, B299-B305.

Chitale, S. V. (1962). Discussion on "Scour at bridge crossing, Laursen, E. M." Trans. ASCE, Part I, Vol. 127, 191-196.

Cunha, V. (1970). Discussion on "Local scour around bridge pier, Shen et al." J. of Hydr. Div., ASCE, Vol. 96, (HY8), 1742-1747.

Cunha, L. V. (1973). Discussion on "Erosion of sand bed around spur-dike, Gill, M. A." J. of Hydr. Div., ASCE, Vol. 99, No. HY9, 1637-1639.

Cunha, L. V. (1975). Time evaluation of local scour. Proc. of the XVIth Congress of the IAHR, Sao-Paulo, Brazil, 285-299.

Darghahi, B. (1990). Controlling mechanism of local scour. J. of Hydr. Engrg., ASCE, Vol. 116, No. 10, 1197-1214.

Darghahi, B. (1987). Flow field and local scouring around a cylinder. Bulletin No. 137, Royal Inst. Tech. Hydr. Lab., Stockholm.

Egiazaroff, J. V. (1965). Calculation of nonuniform sediment concentrations. J. of

Hydr. Div., ASCE, vol. 91, (HY4).

Einstein, H. A., and El-Samni, E. S. (1949). Hydrodynamic forces on a rough wall. Rev. Mod. Phys., Vol. 21, No. 3.

Ettema, R. (1980). Scour at bridge piers. Report No. 216, School of Engineering, University of Auckland, Auckland, New Zealand.

Fiorotto, V. (1993). Discussion of "Local scour at bridge abutments, Melville, M. W." J. of Hydr. Engrg., ASCE, Vol. 119, No. 9, 1064-1066.

Forchheimer, P. (1914). See Graf, 1971.

Franzetti, S., Larcan, E., and Mignosa, P. (1982). Influence of test duration on the evaluation of ultimate scour around circular piers. Proc. of Int. Conf. on the Hydra. Modelling of Civil Engineering structures, Coventry, England, 381-396.

Froehlich, D. C. (1989). Local scour at Bridge abutment. Hydraulic Engineering 89, Proc. of the 1989 Nat. Conf. on Hydr. Engrg., Hydr. Div., ASCE. New Orleans, La., 13-18.

Garde, R. G., and Ranga Raju, K. G. (1985). Mechanics of sediment transport and alluvial stream problems (2nd edition). John Wiley & Sons, New Delhi.

Garde, R. G., Subramanya, K., and Nambudripad, K. D. (1961). Study of scour around spur-dikes. J. of Hydr. Div., ASCE, vol. 87, (HY6), 23-37.

Garde, R. G., Subramanya, K., and Nambudripad, K. D. (1963). Closure to the discussion on "Study of scour around spur-dikes" J. of Hydr. Div., ASCE, vol. 89, (HY1), 167-175.

Gill, M. A. (1972). Erosion of sand bed around spur-dikes. J. of Hydr. Div., ASCE, Vol. 98, No. HY9, 1587-1602.

Gill, M. A. (1974). Closure to discussion on "Erosion of sand bed around spur-dike" J. of Hydr. Div., ASCE, Vol. 99, No. HY9, 1265-1267.

Gill, M. A. (1981). Bed erosion in rectangular long contraction. J. of Hydr. Div., ASCE, Vol. 107, No. HY3, 273-284.

Graf, W. H. (1972). Hydraulics of sediment transport. McGraw-Hill Inc.

Hankarachar, D., and Chadrasekhara, T. R. (1970). Discussion on "Local scour around bridge pier, Shen et al." J. of Hydr. Div., ASCE, Vol. 96, (HY8), 1747-1747.

Ippen, A. T., and Verma, R. P. (1953). The motion of discrete particles along the bed of a turbulent stream. Proc. of the Vth Congress of the IAHR, Minneapolis, Minnesota, 7-20.

Jeffreys, H. (1929). On the transport of sediments by streams. Proc. Cambridge Phil. Soc., Vol. XXV.

Joglekar, D. V. (1962). Discussion on "Scour at bridge crossing, Laursen, E. M." Trans. ASCE, Part I, Vol. 127, 183-186.

Jones, J. S. (1984). Comparison of prediction equations for bridge pier and abutment scour. Transportation Research Record, No. 950, Nat. Res. Council, Washington, D. C., 202-209.

Kandasamy, J. K. (1985). Local scour at Skewed abutments. Report No. 375, School of Engineering, University of Auckland, Auckland, New Zealand.

Kandasamy, J. K. (1989). Abutment scour. Report No. 458, School of Engineering, University of Auckland, Auckland, New Zealand.

Kandasamy, J. K. and Melville, B. M. (1989). Bridge damage due to Cyclone Bola. Report No. 459, School of Engineering, University of Auckland, Auckland, New Zealand.

Karaki, S (1960). Laboratory study of spur dikes for highway bridge protection. Highway research board bulletin 286, Washington, D. C., 1-12.

Karaki, S. S. (1959). Hydraulic model study of spur dikes for highway bridge openings. Report No. CER59SSK36, Colorado State University, Civil Engrg. Section, Fort Collins, Co, 1-47.

Knight, D. W. (1975). A laboratory study of local scour at bridge piers. Proc. of the XVIth Congress of the IAHR, Sao-Paulo, Brazil, 243-250.

Knight, D. W. (1981). Boundary shear in smooth and rough channels. J. of Hydr. Div., ASCE, Vol. 107, NO. HY7, 839-851.

Knight, D. W., and Demetriou, J. D. (1983). Flood plain and main channel flow interaction. J. of Hydr. Engrg., ASCE, Vol. 109, No. 8, 1073-1092.

Knight, D. W., and Shinon, K. (1990). Turbulence measurements in a shear layer region of a compound channel. J. of Hydr. Res., IAHR, Vol. 28, No. 2, 175-196.

Kothyari, U. C., Garde, R. G. , and Ranga raju, K. G. (1992). Temporal variation of scour around circular bridge piers. J. of Hydr. Engrg., ASCE, Vol. 118, No. 4, 1091-1106.

Krishnamurthy, M. (1970). Discussion on "Local scour around bridge piers, Shen et al." J. of Hydr. Div., ASCE, Vol. 96, (HY7), 1637-1638.

Kwan, T. F. (1984). A study of abutment scour. Report No. 451, school of Engineering, University of Auckland, Auckland, New Zealand.

Kwan, T. F. (1988). A study of abutment scour. Report No. 451, School of Engineering, University of Auckland, Auckland, New Zealand.

Kwan, T. F., and Melville, B. W. (1994). Local scour and flow measurements at bridge abutments. J. of Hydr. Res., IAHR, Vol. 32, No. 5, 661-673.

Lane, E. W. (1953). Progress report on studies on the design of stable channel of the Bureau of Reclamation, Trans. ASCE, Vol. 79.

Laursen, E. M. (1952). Observation on the nature of scour. Proc. of the fifth hydraulic conf. Bulletin 34, University of Iowa, Iowa city, Iowa, 179-197.

Laursen, E. M. (1958). Scour at bridge crossings, Iowa Highway Research Board Bulletin No. 8.

Laursen, E. M. (1962a). Scour at bridge crossing, Trans. ASCE, Part I, Vol. 127, 166-180.

Laursen, E. M. (1962b). Closure to the discussion on "Scour at bridge crossing" Trans. ASCE, Part I, Vol. 127, 207-209.

Laursen, E. M. (1963). An analysis of relief bridge scour. J. of Hydr. Div., ASCE, Vol. 89, No. HY3, 93-118.

Laursen, E. M. (1970). Discussion on "Local scour around bridge piers, Shen et al." J. of Hydr. Div., ASCE, Vol. 96, (HY9), 1896-1899.

Laursen, E. M. (1980). Predicting scour at bridge piers and abutments. General report No. 3, Engineering Experiment Station, College of Engineering, University of Arizona, 1-105.

Laursen, E. M. (1984). Assessing vulnerability of bridges to floods. Transportation Research Record, No. 950, Nat. Res. Council, Washington, D. C., 222-229.

Laursen, E. M. (1988). Bridge are expensive-- bridge failures are more expensive. Transportation Research Record, No. 1201, Nat. Res. Council, Washington, D. C., 43-45.

Laursen, E. M., and Christofferson, J. R. (1962). Discussion on "Study of scour around spur-dikes. Garde et al." J. of Hydr. Div., ASCE, vol. 88, (HY3), 225-229.

Laursen, E. M., and Toch, A. (1953). A generalized model study of scour around bridge piers and abutments. Proc. International Hydraulics Convention, Minneapolis, Minnesota, 123-131.

Laursen, E. M., and Toch, A. (1956). Scour around bridge piers and abutments. Bulletin No. 4, Iowa Highway Research Board, 1-60.

Lim, S. Y. (1993). Discussion on "Local scour at bridge abutments, Melville, M. W." J. of Hydr. Engrg., ASCE, Vol. 119, No. 9, 1066-1069.

Liu, H. K., and Skinner, M. M. (1961). Effect of bridge constriction on scour and backwater. Report No. CER60HKL22, Civil Engineering Section, Colorado State University, Fort Collins, Co, 1-118.

Mavis, F. t. and Laushey, L. M. (1948). A reappraisal of the beginning of bed movement-competent velocity. Proc. of the IInd meeting of IAHR, Stockholm.

Melville, B. W. (1975). Local scour at Bridge sites. Report No. 117 School of Engineering, University of Auckland, Auckland, New Zealand.

Melville, B. M. (1984). Live bed scour at bridge piers. J. of Hydr. Engrg., ASCE, Vol. 110, No. 9, 1234-1247.

Melville, B. W. (1992). Local scour at bridge abutments. J. of Hydr. Engrg., ASCE, Vol. 118, No. 4, 615-631.

Melville, B. W. (1993). Closure to the discussion on "Local scour at bridge abutments" J. of Hydr. Engrg., ASCE, Vol. 119, No. 9, 1071-1073.

Melville, B. W. (1995). Bridge abutment scour in compound channels. J. of Hydr. Engrg., ASCE, Vol. 121, No. 12, 863-868.

Melville, B. M., Ettema, R., and Jain, S. C. (1989). Measurement of bridge scour. Report No. FHWA-RD-90-035, Proc. of the bridge scour symp., Turner-Fairbank

Highway Research Center, Federal Highway Administration, 183-94.

Melville, B. W., and Ettema, R. (1993). Bridge abutment scour in compound channels. Hydraulic Engineering 93, Proc. of the 1993 Nat. Conf. on Hydr. Engrg., Hydr. Div., ASCE. Sanfrancisco, Ca., 767-772.

Melville, B. W., and Parola, A. (1995). The need for additional abutment scour research. Proc. of the First Inter. Conf. on Water Resources Engineering, ASCE, San Antonio, Texas, 1239-1243.

Melville, B. W., and Raudkivi, A. J. (1977). Flow characteristics in local scour at bridge piers. J. of Hydr. Res., IAHR, Vol. 15, No. 4, 373-380.

Melville, M. A. and Raudkivi, A. J. (1984). Local scour at bridge abutments, Road Research Unit, Bulletin 73, National Road Board, Wellington, New Zealand.

Melville, B. W., and Sutherland, A. J. (1988). Design method for local scour at bridge piers. J. of Hydr. Engrg., ASCE, Vol. 114, No. 10, 1210-1226.

Myers, R. C., and Elsawy, E. M. (1975). Boundary shear in channel with floodplain. J. of Hydr. Div., ASCE, Vol. 101, No. HY7, 933-946.

Myers, W. R. C. (1977). Momentum transfer in compound channel. J. of Hydr. Res., IAHR, Vol. 16, No. 2, 139-150.

Myers, W. R. C. (1991). Influence of geometry on discharge capacity of open channels. J. of Hydr. Engrg., ASCE, Vol. 117, No. 5, 676-680.

Myers, W. R. C., and Brennan, E. K. (1990). Flow resistance in compound channel. J. of Hydr. Res., IAHR, Vol. 28, No. 2, 141-155.

Nakagawa, H., and Suzuki, K. (1975). An application of stochastic model of sediment motion to local scour around a bridge pier. Proc. of the XVIth Congress of the IAHR, Sao-Paulo, Brazil, 228-235.

Nazarul Islam, M. D., Garde, R. J., and Ranga Raju, K. G. (1986). Temporal variation of local scour. Proc. of the 1986 IAHR symp. on scale effects in modelling sediment transport phenomena, Toronto, Canada, 253-261.

Neill, C. R. (1970). Discussion on "Local scour around bridge piers, Shen et al." J. of Hydr. Div., ASCE, Vol. 96, (HY5), 1224-1227.

Neill, C. R. (1973). Discussion on "Erosion of sand bed around spur-dike, Gill, M. A." J. of Hydr. Div., ASCE, Vol. 99, No. HY5, 860-862.

Neill, C. R., and Chaplain, T. K. (1962). Discussion on "Study of scour around spur-dikes. Garde et al." J. of Hydr. Div., ASCE, vol. 88, (HY2), 191-192.

Neill, C. R. (1967). Mean velocity criterion for scour of coarse uniform bed-material. Proc. of the 12th congress of the IAHR, Vol. 3, Fort collins, Co.

Nikuradse, J. (1933). Law of flow in rough pipes. Translation of "Strömungsgesetze in rauhen rohren" Technical memorandum 1292, National Advisory Committee for Aeronautics, Washington, 1950.

Nikuradse, J. (1932). See Schlichting, 1968.

Nwachukwu, B. A. and Rajaratnam, N. (1980) Flow and erosion near groyne-like structures. Dept. of Civil Engrg., University of Alberta, Edmonton, Alberta, Canada.

Prandtle, L. (1929). See Schlichting 1968.

Rajaratnam, N., and Ahmadi, R. M. (1979). Interaction between main channel and floodplain flows. J. of Hydr. Div., ASCE, Vol. 105, No. HY5, 573-588.

Rajaratnam, N., and Nwachukwu, B. A. (1983a). Flow near groin-like structures. J. of Hydr. Engrg., ASCE, Vol. 109, No. 3, 463-480.

Rajaratnam, N., and Nwachukwu, B. A. (1983b). Erosion near groin-like structures.

J. of Hydr. Res., IAHR, Vol. 21, No. 4, 277-287.

Raudkivi, A. J. (1990). Loose boundary hydraulics. 3ed edition.

Raudkivi, A. J. (1984). Scour at bridge piers. Proc. of the 4th. Int. Conf. on Applied Numerical Modelling, Vol. 63, Tainan, Taiwan, 283-289.

Raudkivi, A. J. (1986). Functional trends of scour at bridge piers. J. of Hydr. Engrg., ASCE, Vol. 112, No. 1, 1-13.

Raudkivi, A. J. (1967). Analysis of resistance in fluvial channels. J. of Hydr. Div., ASCE, Vol. 93, (HY5), 73-84.

Raudkivi, A. J., and Ettema, R. (1977). Effect of sediment gradation on clear water scour. J. of Hydr. Div., ASCE, Vol. 103, No. HY10, 1209-1213.

Raudkivi, A. J., and Ettema, R. (1982). Clear-water scour at cylindrical piers. J. of Hydr. Engrg., ASCE, Vol. 109, No. 3, 338-350.

Raudkivi, A. J. and Sutherland, A. J. (1981). Scour at bridge crossings, Bulletin No. 54, Road Research Unit, National Roads Board, New Zealand.

Richardson, E. V., Harrison, L. J., Davis, S. R. (1991a). Evaluating scour at bridges. Hydraulic Engineering Circular No. 18, Pub. No. FHWA-IP-90-017, Federal Highway Administration, Washington, D.C.

Richardson, E. V., and Huber, F. W. (1991). Evaluation of bridge vulnerability to hydraulic forces, stream instability, and scour. Transportation Research Record, No. 1290, Nat. Res. Council, Washington, D. C., 25-38.

Richardson, E. V., and Richardson, J. R. (1994). Practical method for calculating contraction scour. Hydraulic Engineering 94, Proc. of the 1994 Nat. Con. on Hydr. Engrg., Hydr. Div., ASCE. Buffalo, N.Y., 6-10.

Richardson, E. V., and Richardson, J. R., and Abed, L. (1991b). Estimating scour at bridges. Transportation Research Record, No. 1290, Nat. Res. Council, Washington, D. C., 245-254.

Richardson, E. V., and Simons, D. B. (1984). Use of spur and guidebanks for highway crossings. Transportation Research Record, No. 950, Nat. Res. Council, Washington, D. C., 184-193.

Richardson, E. V., Simons, D. B., Julien, P.Y. (1990). Highway in the river environment. Publication No. FHWA-HI-90-016, National Highway Institute Federal Highway Administration, McLean, Virginia.

Richardson, J. R., and Richardson, E. V. (1993a). The fallacy of local abutment scour equations. Hydraulic Engineering 93, Proc. of the 1993 Nat. Conf. on Hydr. Engrg., Hydr. Div., ASCE. Sanfrancisco, Ca., 749-754.

Richardson, J. R., and Richardson, E. V. (1993b). Discussion of "Local scour at bridge abutments, Melville, M. W." J. of Hydr. Engrg., ASCE, Vol. 119, No. 9, 1069-1071.

Richardson, J. R., and Richardson, E. V. (1994). Practical method for scour prediction at bridge piers. Hydraulic Engineering 94, Proc. of the 1994 Nat. Con. on Hydr. Engrg., Hydr. Div., ASCE. Buffalo, N.Y., 1-5.

Romita, P. L. (1962). Discussion on "Scour at bridge crossing, Laursen, E. M." Trans. ASCE, Part I, Vol. 127, 206-207.

Roper, A. T. (1970). Discussion on "Local scour around bridge piers, Shen et al." J. of Hydr. Div., ASCE, Vol. 96, (HY7), 1636-1637.

Rouse, H. (1939). An analysis of sediment transport in the light of fluid turbulence. Soil conservation service Report No. SCS-TP-25 U.S. Dept. of Agriculture. Washington D.C.

Schlichting, H. (1968). Boundary-layer theory, 6th edition, McGraw-Hill Inc.

Sellin, R. H. J. (1964). A laboratory investigation into the interaction between the flow in the channel of a river and that over its flood plain. La Houille Blanche, Vol. 7, 793-801.

Shen, H. W., Schneider, V. R., and Karaki, S. (1969). Local scour around bridge piers. J. of Hydr. Div., ASCE, Vol. 95, (HY6), 1919-1940.

Shen, H. W., Schneider, V. R., and Karaki, S. S. (1966). Mechanics of local scour. Report No. CER66HWS22 Civil Engineering Department, Colorado State University, Fort Collins, CO.

Shen, H. W., Schneider, V. R., Karaki, S. (1971). Closure to the discussion on "Local scour around bridge piers" J. of Hydr. Div., ASCE, Vol. 97, (HY9), 1513-1517.

Shields, A. (1936). See Vanoni, 1975.

Shirole, A. M., and Holt, R. C. (1991). Planning for a comprehensive bridge safety assurance program. Transportation Research Record, No. 1290, Nat. Res. Council, Washington, D. C., 39-50.

Simons, D. B., and Albertson, H. (1960). See Simons, D. B., and Senturk, F. (1992)

Simons, D. B., and Senturk, F. (1992). Sediment transport technology. WRP, Littleton, Co. USA.

Sturm, T. W., and Janjua, N. S. (1994). Clear-water scour around abutments in floodplains. J. of Hydr. Engrg., ASCE, Vol. 120, No. 8, 956-972.

Sturm, T. W., and Janjua, N. S. (1993). Bridge abutment scour in floodplain. Hydraulic Engineering 93, Proc. of the 1993 Nat. Conf. on Hydr. Engrg., Hydr. Div., ASCE. Sanfrancisco, Ca., 761-766.

Tarapore, Z. S. (1967). Determination of the depth of scour around an obstruction in an alluvial channel. Proc. of the 12th congress of the IAHR, Vol. 3, Fort collins, Co., C3.1-C3.9.

Thomas, A. R. (1962). Discussion on "Scour at bridge crossing, Laursen, E. M." Trans. ASCE, Part I, Vol. 127, 196-198.

Thomas, A. R. (1970). Discussion on "Local scour around bridge piers, Shen et al." J. of Hydr. Div., ASCE, Vol. 96, (HY9), 1894-1896.

Tison, G. Jr. (1962). Discussion on "Study of scour around spur-dikes. Garde et al." J. of Hydr. Div., ASCE, vol. 88, (HY4), 301-306.

Tison, L. J. (1962). Discussion on "Scour at bridge crossing, Laursen, E. M." Trans. ASCE, Part I, Vol. 127, 188-191.

Townsend, D. R. (1968). An investigation of turbulence characteristics in a river model of complex cross section. Proc. of the institution of Civil Engineers, Vol. 40, 155-175.

Vanoni, V. A. (1966). Sediment transport mechanics: Initiation of motion. J. of Hydr. Div., ASCE, Vol. 92, (HY2).

Vanoni, V. A., and Hwang, Li-San (1967). Relation between bed forms and friction in streams. J. of Hydr. Div., ASCE, Vol. 93, (HY3), 121-144.

Vanoni, V. A. (1975). Sedimentation engineering. Engineering Monograph No. 54. ASCE.

Ward, B. D. (1969). Relative density effects on incipient bed movement. Water Resources Res. Vol. 5, No. 5.

White, C. M. (1940). The equilibrium of grains on the bed of a stream. Proc. Roy. Soc. London. Vol. 174A.

Wong, W. H. (1982). Scour at bridge abutments. Report No. 275, School of Engineering, University of Auckland, Auckland, New Zealand.

Wright, R. R., and Carstens, M. R. (1970). Linear-momentum flux to overbank sections. J. of Hydr. Div., ASCE, Vol. 96, No. HY9, 1781-1793.

Zaghloul, N. (1983). Local scour around spur-dikes. J. of Hydrology, Vol. 60, 123-139.

Zheleznyakov, C. V. (1965). Relative deficit of mean velocity of unstable river flow, kinematic defect in river beds with flood plains. Proc. of the 11th congress of the IAHR, Leningrad, USSR, 1-12.

Zheleznyakov, C. V. (1971). Role of flood plain in flood discharge of a river channel. Proc. of the 14th Int. congress of the IAHR, Paris France, 141-144.

Zheleznyakov, C. V. (1971). Interaction of channel and flood plain streams. Proc. of the 14th Int. congress of the IAHR, Paris, France, 145-148.

Appendices

Appendix A

PARTICLE MOVEMENT
AND
LOG VELOCITY LAW

A.1- PARTICLE MOVEMENT

The equations describing the initial movement of bed particles were founded on several bases: the critical velocity (fluid impact on particles), the critical shear stress (the frictional drag of the flow on the particles), and the lift force criteria (the pressure differences due to the gradient of the velocity). Although the approaches seem to be different, it can be shown that they are not entirely dissimilar.

A.1.1- Critical velocity equations

A.1.1.1- Theoretical formulation

Considering the angle of repose, φ, and the forces acting parallel, F_t, and normal, F_n, to it, the initial movement condition for a mass of cohesionless, loose, and solid particles can be described as:

$$\tan \varphi = \frac{F_t}{F_n} \qquad \textbf{(A.1)}$$

Substituting the resultants of the hydrodynamic drag, F_D, the lift force, F_L, and the submerged weight, W, for F_t and F_n in Equation A.1, the condition of incipient movement becomes:

$$\tan \varphi = \frac{W \sin \alpha + F_D}{W \operatorname{Cos} \alpha - F_L} \tag{A.2}$$

in which α is the inclination of the bed from the horizontal at which incipient sediment movement takes place. This situation is illustrated in Figure 3.1.

Usually, drag and lift forces and the submerged weight of the particle are expressed as:

$$F_D = C_D\, k_1\, D^2\, \frac{\rho\, u_b^2}{2} \tag{A.3}$$

$$F_L = C_L\, k_2\, D^2\, \frac{\rho\, u_b^2}{2} \tag{A.4}$$

$$W = k_3\, (\rho_s - \rho)\, g\, D^3 \tag{A.5}$$

in which u_b = flow velocity at the bottom of the channel, C_D, C_L = drag and lift coefficients, respectively, D = particle diameter, and k_1, k_2, and k_3 = particle shape factors.

Introducing Equations A.3, A.4, and A.5 into Equation A.2, yields:

$$\frac{u_{b_c}^2}{(\rho_s/\rho - 1)\, gD} = \frac{2k_3\, (\tan \varphi \cos \alpha - \sin \alpha)}{C_D\, k_1 + C_L\, k_2 \tan \varphi} \tag{A.6}$$

in which u_{b_c} is the critical bottom velocity at which incipient sediment motion takes place. The right-hand side of Equation A.6 is termed the *sediment coefficient* A':

$$A' = \frac{2k_3\,(\tan\varphi\cos\alpha - \sin\alpha)}{C_D\,k_1 + C_L\,k_2\tan\varphi} \tag{A.7}$$

Equation A.7 shows that the *sediment coefficient*, A', is a function of: (*i*) the bed material (grain size, size distribution, shape, texture, etc.), (*ii*) the flow characteristics which determine C_D and C_L values, (*iii*) the channel slope, and (*iv*) the angle of repose, which depends on particle properties.

A.1.1.2- Experimental verifications

The lack of good definition of the bottom velocity, u_b, on one hand and the encountered difficulty in its measurements on the other, make it difficult to experimentally evaluate Equation A.6. Nevertheless, applying this equation in some circumstances in which the effect of some parameters is negligible might be useful.

Analysing the results of 400 tests, Mavis and Luashey (1948) proposed an equation to determine the critical bottom velocity in alluvial streams. Their proposed model takes the form:

$$u_{b_c} = \frac{1}{2}\,D^{4/9}\sqrt{\frac{\rho_s}{\rho} - 1} \tag{A.8}$$

in which the grain diameter is in mm and the flow velocity in ft/s. Another equation which relates the initiation of sediment motion to the bottom velocity was proposed by Carstens (1966). Based on analysis of relatively large amounts of the published data collected on incipient motion, Carstens suggested his model in the following form:

$$\frac{u_{b_c}^2}{(\rho_s/\rho - 1)\, gD} = 3.612\ (\tan\varphi \cos\alpha - \sin\alpha) \tag{A.9}$$

Among the numerous studies that relate U_c to the initiation of bed motion only Neill's (1967) relationship and Levi's work (reported by Graf, 1971) are presented here, by Equations A.10 and A.11 respectively.

$$U_c = 1.4\sqrt{gD}\ \ln\frac{y_o}{7D} \qquad (SI\ units) \tag{A.11}$$

$$\frac{u_c^2}{(\rho_s/\rho - 1)gD} = 2.50\left(\frac{D}{y_o}\right)^{-0.20} \tag{A.10}$$

Equation A.11 is applicable when the relative roughness $y_o/D > 60$, in which y_o = the uniform depth of flow.

A.1.2- Critical shear stress equations

A.1.2.1- Theoretical formulation

According to Forchheimer (1914) the friction force at the bottom of a channel is related to the weight component of a water column by the following equation:

$$\gamma\, y_o\, S = k_5\, u_b^2 \tag{A.12}$$

in which S = slope of the energy grade line, and k_5 = a constant. The left hand side of Equation A.12 is the *tractive force* per unit surface area, τ_o, or the *shear stress:*

$$\tau_o = \gamma \, y_o \, S \tag{A.13}$$

Equation A.13 is applicable to wide rectangular channels; however, for narrow or irregular channels the average flow depth should be substituted by the hydraulic radius, $R = A/P$, of the watercourse, in which A= the channel cross-sectional area and P= the wetted perimeter

Based on the relation between τ_o and u_b (Equations A.12 and A.13) Equation A.6 can be written in terms of the critical shear stress, τ_c, at the incipient condition as:

$$\frac{\tau_c}{(\gamma_s - \gamma)D} = A'' \tag{A.14}$$

in which A''= a sediment coefficient.

Application of *friction velocity* or the *shear velocity*, u_*, which represents a measure of the intensity of the turbulent fluctuations, was suggested by the modern advancements in fluid mechanics. As mentioned earlier, the relation between *friction velocity* and *shear stress* is given by:

$$u_* = \sqrt{\frac{\tau_o}{\rho}} \tag{A.15}$$

The threshold condition of particle motion might be presented in a functional form as follows (Simons and Senturk, 1992):

$$\frac{\tau_c}{(\gamma_s - \gamma)\, D_s} = \frac{\rho \, u_{*c}^2}{(\gamma_s - \gamma)\, D_s} = f\,(B,\, y_o,\, D_s,\, g,\, \rho_s,\, \rho,\, \nu,\, u_{*c}) \tag{A.16}$$

in which B= the channel width, D_s= the effective grain size or roughness element, ν= the kinematic viscosity of the fluid, and u_{*c}= the shear velocity at the threshold condition.

With the aid of dimensional analysis, Equation A.16 can be presented in the following form:

$$\frac{\tau_c}{(\gamma_s-\gamma)\ D_s} = \frac{\rho\ u_{*c}^2}{(\gamma_s-\gamma)\ D_s} = f\left(\frac{D_s}{b}, \frac{D_s}{y_o}, \frac{\rho_s}{\rho}, \frac{u_{*c}\ D_s}{\nu}\right) \qquad \textbf{(A.17)}$$

The influence of D_s/b and D_s/y_o on particle equilibrium for fine particles may practically be neglected. Since ρ_s and ρ are constant quantities, the effect of ρ_s/ρ can be included in the coefficient of the final equation. Hence Equation A.17 reduces to:

$$\frac{\tau_c}{(\gamma_s-\gamma)\ D_s} = f\left(\frac{u_{*c}\ D_s}{\nu}\right) \qquad \textbf{(A.18)}$$

The left term of Equation A.18 is the ratio of the drag force to the gravitational force, i.e., it is a type of Froude number expressed in terms of the shear velocity ratio and the grain size. The right hand side, however, is the Reynolds number of the particle which is usually refer to as the *shear Reynolds number*, R_{e*}.

A.1.2.2- Experimental verifications

During the past many investigators tried to experimentally establish a relation like Equation A.14. A few of the important findings are mentioned here, (for further information see Graf (1971), Vanoni (1975), Raudkivi (1990), and Simons and Senturk (1992)). Field data for a wide range of grain sizes from fine to coarse noncohesive material were studied by Lane (1953) to establish the limiting tractive force diagram (Figure 3.2). The diagram, which has been used for design purposes, clearly shows that considerably lower critical shear stress is allowed for clear water than for water carrying sediment.

Leliavsky (1955) believed that a simple relationship such as:

$$\tau_c = 166\ D \qquad g/m^2 \tag{A.19}$$

satisfactorily relates the critical shear stress to the grain size. In this equation the mean particle diameter, D, is given in mm and should be smaller than 3.5 mm. Figure 3.3 is a plot of Equation A.19 along with the data of different researchers. Equation A.19 is simple in form. Graf (1971), however, declared that it apparently applies to most of the data.

Many experimental programs have been conducted by researchers to establish an explicit solution of the functional relationship, as given in Equation A.18,. The first was that of Shields (1936) who proposed a graphical solution, which was later modified by Rouse (1939) to take the form given in Figure 3.4. On this graph a number of interesting facts can be observed. For a particular value of R_{c*} the corresponding value of F_* falling on the curve indicates the threshold condition of particle movement, while lower and higher values respectively correspond to no bed motion and general bed motion. Also, the curve is very similar to the friction diagram for artificially-roughened pipes and the drag coefficients relationship for a sphere or a cylinder which might indicate that these phenomena are related through fluid mechanics (Graf, 1971).

Many investigators, including White (1940), Ippen and Verma (1953), and Ward (1969), verified Shields diagram (Figure 3.4) and it is widely accepted now. Shields diagram, however, is applied to uniform sand, therefore nonuniform grain material, cohesive or flocculant material, as well as flat sand grains might move at τ_c different than that given by Shields diagram for uniform sand. For incipient motion of nonuniform mixtures, Egiazaroff (1965) proposed the following equation, which is only applicable in fully turbulent flow:

$$\frac{\tau_c}{(\gamma_s-\gamma)\ D_{50}} = \frac{0.1}{[\log\ 19\ (D_{50}/\overline{D})]^2} \tag{A.20}$$

where D_{50} and $\overline{D}$= the median and the average diameter of grains, respectively, for grains in movement and for total sediments. For a fine-graded mixture, $D_{50}<\overline{D}$, the resistance to incipient motion is increased, while according to Equation A.20, the opposite is true for a coarse-graded mixture, where $D_{50}>\overline{D}$.

A.1.3- Lift force mechanisms

The lift forces were incorporated in the derivation of the basic equation of scour, i.e. Equation A.2. However, its quantitative effect has not been stressed yet. In this section the lift force and its effects are discussed in greater detail.

A.1.3.1-Theoretical formulation

At the invert level of a channel lift forces develop and affect particles resting on the channel bed. The generation of the lift forces might be attributed to at least two reasons: the velocity gradient in the vertical direction and turbulence fluctuations. Considering the vertical velocity distribution in a channel flow, the bottom zone experiences a steeper velocity gradient, therefore, a pressure difference is set up which results in lifting of the bed particles. Also, the upward velocity component, resulting from the turbulence, might lift the same particles.

For a horizontal channel bed ($\alpha=0$) Equation A.2 takes the form:

$$\tan\varphi = \frac{F_D}{W-F_L} \tag{A.21}$$

which indicates that as soon as the magnitude of the lift becomes equal to the particle weight ($W=F_L$), the smallest drag force would cause the initiation of motion. Therefore, it is important to investigate the magnitude of the lift force (Equation A.4) to compare its value to both the drag force (Equation A.3) and the submerged weight of the particle (Equation A.5).

Assuming a potential flow over a long, circular cylinder with its major axis perpendicular to the flow, Jeffreys (1929) presented a criterion for the occurrence of lift force. He showed that lift takes place if Equation A.22 is satisfied.

$$\left(\frac{1}{3}+\frac{1}{9}\pi^2\right)u_\infty^2 > \frac{\rho_s-\rho}{\rho}ga \tag{A.22}$$

in this equation u_∞ = the free-stream velocity, and a = the radius of the particle ($a=D/2$). An experimental investigation indicated that values obtained with Equation A.22 seem to be of the right order of magnitude. Flow passing a grain is a three-dimensional flow, however, Equation A.22 was derived for a two-dimensional flow. Therefore, consideration of a modifying factor in this case is essential. Also, the shortcoming of Jeffreys' model is that drag forces are altogether disregarded.

The qualitative functional relationship in the Shields diagram (Figure 3.4) can also be derived with a model for lift forces rather than for shear forces. This fact, however, only adds further confidence to the Shields diagram.

A.1.3.2-Experimental verifications

Einstein and El-Samni (1949) studied the average lift force on two sediment beds, which was measured directly as a pressure difference. The experiments should be viewed as a step forward in understanding the lift mechanism. Plastic spherical balls 68.5 mm in diameter and natural gravel of about the same average size but with a considerable spread of grain size, were used. All the data are represented by Equation A.23 which is similar to Equation A.4:

$$\Delta P = \frac{1}{2} C_L \, \rho u_y^2 \tag{A.23}$$

in which ΔP= is the mean static-pressure difference in the bed at the top and bottom of the grain. The velocity u_y is measured at a distance 0.35D from the theoretical wall. Vanoni (1966) used the result of this study to calculate the ratio $\Delta P/\tau_c$. His calculations showed that $\Delta P/\tau_c \approx 2.5$, which indicates that lift forces are highly important in the initial-motion mechanism. However, once a particle is displaced, lift forces tend to diminish and drag forces tend to increase.

A.2- LOG VELOCITY LAW

The velocity and shear stress distributions play key roles in any *loose-boundary* hydraulics study. Although deviating from the undisturbed floodplain and main channel values, the velocity distributions in these regions still follow the universal log-law. Accordingly, the theoretical basis of the velocity distribution and the approach by which the bed roughness is evaluated are presented here.

A.2.1- THE UNIVERSAL VELOCITY DISTRIBUTION LAW

Prandtl's (1925) hypothesis for turbulent shearing stress is given in the following form:

$$\tau=\rho l^2\left(\frac{du}{dy}\right)^2 \qquad \textbf{(A.24)}$$

in which du/dy = time average of velocity gradient in the y direction, and l = Prandtl's mixing length (a mean distance over which fluid particles are transported by turbulence from regions of one velocity to regions of another and in so doing these particles suffer changes in their general velocities of motion).

Under the assumptions that the mixing length is proportional to the distance from the wall, $l=\kappa y$, and that the shearing stress remains constant, Prandtl's turbulent shearing stress hypothesis led to the derivation of a relationship describing the velocity distribution which is valid for small wall distances. For the case of a turbulent stream over a smooth flat wall, the velocity-distribution law takes the form:

$$u=\frac{u_*}{\kappa}\ln y+C \qquad \textbf{(A.25)}$$

in which κ = Von Karman's universal constant, and C= the constant of integration (determined so that at a certain distance from the wall, $u=0$). Therefore, Equation A.25 takes the form:

$$u = \frac{u_*}{\kappa}\left(\ln y - \ln Y\right) \qquad \text{(A.26)}$$

Using dimensional argument, which indicates that y_o is proportional to $\frac{\nu}{u_*}$ (Schlichting, 1968), and substituting $\beta \frac{\nu}{u_*}$ for Y in Equation A.26 yields:

$$\frac{u}{u_*} = \frac{1}{\kappa}\left(\ln \frac{yu_*}{\nu} - \beta\right) \qquad \text{(A.27)}$$

or

$$\frac{u}{u_*} = \frac{1}{\kappa}\left(\ln \frac{yu_*}{\nu}\right) + \beta' \qquad \text{(A.28)}$$

Equation A.28, the logarithmic universal velocity-distribution law, gives the relation between $\frac{yu_*}{\nu}$ and the dimensionless velocity u/u_* on a smooth bed.

Although the universal velocity-distribution law was derived for the case of a flat wall (rectangular channel), measurements by Nikuradse (1933, 1932) for flow through circular smooth pipes showed excellent agreement with it. Not only is the concordance between Nikuradse's data and Equation A.28 obtained for the wall region, it is also true for the whole range of flow up to the pipe axis (Schlichting, 1968). Hence, based on Nikuradse's measurements, the numerical values of κ and β' of Equation A.28 were found to be 0.4 and 5.5 respectively. Therefore, the universal velocity-distribution laws for turbulent flow in smooth pipes (using natural and common logarithms respectively), take the form:

$$\frac{u}{u_*} = 2.5 \ln \frac{yu_*}{\nu} + 5.5 \tag{A.29}$$

and

$$\frac{u}{u_*} = 5.75 \log \frac{yu_*}{\nu} + 5.5 \tag{A.30}$$

In a region very close to the boundary, the laminar shearing stress is dominant, while the turbulent shearing stress vanishes. This causes a deviation in the velocity distribution from the universal law in the immediate neighbourhood of the wall. In this laminar flow region the velocity distribution takes the form:

$$\frac{u}{u_*} = \frac{yu_*}{\nu} \tag{A.31}$$

Further measurements (Nikuradse, 1933) indicated that the assumption of the proportionality of mixing length to the distance from the wall, $l=\kappa y$, is also valid for rough pipes in the neighbourhood of the wall. Therefore, the logarithmic velocity-distribution law (Equation A.25) is also valid for rough pipes provided that a different numerical value is assigned to the constant of integration, Y. That is, in the case of a rough pipe, Y is proportional to a characteristic length of roughness height k (Schlichting, 1968). Introducing $Y=\lambda k$ into Equation A.26 yields:

$$\frac{u}{u_*} = \frac{1}{\kappa}\left(\ln \frac{y}{k} + \lambda\right) \tag{A.32}$$

Equation A.33 can be written in the following general form:

$$\frac{u}{u_*} = \frac{1}{\kappa} \ln \frac{y}{k} + B \tag{A.33}$$

Since the numerical values of Equation A.33 were evaluated according to Nikuradse's (1933) measurements, it is common practice to define the characteristic length of roughness, k, in terms of Nikuradse's equivalent (or effective) sand roughness, k_s. Effective roughness in the sense that k_s is no longer an actual linear dimension of the roughness but a parameter signifying behaviour in comparison with Nikuradse's experiments for which the constants were chosen. Hence, Equation A.34 might be arranged according to Nikuradse's equivalent sand roughness, k_s, as:

$$\frac{u}{u_*} = \frac{1}{\kappa} \ln \frac{y}{k_s} + B_s \tag{A.34}$$

in which B_s, the roughness function, takes different values according to the predominant flow regime.

According to Nikuradse's measurements, three regimes are distinguished based on the value of roughness Reynolds number, $\frac{k_s u_*}{\nu}$, and the value of B_s in these regimes was evaluated as follows:

- In the range $0 < \frac{k_s u_*}{\nu} < 3.5$ the flow regime is hydraulically *smooth* and the height of the roughness elements is so small that they are completely submerged within the laminar sub-layer. According to Figure 3.5, B_s might be evaluated as:

$$B_s = 5.5 + 2.5 \ln \frac{k_s u_*}{\nu} \tag{A.35}$$

which, when substituted in Equation A.34 yields the universal velocity-distribution law (Equation A.29) for turbulent flow on *smooth* boundaries.

- A transition regime exists when $3.5 < \frac{k_s u_*}{\nu} < 70$. In this instance partial height of some of the roughness elements extends outside the laminar sub-layer and introduce additional resistance due to form drag. To determine B_s in this range of $k_s u_*/\nu$ different straight line segments might be fitted to the data of Figure 3.5 which give the following values:

$$B_s = 6.75 + 3.27 \log \frac{k_s u_*}{\nu} \; ; \; for \;\; 3.5 \leq \frac{k_s u_*}{\nu} < 7.1 \qquad \textbf{(A.36)}$$

$$B_s = 9.5 \; ; \; for \;\; 7.1 \leq \frac{k_s u_*}{\nu} < 16 \qquad \textbf{(A.37)}$$

$$B_s = 11.46 - 1.607 \log \frac{k_s u_*}{\nu} \; ; \; for \;\; 16 \leq \frac{k_s u_*}{\nu} \leq 70 \qquad \textbf{(A.38)}$$

- In the Rough flow regime $\frac{k_s u_*}{\nu} > 70$ and all the roughness elements extend beyond the laminar sub-layer. The resistance to flow in this regime is mainly due to form drag, which acts on the roughness elements. In this case B_s maintains a constant value of 8.5, which when substituted in Equation A.34 along with the value of $\kappa=0.4$ yields the well known equation of the universal velocity-distribution in *rough* flows:

$$\frac{u}{u_*} = 2.5 \ln \frac{y}{k_s} + 8.5 \qquad \textbf{(A.39)}$$

or in terms of common logarithms:

$$\frac{u}{u_*} = 5.75 \log \frac{y}{k_s} + 8.5 \tag{A.40}$$

Integrating A.40 over the depth of flow yields the flow rate per unit width of the channel, and dividing the result by the flow depth gives the mean velocity U_a as (Raudkivi, 1990):

$$\frac{U_a}{u_*} = 5.75 \log \frac{y_a}{k_s} + 6.0 \tag{A.41}$$

Appendix B

DEVELOPMENT OF DATA ACQUISITION SYSTEM

To measure the flow velocity, first the frequency should be scanned visually and recorded manually from the analog display of the AI. The average of the recorded values, then, is used to compute the actual velocity utilizing the calibration curves supplied with the sensing probe. During the preliminary tests it became apparent that the movements of the analog display are too fast to be scanned and recorded manually, making accurate data collection impossible. Moreover, processing velocity measurement in this manner is both time consuming and tedious. High accuracy in recording flow velocity could only be achieved using a computer-based data acquisition system. An appropriate system was designed for this particular application.

The signal provided by Streamflo Instruments can not be digitally recorded without modifying it to an acceptable form prior to feeding to a computer. A special outlet is available on the rear panel of the AI unit which provides a standard *precision current* with the range 0 to 200 μA. However, this current and the output range can not be accepted by a data acquisition board. Instead, it is specifically designed to feed a Nixon Instruments graphical record. An analog signal can be recorded by a computer if the computer is equipped with an Analogue to Digital (A/D) conversion board. A/D conversion boards usually accept *voltage signals* with a specific range and provide a conversion of the received signals to a digital form. Consequently, applying a specific A/D conversion board dictates necessary changes to the output of the AI prior to being accepted by the board. The A/D conversion board model DT2811 of Data Translation, Inc. was selected for this purpose and the output of the applied AI was modified to match the board requirements.

The DT2811 board is a 12-bit A/D convertor with three main features: Analogue to Digital (A/D) conversion, Digital to Analogue (D/A) conversion, and Digital Input/Output (I/O) transfer operations. The DT2811 has three different input modes, i.e. Single-Ended (SE), Differential (DI), and Pseudo-Differential (PDI) inputs. Furthermore, three input ranges are accepted by this board: ± 5 volts, 0 to +5 volts, and ± 2.5 volts. For this study the A/D conversion board was configured with the first input range (± 5 volt).

The number of the available channels to acquire data and the sensitivity to the electrical noise are the most important characteristics of each input mode. In the SE input mode, since input signals share a common low side, it provides maximum channel density (16 channel). However, the inputs in this mode are more sensitive to electrical noise which somewhat restricted the usage of this mode due to our electrically noisy environment. In a DI input mode, on the other hand, two multiplexer switches are used on each channel. Thus, the number of channels which can be connected is cut in half. The main advantage of this input mode is that it is less sensitive to electrical noise because noise is significantly reduced due to high common mode rejection of this mode, therefore, input cable length will not affect the noise figure and it may suit user requirements. Nevertheless, all cables should be kept as short as possible. The PDI input mode is a variation of the SE input mode and provides the user with partial common mode noise rejection without reducing the number of input channels. This Input mode, however, is as sensitive to the electrical noise as the SE mode, consequently, they share common restrictions in their applications.

The selected DT2811 A/D conversion board of Data Translation Inc. does not accept the precision current output of the Nixon AI. That current must be converted to a ±5 volts, suitable for the A/D card input range. To accomplish that, a new device was designed and built to receive the original *precision current* output of the AI and convert it to an acceptable voltage within the A/D board's range. Termed: *Precision Current to Voltage Current* (PCVC), this device, along with the other components of the whole system (Streamflo Instruments, and the A/D conversion board) went under comprehensive tests to check overall accuracy prior to application.

First the DT2811 A/D conversion board itself was tested to check its accuracy and to examine the possible meed for calibration. During this step, the A/D conversion board was installed inside an IBM Personal computer having an 8088 processor, then, its driver was installed and configured for that particular machine. The adopted configuration includes SE input mode, ±5 volts input range, and gain of one. Also, an interactive computer program was developed to scan and record the converted data acquired by the first channel of the A/D conversion board. A very constant voltage source was connected to the first channel of the board for a long period to observe the accuracy of the recorded data. The variation of the recorded data is shown in Figure 4.4; each data point of this graph is the average of eighty records scanned during eight seconds (ten records per second). Stable and reliable data were recorded during this step of the test. The maximum variations of the recorded data observed in this step were less than ±0.0015 volts (less than 0.2% of the full scale) which indicate that reliable data were acquired. Therefore, further calibration of the A/D conversion board was not necessary.

In the second step, The sensing probe was installed in a flume and connected to the AI to test the output of the PCVC. The output of the AI was fed to the PCVC while a precise digital voltameter was connected to the output of the PCVC to measure the produced voltage. Then, water was allowed to flow in the flume and by changing the discharge a flow velocity range of 0.1 to 1.2 m/s was generated. For the given flow velocity range the output voltage of PCVC showed complete concordance with the frequency values displayed by the AI. In other words, the output of the PCVC fell in the range 0 to 5 volts, which is accepted by the A/D conversion board. The results of this step along with that of the first step indicated that the components of the system produced accurate results when tested individually and were ready for the next step of the test as a complete data acquisition system.

In the third step of the test, the voltameter used in the second step was substituted by the A/D conversion board. In other words, the voltage of the PCVC was fed to the A/D conversion board, while other connections and test conditions were kept the same as those applied in the second step. As soon as the output of the PCVC was connected to the A/D conversion board, the voltage dropped and fluctuated 15 to 35% below the actual value. Numerous observations and tests carried out to detect the cause of this phenomenon led to the detection of 25 to 35 μA of leakage current between the flowing water and the computer's ground. Although the leakage current was small, it represented a significant percentage of the original range produced by the AI and could not be ignored in this case.

Theoretically, no current should be detected between the grounding of the system and the flowing water, therefore, a solution to this problem could not be supplied by the A/D conversion board manufacturer. Many large electrical devices and pumps running in the laboratory seem to produce electrical noise which affects the working condition of the system. Therefore, changing the input mode of the A/D conversion board to the DI mode which is not sensitive to the electrical noise seemed the only solution to the problem. This change of the input mode meant repeating steps I and II of the tests which led to the next phase of the test.

During the second phase of the tests, the A/D conversion board was configured to accept input in the DI mode, while the input range and the gain were kept the same. To observe the reliability of the data acquired by the A/D conversion board in the DI mode, the first step was repeated. A constant voltage source was fed to it. The acquired data showed large instability in the records (Figure 4.5). Therefore, reliable records using the DI mode might be obtained, provided a solution to the instability of the acquired data existed.

Careful supplementary tests indicated that referencing the low end of the used differential input channel to the Analogue Ground of the board improved the A/D conversion results. Further investigations revealed that the instability could be entirely eliminated, provided the aforementioned connection was externally accomplished through a resistor. Different resistors were installed and tested to find the most suitable one that removed the instability entirely and produced the smallest deviation from the mean of the recorded data. Applying a 1 kΩ resistor yielded the most accurate results (Figure 4.6). Figure 4.6 shows the recorded data using the full scale (compare with Figure 4.5), while Figure 4.7 shows the deviation of each data point from the original voltage. It should be mentioned that each data point of these figures is the average of eighty readings accomplished within eight seconds (ten records per second). Accordingly, the 1 kΩ resistor was selected to stabilize the A/D conversion operation of the board in the DI input mode. The resistor was externally and permanently installed between the low end of the first channel (the utilized channel) and the AG of the board (pin 17). Hence, the A/D conversion board was ready for the next test step --step II.

During the third test step of the second phase, the output of the PCVC was directly connected to the A/D conversion board, which was configured for the DI input mode, ± 5 volts input range, and gain of one. Also, other connection and flow conditions remained the same as that used in the third step of earlier phase of the tests. No improvements in the recorded data were observed, i.e. the drop in the recorded values still remained and changing the input mode to the DI did not resolve the problem. The results of the tests revealed that the measured output (using the voltameter) of the PCVC was in complete agreement with the results displayed by the AI and the drop in the voltage occurred as soon as the PCVC was connected to the A/D conversion board. Isolating the computer ground was the only solution. This was achieved by designing and applying a new device, i.e. a Ground Isolation Device (GID). In other words, by installing the GID between the PCVC and the A/D conversion board, direct connection was avoided and accurate data were captured and converted by the board.

The idea behind the GID is the deployment of a matched pair of photo voltaic optical isolators working in harmony on both sides of the isolation barrier to produce two equal voltages. An infrared beam is emitted on the PCVC side forcing a voltage to a pear on the computer side. Likewise, the computer side will emit a beam proportion to voltage it received back to PCVC side to ensure solid and repeatable results. Implementing the system with the GID removed the drop in the recorded voltage and reliable data were acquired thereafter. A schematic sketch of the complete data acquisition system is shown in Figure 4.8. Also, Figure 4.9 shows the acquired velocity measurements using the implemented system during a prolonged period (7000 seconds). The fluctuations in the recorded data are related to the turbulence structure.

Appendix C

Table C.1- D_s-y_a-S_o relationship for threshold conditions

S_o	y_a	τ_c	u_{*c}	D_{50}
-----	mm	N/m^2	m/s	mm
0.0006	27	0.1763	0.0133	0.24
0.0006	31.5	0.2056	0.0144	0.34
0.0006	36.1	0.235	0.0153	0.41
0.0006	40.6	0.2644	0.0163	0.48
0.0006	45.1	0.2938	0.0172	0.55
0.0006	49.6	0.3231	0.018	0.61
0.0006	54.1	0.3525	0.0188	0.67
0.0006	58.6	0.3819	0.0196	0.73
0.0006	63.1	0.4113	0.0203	0.78
0.0006	67.6	0.4407	0.021	0.83
0.0006	72.2	0.47	0.0217	0.88
0.00075	22.5	0.1836	0.0136	0.26
0.00075	27	0.2203	0.0149	0.38
0.00075	31.5	0.257	0.016	0.47
0.00075	36.1	0.2938	0.0172	0.55
0.00075	40.6	0.3305	0.0182	0.62
0.00075	45.1	0.3672	0.0192	0.70
0.00075	49.6	0.4039	0.0201	0.77
0.00075	54.1	0.4407	0.021	0.83
0.00075	58.6	0.4774	0.0219	0.89
0.00075	63.1	0.5141	0.0227	0.95
0.00075	67.6	0.5508	0.0235	1.01
0.00075	72.2	0.5875	0.0243	1.07
0.0009	18	0.1763	0.0133	0.24
0.0009	22.5	0.2203	0.0149	0.38
0.0009	27	0.2644	0.0163	0.48
0.0009	31.5	0.3085	0.0176	0.58
0.0009	36.1	0.3525	0.0188	0.67
0.0009	40.6	0.3966	0.0199	0.75
0.0009	45.1	0.4407	0.021	0.83
0.0009	49.6	0.4847	0.022	0.91
0.0009	54.1	0.5288	0.023	0.98

Appendix C

Table C.1- D_s-y_a-S_o relationship for threshold conditions

S_o	y_a	τ_c	u_{*c}	D_{50}
-----	mm	N/m^2	m/s	mm
0.0009	58.6	0.5729	0.024	1.05
0.0009	63.1	0.6169	0.0249	1.12
0.0009	67.6	0.661	0.0257	1.18
0.0009	72.2	0.705	0.0266	1.24
0.0015	13.5	0.2203	0.0149	0.38
0.0015	18	0.2938	0.0172	0.55
0.0015	22.5	0.3672	0.0192	0.70
0.0015	27	0.4407	0.021	0.83
0.0015	31.5	0.5141	0.0227	0.95
0.0015	36.1	0.5875	0.0243	1.07
0.0015	40.6	0.661	0.0257	1.18
0.0015	45.1	0.7344	0.0271	1.28
0.0015	49.6	0.8079	0.0284	1.38
0.0015	54.1	0.8813	0.0297	1.47
0.0015	58.6	0.9548	0.0309	1.55
0.0015	63.1	1.0282	0.0321	1.64
0.0015	67.6	1.1016	0.0332	1.71
0.0015	72.2	1.1751	0.0343	1.78

$u_*/u_{*c} = 0.95$

$u_* = (g\,S_o\,y)^{0.5}$

$\tau_c = u_{*c}^{\,2}\,\rho$

Appendix D

Table D.1- Scour data for interacting flow conditions; D_{50}= 0.5 mm

S_o	abut. shape	L	y_a	y_{se}	y_{se}/y_a	L/y_a	y_{se}/L	y_a/L
—	—	cm	mm	mm	----	----	----	----
0.0006	VW	21	42	181.7	4.325	5.000	0.865	0.200
0.0006	VW	15	42	135.0	3.214	3.571	0.900	0.280
0.0006	VW	9	42	100.0	2.381	2.143	1.111	0.467
0.0006	WW	21	42	140.0	3.333	5.000	0.667	0.200
0.0006	WW	15	42	115.0	2.738	3.571	0.767	0.280
0.0006	WW	9	42	100.0	2.381	2.143	1.111	0.467
0.0006	SC	21	42	131.7	3.135	5.000	0.627	0.200
0.0006	SC	15	42	105.0	2.500	3.571	0.700	0.280
0.0006	SC	9	42	91.7	2.183	2.143	1.019	0.467
0.0006	ST	21	42	131.7	3.135	5.000	0.627	0.200
0.0006	ST	15	42	110.0	2.619	3.571	0.733	0.280
0.0006	ST	9	42	86.7	2.063	2.143	0.963	0.467
0.00075	VW	21	33	162.5	4.924	6.364	0.774	0.157
0.00075	VW	15	33	133.3	4.040	4.545	0.889	0.220
0.00075	VW	9	33	96.7	2.929	2.727	1.074	0.367
0.00075	WW	21	33	133.3	4.040	6.364	0.635	0.157
0.00075	WW	15	33	109.2	3.308	4.545	0.728	0.220
0.00075	WW	9	33	96.7	2.929	2.727	1.074	0.367
0.00075	SC	21	33	130.0	3.939	6.364	0.619	0.157
0.00075	SC	15	33	105.0	3.182	4.545	0.700	0.220
0.00075	SC	9	33	90.0	2.727	2.727	1.000	0.367
0.00075	ST	21	33	132.5	4.015	6.364	0.631	0.157
0.00075	ST	15	33	105.0	3.182	4.545	0.700	0.220
0.00075	ST	9	33	81.7	2.475	2.727	0.907	0.367
0.0009	VW	21	28	141.7	5.060	7.500	0.675	0.133
0.0009	VW	15	28	130.0	4.643	5.357	0.867	0.187
0.0009	VW	9	28	90.0	3.214	3.214	1.000	0.311
0.0009	WW	21	28	125.0	4.464	7.500	0.595	0.133
0.0009	WW	15	28	108.3	3.869	5.357	0.722	0.187
0.0009	WW	9	28	86.7	3.095	3.214	0.963	0.311
0.0009	SC	21	28	121.7	4.345	7.500	0.579	0.133
0.0009	SC	15	28	104.2	3.720	5.357	0.694	0.187
0.0009	SC	9	28	83.3	2.976	3.214	0.926	0.311
0.0009	ST	21	28	120.0	4.286	7.500	0.571	0.133
0.0009	ST	15	28	105.0	3.750	5.357	0.700	0.187
0.0009	ST	9	28	70.0	2.500	3.214	0.778	0.311

Table D.2- Scour data for non-interacting flow conditions; D_{50}= 0.5 mm

S_o	abut. shape	L	y_a	y_{se}	y_{se}/y_a	L/y_a	y_{se}/L	y_a/L
—	—	cm	mm	mm	—	—	—	—
0.00075	VW	21	33	129.2	3.916	6.364	0.615	0.157
0.00075	VW	15	33	112.3	3.403	4.545	0.749	0.220
0.00075	VW	9	33	76.9	2.331	2.727	0.855	0.367
0.00075	WW	21	33	105.4	3.193	6.364	0.502	0.157
0.00075	WW	15	33	97.7	2.960	4.545	0.651	0.220
0.00075	WW	9	33	76.9	2.331	2.727	0.855	0.367
0.00075	SC	21	33	107.7	3.263	6.364	0.513	0.157
0.00075	SC	15	33	92.3	2.797	4.545	0.615	0.220
0.00075	SC	9	33	70.0	2.121	2.727	0.778	0.367
0.00075	ST	21	33	109.2	3.310	6.364	0.520	0.157
0.00075	ST	15	33	94.6	2.867	4.545	0.631	0.220
0.00075	ST	9	33	66.9	2.028	2.727	0.744	0.367
0.0009	VW	21	28	118.7	4.240	7.500	0.565	0.133
0.0009	VW	15	28	107.0	3.822	5.357	0.713	0.187
0.0009	VW	9	28	66.4	2.371	3.214	0.738	0.311
0.0009	WW	21	28	112.9	4.031	7.500	0.538	0.133
0.0009	WW	15	28	102.0	3.643	5.357	0.680	0.187
0.0009	WW	9	28	84.2	3.008	3.214	0.936	0.311
0.0009	SC	21	28	102.8	3.673	7.500	0.490	0.133
0.0009	SC	15	28	95.3	3.404	5.357	0.635	0.187
0.0009	SC	9	28	69.6	2.487	3.214	0.774	0.311
0.0009	ST	21	28	103.7	3.703	7.500	0.494	0.133
0.0009	ST	15	28	89.5	3.195	5.357	0.596	0.187
0.0009	ST	9	28	62.3	2.225	3.214	0.692	0.311

Table D.3- Scour data for interacting flow conditions; D_{50}= 0.7 mm

S_o	abut. shape	L	y_a	y_{se}	y_{se}/y_a	L/y_a	y_{se}/L	y_a/L
----	----	cm	mm	mm	----	----	----	----
0.0009	VW	21	38	180.0	4.737	5.526	0.857	0.181
0.0009	VW	15	38	152.3	4.008	3.947	1.015	0.253
0.0009	VW	9	38	117.7	3.097	2.368	1.308	0.422
0.0009	WW	21	38	153.8	4.049	5.526	0.733	0.181
0.0009	WW	15	38	124.6	3.279	3.947	0.831	0.253
0.0009	WW	9	38	104.6	2.753	2.368	1.162	0.422
0.0009	SC	21	38	147.7	3.887	5.526	0.703	0.181
0.0009	SC	15	38	127.7	3.360	3.947	0.851	0.253
0.0009	SC	9	38	100.0	2.632	2.368	1.111	0.422
0.0009	ST	21	38	152.3	4.008	5.526	0.725	0.181
0.0009	ST	15	38	126.2	3.320	3.947	0.841	0.253
0.0009	ST	9	38	92.3	2.429	2.368	1.026	0.422

Table D.4- Scour data for non-interacting flow conditions; D_{50}= 0.7 mm

S_o	abut. shape	L	y_a	y_{se}	y_{se}/y_a	L/y_a	y_{se}/L	y_a/L
----	—	cm	mm	mm	----	----	—	----
0.0009	VW	21	38	135.0	3.553	5.526	0.643	0.181
0.0009	VW	15	38	108.6	2.857	3.947	0.724	0.253
0.0009	VW	9	38	84.3	2.218	2.368	0.937	0.422
0.0009	WW	21	38	142.1	3.739	5.526	0.677	0.181
0.0009	WW	15	38	115.7	3.044	3.947	0.771	0.253
0.0009	WW	9	38	91.7	2.414	2.368	1.019	0.422
0.0009	SC	21	38	119.3	3.139	5.526	0.568	0.181
0.0009	SC	15	38	105.0	2.763	3.947	0.700	0.253
0.0009	SC	9	38	75.7	1.992	2.368	0.841	0.422
0.0009	ST	21	38	124.3	3.271	5.526	0.592	0.181
0.0009	ST	15	38	109.3	2.876	3.947	0.729	0.253
0.0009	ST	9	38	81.4	2.143	2.368	0.905	0.422

Appendix E

Table E.1 - Scour data for interacting flow conditions

y_{se}/y_a	Q_w/Q_a	F_a	F_c	y_a	log (y_w/y_a)	log (Q_w/Q_a)	log (F_a)	log (F_c)
-------	-------	-------	-------	mm	-------	-------	-------	-------
3.460	0.84	0.444	0.429	42	0.539	-0.076	-0.353	-0.367
2.571	0.81	0.430	0.381	42	0.410	-0.092	-0.367	-0.419
1.905	0.78	0.400	0.413	42	0.280	-0.108	-0.398	-0.384
3.067	0.84	0.444	0.429	42	0.487	-0.076	-0.353	-0.367
2.519	0.81	0.430	0.381	42	0.401	-0.092	-0.367	-0.419
2.190	0.78	0.400	0.413	42	0.341	-0.108	-0.398	-0.384
3.135	0.84	0.444	0.429	42	0.496	-0.076	-0.353	-0.367
2.500	0.81	0.430	0.381	42	0.398	-0.092	-0.367	-0.419
2.183	0.78	0.400	0.413	42	0.339	-0.108	-0.398	-0.384
3.135	0.84	0.444	0.429	42	0.496	-0.076	-0.353	-0.367
2.619	0.81	0.430	0.381	42	0.418	-0.092	-0.367	-0.419
2.063	0.78	0.400	0.413	42	0.315	-0.108	-0.398	-0.384
3.939	0.87	0.450	0.434	33	0.595	-0.060	-0.347	-0.363
3.232	0.82	0.431	0.406	33	0.510	-0.086	-0.366	-0.391
2.343	0.79	0.406	0.379	33	0.370	-0.102	-0.391	-0.421
3.717	0.87	0.450	0.434	33	0.570	-0.060	-0.347	-0.363
3.043	0.82	0.431	0.406	33	0.483	-0.086	-0.366	-0.391
2.695	0.79	0.406	0.379	33	0.431	-0.102	-0.391	-0.421
3.939	0.87	0.450	0.434	33	0.595	-0.060	-0.347	-0.363
3.182	0.82	0.431	0.406	33	0.503	-0.086	-0.366	-0.391
2.727	0.79	0.406	0.379	33	0.436	-0.102	-0.391	-0.421
4.015	0.87	0.450	0.434	33	0.604	-0.060	-0.347	-0.363
3.182	0.82	0.431	0.406	33	0.503	-0.086	-0.366	-0.391
2.475	0.79	0.406	0.379	33	0.394	-0.102	-0.391	-0.421
3.977	0.88	0.490	0.467	28	0.600	-0.056	-0.310	-0.331
3.649	0.83	0.477	0.453	28	0.562	-0.081	-0.322	-0.344
2.526	0.8	0.454	0.425	28	0.402	-0.097	-0.343	-0.371
4.035	0.88	0.490	0.467	28	0.606	-0.056	-0.310	-0.331
3.497	0.83	0.477	0.453	28	0.544	-0.081	-0.322	-0.344
2.798	0.8	0.454	0.425	28	0.447	-0.097	-0.343	-0.371
4.269	0.88	0.490	0.467	28	0.630	-0.056	-0.310	-0.331
3.655	0.83	0.477	0.453	28	0.563	-0.081	-0.322	-0.344
2.924	0.8	0.454	0.425	28	0.466	-0.097	-0.343	-0.371
4.211	0.88	0.490	0.467	28	0.624	-0.056	-0.310	-0.331
3.684	0.83	0.477	0.453	28	0.566	-0.081	-0.322	-0.344

Table E 1- Scour data for interacting flow conditions

y_w y_a	Q_w Q_a	F_a	F_c	y_a	log (y_w y_a)	log (Q_w Q_a)	log (F_a)	log (F_c)
-------	-------	-------	-------	mm	-------	-------	-------	-------
2.456	0.8	0.454	0.425	28	0.390	-0.097	-0.343	-0.371
3.789	0.85	0.483	0.363	38	0.579	-0.071	-0.316	-0.440
3.206	0.81	0.460	0.349	38	0.506	-0.092	-0.337	-0.457
2.478	0.78	0.429	0.335	38	0.394	-0.108	-0.367	-0.475
3.725	0.85	0.483	0.363	38	0.571	-0.071	-0.316	-0.440
3.017	0.81	0.460	0.349	38	0.480	-0.092	-0.337	-0.457
2.533	0.78	0.429	0.335	38	0.404	-0.108	-0.367	-0.475
3.887	0.85	0.483	0.363	38	0.590	-0.071	-0.316	-0.440
3.360	0.81	0.460	0.349	38	0.526	-0.092	-0.337	-0.457
2.632	0.78	0.429	0.335	38	0.420	-0.108	-0.367	-0.475
4.008	0.85	0.483	0.363	38	0.603	-0.071	-0.316	-0.440
3.320	0.81	0.460	0.349	38	0.521	-0.092	-0.337	-0.457
2.429	0.78	0.429	0.335	38	0.385	-0.108	-0.367	-0.475